



2011

annual progress report

Advanced Power Electronics and Electric Motors

**U.S. Department of Energy
Office of Vehicle Technologies, EE-2G
1000 Independence Avenue, S.W.
Washington, D.C. 20585-0121**

FY 2011

Advanced Power Electronics and Electric Motors Annual Progress Report

**Energy Efficiency and Renewable Energy
Vehicle Technologies Program**

Susan A. Rogers, Technology Development Manager

January 2012

Contents

| | |
|--|-----|
| Acronyms and Abbreviations | vi |
| 1. Introduction..... | 1 |
| 2. Power Electronics Research and Technology Development..... | 8 |
| 2.1 Wide Bandgap Materials..... | 8 |
| 2.2 Power Device Packaging | 20 |
| 2.3 Converter Topologies for Wired and Wireless Battery Chargers | 31 |
| 2.4 Inverter Using Current Source Topology..... | 42 |
| 2.5 A Segmented Drive Inverter Topology with a Small dc Bus Capacitor | 55 |
| 2.6 High Dielectric Constant Capacitors for Power Electronic Systems | 67 |
| 2.7 Glass Ceramic Dielectrics for DC Bus Capacitors..... | 79 |
| 2.8 High Temperature Thin Film Polymer Dielectric Based Capacitors for HEV Power Electronic Systems | 86 |
| 2.9 Development, Test and Demonstration of a Cost-Effective, Compact, Light-Weight, and Scalable High Temperature Inverter for HEVs, PHEVs, and FCVs..... | 98 |
| 2.10 Development of SiC Large Tapered Crystal Growth..... | 106 |
| 3. Electric Motors Research and Technology Development..... | 118 |
| 3.1 A New Class of Switched Reluctance Motors Without Permanent Magnets | 118 |
| 3.2 Novel Flux Coupling Machine without Permanent Magnets..... | 133 |
| 3.3 Motor Packaging with Consideration of Electromagnetic and Material Characteristics..... | 141 |
| 3.4 Permanent Magnet Development for Automotive Traction Motors | 156 |
| 3.5 Scalable, Low-Cost, High Performance IPM Motor for Hybrid Vehicles..... | 171 |
| 4. Traction Drive Systems Research and Technology Development..... | 188 |
| 4.1 Benchmarking of Competitive Technologies..... | 188 |
| 4.2 High Power Density Integrated Traction Machine Drive | 204 |
| 4.3 Novel Packaging to Reduce Stray Inductance in Power Electronics | 218 |
| 4.4 Integration of Novel Flux Coupling Motor and Current Source Inverter | 230 |
| 4.5 Advanced Integrated Electric Traction System..... | 236 |
| 5. Thermal Management Research and Technology Development | 246 |
| 5.1 Air Cooling Technology for Power Electronics Thermal Management | 246 |
| 5.2 Thermal Performance and Reliability of Bonded Interfaces..... | 262 |

| | | |
|-----|--|-----|
| 5.3 | Light-Weight, Single-Phase Liquid-Cooled Heat Exchanger/Cold Plate | 277 |
| 5.4 | Integrated Vehicle Thermal Management – Combining Fluid Loops on Electric Drive Vehicles..... | 291 |
| 5.5 | Electric Motor Thermal Management..... | 306 |
| 5.6 | Physics of Failure of Electrical Interconnects..... | 323 |
| 5.7 | Two-Phase Cooling Technology for Power Electronics with Novel Coolants..... | 334 |
| 6. | Small Business Innovative Research Grants | 348 |
| 6.1 | Small Business Innovative Research Projects..... | 348 |

Acronyms and Abbreviations

| | |
|---------------|---|
| 2D | two dimensional |
| 3D | three dimensional |
| ac | alternating current |
| Adc | amps direct current |
| AFM | atomic force microscopy |
| ANSYS | modeling and simulation workbench |
| APEEM | Advanced Power Electronics and Electric Motors (program, DOE) |
| ASTM | American Society for Testing and Materials |
| AT | automatic transmission |
| bcc | body centered cubic |
| BHT | 3,5-di- <i>t</i> -butyl-4-hydroxytoluene |
| BIC | best-in-class |
| BIM | bonded interface material |
| BNC | Bayonet-Neill-Concelman (connector) |
| BNC | Birck Nanotechnology Center |
| BOPP | baseline biaxially-oriented polypropylene |
| BREM | beyond rare earth magnets |
| C-SAM | C-mode scanning acoustic microscope |
| CAN | controller area network |
| Cdg | drain-to-gate capacitance |
| Cds | drain-to-source capacitance |
| CF-trans-qZSI | current-fed trans-quasi-ZSI |
| CF-trans-ZSI | current-fed trans-ZSI |
| CFD | computational fluid dynamics |
| CHF | critical heat flux |
| COP | coefficient of performance |
| CSD | chemical solution deposition |
| CSI | current source inverter |
| CTE | coefficient of thermal expansion |
| CVD | chemical vapor deposition |
| DBA | direct bonded aluminum |
| DBC | direct bonded copper |
| dc | direct current |
| DFT | density functional theory |
| DOE | U.S. Department of Energy |
| DPT | double pulse tester/testing |
| DSC | differential scanning calorimeter |

| | |
|----------|--|
| DUT | device under test |
| ECI | Electronic Concepts, Inc. |
| EDS | energy dispersive spectroscopy |
| EDV | electric drive vehicle |
| EDX | energy dispersive x-ray spectroscopy |
| EETT | Electrical and Electronics Technical Team (U.S. Drive) |
| EM | electric motor |
| emf | electromotive force |
| EMI | electromagnetic interference |
| ESC | electro-slag casting |
| ESL | equivalent series inductance |
| ESR | equivalent series resistance |
| ESS | energy storage system |
| ETS | electric traction system |
| EV | electric vehicle |
| EWG | ethylene water glycol |
| FE | finite element |
| FEA | finite element analysis |
| GA | genetic algorithm |
| GE | General Electric |
| GOSS | grain oriented silicon steel |
| GUI | graphical user interface |
| GWP | global warming potential |
| HALT | highly accelerated lifetime tests |
| HD | hydrogen decrepitation |
| HEV | hybrid electric vehicle |
| HSG | hybrid starter-generator |
| HVAC | heating, ventilation and air conditioning |
| ICE | internal combustion engine |
| ID | inner diameter |
| IGBT | insulated gate bipolar transistor |
| IMFP | isolated multiple flux path |
| IMMD | integrated modular motor drive |
| INV/CONV | inverter/converter |
| IPM | interior permanent magnet |
| JBS | junction barrier Schottky |
| JEDEC | Joint Electron Device Engineering Council |
| KULI | thermal management system for automotive applications |

| | |
|--------|--|
| LCR | inductance, capacitance and resistance |
| LFE | laminar flow element |
| LNO | LaNiO ₃ |
| Lp | parasitic inductance |
| MEC | magnetic equivalent circuit |
| M/G | motor/generator |
| mmf | magnetomotive force |
| MOSFET | metal-oxide semiconductor field-effect transistor |
| MRE | mixed rare earth |
| NREL | National Renewable Energy Laboratory |
| NFC | novel flux coupling |
| NIH | number-in-hand |
| Nm | Newton meter |
| OD | outer diameter |
| ORNL | Oak Ridge National Laboratory |
| OVT | Office of Vehicle Technologies |
| PCU | power control unit |
| PD | power density (peak) |
| PE | power electronics |
| PEEM | Power Electronics and Electric Machines (subprogram, ORNL) |
| PEI | polyetherimide |
| PEM | power electronics module |
| PEPL | Power Electronics Packaging Laboratory (ORNL) |
| PEV | plug-in electric vehicle |
| PF | power factor |
| PFC | power factor correction |
| PHEV | plug-in hybrid electric vehicles |
| PID | proportional-integral-derivative |
| PLZT | (Pb,La)(Zr,Ti)O ₃ |
| PM | permanent magnet |
| PMSM | permanent magnet synchronous motor |
| PWM | pulse width modulated/modulation |
| PoF | physics of failure |
| PoP | Proof-of-principle |
| PWB | printed wire board |
| R&D | research and development |
| R-L | inductor-resistor |
| RB | reverse-blocking |

| | |
|-------------------|--|
| RE | rare earth |
| regen | regenerative braking |
| rms | root mean square |
| R _p | parasitic resistance |
| SEM | scanning electron microscopy |
| SF | specific force |
| SOA | state of the art |
| SJT | super junction transistor |
| SP | specific power (peak) |
| SPICE | Simulation Program with Integrated Circuit Emphasis |
| SPM | surface permanent magnet |
| SSRL | Stanford Synchrotron Research Laboratory |
| SR | switched reluctance |
| SRM | switched reluctance motor |
| T3Ster | Transient Thermal Tester |
| TC | thermal conductivity |
| TEM | transmission electron spectroscopy |
| THD | total harmonic distortion |
| TIM | thermal interface material |
| T _j | junction temperature |
| T _{jmax} | maximum junction temperature |
| TMC | Toyota Motor Company |
| TSDPSR | total switching device power stress ratio |
| TSI | Thermal Anemometry Systems |
| TXV | thermal expansion valve |
| U.S. DRIVE | Driving Research and Innovation for Vehicle efficiency and Energy sustainability (cooperative research effort between DOE and industry partners) |
| UW | University of Wisconsin |
| V2G | vehicle-to-grid |
| V _{ac} | volts of alternating current |
| V _{dc} | volts of direct current (operating voltage) |
| V _{ds} | drain-to-source voltage |
| V _{gs} | gate-to-source voltage |
| VSA | vehicle systems analysis |
| VSATT | Vehicle Systems Analysis Technical Team (U.S. Drive) |
| VSI | voltage source inverter |
| VTP | Vehicle Technologies Program (DOE) |
| WBG | wide bandgap |

| | |
|------|----------------------------------|
| WEG | water-ethylene glycol |
| XRD | x-ray diffraction |
| ZCSI | Z-source current source inverter |
| ZSI | Z-source inverter |

1. Introduction

The U.S. Department of Energy (DOE) announced in May 2011 a new cooperative research effort comprising DOE, the U.S. Council for Automotive Research (composed of automakers Ford Motor Company, General Motors Company, and Chrysler Group), Tesla Motors, and representatives of the electric utility and petroleum industries. Known as U.S. DRIVE (Driving Research and Innovation for Vehicle efficiency and Energy sustainability), it represents DOE's commitment to developing public-private partnerships to fund high risk-high reward research into advanced automotive technologies. The new partnership replaces and builds upon the partnership known as FreedomCAR (derived from "Freedom" and "Cooperative Automotive Research") that ran from 2002 through 2010 and the Partnership for a New Generation of Vehicles initiative that ran from 1993 through 2001.

The Advanced Power Electronics and Electric Motors (APEEM) program within the DOE Vehicle Technologies Program (VTP) provides support and guidance for many cutting-edge automotive technologies now under development. Research is focused on developing revolutionary new power electronics (PE), electric motor (EM), thermal management, and traction drive system technologies that will leapfrog current on-the-road technologies. The research and development (R&D) is also aimed at achieving a greater understanding of and improvements in the way the various new components of tomorrow's automobiles will function as a unified system to improve fuel efficiency.

In supporting the development of advanced vehicle propulsion systems, the APEEM program has enabled the development of technologies that will significantly improve efficiency, costs, and fuel economy.

The APEEM program supports the efforts of the U.S. DRIVE partnership through a three phase approach intended to

- identify overall propulsion and vehicle related needs by analyzing programmatic goals and reviewing industry's recommendations and requirements and then develop the appropriate technical targets for systems, subsystems, and component R&D activities;
- develop and validate individual subsystems and components, including EMs and PE; and
- determine how well the components and subsystems work together in a vehicle environment or as a complete propulsion system and whether the efficiency and performance targets at the vehicle level have been achieved.

The research performed under this program will help remove technical and cost barriers to enable the development of technology for use in such advanced vehicles as hybrid electric vehicles (HEVs), plug-in HEVs (PHEVs), battery electric vehicles, and fuel-cell-powered automobiles that meet the goals of the VTP.

A key element in making these advanced vehicles practical is providing an affordable electric traction drive system. This will require attaining weight, volume, efficiency, and cost targets for the PE and EM subsystems of the traction drive system. Areas of development include

- novel traction motor designs that result in increased power density and lower cost;
- inverter technologies involving new topologies to achieve higher efficiency with the ability to accommodate higher temperature environments while achieving high reliability;
- converter concepts that use methods of reducing the component count and integrating functionality to decrease size, weight, and cost;
- new onboard battery charging concepts that result in decreased cost and size;
- more effective thermal control through innovative packaging technologies; and

- integrated motor-inverter traction drive system concepts.

Thermal management of electronics and electronic systems represents a major technical barrier to achieving specific APEEM technical targets. Excessive temperature, temperature cycling, and power cycling can degrade the performance, life, and reliability of power electronic components. Advanced thermal management technologies can enable higher power density and higher specific power as well as lowering system costs by facilitating the use of lower-cost package configurations and lower-cost materials with minimal impact on performance and reliability.

The Thermal Management of Advanced Power Electronics and Electric Motors research activity is focused on developing thermal management technologies that enable advanced power electronics and electric motor technologies that are efficient, small, lightweight, low cost, and reliable. Specifically, we are concerned with addressing and overcoming any and all thermal barriers to these systems within the systems context of the entire vehicle—ultimately working towards a total vehicle electric traction drive system that is low-cost, small, lightweight, reliable, effective, and efficient.

These thermal management and reliability enhancements will permit U.S. industry to improve the range and reduce the purchase, operating and maintenance costs of electric vehicles leading to a widening of their acceptance by the public. The larger volume of advanced fuel saving vehicles manufactured in the United States will result in higher domestic employment, while significantly reducing the trade deficit by reducing the amount of imported oil.

DOE's continuing R&D into advanced vehicle technologies for transportation offers the possibility of reducing the nation's dependence on foreign oil and the negative economic impacts of crude oil price fluctuations. It also supports the Administration's goal of deploying 1 million PHEVs by 2015.

Highlights

Task 2: Power Electronics Research and Technology Development

Task 2.1 Wide Bandgap Materials

- Acquired, tested, and characterized SiC metal-oxide semiconductor field-effect transistors (MOSFETs), super junction transistor switches, and junction barrier Schottky diodes both dynamically and statically over expanded temperature ranges.
- Optimized a traction drive model for use in determining the benefit of wide bandgap devices for automotive applications.
- Developed a SPICE* model for a 1,200 V, 33 A, SiC MOSFET for use in packaging efforts.

Task 2.2 Power Device Packaging

- Designed an integrated planar package power module structure featuring double sided planar interconnections and integrated cooling that offers cost reductions of 30% or more compared to state-of-the-art packages.
- Fabricated a 1,200 V, 200 A, phase leg using the new module, and completed thermal and electrical characterization.
- Developed a simulation program to comprehensively evaluate power module technologies.
- Established a thermal performance test station.
- Benchmarked four state-of-the-art power device packaging technologies.
- Manufactured four different types of power modules for other APEEM projects.

* Simulation Program with Integrated Circuit Emphasis.

Task 2.3 Converter Topologies for Wired and Wireless Battery Chargers

- Wired charger
 - Developed a new approach that uses the onboard PE components to reduce the cost, weight, and volume of onboard chargers; accomplish galvanic isolation; and accommodate a wide range of battery voltages.
 - Completed a converter design for a 5 kW integrated wired charger with an estimated cost reduction of 80% compared to a stand-alone onboard battery charger.
- Wireless charger
 - Developed two converter topologies with reduced switch count and passive component requirements. Simulation results proved the concepts.

Task 2.4 Inverter using Current Source Topology

- Completed a design for a 10 kW Z-source current source inverter based on the current-fed trans-quasi Z-source inverter using first generation reverse-blocking–insulated gate bipolar transistor (IGBT) technology. The design yields a specific power of 4.85 kW/kg, a power density of 14.2 kW/L, and efficiency of 97.7% in boost mode and 97.1% in buck mode.
- Test results with a 10 kW prototype demonstrate
 - capacitance reduction to 80 μF [200 μF for a voltage source inverter (VSI)],
 - output voltage capability range from 0–3 times the battery voltage (0–0.99 \times for a VSI),
 - output voltage total harmonic distortion of 6%–12 % (70%–200% for a VSI), and
 - high efficiency (more than 97% even at a relatively low source voltage of 250 V).

Task 2.5 A Segmented Drive System with a Small dc Bus Capacitor

- Demonstrated a 55 kW segmented inverter prototype with a 60% reduction of dc bus capacitance compared to a standard VSI.
- Tested prototype with both carrier based and space vector based pulse width modulation control methods to show
 - 55% to 75% reduction in capacitor ripple current,
 - 70% to 90% reduction in battery ripple current, and
 - 60% to 80% reduction in motor ripple current.
- Completed design and fabrication of a ring-shaped 55 kW segmented inverter that is suitable for integration with a motor.

Task 2.6 High Dielectric Constant Capacitors for Power Electronic Systems

- Fabricated & measured a 20-mm diameter film-on-foil ($\approx 0.7 \mu\text{m}$ -thick PLZT) with capacitance of $\approx 3 \mu\text{F}$ @ 15 V/ μm bias.
- Built a $\approx 9 \mu\text{F}$ (4 μF @ 15 V) prototype capacitor by stacking four 1" x 1" film-on-foils (volumetric capacitance density of $\approx 4.8 \mu\text{F}/\text{cm}^3$).
- Demonstrated film-on-foil PLZT dielectrics with dielectric breakdown field $> 2.6 \text{ MV}/\text{cm}$, and leakage current $< 10^{-8} \text{ A}/\text{cm}^2$ at room temperature.
- Demonstrated graceful failure mode by self-clearing method in single layer film-on-foil dielectrics.
- Fabricated and characterized PLZT dielectrics on nickel metal foils with self-clearing electrodes. The key to large-area yield is to electrically isolate the defect spots that compromise the integrity of the dielectric layer.

Task 2.7 Glass Ceramic Dielectrics for DC Bus Capacitors

- Demonstrated that flat panel display glass can operate as a capacitor up to temperatures of 250 $^{\circ}\text{C}$.
- Invented self-healing in a glass capacitor.

- Fabricated and tested the first prototype capacitor made by winding glass ribbon.

Task 2.8 High Temperature Thin Film Polymer Dielectric Based Capacitors for HEV Power Electronic Systems

- Demonstrated extrusion in-house using the new hydrogenated polymer
- Fabricated and characterized two 0.5 μF stacked capacitors in-house using the improved hydrogenated polymer formulation. One of the capacitors was potted in high temperature epoxy and the other capacitor was wrapped with a Kapton wrapper and sealed with heat-shrink tubing.
- Began working with the Natick Soldier Center in Boston MA and Dr. Collin in order to identify bench top film forming extrusion equipment and to extrude thin polymer film suitable for capacitor

Task 2.9 Development, Test and Demonstration of a Cost-Effective, Compact, Light-Weight, and Scalable High Temperature Inverter for HEVs, PHEVs, and FCVs

- Various resins (PEI, PPS, PC) were identified as high temperature dielectrics for capacitors.
- Comparisons showed Delphi's power device packaging provides at least 30% improvement in thermal resistance junction-to-coolant, compared to the "best" commercially available double-side cooled product today (in the Lexus LS 600h, see figure under "Technical Discussion")

Task 3: Electric Machinery Research and Technology Development

Task 3.1 A New Class of Switched Reluctance Motors without Permanent Magnets

- Developed, fabricated, and tested an unconventional switched reluctance machine design.
- Developed custom design software.
- Developed iterative self-learning pseudo-flux observer-based control algorithm capable of tracking/producing abstract current waveforms, which is essential for torque ripple control.
- Tested machine up to 5,000 rpm.

Task 3.2 Novel Flux Coupling Machine without Permanent Magnets

- Machined prototype motor parts; fabricated and assembled the motor.
- Completed locked rotor test on the prototype. It confirmed that the concept is workable. The full testing will be completed during FY 2012 due to scheduling issues with the Dyne cells in FY 2011.
- Completed studies on the issues with power factor performance of interior permanent magnet (IPM) motors.

Task 3.3 Motor Packaging with Consideration of Electromagnetic and Material Characteristics

- Analyzed ORNL benchmarking data on the 2010 Prius IPM, and extracted key parameters for development of an electrical equivalent d-q axis circuit model.
- Developed a computer model for the lamination material reluctivity to be used in magnetic equivalent circuit model and simulation.
- Developed baseline IPM technology trajectory.
- Developed a thermal model of the baseline IPM, and validated it against ORNL benchmarking data. The thermal model provides ORNL researchers a finite element analytical model for predicting IPM copper, lamination iron, and rotor magnet dissipation mechanisms.

Task 3.4 Permanent Magnet Development for Automotive Traction Motors

- For RE magnets, a large Dy reduction was enabled by targeted diffusion (at 900°C) of DyF_3 "paint" to the interior microstructure in anisotropic sintered $\text{MRE}_{2.5}(\text{Fe, Co})_{14}\text{B}$ magnets, where $\text{MRE} = [\text{Nd}_{0.45}(\text{Y}_3\text{Dy}_1)_{0.55}]$, which achieved an energy product, $(\text{BH})_{\text{max}}$, of 31.4 MGOe and a coercivity, H_{ci} ,

of 15 kOe, both at ambient temperature, and a temperature coefficient of H_{ci} , β , of $-0.5\%/^{\circ}\text{C}$, all equivalent to commercial Nd-based $\text{Nd}_2\text{Fe}_{14}\text{B}$ magnets that are used in drive motors for 200°C operation (EH grade, containing 8-10% Dy), but by using only 5.3wt.% Dy or about 45% less Dy for large magnet cost decrease.

- In development of particulate for anisotropic bonded $\text{MRE}_{2.2}\text{Fe}_{14}\text{B}_{1.1}$ magnets without Dy, where $\text{MRE} = [\text{Y}_{0.55}\text{Nd}_{0.45}]$, highly aligned columnar solidification patterns resulted from a novel Ag micro-alloying ($<1\text{at.}\%\text{Ag}$) effect that achieved strong and unique texture control in ribbon samples that were melt spun at low speed (5m/s), producing an anisotropic particulate that was crushed for epoxy bonding and testing.
- In our search for non-RE permanent magnets, a genetic algorithm (GA) method was adapted to enable computational phase diagram exploration for alloys based on Fe-Co, speeding up by at least 1000 times the search for candidate chemical compositions with desirable structures and properties.
- As a tool for rapid structural analysis in our “beyond RE magnets” (BREM) thrust, a multiple sample staging system was developed at the DOE synchrotron X-ray source at Stanford Synchrotron Research Laboratory and demonstrated by characterization of thin film samples from a Fe-Co-W combinatorial “library” of compositions, determining that an upper W content of about 15 at.% is set in this system by the onset of dominant amorphous phase formation.
- In the portion of the BREM thrust devoted to improvement of existing Alnico magnets, a series of density functional theory (DFT) calculations predicted that the magnetic anisotropy of Fe-Co layers at the interface of Fe-Co precipitates and the NiAl matrix phase is increased by two orders of magnitude, indicating that a significant coercivity benefit could result from reducing the spinodal spacing to far less than the typical 50 nm.

Task 3.5 Scalable, Low-Cost, High Performance IPM Motor for Hybrid Vehicles

- 2 rotor & 2 stator EM concepts developed & analyzed in detail
- Scalable rotor and stator cooling concepts selected to meet performance, simplicity and scalability requirements
- First proof-of-principle motor built and fully tested
- Second proof-of-principle machine (different rotor structure) is built and fully tested
- Third and final 30kW/55kWpk machine built and fully tested
- Achieved kilogram scale production of $\text{Nd}_{15}\text{Fe}_{77}\text{B}$ permanent magnet powder for scaled processing
- Identified insulating layer compositions whose densification behavior approaches that of NdFeB with minimal reaction with NdFeB

Task 4: Systems Research and Technology Development

Task 4.1 Benchmarking of Competitive Technologies

- Conducted design/package studies of the 2011 Hyundai Sonata power converter unit, hybrid starter-generator, and primary motor.
- Assessed mass, volume, power density, and specific power of various hybrid system subsystems.
- Evaluated efficiency, performance, and other operational characteristics of the 2011 Sonata subsystems.

Task 4.2 High Power Density Integrated Traction Machine Drive

- Designed, built, and tested a 10 kW, six phase, 10-pole permanent magnet (PM) machine.
- Developed a modular integrated modular motor drive (IMMD) power converter that conforms to the dimensions of the 10 kW concept demo PM machine, providing a testbed for implementing the IMMD distributed control software.
- Tested ruggedness of selected IGBT at various temperatures, concluding that the device has good latch-up immunity and adequate short circuit capability for operation at 200°C .

- Designed and fabricated a 10 kW phase leg power module, and tested its electrical and thermal characteristics up to 200°C.
- Designed the gate driver boards and main board for the IGBT phase leg modules.

Task 4.4 Integration of Novel Flux Coupling Motor and Current Source Inverter

- Validated the concept of the integration of the novel flux coupling motor and the current source inverter through laboratory tests.
- Studied methods to increase the efficiency of the system.

Task 4.5 Advanced Integrated Electric Traction System

- Built, demonstrated, and verified through test Electric Traction System that met all DOE 2010 objectives and met DOE 2015 objectives for specific power and power density
- Built, demonstrated, and tested bi-directional charger

Task 5: Thermal Management Research and Technology Development**Task 5.1 Air Cooling Technology for Power Electronics Thermal Management**

- Applied system-level analysis to an inverter for both air-cooled and liquid-cooled approaches. This analysis showed that by using an allowable junction temperature of 200°C or 150°C plus the use of an advanced spreader, the air-cooled system is able to match the power density of the liquid-cooled approach. It also showed that equal or higher electric current per silicon area could be achieved. This feasibility study demonstrates that there are several possible pathways for successful air-cooled thermal design.
- Improved the Air Cooling Characterization Platform and used it to study steady jet and synthetic jet heat transfer. The synthetic jet was found to have up to a 40% improvement in Nusselt number for the same Reynolds number. For the synthetic jet, the best heat transfer was observed at $H/D_h = 10$. A correlation was also developed that accurately describes the steady jet performance.

Task 5.2 Thermal Performance and Reliability of Bonded Interfaces

- Bonded interfaces were established between 50.8 mm x 50.8 mm cross-sectional area DBC and copper base plate samples for lead-based solder, thermoplastics with embedded carbon fibers, and silver sintered materials. Initial thermal cycling (up to 100 cycles) was performed on these samples.

Task 5.3 Light-Weight, Single-Phase Liquid-Cooled Heat Exchanger/Cold Plate

- Completed design of the new heat exchangers using FEA and CFD modeling. These heat exchangers were designed to be a replacement for the baseline heat exchanger on the UQM inverter.
- Completed experiments with the transient thermal tester to characterize the thermal performance of the baseline channel-flow-based heat exchanger. Obtained good correlation between CFD results and experimental data on the baseline heat exchanger.
- Though modeling, demonstrated improvements in thermal resistance, coefficient-of-performance (COP), power density and specific power for the new heat exchangers with respect to the baseline.

Task 5.4 Integrated Vehicle Thermal Management – Combined Fluid Loops on Electric Drive Vehicles

- High quality data provided by Visteon formed the basis of the detailed KULI component models
- Using KULI thermal software, built the A/C, cabin, power electronics cooling loop, and battery cooling loop models

Task 5.5 Electric Motor Thermal Management

- NREL developed a parametric thermal finite element analysis motor model representing interior permanent magnet motors to enable sensitivity studies related to cooling electric motors. In addition, the lab partnered with the University of Wisconsin–Madison to develop methods to rapidly estimate the heat loads in various motor locations. The results will support the development of motor cooling technologies to improve motor performance and reliability and reduce the use of rare earth materials with the transition to more electrically dominant vehicle propulsion.

Task 5.6 Physics of Failure of Electrical Interconnects

- Established capabilities at NREL for accelerated testing and mechanical evaluation of ribbon bond interconnects.
- Finalized ribbon layout geometry and obtained direct bond copper (DBC) substrates.
- Selected industry partners for the supply of ribbon material and the bonding process.
- Generated finite element analysis (FEA) models to predict heel stresses within wire and ribbon bonds.

Task 5.7 Two-Phase Cooling Technology for Power Electronics with Novel Coolants

- The pool boiling performance of a new refrigerant, HFO-1234yf, was characterized and compared to the performance of HFC-134a (R134a). Experiments were carried out at various saturation temperatures (25°C–60°C), with and without boiling enhancement techniques, up to the critical heat flux condition. Results from this study will be published in the 2011 ASME IMECE Conference Proceeding [1] making the National Renewable Energy Laboratory (NREL) the first institution to publish this information. This work was a collaborative effort between NREL, 3M, and DuPont.
- NREL in collaboration with 3M, Delphi, and Oak Ridge National Laboratory (ORNL) demonstrated a 60% reduction in thermal resistance of an automotive power electronics module using immersion boiling (two-phase) in conjunction with surface enhancement techniques [2-4]. The thermal performance enhancement was in comparison to the existing automotive cooling system.

Looking Forward

The following reports provide a detailed description of APEEM activities and technical accomplishments during FY 2011. Numerous project reviews, technical reports, and papers have been published for these efforts, and they are indicated at the end of each section for readers interested in pursuing details of the work. In collaboration with industry, universities, and national laboratories, DOE continues to develop advanced PE and EM technologies for the next generation of automotive vehicles.

2. Power Electronics Research and Technology Development

2.1 Wide Bandgap Materials

Principal Investigator: Madhu Sudhan Chinthavali

Oak Ridge National Laboratory

National Transportation Research Center

2360 Cherahala Boulevard

Knoxville, TN 37932

Voice: 865-946-1411; Fax: 865-946-1262; E-mail: chinthavalim@ornl.gov

DOE Technology Development Manager: Susan A. Rogers

Voice: 202-586-8997; Fax: 202-586-1600; E-mail: Susan.Rogers@ee.doe.gov

ORNL Program Manager: Mitch Olszewski

Voice: 865-946-1350; Fax: 865-946-1262; E-mail: olszewskim@ornl.gov

Objectives

- To keep up to date with the state-of-the-art wide bandgap (WBG) power devices and acquire, test, and characterize newer technology WBG power devices.
- Assess the system level impact of WBG semiconductor devices on hybrid electric vehicles.

Approach

- Evaluate device performance: Acquire, test, and characterize newer technology WBG power devices including the following:
 - Static characteristic tests
 - Dynamic characteristic tests
 - Behavioral modeling
- Develop behavioral SPICE* models for packaging projects: Specific device tests will be performed to extract the parameters required for behavioral SPICE models. These models will be used to study the parasitic parameters in a package.
- Perform inverter simulations with selected device models: The inverter simulations will be performed to evaluate the impact of the device performance at system level.
- Prepare a summary report that includes the test results of devices and SPICE modeling results to be incorporated into the annual DOE Vehicle Technologies Program report.

Major Accomplishments

- Acquired, tested, and characterized SiC metal-oxide semiconductor field-effect transistor (MOSFET), SiC super junction transistor (SJT), and SiC junction barrier Schottky (JBS) diodes.
- Developed SPICE model for a 1,200 V, 33 A SiC MOSFET.
- Developed a traction drive model to simulate the performance of the WBG devices over different drive cycles.

*Simulation Program with Integrated Circuit Emphasis.

Future Direction

- The state-of-the-art WBG power devices and newer technology WBG power devices will be acquired, tested, and characterized.
- SPICE models of the devices will be developed.

Technical Discussion

Device Testing

The new WBG devices acquired this year are SiC MOSFETs, SiC JBS diode copacks with silicon insulated gate bipolar transistors (IGBTs), and SiC SJTs. On-state characteristics and switching energy losses of the devices were obtained, and the voltage blocking capability of the devices over the wide temperature range was tested. The test results for these devices will be presented in the following sections. All the devices obtained were experimental samples.

1. 1,200 V, 35 A SiC JBS Diode

The static characteristics of a 1,200 V, 35 A SiC JBS diode were obtained over a wide temperature range (25°C–175°C) (Fig. 1). The on-state resistance over temperature is shown in Fig. 2. It is evident that the SiC JBS diode has a positive temperature coefficient. The leakage current of the diode at a blocking voltage of 600 V is about 0.5 μ A at 25°C and increases to 350 μ A at 175°C (Fig. 3). The leakage current increased dramatically from 150°C to 175°C. Fig. 4 shows the switching losses at 600 V.

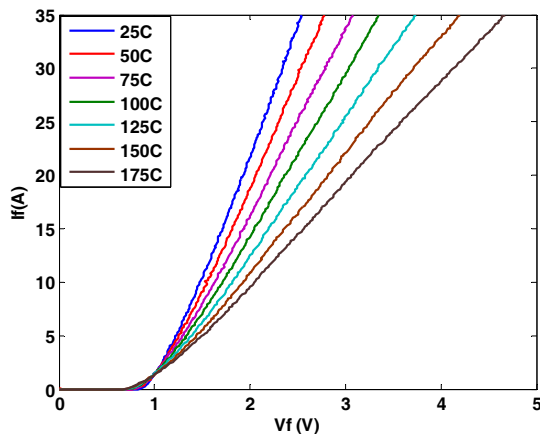


Fig. 1. Forward characteristic of 1,200 V, 35 A JBS diode.

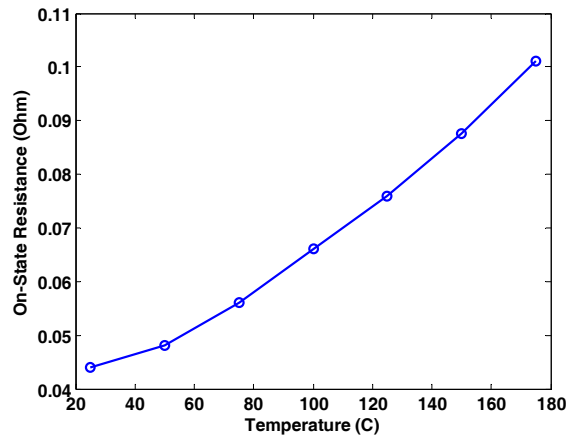


Fig. 2. On-state resistance of 1,200 V, 35 A JBS diode.

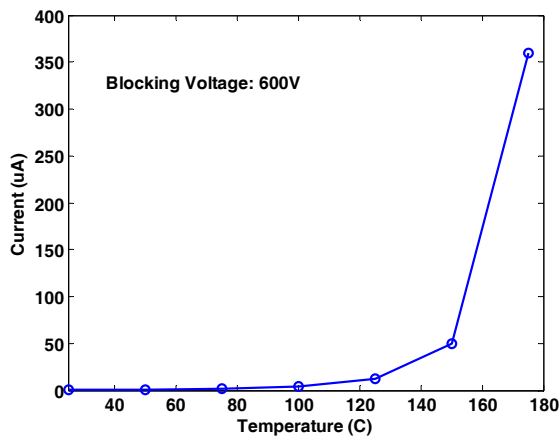


Fig. 3. Leakage current of 1,200 V, 35 A JBS diode.

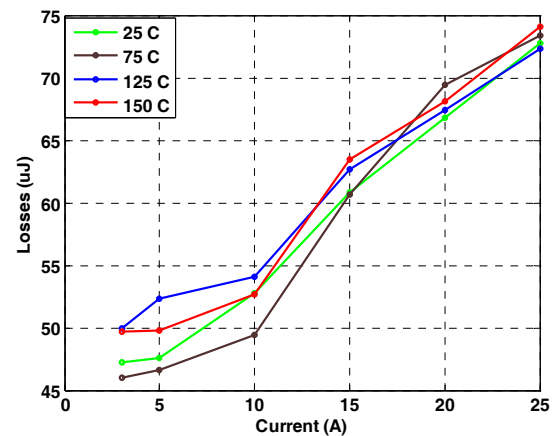


Fig. 4. Energy losses at 600 V.

2. 1,200 V, 100 A SiC JBS Diode

The static characteristics of a 1,200 V, 100 A SiC JBS diode were obtained over a wide temperature range (25°C–175°C) (Fig. 5). The on-state resistance over temperature is shown in Fig. 6. The diodes were specifically designed for high temperature operation. Figures 7 to 9 are the switching losses at different voltages and temperatures. As can be seen, the losses increase greatly with voltage; however, they decrease with current increases and stay almost constant with temperature.

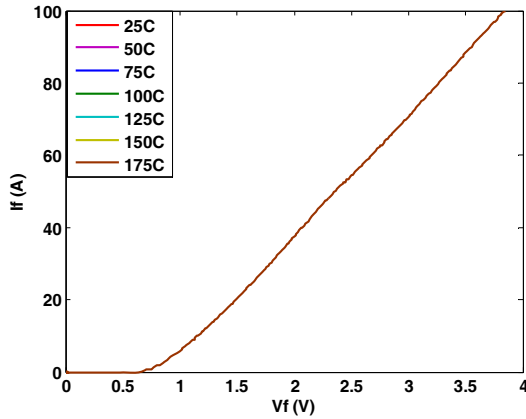


Fig. 5. Forward characteristic of 1,200 V, 35 A JBS diode.

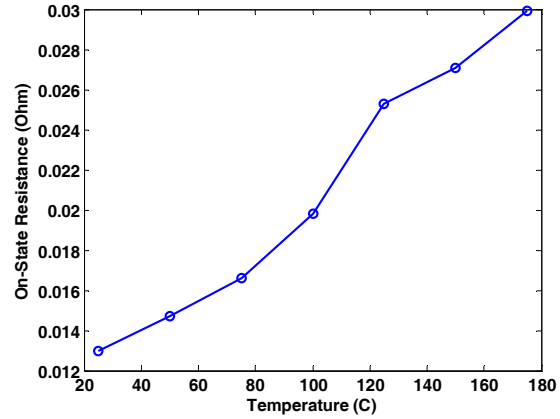


Fig. 6. On-state resistance of 1,200 V, 35 A JBS diode.

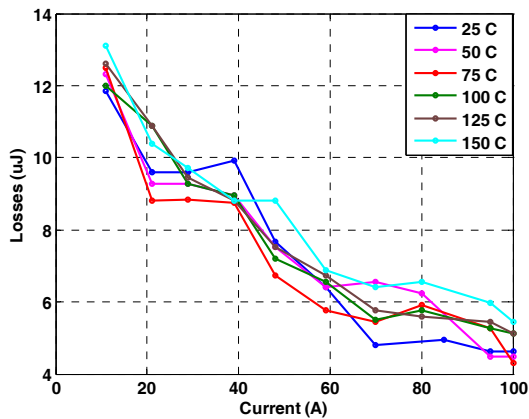


Fig. 7. Energy losses at 200 V.

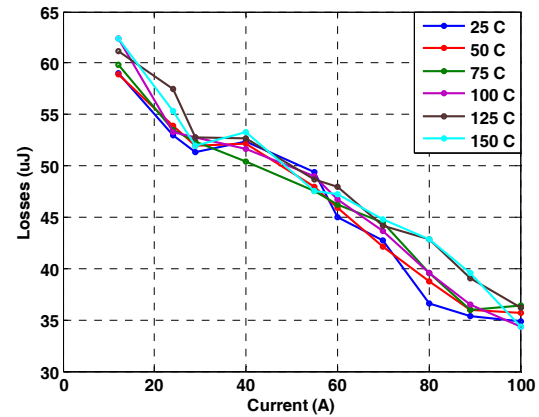


Fig. 8. Energy losses at 400 V.

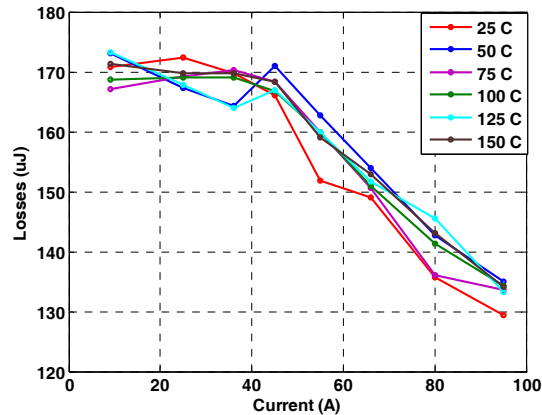


Fig. 9. Energy losses at 600 V.

3. 1,200 V, 20 A SiC MOSFET

Both static and switching characteristics of a 1,200 V, 33 A SiC MOSFET have been tested. Figure 10 shows the forward characteristic at different temperatures. The on-state resistance has also been calculated accordingly and is shown in Fig. 11. One thing to be noticed is that the SiC MOSFET has a negative temperature coefficient around 50°C. This might be an issue when paralleling those devices because the current could not be shared evenly among devices. Figure 12 is the transfer function of the device over a wide temperature range at $V_{ds} = 10$ V. Figure 13 shows the threshold voltage obtained from the transfer curves. The threshold voltage decreases as temperature increases. Figure 14 is the leakage current at different temperatures for 600 V blocking voltage.

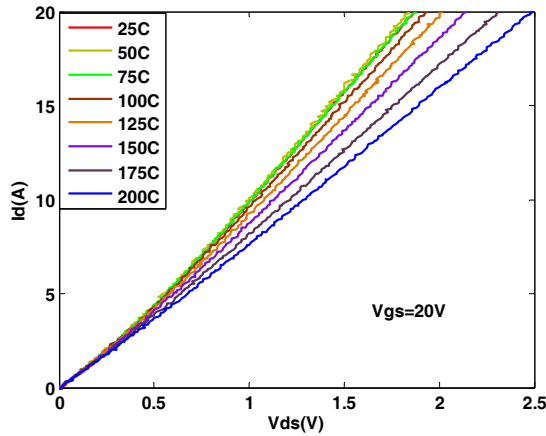


Fig. 10. Forward characteristic of 1,200 V, 33 A MOSFET.

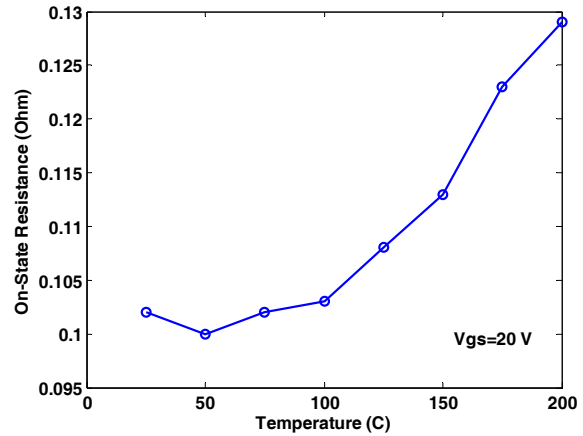


Fig. 11. On-state resistance of 1,200 V, 33 A MOSFET.

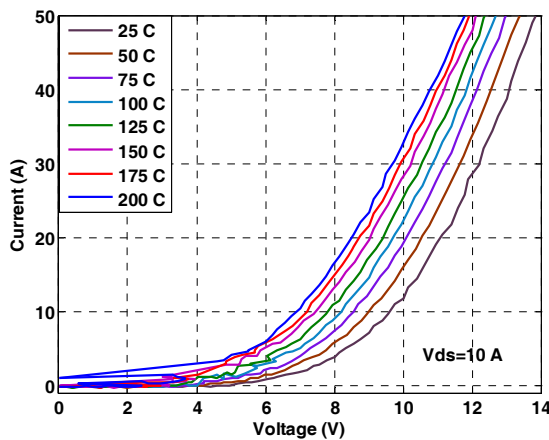


Fig. 12. Transfer characteristic of 1,200 V, 33 A MOSFET.

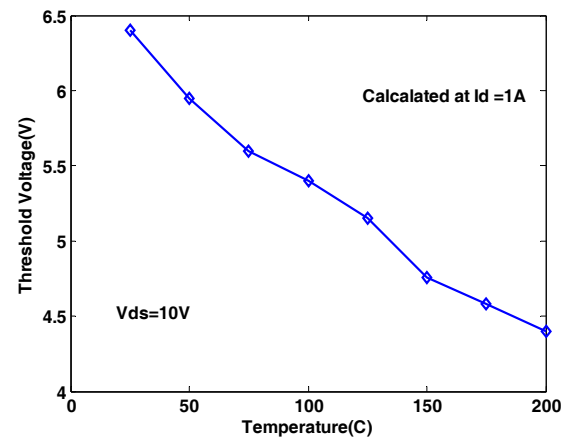


Fig. 13. Threshold voltage of 1,200 V, 33 A MOSFET.

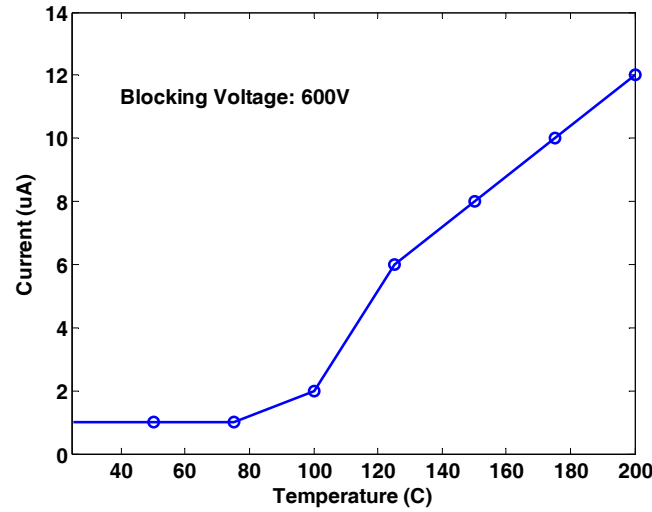


Fig. 14. Leakage current of 1,200 V, 33 A MOSFET.

Figure 15 is the switching waveform of the SiC MOSFET at 600 V and 12 A in a double pulse testing (DPT) circuit. The turn-on and turn-off energy losses were obtained with a load inductance of 140 μ H, and a 1,200 V, 30 A SiC JBS diode was used as the clamping diode in the circuit. The gate driver used for this testing was a commercial gate driver IXDD414. The data were obtained at 600 V and 400 V dc for various currents from 25°C to 175°C. The total energy losses increase with increase in current; however, the losses do not change much with increase in temperature (Figs. 16 and 17).

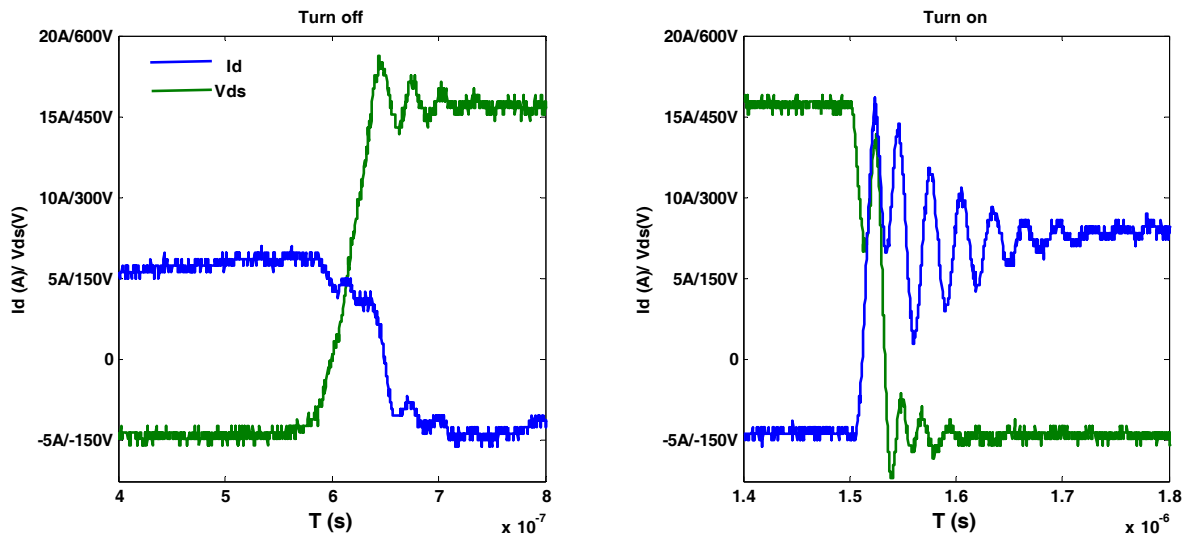


Fig. 15. Switching waveforms of 1,200 V, 33 A MOSFET.

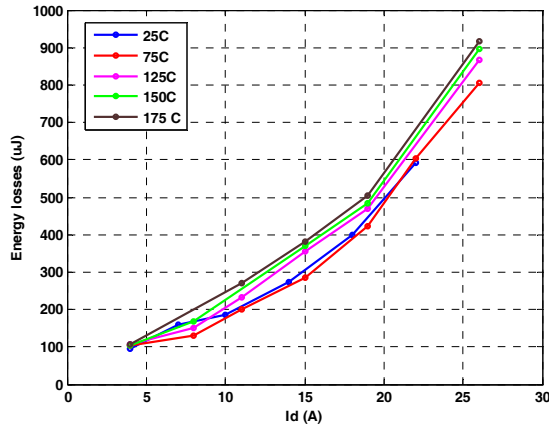


Fig. 16. Switching losses of 1,200 V, 33 A MOSFET at 400 V.

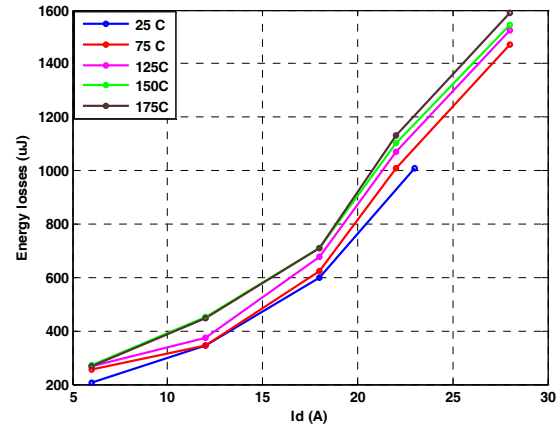


Fig. 17. Switching losses of 1,200 V, 33 A MOSFET at 600 V.

4. 1,200 V, 10 A SiC SGT

The SiC SGT is a current controlled normally off device. Figure 18 shows the forward characteristics of the SGT at different temperatures for a 350 mA base current. The gain of SGT was calculated correspondingly for different base current in the saturation region (shown in Fig. 19). It can be seen that the gain is decreasing with both temperature and collector current. Figure 20 is the on-state resistance of the SGT, which increases with temperature.

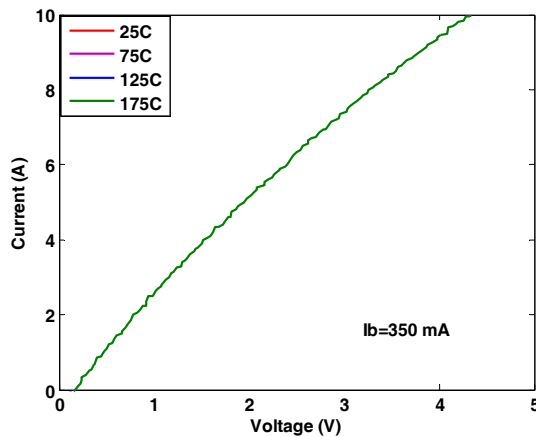


Fig. 18. Forward characteristic of 1,200 V, 10 A SGT.

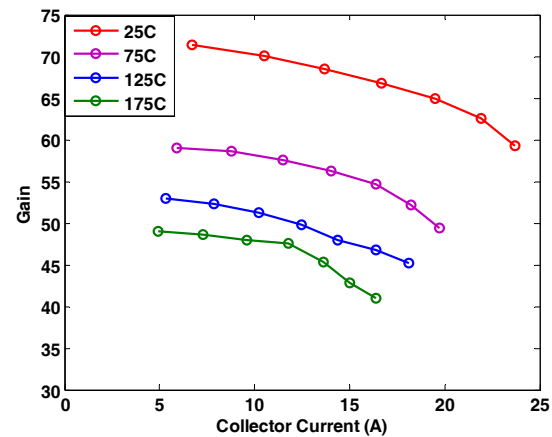


Fig. 19. Gain of 1,200 V, 10 A SGT.

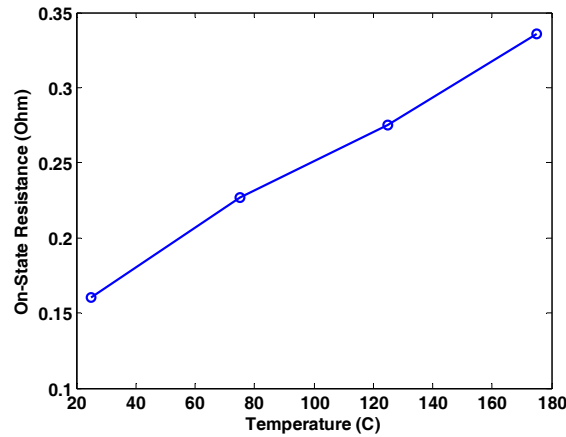


Fig. 20. On-state resistance of 1,200 V, 10 A SiC MOSFET.

Device Modeling

1. PSPICE Model of SiC MOSFET

A behavioral model of a 1,200 V, 33 A SiC MOSFET was built in PSpice.* The parameters used to build the model were obtained from test data. The model has been verified through comparison of the simulation and testing data and will be discussed in detail in the following section.

The SiC MOSFET has three ports (gate, drain, and source), several internal capacitors, and several layers. The values of the internal capacitors change as the bias voltage changes. They affect the switch transient as these capacitors need to be charged or discharged every time the device is switched. The MOSFET has been simplified to be the equivalent circuit shown in Fig. 21. It includes a voltage controlled current source, three junction capacitors, reverse body diode, and other parasitic elements.

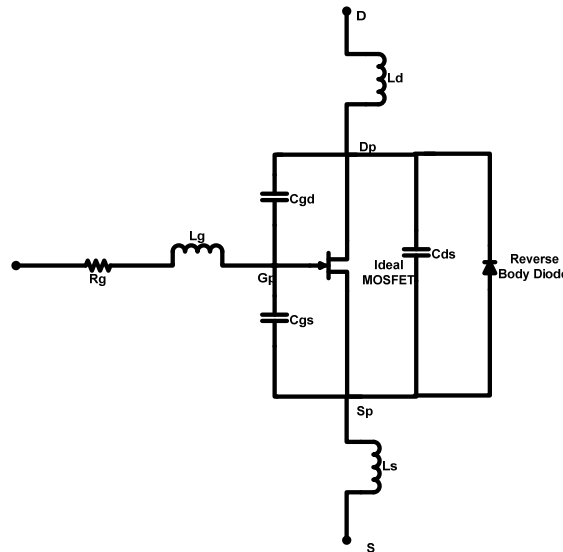


Fig. 21. Equivalent circuit of SiC MOSFET.

*PC version of SPICE.

Figures 22 and 23 show the relationship between junction capacitance [drain-to-source (C_{ds}) and drain-to-gate (C_{dg})] and drain-to-source voltage (V_{ds}). The corresponding equations are as follows.

$$C_{ds} = 10^{-12} * ((1781 * \exp(-0.09048 * V_{ds}) + 420.8 * \exp(-0.004418 * V_{ds})) \quad (1)$$

$$C_{dg} = 10^{-12} * ((1613.6 * \exp(-0.0839 * V_{ds}) + 52.84 * \exp(-0.00381 * V_{ds})) \quad (2)$$

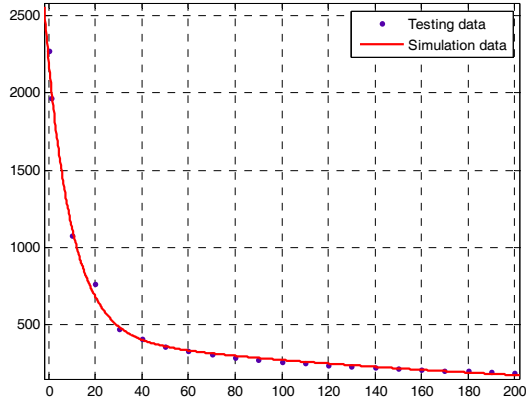


Fig. 22. Drain-to-source capacitance vs drain-to-source voltage.

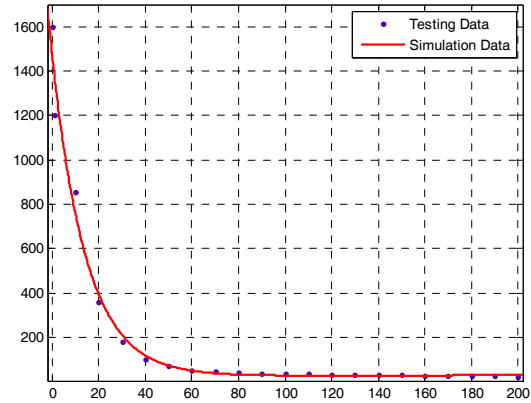


Fig. 23. Drain-to-gate capacitance vs drain-to-source voltage.

The following are the equations used to describe the voltage controlled current source. In these equations, λ is the channel-length modulation parameter; V_{TO} is threshold voltage; I_{DSAT} and V_{DSAT} are the saturation current and voltage, which are derived from [1,2]; B and n are constants that control the saturation current; and K and m are constants that control the saturation voltage.

$$I_D = 0 \quad V_{GS} - V_{TO} \leq 0 \quad (\text{Pinch-off}) \quad (3)$$

$$I_D = I_{DSAT}(1 + \lambda V_{DS}) \quad V_{DS} > V_{DSAT} \quad (\text{Saturation region}) \quad (4)$$

$$I_D = I_{DSAT}(1 + \lambda V_{DS}) * \left(2 - \frac{V_{DS}}{V_{DSAT}}\right) * \frac{V_{DS}}{V_{DSAT}} \quad V_{DS} < V_{DSAT} \quad (\text{Linear region}) \quad (5)$$

$$V_{DSAT} = K(V_{GS} - V_{TO})^m \quad (6)$$

$$I_{DSAT} = B(V_{GS} - V_{TO})^n \quad (7)$$

The value of threshold voltage V_{TO} is directly from measured data. The values of B , K , m , n , and λ in the model are extracted from the forward curves of the device by solving linear equations with five points located at both linear and saturation regions from testing. All those parameters are temperature dependent.

Figure 24 is the comparison between simulation and testing for the forward characteristics at multiple gate voltages and temperatures with currents up to 70 A. Notice this is a 20 A rated device, so currents usually are lower. It can be seen that at lower current, higher temperature (125°C and 200°C) simulations have better agreement with testing. At room temperature, the simulation has an error less than 10% compared to the testing results, caused by curve fitting which will lose some accuracy at some operating

points. Figure 25 shows the on-state resistance calculated. Most of the resistance under a certain temperature is consistent; however, at room temperature the simulated resistance is higher than the testing results. Figure 26 shows the comparison of transfer characteristics between simulation and testing at different temperatures. The comparison shows good agreement.

The parasitic parameters, like inductance and resistance, were extracted using simulation to get a good match with the experimental data. As shown in Fig. 27, there are two dc inductances, L4 and L5. These two inductors affect the switching transient time and oscillation value. For L4 equals 200 nH and L5 equals 10 nH, the transient time has a good match, but the oscillation value is larger than the testing waveform, which is why a 2 Ω resistor R3 was added to the circuit to minimize the oscillation. Gate inductance L7 and drain inductance L3 also have influence on the transient time, but not as much as loop inductance. Values shown in the schematic are the final values used for the comparison. Figure 28 shows the comparison of switching voltage and current. The simulation results show some aspects of the actual switching behavior of the device in the circuit, like the overshoot and oscillation of both current and voltage and the transient time. However, some of the performance is not reflected in the simulation, like the double hump of the current and notch of voltage during turn-on. This could be caused because of some of the other parasitic parameters associated with the circuit that could not be evaluated.

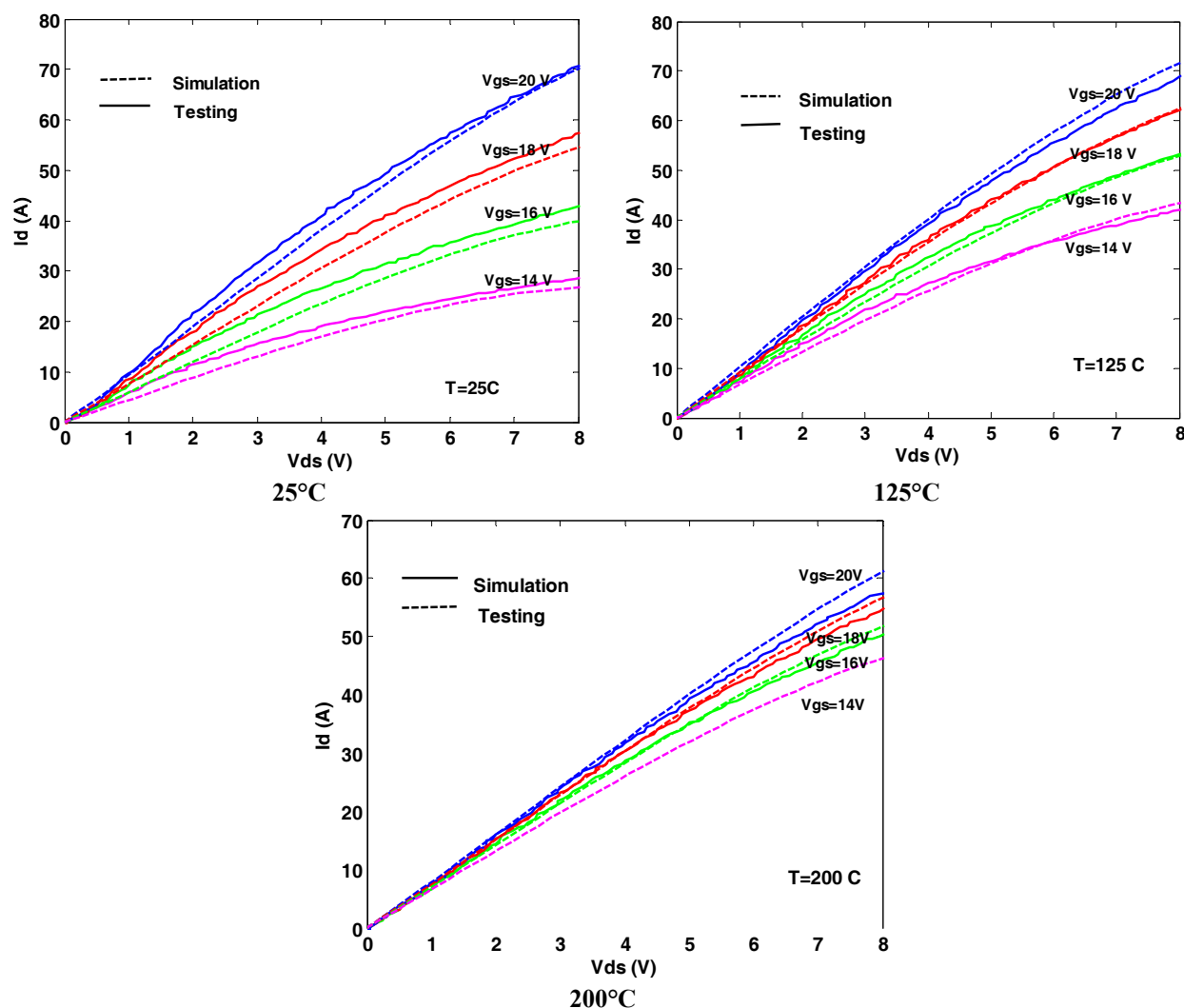


Fig. 24. Comparison at various temperatures of forward characteristics between testing and simulation.

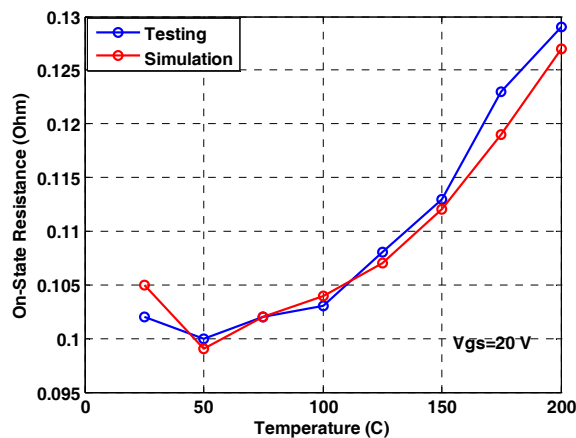


Fig. 25. Comparison of on-state resistance.

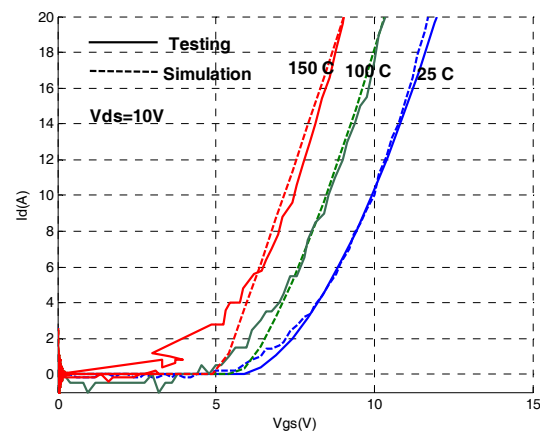


Fig. 26. Comparison of transfer characteristics.

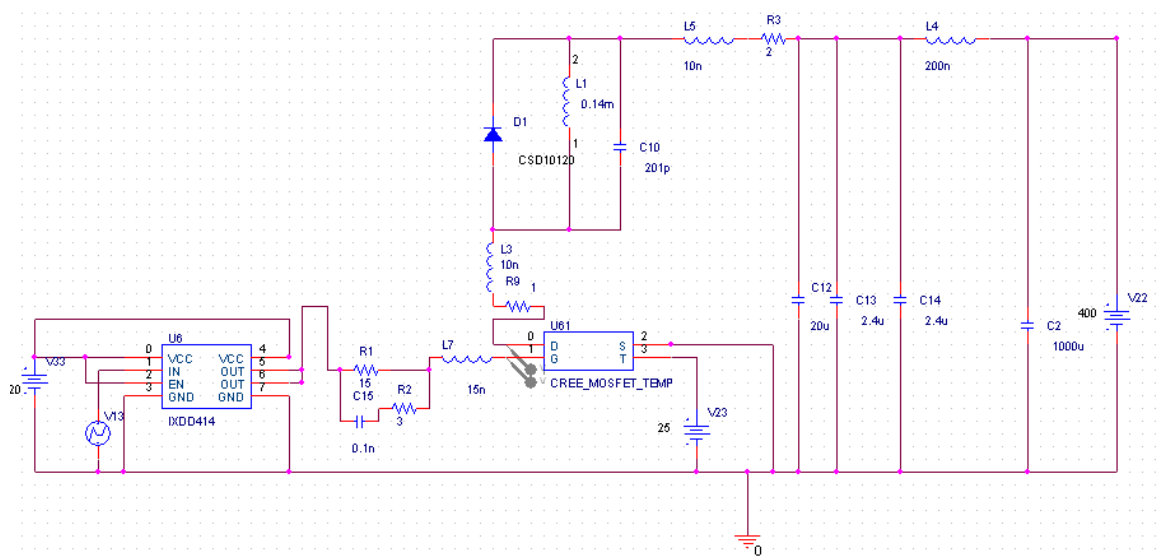
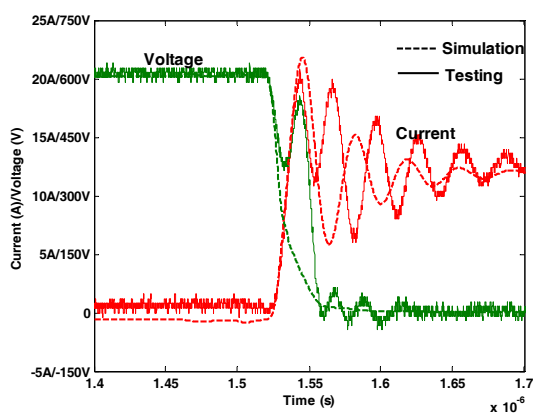
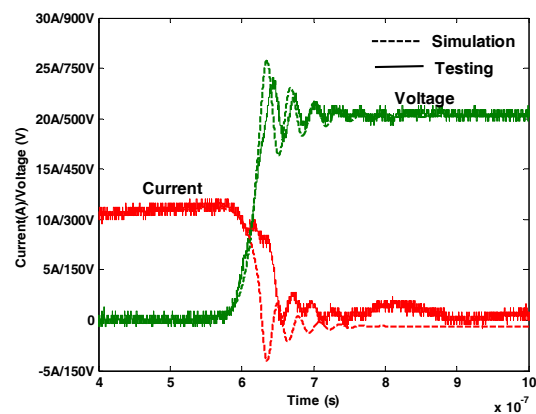


Fig. 27. Schematic of DPT in PSpice.



(a)



(b)

Fig. 28. Comparison of switching characteristics between testing and simulation:
(a) turn-on; (b) turn-off.

2. Traction Drive Model

The traction drive model consists of two parts: (1) an electric motor/generator model that computes the current, voltage, and phase angle that will produce optimally 100% of the torque required at each time step and (2) an inverter loss model that computes the temperature dependent device losses associated with the voltages, currents, and frequencies demanded by the motor. The details of the motor model were presented in the FY 2010 annual report.

3. Inverter Loss Model

The inverter loss model was implemented by using silicon IGBT and SiC JBS diodes in a hybrid configuration. The temperature dependent conduction loss parameters, on-state resistance and voltage drop, and switching losses were obtained from testing the 1, 200 V, 100 A IGBT module. The details of the inverter model were also presented in the FY 2010 annual report.

Simulation Results

The drive model was simulated for the US06 drive cycle with silicon IGBT and diode models at switching frequencies of 10 kHz and 20 kHz and two different coolant temperatures, 70°C and 105°C. The drive model outputs time dependent, cycle average, and cumulative values of interest for all pertinent parameters. The average inverter efficiency and inverter losses over the drive cycle for 10 and 20 kHz with 70°C and 105°C cooling are shown in Table 1.

Table 1. Simulation results of traction drive for the US06 drive cycle

| 10 kHz | | 20 kHz | |
|---------------------------|-------|--------|--------|
| Inverter efficiency (%) | | | |
| 70°C | 105°C | 70°C | 105°C |
| 95.97 | 95.76 | 92.67 | 92.28 |
| Inverter energy loss (kJ) | | | |
| 70°C | 105°C | 70°C | 105°C |
| 536.4 | 565.2 | 1004.5 | 1061.5 |

The inverter efficiency corresponds to the losses of devices in the inverter only, and the losses in the boost converter are not included. For 10 kHz operation, the efficiency of the inverter decreased by only 0.21% for the 70°C to 105°C coolant temperature condition. For 20 kHz operation, the efficiency of the inverter decreased by 0.39% for the 70°C to 105°C coolant temperature condition. However, when the switching frequency was increased from 10 kHz to 20 kHz, the efficiency of the silicon IGBT and SiC diode hybrid inverter decreased by 3.3% and 3.48% at 70°C and 105°C coolant temperature, respectively.

Conclusion

Several new SiC MOSFETs, JBS diodes, and SJTs were acquired, tested, and modeled. The traction drive was successfully completed, and the simulation results for the Si-SiC hybrid inverter, developed based on 1,200 V, 100 A SiC JBS diode module testing, were presented. A behavioral SPICE model of a 1,200 V, 33 A SiC MOSFET was developed by obtaining the model parameters from testing the device. The SPICE model was validated through testing.

Patents

None.

Publications

1. M. Chinthavali, P. Ning, Y. Cui, and L. M. Tolbert, "Investigation on the parallel operation of the discrete SiC BJTs and JFETs," in *Applied Power Electronics Conference (APEC)*, Dallas, 2011, pp. 1076–1083.

References

1. T. Sakurai and A. R. Newton, "A simple MOSFET model for circuit analysis," *IEEE Transactions on Electron Devices*, vol. 38, pp. 887–894, 1991.
2. N. Phankong, T. Funaki, and T. Hikihara, "A static and dynamic model for a silicon carbide power MOSFET," in *Power Electronics and Applications, 2009, EPE '09, 13th European Conference*, September 8–10, 2009, pp. 1–10.

2.2 Power Device Packaging

Principal Investigator: Zhenxian Liang

Oak Ridge National Laboratory

National Transportation Research Center

2360 Cherahala Boulevard

Knoxville, TN 37932

Voice: 865-946-1467; Fax: 865-946-1262; E-mail: liangz@ornl.gov

DOE Technology Development Manager: Susan A. Rogers

Voice: 202-586-8997; Fax: 202-586-1600; E-mail: Susan.Rogers@ee.doe.gov

ORNL Program Manager: Mitch Olszewski

Voice: 865-946-1350; Fax: 865-946-1262; E-mail: olszewskim@ornl.gov

Objectives

Overall project objectives

- Identify the limitations and shortcomings of existing device packaging approaches.
- Develop new packaging concepts for improved electrical performance, thermal management, reliability, and manufacturability.
- Complement other packaging and thermal management research efforts within the DOE Vehicle Technologies Program (VTP).

FY 2011 objectives

- Develop new power module packaging, including electrical, thermal, and thermomechanical performance evaluation and characterization and material/structure selection.
- Fabricate, test, and analyze sample modules.
- Continue to benchmark state-of-the-art technologies and share information.
- Provide packaging support for other DOE Advanced Power Electronics and Electric Motors (APEEM) projects.

Approach

- Optimize the new package structure, which incorporates advanced die attach, double sided cooling, and non-wire-bond interconnect, through simulation of its electrical, thermal, and thermomechanical properties.
- Based on the optimization information, fabricate a sample module. Fabrication will include process development and integration of substrate patterning, die attach, interconnect, encapsulation, etc.
- Test the fabricated sample electrically and thermally. Analyze the results for design verification and improvement.
- Implement an inverter-level package study.
- Benchmark promising new packaging concepts through survey, experimental analysis, and simulation.
- Develop key materials and processes such as paste materials and processes for sintering, substrates, and cooling through experimental tests and microstructural analysis.
- Provide packaging support for other projects: The support will mainly be through fabrication and testing of selected prototypes.
- Prepare a summary report that includes evaluation results (incorporate into the annual VTP report).

Major Accomplishments

- Designed an integrated planar package power module structure for automotive applications featuring double sided planar interconnection and integrated cooling (Planar_Bond_All).
- Fabricated a 200 A, 1,200 V phase leg planar bond power module prototype, and completed thermal and electrical characterization.
- Developed a simulation program to comprehensively evaluate the power module technology.
- Established a module thermal performance test station and performed tests.
- Benchmarked four state-of-the-art power device packaging technologies.
- Manufactured four different types of power modules for other APEEM projects.

Future Direction

Develop high temperature (up to 200°C), high reliability planar packaging through thermomechanical structure optimization, material tailoring, and process innovations.

Technical Discussion

Introduction

From a power electronics (PE) system point of view, the major criteria to appraise an automotive power module consist of its cost, reliability, functionality, power density, and efficiency. All these aspects are generally determined by its components (e.g., power semiconductors and package components) and manufacturing/processing technology. The power semiconductors include multiple power switches such as insulated gate bipolar transistors (IGBTs); metal-oxide semiconductor field-effect transistors (MOSFETs); and diodes made of Si, SiC, GaN, etc. The package components include the bonding wire and solder, power substrate, power and signal terminals, baseplate, encapsulate, thermal interface greases, etc. Power modules are made using all these diverse materials and multiple manufacturing processes. Figure 1 is a flowchart illustrating the relationship between the power module's performance criteria; electrical, thermal, thermomechanical, and mechanical properties; and components, materials, and manufacturing processes, with the electrical, thermal, etc. properties the critical link. These various properties can be further broken down into subcategories such as thermal impedance (resistance and capacitance), operation temperature, parasitic electric resistance, conductance, power cycling, thermal cycling/shock, vibration ruggedness, etc.

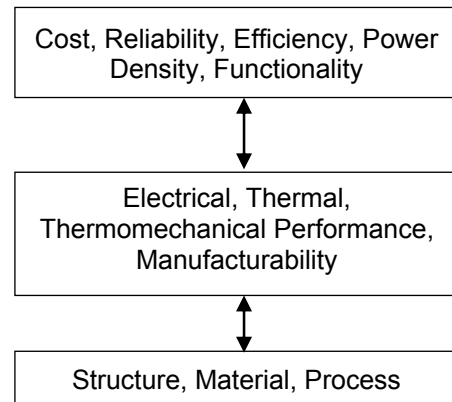


Fig. 1. Technology analysis flowchart for automotive power modules.

Looking at things in terms of these categories and their relationships makes evaluation of power module technologies to identify the shortcomings of existing technology and develop new power module concepts relatively easier.

Using this as a guideline, in FY 2011 ORNL developed a program dealing with the effects of the module's electrical, thermal, and thermomechanical performance on cost, efficiency, reliability, etc. Experimental setups were developed for characterizing these parameters and running simulations. Then a novel packaging structure was proposed, and an innovative packaging process technology was developed. Based on these, a new 200 A, 1,200 V phase leg power module prototype with tremendous improvement in performance and manufacturability was fabricated, resulting in considerable strides toward achieving power density and cost targets for PE systems. Furthermore, these automotive power modules were

benchmarked with microstructure analysis tools in addition to thermal performance comparisons. Based on in-house packaging capability, four types of power modules were prototyped for other APEEM projects.

Automotive Power Module Evaluation

To obtain the relationships between performance parameters and final criteria, an evaluation software program has been developed that incorporates a set of metrics (control factors) to represent the power module's performance based on standard operating conditions such as drive cycles. Figure 2(a) illustrates the computational flow chart of this program. The various parts are used to calculate the power semiconductor device's power loss and junction temperature with a certain die area under a typical driving cycle (in this case, the US06 drive cycle). The control factors include the module's thermal and reliability performance and semiconductor properties [V_{ce-J} , (T_j) , $E_{sw-J}(T_j)$]; packaging parasitic electric parameters, L_p and R_p ; thermal impedance, θ_{ja} ; and reliability characterization, $N_f-\Delta T_j$. Ultimately the program will be used to simulate power loss under various conditions, including change in junction temperature, ΔT_j ; maximum junction temperature, T_{jmax} ; and IGBT/diode die size. Power loss data can be correlated to the module's efficiency; ΔT_j and T_{jmax} can be used to assess lifetime (reliability) as well as coolant temperature. Die size data from these computations will be critical for calculating module cost (die costs are known to be a significant factor in overall power module cost).

This computational tool was used to perform a comprehensive evaluation of a conventional silicon IGBT module. As shown in Fig. 2(a), the US06 drive cycle over a 10 min regimen was selected as a standard operating condition for these simulations. The semiconductor characterization has been extracted. The thermal performance and thermal resistance versus die area relationship have been obtained by measurement and simulation. The module's reliability characterization, the number of thermal cycles to failure versus ΔT_j or ΔT_c (change in either junction or case temperatures) is based on experiment data along with Coffin-Manson modeling.

The IGBT power loss can vary greatly during one cycle, from 20 W to 230 W. To account for the total energy loss, the power loss is integrated for the total time duration. The dependence of this total energy loss on die area is shown in Fig. 2(b). As can be seen from the figure, increasing die area from 1 cm² to 3 cm² only reduces total energy loss by 5.6%. The main reason is that IGBTs have a cutoff voltage drop, V_{ce0} (0.7 V), and the die area just affects the slope of I-V curve that is a minor part in conduction power loss.

The IGBT junction temperature variation, ΔT_j , is dependent on both the die area and coolant temperature. The die area affects the IGBT maximum junction temperature, T_{jmax} , two ways: through power loss and through thermal impedance. Figure 2(c) shows the great dependence of T_{jmax} on die area. Because there is a rigid limitation on semiconductor operating temperature (T_{jmax} , 150°C for silicon devices), a minimum die area requirement can be set for specific cooling performance and coolant temperature. The computational program can also predict the penalty in die area if coolant temperature rises from 65°C to 105°C, a scenario in which the PE system shares a coolant loop with the internal combustion engine. So the tradeoffs in cost vs die area increase vs reduction of cooling loop requirements can be evaluated using the program.

To examine the power module lifetime vs die area, the temperature excursion, ΔT , with different die sizes has been calculated. Figure 2(d) shows the ΔT_j distribution with a die size of 3 cm² during the 10 min drive cycle.

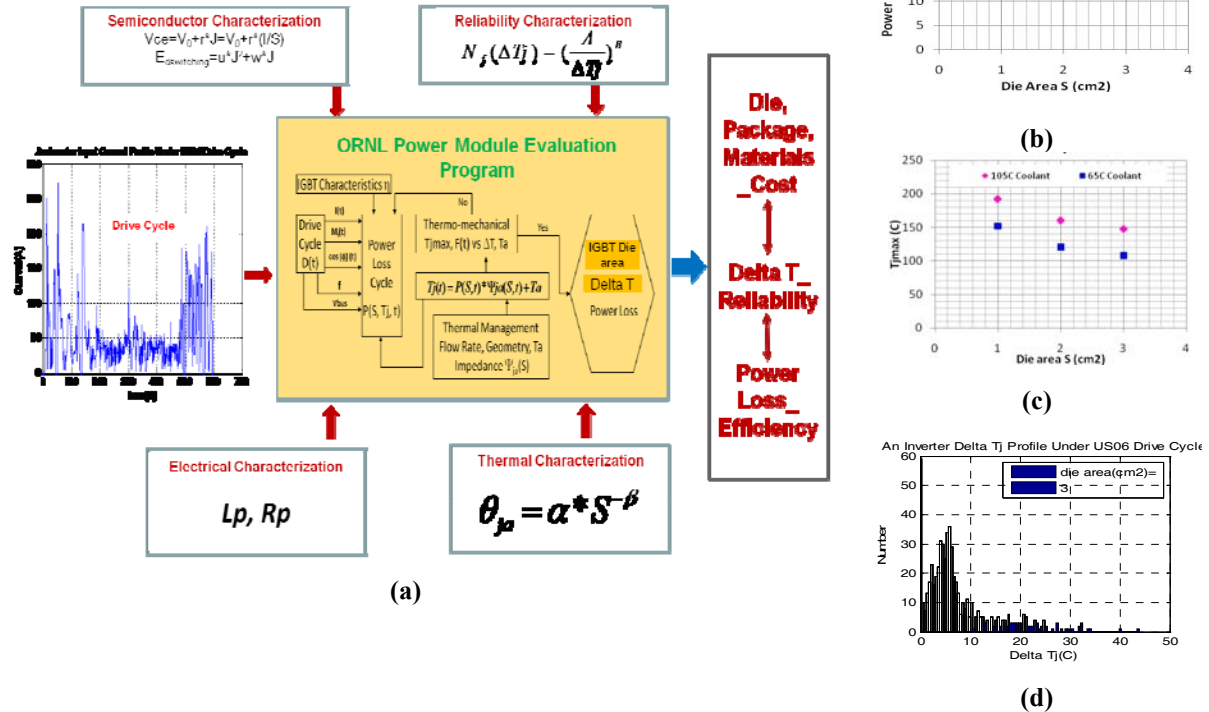


Fig. 2. ORNL automotive power module evaluation program: (a) computation flow chart of ORNL comprehensive evaluation program, showing individual components; (b) die area–power loss relationship; (c) die area–maximum junction temperature (T_{jmax}) relationship; (d) the number of times specific values of ΔT_j occur during the US06 drive cycle.

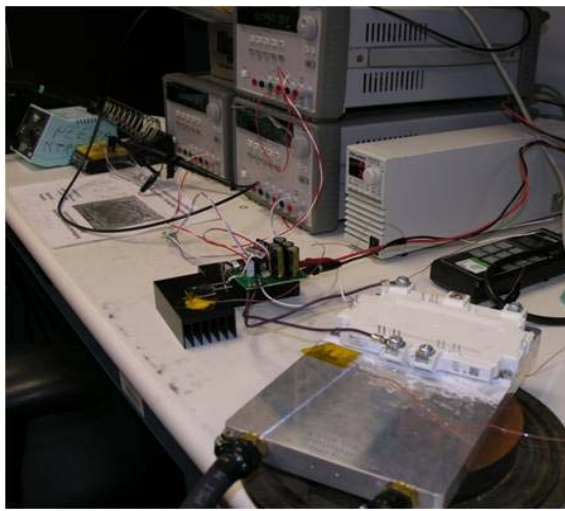
In conclusion, the outputs from this program such as die size, power loss, and temperature and its excursion can be easily transferred to relationships of power conversion efficiency and reliability (lifetime) versus performance parameters. Using the algorithms developed as part of the ORNL automotive power module evaluation program, the best tradeoffs between the three major aspects of cost, efficiency, and lifetime can be made for a power module with specific technology.

Benchmarking Automotive Power Module Packaging Technologies

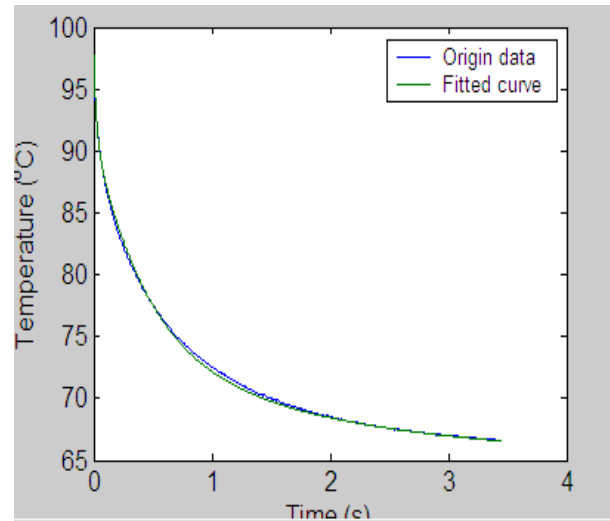
As described in the FY 2010 report, state-of-the-art automotive power modules are manufactured with different technologies. Many concepts for improvements in packaging structure, materials, and packaging process techniques have been pursued. All these advancements will affect the module's electrical, thermal, and thermomechanical performance, in turn leading to improvements in cost, reliability, and efficiency, as discussed in the previous section.

To comprehensively compare or benchmark advanced packaging technologies, in FY 2011 ORNL developed test techniques for characterization of various power module performance aspects. These data can be directly used in the evaluation program described previously. Figure 3 shows an example of these test techniques. Figure 3(a) shows the thermal impedance test facilities. The 2010 Toyota Prius (Prius 10) [1] and Infineon HP1 [2] module assemblies (power module + cold plate) were tested. Figure 3(b) shows a typical cooling down curve for IGBT junction temperature. The thermal impedance (resistance and time constant) can be extracted from it. Figure 3(c) presents the thermal time constant of three assemblies with five-order thermal network assumption. The difference between modules is attributable to the different

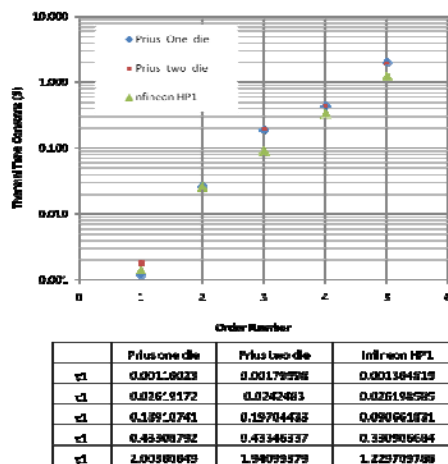
stacking components in the module structures. Figure 3(d) shows the thermal resistance of three module assemblies.



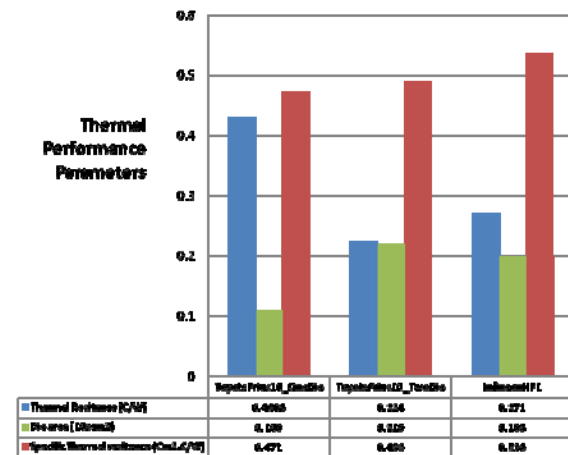
(a)



(b)



(c)



(d)

Fig. 3. Example of ORNL's comprehensive testing facilities/techniques: (a) thermal performance test setup, (b) typical cooling curves for a module assembly, (c) thermal time constant in a five-order network, and (d) thermal resistance comparison of power modules.

It is not fair to singularly compare packaging technologies by using thermal resistance data because of its dependence on die size. Therefore, a parameter referred to as “specific thermal resistivity,” a product of die size and thermal resistance, was used to represent the package’s thermal performance in Fig 3(d). It can be seen that there is little difference in the specific thermal resistance of a one-die device and a two-die device in Prius10 [0.471 cm²·°C/W (one die) and 0.489 cm²·°C/W (two die)] due to thermal spreading/coupling effects. The Prius10 offers 10% lower specific thermal resistance (0.489 cm²·°C/W) than the Infineon HP1 one (0.536 cm²·°C/W). This is attributable to its integrated cooling structure [direct bonded aluminum (DBA) bonded directly onto cold plate] compared to a conventional module mounted on a cold plate with thermal grease. The modules were also measured at different coolant temperatures (25°C, 65°C, 90°C, and 105°C). The thermal resistance of the HP1 module is 0.2234°C/W and

0.2211°C/W at 25°C and 105°C, respectively (only 1% difference). This illustrates that the effect of coolant temperature on a module's thermal resistance is negligible.

Figure 4 shows an example of parasitic electric parameters acquisition from the Prius10 module. A three-dimensional (3D) interconnection model was built [Figure 4(a)]. Using electromagnetic simulation software, the parasitic inductance (L_p) and resistance (R_p) associated with each section of the current paths were obtained, as shown in Fig. 4(b). For a power module, the sums of these parameters along the so-called main loop from the positive terminal through neutral to negative terminals are representative parameters for the package. For the Prius 10 module, they are $L_p = 39.5$ nH and $R_p = 1.12$ m Ω .

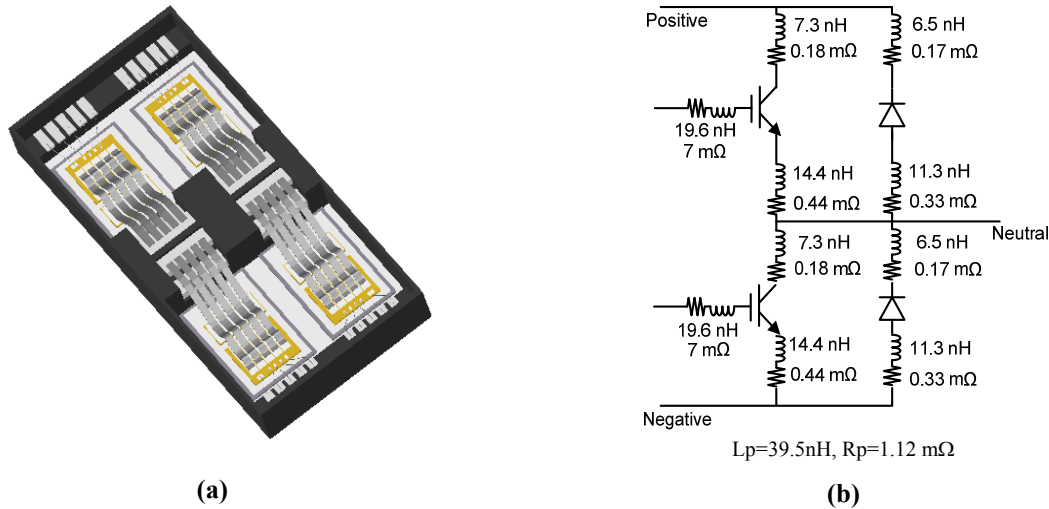


Fig. 4. Electrical performance simulation of the Toyota Prius10 power module: (a) 3D interconnection model and (b) parasitic electric parameters.

Packaging materials and the associated processing are critical factors in determining the mechanical and thermomechanical performance of power modules. During 2011, ORNL continued to perform microstructural analyses of selected packages. Figure 5 gives a few examples. Figure 5(a) shows the solder composition in the die attach layer in an Infineon HP1 module. This lead-free solder contains multiple elements such as tin, copper, and silver. The metallurgical compositions change also along the bond line. Among recent packaging advancements, the planar bond top interconnection of die, instead of wire bond, has become popular, such as that used in modules by Mitsubishi [3], IR [4], and Semikron [5]. The metallization on top of these dies is specially required to match with the bonding materials. Figure 5(b) shows the microstructure of the top metalized layer of a silicon IGBT die in the Mitsubishi TPM_II module, where a lead-free solder was used to bond a copper lead to the die. The metallization and bonding alloys have been identified by energy dispersive x-ray spectroscopy (EDX) and marked in the photo. The newly developed Nissan Leaf module [6] doesn't feature conventional direct bonded copper or DBA substrates; instead, a larger polymer insulation sheet is put on top of the cold plate. The power module built up on a metal frame (bus bar) is directly mounted on this layer with thermal grease, as shown in the photo in Fig. 5(c). Fourier transform infrared spectroscopy indicates that it is a silicone polymer. The EDX spectrum [Fig. 5(c), middle inset] discloses that it contains fluorine, calcium, carbon, and oxygen as part of its composition. Figure 5(d) shows the microstructure of a bonded copper tabs sandwich, which is designed to test the high temperature bonding capability of a polyimide paste/sheet. The photos give the details of bond line as well as failure modes under shear stress.

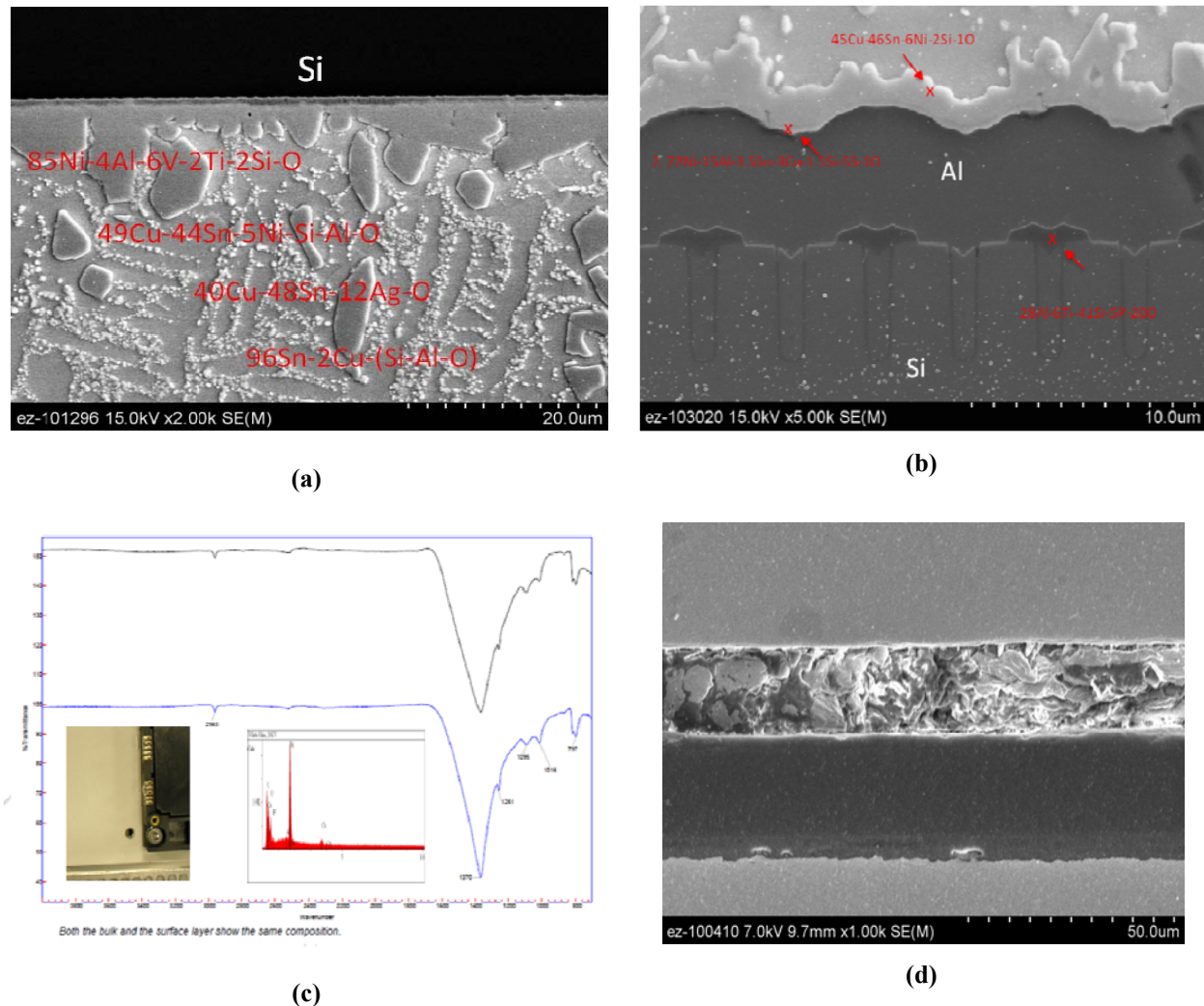


Fig. 5. Examples from microstructural analyses of packaging materials: (a) composition of die attach solder in Infineon HP1 module, (b) metallurgical composition on top of silicon die in Mitsubishi TPM_II, (c) insulator sheet in Nissan Leaf, and (d) a high temperature bonding polyimide layer.

New Automotive Power Module Packaging

An important objective of this project is to develop advanced automotive PE packaging technologies. To this end, multidisciplinary research has been performed including research on power module packaging processes and electrical, thermal, mechanical, and thermomechanical design and analysis.

Figure 6 illustrates a new 200 A, 1,200V phase leg power module, *Planar_Bond_All*, based on innovative ORNL packaging technology and fabricated at the NTRC packaging laboratory. The module features double sided planar electrical interconnections and integrated mini-coolers, resulting in tremendous improvement for automotive power modules.

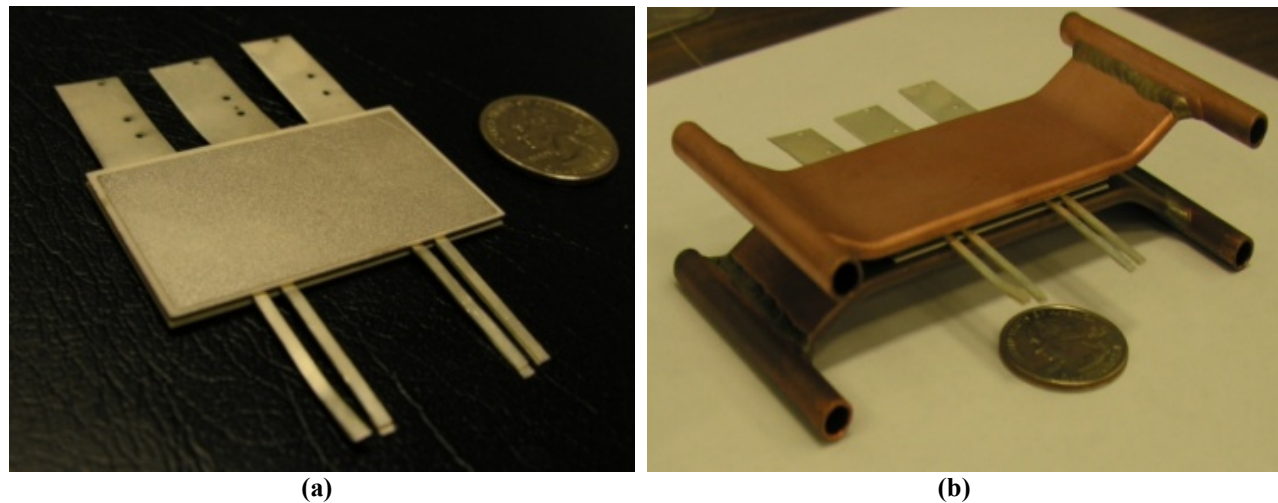


Fig. 6. Photos of the prototype of a 200 A, 1,200 V phase leg power module with (a) double sided planar interconnections and (b) integrated mini-coolers.

Planar_Bond_All is a paradigm shift in power module packaging technologies. It reduces the conventional multiple hybrid packaging processes to two steps, as shown in Fig. 7. In the first step, all the components are assembled into a fixture. The second step involves heating the assembly to form the bonds and create the final package. The simplicity of the process helps reduce costs and improve the manufacturability of the modules.

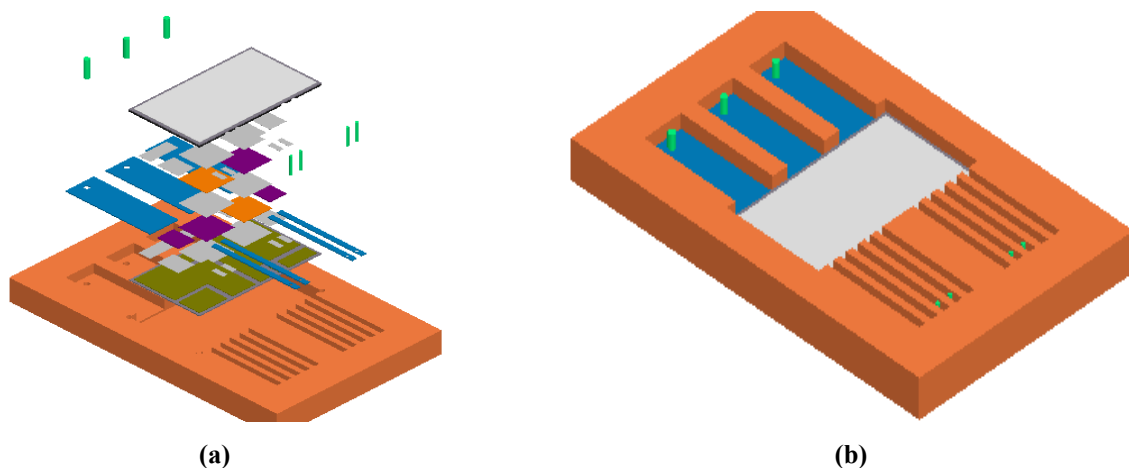


Fig. 7. *Planar_Bond_All* process flow: (a) assembling all components into a fixture; (b) heating of assemblies in oven.

Planar interconnection allows large contact and switch unit orientation of face up-face down switch die pairs (IGBT/diode) as depicted in Fig. 8(a), leading to lower parasitic electric parameters [Fig. 8(b)]. In comparisons with the Prius 10 [Fig. 8(c)], the *Planar_Bond_All* showed an 80% reduction in main path parasitic induction and resistance ($L_p = 12.8 \text{ nH}$ and $R_p = 0.22 \text{ m}\Omega$).

Figure 9(a) shows the temperature distribution for the *Planar_Bond_All* under typical application conditions. The double sided cooling reduces the specific thermal resistivity of the whole module assembly to $0.33 \cdot \text{cm}^2 \text{ C/W}$, which is 30% lower than the Prius10 [Fig. 9(b)].

The improved performance and anticipated cost reduction of the *Planar_Bond_All* package should result in considerable strides toward achieving power density and cost targets for PE systems.

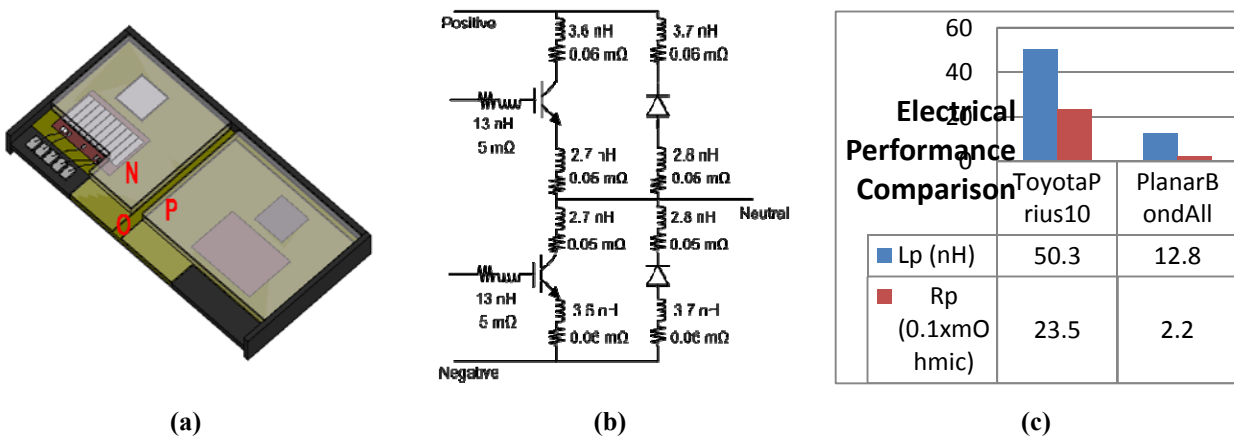


Fig. 8. Advantages of planar interconnection: (a) orientation of face up-face down switch die pairs, (b) parasitic electric parameters (main path $L_p = 12.8$ nH, $R_p = 0.22$ mΩ), and (c) comparison to Prius 10.

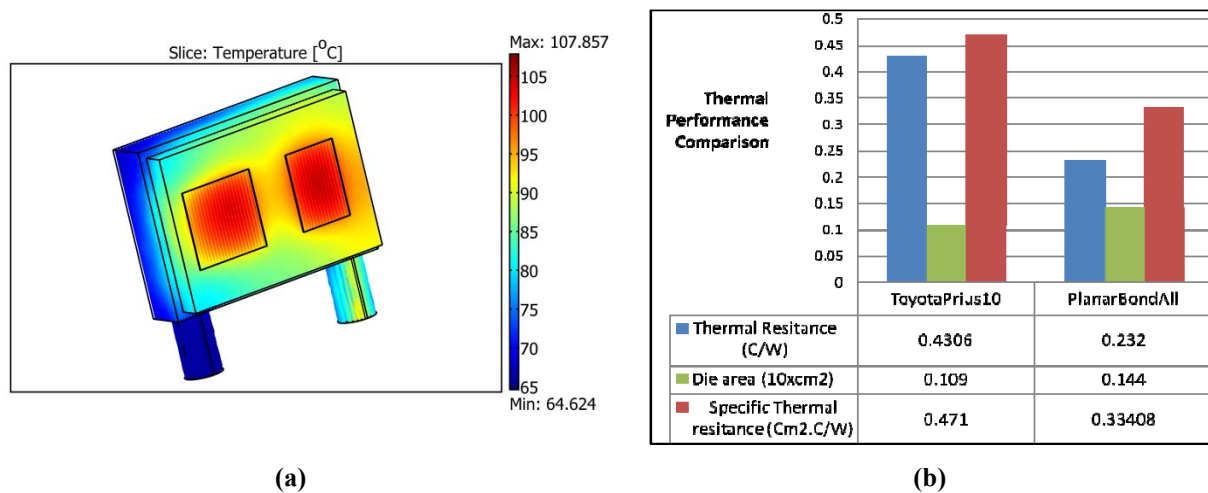


Fig. 9. Thermal performance characterization of ORNL planar bond power module: (a) temperature distribution from simulation; (b) test results and comparison to Prius 10.

Power Module Prototyping

The ORNL Power Electronics Packaging Laboratory (PEPL) supports projects for advancing packaging technology with materials development, structure optimization, and process innovation such as all planar bonding, double sided cooling, and coefficient of thermal expansion matching. Combining these technologies and advanced power semiconductors (Si, SiC, GaN, and diamond) produces PE modules with superior electrical performance, thermal management, high temperature operation, power density, and integration, which will improve cost-effectiveness, efficiency, and reliability of power conversion systems.

Equipped with modern facilities, PEPL provides advanced processing capabilities for PE module packaging. The laboratory includes (1) chemical processing stations for electrical or electroless thin metal plating, metal etching, parts cleaning, etc.; (2) class 100 clean operation bench and screen/stencil printer

for paste coating, assembling, etc.; (3) three furnaces for various large area semiconductor die attach techniques (vacuum reflow, pressure assisted sintering, environment controlled reflow); (4) wire bonder machine for thick wire and ribbon bonding for interconnection; and (5) encapsulant set for polymer spin coating, dispensing, curing, etc. Based on these capabilities, we have completed fabrication of customized specific power module prototypes for other projects within the DOE APEEM program. Figure 10 presents examples of such modules. The prototypes offer flexibility of power semiconductor selection and package forms, which will greatly improve system efficiency and further integration.

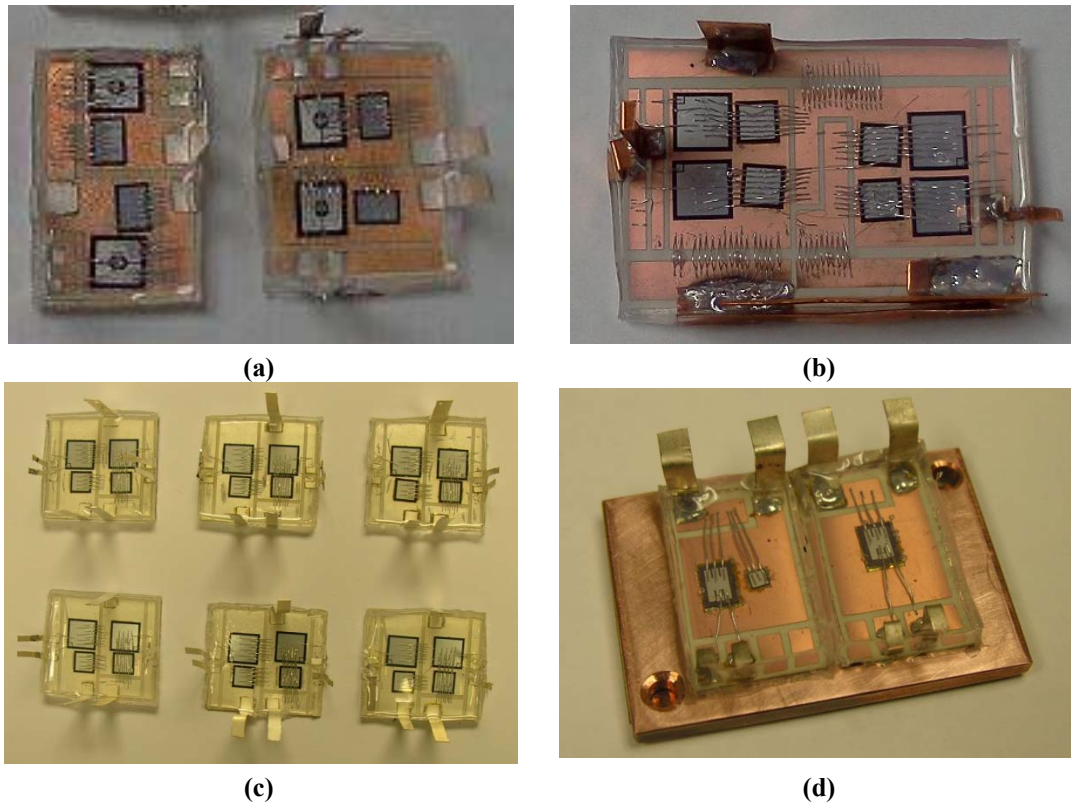


Fig. 10. Prototypes fabricated in the ORNL PEPL for other APEEM projects: (a) high power density integrated traction machine drive, (b) reduced stray inductance power module, (c) segmented drive phase legs, and (d) coupon for wide bandgap package.

Conclusion

In FY 2011, ORNL continued power device packaging research in three key areas: benchmarking, support for APEEM projects, and advanced power module development.

- Four advanced automotive power modules (Prius10, Infineon HP1, Mitsubishi TPM_II, and Nissan Leaf) have been benchmarked using ORNL's comprehensive automotive power module evaluation system.
- Four new prototype modules have been packaged for further system improvement.
- An innovative packaging technology has been invented featuring comprehensive improvement in performance, reliability, and cost effectiveness by structure optimization and material and processing development.
- A phase leg power module prototype with double sided planar interconnection and integrated heat exchangers has been developed. Initial analysis has confirmed its features of low parasitic electric parameters, low thermal resistance, and low manufacturing cost.

All these efforts contribute toward meeting 2015 DOE APEEM program challenging targets in PE systems cost, power density, and efficiency.

Patents

Zhenxian Liang, Fred Wang, Puqi Ning, and Laura Marlino, *Power Module Packaging with Double Sided Planar Interconnection and Heat Exchangers*, serial number 61/509312, filed 07/19/2011.

Publications

1. Zhenxian Liang, "Power Device Packaging," DOE VTP APEEM Kickoff Meeting, Oak Ridge, Tennessee, November 16–19, 2010.
2. Zhenxian Liang, Fred Wang, and Laura Marlino "Automotive Power Module Packaging: Issues and Technologies," APEC'11, Session 2.1, Fort Worth, Texas, March 8, 2011.
3. Zhenxian Liang, "Power Device Packaging," DOE AMR, Washington, DC, June 9, 2011.
4. Zhenxian Liang, Laura Marlino, and Fred Wang, "Challenges and Technologies of Power Semiconductor Module Packaging for Electric and Hybrid Electric Vehicles," SEMICON WEST'11 Keynote presentation, July 12, 2011.
5. Zhenxian Liang, Puqi Ning, Fred Wang, and Laura, Marlino, "Power Module Packaging with Double Sided Planar Interconnection and Heat Exchanger," ORNL PE Symposium, July 22, 2011.
6. Zhenxian Liang and Laura Marlino, "Power Semiconductor Module Packaging for Electric and Hybrid Electric Vehicles," Power Electronics Summit, Detroit, Michigan, Aug 8, 2011.
7. Zhuxian Xu, Ming Li, Fred Wang, and Zhenxian Liang, "Investigation of Si IGBT Operation at 200°C for Traction Application," ECCE'11, Phoenix, Arizona, September 19–22, 2011.

References

1. Natsuki Nozawa, Takeshi Maekawa, Shigeyuki Nozawa, and Ken Asakura, "Development of Power Control Unit for Compact-Class Vehicle," in Procs. 2009 SAE International Conference, p. 2009-01-1310.
2. Infineon Technologies, HybridPack 1, product information, available online at <http://www.infineon.com/cms/en/product/power-modules-and-discs/hybridpack%E2%84%A2-modules/hybridpack%E2%84%A21/channel.html?channel=db3a3043136fc1dd011370f45ed90441>.
3. Tetsuya Ueda, Naoki Yoshimatsu, Nobuyoshi Kimoto, Dai Nakajima, Masao Kikuchi, and Toshiaki Shinohara, "Simple, Compact, Robust and High-Performance Power module T-PM (Transfer-molded Power Module)," in *Proceedings of the 22nd International Symposium on Power Semiconductor Devices & ICs*, Hiroshima, Japan, June 6–10, 2010, pp. 47–50.
4. Hsueh-Rong Chang, Jiankang Bu, George Kong, and Ricky Labayen, "300 A, 650 V, 70 um Thin IGBTs with Double-Sided Cooling," in *Proceedings of The 23rd International Symposium on Power Semiconductor Devices & ICs*, San Diego, California, May 23–26, 2011, pp. 320–323.
5. Thomas Stockmeier, Peter Beckedahl, Christian Goebel, and Thomas Malzer, "Skin: Double side Sintering Technology for New Packages," in *Proceedings of the 23rd International Symposium on Power Semiconductor Devices & ICs*, San Diego, California, May 23–26, 2011, pp. 324–327.
6. Yoshinori Sato, Shigeaki Ishikawa, Takahito Okubo, Makoto Abe, and Katsunori Tamai, "Development of High Response Motor and Inverter System for the Nissan LEAF Electric Vehicle," International World Congress and Exhibition, Detroit, Michigan, April 12–14, 2011, paper 2011-01-0350.

2.3 Converter Topologies for Wired and Wireless Battery Chargers

Principal Investigator: Gui-Jia Su

Oak Ridge National Laboratory

National Transportation Research Center

2360 Cherahala Boulevard

Knoxville, TN 37932

Voice: 865-946-1330; Fax: 865-946-1262; E-mail: sugj@ornl.gov

DOE Technology Development Manager: Susan A. Rogers

Voice: 202-586-8997; Fax: 202-586-1600; E-mail: Susan.Rogers@ee.doe.gov

ORNL Program Manager: Mitch Olszewski

Voice: 865-946-1350; Fax: 865-946-1262; E-mail: olszewskim@ornl.gov

Objectives

- Overall project objectives
 - Develop a 5 kW integrated wired battery charger that fully utilizes the existing onboard power electronics components to reduce the cost, volume, and weight and simultaneously provide galvanic isolation and the capability of charging fully depleted batteries.
 - Develop converter topologies suitable for wireless charging systems and design, build, and test prototypes.
- Objectives for FY 2011 effort
 - Perform circuit simulation study and generate a converter design for a 5 kW integrated wired charger.
 - Develop converter topologies for wireless chargers through circuit simulation.

Approach

- Wired charger
 - Use the existing onboard power electronics components to reduce cost, weight, and volume and accomplish galvanic isolation.
- Wireless charger
 - Investigate converters suitable for wireless charging systems by simulation and bench tests. Converter topology candidates include the following:
 - ▶ ac-dc plus dc-dc, and
 - ▶ ac-ac plus ac-dc.
 - The following control methods for efficiency improvements will also be included:
 - ▶ alternative resonant modes that can significantly reduce circulating current,
 - ▶ soft-switching to reduce switching loss and electromagnetic interference (EMI) noises, and
 - ▶ synchronous rectification to reduce conduction loss.

Major Accomplishments

- Wired charger
 - Developed a new approach that utilizes the onboard power electronics components to reduce the cost, weight, and volume of onboard chargers; accomplish galvanic isolation; and accommodate a wide range of battery voltages.
 - Proved the concept using detailed circuit simulations, and confirmed high power quality performance.

- ▶ Total harmonic distortion (THD) factors range from 2.8% to 6.6% and are less than 5% when charging rates are more than 1 kW.
- ▶ Power factors range from 97% to 99.6% and are greater than 98% when charging rates are more than 1 kW.
- Completed a converter design for a 5 kW integrated wired charger with an estimated cost reduction of 80% compared to a standalone onboard battery charger.
- Wireless charger
 - Developed two converter topologies with reduced switch count and passive component requirements. Simulation results proved the concepts.
 - Confirmed a high power factor resonant circuit was effective in reducing the circulating current and the associated losses. Simulation results showed reductions in the range of 70% to 75% for the current and 14% to 38% for the losses.

Future Direction

- Design, build, and test a 5 kW integrated wired charger prototype.
- Design, build, and test a 5 kW wireless charger converter prototype.
- Demonstrate a wireless charger prototype in a vehicle charging system.

Technical Discussion

Background

Plug-in electric vehicles (PEVs) are emerging as a pre-fuel-cell technology that offers greater potential to reduce oil consumption and carbon dioxide emissions than hybrid vehicles currently on the market. In PEVs, the energy storage capacity of the battery needs to be increased significantly to enable a driving distance of at least 40 miles in an all-electric mode, the distance needed to substantially reduce oil consumption for daily commuting. A charger is also required to replenish the battery after it is depleted, typically done overnight to leverage energy costs by taking advantage of off-peak electricity rates [1].

Stand-alone battery chargers, however, impose an extra cost on already expensive hybrid electric vehicles (HEVs) and have other limitations. A typical stand-alone battery charger for PEVs consists of a diode rectifier with power factor correction (PFC) and a unidirectional dc-dc converter (i.e., it can only charge the battery) that uses power semiconductor switches, diodes, inductors, and capacitors, as shown in Fig. 1. A charger with a low charging capability of 1 to 3 kW can cost almost 30% as much as the electric traction system for a mid-size PEV car (estimated at \$300 to \$400, about half of the DOE 2015 cost target of \$660 for the entire traction drive system). The limited charging capability results in a long charging time (6–8 h), which could negatively impact the acceptance of PEVs. Moreover, most of the onboard chargers on the market are unidirectional [can only charge the battery but are not capable of vehicle-to-grid (V2G) support] to keep costs low.

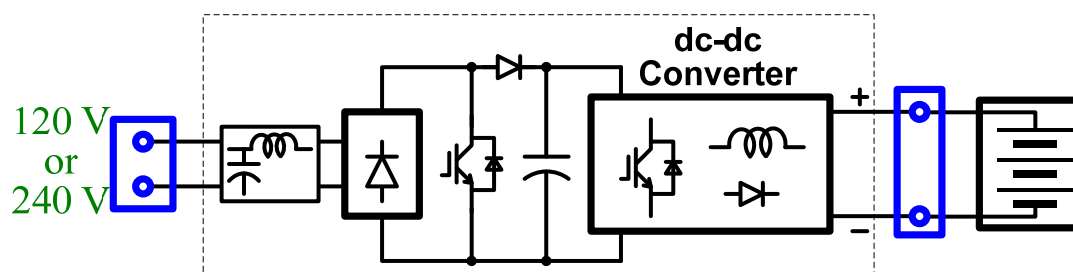


Fig. 1. A schematic showing major components in a stand-alone wired battery charger.

To minimize the cost of the charger while simultaneously providing other desirable functionalities such as V2G support and mobile power generation, a previous project finished in FY 2009 examined the use of the power electronics and motors already aboard the vehicle to fulfill the charging requirements [2,3]. The project demonstrated that, compared with a stand-alone battery charger, this approach imposes virtually no additional cost or significantly reduces the cost, depending on the configuration of the onboard traction drive system. The proposed approach is to integrate the battery charging function into the traction drive system and eliminate or minimize the number of additional components. Because traction power inverters have a greater current-carrying capability, the integrated charger can reduce the charging time significantly. Another benefit of this approach is that it enables PEVs to function as mobile power generators and provide V2G support capabilities at little or no additional cost. An integral charger prototype (Fig. 2) utilizing a traction drive comprising a 55 kW motor inverter and a 30 kW generator inverter was demonstrated with (1) capability of providing charging power of 20 kW; (2) 90% cost reduction compared to a standalone charger; (3) high efficiencies of 93% to 97%; and (4) charging, mobile power generation, and vehicle-to-grid operations.

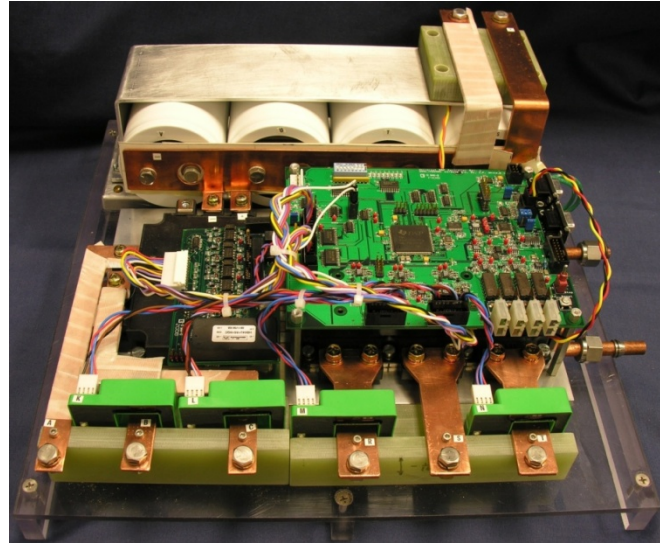


Fig. 2. An integral charger prototype utilizing a traction drive comprising a 55 kW motor inverter and a 30 kW generator inverter.

It has been found, however, that the integrated charger lacks galvanic isolation, which makes it difficult to meet safety requirements and the ability to charge “dead” batteries. One main task of this project is, therefore, to propose an integrated charger topology that utilizes the onboard traction drive system and the low-voltage converter to reduce the cost, volume, and size while simultaneously providing galvanic isolation and the capability to charge fully depleted batteries.

On the other hand, in the long term it is highly desirable to have charging systems that can transfer electric power from the grid to a vehicle to charge the batteries with minimal or no user intervention, not only because they offer ultimate convenience but also because they prevent users forgetting to plug in their vehicles. These desirable capabilities can be fulfilled with magnetically coupled wireless chargers. Until recently, conventional magnetically coupled systems required a gap of less than a centimeter. This is not practical for vehicles of the future. Power transferred by standing electromagnetic waves induced by the magnetic dipole of a loosely coupled air core transformer can theoretically provide the mechanism for this power transfer over a significant fraction of a meter without physical contact, eliminating the need for precision alignment between a vehicle and its power source. The air core is responsible for the loose coupling of this transformer’s primary (transmitter) and secondary (receiver). By comparison, the wireless power transfer technology used by most systems on the market today is inductive power transfer, which uses a fair amount of magnetic core material to increase the coupling. Figure 3 illustrates a conceptual block diagram for wireless chargers based on a loosely coupled transformer in which an ac 50/60 Hz voltage is converted by the ac-ac converter into a high frequency voltage in the range of tens of kilohertz to several megahertz and transmitted to the onboard ac-dc converter through the loosely coupled transformer, where it is converted to a dc voltage and charges the battery.

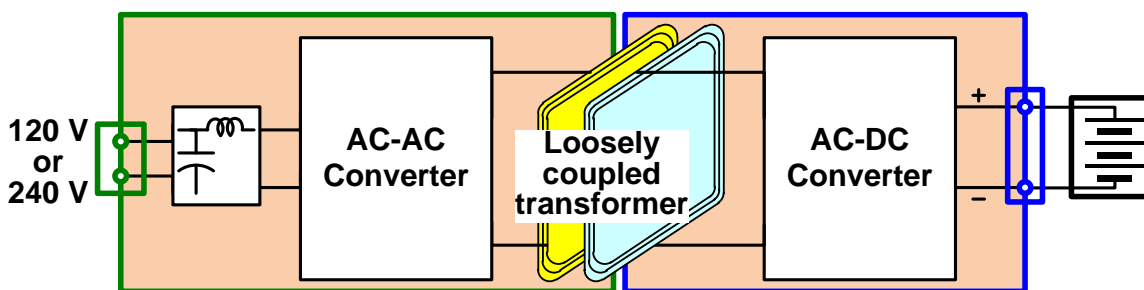


Fig. 3. A conceptual block diagram for wireless chargers based on a loosely coupled transformer.

ORNL is investigating an air core based wireless charger that is divided into two parts—one part installed in a vehicle with a receiver antenna and the other part positioned in garages or other charging stations with a transmitter antenna buried underground—and transfers power across the antennas without the need of plugging a cable into the vehicle. With the help of sensors and wireless communication systems, battery charging can be initiated and managed by a charger controller without user intervention other than parking a vehicle at a specified location. The ORNL work has been focused on antenna design and power transfer capability against misalignments of the antennas and has demonstrated power transfer greater than 4 kW in a full-scale laboratory apparatus (Fig. 4) with an efficiency of 95% from the transmitting antenna to a battery-like load with an antenna separation of 25.4 cm. Higher power transfer levels will only require components with higher voltage and current ratings. However, efficiency becomes a significant factor in overall cost. Converters with high efficiency and power factor and suitable for the wireless charging system are needed and thus developing such converter topologies is the second main task for this project.

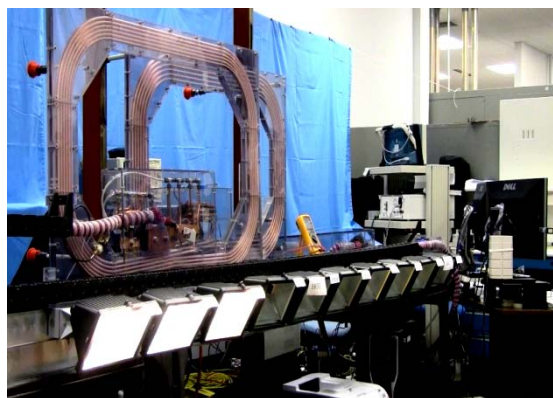


Fig. 4. ORNL laboratory test apparatus with alignment-adjustable antennas for wireless power transfer.

Integrated Wired Charger

Figure 5 shows the previous topologies for using the onboard electrical drive system (without galvanic isolation) to provide plug-in charging and mobile generation capabilities for HEVs. The new approach under investigation in this project will similarly utilize the traction drive system components but also add galvanic isolation. Details of the new circuit topology, however, will not be disclosed in this report because it is under patent review.

The onboard electrical drive system may consist of one or more electrical motor drive units, all connected to a common dc bus. Each motor drive unit typically employs a three phase inverter/converter (INV/CONV) and a three phase motor/generator (M/G) with a Y-connection of stator windings with a neutral point ($N_{M/G}$). At least one drive unit is coupled to the engine shaft through a mechanical transmission device. The basic idea is to use the M/Gs as inductors by connecting their neutral points to an external charging source to charge the battery or to external loads to supply power to them. The external charging source can be a dc or single phase or three phase ac power supply, depending on the number of onboard drive units. Figure 5(a) illustrates an arrangement for a series HEV in which two INV/CONVs and two M/Gs are used. For such vehicles, virtually no additional components except some wiring and connectors are required. An ac filter capacitor may also be needed to meet grid interface power quality requirements. For parallel HEVs, in which only one INV/CONV and M/G are used, two switches must be added, as shown in Fig. 5(b).

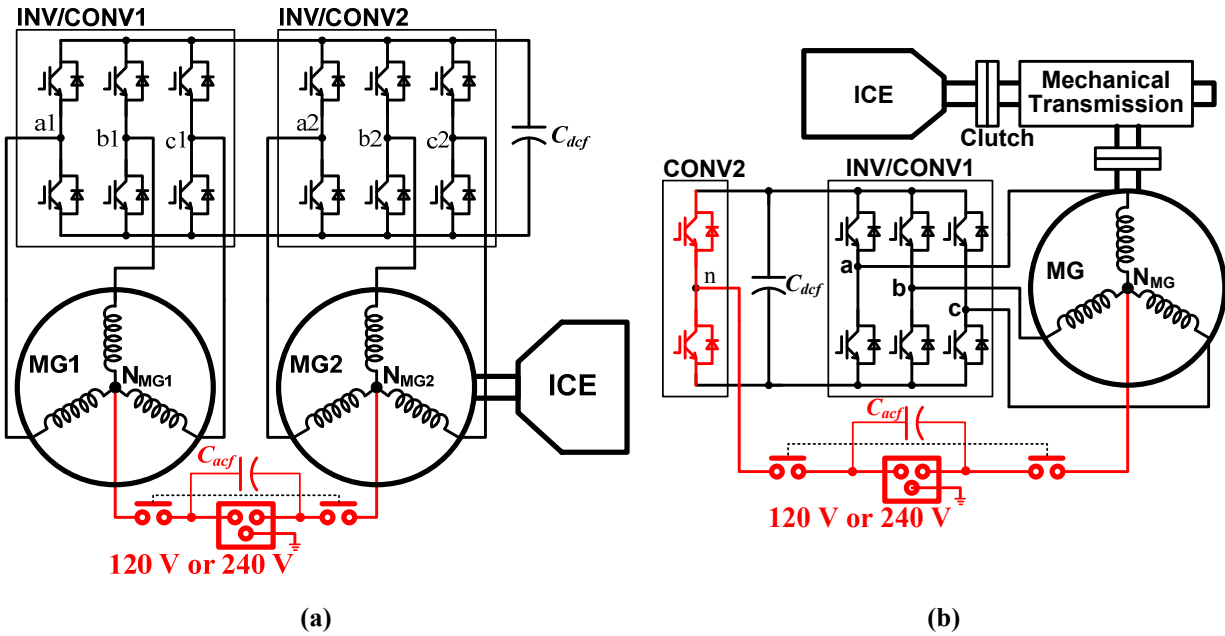


Fig. 5. The previous topologies for using the onboard electrical drive system to provide plug-in charging and mobile generation capabilities for HEVs: (a) for HEVs using two inverters and motors and (b) for HEVs using a single inverter and motor. (Red denotes added components.)

All the switch legs in each INV/CONV collectively function as a single switch leg and the M/G as an inductor (i.e., its stator zero sequence impedance network, consisting of three branches and each branch comprising the stator winding phase resistance and the stator phase leakage inductance). Together, the drive units form a single phase or multiphase converter, operating in the charging mode, to regulate the dc bus voltage. In the generation mode, the drive units form a single phase or multiphase inverter to supply external loads. In this mode, the M/G of the drive unit coupled to the engine shaft is driven by an engine to generate power to supply the dc bus and ultimately the external loads. Or power can be drawn from the battery for short operating intervals. An additional benefit of operating the three phase converters as single leg converters is the reduction in harmonic current components resulting from interleaving the gating signals of the three legs.

Detailed circuit simulations were performed in PSIM^{*} to prove the concept and provide circuit design data for use in development of a prototype 5 kW integrated wired charger in FY 2012. Figure 6 gives simulation waveforms of input source voltage and current, “*vs*” and “*is*,” and battery voltage and current, “*V_{batt}*” and “*I_{bat}*,” for charging at the rated power of 5 kW from a 240 V source showing capability for charging at the nominal battery voltage of 325 V [6(a)] and fully depleted battery voltage of 200 V [6(b)]. Figure 7 gives the same simulated waveforms for charging off a 120 V source at a rate of 2 kW, which is below half the rated power but slightly higher than the power limits of typical household 120 V outlets. The results again illustrate the capability for charging at the nominal [7(a)] and fully depleted [7(b)] battery voltage levels. In both cases, the input source currents are sinusoid shaped and are in phase with the source voltages because the charger produces very low THD factors but high power factors.

Figure 8 plots simulated THD factors against charging power, and Fig. 9 power factor vs charging power. The THD factors are in the range of 2.8% to 6.6% and lower than 5% when charging rates are more than

^{*}Simulation software from Powersim Inc.

1 kW. The power factors are in the range of 97% to 99.6% and greater than 98% when charging rates are more than 1 kW.

The simulation results generated voltage and current requirements for the switches and passive components. A converter design for a 5 kW integrated wired charger incorporating these requirements was completed. From the bill of material, it was estimated that a cost reduction of 70% could be achieved compared to a stand-alone onboard battery charger.

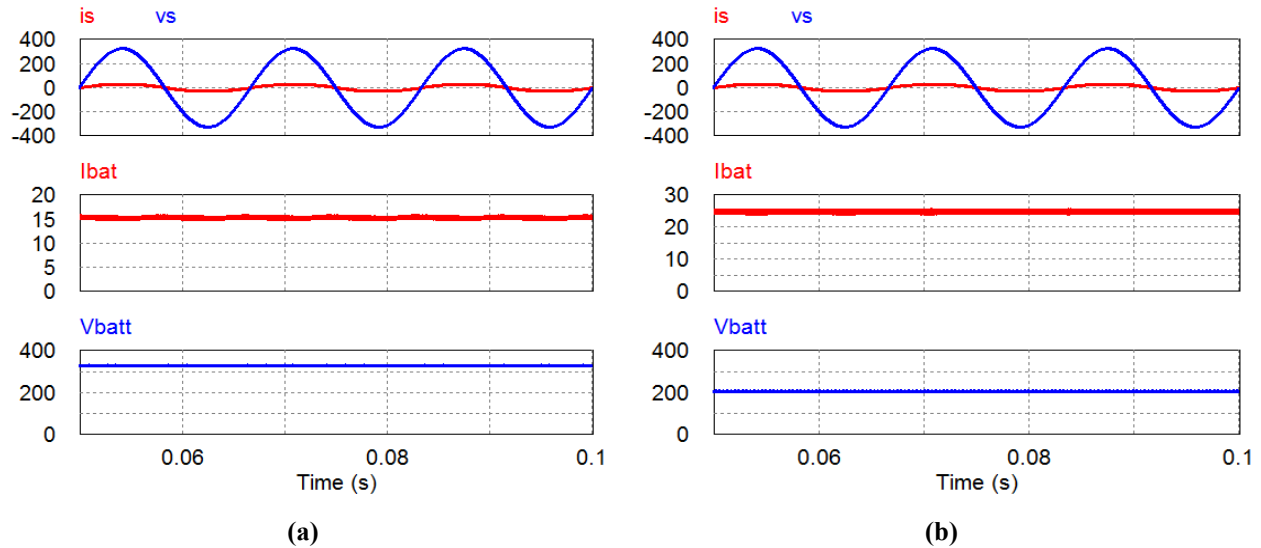


Fig. 6. Simulation results for charging at 5 kW from 240 V input showing capability for charging at (a) nominal battery voltage of 325 V and (b) fully depleted battery voltage level of 200 V.

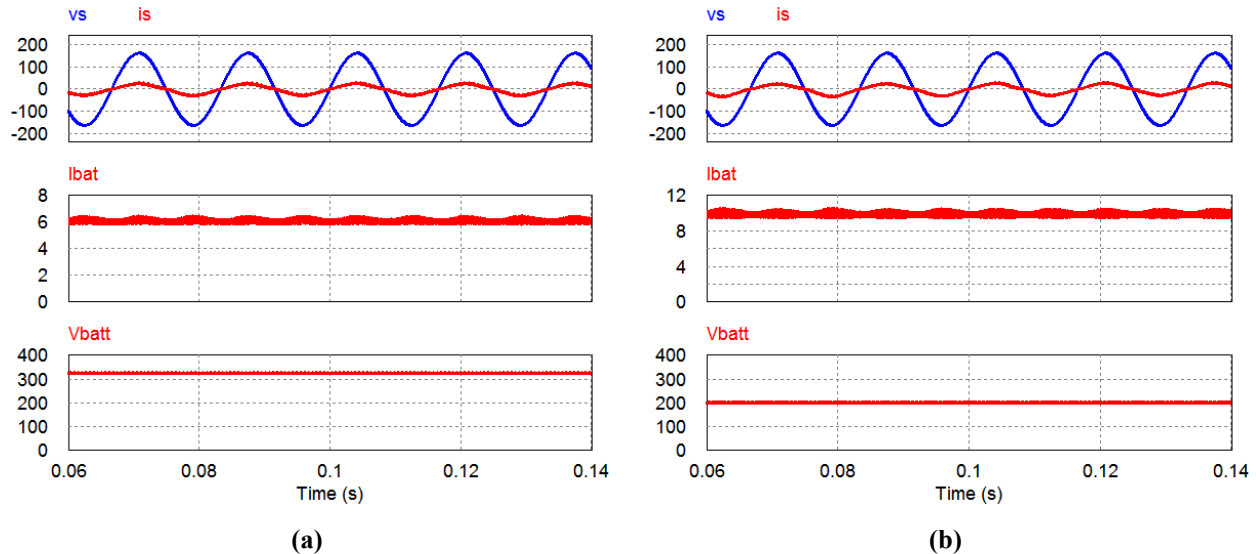


Fig. 7. Simulation results for charging at 2 kW from 120 V input showing capability for charging at (a) nominal battery voltage of 325 V and (b) fully depleted battery voltage level of 200 V.

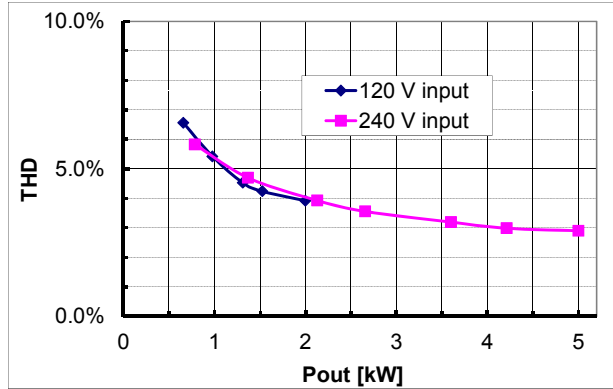


Fig. 8. THD vs charging power.

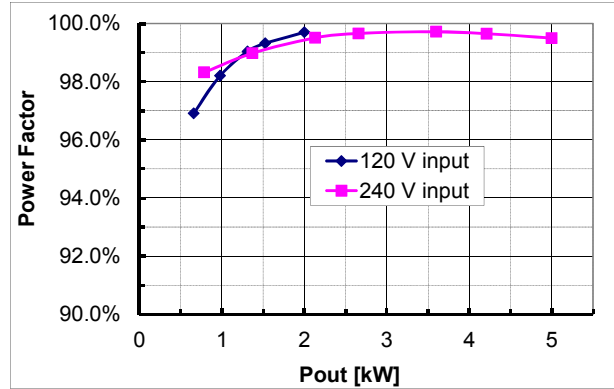


Fig. 9. Power factor vs charging power.

Wireless Charger

A converter topology study through simulation was carried out. In particular, two new topologies with reduced switch count and passive components were investigated through modeling and simulation. The first one comprises an ac-dc and dc-dc converter, and the second one is based on ac-ac-dc conversion. Details of the topologies will not be discussed in this report because they are under patent review. Compared to a typical wireless charger converter shown in Fig. 10, the proposed converters can either reduce the number of switches or significantly reduce the dc bus capacitance. In addition, an investigation on resonant circuit designs was also conducted to minimize the reactive power requirements by the air core transformer through increasing its power factor, thus reducing the circulating current and losses in the resonant circuit and converter and increasing the system efficiency. Furthermore, the following efficiency improvement techniques were included in the topology study: (1) soft switching to reduce switching loss and EMI noises and (2) synchronous rectification to reduce conduction loss.

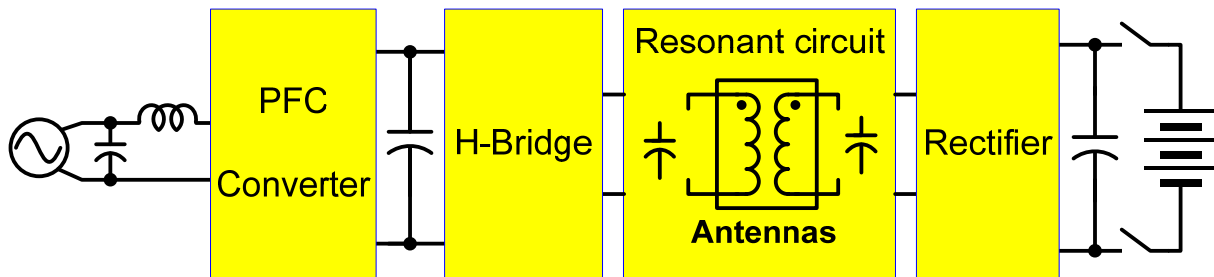


Fig. 10. A simplified block diagram for a typical wireless charger converter.

Figure 11 shows typical simulated operating waveforms for the ac-dc + dc-dc converter: source voltage and current, dc bus voltage, and high frequency output current to the transformer. The source current is sinusoidal and in phase with the source voltage, indicating a low THD and high power factor. Figure 12 gives typical simulation results for the ac-ac-dc converter: source voltage and current, high frequency ac link voltage, and high frequency output current to the transformer. Again, the source current is sinusoidal and in phase with the source voltage. These simulation results confirmed the operating principles of the converters.

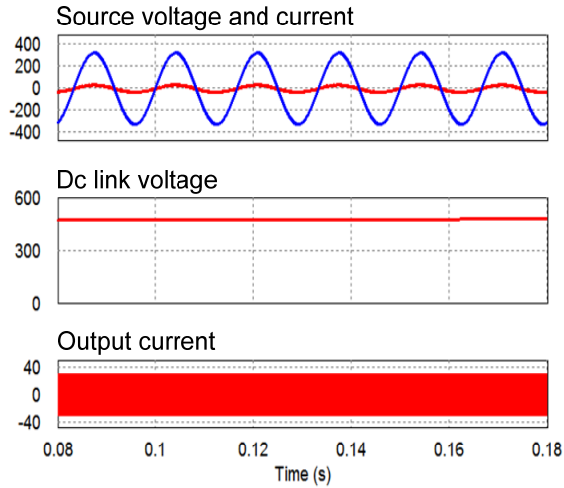


Fig. 11. Simulated operating waveforms for the ac-dc + dc-dc converter.

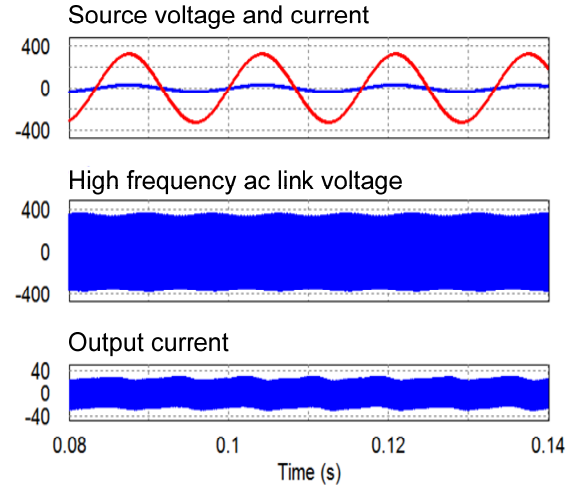


Fig. 12. Simulation results for the ac-ac-dc converter.

Figure 13 gives simulation results for charging the battery at the rated power of 5 kW to show the impact of the power factor of the resonant circuit on the primary current in which “vs” and “is” are source voltage and current; “Vbatt” and “Ibat” battery voltage and current; and “vab” and “io” primary voltage and current. Figure 13(a) is for a low power factor resonant circuit that produced a high primary current of $i_o = 64.33$ Arms, while Fig. 13(b) is for a high power factor resonant circuit that significantly reduced the primary current of i_o to 19.33 Arms.

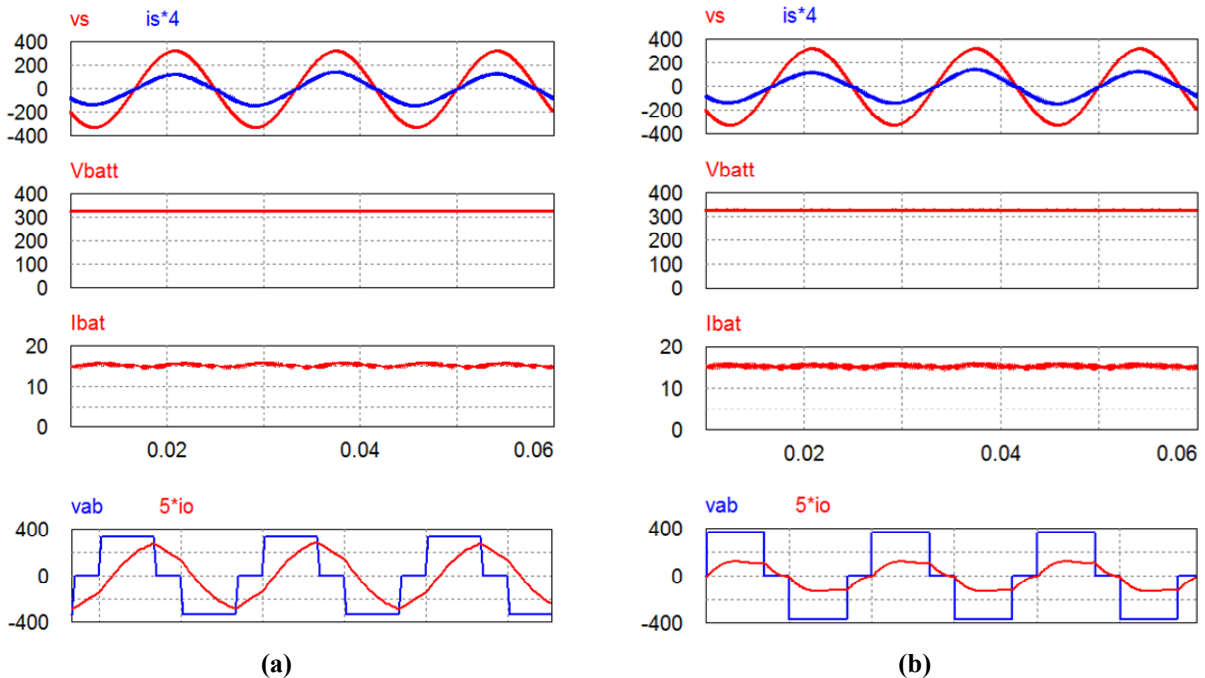


Fig. 13. Simulation results for charging at 5 kW showing the impact of the power factor of the resonant circuit on the primary current for (a) a low power factor resonant circuit that produced a high primary current of 64.33 Arms and (b) a high power factor resonant circuit that produced a significantly lower primary current of 19.33 Arms.

Figure 14 gives simulation results for charging the battery at half the rated power of 2.5 kW. With the low power factor resonant circuit, the primary current of $i_o = 63.07$ Arms remains at almost the same level for charging at 5 kW, while i_o is reduced to 16.42 Arms for the high power factor resonant circuit. In both cases, the source currents are sinusoidal and in phase with the source voltages, indicating low THD factors and high power factors.

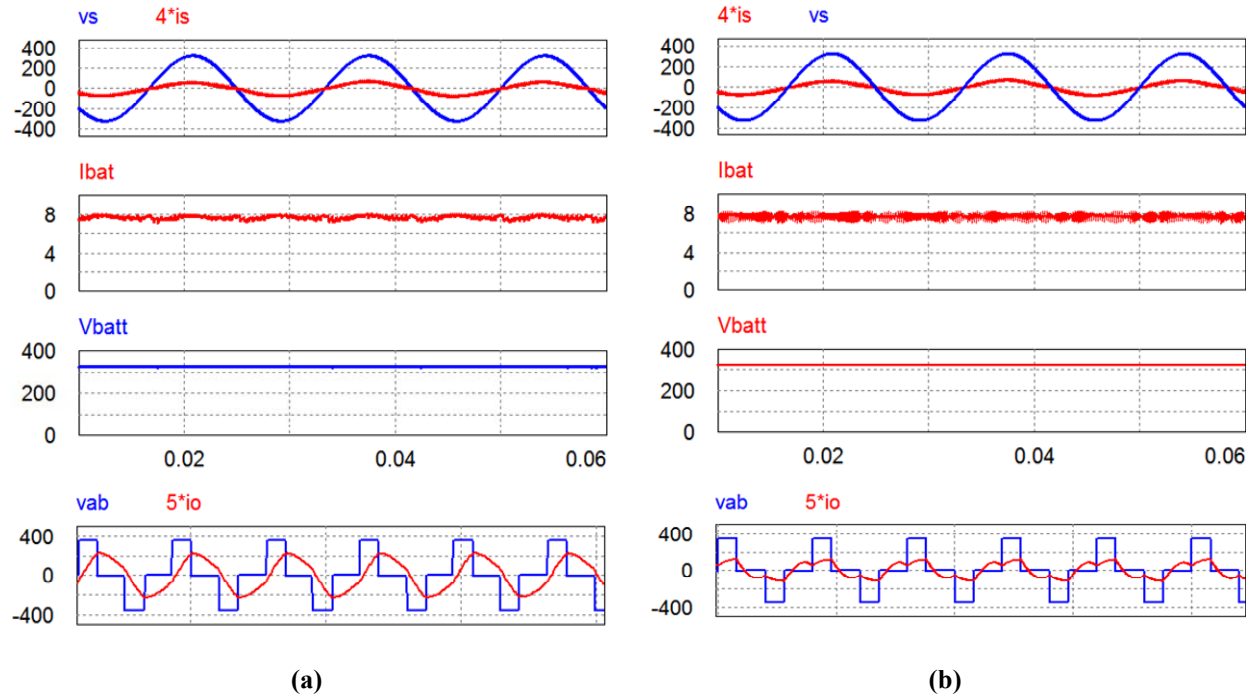


Fig. 14. Simulation results for charging at 2.5 kW showing the impact of the power factor of the resonant circuit on the primary current for (a) the low power factor case, resulting in a primary current of 63.07 Arms, and the high power case, with a primary current of 16.42 Arms.

The lower primary current levels with the high power factor resonant circuit lead to lower losses. For a comparison of losses and primary currents between the two resonant circuits, Fig. 15 plots the losses and primary current of the high power factor resonant circuit as percentages of those for the low power factor resonant circuit at various charging rates. The chart shows a range of 25% to 30% for the current and 62% to 86% for the losses. The chart also illustrates a significant reduction in the losses with the high power factor resonant circuit that increases as the charging power decreases.

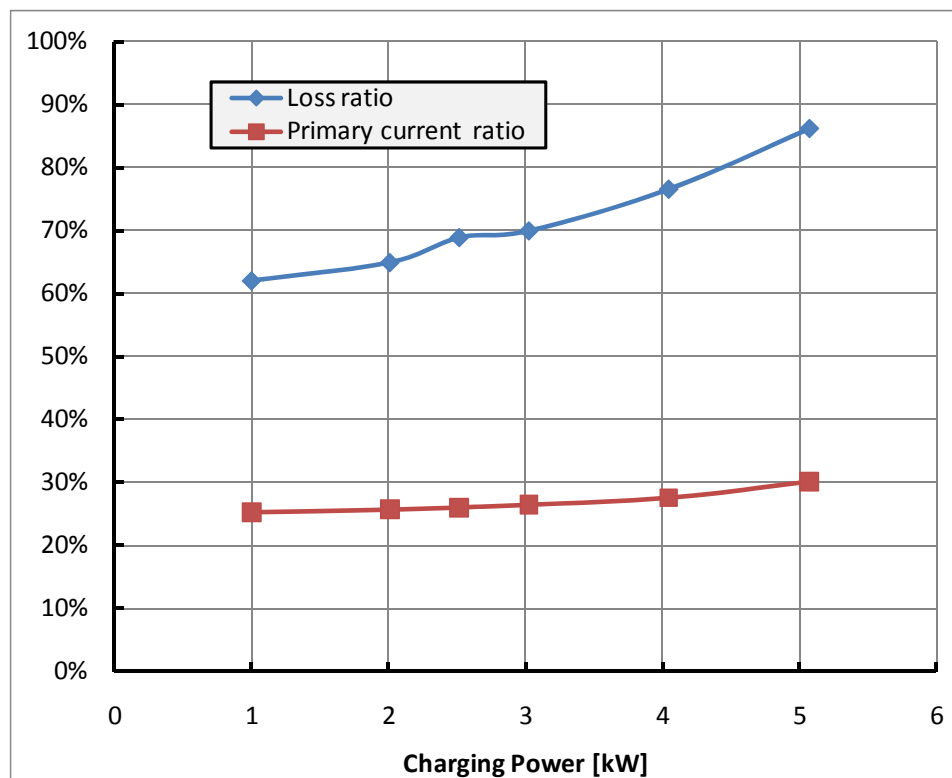


Fig. 15. Comparison of losses and primary currents between the high power factor and low power factor resonant circuits at various charging rates.

Conclusion

This project extends the previous approach of using the onboard power electronics components to provide plug-in charging functionality. The new approach under investigation in this project similarly utilizes the traction drive system components to reduce the cost, weight, and volume but also accomplishes galvanic isolation. Detailed circuit simulations were carried out, and the simulation results proved the concept and showed high performance in meeting the utility connection requirements for power quality: (a) THD factors are in the range from 2.8% to 6.6% and lower than 5% when charging rates are more than 1 kW and (b) the power factors are in the range from 97% to 99.6% and greater than 98% when charging rates are more than 1 kW. Based on the simulation results a converter design for a 5 kW integrated wired charger was completed with an estimated cost reduction of 80% compared to a stand-alone onboard battery charger.

Two converter topologies with reduced switch count and passive component requirements for wireless chargers were also investigated through modeling and simulation. A high power factor resonant circuit was found effective in reducing the circulating current and the associated losses. Simulation results showed reductions in the range of 70% to 75% for the current and 14% to 38% for the losses.

Patents

G. J. Su, Invention disclosure 201002409, "AC-DC Power Conversion Apparatus and Method," March 2011.

Publications

None.

References

1. *Advanced Batteries for Electric-Drive Vehicles*, Report 1009299, Electric Power Research Institute: Palo Alto, California, May 2004.
2. G. J. Su, US Patent 7,733.039B2, *Electric Vehicle System for Charging and Supplying Electrical Power*, June 8, 2010.
3. L. Tang and G. J. Su, "A Low-Cost, Digitally-Controlled Charger for Plug-In Hybrid Electric Vehicles," *IEEE Energy Conversion Congress and Exposition (ECCE)*, September 20–24, 2009, San Jose, California, pp. 3923–3929.

2.4 Inverter Using Current Source Topology

Principal Investigator: Gui-Jia Su

Oak Ridge National Laboratory

National Transportation Research Center

2360 Cherahala Boulevard

Knoxville, TN 37932

Voice: 865-946-1330; Fax: 865-946-1262; E-mail: sugj@ornl.gov

DOE Technology Development Manager: Susan A. Rogers

Voice: 202-586-8997; Fax: 202-586-1600; E-mail: Susan.Rogers@ee.doe.gov

ORNL Program Manager: Mitch Olszewski

Voice: 865-946-1350; Fax: 865-946-1262; E-mail: olszewskim@ornl.gov

Objectives

- Overall project objectives
 - Develop novel Z-source current source inverter (ZCSI) topologies that combine the benefits of ORNL's current source inverter (CSI) efforts and Michigan State University's work on Z-source inverters (ZSIs) to significantly reduce cost and volume through the integration of voltage boost, inverter, regenerative braking (regen), and plug-in electric vehicle charging functions.
- Objectives for FY 2011 effort
 - Perform a simulation study on ways to reduce passive component requirements for ZCSI on the selected ZCSI topology.
 - Design, assemble and test a 10 kW ZCSI setup using reverse-blocking (RB) insulated gate bipolar transistors (IGBTs) to validate the simulation study.

Approach

- Use ORNL's CSI with a quasi-Z network of passive components to enable
 - single stage voltage buck and boost power conversion,
 - battery charging,
 - safe operation in open- and short-circuit events,
 - reduction of total capacitance,
 - supply of sinusoidal voltages and currents to the motor, and
 - extension of constant-power speed range without using a dc-dc boost converter.
- Eliminate antiparallel diodes with RB-IGBTs.

Major Accomplishments

- Confirmed through simulation that using the modulation signal angle control method can significantly increase the output voltage to the point that is only limited by the voltage rating of the switches in the inverter, thus eliminating the need for high numbers for the turns ratio of the coupled inductor.
- Completed a design for a 10 kW ZCSI based on the current-fed trans-quasi-ZSI (CF-trans-qZSI) using first generation RB-IGBT technology. The design yields a specific power of 4.85 kW/kg, power density of 14.2 kW/L, and efficiency of 97.7% in boost mode and 97.1% in buck mode. With next generation RB-IGBT technology, the efficiency numbers can be increased to 98.7% and 98%, respectively.
- Test results with a 10 kW prototype demonstrate the following:

- Capacitance reduction to 80 μF [200 μF for a voltage source inverter (VSI)]
- Output voltage capability range from 0 to 3 times the battery voltage (0–0.99 \times for a VSI)
- Output voltage total harmonic distortion (THD) factors of 6%–12% (70%–200% for a VSI)
- High efficiency (more than 97% even at a relatively low source voltage of 250 V)

Future Direction

- Design, fabricate, and test 55 kW ZCSI prototypes when new RB switching devices become available.

Technical Discussion

Background

Current electric vehicles (EVs) and hybrid electric vehicles (HEVs) use a type of inverter called a voltage source inverter (VSI) [Fig. 1(a)]. The VSI, while well suited to operate off a battery as the voltage source, possesses several drawbacks that make it difficult for it to meet the U.S. DRIVE goals for inverter volume, lifetime, and cost established by the U.S. Department of Energy and its industrial partners. The VSI requires a very high performance direct current (dc) bus capacitor to maintain a near ideal voltage source and absorb the ripple current generated by the switching actions of the inverter. The root mean square (rms) value of the ripple current can reach 50% to about 80% of the motor current. Concerns about the reliability of electrolytic capacitors have forced HEV makers to use film capacitors, and currently available film capacitors that can meet the demanding requirements of this environment are costly and bulky, taking up one-third of the inverter volume and making up one-fifth of the cost. The reliability of the inverter is also limited by the capacitors and further hampered by the possible shoot-throughs of the phase legs making up a VSI [S_1 – S_2 , S_3 – S_4 , and S_5 – S_6 in Fig. 1(a)]. Steep rising and falling edges of the pulse width modulated (PWM) output voltage generate high dv/dt related electromagnetic-interference noises, cause motor insulation degradation due to the voltage surges resulting from these rapid voltage transitions, produce high frequency losses in the windings and cores of the motor, and generate bearing-leakage currents that erode the bearings over time. Furthermore, for the VSI to operate from a low voltage battery, a bidirectional boost converter is needed.

All these problems can be eliminated or significantly reduced by the use of another type of inverter, the CSI [Fig. 1(b)]. The CSI requires no dc bus capacitors and uses only three alternating current (ac) filter capacitors of a much smaller capacitance. The total capacitance of the ac filter capacitors is estimated to be about one-fifth that of the dc bus capacitors in the VSI. In addition, the CSI offers many other advantages important for EV/HEV applications: (1) it does not need antiparallel diodes in the switches, (2) it can tolerate phase leg shoot-throughs, (3) it provides sinusoid-shaped voltage output to the motor, and (4) it can boost the output voltage to a higher level than the source voltage to enable the motor to operate at higher speeds. These advantages could translate into a significant reduction in inverter cost and volume, increased reliability, a much higher constant-power speed range, and improved motor efficiency and lifetime. Furthermore, by significantly reducing the amount of capacitance required, the CSI based inverter with silicon IGBTs will be able to substantially decrease the requirements for cooling systems and, further, could enable air-cooled power inverters in the future when silicon carbide based switches become commercially viable.

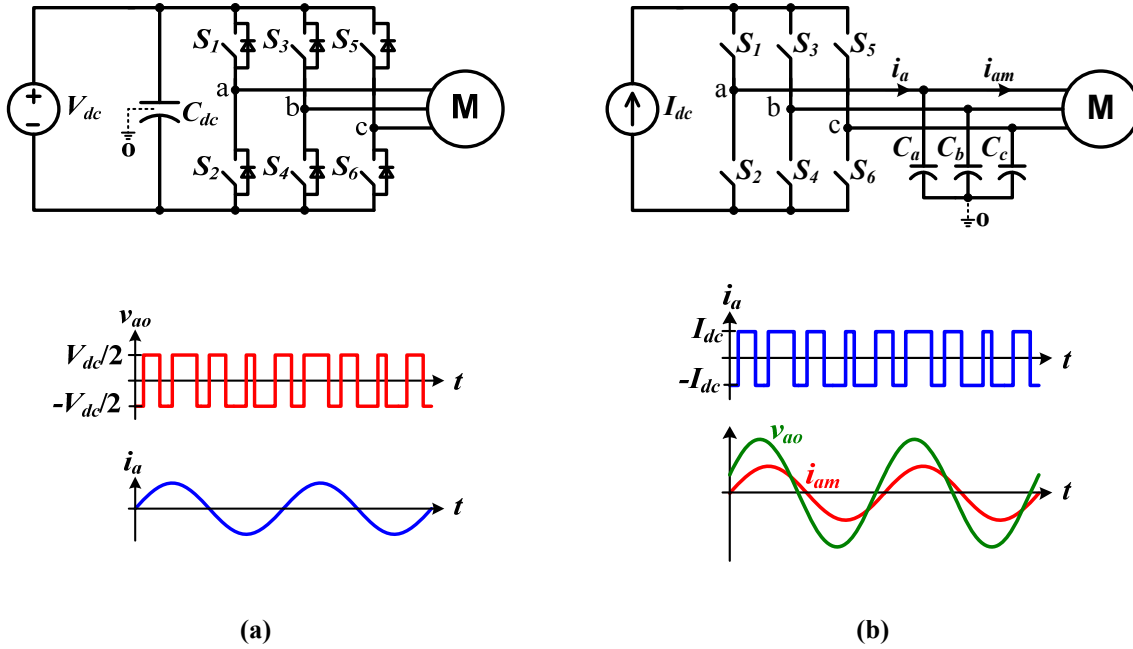


Fig. 1. Schematics of the two types of inverters and typical output voltage and current waveforms: (a) VSI and (b) CSI.

Two factors, however, have so far prevented the application of CSIs in HEVs. The first is the difficulty of incorporating batteries into a CSI as energy storage devices while controlling the motor at low speeds; the second is the limited availability of power switches that can block voltages in both forward and reverse directions. However, IGBTs with RB capability are being offered as engineering samples [1, 2], and the technology is rapidly reaching the maturity needed for commercial production. This project aims to take advantage of the latest technologies to remove the remaining hurdles and bring the CSI to HEV applications by offering new inverter topologies based on the CSI but with novel schemes to incorporate energy storage devices. Two approaches have been examined: one uses a V-I converter and the other uses a passive Z-network of inductors, capacitors, and diodes. The former, although it requires switches, has the advantage of being able to be applied in multiple-motor traction drive systems. This report discusses the work in FY 2011 on the latter approach.

Z-Network Based Current Source Inverter

Two new Z-network based CSI (ZCSI) topologies, CF-trans-qZSI and CF-trans-ZSI, were developed in FY 2010. The CF-trans-qZSI was selected for prototype development in FY 2011. Figure 2 shows a schematic drawing of the CF-trans-qZSI. The inverter topology uses a passive Z-network consisting of a diode, D_1 ; a capacitor, C_1 ; and coupled inductors, L_1 and L_2 . In addition, a contact switch is used for selecting between the motor/generator (M/G) and a charger port that can be plugged into a single- or three-phase grid to charge the battery. Compared to previous ZCSIs, the new topologies eliminate one capacitor and can extend the constant-power speed range by increasing the coupled-inductor turns ratio to provide a higher voltage boost ratio. Compared to the traditional CSI, the ZCSIs can buck and boost the output voltage in a single stage, charge the battery during regen operation, and tolerate open-circuit conditions in the CSI bridge.

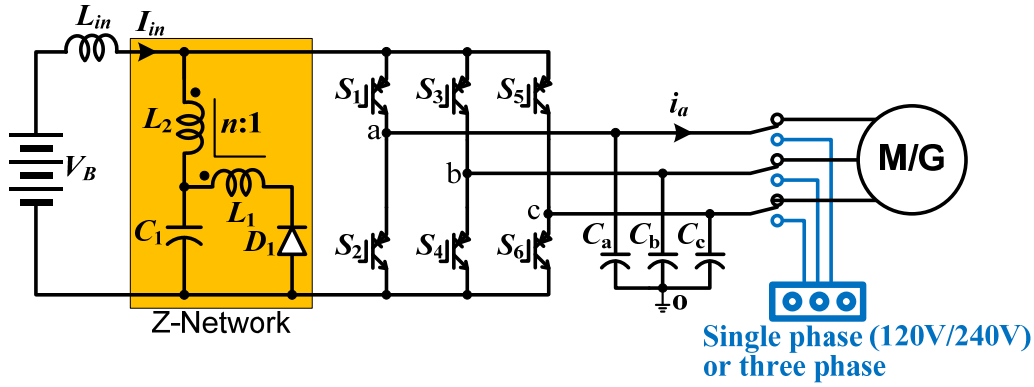


Fig. 2. Schematic of the CF-trans-qZSI with PHEV battery charging ability.

ZCSIs introduce a new zero current state, open-circuit zero state, in which all switches are turned off, in addition to the short-circuit-zero current vector and use this new current vector to step down the output voltage (buck mode) and perform the regenerative function to charge the battery. To control the duty ratio of the open-circuit zero state, in addition to the traditional CSI control method, two open-circuit-zero state references are added to the current references, as shown by the shaded intervals in Fig. 3. During these intervals, the shoot-through zero states, in which both switches, S_1 and S_2 , are conducting, are changed to open-circuit zero state by turning off both switches.

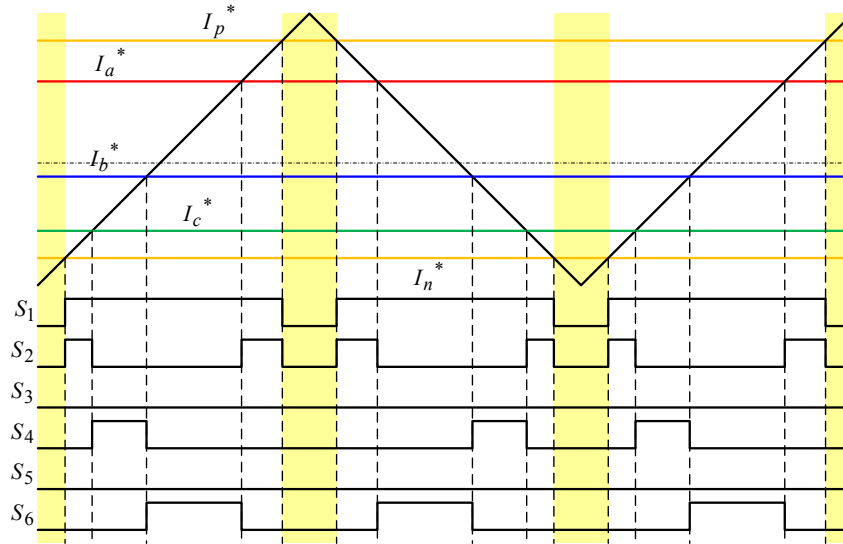


Fig. 3. PWM control method with open-circuit-zero state references inserted.

Depending on how the open-circuit-zero state reference is generated, there are three ways to insert it: (1) simple boost control, in which two straight lines are added as the open-circuit-zero state reference; (2) maximum boost control, which uses the envelop of the three phase current references; and (3) constant boost control, in which the reference is produced by injecting a third harmonic into the current commands, as shown in Fig. 4. The maximum boost control transfers the entire shoot-through-zero state interval to open-circuit zero state, while the simple boost and constant boost control have the same open-state duty cycle over every switching cycle.

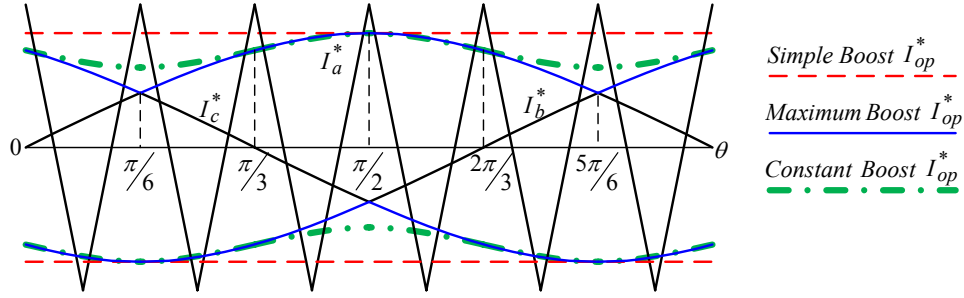


Fig. 4. PWM control methods using three different references to generate the open-circuit zero state.

Figure 5 shows the equivalent circuits of the CF-trans-qZSI for the three operation states: active, shoot-through zero, and open-circuit zero. Figure 5(a) shows the active state, in which the inverter operates in one of the six active states and the diode, D_1 , (ref. Fig. 2) is not conducting. Figure 5(b) shows the shoot-through zero state, in which one of the inverter legs is short-circuited and the diode, D_1 , is not conducting. Figure 5(c) shows the open-circuit zero state, in which all the switches of the inverter are off and the motor is disconnected from the battery. The diode, D_1 , is conducting during this state.

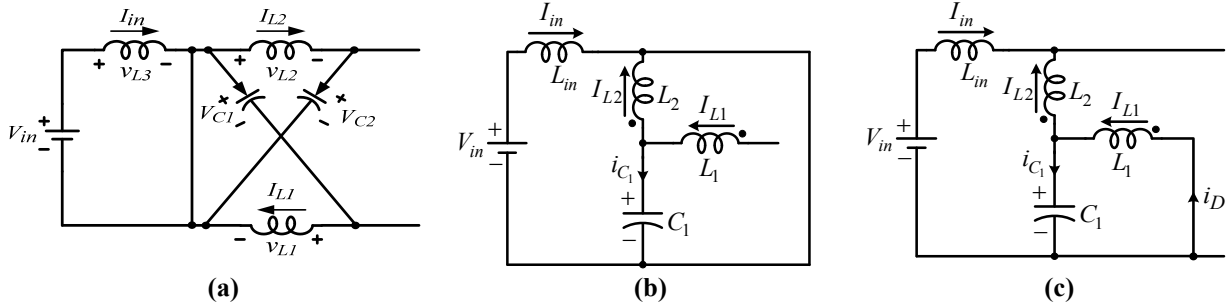


Fig. 5. CF-trans-qZSI equivalent circuit: (a) active state, (b) shoot-through zero state, and (c) open-circuit zero state.

The dc voltage gain of the CF-trans-qZSI can be derived from the equivalent circuits as

$$\frac{V_{out}}{V_{in}} = \frac{1 - D_{op}(n+1)}{D_A},$$

where n is the turns ratio of the coupled inductor and D_A and D_{op} represent the duty cycles for the active and open-circuit states, respectively.

For a turns ratio of 2 (i.e., $n = 2$) and taking into account that $D_A + D_{op} + D_{sh} = 1$, the above equation becomes

$$\frac{V_{out}}{V_{in}} = \begin{cases} \frac{1}{D_A} & \text{if } D_{op} = 0 \\ 3 - \frac{2}{D_A} & \text{if } D_{sh} = \end{cases},$$

where D_{sh} represents the short-circuit-zero state duty ratio.

Figure 6 shows the dc output voltage gain of the CF-trans qZSI. There are three operation regions, A, B, and C. In region B the inverter operates in the motoring mode and can produce an equivalent dc output voltage in the range of 0 to $3V_{in}$. Region C is the regen region, as indicated by the negative output voltage gain. In this region, the inverter can operate as a PWM rectifier and plug in the grid to charge the battery. Region A is a prohibited region because the diode of the Z-network will conduct automatically, interrupting the proper operation of the inverter. The output voltage will get distorted due to the unwanted conduction of the diode. If it is desired to extend the motoring operation region, the diode will have to be replaced with an RB switch. Alternatively, increasing the transformer turns ratio can also extend the motoring operation region. In addition, the line marked “Mode 1” represents the motoring operation region boundary on which no open-circuit zero states are introduced and the highest voltage gain is achieved. The line marked “Mode 2” is the regen region boundary line where all the shoot-through zero states are replaced by open-circuit zero states. During this mode, the inverter produces the lowest possible voltage.

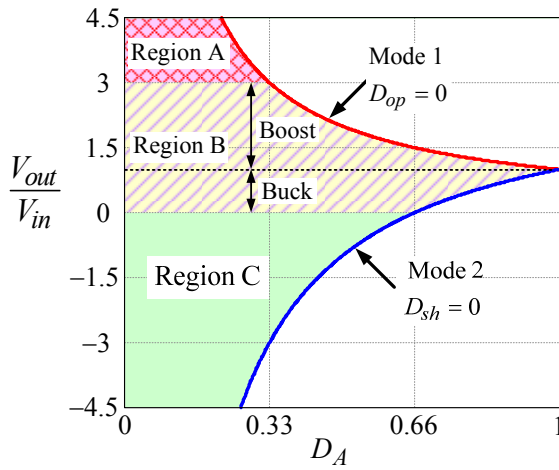


Fig. 6. CF-trans-qZSI dc output voltage gain.

Table 1 summarizes the open-circuit duty cycle, D_{op} , voltage and current gains corresponding to the modulation index, M , for the three control strategies. In the table, n is the turns ratio of the coupled inductor and $\cos\theta$ is the power factor (PF) of the motor.

Table 1. Comparison of the three different control strategies

| Control method | D_{op} | Voltage gain | Current gain |
|----------------|-------------------------------|---|--|
| Simple boost | $1 - M$ | $\frac{4}{3M \cos \theta} [M(n+1) - n]$ | $\frac{M}{M(n+1) - n}$ |
| Maximum boost | $1 - \frac{3\sqrt{3}M}{2\pi}$ | $\frac{4}{3M \cos \theta} \left(\frac{3\sqrt{3}M}{2\pi} (n+1) - n \right)$ | $\frac{2\pi M}{3\sqrt{3}M(n+1) - 2n\pi}$ |
| Constant boost | $1 - \frac{\sqrt{3}M}{2}$ | $\frac{4}{3M \cos \theta} \left(\frac{\sqrt{3}M}{2} (n+1) - n \right)$ | $\frac{2M}{\sqrt{3}M(n+1) - 2n}$ |

Figure 7 plots the output line-to-line peak voltage gain of the CF-trans-qZSI versus the modulation index at $n = 2$ and $\text{PF} = 1$ for the three control methods. The simple boost method produces the narrowest operation area, while the maximum boost method leads to a slightly wider regen area than that of the constant boost scheme.

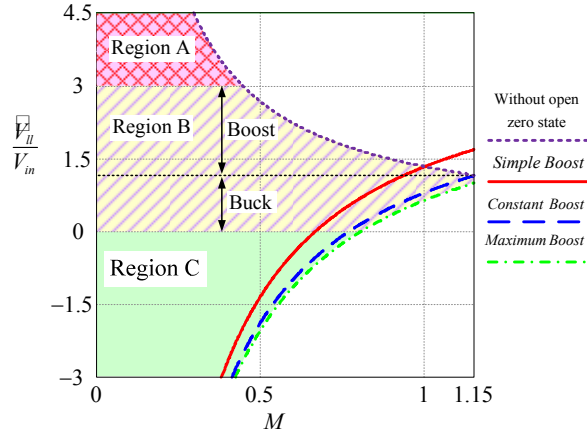


Fig. 7. Output voltage gain at $n = 2$ vs modulation index for the three control methods.

Table 2 shows the switching device stress comparison. The product of the line current, I_{l_rms} , and the maximum input voltage, V_{max} , is used as the base for the power. Because the maximum boost control may lead to discontinuous buck and boost modes, the constant boost control is used to calculate the total switching device power stress ratio (TSDPSR).

Table 2. Switching device stress

| | |
|---|---|
| Switching device voltage stress, V_S | $(n + 1)V_{max}$ |
| Diode voltage stress, V_D | $\left(1 + \frac{1}{n}\right)V_{max}$ |
| Switch average current stress, I_{ave} | $\frac{\sqrt{2}}{3}I_{l_rms}$ |
| Diode average current stress, I_D | $\frac{\sqrt{2}n(2 - \sqrt{3}M)}{\sqrt{3}M}I_{l_rms}$ |
| Average TSDPSR, $(6V_S I_{ave} + V_D I_D)/V_{max} I_{l_rms}$ | $4\sqrt{2} + \frac{2\sqrt{2}n(2 - \sqrt{3}M)}{\sqrt{3}M}$ |
| Switching peak current stress, I_{pk} | $\frac{2\sqrt{2}}{\sqrt{3}M}I_{l_rms}$ |
| Diode peak current stress, I_{Dpk} | $\frac{2\sqrt{2}n}{\sqrt{3}M}I_{l_rms}$ |
| Peak TSDPSR , $(6V_S I_{pk} + V_D I_{Dpk})/V_{max} I_{l_rms}$ | $\frac{24\sqrt{2} + 4\sqrt{2}n}{\sqrt{3}M}$ |

Using Phase Angle Control to Extend the Boost Voltage Factor

Because the voltage boost gain is limited by the turns ratio, n , of the coupled inductor, higher voltage boost ratios require a higher n , which is not desirable because it increases the size and weight of the coupled inductor and generates high leakage inductance that causes high transient voltages. There is another way to increase the voltage gain without increasing n .

The voltage, V_{out} , is determined by

$$V_{out} = \frac{3}{4}V_{ll_pk}M \cos \theta ,$$

where V_{ll_pk} and θ are the line-to-line peak voltage and phase angle of modulation signal. For a given V_{out} , decreasing leads to a higher V_{ll_pk} , effectively raising the voltage boost ratio defined as V_{ll_pk}/V_{in} . This method of increasing the output voltage is suited for controlling motors in the field weakening region to extend the motor constant power speed range. A simulation study was carried out, and the results indicated that by using this control method, the output voltage can be increased significantly and is only limited by the voltage rating of the switches in the inverter.

10 kW ZCSI Design, Fabrication, and Test

A design for a 10 kW ZCSI using the CF-trans-qZSI topology was generated for the following conditions.

- Peak power rating: 10 kW
- Battery voltage, V_{in} : 265 V
- Output line-to-line voltage: 0~500 V
- Switching frequency: 7.5 kHz
- Coupled inductor turns ratio: 2

Based on the calculated voltage stress of 780 V and current stresses of 44 A peak and 13 A average for the switches, an RB-IGBT rated at 1,200 V and 50 A should be chosen. The RB-IGBT engineering sample from Fuji that contains 18 switches with those ratings is used to estimate the losses and efficiency of the inverter design. At $V_{ce(sat)} = 2.8$ V and an average switch current of 13 A, conduction losses of the six switches are estimated to be 109.2 W. Assuming the RB-IGBT switching loss is proportional to the peak current, the total switching loss of the six devices under 7.5 kHz switching would be 101.2 W in the boost mode and 67.5 W in the buck mode. The estimated volume and weight of a six-pack RB-IGBT module are 0.047 L and 0.144 kg, respectively.

Based on the calculated diode voltage stress of 390 V and current stresses of 21 A peak and 7.1 A average, a diode rated at 600 V and 30 A could be sufficient for the design. The readily available diode from Microsemi (APT2X101D60J, dual diode rated at 600 V and 100 A) was, however, chosen for the design. The weight and volume of the diode are 0.029 kg and 10.45 mL, respectively. The diode conduction and reverse recovery losses are estimated at 9.95 W and 1.57 W, respectively.

Requirements for the Z-network capacitor are 300 V, 18.1 Arms, and 50 μ F. To meet the ripple current requirement, the Electronic Concepts film capacitor, 5MPA1506K, was chosen for the design, giving a capacitance of 50 μ F, a volume of 0.163 L, and a weight of 0.213 kg. The loss due to the electric series resistance is 0.55 W.

Requirements for the Z-network coupled inductors, L_1 and L_2 , are 69 μ H/14.7 Arms and 280 μ H/10.4 Arms, respectively. With the selected amorphous core, AMCC-40, and 14 turns for L_1 and 28 turns for L_2 , the resulting coupled inductor has $L_1 = 68$ μ H, $L_2 = 274$ μ H, core weight of 0.53 kg, core loss of 46.7 W, copper loss of 33.8 W, litz wire weight of 0.073 kg, and a total inductor volume of 0.101 L.

Requirements for the input inductor, L_{dc} , are 38 A and 310 μ H. With the selected amorphous core, AMCC-50, and 30 turns, the resulting inductor has inductance of 315 μ H, core weight of 0.586 kg, core loss of 9.8 W, copper loss of 10.26 W, litz wire weight of 0.102 kg, and a total inductor volume of 0.152 L.

The voltage stress of the output ac filter capacitors is around 300 Vrms, and the required capacitance is 10 μ F per phase. The film capacitor made by Genteq Capacitors, 41L6100, rated at 330 Vac and 10 μ F, was selected. Using three of these capacitors gives a total volume of 0.154 L and weight of 0.138 kg.

A water-cooled heat sink about twice the size of the switch module was chosen for the design. The volume and weight of the heat sink are 0.079 L and 0.248 kg, respectively.

Figure 8 is a three-dimensional drawing of the 10 kW ZCSI design. Table 3 provides a summary of component volumes and weights and the resulting power density. Figure 9 shows inverter volume breakdown by component; the capacitors and inductors are the major volume-contributing parts, constituting 81% of the total inverter volume. Figure 10 illustrates weight breakdown by component; the inductors contribute the most to the inverter weight (63%).

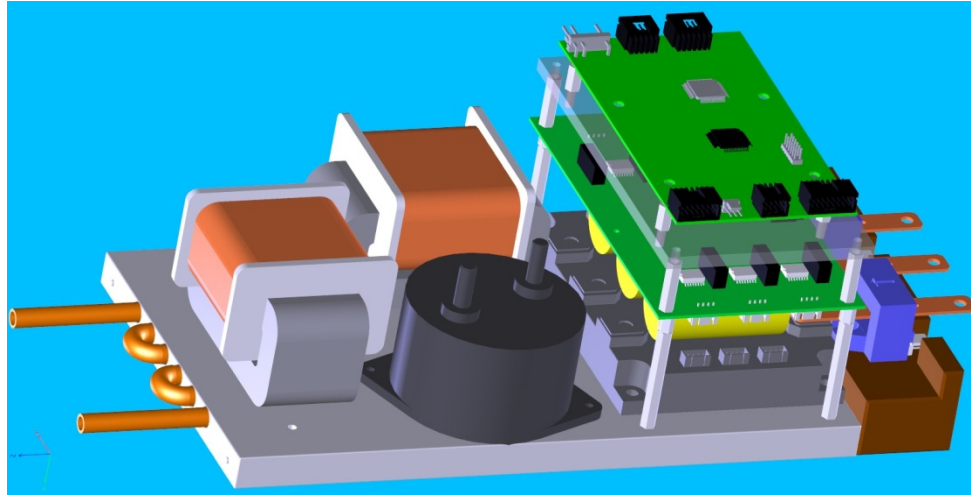


Fig. 8. A three-dimensional drawing of the 10 kW ZCSI design.

Table 3. Summary of component volume, weight, and power density for the 10 kW inverter design

| | Switches | Diode | Capacitors | Inductors | Heat Sink | Total | Power Density |
|-------------|----------|-------|------------|-----------|-----------|-------|---------------|
| Weight (kg) | 0.144 | 0.029 | 0.351 | 1.291 | 0.248 | 2.063 | 4.85 kW/kg |
| Volume (L) | 0.047 | 0.010 | 0.317 | 0.253 | 0.079 | 0.706 | 14.16 kW/L |

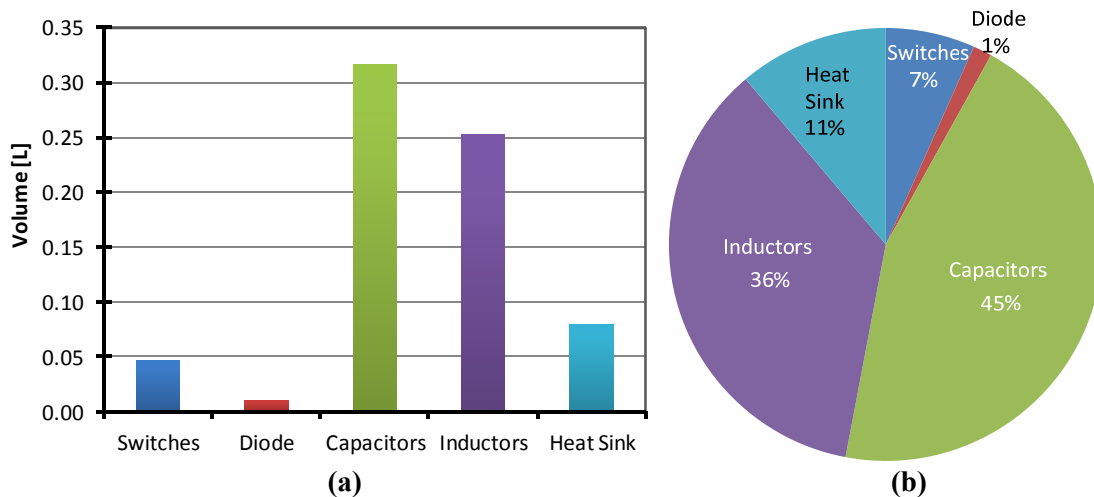


Fig. 9. Volume breakdown by component for the 10 kW ZCSI design: (a) component volume in liters; (b) component percentage of total.

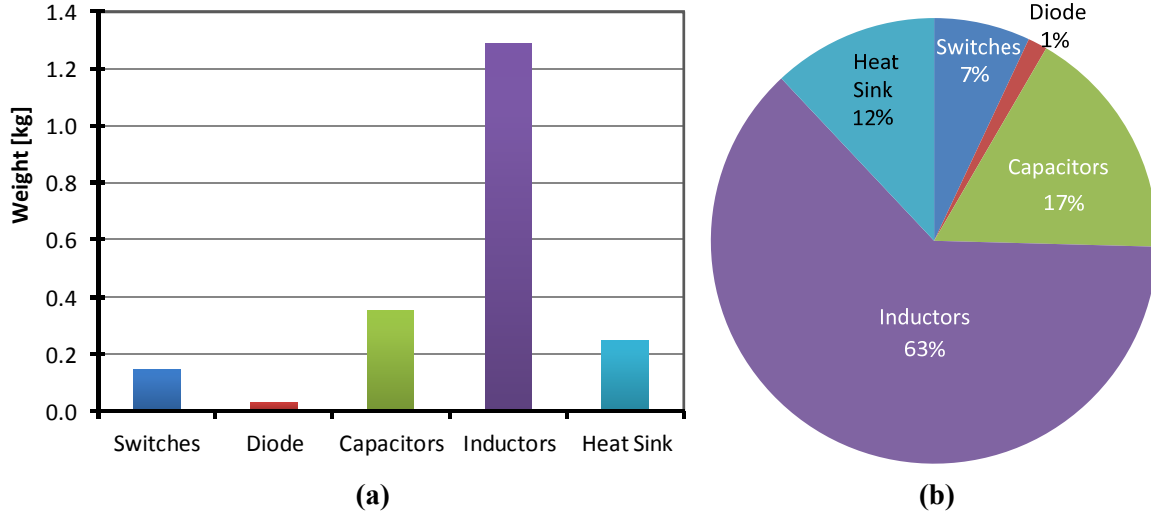


Fig. 10. Weight breakdown by component for the 10 kW ZCSI design: (a) component weight in kilograms; (b) component percentage of total.

Table 4 shows loss breakdown in boost mode and buck mode. As the Z-network is not activated in the boost mode, losses in the coupled inductor, diode, and capacitor are negligible. The estimated efficiency is 97.7% in boost mode and 97.1% in buck mode. The switching device loss is the major contributor to the total loss. To achieve higher power density and reduce the size of the inductor, the switching frequency should be increased. But the device switching loss will also increase, negatively impacting the converter efficiency. Currently available first generation RB-IGBT technology was used in this design. Assuming 100% reductions in switching and conduction losses with next generation RB-IGBTs, the boost mode and buck mode efficiency numbers can be increased to 98.7% and 98%, respectively. Further, future wide bandgap based devices, which can switch at high frequencies while still maintaining low switching losses, can be used to shrink the size of the inductors and improve the power density and efficiency.

Table 4. Summary of component loss and efficiency for the 10 kW ZCSI design

| | Switches | Diode | Capacitors | Inductors | Total | Efficiency |
|----------------|----------|-------|------------|-----------|--------|------------|
| Boost Mode (W) | 210.4 | | | 20.06 | 230.46 | 97.70% |
| Buck Mode (W) | 176.7 | 11.52 | 0.550 | 100.60 | 289.37 | 97.11% |

A 10 kW prototype was fabricated using the design and tested. Figure 11 shows a photo of the 10 kW ZCSI prototype. An 18-pack RB-IGBT rated at 600 V and 200 A was available and thus used to assemble the prototype. The control scheme was implemented with a Texas Instruments digital signal processor, TMS320F28335, and a complex programmable logic device for synthesizing the gate control PWM signals. Figures 12 and 13 show experimental waveforms of input voltage, V_{in} ; output line-to-line voltages, V_{ab} and V_{bc} ; input current, I_{in} ; and output currents, i_a and i_c , for the 10 kW ZCSI prototype operating in boost and buck modes. Figures 14 and 15 show experimental waveforms for charging a capacitor-resistor load at source voltages of 60 V in the boost mode and 120 V in the buck mode, illustrating the buck and boost capability of the ZCSI based charger. All the output voltage waveforms are sinusoidal with very low THD factors (in the range of 6%–12%). Figure 16 shows an efficiency chart at $V_{in} = 250$ V, indicating a maximum efficiency of 97.6%.

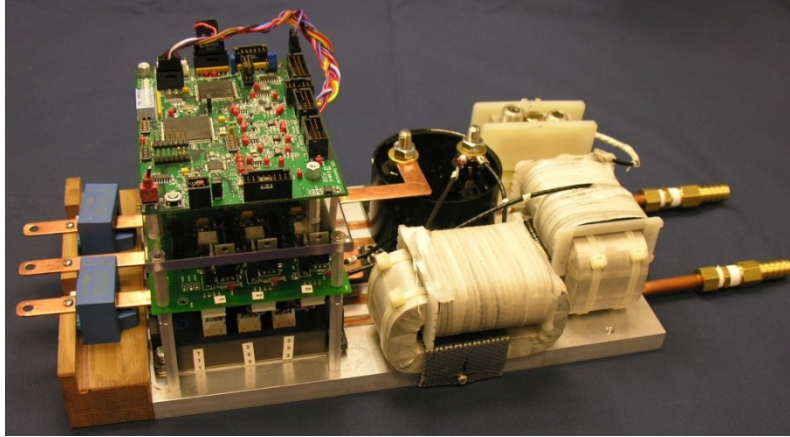


Fig. 11. Photo of the 10 kW ZCSI prototype.

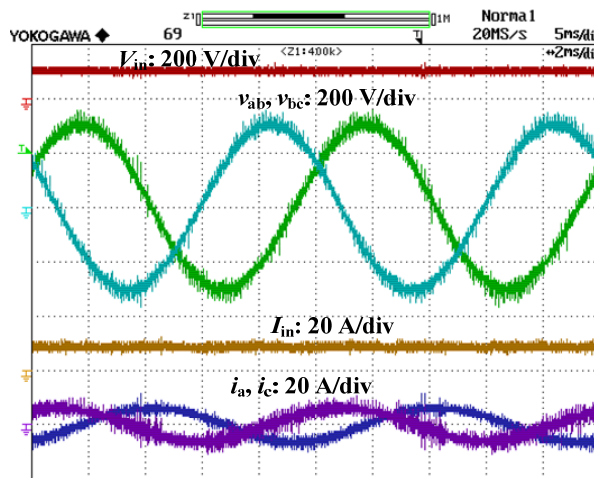


Fig. 12. Test waveforms in the boost mode showing a voltage boost factor of 3.

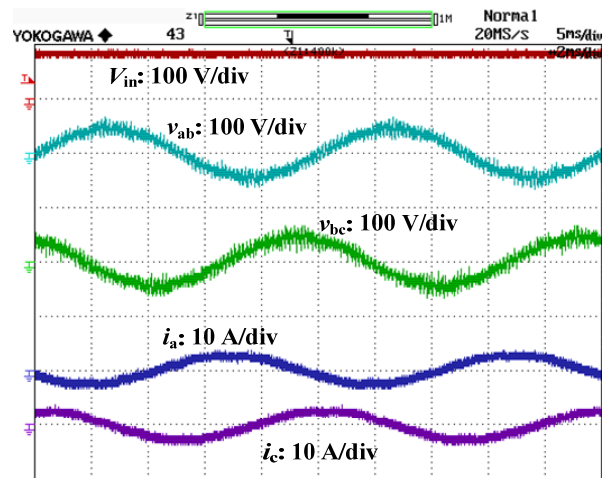


Fig. 13. Experimental waveforms in buck mode.

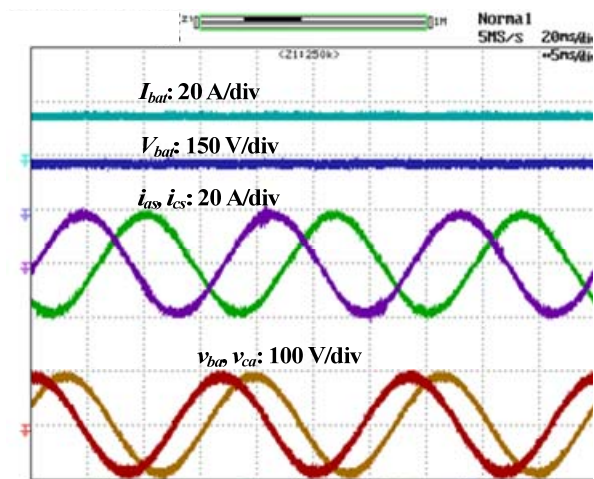


Fig. 14. Test waveforms for charging in boost mode.

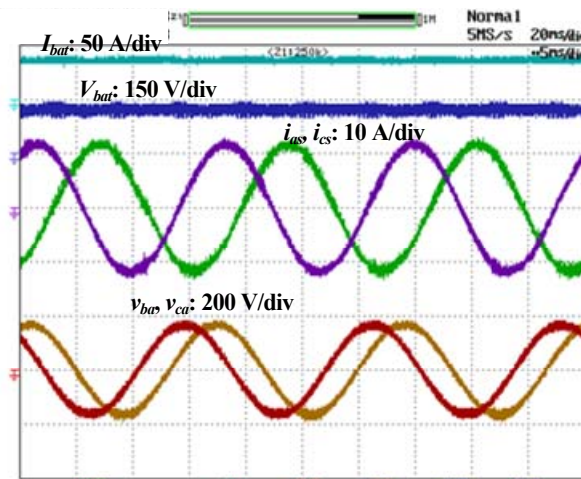


Fig. 15. Test waveforms for charging in buck mode.

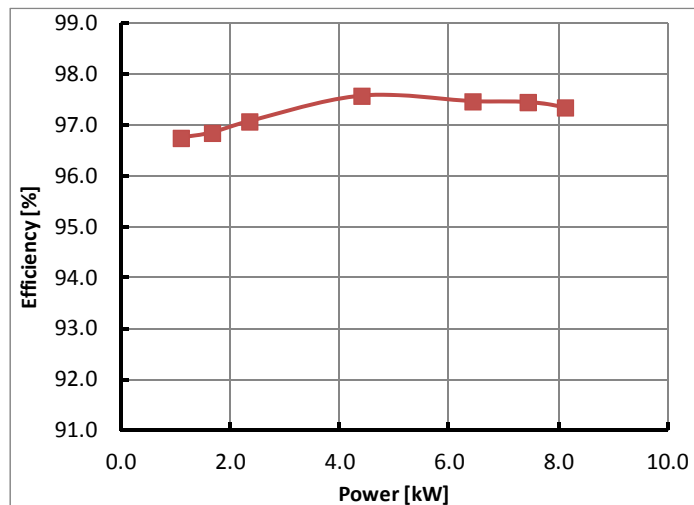


Fig. 16. Efficiency chart.

Conclusion

A simulation study verified that using the modulation signal angle control method can significantly increase the output voltage to the point that it is only limited by the voltage rating of the switches in the inverter, thus eliminating the need for high numbers for the turns ratio of the coupled inductor.

A 10 kW ZCSI based on the CF-trans-qZSI was designed using the first generation RB-IGBT technology, fabricated, and tested. The design yields a specific power of 4.85 kW/kg, power density of 14.2 kW/L, and efficiency of 97.7% in boost mode and 97.1% in buck mode. With next generation RB-IGBT technology, it is estimated the efficiency numbers can be increased to 98.7% and 98%, respectively. Test results with the 10 kW prototype demonstrate the following.

- Capacitance reduction to 80 μ F (200 μ F for a VSI)
- Output voltage capability range from 0 to 3 times the battery voltage (0–0.99 \times for a VSI)
- Output voltage THD factors of 6%–12% (70%–200% for VSI)
- High efficiency (more than 97% even at a relatively low source voltage of 250 V)

Patents

G. J. Su, *Power Conversion Apparatus and Method*, application US12/399,486, March 6, 2009, patent pending.

Publications

1. G. J. Su and L. Tang, "A Current Source Inverter Based Motor Drive for EV/HEV Applications," presented at the SAE 2011 World Congress, 2011-01-0346, April 21–25, 2011, Detroit, Michigan.
2. G. J. Su and L. Tang, "Current Source Inverter Based Traction Drive for EV Battery Charging Applications," presented at the 7th IEEE Vehicle Power and Propulsion Conference (VPPC '11), September 6–9, 2011, Chicago, Illinois.
3. L. Tang and G. J. Su, "A Novel Current Angle Control Scheme in a Current Source Inverter Fed Surface-Mounted Permanent Magnet Synchronous Motor Drive," in *3rd IEEE Energy Conversion Congress and Exposition (ECCE 2011)*, September 17–22, 2011, Phoenix, Arizona, pp. 2358–2364.

References

1. M. Takei, Y. Harada, and K. Ueno, “600 V-IGBT with Reverse Blocking Capability,” in *Proceedings of IEEE ISPSD '2001*, 2001, pp. 413–416.
2. E. R. Motto, et al., “Application Characteristics of an Experimental RB-IGBT (reverse blocking IGBT) Module,” in *Proceedings of IEEE IAS 2004 Annual Meeting*, 2004, pp. 1504–1544.

2.5 A Segmented Drive Inverter Topology with a Small dc Bus Capacitor

Principal Investigator: Gui-Jia Su

Oak Ridge National Laboratory

National Transportation Research Center

2360 Cherahala Boulevard

Knoxville, TN 37932

Voice: 865-946-1330; Fax: 865-946-1262; E-mail: sugj@ornl.gov

DOE Technology Development Manager: Susan A. Rogers

Voice: 202-586-8997; Fax: 202-586-1600; E-mail: Susan.Rogers@ee.doe.gov

ORNL Program Manager: Mitch Olszewski

Voice: 865-946-1350; Fax: 865-946-1262; E-mail: olszewskim@ornl.gov

Objectives

- Overall project objectives
 - Design, develop, build, and test a 55 kW integrated segmented traction drive system that can reduce the inverter dc bus ripple current and thus the capacitance by at least 60%.
 - Address the 2015 inverter target of 12 kW/kg and the 2020 inverter target of 13.4 kW/L.
 - Eliminate the capacitor related hurdle for high temperature operations.
- Objectives for FY 2011 effort
 - Test the 55 kW segmented inverter prototype developed in FY 2010 with a higher dc bus voltage for higher power levels and motor speeds.
 - Test the 55 kW segmented inverter prototype with space vector based pulse width modulation (PWM) schemes.
 - Design and fabricate a 55 kW segmented inverter that is suitable for integrating with a motor.

Approach

- Use a segmented drive system topology that does not need additional switches or passive components but can significantly reduce the dc link ripple current and the amount of capacitance.
- Perform simulation study of various PWM schemes using commercial circuit simulation software to assess their impact on the capacitor ripple current.
- Design, build, and test a 55 kW inverter prototype to experimentally validate the simulation study.
- Integrate the segmented inverter and motor into a single package drive system to eliminate cable connections and reduce the drive system cost.
- Test, characterize, and refine a 55 kW prototype of an integrated segmented inverter-motor drive system (FY 2012).

Major Accomplishments

- Demonstrated a 55 kW segmented inverter prototype with a 60% reduction of dc bus capacitance compared to a standard voltage source inverter (VSI).
- Tested prototype with both carrier based and space vector based PWM control methods to show
 - 55% to 75% reduction in capacitor ripple current,
 - 70% to 90% reduction in battery ripple current, and
 - 60% to 80% reduction in motor ripple current.

- Completed design and fabrication of a ring-shaped 55 kW segmented inverter that is suitable for integration with a motor.
 - Finite element analysis (FEA) results indicated satisfactory thermal performance of a toroidal heat exchanger design.
 - Use of heavy copper printed circuit board technology for interconnecting the power modules eliminated the need for bus bars and greatly simplified the inverter assembly steps

Future Direction

- Test, characterize, and refine the 55 kW integrated segmented inverter and motor drive prototype developed in FY 2011.

Technical Discussion

Background

The dc bus capacitor is an indispensable component for maintaining a stable dc bus voltage and smooth battery current for the voltage source inverter (VSI) based traction drive systems in electric vehicles (EVs), hybrid EVs (HEVs), and plug-in HEVs. Figure 1 is a schematic drawing of the standard VSI based drive system. The VSI, mainly comprising six power semiconductor switches—typically insulated gate bipolar transistors (IGBTs)—and a dc bus filter capacitor, switches the battery dc voltage to produce a desired set of three phase ac voltages according to a chosen PWM scheme. The ac voltages in turn regulate the motor current to control the motor torque and speed. In doing the switching operations, the inverter generates large ripple components in the dc link current, i_{inv} , thus necessitating the use of the dc bus filter capacitor to absorb the ripple currents and suppress voltage transients, which occur on the dc bus at every instant of inverter switching and, if not sufficiently constrained, are detrimental to the battery life and reliability of the semiconductor switches in the inverter.

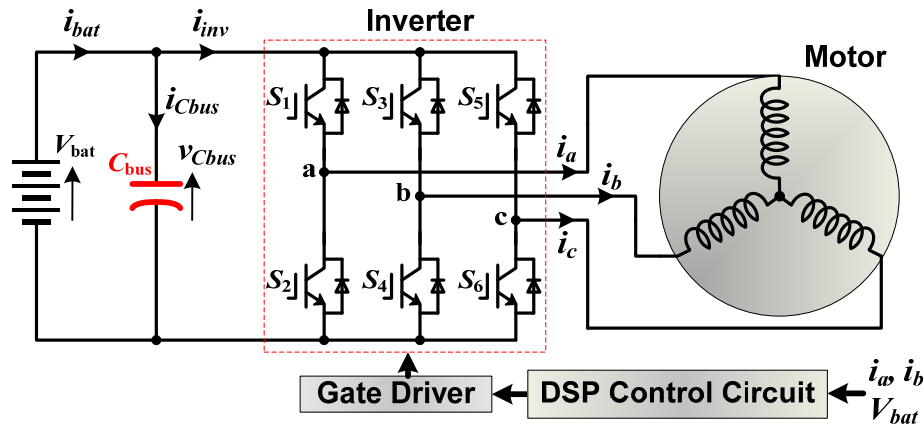


Fig. 1. Standard VSI based drive system in HEVs.

Figure 2 shows simulated motor currents, i_a , i_b , and i_c ; capacitor ripple currents, i_{Cbus} and $i_{Cbus(rms)}$; inverter dc link current, i_{inv} ; battery current, i_{bat} ; and bus voltage, v_{Cbus} , in a typical 55 kW HEV inverter. The capacitor ripple current reaches as large as 200 Arms, which is more than 70% of the motor current. As a result, a bulky and costly dc bus capacitor of about 1,000 μF is required to prevent this large ripple current from flowing into the battery and to maintain a smooth dc bus voltage. Even with the large bus capacitor, there is still a relatively large ripple component of 70 A peak-to-peak in the battery current, i_{bat} .

Concerns about the reliability of electrolytic capacitors have forced HEV makers to use self-healing film capacitors, and currently available film capacitors that can meet the demanding requirements are costly

and bulky, taking up one-third of the inverter volume and making up one-fifth of the cost. The dc bus capacitor, therefore, presents significant barriers to meeting the requirements of the USDRIVE program goals for inverter volume, lifetime, and cost established by DOE and its industrial partners [1].

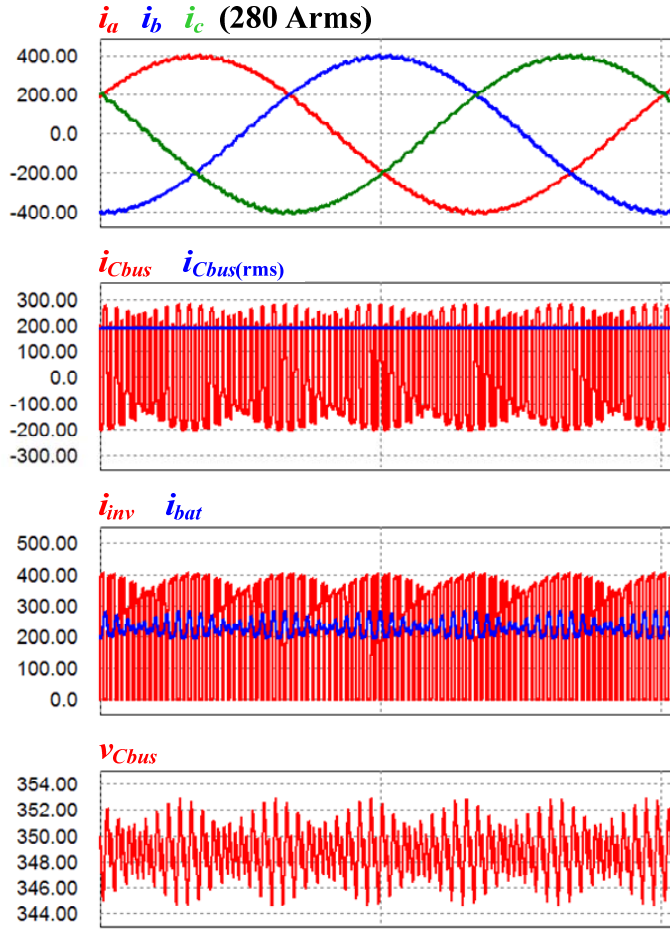


Fig. 2. Simulated waveforms in the standard VSI based drive system.

currents have frequencies of multiples of the switching frequency (nf_{sw}) or their side bands ($nf_{sw} \pm f_m$, $nf_{sw} \pm 2f_m$, ...), as given by the equation below and illustrated in Fig. 4. The high frequency nature makes it impractical to actively filter out the ripple components because doing so requires the use of very high switching frequencies in the active filter.

$$i_{inv} = I_{dc} + \sum_{k=0}^{\infty} \sum_{n=1}^{\infty} I_{n,k} \sin[2\pi(nf_{sw} \pm kf_m)t + \alpha_{n,k}]$$

where

- f_{sw} is inverter switching frequency,
- f_m is motor current fundamental frequency,
- I_{dc} is dc component,
- $I_{n,k}$ is ripple current amplitude,
- $\alpha_{n,k}$ is ripple current phase angle.

The large ripple currents become even more problematic for the film capacitors in high temperature environments as their ripple current handling capability decreases rapidly with rising temperatures, as indicated in Fig. 3 for one of the best film capacitors at 150 μ F available on the market. For example, as the ambient temperature rises from 85°C to 105°C, weight, volume, and cost of capacitors could increase by a factor of 5 due to the decrease of ripple current capability from 50 A to 11 A.

To help achieve the USDRIVE targets, there is thus an urgent need to minimize this bulky component by significantly reducing the inverter ripple current. A much smaller dc bus capacitor would also enable inverters to operate at higher temperatures. The following factors, however, make this a difficult task: (1) increasing the switching frequency, which is one of the anticipated benefits with future wide-bandgap-based switches, has little impact on the bus capacitor ripple currents because the capacitor ripple currents depend on the motor peak current, although so increasing switching frequency does reduce the dc bus voltage and motor current ripples, and (2) the major components of the capacitor ripple

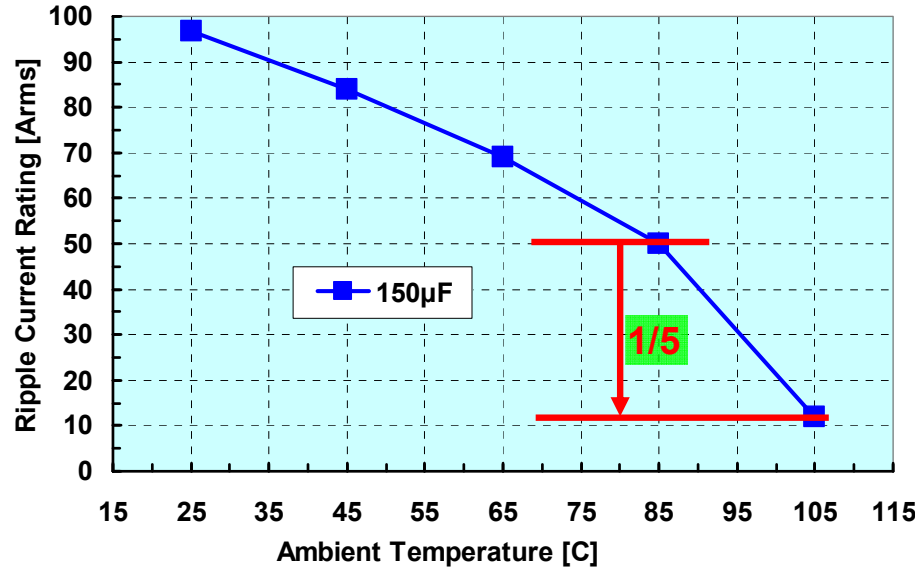


Fig. 3. Film capacitor ripple current capability vs ambient temperature (Electronic Concepts UL31 Series) [2].

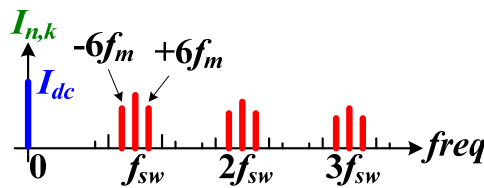


Fig. 4. Ripple components in the dc link current in the standard VSI based drive system.

Features of the Proposed Segmented Drive

A segmented drive system (Fig. 5) that does not add switches or passive components has been developed in this project to significantly reduce the ripple current and thus the requirement on bus capacitance. Because the technology is under patent review, details of the topology will not be shown in this report. However, the segmented topology does not need additional switches or passive components but enables the use of optimized PWM schemes to significantly reduce the dc link ripple current generated by switching of the inverter output currents. In addition, integrated inverter/motor packaging techniques are being explored to reduce inverter/motor connection cable length.

The uniqueness of this technology is that, while being able to significantly reduce the capacitor ripple current and bus capacitance, it *does not*

- need additional silicon or passive (L or C) components,
- need additional sensors, or
- add control complexity.

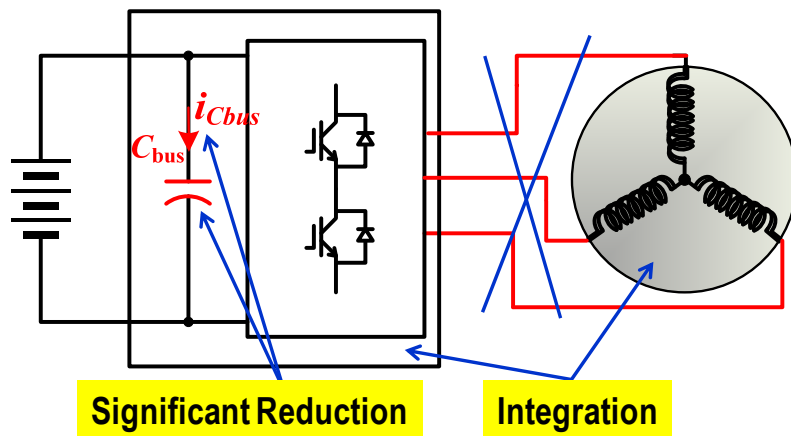


Fig. 5. Proposed segmented drive system.

The following positive impacts are expected.

- Substantially reduced bus capacitance (at least 60%) and thus reduced inverter volume and cost.
- Reduced battery losses and improved battery operating conditions (by eliminating battery ripple current).
- Significantly reduced motor torque ripples (up to 50%).
- Reduced switching losses (by 50%).
- Improved high temperature operating capability.

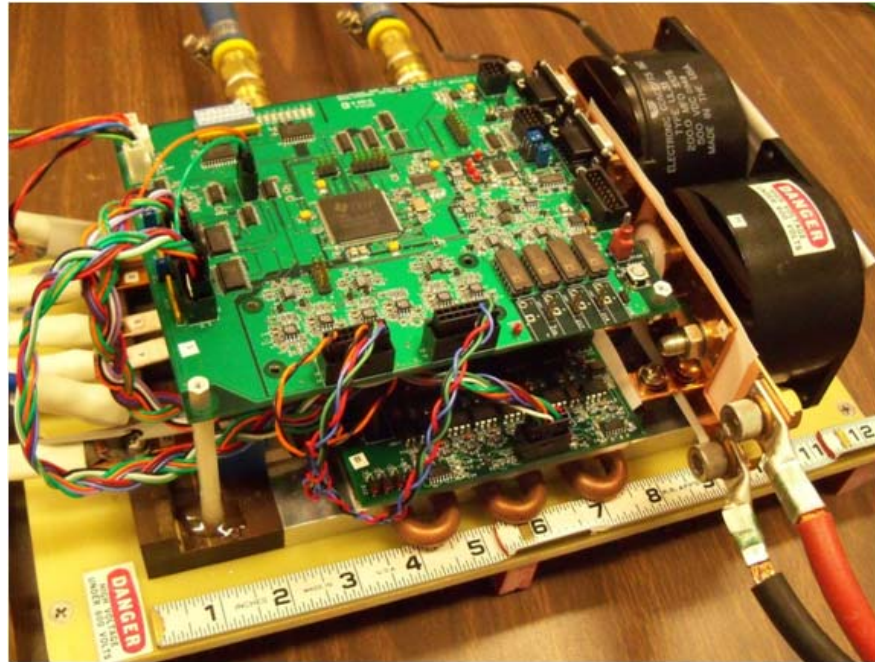
A simulation study using PSIM carried out in FY 2009 has validated the segmented drive concept and indicated that the bus capacitance can be reduced by 60% from that needed for a standard VSI. The simulation results also show that, compared to the standard inverter configuration, the segmented drive inverter can achieve (1) more than 65% reduction in capacitor ripple current, (2) 80% reduction in battery ripple current, (3) 70% reduction in dc bus ripple voltage, and (4) 50% reduction in motor ripple current.

Inverter Prototype Design and Test Results

Incorporating the simulation study, a 55 kW prototype was designed, built, and tested in FY 2010. A 55 kW baseline standard VSI was also designed for comparison. Both designs use the same IGBT modules, purchased from Powerex, and the same water-cooled cold plate, measuring 6 in. by 7 in., for fixing and cooling the IGBT modules. Capacitor requirements for the segmented inverter are 400 μF and are fulfilled with two film capacitors, each rated at 500 V and 200 μF . In comparison, a total amount of capacitance of 1,000 μF is needed for the baseline VSI design and is furnished with five film capacitors, each rated at 500 V and 200 μF . The capacitors are mounted on an aluminum heat sink attached to the cold plate. Because of the larger capacitance requirement (more than twice that of the segmented inverter), the baseline design requires a significantly larger heat sink for mounting the capacitors. Table 1 gives a comparison of heat sink size and capacitor volume for the two designs. Figure 6 shows a photo of the assembled 55 kW segmented inverter prototype. A Texas Instruments 32 bit fixed-point digital signal processor chip, TMS320F2812, is used to implement the motor control and PWM switching schemes.

Table 1. Comparison of heat sink sizes and capacitor volumes of 55 kW segmented inverter and baseline standard inverter designs

| | Baseline | Segmented |
|---------------------------|-------------------------------|--------------------------------------|
| Heat sink footprint (in.) | $6 \times 7 + 6.6 \times 9.6$ | $6 \times 7 + 6.6 \times 2.2$ |
| Capacitor volume | 1.39 L | 0.56 L —————→ a 60% reduction |

**Fig. 6. A 55 kW segmented inverter prototype.**

During FY 2010, the prototype was first tested with an inductor-resistor (R-L) load bank with nominal circuit parameters of 0.45 mH and 1.6 Ω . A dc power supply was used to simulate a 300 V battery. For comparison, the prototype was reconfigured as the baseline VSI, but without the added capacitors, and tested at the same load conditions. Because the limitation of the maximum dc power supply voltage renders the inverter unable to supply the rated voltage to the load bank, the R-L load tests were performed with power levels up to 27 kW. The prototype was then tested with a commercial, off-the-shelf, induction motor rated at 15 HP, 230 Vrms, 37.5 Arms, 91 Nm, and 1,175 rpm. The motor is in delta connection and has six pole pairs. Again due to the limitation of the maximum dc power supply voltage of 300 V, tests could not be done at the rated speed region. All the tests were performed with carrier based PWM schemes.

In FY 2011, as a dc power supply with a maximum output voltage of 450 V became available, R-L load tests were conducted at a higher inverter dc bus voltage and power levels up to 43 kW. Tests were then repeated with space vector based PWM schemes, and the results were similar to those with the carrier based PWM methods. Figure 7 plots the capacitor ripple currents at various levels of input dc power for both the baseline and segmented inverters. The graph shows the same results as the tests in FY 2010 did [i.e., the segmented inverter offers a significant reduction of capacitor ripple current (in the range of 55% to 75%)].

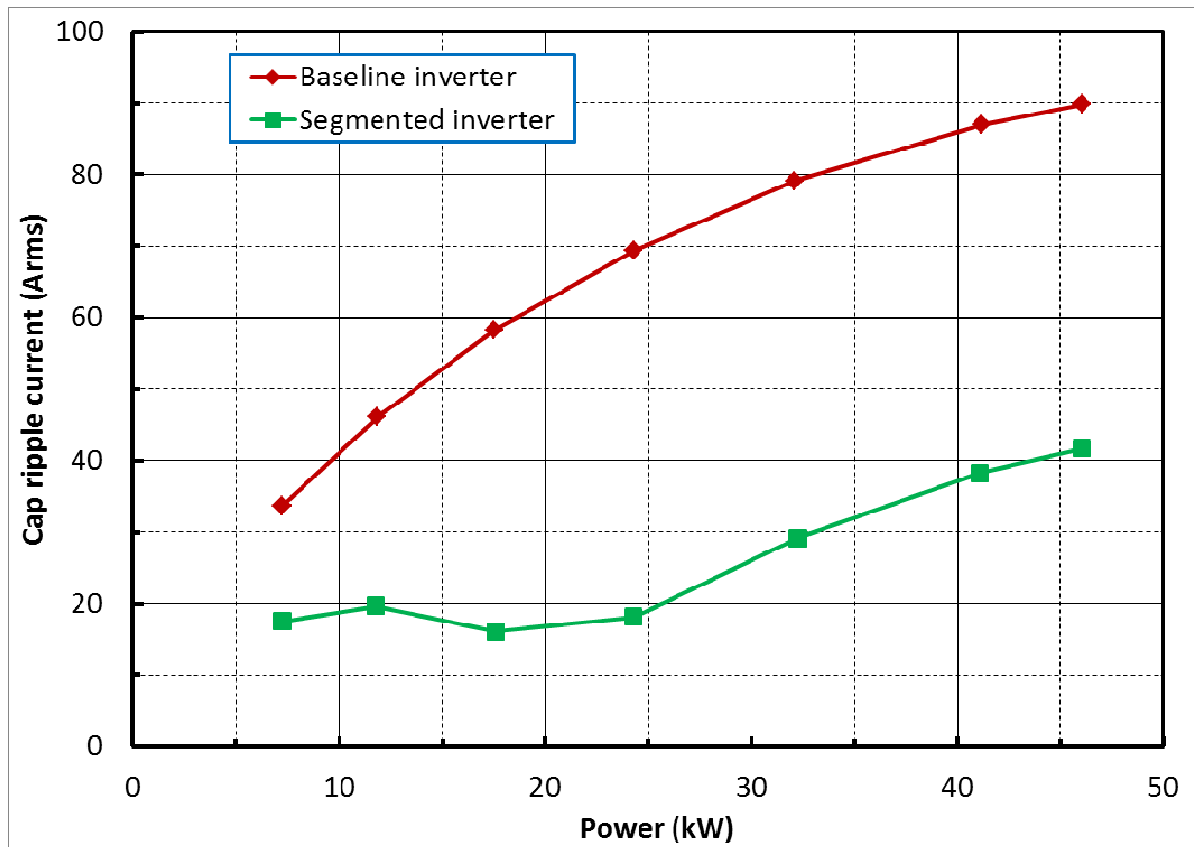


Fig. 7. Comparison of capacitor ripple current vs dc input power for an R-L load.

Figure 8 plots the battery ripple currents at various levels of input dc power for both the baseline and segmented inverters. Again, the segmented inverter offers a significant reduction of battery ripple current (in the range of 70% to 80%).

The prototype was then tested again with the commercial off-the-shelf induction motor at a higher dc bus voltage that enabled the inverter to operate the motor at the rated speed of 1,175 rpm. The motor tests were also repeated with the space vector PWM schemes, and nearly identical results were obtained. Figure 9 shows battery current, I_{bat} ; motor currents, i_a , i_b , and i_c ; and capacitor ripple current, i_{Cbus} , at 1,185 rpm and rated torque of 91 Nm for the baseline inverter and the segmented inverter. The measured capacitor ripple currents are 31.72 Arms for the baseline inverter and 13.87 Arms for the segmented inverter, and the measured peak-to-peak battery ripple currents are 35 A and 10 A, respectively. These measurements show a reduction of 56% for capacitor ripple current and 71% for battery ripple current with the segmented inverter. The motor current waveforms also illustrate significantly lower ripple components with the segmented inverter. Figure 10 plots the capacitor ripple currents at various levels of load torque vs motor speed for both the baseline and segmented inverters. Again, the segmented inverter offers a significant reduction of capacitor ripple current, in the range of 55% to 75%, at the rated torque; 50% to 70% at 75% of rated torque; and 50% to 60% at 50% of rated torque. It is also worth noting that the maximum ripple current with the baseline VSI approaches the rated motor current of 37.5 Arms.

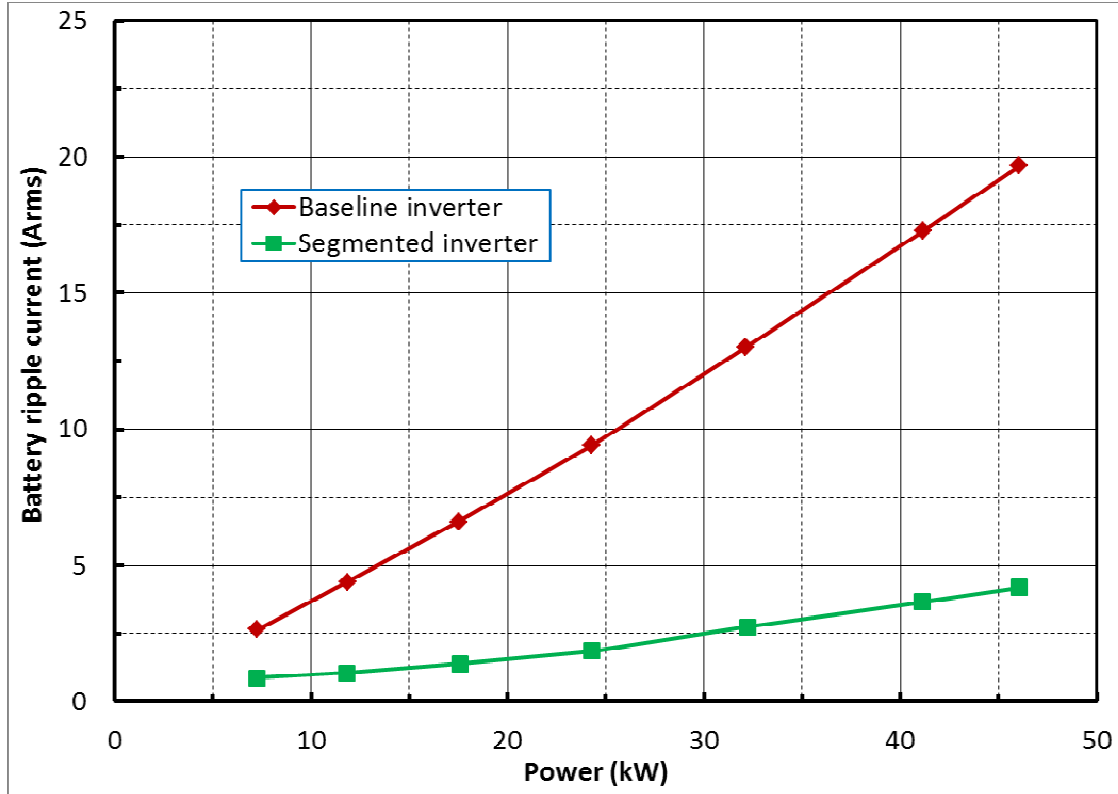


Fig. 8. Comparison of battery ripple current vs dc input power for an R-L load.

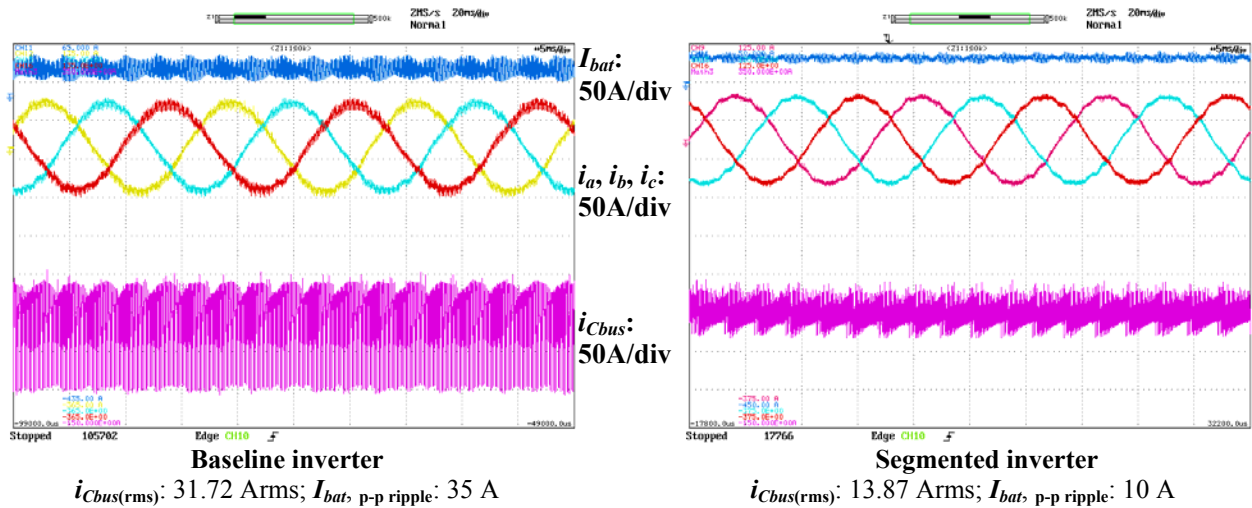


Fig. 9. Waveforms with an induction motor at 1,185 rpm and rated torque of 91 Nm showing a reduction of 56% for capacitor ripple current [$i_{Cbus(rms)}$] and 71% for peak-to-peak battery ripple current (I_{bat} p-p ripple) with the segmented inverter.

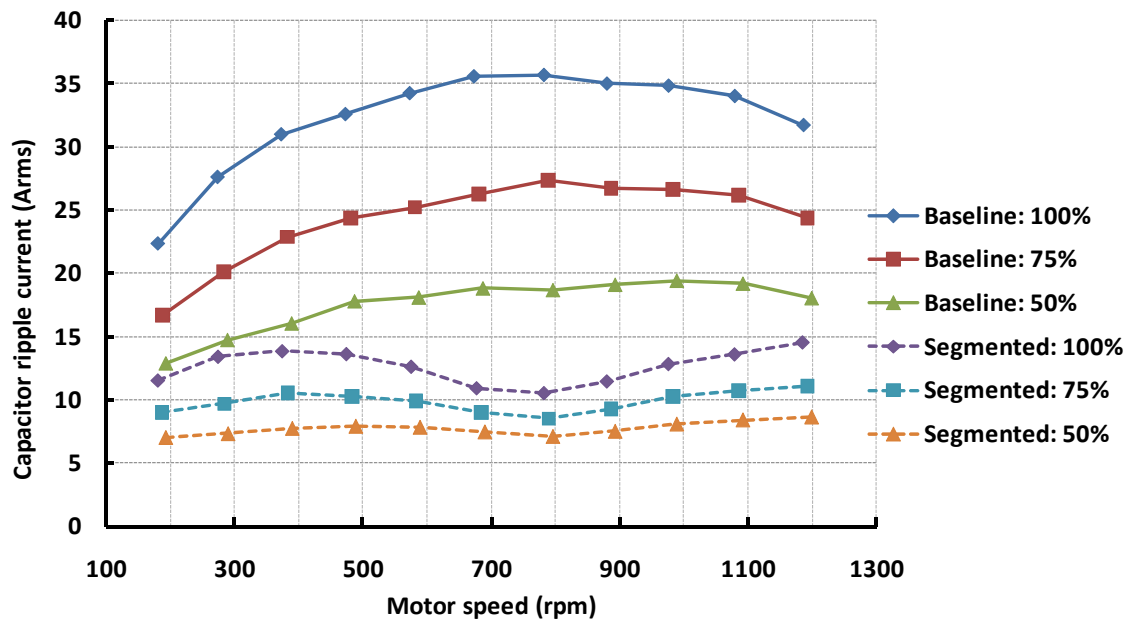


Fig. 10. Comparison of capacitor ripple current vs motor speed at load torque of 100%, 75%, and 50% of rated torque of 91 Nm.

Table 2 shows estimated performance improvements when the technology is applied to the 2009 Toyota Camry motor inverter: 40% and 35% increases in specific power and power density, respectively, and 11% decrease in cost (\$/kW). It also indicates that the segmented inverter would exceed the DOE 2015 target for specific power and the 2020 target for power density.

Table 2. Estimated performance improvements^a

| | Camry inverter | | | Segmented inverter | | |
|----------------|----------------|-------------|--------------|--------------------|-------------|--------------|
| | Weight (kg) | Volume (L) | Cost (\$) | Weight (kg) | Volume (L) | Cost (\$) |
| Bus Cap | 3.57 | 2.6 | 182 | 1.43 | 1.04 | 73 |
| Others | 3.99 | 3.36 | 728 | 3.99 | 3.36 | 737 |
| Subtotal | 7.56 | 5.96 | 910 | 5.42 | 4.4 | 810 |
| Metrics | kW/kg | kW/L | \$/kW | kW/kg | kW/L | \$/kW |
| | 9.3 | 11.7 | 13 | 12.9 | 15.9 | 11.6 |
| DOE targets | 12 | 12 | 5 | 14.1 | 13.4 | 3.3 |
| | | 2015 | | | 2020 | |

^aAssumptions: Camry inverter: capacitor costs 20%

Segmented inverter: a reduction of 60% in bus capacitor requirements

Segmented inverter performance on significant DOE targets highlighted.

Design and Fabrication of a 55 kW Inverter Prototype for Integrating with a Motor

One of the goals of the project is to develop an integrated segmented inverter and motor traction drive system (Fig. 11) that can substantially reduce cost, volume, and weight of the drive system through a reduction of the dc bus capacitance by 60% and elimination of cable connections between the inverter and motor. Toward this goal, a ring-shaped segmented inverter that is suited to be integrated into typical cylindrical motors was designed and fabricated. Figure 12 shows three-dimensional drawings of the hardware design for the 55 kW prototype. The design comprises a toroidal heat exchanger with circular water channels, IGBT modules, a dc bus capacitor board that is constructed using heavy copper printed circuit technology and also functions as bus bars to interconnect the IGBT power modules, and a gate

drive and control logic board. The toroidal heat exchanger has an outer diameter of 9 in., inner diameter of 4 in., and thickness of 0.75 in. Although the required capacitance was fulfilled using multiple discrete block capacitors for this prototype design, a custom built ring-shaped capacitor would fully use the spaces and thus reduce the inverter volume. Such a capacitor is under examination and will be used in a refined design. Also, the gate drive board is divided into six identical arc sections to save design time and cost. Future designs could put all the gate drive and control circuits on a single ring-shaped board.

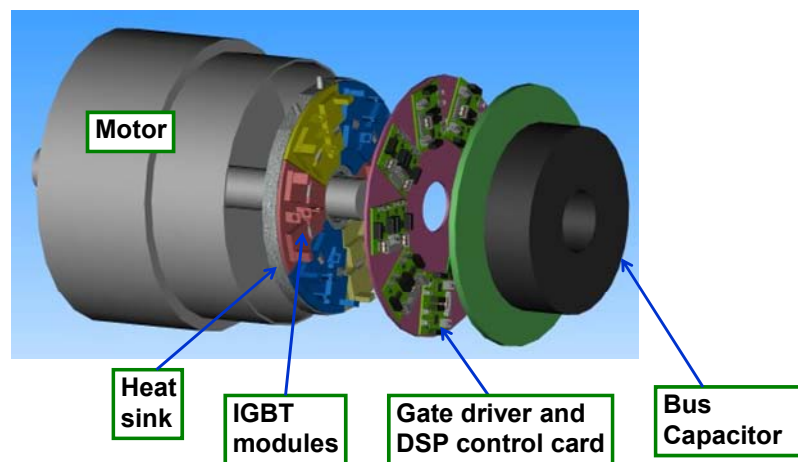


Fig. 11. Design concept for an integrated segmented inverter-motor.

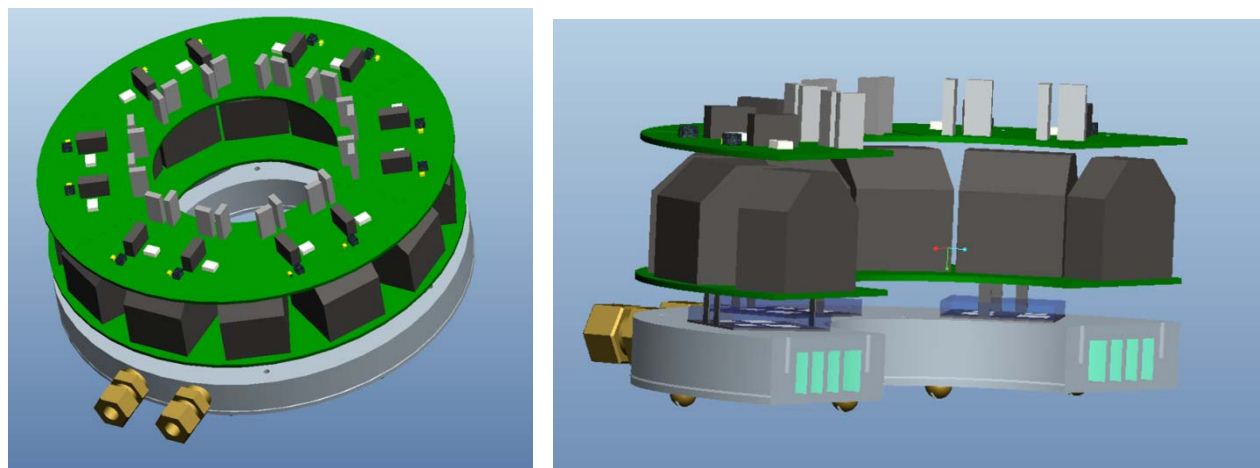


Fig. 12. Hardware design for a 55 kW ring-shaped segmented inverter that is suited to be integrated with typical cylindrical motor prototypes.

The IGBT modules (Fig. 13) were designed and packaged at the ORNL packaging laboratory using ABB IGBT and diode dies rated at 1,200 V and 75 A. The dies are soldered on a rectangular aluminum oxide double bond copper substrate with a footprint of 1.5 in. by 1.38 in. The modules use wire bonds for interconnections and are potted with a type of relatively high temperature silicone gel. A double side cooled, “wirebondless,” planar IGBT module is under development at ORNL and could be used in future prototype designs, which could substantially improve thermal performance and decrease parasitic resistance and inductance.

FEAs were carried out to evaluate the thermal performance of the toroidal heat exchanger. Inlet water flow was set to 0.2 m/s. Water properties were that of a 66°C water-ethylene glycol (WEG) mixture. Water flow was solved then coupled with the heat transfer. The cooling chamber material was aluminum, with a thermal conductivity (TC) of 160 W/(m/K). The silicon chip, with a TC of 163 W/(m/K), was mated to a copper plate with a copper TC of 400 W/(m/K). The chip-copper set was mated to Duralco thermally conductive adhesive with a TC of 5.8 W/(m/K). The chip was set to produce a total of 165 watts of waste heat. This waste heat was applied as a volumetric heat load. The WEG was set to an inlet temperature of 70°C. The FEA (Fig. 14) gave a maximum junction temperature of 110.7°C, well below the typical safe operation limit of 125°C. FEA results indicated that the toroidal heat exchanger design presents a relatively low pressure drop, with the bulk of it occurring at the narrow inlet and outlet fixtures. This provides an opportunity for further optimization of the cooling channels in terms of the number and width of the channels for higher coolant temperature operations. A feasibility study will be carried out once the FEA results are validated by prototype testing in FY 2012 to assess the possibility of using the motor coolant for the inverter with a heat-transfer-enhanced heat exchanger design, higher junction temperature silicon switches, and better power module packages.

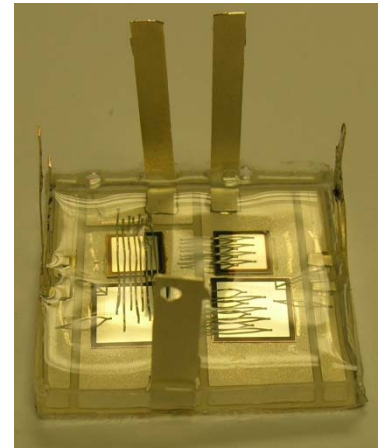


Fig. 13. ORNL packaged IGBT module.

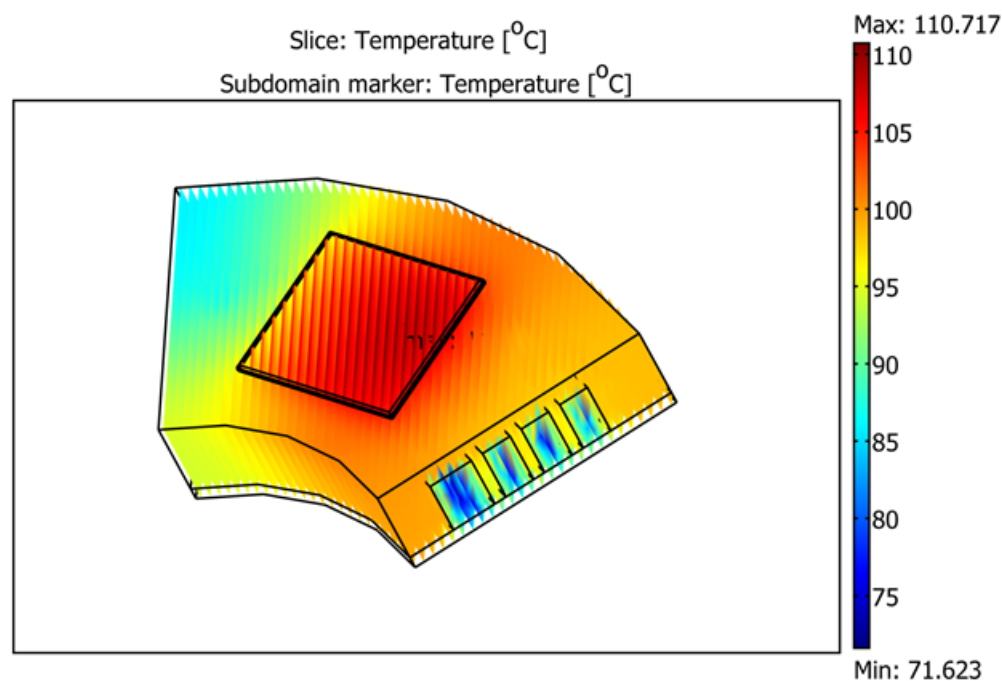


Fig. 14. FEA results for the toroidal heat exchanger.

After the FEA results showed satisfactory thermal performance with the toroidal heat exchanger design, a 55 kW ring-shaped segmented inverter was fabricated (Fig. 15). The use of heavy copper printed circuit board technology for interconnecting the power modules eliminates the need for bus bars and greatly simplifies the inverter assembly steps. Testing of the prototype is planned for FY2012.



Fig. 15. A 55 kW ring-shaped segmented inverter prototype that is suited to be integrated into typical cylindrical motors.

Conclusion

The 55 kW segmented inverter prototype with a 60% reduction of dc bus capacitor developed in FY 2010 was successfully tested with both R-L load and an induction motor at higher power levels and motor speeds. Test results show a significant reduction of 55% to 75% in capacitor ripple current, reduction of 70% to 90% in battery ripple current, and reduction of 60% to 80% in motor ripple current. The tests were then repeated with space vector based PWM schemes, and the same results were obtained. Moreover, with the segmented inverter a lower switching frequency can be used to increase the inverter efficiency while still maintaining a low level of harmonic components in motor currents, even for low inductance motors such as permanent magnet motors.

One of the objectives for the project is to demonstrate an integrated segmented inverter and motor traction drive system that can substantially reduce system cost, volume, and weight through a reduction of the dc bus capacitance by 60% and elimination of cable connections between the inverter and motor. Toward this goal, a 55 kW ring-shaped segmented inverter that is suited to be integrated into typical cylindrical motors was designed and fabricated. FEA results indicated satisfactory thermal performance with the toroidal heat exchanger design. Testing of the prototype is planned in FY 2012.

Patents

G. J. Su, *Electrical Motor/Generator Drive Apparatus and Method*, App. serial no. 12/887,110, filing date: September 21, 2010.

Publications

None.

References

1. U.S. Department of Energy, *Electrical and Electronics Technical Team Roadmap*, December 7, 2010, available online at http://www1.eere.energy.gov/vehiclesandfuels/about/partnerships/roadmaps-other_docs.html.
2. Electronic Concepts, Inc., *Electronic Concept Datasheets*, available online at <http://www.ecicaps.com/capacitors/features/ul3-series-unlytic-lt-sup-gt-reg-lt-sup-gt-ul3-ul31-ul32-ul34-ul35-series>.

2.6 High Dielectric Constant Capacitors for Power Electronic Systems

Principal Investigator: U. (Balu) Balachandran

Argonne National Laboratory

9700 S. Cass Avenue

Argonne, IL 60439

Voice: 630-252-4250; Fax: 630-252-3604; E-mail: balu@anl.gov

DOE Technology Development Managers: Susan A. Rogers and Steven Boyd

Voice: 202-586-8997; Fax: 202-586-1600; E-mail: Susan.Rogers@ee.doe.gov

Voice: 202-586-8967; Fax: 202-586-1600; E-mail: Steven.Boyd@ee.doe.gov

Objectives

- Develop ceramic dielectric films that have potential to reduce size, weight, and cost, concomitant with increased capacitance density and high temperature operation, for capacitors in electric drive vehicle inverters.
- Current DC bus capacitors occupy a significant fraction of volume ($\approx 35\%$) and weight ($\approx 25\%$) of the inverter module, cannot tolerate temperatures $>120^\circ\text{C}$, and suffer from poor packaging, and inadequate reliability.
- Traditional capacitor architectures with conventional dielectrics cannot adequately meet all of the performance goals for capacitance density, weight, volume, and cost.
- Meeting these goals requires a dielectric with high permittivity and breakdown field that tolerates operating at high temperature, is packaged in architecture with high volumetric efficiency, and exhibits benign failure features.

Approach

- Develop high-dielectric constant, high-temperature, low-cost ferroelectric $(\text{Pb},\text{La})(\text{Zr},\text{Ti})\text{O}_3$ (abbreviated as PLZT) dielectric films on base-metal foils (“film-on-foil”) that are either stacked on or embedded directly into the printed wire board (PWB).
- Stack high performance film-on-foils, produce prototype capacitor with termination, and characterize its properties.
- Use of base-metals and solution-based deposition techniques reduce the cost.
- Ferroelectrics possess high dielectric constants, breakdown fields, and insulation resistance. With their ability to withstand high temperatures, they can tolerate high ripple currents at under-the-hood conditions.
- Stacked and/or embedded capacitors significantly reduce component footprint, improve device performance, provide greater design flexibility, achieve high degree of volumetric efficiency with less weight, and offer an economic advantage.
- R&D efforts focus on examining the issues that underpin the performance of film-on-foil capacitors, establishing fabrication protocols that are commercially robust and economically viable.

Major Accomplishments

- Measured $k \approx 110$ & loss ≈ 0.004 (0.4%) at 300 V bias voltage ($\approx 100 \text{ V}/\mu\text{m}$ bias field) on a $\approx 3.0 \mu\text{m}$ -thick film (for comparison, k of polymer films are ≈ 6).
- Fabricated & measured a 20-mm diameter film-on-foil ($\approx 0.7 \mu\text{m}$ -thick PLZT) with capacitance of $\approx 3 \mu\text{F}$ @ 15 V/ μm bias.
- Built a $\approx 9 \mu\text{F}$ (4 μF @ 15 V) prototype capacitor by stacking four 1” x 1” film-on-foils (volumetric capacitance density of $\approx 4.8 \mu\text{F}/\text{cm}^3$).

- Measured energy density $\approx 85 \text{ J/cm}^3$ on a $\approx 3.0 \text{ }\mu\text{m}$ -thick PLZT film-on-foil at room temperature.
- Demonstrated film-on-foil PLZT dielectrics with dielectric breakdown field $> 2.6 \text{ MV/cm}$, and leakage current $< 10^{-8} \text{ A/cm}^2$ at room temperature.
- Demonstrated graceful failure mode by self-clearing method in single layer film-on-foil dielectrics.
- Fabricated and characterized PLZT dielectrics on nickel metal foils with self-clearing electrodes. The key to large-area yield is to electrically isolate the defect spots that compromise the integrity of the dielectric layer.
- Dielectric films are thermally cycled (about 1000 cycles) between -50°C and $+150^\circ\text{C}$ with no measurable degradation in k.
- Highly accelerated lifetime tests (HALT) were performed at elevated temperature and high field stress to predict the lifetime of film-on-foils.
- Presented program status and future direction to DOE APEEM projects kickoff, EE Tech Team, and Annual Merit Review meetings.
- Published three papers in peer reviewed international journals and three papers in conference proceedings.
- Filed three patent applications.
- Presented the results at seven scientific conferences.

Future Direction

- The primary emphasis of FY 2012's effort is toward advancing the proven laboratory scale film-on-foil technology and fabricating a high-voltage capable $\approx 10 \text{ }\mu\text{F}$ capacitor with termination. The effort will be focused on optimizing processing conditions investigated in FY11 to produce high-voltage capable film-on-foils. The R&D effort in FY11 has demonstrated that the properties of PLZT film-on-foils are suitable for power electronics operating at under-the-hood temperatures. Important processing issues such as substrate polishing, humidity control, organic removal, clean room processing, and rapid thermal annealing have been identified to make large area capacitors with the desired dielectric properties.
- Optimize processing conditions to produce high-voltage capable film-on-foils with uniform properties.
- Stack high-voltage capable film-on-foils and produce a $\approx 10 \text{ }\mu\text{F}$ capacitor with termination.
- In collaboration with Pennsylvania State University and Delphi Automotive Systems, characterize the dielectric properties & high temperature behavior of film-on-foils and the stacked, multilayer capacitor.
- Investigate electrode material and architecture to achieve benign failure in multilayers.
- Develop methodology for segmented electrodes to achieve benign failure at high voltages.
- Utilize thick film fabrication methodology (sol-gel with nano-particle seeds and aerosol deposition) to reduce the processing steps (i.e., capacitor cost).
- Fabricate films with improved breakdown strength and reduced loss via novel superstructure film growth.
- Develop new fabrication methodology (sol-gel with nano-particle seeds and aerosol deposition) to reduce the capacitor cost.
- Identify industrial partner to manufacture multilayer capacitors.

Technical Discussion

The overall project objective is to develop ceramic dielectric films that have potential to reduce size, weight, and cost, concomitant with increased capacitance density and high temperature operation, for capacitors in electric drive vehicle inverters. The purpose of this project is to build and test a prototype capacitor capable of meeting APEEM requirements. The performance of presently available capacitors

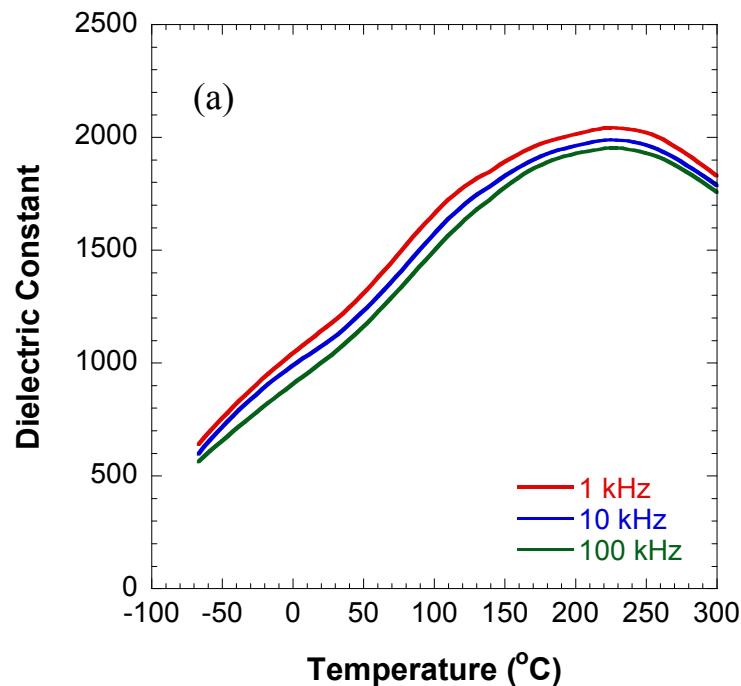
degrade rapidly with increasing temperature and they occupy significant fraction of the inverter volume ($\approx 35\%$), weight ($\approx 25\%$), and cost ($\approx 23\%$). The ceramic dielectric capacitor R&D program at Argonne National Laboratory (Argonne) addresses the technology gap in an innovative manner. We are developing high performance, low cost capacitors that are either stacked on or embedded directly into the printed wire board (PWB). In these “film-on-foil” capacitors, a base-metal foil (nickel or copper) is coated with a high permittivity ferroelectric material, PLZT, via a chemical solution deposition (CSD) technique. Ferroelectrics possess high permittivity, breakdown electric fields, and insulation resistance. They can withstand high temperatures such that high ripple currents can be tolerated at under-the-hood temperatures. Use of base-metals and solution-based deposition techniques reduce the cost. The stacked and embedded capacitors approaches significantly reduces component footprint, improves device performance, provides greater design flexibility, and offers an economic advantage for commercialization. This technology will achieve the high degree of packaging volumetric efficiency with less weight. Device reliability is improved because the number and size of interconnections are reduced. While this technology has primarily received attention for low voltage, high frequency decoupling capacitors, it can potentially be extended to the higher voltages of electric drive vehicle systems. The vision of embedded DC bus capacitors is compelling and offers US automotive companies a substantial technological advantage over their foreign counterparts. The bulky coke-can-like banks of capacitors can be replaced by lengths of capacitors tucked flat and neatly underneath the active components and bus structure. While embedding the film-on-foil capacitors into the PWB is the ultimate goal, the short-term practical approach is to target high voltage, high temperature, stacked capacitors for the inverter applications using film-on-foil dielectric layers. The short-term target will address the important issues, namely, weight, volume, and cost advantages of the film-on-foils compared to the conventional, bulky, wound polymer capacitors. Our R&D efforts focus on examining the issues that underpin the performance of film-on-foil capacitors, establishing fabrication protocols that are commercially robust and economically viable.

We have developed a core technology for fabricating CSD PLZT on Ni foils with LaNiO_3 (LNO) buffer layers. CSD solutions were synthesized at Argonne, and films were deposited by spin coating. Nickel substrates ($25 \text{ mm} \times 25 \text{ mm}$, 0.5 mm thickness, 99.8% pure, ESPI Metals) were polished to $1\text{-}\mu\text{m}$ finish ($\approx 0.4 \text{ mm}$ final thickness) and ultrasonically cleaned in acetone and methanol prior to coating. Stock solutions of 0.3M LaNiO_3 (LNO) and 0.5M $\text{Pb}_{0.92}\text{La}_{0.08}\text{Zr}_{0.52}\text{Ti}_{0.48}\text{O}_3$ (PLZT) were prepared by modified sol-gel synthesis using 2-methoxyethanol as the solvent. The detailed procedure is reported elsewhere [1-5]. The LNO solution was spin-coated onto the substrate at 3000 rpm for 30 sec , pyrolyzed at $\approx 450^\circ\text{C}$ for $5\text{-}10 \text{ min}$, and crystallized at $\approx 650^\circ\text{C}$ for $2\text{-}5 \text{ min}$. This process was repeated five times to build the desired thickness with a final annealing at $\approx 650^\circ\text{C}$ for 20 min . The PLZT stock solution was spin-coated onto the LNO-buffered substrate at 3000 rpm for 30 sec . Films were then pyrolyzed at $\approx 450^\circ\text{C}$ for 10 min and crystallized at $\approx 650^\circ\text{C}$ for $2\text{-}5 \text{ min}$, followed by a final annealing at $\approx 650^\circ\text{C}$ for 20 min after repeating the coating steps to build up layers of sufficient thickness. By this process, we have fabricated PLZT films with thicknesses up to $\approx 3 \mu\text{m}$. Platinum top electrodes were then deposited by electron beam evaporation using a shadow mask. These electrodes had diameters of $250 \mu\text{m}$, $750 \mu\text{m}$, and 20 mm and thickness of $\approx 100 \text{ nm}$. Films with top electrodes were annealed at $\approx 450^\circ\text{C}$ in air for 2 min for electrode conditioning. A Signatone QuieTemp® probe system with heatable vacuum chuck (Lucas Signatone Corp., Gilroy, CA) was used for electrical characterization. For the electrical measurements, the Pt/PLZT/LNO/Ni heterostructure was contacted by a Pt top electrode pad with one probe and the substrate (bottom electrode) with the other. A positive applied voltage corresponds to the configuration where the top electrode is at a higher potential than the bottom electrode. An Agilent E4980A Precision LCR Meter measured the capacitance and dissipation factor under applied bias field. A Radiant Technologies' Precision Premier II tester measured the hysteresis loops. The capacitor samples were immersed in Fluka silicone oil (Sigma-Aldrich) during high-field hysteresis loops and dielectric breakdown measurements. A Keithley 237 high-voltage source meter measured the current-voltage

characteristics. The leakage current density was determined by fitting the current density relaxation data to the Curie-von Schweidler equation [6].

The PLZT films grown on LNO-buffered Ni foils were phase pure with no preferred crystallographic orientation as shown by X-ray diffraction, and no crack or delamination was observed from SEM [1]. Average grain size of ≈ 60 nm was determined from SEM and confirmed by AFM [4]. The use of LNO buffer allows the film-on-foils to be processed in air without the formation of a parasitic interfacial nickel oxide layer. The LNO also compensates for the roughness of the Ni foil and provides a smooth interface for the PLZT films, resulting in higher breakdown strengths. In addition, the LNO buffer helps to reduce the compressive strain in the PLZT films deposited on nickel substrates due to the thermal expansion coefficient mismatch between PLZT and metal foils [7].

Fig. 1 shows the dielectric constant and loss measured as a function of temperature measured at three different frequencies on a ≈ 3 - μm -thick PLZT deposited on a 0.4 - μm -thick LNO buffered Ni substrate coated with Pt top electrodes. At 1 kHz, we measured dielectric constant of 700 and dielectric loss of 0.04 at -50°C , dielectric constant of 1150 and dielectric loss of ≈ 0.05 at room temperature, and dielectric constant of 1900 and dielectric loss of ≈ 0.03 at 150°C , respectively. Under zero bias, dielectric constant (hence the capacitance) increases and dielectric loss decreases with increase in temperature up to 200°C . Increase in capacitance lowers the ESR and the ripple current capability of the capacitor improves with increase in temperature. This improvement in performance is desired for DC bus capacitors in high temperature inverters for electric drive vehicles.



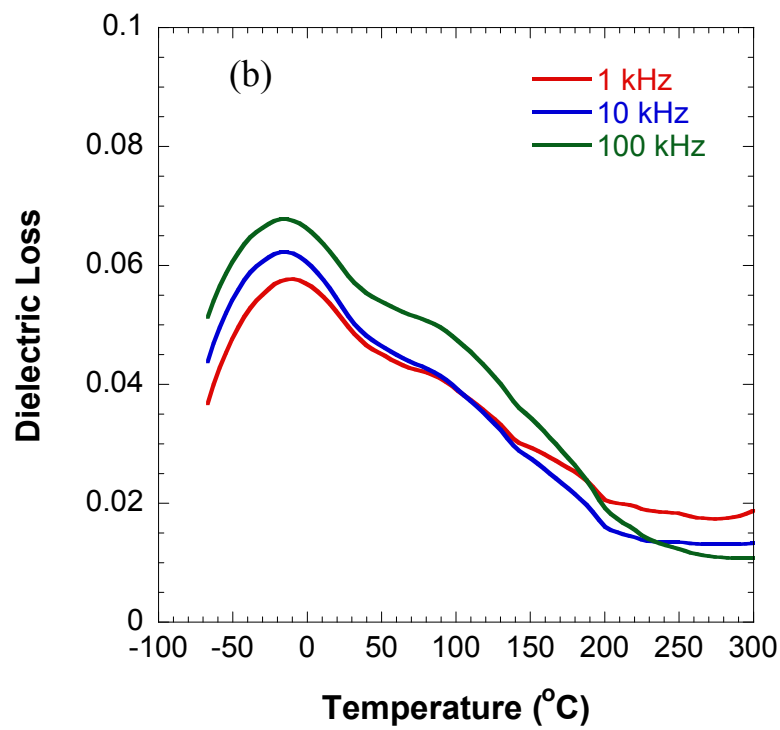
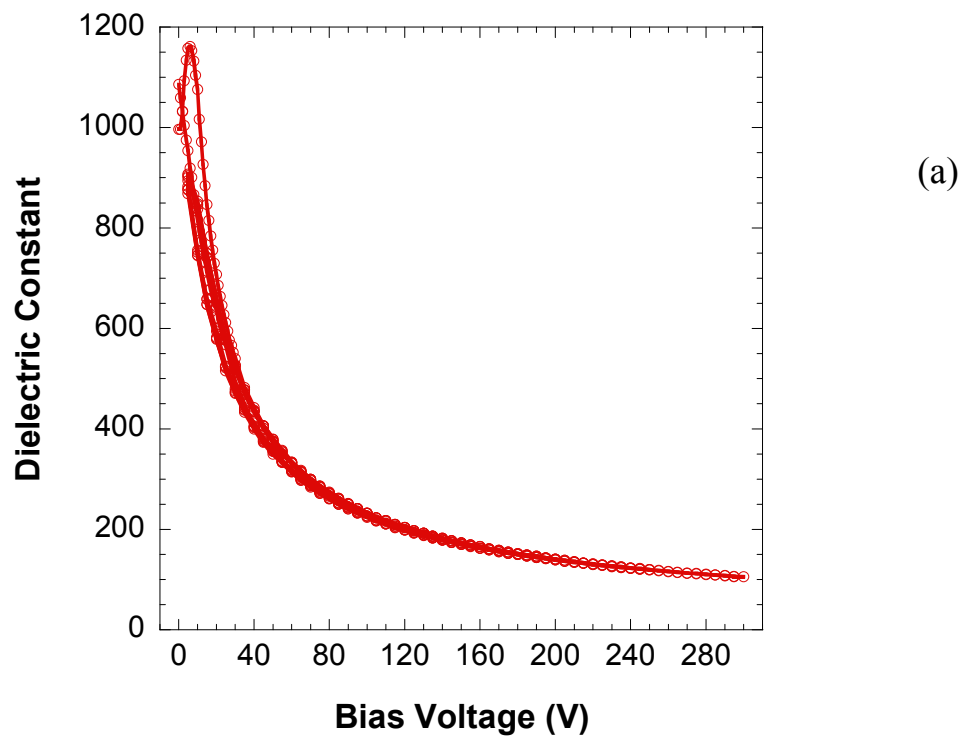


Fig. 1. Dielectric constant (a) and loss (b) measured at various frequencies as a function of temperature.



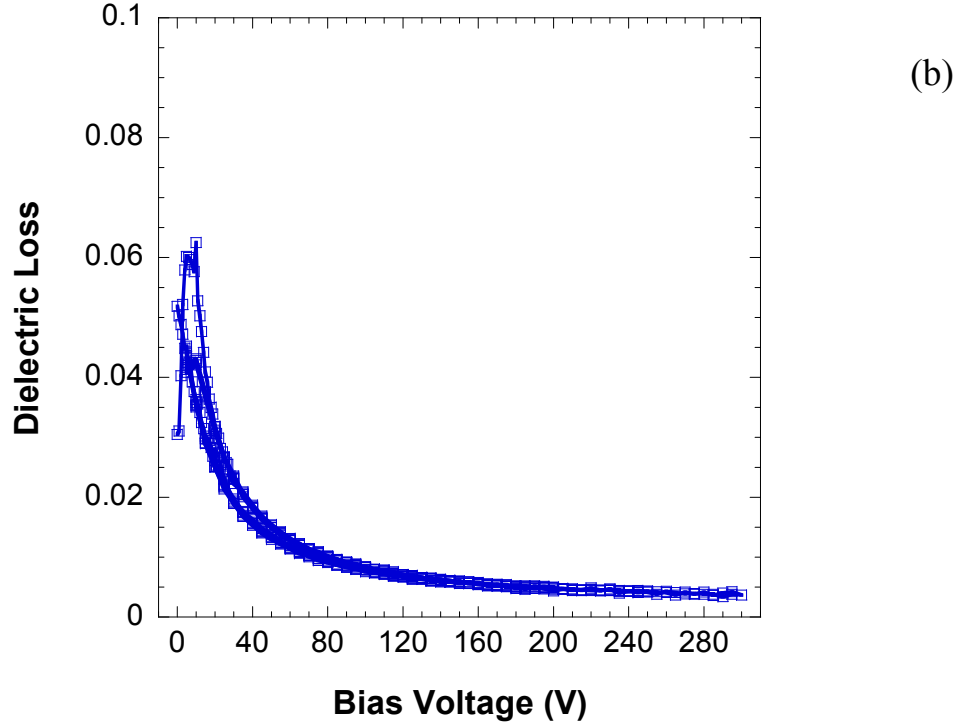


Fig. 2. Dielectric constant (a) and loss (b) measured at 10 kHz as a function of bias voltage.

Fig. 2 shows the dielectric constant and dielectric loss measured at room temperature and 10 kHz as a function of applied bias voltages from 0 to 300 V. Again this measurement was conducted on a $\approx 3\text{-}\mu\text{m}$ -thick PLZT deposited on a $0.4\text{-}\mu\text{m}$ -thick LNO buffered Ni substrate coated with Pt top electrode. Dielectric constant and loss decreases with increase in applied bias field. We measured dielectric constant of ≈ 230 and loss of ≈ 0.008 (0.8%) at 100 V bias, dielectric constant of ≈ 140 and loss of ≈ 0.005 at 200 V bias, dielectric constant of ≈ 110 and loss of ≈ 0.004 at 300 V bias on this $\approx 3\text{-}\mu\text{m}$ -thick PLZT film-on-foil.

Fig. 3 shows the dielectric constant and loss measured on a $\approx 3\text{-}\mu\text{m}$ -thick PLZT film-on-foil capacitor at 10 kHz as a function of temperature under bias voltages of 100 V, 200 V, and 300 V. Dielectric constant increases with increasing temperature. We measured low dielectric loss ($<1\%$) at temperature between room temperature and 150°C with applied bias voltage greater than 100 V. Low dielectric loss translates to low ESR which is desirable for power electronics applications.

Fig. 4 shows P-E hysteresis loops measured on a $\approx 3\text{-}\mu\text{m}$ -thick PLZT film-on-foil at temperatures from 20 to 150°C . Well defined ferroelectric loops were observed with remanent polarization (P_r) of $\approx 2.7 \times 10^{-5} \text{ C/cm}^2$ and coercive electric field (E_c) of $\approx 4.2 \times 10^4 \text{ V/cm}$. We observed slim PE loops at all temperatures, indicative of low energy loss. Low energy loss is desirable for energy storage/conversion applications.

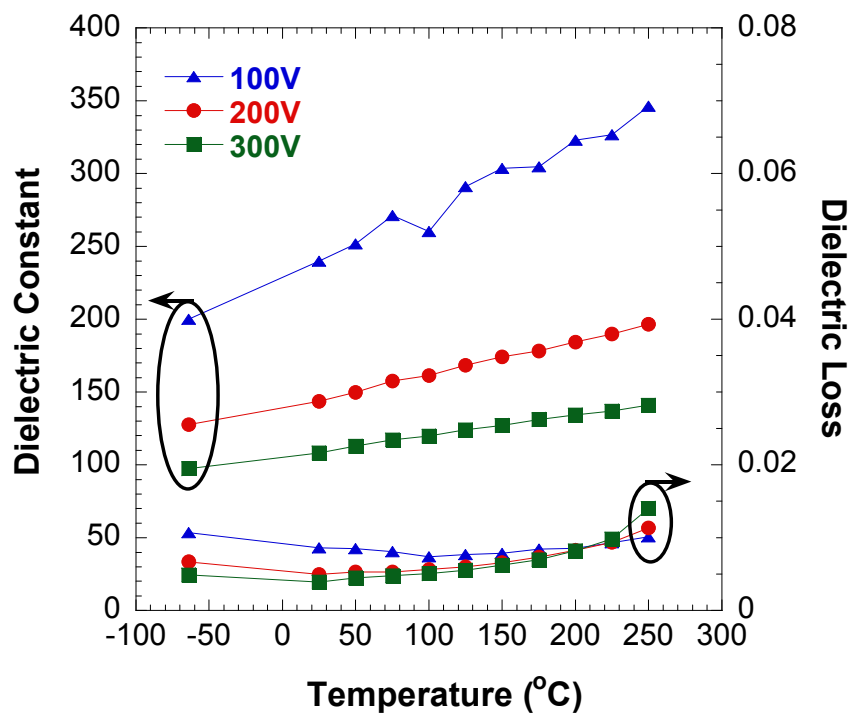


Fig. 3. Dielectric constant and loss as a function of temperature measured under high bias voltages.

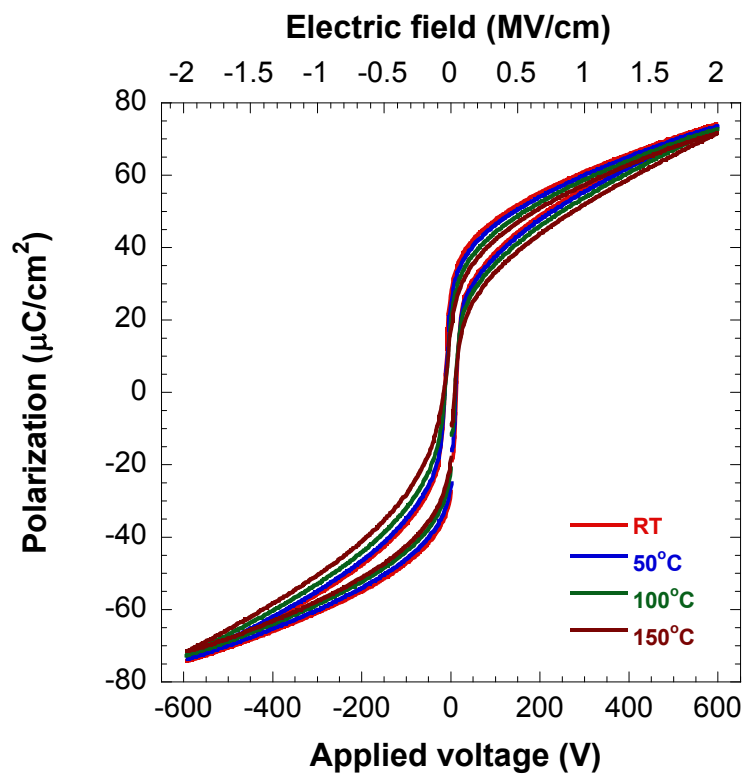


Fig. 4. P-E hysteresis loops measured on a $\approx 3\text{-}\mu\text{m}$ -thick PLZT film-on-foil at various temperatures.

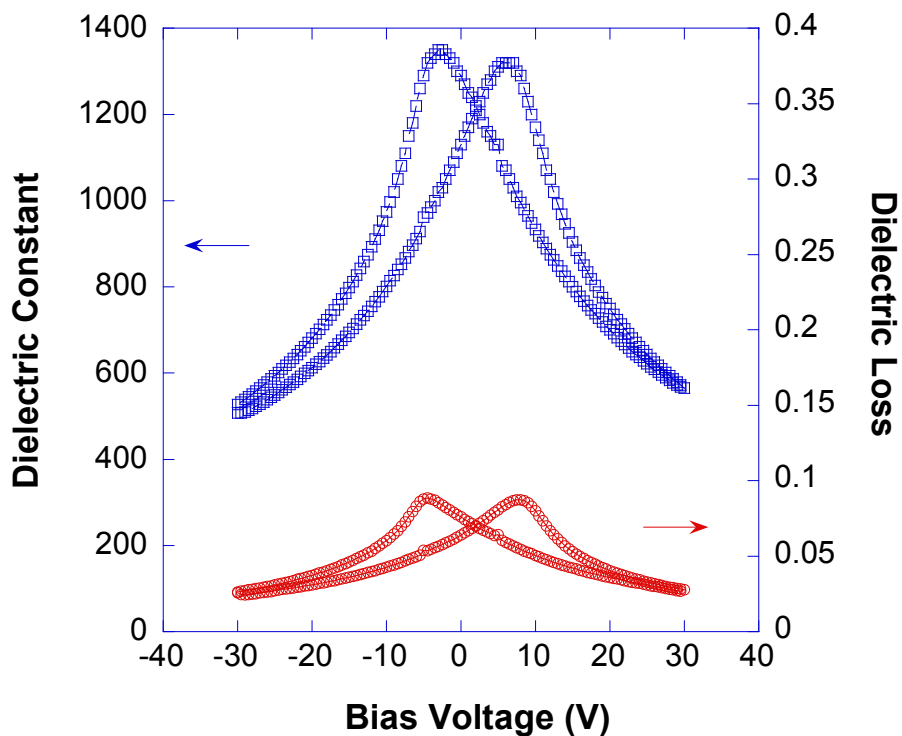


Fig. 5. Dielectric properties of a 20-mm-diameter, $\approx 3\text{-}\mu\text{m}$ -thick PLZT film-on-foil measured at room as a function of bias voltage.

Fig. 5 shows dielectric constant and dielectric loss of a large area (20-mm-diameter), $\approx 3\text{-}\mu\text{m}$ -thick PLZT on Ni foil measured as a function of applied bias. The $\approx 200\text{-nm}$ -thick and 20-mm-diameter Pt top electrode was deposited on PLZT/LNO/Ni by electron-beam evaporation. Sample was annealed at $\approx 450^\circ\text{C}$ for 2 minutes for electrode conditioning before the dielectric property measurement. At room temperature, we measured dielectric constant ≈ 1300 and dielectric loss ≈ 0.08 under zero-bias field and dielectric constant ≈ 500 and dielectric loss ≈ 0.025 under 30 V bias, respectively, on this large area film-on-foil.

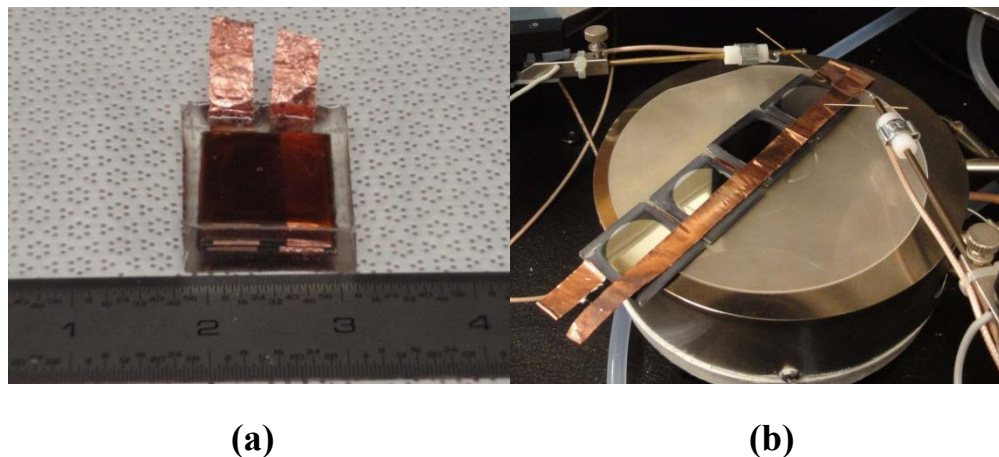


Fig. 6. Photos of (a) a stacked ceramic film capacitor made using four PLZT film-on-foils and (b) four film-on-foils interconnected in parallel on a testing stage.

Fig. 6a shows a photo of a prototype stacked film-on-foil capacitor with electrical leads connected. This capacitor was made using four film-on-foils, as shown in Fig. 6b, each of which has $\approx 1 \mu\text{m}$ thick PLZT with a 20-mm-diameter top electrode. They were interconnected electrically via conductive copper ribbons and then folded before being encapsulated in epoxy. This stacked capacitor has capacitance of $\approx 8.5 \mu\text{F}$ at room temperature and 1 kHz under zero bias. Capacitance density of this multilayer capacitor is $\approx 4.8 \mu\text{F}/\text{cm}^3$.

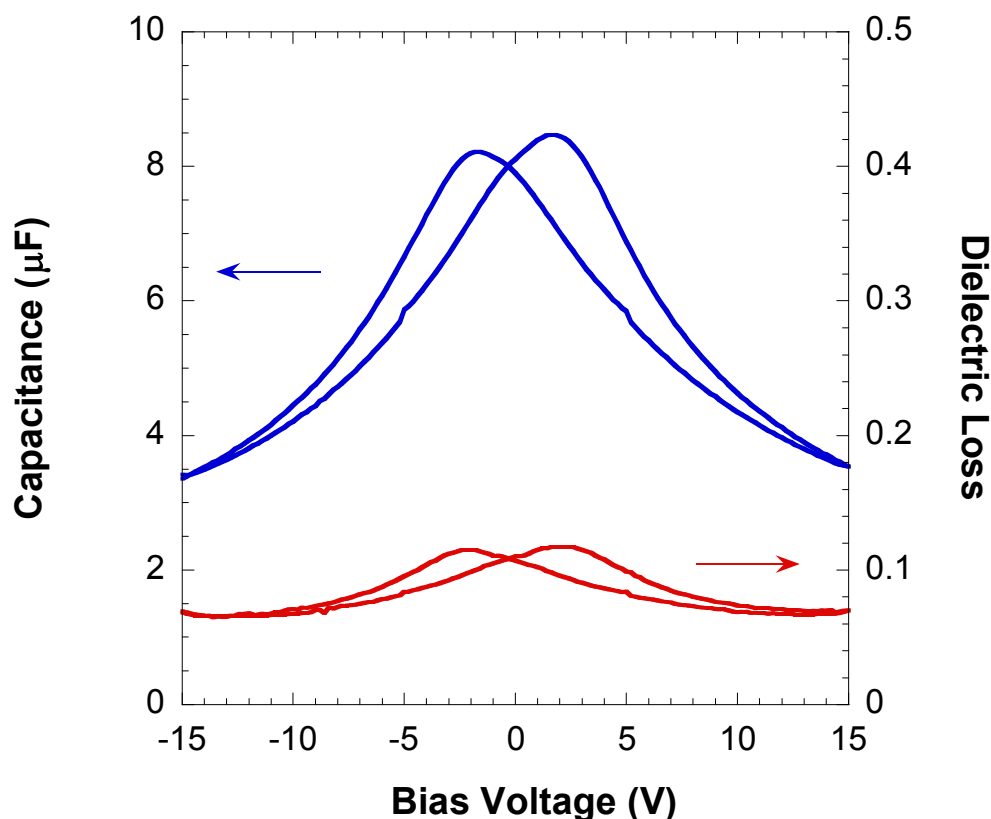


Fig. 7. Capacitance and dielectric loss of a stacked ceramic film capacitor measured at room temperature and 1 kHz under applied bias.

Fig. 7 shows capacitance and dielectric loss measured at room temperature and 1 kHz on this stacked capacitor as a function of applied bias. Butterfly shaped curves are indicative of ferroelectric characteristic of the stacked capacitor. Capacitance of $\approx 3.5 \mu\text{F}$ and dielectric loss of ≈ 0.07 was measured under 15 V applied bias at room temperature and 1 kHz.

Fig. 8 shows frequency dependent capacitance and dielectric loss of a stacked ceramic film capacitor measured at room temperature and 1 kHz. Capacitance (and hence dielectric constant) decrease with increasing frequency; while dielectric loss is nearly independent of measuring frequency under 1 kHz. At 10 kHz, capacitance of $\approx 6 \mu\text{F}$ and dielectric loss of ≈ 0.5 was measured.

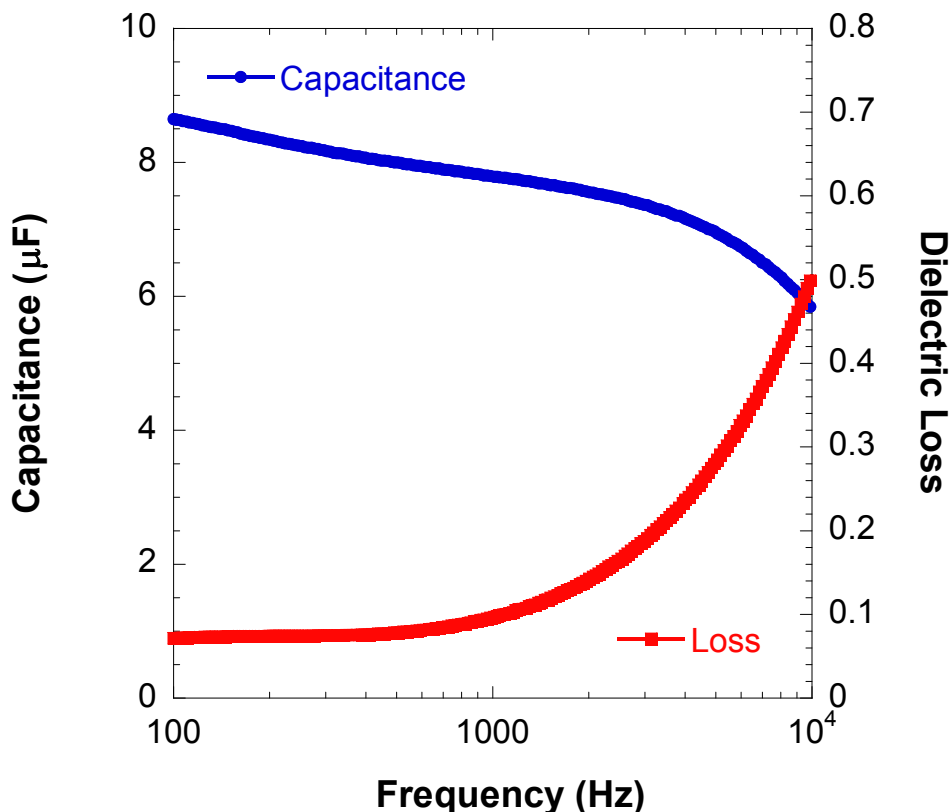


Fig. 8. Frequency dependent capacitance and dielectric loss of a stacked ceramic film capacitor measured at room temperature.

Conclusion

We have developed a core technology for fabricating high capacitance density ceramic PLZT films on base metal foils, called “film-on-foil” technology. PLZT film-on-foils have been fabricated with LNO buffer layers atop Ni foils, allowing the capacitors to be processed in air. At 1 kHz and zero bias, we measured dielectric constant of 700 and dielectric loss of 0.04 at -50°C , dielectric constant of 1150 and dielectric loss of ≈ 0.05 at room temperature, and dielectric constant of 1900 and dielectric loss of ≈ 0.03 at 150°C , respectively. Film-on-foil samples were characterized under high bias fields. We measured dielectric constant of ≈ 230 and loss of ≈ 0.008 (0.8%) at 100 V bias, dielectric constant of ≈ 140 and loss of ≈ 0.005 (0.5%) at 200 V bias, dielectric constant of ≈ 110 and loss of ≈ 0.004 (0.4%) at 300 V bias on a $\approx 3\text{-}\mu\text{m}$ -thick PLZT film-on-foil sample. A prototype stacked capacitor with electrical leads was fabricated using four film-on-foil capacitors. This stacked capacitor measured capacitance of $\approx 8.5\text{ }\mu\text{F}$ (unbiased condition) at room temperature (capacitance density of $\approx 4.8\text{ }\mu\text{F}/\text{cm}^3$). The properties measured show that these ceramic film capacitors have potential to meet the APEEM goals. Our results and the research plans were presented at the VT program’s APEEM project kickoff, Annual Merit and Peer Review, and EE Tech Team meetings. Argonne’s ceramic film capacitor technology was selected as a winner of 2011 R&D 100 Award. The primary emphasis of FY12’s effort is toward advancing the proven laboratory scale film-on-foil technology towards fabricating a $\approx 10\text{ }\mu\text{F}$, high voltage capable capacitor with termination.

Publications

We have over 50 publications and presentations, and few selected recent publications are listed below.

1. B. Ma, S. Tong, M. Narayanan, S. Liu, S. Chao, U. Balachandran, *Fabrication and dielectric property of ferroelectric PLZT films grown on metal foils*, Mater. Res. Bull., 46, 1124, 2011.
2. S. Tong, M. Narayanan, B. Ma, R. E. Koritala, S. Liu, U. Balachandran, D. Shi, *Effect of dead layer and strain on the diffuse phase transition of PLZT relaxor thin films*, Acta Mater., 59, 1309, 2011.
3. M. Narayanan, S. Tong, R. E. Koritala, B. Ma, V. Pol, U. Balachandran, *Sol-Gel Synthesis of High-Quality SrRuO₃ Thin-Film Electrodes Suppressing the Formation of Detrimental RuO₂ and the Dielectric Properties of Integrated Lead Lanthanum Zirconate Titanate Films*, Chem. Mater., 23, 106, 2011.
4. B. Ma, M. Narayanan, S. Liu, S. Chao, U. Balachandran, *Ferroelectric PLZT films grown on metal foils for power electronic applications*, proceedings of the 20th IEEE International Symposium on Applications of Ferroelectrics and International Symposium of Piezoresponse Force and Microscopy & Nanoscale Phenomena in Polar Materials, Vancouver, Canada, Jul. 24 - 27, 2011
5. U. Balachandran, M. Narayanan, B. Ma, *Ferroelectric films on metal foils for power electronics in electric drive vehicles*, presentation at the 9th International Meeting of Pacific Rim Ceramic Societies, Cairns, Australia, Jul. 10, 2011.
6. U. Balachandran, M. Narayanan, B. Ma, *Ferroelectric film capacitors with high energy density for electric drive vehicles*, presentation at Conference on Materials for Advanced Technologies, Suntec, Singapore, Jun. 26 - Jul. 1, 2011.
7. U. Balachandran, B. Ma, M. Narayanan, S. Liu, S. Chao, S. Tong, S. E. Dorris, *High-dielectric-constant capacitors for power electronic systems*, presentation at the 2011 DOE Vehicle Technologies Program Annual Merit Review & Peer Evaluation Meeting, Washington, DC, May 9 - 13, 2011.
8. M. Narayanan, B. Ma, R. Koritala, S. Tong, U. Balachandran, *Chemical solution deposition of high-quality SrRuO₃ thin film electrodes and the dielectric properties of integrated lead lanthanum zirconate titanate films*, proceedings of the 7th International Conference and Exhibition on Ceramic Interconnect and Ceramic Microsystems Technologies, San Diego, CA, Apr. 5-7, 2011.
9. B. Ma, M. Narayanan, S. Tong, U. Balachandran, *Fabrication and Characterization of Ferroelectric PLZT Film Capacitors on Metallic Substrates*, J. Mater. Sci., 45, 152, 2010.
10. U. Balachandran, D. K. Kwon, M. Narayanan, B. Ma, *Development of PLZT Dielectrics on Base-Metal Foils for Embedded Capacitors*, J. European Cer. Soc., 30, 365, 2010.
11. B. Ma, M. Narayanan, U. Balachandran, *High-dielectric constant PLZT films on metal foils for embedded passives*, proceedings of the 43rd International Symposium on Microelectronics, Research Triangle, NC, Oct. 31 - Nov. 4, 2010
12. M. Narayanan, B. Ma, and U. Balachandran, *Improved Dielectric Properties of Lead Lanthanum Zirconate Titanate Thin Films on Copper Substrates*, Mater. Lett., 64, 22, 2010.
13. M. Narayanan, B. Ma, U. Balachandran, and W. Li, *Dielectric Spectroscopy of Pb_{0.92}La_{0.08}Zr_{0.52}Ti_{0.48}O₃ Films on Hastelloy Substrates with and without LaNiO₃ Buffer Layers*, J. Appl. Phys. Lett., 107, 024103, 2010.
14. B. Ma, D. K. Kwon, M. Narayanan, U. Balachandran, *Dielectric Properties and Energy Storage Capability of Antiferroelectric Pb_{0.92}La_{0.08}Zr_{0.95}Ti_{0.05}O₃ Film-on-Foil Capacitors*, J. Mater. Res., 24, 2993, 2009.

15. B. Ma, D. K. Kwon, M. Narayanan, and U. Balachandran, J. Electroceram., *Chemical Solution Deposition of Ferroelectric Lead Lanthanum Zirconate Titanate Films on Base-Metal Foils*, 22, 383, 2009.
16. B. Ma, D. K. Kwon, M. Narayanan, U. Balachandran, *Fabrication of Antiferroelectric PLZT Films on Metal Foils*, Mater. Res. Bull., 44, 11, 2009.
17. B. Ma, M. Narayanan, U. Balachandran, *Dielectric Strength and Reliability of Ferroelectric PLZT Films Deposited on Nickel Substrates*, Mater. Lett., 63, 1353, 2009.
18. B. Ma, D. K. Kwon, M. Narayanan, and U. Balachandran, *Leakage Current Characteristics and Dielectric Breakdown in Antiferroelectric $Pb_{0.92}La_{0.08}Zr_{0.95}Ti_{0.05}O_3$ Film Capacitors Grown on Metal Foils*, J. Phys D: Appl. Phys., 41, 205003, 2008.
19. B. Ma, D. K. Kwon, M. Narayanan, and U. Balachandran, *Dielectric Properties of PLZT Film-on-Foil Capacitors*, Mater. Lett., 62, 3573, 2008.
20. M. Narayanan, D. K. Kwon, B. Ma, U. Balachandran, *Deposition of Sol-gel Derived PLZT Thin Films on Copper Substrate*, Appl. Phys. Lett., 92, 252905, 2008.

References

1. B. Ma, D.-K. Kwon, M. Narayanan, and U. Balachandran, J. Electroceram. **22**, 383-389, (2009).
2. U. Balachandran, D. K. Kwon, M. Narayanan, B. Ma, *J. European Cer. Soc.*, 30, 365, 2010.
3. D.Y. Kaufman, S. Saha, and K. Uprety, Proc. 12th US-Japan Seminar on Dielectric and Piezoelectric Ceramics, Annapolis, MD, 305-308 (2005).
4. B. Ma, D.-K. Kwon, M. Narayanan, and U. Balachandran, Mater. Lett. **62**, 3573-3575, (2008).
5. Q. Zou, H. E. Ruda, and B. G. Yacobi, Appl. Phys. Lett. **78**, 1282-1285, (2001).
6. K. Jonscher, *Dielectric Relaxation in Solids*, Chelsea Dielectrics Press, London (1983).
7. J. Chen, L. He, L. Che, and Z. Meng, Thin Solid Films **515**, 2398-2402, (2006).

Patents

1. B. Ma, M. Narayanan, S. E. Dorris, and U. Balachandran, *Method for Fabrication of Ceramic Dielectric Films on Copper Foils*, Patent Application US 2010/0302706A1, published Dec. 2, 2010.

Awards

1. The ceramic film capacitor technology developed at Argonne National Laboratory, *Advanced Ceramic Film Capacitor for Power Electronics*, received the 2011 R&D 100 Award.

2.7 Glass Ceramic Dielectrics for DC Bus Capacitors

Principal Investigators: Michael Lanagan and Carlo Pantano

Penn State University, 278 Materials Research Laboratory University Park, PA 16802

Voice: 814-865-6992 ; Fax: 814-865-2326; E-mail: mlanagan@psu.edu

DOE Technology Development Manager: Susan A. Rogers

Voice: 202-586-8997; Fax: 202-586-1600; E-mail: Susan.Rogers@ee.doe.gov

Objectives

Commercial capacitors for hybrid electric vehicles (HEVs) and plug-in hybrid electric vehicles (PHEVs) do not meet US automaker's specifications for high temperature operation, cost and reliability. The objectives of this project are to develop high temperature capacitors that go beyond what is commercially available and to minimize the need for costly coolant systems within the HEVs and PHEVs. Ceramic capacitors have excellent high temperature performance and meet a majority of HEV and PHEV specifications for power electronic converters; however, low reliability is a primary impediment to their use in hybrid vehicles. The goal of this project is to produce reliable glass capacitors without compromising the energy density (related to capacitor volumetric efficiency). Specific goals include:

- Characterize fundamental relationships between conductor thickness and dielectric breakdown, which is important for glass capacitor reliability.
- Collaborate with Argonne National Laboratory to understand coated conductor breakdown strength and reliability.
- Scale-up glass capacitor technology by coupling with glass manufacturers and capacitor companies.

Approach

- Adapt low-cost production methods and materials, already developed for flat panel displays, to high temperature capacitors.
- Characterize glass materials at high temperature to predict reliability.
- Develop self-healing modes in glass capacitors to avoid catastrophic failure.
- Manufacture prototype capacitors in collaboration with industrial partners.

Major Accomplishments

- Demonstrated that flat panel display glass can operate as a capacitor up to temperatures of 250 °C.
- Invented self-healing in a glass capacitor.
- Fabricated and tested the first prototype capacitor made by winding glass ribbon.

Future Direction

- Scale-up glass capacitors to 10 μF 1,000 V levels - large-scale capacitors that are based on flat-panel display glass will require a multilayer construction. This project will develop robust terminations for multilayer glass capacitors.
- Penn State has been working with flat-panel display manufacturers to reduce the glass layer thickness. Currently 50 μm thick glass sheets are available and 10 μm thick sheets have been fabricated at the laboratory scale. The final design for a high-temperature DC link capacitor will require glass layer thicknesses between 5 and 10 μm .

Technical Discussion

There is general agreement within the automotive and power electronic communities that revolutionary approaches, drawing on diverse disciplines, will be necessary to develop the next generation of power systems for electric vehicles. New active and passive components need to be manufactured which can operate at high temperature for long periods of time. In addition, component miniaturization is important to reduce the total volume of the power electronic circuitry on board an electric vehicle. A summary of the results of this study is shown in Figure 1.

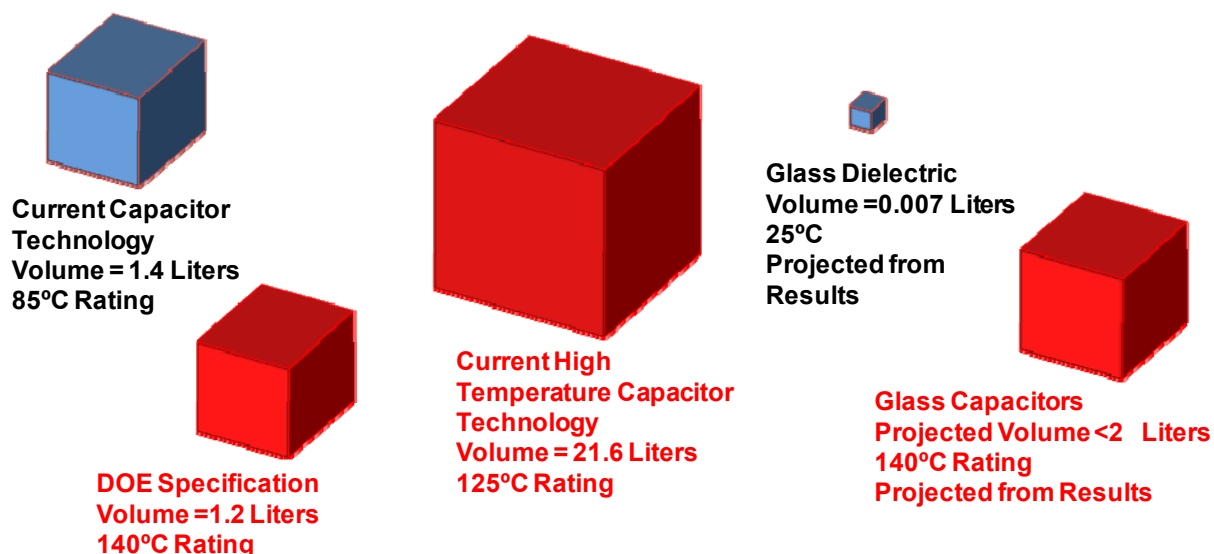


Figure 1. Volumetric comparison between DOE capacitor specifications, commercial capacitors and the projected capacitor volumes from the research at Penn State. All volumes shown are for a 1000 μ F 1000 V capacitor.

The DOE specifications (Figure 1 lower left corner) were derived from discussions with the EE Tech Team and component manufacturers. Presently, high-temperature film capacitors (middle of Figure 1) have 18 times the volume of the DOE specification. The glass dielectrics explored in this study have the potential to operate above 140°C and the volume is much smaller than commercial high temperature capacitors (Figure 1 right side).

Thin glass sheet production has grown substantially because of strong demand from the flat panel display industry and a large investment in the development of new glass fabrication methods. Glass manufacturers have been able to develop a continuous sheet casting process with sufficient control to make significant lengths of thin flexible sheet. Within the past year, Penn State has collaborated with NEG Corporation to manufacture the first wound glass capacitor (Figure 2). It is now possible to manufacture glass capacitors in a similar manner to polymer film capacitors that are presently used in hybrid electric vehicles. The manufacturing process will be a major part of the component cost. This is a major step in demonstrating that flat panel display glass is a viable material for high temperature DC bus capacitors for electric vehicles. The fabrication process for the coiled glass capacitors are shown in Table 1, which outlined the series of stages from the material to the final device.

Figure 2: (a) 3 meters of glass ribbon wound around a 10 cm diameter cylinder. The glass is co-wound with a mylar sheet to avoid electrical shorting between the electrodes. (b) Demonstrating the mechanical flexibility and strength of glass ribbon that was wound to make a capacitor. A sprayed silver electrode has been deposited on both sides of the glass before winding.

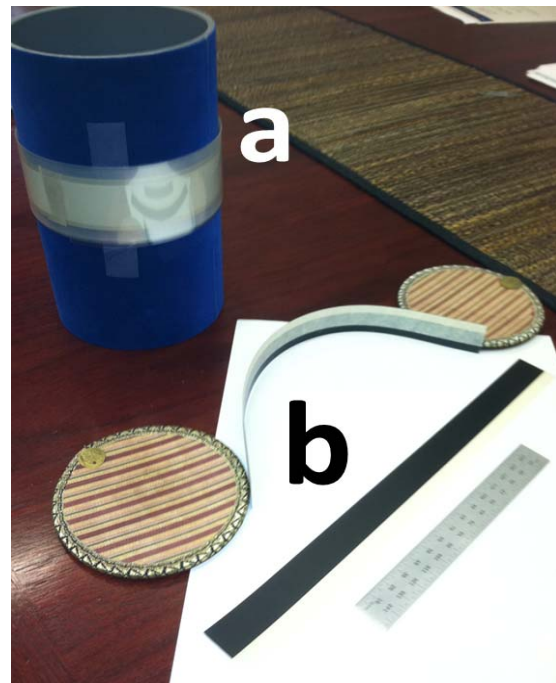


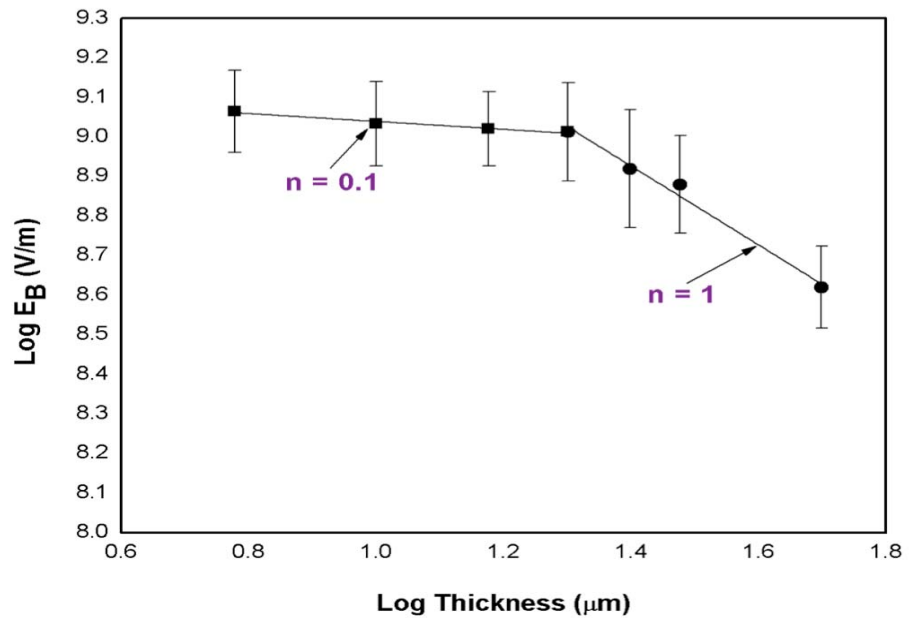
Table 1. Fabrication Process for Wound Glass Capacitors

| | |
|-------------------|---|
| Draw Glass Ribbon | <ul style="list-style-type: none"> Thin glass ribbon is manufactured by a down-draw process and redrawn to reduce the ribbon thickness. The key challenge is to produce glass ribbon from 50μm to 10 μm. |
| Deposit Electrode | <ul style="list-style-type: none"> Electrodes are placed on top and bottom surfaces of glass ribbon and candidate electrodes include copper foil, aluminum and silver film. Equivalent Series Resistance (ESR) and self-healing mechanisms are controlled by the electrode properties. |
| Wind glass | <ul style="list-style-type: none"> Glass ribbon up to a 100 meters in length has been produced by glass manufacturers, which will need to be coiled into a capacitor configuration. Coil diameters of 10 cm have been demonstrated for 50μm thick ribbon. Substantially smaller diameters (1 cm) are possible with thinner glass. |
| Package | <ul style="list-style-type: none"> Packaging includes end termination, lead attachment and encapsulation. Thermal, mechanical and electrical performance must be considered in package design. |
| Test | <ul style="list-style-type: none"> The capacitance and loss is characterized as a function of frequency, temperature and AC voltage strength. Reliability tests to predict capacitor performance under operating conditions. |

In addition to the capacitor scale-up, the fundamental electrical properties of the glass and electrodes were explored. The dielectric breakdown statistics of alkali-free glass were determined for thinned substrates with electrodes having controlled morphology and continuity. The characteristic electrical breakdown field strength increased from 400 MV/m to 1100 MV/m as the glass substrate thickness decreased from 58 μm to 5 μm , respectively. This translates to a breakdown voltage of 4,000 V for a 10 μm thick glass sheet. These breakdown strengths are among the highest ever reported for a material. Surface roughness RMS values of as-drawn and etched glass substrates are in the 0.9-1.8 nm range, which are small in comparison to the glass substrate thickness. Glass etching did not have significant effect on the dielectric breakdown strength. Dielectric breakdown strength was also independent of sputtered electrode composition (Au, Pt); however, electrode thickness played an important role in controlling the breakdown process. The Au electrode morphology transitioned from a continuous sheet for thicker electrodes to discrete islands for very thin electrodes (< 2 nm thick) that limit electrode continuity. The thin electrode morphology provides a unique opportunity to explore a high dielectric breakdown strength regime (1100 MV/m) in glasses with Weibull modulus values approaching 100. The high Weibull modulus is important for scale-up.

Thickness-dependent dielectric breakdown strength of OA-10G glass (commercial glass from NEG) is shown in Figure 3. There is a reduction of the breakdown strength as thickness increases, and this behavior follows power law dependence, similar to the breakdown behavior for another alkali-free glass system [1]. The two regimes corresponding to $n = 0.1$ and $n = 1$ indicates two different breakdown mechanisms with a transition around 20 μm thick glass. The highest characteristic breakdown field (933 MV/m) was found for 5- μm thick glass, which corresponds to an energy density of 20 J/cm³.

Figure 3: Breakdown strength of as-drawn glass with gold (20nm) and platinum (10, 20 and 50nm) electrodes as a function of glass thickness. The error bars denote the standard deviation of 1σ (Weibull distribution approximates as a Gaussian distribution for a Weibull modulus exceeding 3) in this figure.



The breakdown strength of the glass samples with large area (900mm²) electrodes is shown in Figure 4, in which the probe is moved to a fresh spot after each breakdown event. The breakdown strength is very uniform for the thin electrodes. This is an important point because the electrode thickness needs to be optimized. Thin electrodes are required for high reliability and thick electrodes for low equivalent series resistance (ESR). Atomic Force Microscopy (AFM) results in Figure 5 show that the 2-nm thick sputtered gold film has a microstructure that is comprised of isolated sub-10 nm particles with sparse glass coverage. In contrast, the 5-nm thick electrode has 25 nm in-plane gold particles in close proximity with each other.

Figure 4:
Breakdown strength of as-drawn glass with Au electrode (Area: 900mm^2 , thickness 2nm and 5nm) measured at 20 different probe positions.

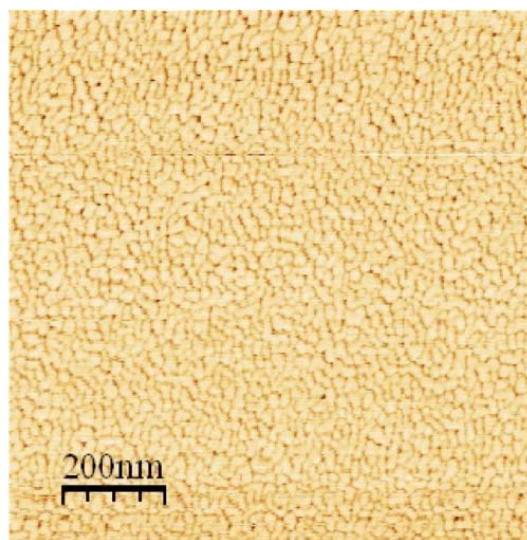
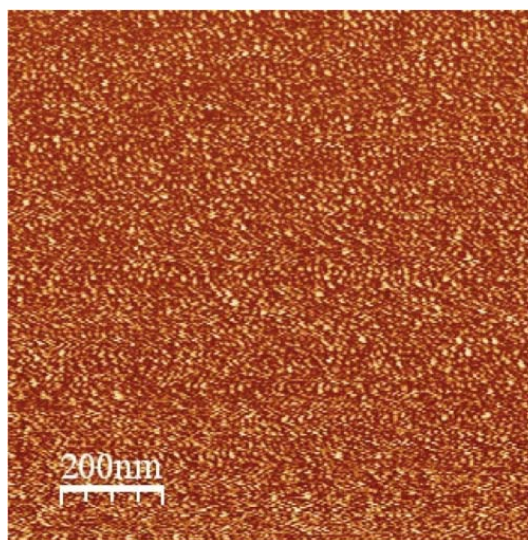
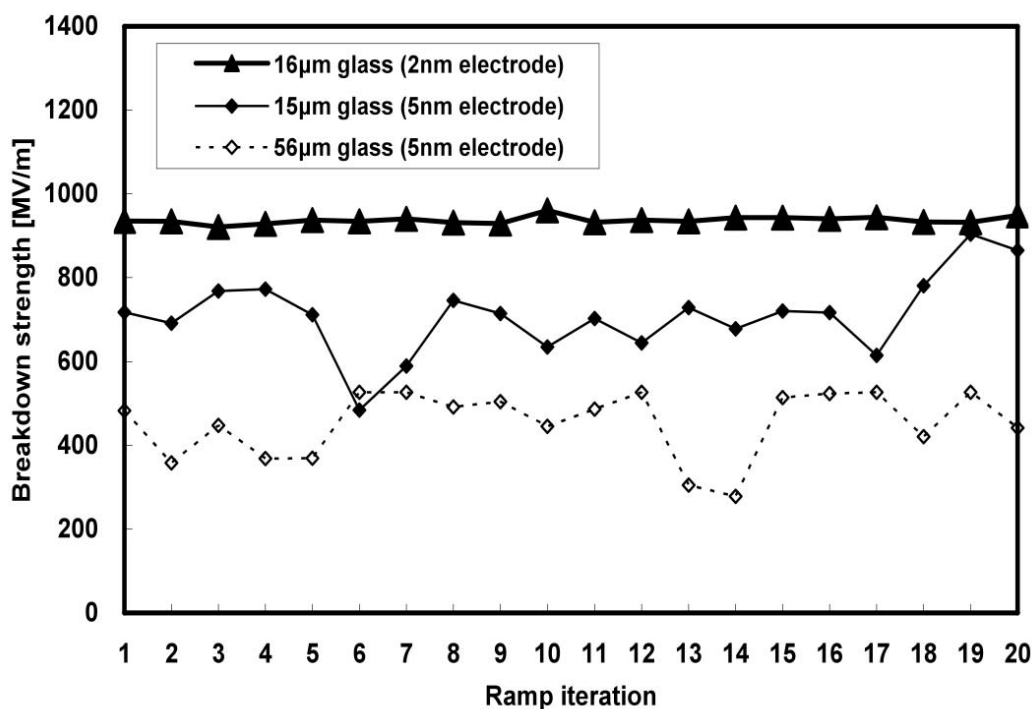


Figure 5: AFM images of the glass with (a) 2nm and (b) 5nm Au electrode.

The capacitance for the glass samples with large area electrode is plotted as a function of top gold electrode thickness and is shown in Figure 6. The capacitance (~ 800 pF) is independent of electrode thickness down to 10 nm and then the capacitance precipitously drops towards zero. Given the permittivity of 5.3 and the sample dimensions, a capacitance of 750 pF is expected. The corresponding thickness-dependent electrical resistivity for the gold electrode is also shown in Figure 6. A percolation threshold for the regions constituting top electrode is observed for electrode thicknesses below 10 nm.

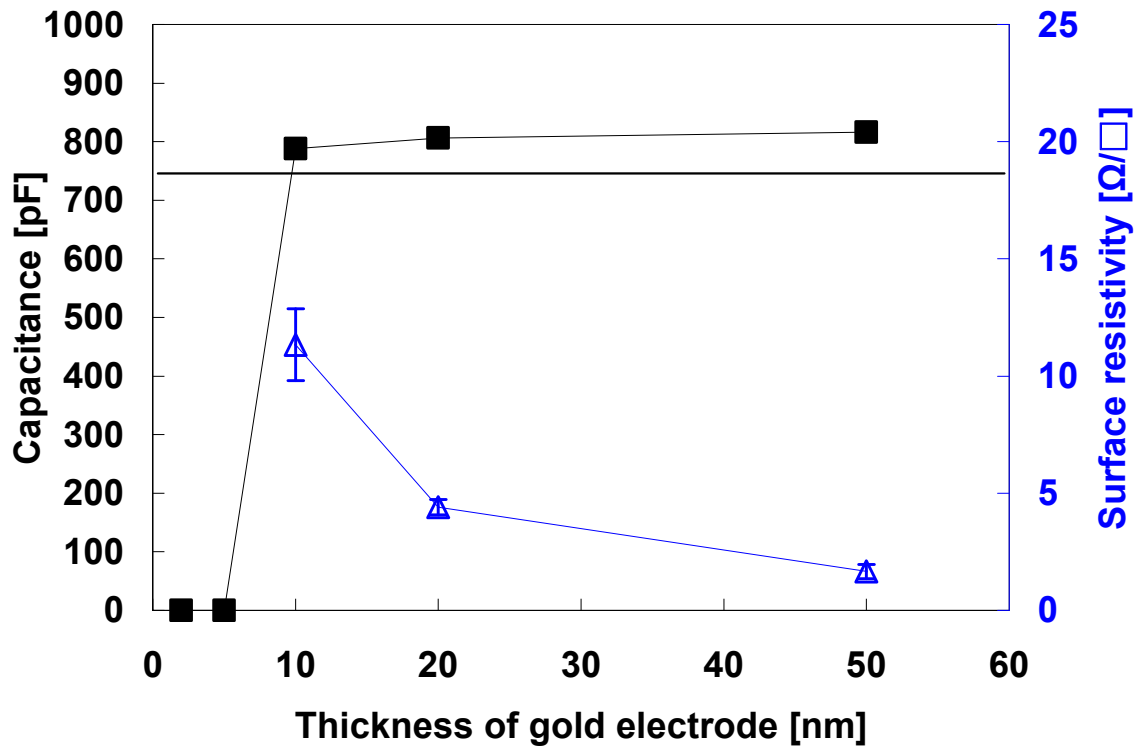


Figure 6: Capacitance and surface resistivity as a function of Au electrode thickness.

Conclusion

The outcome of this project is a cost effective manufacturing process for high temperature capacitors that will meet the US automaker specifications for HEV and PHEV applications. Penn State has collaborated with a glass manufacturer (NEG) to investigate reliable prototype capacitors from glass-ceramic materials. Penn State has developed a polymer/glass composite laminate that promotes self-healing and this technology is currently being explored for large scale glass capacitors.

The dielectric breakdown strength of thin glass substrates was explored for several test conditions. There was an increase in the breakdown strength as the glass thickness decreased. There were a significantly larger number of extrinsic breakdown events for thicker samples compared to thinner ones suggesting bulk defects contribute to breakdown. The two slopes in the thickness dependence of the dielectric breakdown strength indicated two different breakdown mechanisms with a transition between them at around 20 μm thick glass. The highest known to us Weibull modulus (~ 100) of any solid dielectric was observed in the glass samples with the intrinsic breakdown. A combination of a high intrinsic breakdown strength, high intrinsic Weibull modulus, high-temperature capability, low dielectric loss and graceful failure observed in the thin glass samples point to their utility as energy storing dielectrics for power electronics.

Publications

1. G. Sethi*, B. Koch*, E. Furman and M. Lanagan, "Influence of Permittivity Contrast on Electrical Breakdown and Tree Growth in Heterogeneous Laminate Dielectrics," submitted to Modeling and Simulation in Materials Science and Engineering, 2011.

2. T. Murata, P. Dash, E. Furman, C. Pantano and M.I Lanagan, "Electrode Limited Dielectric Breakdown of Alkali Free Glass," submitted to the J. Amer. Ceram. Soc. 2011.
3. S. Kwon, W. Hackenberger, E. Furman and M. Lanagan "Nonlinear Dielectric Ceramics and their Application to Capacitors and Dielectrics," IEEE Dielectric and Insulation 27(2): 43-55, 2011.
4. B. Rangarajan*, S.S.N. Bharadwaja, E. Furman, T. Shrout and M. Lanagan, "Impedance Spectroscopy Studies of Fresnoites in BaO-TiO₂-SiO₂ System," J. Amer. Ceram. Soc., 93(2):522-530, 2010.
5. M.Li, A. Feteira, M. Mirsaneh, S. Lee, M.T. Lanagan, C. A. Randall and D.C. Sinclair, "Influence of Nonstoichiometry on Extrinsic Electrical Conduction and Microwave Dielectric Loss of BaCo_{1/3}Nb_{2/3}O₃ Ceramics," J. Amer. Ceram. Soc. 93(12):4087, 2010.
6. P. Tewari*, R. Rajagopalan, E. Furman, and M. Lanagan, "Effects of Interfacial Modifications on Electrical Properties of Laminar Composite Dielectrics," Langmuir, 26(24):18817-18823, 2010.
7. M. Mirsaneh, E. Furman, J. V. Ryan*, M. T. Lanagan, and C. G. Pantano, "Frequency dependent electrical measurements of amorphous GeSbSe chalcogenide thin films," Appl. Phys. Lett., 96, 112907, 2010.
8. Feteira, D.C. Sinclair and M. Lanagan, "A link between p-type electrical conduction and microwave dielectric loss in highly ordered Ba(Co_{1/3}Nb_{2/3})O₃ ceramics," J. Mater. Res., 25(6):1011-1014, 2010.
9. H. Lee, N. J. Smith*, C. G. Pantano, Eugene Furman, and Michael T. Lanagan, "Dielectric Breakdown of Thinned BaO-Al₂O₃-B₂O₃-SiO₂ Glass," J. Am. Ceram. Soc., 93(8):2346-2351, 2010.

* Indicates PhD students that are now working in the US manufacturing industry and National Labs

References

1. H. Lee, N.J. Smith, C.G. Pantano, E. Furman, and M.T. Lanagan, "Dielectric Breakdown of Thinned BaO-Al₂O₃-B₂O₃-SiO₂ Glass," Journal of the American Ceramic Society, vol. 93, 2010, pp. 2346-2351.

Patents

1. M. Lanagan, N. Smith, H. Lee, C. Pantano, " Self-Healing High Energy Density Capacitors," Full patent submitted 2011.

2.8 High Temperature Thin Film Polymer Dielectric Based Capacitors for HEV Power Electronic Systems

Shawn M. Dirk,[†] Leah N. Appelhans,[†] Michele L. B. Denton,[†] Kylene Johns,[†] Jacob Haworth,[†] Ross S. Johnson,[†] Thang Vuong,[±] and Joseph Bond[±]

[†]*Organic Materials Department
Sandia National Laboratories[1]*

P.O. Box 5800

Albuquerque, NM 87185

Voice: 505-844-7835; Fax: 505-844-9624; E-mail: smdirk@sandia.gov

[±]*Electronic Concepts Inc. (ECI)*

P.O. Box 1278

526 Industrial Way

Eatontown,

New Jersey 07724

DOE Technology Development Manager: Susan A. Rogers

Voice: 202-586-8997; Fax: 202-586-1600; E-mail: Susan.Rogers@ee.doe.gov

Objectives

DC bus capacitors are currently the largest and the lowest reliability component of fuel cell and electric hybrid vehicle inverters. Capacitors represent up to 23% of both inverter weight and inverter cost and up to 35% of the inverter volume. Furthermore, existing DC bus capacitors cannot tolerate temperatures greater than 120 °C. Our project goal is to develop an inexpensive high energy density, high temperature polymer-based dielectric for DC bus capacitors for use in next generation hybrid electric vehicles (HEVs), plug in hybrid electric vehicles (PHEVs), and electric vehicles (EV). The improved capacitors will be based on novel inexpensive, high temperature polymer thin film dielectrics that have much of the chemical functionality of the known high temperature polymer Kapton®. Our technical goal is to enhance high temperature performance and volumetric efficiency compared to present dielectrics. Specific metrics include the development of polymer film dielectrics with dissipation factors of 0.02 or less at 150 °C. Synthesis, fabrication, and high temperature (room temperature to 150 °C) characterization of these dielectric materials is an integral part of the material development program. Inexpensive nanoparticle fillers will be utilized to further reduce the capacitor size as both dielectric breakdown and relative permittivity are improved, while still maintaining the benign failure mode of polymer dielectrics. In addition, work will focus on transitioning the material to industry to produce rolls of the novel high temperature polymer dielectric film which will lead directly to the production of a prototype capacitor.

Approach

Sandia National Laboratory's (Sandia) capacitor research and development (R&D) program addresses the high temperature capacitor technology gap in an innovative manner. We are developing high performance, high temperature, low cost capacitors that are based on a novel Sandia developed polymer chemistry. Capacitors fabricated using this polymer technology will achieve a high degree of packaged volumetric efficiency with less weight while maintaining a cost of less than \$0.03 per μF dramatically reducing high temperature polymer capacitor volume. Our R&D specific efforts focus on producing polymer film at Electronic Concepts, Inc. (ECI) using a solvent casting technique and at the Natick

Soldier Center using an extrusion technique. In both cases, material will be produced in an appropriate quantity to fabricate prototype capacitors. Inexpensive nanoparticle fillers will also be used to further increase dielectric breakdown strength and improve relative permittivity in order to decrease capacitor volume.

Major Accomplishments

- Solved initial problems associated with thin film production at ECI. The polymer was modified to remove the reactive double bonds via a hydrogenation process. Polymer solution lifetime was greatly improved and longer lengths of polymer film have been produced
- Demonstrated extrusion in-house using the new hydrogenated polymer
- Fabricated and characterized two 0.5 μF stacked capacitors in-house using the improved hydrogenated polymer formulation. One of the capacitors was potted in high temperature epoxy and the other capacitor was wrapped with a Kapton wrapper and sealed with heat-shrink tubing.
- Began working with the Natick Soldier Center in Boston MA and Dr. Collin in order to identify bench top film forming extrusion equipment and to extrude thin polymer film suitable for capacitor formation.

Future Direction

The R&D effort has demonstrated feasibility of using high temperature dielectrics for power electronics operating at high temperatures (150 °C). A four pronged approach is being used to ensure polymer thin film production. Two approaches rely on solvent casting which is being done in house at Sandia National Laboratories as well as with our industrial partner (ECI). Extrusion of the Sandia developed dielectric was demonstrated in FY12 and efforts are underway in collaboration with the Natick Soldier Center and Dr. Collin to develop techniques to extrude or blow mold thin films of the Sandia developed dielectric. Fabrication of larger capacitance prototype high temperature capacitors has begun using a stacked approach. Large scale film fabrication will require further development of polymer casting and/or polymer extrusion techniques that enable the production of large spools (>100 m length) of polymer dielectric films. The spools of polymer dielectric will then be slit, metalized and rolled into capacitors. We have worked with our industrial partner (ECI) to produce a desired amount of polymer dielectric film capable of prototype capacitor formation. Research in FY09 led to the identification of the side reaction that was occurring in solution leading to polymer gel formation which was inhibiting the large-scale film formation. Work in FY10 was focus on the removal of the crosslinkable double bonds in the backbone of the polymer to yield polymer film solutions with greatly enhanced shelf life. Research in FY11 focused on the fabrication of larger capacitance prototype capacitors and the demonstration of extrusion. Work for FY12 will focus on continued work with ECI, Natick Soldier Center, and Dr. Collin to produce several prototype capacitors. At least six prototype capacitors with capacitances of 5.0 μF or greater will be evaluated and benchmarked against APEEM goals. In addition, we will produce at least two “stacked” capacitors at Sandia National Labs in the event that we are unable to produce six rolled prototype capacitors at ECI. These initial prototype capacitors (rolled or stacked) will be evaluated by ORNL as well as other research institutions. We will continue our effort in developing dielectric materials with improved performance focusing on the incorporation of nanoparticle fillers to increase the dielectric breakdown strength and relative permittivity in order to further increase the energy density and decrease the capacitor volume.

Technical Discussion

1.0. Commercially Available Capacitor Limitations

Polymer dielectric-based direct current (DC) bus capacitors are a required component within current inverters used in fuel cell, electric, and electric hybrid vehicle inverters. One of the reasons polymer-based capacitors are used in the inverter application is due the failure mode. If the capacitor fails, it fails

safely as an open (known as begin failure) rather than a potential fire or explosion inducing short. However, these polymer-based capacitors are currently the largest and the lowest reliability component within the inverter and represent up to 23% of both inverter weight and inverter cost and up to 35% of the inverter volume. Furthermore, existing polymer DC bus capacitors cannot tolerate temperatures greater than 120 °C. The main goal of this project is to develop a polymer-based dielectric which leads to capacitors that are capable of meeting the APEEM program goals.

2.0. Polymer Film Production Leading to Capacitors

We have studied a high temperature polymer dielectric which has been synthesized from very inexpensive monomers using a controlled polymerization based on the ring opening metathesis polymerization (ROMP).[2-5] The polymer has many of the same functional groups that are present in the known high temperature polymer Kapton® including the imide, ether and aromatic moieties. The polymer is shown in figure 1A.

Previous attempts to cast dielectric films on a large scale using dichloroethane as the casting solvent at ECI yielded only small amounts of polymer dielectric film (1B) when using the initial Sandia developed dielectric shown in figure 1A.

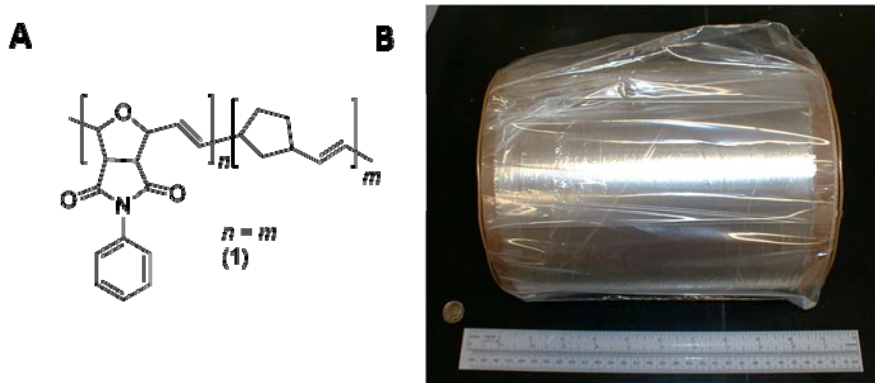


Figure 1. A) Structure of the high temperature polymer dielectric polymer and B) Spool of the high temperature polymer dielectric produced at ECI

It was noted during this time that the polymer solutions used for solvent casting were not stable for long periods of time. For example, a typical procedure to produce polymer film started by dissolving the polymer into an appropriate solvent such as dichloroethane to produce a solution suitable for casting experiments. Unused polymer solution would be stored in air usually over a weekend. Polymer was precipitating out of solution and did not go back into solution upon heating or stirring when the polymer solution was examined later. These results are consistent with the crosslinking of the double bonds in the backbone of polymer **1** as shown in Figure 2.

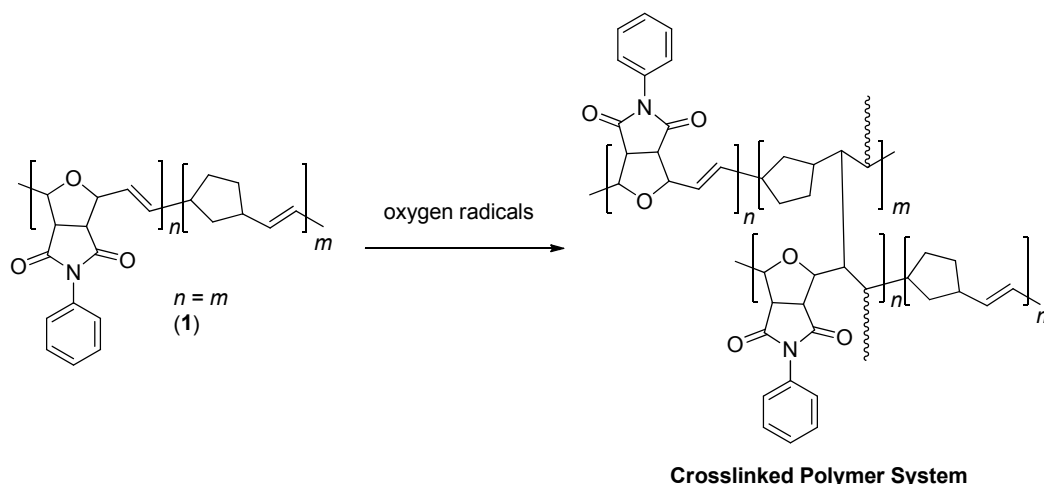


Figure 2. Crosslinking reaction that results in polymer precipitation from casting solutions

Several experiments confirmed the initially observed crosslinking reactions. In one such experiment, free radical inhibitors were added to the dielectric polymer solutions. In all cases, the polymer solution stability was greatly improved by the addition of free radical inhibitor to dielectric polymer solutions. Figure 3, illustrates the difference between two solutions of polymer both formed at concentrations of 7% (w/w). Solution A contained no free radical inhibitor, whereas, solution B contained the common free radical inhibitor 3,5-di-*t*-butyl-4-hydroxytoluene (BHT).[6] Solution A became cloudy after 48 h, whereas the solution B was still transparent. The solution that contained the free radical inhibitor BHT was not crosslinking due to inhibition of the side reactions that were leading to crosslinking.

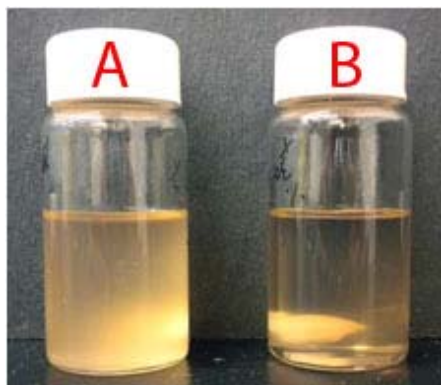


Figure 3. A) Solution of polymer (7% (w/w)) dissolved in chloroform without removal of ambient atmosphere after 48 hours. B) Solution of polymer (7% (w/w)) containing (0.1 % (w/w)) 3,5-di-*t*-butyl-4-hydroxytoluene (BHT) dissolved in chloroform without removal of ambient atmosphere after 48 hours.

Polynorbornene based polymers are highly unsaturated polymers which are quite prone to oxidative degradation which limits solubility in organic solvents (as shown above). Removal of the reactive double bonds was evaluated as a potential method to enhance polymer solution lifetimes, and improve processing, and film formation. Hydrogenation of the olefin containing polymers was accomplished using tosylhydrazide as the diimide hydrogenation precursor. The hydrazide undergoes decomposition at elevated temperatures to form diimide at high temperatures, which is the reactive species responsible for hydrogenation.[7, 8] In large-scale production, less expensive hydrogenation processes could be used such as hydrogen gas used in combination with a heterogeneous or homogeneous catalyst.[9, 10]

Hydrogenation of the polymer system **1** produced the desired hydrogenated polymer (**2**) which is shown in Figure 4.

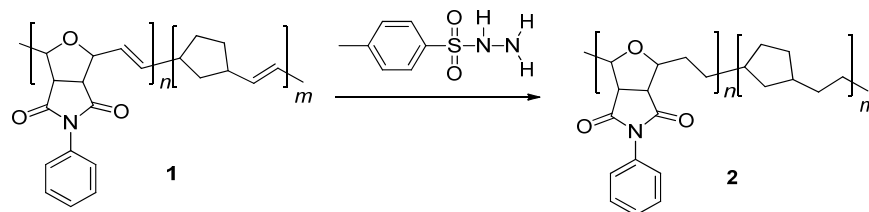


Figure 4. Hydrogenation of a model polymer dielectric

Polymer 2 stoichiometry was optimized to provide optimal dielectric properties including breakdown strength, which is shown in Figure 6. The breakdown strength of the hydrogenated polymer increases as the imide content increases. The polymer with the greatest breakdown strength was scaled up and further characterized thermally. Between 26 and 30 parallel plate capacitors were fabricated with top-side electrodes having diameters of 6.3 mm. The bottom electrodes were a continuous film. All electrodes were Au, deposited using a sputter coater at rate of 16 nm/min for a total Au thickness of 50 nm. The metalized dielectric film was placed on a Cu ground plate and the top electrodes were immersed in Fluorinert FC-40 (Aldrich) prior to electrical testing to prevent arcing and surface discharge. Weibull statistics were used to analyze the breakdown field, which was determined to be 326 V/ μm (Figure 5), resulting in a calculated energy density of 1.54 J/cm³ for the polymer formulation where $n = 3m$ (72% imide).[6-8] No special effort was undertaken to ensure that particulates were not in the film which would lower breakdown strength. Presumably, if additional steps were taken to ensure minimal particulate inclusion by casting films within a clean room the breakdown strength could be greatly enhanced.

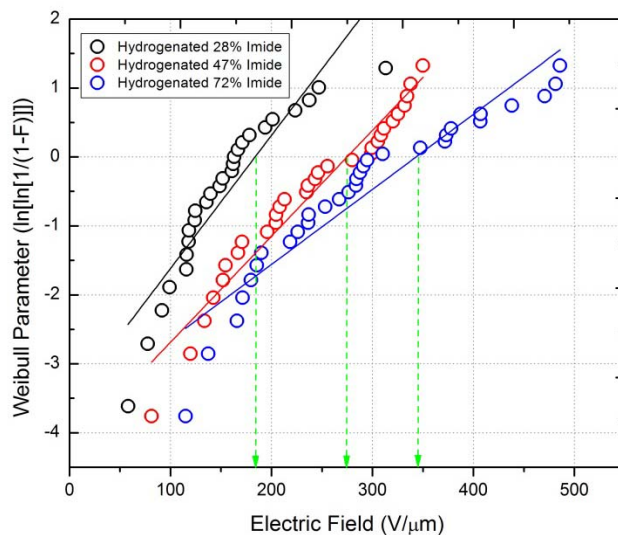


Figure 5. Breakdown strength of hydrogenated polymers as a function of imide content

Thermal characterization of polymer 2 where $n = m$ produced a polymer with a relatively low glass transition temperature (T_g) 100 °C (data not shown) and capacitors produced using hydrogenated polymers with $n = m$ (48% imide) failed at temperatures less than 150 °C (Figure 6). For these applications, a capacitor is considered to have failed if the normalized capacitance drops below 90% of the original value. The data shown in Figure 6 is an average of five capacitor capacitances as a function

of temperature. The hydrogenated polymer with $n = 3m$ (72% imide) maintains greater than 90% relative capacitance up to 165 °C. Thermal characterization of polymer 2 where $m = 0$, resulted in a polymer with a T_g of 250 °C (data not shown). Changing the copolymer stoichiometry to $n = 3m$, followed by hydrogenation resulted in a polymer with a T_g of 175 °C. Differential scanning calorimeter (DSC) data is shown in Figure 7. The lower T_g of the hydrogenated polymer containing $n = 3m$ 72% imide improves its processing characteristics and enables extrusion at a reasonable temperature.

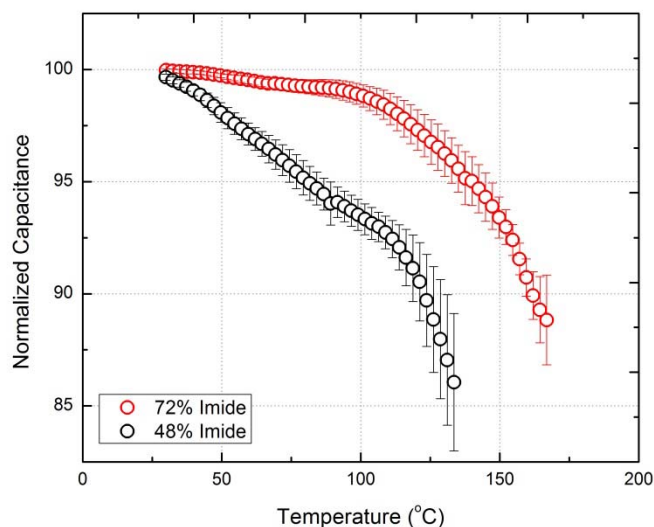


Figure 6. Average capacitor thermal performance for $n = m$ (48% imide) and $n = 3m$ (72% imide), average of 5 capacitors.

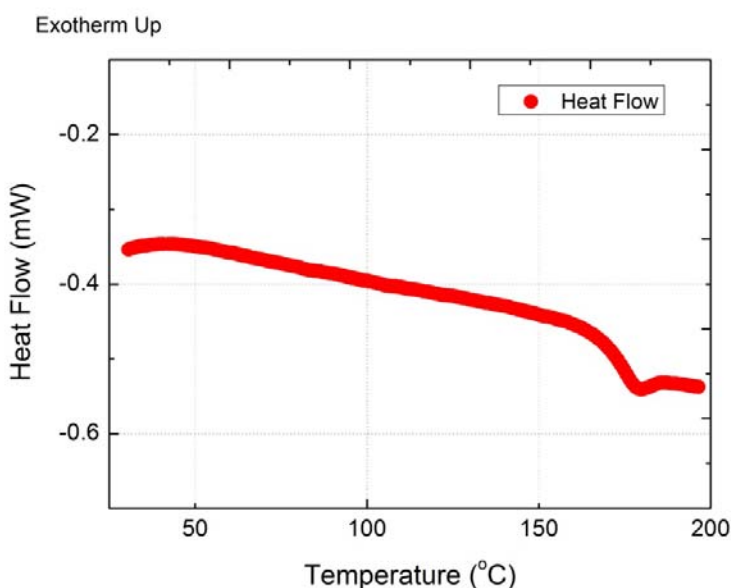


Figure 7. DSC data on polymer 2 where $n = 3m$ (72% imide)

Electrical characterization on 2 where $n = 3m$, were performed as a function of frequency to determine what affect removal of the double bond had on the dissipation factor and dielectric constant. Removal of the double bond decreased the relative permittivity of the polymer but had little effect on the dissipation factor as shown in Figure 8.

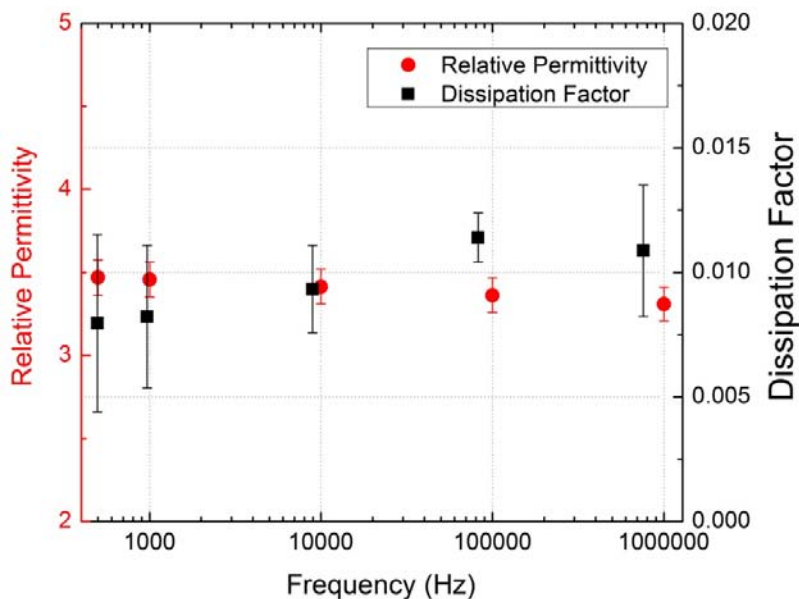


Figure 8. Dielectric properties as a function of frequency

With initial electrical and thermal characterization in hand, the hydrogenated polymer synthesis was scaled-up and two kilograms of material synthesized. One kilogram was delivered to ECI for casting experiments. A much larger length of polymer film was cast. The film is shown in figure 9 as the material exits from the casting apparatus.



Figure 9. Casting of hydrogenated polymer with stoichiometry $n = 3m$ at ECI

3.0 Stacked Capacitor Fabrication and Characterization

Multilayer stacked capacitor formation has been demonstrated previously by using a hot press technique where the polymer dielectric ($n = 3m$, $\sim 12 \mu m$) was layered iteratively with discrete Al layers ($4 \mu m$ thick). A schematic of the process is shown in Figure 10. Heat was applied to raise the temperature of the polymer above the polymers T_g while applying a load of 500-1000 lbs. Dozens of capacitors were fabricated using the discrete Al/polymer dielectric configuration to confirm this techniques viability. Capacitors fabricated using this technique had capacitances ranging from 2 to 16 nF. An image of one of the many capacitors fabricated is shown in Figure 11. Device yield was only $\sim 50\%$ using the hot-press combined with discrete Al layers so two layers of polymer dielectric were used for a total of $24 \mu m$ thick dielectric layer, which greatly exceeds the DOE OVT program goals, but still provides a demonstration of capacitor fabrication. Future capacitor fabrication will focus on using the two dielectric layer process except thinner polymer films will be used ($\sim 2 \mu m$ per layer).

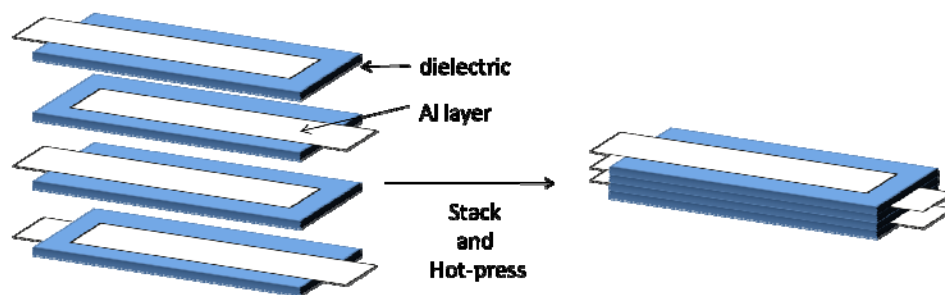


Figure 10. Scheme for fabrication of larger value capacitors

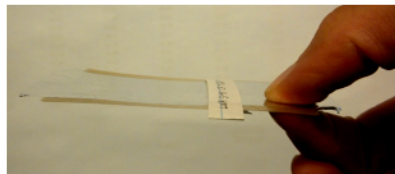


Figure 11. Image of hot pressed stacked capacitor using discrete Al layers

Several stacked capacitors fabricated using discrete Al layers and one layer of polymer dielectric were characterized electrically at temperatures ranging from room temperature to $150^\circ C$. None of the stacked capacitors failed when taken to a temperature of $150^\circ C$. An example of the data collected for normalized capacitance and dissipation factor as a function of temperature is shown in Figure 12.

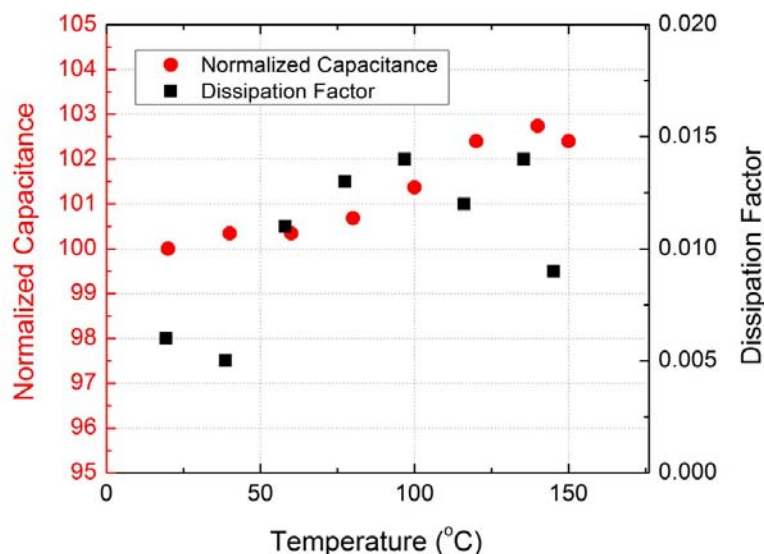


Figure 12. Electrical Characterization of discrete Al based stacked capacitors.

Better yields for capacitor fabrication were obtained when Au electrodes were sputter coated directly onto the polymer dielectric. Thin Au films deposited using a sputter coater at rate of 16 nm/min for a total Au thickness of 50 nm. Polymer films containing one Au electrode were then hot pressed with a force ranging from 500 to 1000 lbs. at a temperature above the T_g of the polymer dielectric. Silver filled epoxy was used to establish an electrical connection to half of the Au layers on one end of the stacked capacitor. The process was repeated on the other end of the capacitor to form a complete capacitor. Two capacitors were fabricated using this technique and each capacitor had a capacitance of between 5-6 nF. Fabrication of capacitors using the sputter coating technique resulted in a device yield of 100%. An image of a capacitor fabricated using the sputter coating technique is shown in figure 12.



Figure 13. Scheme for fabrication of larger value capacitors

Two larger capacitors ($\sim 0.5 \mu\text{F}$) were fabricated in-house using the layering technique. Discrete aluminum foil was used as the metal layer ($5.6 \mu\text{m}$ thick). Two layers of polymer dielectric ($\sim 12 \mu\text{m}$ thick) were used to minimize the possibility of film defect causing a short. Total film length used to fabricate the two capacitors was $\sim 110 \text{ m}$ in length. In the case of the in-house fabricated stacked capacitors, films were produced using a drawdown-based solvent casting technique.

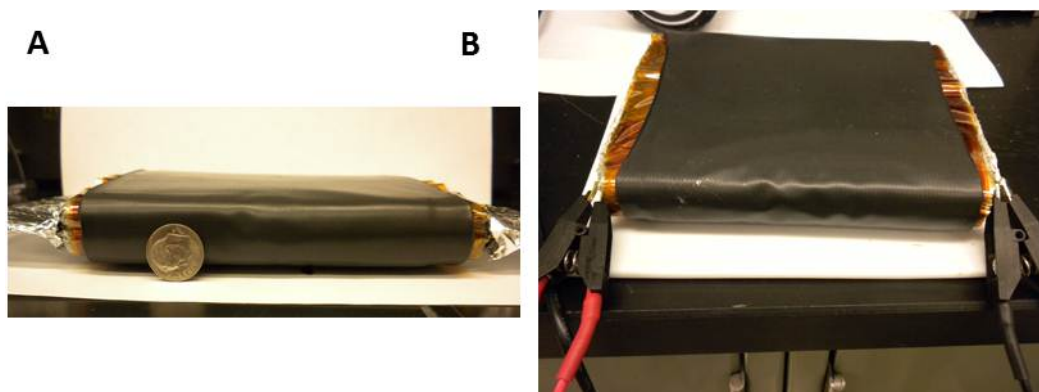


Figure 14. A) Packaged capacitor with foil electrode contacts and Dime to show scale and B) a capacitor with trimmed foil contacts hardened by high temperature conducting epoxy.

Electrical characterization of the capacitor was performed to determine the capacitance and dissipation factor as a function of frequency. The capacitance was under 500 nF, however, if pressure was applied to the face of the capacitor the capacitance would increase to over 500 nF indicating that the stacked capacitor fabrication method included void volumes filled with air. Capacitance and dissipation factor measured with no pressure applied are displayed in figure 15.

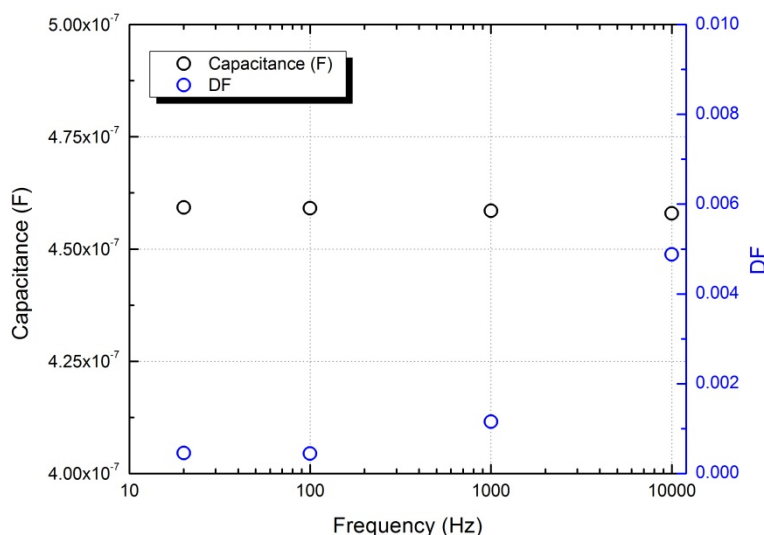


Figure 15. Electrical Characterization as a function of frequency of larger value capacitor fabricated from Sandia developed high temperature polymer dielectric

Work for FY12 will continue the scale-up of the hydrogenated polymer synthesis followed by and production of large lengths of polymer thin film followed by the fabrication and characterization of capacitors with capacitances $>5 \mu\text{F}$. In addition, further improvements in the relative permittivity and breakdown strength will be gained by the incorporation of nanoparticles.

Conclusion

We have developed a novel polymeric material that has superior high temperature dielectric properties. We have been and will continue to work with our industrial partner (ECI) to fabricate large rolls (> 100 m length) of polymer dielectric film leading to prototype capacitor fabrication. Furthermore, we have initiated collaborations with the Natick Soldier Center and Dr. Collin to demonstrate extrusion of the dielectric polymer which does not contain double bonds. Two larger value stacked capacitors (~0.5 μ F) were fabricated and the electrical performance was characterized as a function of frequency. Two approaches were evaluated to pot or encase the larger capacitors including epoxy potting and winding with Kapton and shrink tubing. Fabricated Capacitors will be sent to ORNL for further characterization and evaluation of ability to handle ripple current. Work in FY12 will remain focused on the scale-up of both film and capacitor production. Further research will be focused on the inclusion of inexpensive nanofiller additives to increase the final capacitor energy density. The Sandia developed polymer film and nanofiller are critical components that should enable high temperature, thin film, polymer dielectrics will be used to fabricate high temperature DC bus capacitors with significantly reduced size and weight, and improved performance and reliability.

Publications

1. Dirk, S. M.; Sawyer, P. S.; Wheeler, J.; Stavig, M.; Tuttle, B., High Temperature *Polymer Dielectrics from the Ring Opening Metathesis Polymerization (ROMP)* Proc. - IEEE Int. Pulsed Power Conf., 2009.
2. Dirk, S. M., Cicotte, K. N., Sawyer, P. S., Johns, K. S., Mahoney, P., Tuttle, B. A. *Thiol-ene coupling modifications of polynorbornene polymers for the synthesis of novel dielectric materials*. Polymer Preprint, 2010, POLY-442.
3. Dirk, S.M., et al., *High temperature polynorbornene copolymer dielectric materials*. PMSE Prepr., 2009. **100**: p. 331-332.

References

1. Sandia Corporation, a wholly owned subsidiary of Lockheed Martin Corporation, for the U.S. Department of Energy's National Nuclear Security Administration under contract DE-AC04-94AL85000.
2. Dirk, S.M., et al., *Thiol-ene coupling modifications of polynorbornene polymers for the synthesis of novel dielectric materials*. Polym. Prepr. (Am. Chem. Soc., Div. Polym. Chem.), 2010. **51**(1): p. 698-699.
3. Dirk, S.M., et al., *High temperature polynorbornene copolymer dielectric materials*. PMSE Prepr., 2009. **100**: p. 331-332.
4. Tlenkopatchev, M.A., et al., *Gas Transport in Polymers Prepared via Metathesis Copolymerization of exo-N-Phenyl-7-oxanorbornene-5,6-dicarboximide and Norbornene*. Macromolecules, 2003. **36**(22): p. 8483-8488.
5. Vargas, J., E.S. Colin, and M.A. Tlenkopatchev, *Ring-opening metathesis polymerization (ROMP) of N-cycloalkyl-7-oxanorbornene dicarboximides by well-defined ruthenium initiators*. Eur. Polym. J., 2004. **40**(7): p. 1325-1335.
6. Brown, D.E., E.E. Poirot, and R.A. Speed, *Polyolefin stabilizers composed of a boric acid ester, a phenolic inhibitor, and a sulfur-containing costabilizer*, 1966, (Esso Research and Engineering Co.). Application: US
US. p. 5 pp.

7. Cataldo, F., *FTIR spectroscopic characterization of hydrogenated polyoctenamer and polynorbornene and DSC study of their thermal properties*. Polymer International, 1994. **34**(1): p. 49-57.
8. Mango, L.A. and R.W. Lenz, *Hydrogenation of unsaturated polymers with diimide*. Makromolekulare Chemie, 1973. **163**: p. 13-36.
9. Gilliom, L.R., *Catalytic hydrogenation of polymers in the bulk*. Macromolecules, 1989. **22**(2): p. 662-5.
10. Rempel, G.L., Q. Pan, and J. Wu, *Homogeneous catalytic hydrogenation of polymers*. Handbook of Homogeneous Hydrogenation, 2007. **2**: p. 547-583.

Patents

1. S. M. Dirk, D. R. Wheeler, *Norbornylene based polymer systems for polymer dielectric applications*. US Patent Application #12/270,879, 2008.

2.9 Development, Test and Demonstration of a Cost-Effective, Compact, Light-Weight, and Scalable High Temperature Inverter for HEVs, PHEVs, and FCVs

Principal Investigator: Ralph S. Taylor

Delphi Automotive Systems, LLC (Delphi)

2151 E. Lincoln Rd M/C: CTC 1E

Kokomo, IN 46904

Voice: 765-451-3884; Fax: 765-451- 3690; E-mail: ralph.s.taylor@delphi.com

DOE Technology Development Manager: Susan A. Rogers

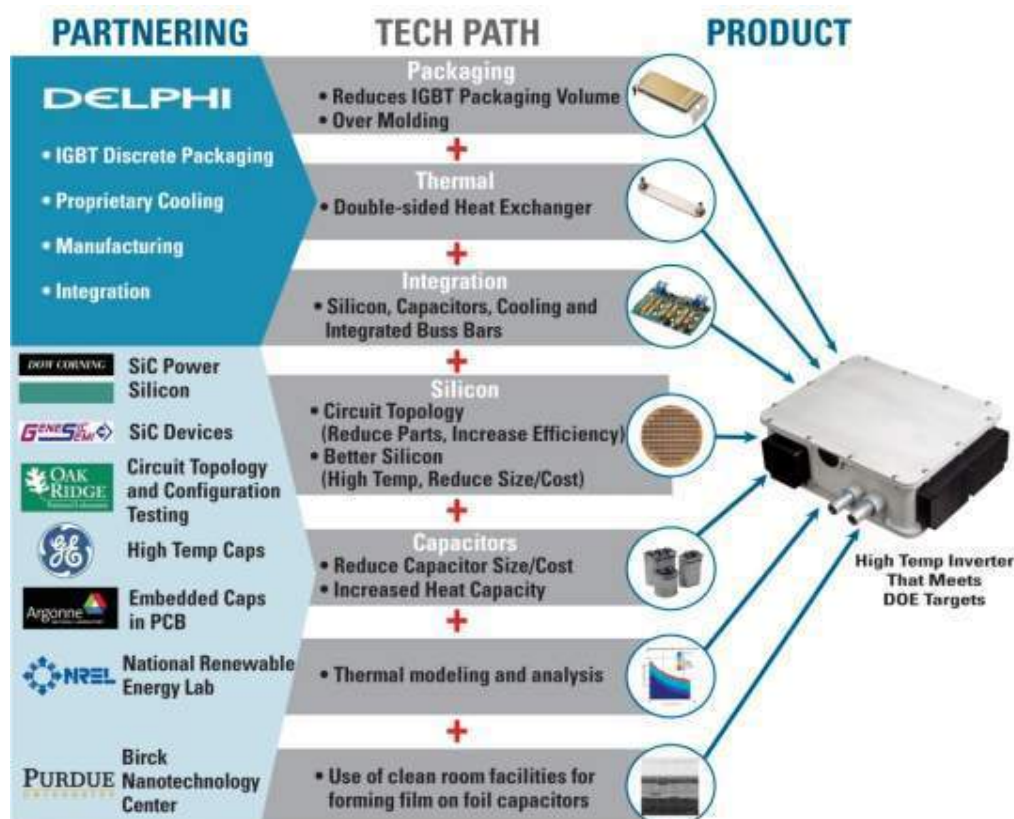
Voice: 202-586-8997; Fax: 202-586-1600; E-mail: Susan.Rogers@ee.doe.gov

Objectives

- Design, Procure Components, Build and Test High Temperature Inverter
 - ♦ Design the previously selected inverter concept, perform component and subsystem development to optimize the inverter system, procure components, build and test the inverter. Identify with DOE an appropriate motor/generator transaxle for testing and test inverter for compliance with DOE performance and cost objectives. Develop manufacturing study from selected design concepts and determine viability to reach the DOE cost and scalability objectives.

Approach

Work with our partners to develop the technologies required for DC bus capacitors, power silicon, packaging, thermal management, and integration.



Major Accomplishments: Film Capacitors (GE)

- Various resins (PEI, PPS, PC) were identified as high temperature dielectrics for capacitors.
- Extrudable PEI and high-Dk PC showed the most promise:
 - ♦ PEI film: $T_g = 217^\circ\text{C}$, $D_k = 3.2$, $D_f = 0.1\%$, 550-600V/m
 - ♦ Experimental PC $T_g = 172^\circ\text{C}$; D_k at RT, 1kHz = 4.0; $D_f < 0.3\%$; BDS = 663 V/ μm
 - ♦ A cost vs. volume model was derived to compare the different film technologies.
 - ♦ Team proposed use of 5 μm thick extruded PEI film to build 800 μF prototype bulk capacitors
 - A 5 μm thick PEI extruded film was metallized and turned into 1 μF POC caps
 - A 5 μm thick PEI extruded film of much improved quality was metallized, and successfully turned into module capacitors of various capacitance
 - 17 μF module capacitors performed satisfactorily when individually tested at 140°C and 700V DC
 - 48 17 μF module capacitors were paralleled into a >800 μF prototype bulk capacitor
 - » This capacitor failed when tested at 700V DC.
 - A new >800 μF prototype capacitor is presently being built

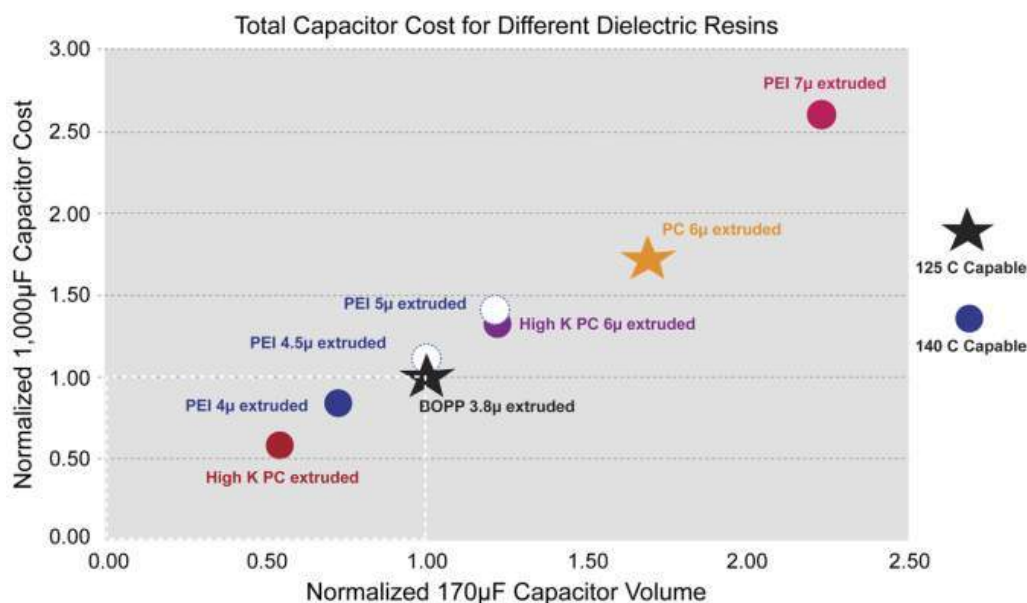
Future Direction

For FY12, we are planning on using an array of 5 μm thick extruded PEI film capacitors to form the bulk capacitor for the inverter deliverable. It should be noted that the 5 μm thick extruded PEI film will be larger than baseline equivalent polypropylene capacitor; however, the 5 μm thick extruded PEI film will be higher temperature capable and will validate the graph shown below, when comparing size to the baseline equivalent polypropylene capacitor.

It is expected that this capacitor will arrive at Delphi the end of November 2011. Once Delphi receives the capacitor the inverter test plan jointly developed with ORNL will be rerun at high temperature to complete Delphi's inverter testing.

Technical Discussion

The graph below summarizes the potential capability of different dielectric resins compared to today's baseline biaxially-oriented polypropylene (BOPP) film capacitors.



For this graphical comparison, the ***processing cost per unit volume of capacitor module was kept constant***, the same as that for the BOPP, although it may be different for resins other than BOPP, especially in those cases in which the raw material cost or the processing cost to make the film by extrusion, or both, are substantially higher than the values assumed for BOPP.

Also, the ***cost to make the High Dk 4 μ m extruded polycarbonate polymer commercially was estimated based on the information presently available***, and it will strongly depend on the cost to make the monomer required to build the polycarbonate molecule and the final volume of resin produced, which are both unknown at this point in time.

The pictures below shows the extruded 5 μ m PEI film and an initial prototype of the bulk capacitor:



5 μ m PEI Film



800 μ F Extruded PEI Film Bulk Capacitor

Major Accomplishments: Film-on-Foil Capacitors (Argonne National Laboratory)

- Transferred process as it exists today to a clean room facility at the Birck Nanotechnology Center (BNC)/Purdue University
- Less variation in dielectric properties observed on samples made in clean room
- Added process controls (inspection of substrate before & after each process step)
- Moved away from polished nickel substrate to metalized silicon wafers and demonstrated good breakdown fields
- Fabricated physically larger size capacitors
- Capacitors that are being fabricated today are larger and better quality than earlier versions.
- By altering the process for forming the capacitors defect free films can be made
 - ◆ This process is not yet optimized, but shows potential for forming larger area thin films
- Still have a long way to go
- Argonne received a R&D 100 award for their work on film-on-foil capacitors

Future Direction

For FY12, continue working at BNC/Purdue to develop a better understanding of the viability of this technology, particularly to reduce capacitor cost and volume.

Technical Discussion

In 2011, Delphi and Argonne National Laboratory continued to fabricate thin-film PLZT capacitors at Purdue University. Three multi-day fabrication trips to Purdue were completed and the electrical test results of the capacitors created during these trips were documented within this report.

During February through June 2011, Delphi Advanced Engineering and Argonne National Laboratory personnel made three capacitor fabrication trips to the Birck Nanotechnology Center at Purdue University, West Lafayette, IN. These three visits were in support of the following deliverables for 2011:

- Produce large area (1" x 1") high-voltage capacitors on silicon
- Confirm a process change to the pyrolyzation profile to eliminate formation of cracks in the PLZT
- Fabricate capacitors with a modified PLZT solution to produce thicker layers – reducing the number of layers required for a high voltage capacitor
- Establish fabrication process to achieve a minimum breakdown voltage of 600 volts
- Test all capacitors for Dk, Vb, from -40°C to +140°C
- Document results

Major Accomplishments: 3C-SiC/Si (Dow Corning)

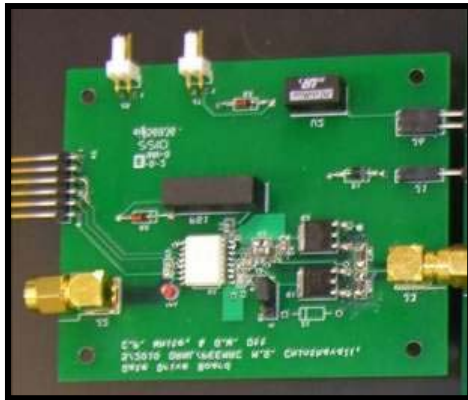
- Objective
 - ♦ Demonstrate functional 3C-SiC on Silicon diodes and MOSFETs
 - ♦ Show materials process and device process cost reduction routes to achieve DOE cost targets for inverter chip set
- Cost model complete
- Epitaxy thickness uniformity good and bow/warp in line with targets
- Demonstrated good crystal quality in CVD processes
- Mechanical samples performed well in package integrity tests using Delphi packaging technology
- Delivered SiC-on-Si wafers to GeneSiC for development of unit process steps
 - ♦ Etching development and oxide growth unit processes completed at GeneSiC

Future Direction

Dow Corning continues work beyond program to improve doping control and demonstrate 150mm 3C-SiC/Si wafers, including reformulation of their precursor material to eliminate N₂ contamination.

Major Accomplishments: Modeling and Test (Oak Ridge National Laboratory)

- Advanced silicon parts, Si IGBT and Si diode, were received from Delphi
- Static characteristics of the Si IGBT and Diode were determined for temperature range 25°C to 150°C
- New gate driver board for power package characterization designed and tested (see following figure)
- Dynamic characteristics of Si IGBT and Diode obtained at 360V, for 10A to 300A, at room temp.
- Results of static and dynamic testing were sent to Delphi for verification of the device behavior
- Obtained device losses at 10A-50A for inverter loss model at low power over simulated drive cycle
- Completed a draft plan for the inverter testing
- Test plan reviewed by Delphi



Gate Drive Board used for Testing



Power Board used for Testing

Future Direction

Verify inverter performance with Delphi using motor supplied by Delphi at Delphi Kokomo.

Technical Discussion

Device loss models received from Delphi were incorporated into the drive model. Results of the modeling show that, by using 3C-SiC devices instead of Si devices, traction inverter energy losses can be reduced by 89%-93% (see the following table).

Modeled Energy Savings with Silicon Carbide

| Federal Urban Driving Schedule (FUDS) | | | | | | | | | | |
|--|-------|------|-------|-------|--|---------------------------------|------|-----|------|-------|
| Energy Savings with SiC vs Si (Joules) | | | | | | % Energy Savings with SiC vs Si | | | | |
| ICE | ISE | DCE | DSE | Total | | ICE | ISE | DCE | DSE | Total |
| 10965 | 35185 | 5609 | 22193 | 73952 | | 76% | 100% | 78% | 100% | 93% |
| | | | | | | | | | | |
| US Aggressive Driving Schedule (US06) | | | | | | | | | | |
| Energy Savings with SiC vs Si (Joules) | | | | | | % Energy Savings with SiC vs Si | | | | |
| ICE | ISE | DCE | DSE | Total | | ICE | ISE | DCE | DSE | Total |
| 9980 | 21836 | 1774 | 13492 | 47082 | | 71% | 99% | 56% | 100% | 89% |

ICE: IGBT Conduction Energy Loss
DCE: Diode Conduction Energy Loss

ISE: IGBT Switching Energy Loss
DSE: Diode Switching Energy Loss

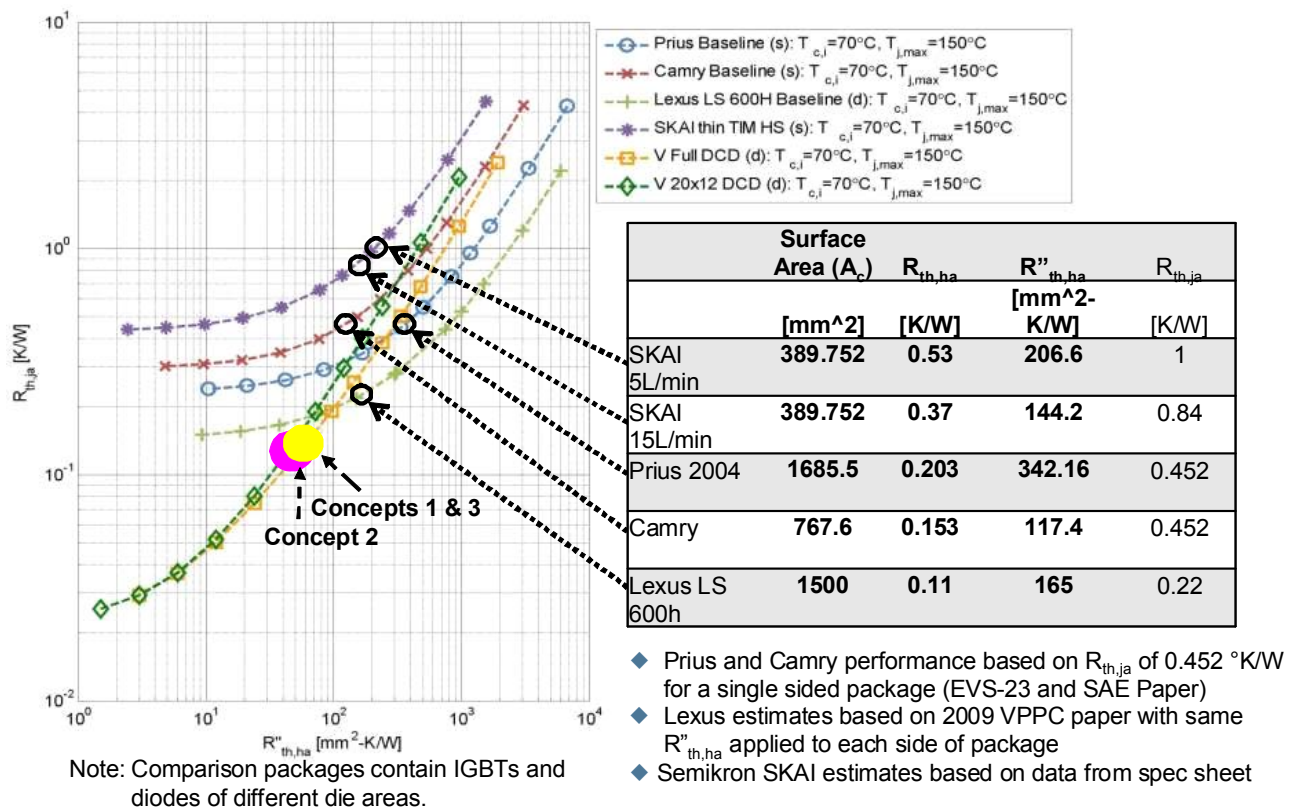
Major Accomplishments: Thermal Modeling of Package (NREL)

- Working with Delphi, NREL has performed analysis of various cooling strategies proposed by Delphi
 - Package comparisons were completed for $R''_{th,ha}$ vs. $R_{th,ja}$
 - In some cases, NREL verified Delphi's results.
- Results of these analysis were compared to commercial systems currently in the marketplace
 - Comparisons showed Delphi's power device packaging provides at least 30% improvement in thermal resistance junction-to-coolant, compared to the "best" commercially available double-side cooled product today (in the Lexus LS 600h, see figure under "Technical Discussion")

Future Direction

In conjunction with suppliers and customers, Delphi will continue to evaluate and develop high performance thermal interface materials, as well as novel thermal stacks, that reduce the thermal resistance junction-to-water below what is being demonstrated today.

Technical Discussion



Major Accomplishments: Packaging Thermal and Integration (Delphi)

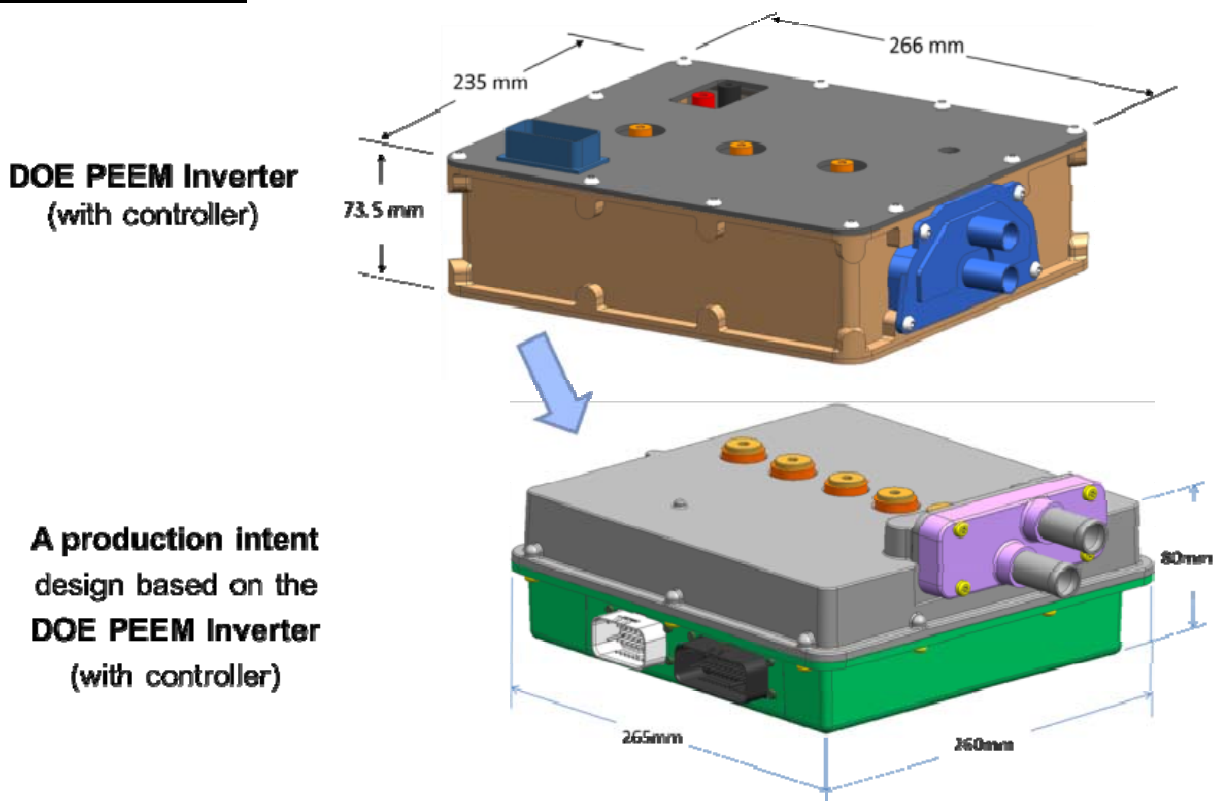
- Inverter that meets the DOE performance requirements has been built and tested.
 - Utilizes advanced Si IGBT and Diodes with improved heat sink
 - Characterized static and dynamic performance of advanced silicon devices over temperature (25°C and 150°C)
 - Conduction losses show substantial reduction vs. baseline and target
 - Switching losses can be optimized to minimize total losses for a given drive cycle

- ♦ Scalable and capable of operating over a wide range of applications
 - Capable of 80A to >300Arms/phase output
 - Parts delete and part substitution
- ♦ Utilizes 105°C engine coolant (waiting on PEI cap for verification)
 - Double-sided cooled power package (discrete power switch)
 - Using light weight, high performance heat rails
 - Thermal performance characterized with 105°C coolant (requires PEI capacitor to verify)
- ♦ Utilizes high performance phase-change thermal interface material
 - Thermal resistance of 0.08 cm² °C/W
- ♦ Utilizes scalable, high current connection system
- ♦ Utilizes PP or extrudable PEI capacitor
 - PEI capacitor will meet 140°C temperature requirement

Future Direction

- Delphi has chosen advanced silicon with an improved heat sink concept for the inverter build. The inverter has been tested at room temperature with 25°C coolant in accordance with ORNL's test plan.
- This inverter is the basis for a Delphi production design inverter for future customer applications.
- Production costing @ 100,000 units per year is currently in process
- Complete inverter testing with 105°C coolant and 140°C ambient air and deliver the test results to DOE/ORNL. Expect ORNL to verify inverter tests in January of 2012.
- Complete final report

Technical Discussion



Conclusions

- Power device packaging provides at least 30% improvement in thermal resistance junction-to-coolant, compared to the “best” commercially available double-side cooled product today
- Advanced Si devices provide conduction losses ~17% lower than target, total loss improvements under characterization
- Developing a technical path to smaller, lower cost, high temperature bulk capacitors
- Lower thermal resistance packaging with lower device losses allows for use of less silicon
- Less silicon implies less silicon packaging
- Less silicon, less silicon packaging and smaller bulk capacitor implies smaller package size
- Results in smaller Inverter with Reduced Volume and Weight – Easier to Manufacture – Lower Cost

Thank you DOE for the Opportunity...

- To work with GE Global Research on high temperature film capacitors - this work done has demonstrated a path to a lower cost, smaller size, higher energy density film capacitors for EDV inverters.
- To work with Dow Corning Compound Semiconductors to develop the best performance to date for a 3C-SiC on Silicon film for use in potential future devices
- To work with Oak Ridge National Laboratory on models comparing Si to SiC power devices, allowing for better tradeoffs of component cost vs. system cost and system efficiency for future commercial programs
- To work with Argonne National Laboratory on film-on-foil capacitors - this work on the material has shown promise for a very compact, high temperature, high energy, and potentially low cost capacitor.
 - ♦ Future efforts to develop a process for this material could be a game-changer for the capacitor industry in the long term
- To work with the National Renewable Energy Laboratory on thermal packaging and integration - this work has provided important insights that could be applied on future commercial programs
- To work with our suppliers on advanced silicon devices – these devices are already being integrated in our development programs for commercial production
- To allow us to explore packaging concepts for inverters as well as inverter components – these concepts will be used on future production inverter programs

2.10 Development of SiC Large Tapered Crystal Growth

Principal Investigator: Dr. Philip G. Neudeck

NASA Glenn Research Center

21000 Brookpark Road, M.S. 77-1

Cleveland, OH 44135

Voice: 216-433-8902; Fax: 216-433-8643; E-mail: Neudeck@nasa.gov

DOE Technology Development Manager: Susan A. Rogers

Voice: 202-586-8997; Fax: 202-586-1600; E-mail: Susan.Rogers@ee.doe.gov

Objectives

1. **Demonstrate initial feasibility of totally new “Large Tapered Crystal” (LTC) approach for growing vastly improved large-diameter wide-band gap wafers.**
2. Open a new technology path to large-diameter SiC and GaN wafers with 1000-fold defect density improvement at 2-4 fold lower cost. This would enable a leapfrog improvement in wide band gap power device capability and cost.

Approach

3. Experimentally investigate and demonstrate the two key unproven LTC growth processes in SiC:
 - Laser-assisted growth of long SiC fiber seeds (Solvent-Laser Heated Floating Zone).
 - Radial epitaxial growth enlargement of seeds into large SiC boules.

Major Accomplishments

4. Completed major design and hardware modifications of two NASA Glenn crystal growth laboratories.
5. First demonstrations of single crystal SiC growth via Solvent-Laser Heated Floating Zone.
 - Growth rates $>100\text{ }\mu\text{m/hour}$ and polycrystalline growth rates $>1.3\text{ mm/hour}$.
6. Initial demonstrations of lateral SiC crystal enlargement via CVD epitaxial growth
 - Growth rates improved more than 2-fold (to $\sim 180\text{ }\mu\text{m/hour}$).
 - Crystal diameter enlargement of 1.5 mm demonstrated.
7. Major setback – Failure of RF generator in NASA SiC CVD epitaxial growth system.

Future Direction

8. Develop optimized SiC mesa seed crystals needed for vertically growing much longer and improved SiC fibers from single screw dislocation and suitable for Solvent-LHFZ
9. Continued development of source material/feed rod compositions and processing for Solvent-LHFZ
10. Repair NASA SiC epitaxial growth system.
11. Eliminate parasitic 3C-SiC from lateral CVD epitaxy by implementing coated graphite parts, improving temperature uniformity and altering gas phase chemistry.

12. Carry out demonstration CVD growth of small 0.5 cm diameter SiC boule.
 - Characterize to see if desired low-defect lateral CVD growth is achieved.
13. Grow larger fibers and boules fully demonstrating feasibility of LTC growth process physics (FY 12 – beyond current NASA/DOE agreement).
14. Launch joint development of full prototype LTC SiC growth system (simultaneous fiber growth + lateral growth to grow full prototype SiC boules) in collaboration with commercial and/or university development partners (FY13-14 - beyond current NASA/DOE agreement).
15. Explore GaN LTC experiments. (FY15-16 - beyond current NASA/DOE agreement).

Technical Discussion

Technical Motivation

It is generally accepted that the use of silicon carbide (SiC) power electronics could enable power systems that are significantly more efficient, lighter, and smaller than systems based on silicon (Si) electronics. Although some SiC devices (e.g. Schottky diodes and field-effect transistors (FETs)) have been developed, the energy-saving performance and reliability of SiC power devices are significantly degraded, and device cost significantly increased, because of a high density of dislocation defects (> 1000 per cm^2) in all commercially-available SiC semiconductor wafers. Eliminating these defects economically (i.e., down to densities < 1 per cm^2 while greatly lowering SiC wafer cost) would unlock SiC's enormous (as yet unfulfilled) promise to revolutionize nearly all high-power electronic systems.

The reason for the high density of defects in commercial SiC wafers is that all current approaches for growing single-crystal SiC boules are fundamentally flawed. The problem with current SiC growth processes is that a high-density of screw dislocation defects (on the order of 10^2 to 10^4 per cm^2) is necessary in order to achieve commercially viable SiC wafer growth rates. Unfortunately, many researchers (including NASA) have now shown that these same dislocation defects harm the yield, performance, reliability, and commercialization of SiC high power devices. If SiC is to fulfill its huge theoretical power device promise, SiC wafer dislocation densities must be brought down 100-1000 fold via a totally new crystal growth approach, yet be able to mass-produce larger-area wafers (at least 6-inches in diameter) at significantly lower cost.

Introduction to Large Tapered Crystal (LTC) Growth

A NASA Glenn Research Center (GRC) team (J. A. Powell, P. G. Neudeck, A. J. Trunek, D. J. Spry) recently patented (US Patent 7,449,065) a radically different, SiC crystal growth concept that can mass-produce large-diameter SiC wafers wherein each wafer ideally contains only a single screw dislocation (in the center of the wafer). This new growth concept utilizes a revolutionary seed crystal configuration and two simultaneous growth processes in connected chambers for rapidly growing large single-crystal SiC boules with only one centrally-located screw dislocation. Because this new process grows a large crystal with a tapered shape, we have named this the Large Tapered Crystal (LTC) growth process. The crystal growth initiates from a small-diameter fiber (with a single screw dislocation at its core) that is grown in a first chamber, from which it is withdrawn, as it elongates, into a second growth chamber where radial growth on the fiber produces a large tapered crystal. Each growth run produces a low-defect (ideally with a single screw dislocation) SiC crystal boule (100 mm diam.) at the top end of the LTC. A comprehensive technical description of the process and apparatus involved can be found in US Patent 7,449,065 that is now available online at the U.S. Patent Office website <http://www.uspto.gov>. This section presents a highly condensed summary of the contents of the patent.

Fig. 1 illustrates schematic cross-sections of SiC crystals during steps S1, S2, and S3 of the LTC growth process. Each LTC growth cycle starts with a large tapered crystal (LTC) as the seed crystal as shown in Fig. 1(a). The central axis of the LTC seed will be parallel to the crystallographic c-axis. During a growth step S1, the small end (the fiber portion in chamber 1), as shown in Fig. 1(b), will be grown in the c-direction and maintained at a diameter of less than 1 mm; the large end of the LTC will be maintained at some designated large diameter (e.g. 100 mm for commercial systems). Simultaneously with the axial growth of the small-diameter fiber in chamber 1, radial epitaxial growth enlargement of the large tapered section takes place in a growth chamber 2 during a growth step S2. Ideally, only a single screw dislocation (along the central axis) will be present in the entire crystal. This single screw dislocation provides the necessary crystal stacking sequence for a given SiC polytype. This stacking sequence also establishes the sequence of atomic steps that propagate radially during growth in chamber 2. It is important to note that defects (i.e., screw dislocations) are not required for the radial growth in chamber 2. Indeed, the bulk of the crystal boule (except for the very small volume of the central fiber) is deposited by “step-flow growth” in chamber 2 (utilizing the crystal stacking sequence established by the small-diameter fiber).

Typically, the vertical growth rate parallel to the c-axis (on the small tip) will be much greater (e.g. the order of 1 mm/hour) than the radial epitaxial growth rate. Because of the large surface area of the tapered portion, moderate radial growth rates (e.g. about 0.1 mm/hour) will yield rapid bulk growth of the LTC in chamber 2. As growth proceeds in steps S1 and S2, the top of the tapered crystal enters an isothermal chamber 3 of inert gas atmosphere where no additional SiC is deposited. This enables a cylindrical (hexagonal cross-section) crystal boule to form as the large end continues to exit chamber 2 into the “no-growth” isothermal chamber 3. The top of the crystal is physically moved upward during growth steps S1 and S2 so that the bottom of the downward-growing small-diameter tip is maintained at the same position inside chamber 1.

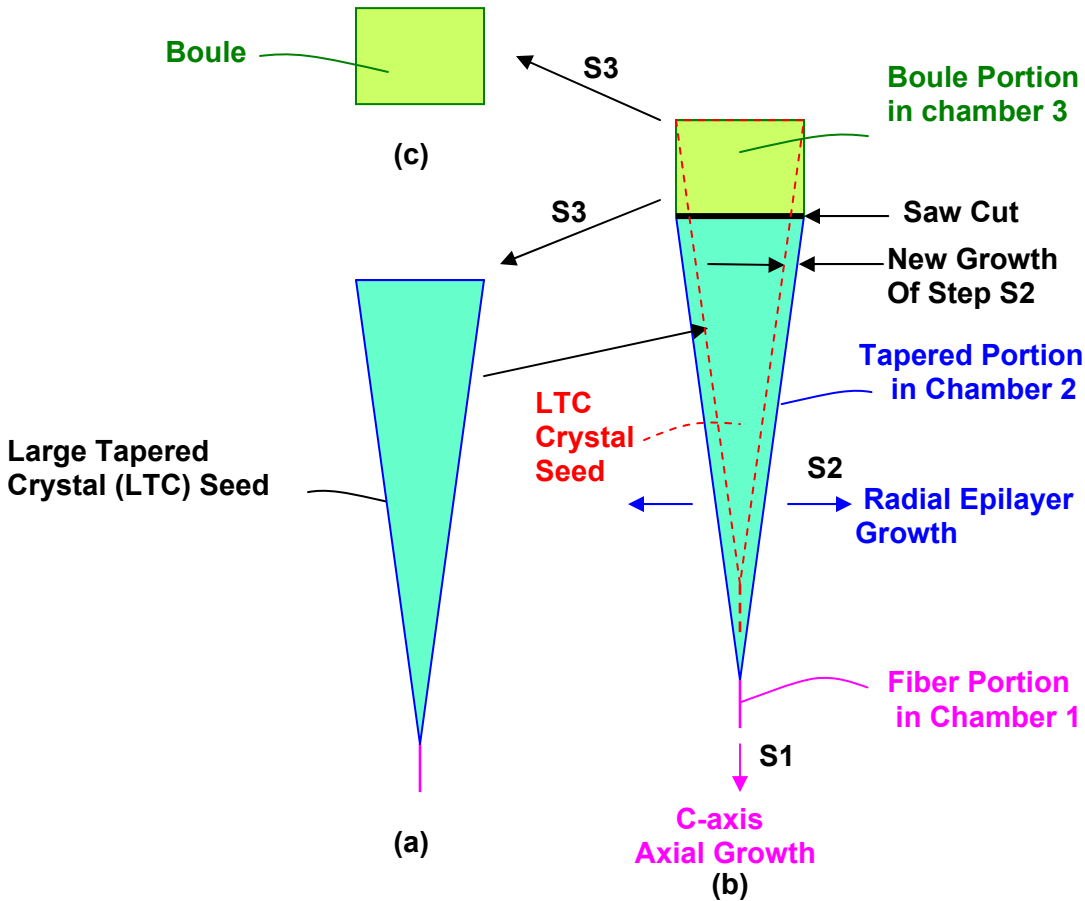


FIG. 1. LTC Growth Process

At the end of each growth cycle, the boule portion will be cut from the whole crystal in step S3 (Fig. 1c), and the remainder of the LTC crystal will be used as a seed crystal in steps S1 and S2 of a subsequent growth cycle. Additional advantages of the LTC process are that boules can be grown at high growth rates and the process can easily be scaled up to larger diameter boules, resulting in increased wafer size and reduced wafer cost. Also, the process should be capable of boules of much greater length than is possible with current SiC growth techniques. Note that only the very first LTC seed crystal will need to be grown in a preliminary and separate process from the LTC process cycle depicted in Fig 1.

The LTC growth process as presented above relies on two separate high-quality SiC growth processes taking place on different surfaces/regions of the same crystal, namely (S1) c-axis fiber growth and (S2) radial epilayer growth. Neither of these processes has been experimentally attempted or demonstrated for SiC in the manner/configuration that is proposed above. Therefore, the immediate first objectives of this work is to separately demonstrate, for the first time, that both of these two new SiC growth processes can be successfully carried out.

SiC Fiber Growth by Solvent-Laser Heated Float Zone Growth

A key (and most challenging) aspect of demonstrating the viability of the LTC process is the demonstration of rapid growth (on the order of 1 mm/hour in the crystal c-axis direction) of a single-crystal SiC small-diameter fiber containing a single screw dislocation (i.e., demonstrating growth S1 of Fig. 1). The basic feasibility goal of initial fiber growth work under this project is to demonstrate single crystal SiC fibers of at least 100 mm in length. To achieve this, a growth method has been chosen which combines the advantages of two well known growth methods: Laser Heated Floating Zone (LHFZ – proven for oxide-based crystals) [1] and Traveling Solvent Method (TSM – demonstrated for SiC) [2] which we have named Solvent-Laser Heated Floating Zone (Solvent-LHFZ).

To perform Solvent-LHFZ, a custom system was constructed during the first year of DOE funding (Figure 2) consisting of a CO₂ laser ($\lambda=10.6\ \mu\text{m}$) and associated optics, vacuum chamber, sample translation system, optical pyrometer and video capture/data collection/experimental control system and vacuum/gas management system, which is designed to pull a vacuum of 5×10^{-5} Torr or better before a growth. During growth ultra high purity Ar gas is brought into the chamber from the top and around the windows and out through the bottom of the chamber in order to keep sensitive areas clean. The pressure in the chamber for these initial experiments is 115 Torr with total Ar flow about 15 slm.

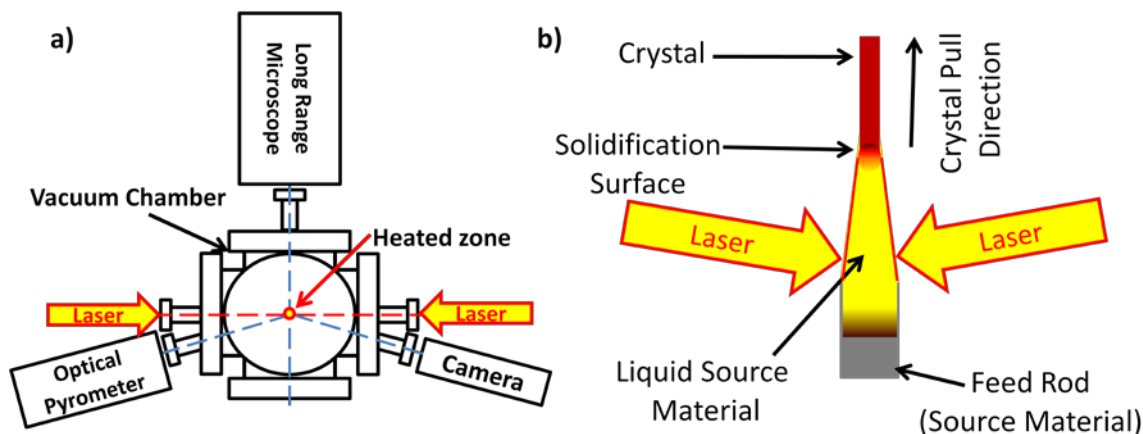


Figure 2. Solvent-LHFZ system. a) Top down view of the configuration of the laser beams and in-situ data collection instruments. Note: that all of the components are co-planar. b) Side view of the laser, liquid source material and solidification surface, seed crystal and feed rod.

Figure 2a, shows the orientation of the laser beams, heated zone and the primary in-situ data collection tools, and Figure 2b, the orientation of the beams to the seed crystal, heated zone and feed rod. The laser beams enter the chamber on a $\sim 5^\circ$ down angle so they cannot exit the chamber through the opposing window, but before the beam enters the chamber, optics are used to focus the beam into an oval shape (long : short axis $\sim 2:1$) with the short axis parallel to the vertical axis of the chamber. The long axis is roughly twice the width of the feed rod in order to ensure even heating. The seed crystal is mounted vertically in the upper mount, so that the growth face is down, while the feed rod is mounted vertically in the lower mount. Both mounts can be moved independent of each other with rates of 50-18,000 $\mu\text{m/h}$ ($\pm 1\ \mu\text{m/h}$).

SiC seed crystals used for this experiment are 0.5 mm x 0.5 mm x 15 mm diced from commercially purchased a-face (11-20) or m-face (1-100) 4H-SiC wafers. The long dimension of the seed is parallel to the c-axis $\langle 0001 \rangle$ making one end the C face (000-1), which is also the growth surface. The growth surface varied from on axis to roughly 10° from the (000-1). Seed crystals were cleaned using a $\text{H}_2\text{SO}_4:\text{H}_2\text{O}_2$ (1:1) bath, and then glued (SiC ceramic paste) into an alumina tube used to mount in the growth system. Next, the crystals were re-cleaned by $\text{HNO}_3:\text{HCl}$ (2:1) dip and then an oxide layer was removed by HF dip and final rinse with de-ionized water).

Growths were conducted by first melting the end of the feed rod (Figure 3a. Pre-contact), and then dipping the end of the seed crystal into the melt allowing the liquid to wet the crystal (Figure 3b.

Wetting). During the entire process the feed rod is continually fed into the heated area, at a rate which maintains approximately the same amount of melted material. The growth ends when the seed/grown crystal is pulled out of the melt. After growth some of the metal solvent remains on the crystal, which is removed using a HF:HNO₃:HCl (1:1:2) bath.

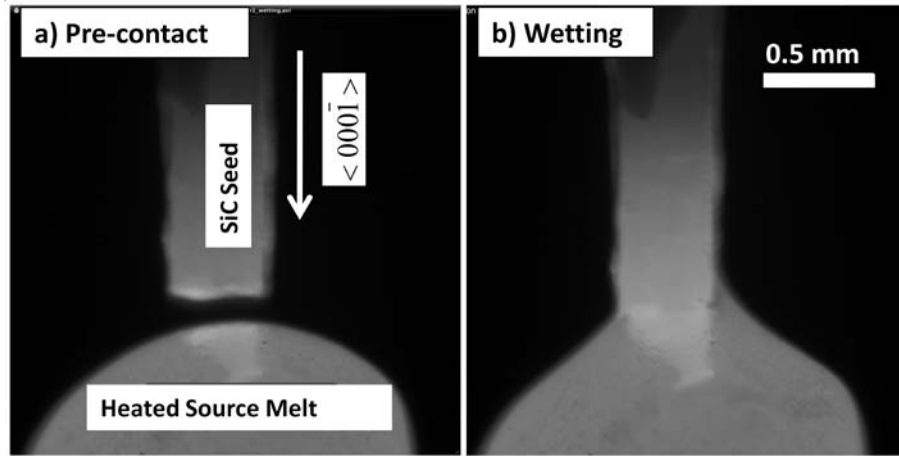


Figure 3. Long-range optical microscope images recorded during a Solvent-LHFZ process experiment. (a) Precontact: Source material is liquid, and the seed approaches the melt. (b) Wetting: Liquid source material wets to the seed crystal.

Both single crystal and polycrystalline SiC growth modes were observed. Figure 4a is an SEM of a thick (85 μm) single crystal grown at a rate of roughly 50 $\mu\text{m}/\text{hour}$. Several of the initial films have been examined by synchrotron white beam x-ray topography (SWBXT) by Prof. Dudley's group at Stony Brook University, which has confirmed the replication of the 4H polytype and epitaxial nature of the grown crystals. Figure 4b is a polycrystalline SiC (confirmed by energy-dispersive X-ray spectroscopy) fiber 800 μm in length which grew at >1.3 mm/hour. The mode of growth is controlled by the placement of the laser beam with respect to the crystal growth front. In the case of single crystal growth, the growth front is kept above laser beam. Conversely, in order to grow polycrystalline SiC, the growth front is kept in the laser beam.

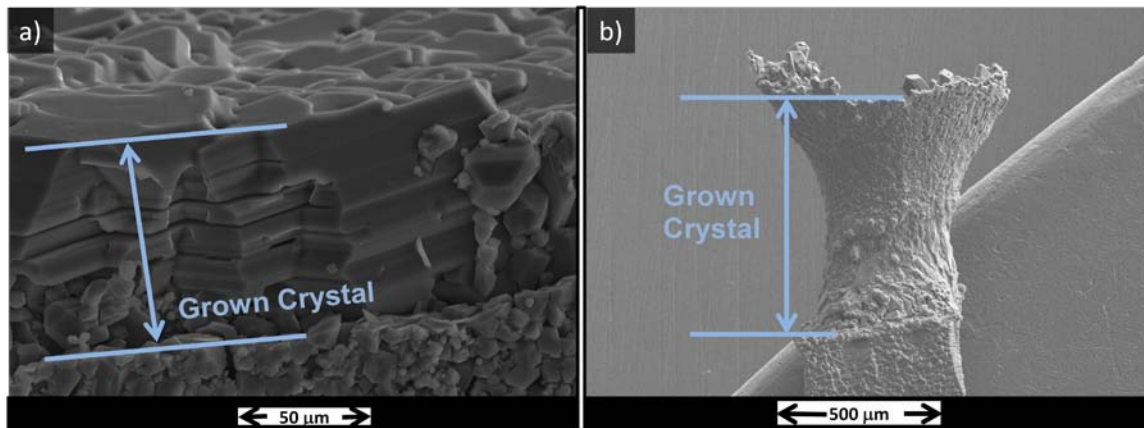


Figure 4: SEM micrographs of a) grown single crystal SiC 85mm grown at ~50 $\mu\text{m}/\text{hour}$ and b) 80 μm long polycrystalline SiC grown at > 1.3mm/hour.

Experiments were also run to examine the nature of single crystal SiC growth. Of particular interest is the impact of source material/feed rod composition and growth temperature. To this end three compositions at were examined: Fe/Si \sim 1.9 (Fe at. %/ Si at. %) with C = 8 at.%, Fe/Si = 0.35 with C = 8 at.% and Fe/Si \sim 0.35 with C = 16 at.%. These were designed to examine the compositions where SiC is known to co-exist with Si-Fe-C liquid [3]. Some results for growths of single crystal SiC are contained Table 1. There are two important notes to make about the data given in Table 1. First due to the possible wide range of emissivity ($\epsilon_{\text{Fe}}=0.3$ [4] to $\epsilon_{\text{graphite}}=0.9$ [5]) and small size ($\sim 2 \text{ mm}^2$) heated zone, none of the listed pyrometer-measured temperatures are corrected for emissivity. Second, the increase in growth rates more closely relates to the change in temperature above the melting point (M.P.) of each feed rod composition than change in total temperature. Therefore, results are referred to relative to the feed rod M.P., instead of absolute temperature. Growth times for these experiments were kept under 2 hours and the rate at which the crystal was pulled away from the melted zone was a constant $100 \mu\text{m/h}$. This pull rate was chosen for two reasons: First, for these short growth times a maximum movement of $200 \mu\text{m}$ will only cause a minimal change in position of the growth front relative to the heated zone. Second, small upward motion ensures that the seed crystal is not pulled further into the heated zone by the considerable surface tension forces present in the melt.

Feed rods with high Fe (Fe/Si \sim 1.9) concentration failed to melt easily. Only with the seed crystal in contact with the feed rod during the initial heating stages could a stable melt be formed, and even then the melted material only partially wetted to the seed crystal. Post-experiment analysis failed to show any growth, and in one case severe etching of the seed crystal occurred ($>200 \mu\text{m}$ in less than 20 seconds). We surmise that a possible cause of this difficulty is caused by the high thermal conductivity of the Fe present in the feed rods.

Both high-Si (Fe/Si \sim 0.35) concentration feed rod compositions had similar melting points and wetted, as shown in Figure 3b. Table 1 data shows that both high-Si concentration feed rods also exhibited growth rates dependent on temperature and initial C concentration. This suggests two things: First, due to the dramatic increase in growth rate with added C, the growth system is currently C limited. Second, keeping in mind that growth is C limited, the increase in growth rate with temperature suggests that the amount of C transported from the feed rod to seed surface is temperature dependent.

The increase in growth rate with temperature is most apparent in a M.P. $+325^\circ\text{C}$, 10 minute growth experiment where Most of the growth surface is covered $22.5 \mu\text{m}$ thick grown at a rate of $133 \mu\text{m/h}$ (64x greater than growth observed at M.P. $+90^\circ\text{C}$. Therefore growth rates can be controlled both by changing the carbon concentration and /or temperature of the melt.

SiC Radial Growth via CVD Epitaxy

The vast majority of the LTC boule will be formed by epitaxial radial growth on the seed fiber via CVD during step S2 (in chamber 2, Fig. 1b). The LTC boule is expected have a hexagonal cross-section whose

| | | | Growth Rates ($\mu\text{m/hour}$) | | |
|-----------------------------|----------|---------------------------|-------------------------------------|----------------------|----------------------|
| Fe/Si (atomic ratio) | C (at.%) | M.P. ($^\circ\text{C}$) | $+90^\circ\text{C}$ | $+190^\circ\text{C}$ | $+325^\circ\text{C}$ |
| High-Si (Fe/Si \sim 0.35) | 8 | 1170 | 4 | 40 | 135+ |
| | 16 | 1195 | 50 | 120 | N/A |
| High-Fe (Fe/Si \sim 1.9) | 8 | N/A | No Growth | | |

Table 1. Summary of Single Growth Crystal Results (M.P.= temperature at which the feed rod formed a melt, at.% =atomic %). Note: Temperatures are not corrected for emissivity and Growth Rate temperatures are referenced to the M.P (e.g. $+90^\circ\text{C} = \text{M.P} +90^\circ\text{C}$).

outer surfaces will be “M-planes”. **It is vital in this initial project to demonstrate that excellent (essentially defect-free) epitaxy can be achieved at sufficiently high growth rates (on the order of 50 to 100 $\mu\text{m}/\text{hour}$) on M-plane surface orientations.** In particular, the project is slated to grow small-diameter fibers (or simulated fibers cut from larger SiC crystals) into 5 mm diameter or larger demonstration boules. Until high quality SiC fiber crystals are grown, development of the radial growth process is proceeding using simulated “pseudo-fiber” SiC crystals commercially purchased and cut with both “a-face” and “m-face” growth surfaces. While these “pseudo-fibers” are not ideal in terms of their defect content and growth surface quality, we nevertheless hope to carry out radial enlargement growth experiments on these fibers. Such experiments will enable optimization of reactor growth conditions (flows, temperature, pressure, etc.) and hardware/procedures (sample loading, mounting, etc.) to achieve significant radial crystal enlargement at high growth rate. One of the task milestones in the present NASA/DOE Agreement is demonstration of a 5 mm diameter SiC boule. Assuming a 0.4mm diameter SiC pseudo fiber as a starting seed crystal an additional 2.2 mm (2200 μm 's) of radial growth must to be accomplished to achieve a completed 5 mm diameter boule. At 100 μm 's/hour growth rate, the total growth time may exceed 22 hours of growth.

The first year of DOE funding was spent carrying out extensive design modification to one NASA Glenn's existing CVD epitaxy reactors, effectively converting it from a cold-wall pancake coil system to a hot-wall barrel coil system (see FY10 report for details). With these modifications completed early during this (second) year, radial growth process experiments were successfully conducted. Results from two of the most important growth runs that represent progress made to date are described in the following paragraphs.

Sample “Fiber 1” was produced during a five-hour growth, while a second sample “Fiber 2” was produced via an 8-hour long epitaxial growth run. The seeds for these growth runs were saw-cut from non-standard “m-face” oriented wafers. In particular, the saw-cutting results in a starting (pre-growth) seed pseudo-fiber with two polished m-plane faces and two saw cut a-plane faces. Prior to growth, fibers were immersed in a 1:1 solution of H_2SO_4 and H_2O_2 for 15 minutes then blown dry with N_2 . Fibers were immediately transferred to an argon filled glove box.

All growth experiments proceeded within four hours of cleaning. Growth runs were accomplished in a custom designed, inductively heated, horizontal flow hot wall CVD reactor. The tantalum carbide coated tubular susceptor has a 40mm inside diameter and a length of 140mm. A carbon foam insulation package was used to reduce heat loss and improve temperature uniformity. The fibers were supported in the reactor by an uncoated graphite carrier shown in the left photo of Figure 5, which also facilitated in the loading and unloading of the fibers. Approximately, two millimeters of the fibers overall length were used for mounting and do not participate in growth. With the exception of the mounted portion of the fiber, the rest of the fiber is uniformly exposed to growth conditions. The carrier gas was hydrogen (H_2) with standard carbon (C_3H_8) and silicon (SiH_4) precursors used for growth. HCl was added to the gas stream to improve pre-growth etching performance and reduce gas phase nucleation during growth. A twelve minute in-situ pre-growth etch was performed on the fibers before transitioning directly to growth. Aggressive etching conditions were employed to remove crystalline damage caused by the saw cutting operation. Growth parameters for both fibers are given in Table 2.

Growth Parameters for five (Fiber 1) and eight (Fiber 2) hour growth runs

| Growth | <i>In-situ</i> etch [min] | Etch Pressure [mb] | Growth [min] | Growth Pressure [mb] | Hydrogen [sccm] | Silane ¹ [sccm] | Propane ¹ [sccm] | HCl ¹ [sccm] | Estimated Temperature ² [°C] |
|--|---------------------------------|--------------------------|-----------------|----------------------------|--------------------|-------------------------------|--------------------------------|----------------------------|---|
| Fiber 1 (five hour) | 12 | 40 | 300 | 325 | 4260 | 0/4 | 1.5/1.5 | 15/20 | 1600 |
| Fiber 2 (eight hour) | 12 | 40 | 480 | 325 | 4260 | 0/8 | 1.5/2.25 | 15/40 | 1590 |
| 1. First number is for etching conditions, second number for growth conditions. 2. No direct observation of temperature by pyrometry was possible. An inferred temperature was calculated based upon the melting points of Si and Pd. | | | | | | | | | |

Table 2. Process parameters for CVD SiC radial epitaxial growth experiments. There is a substantial and unknown quantity of carbon contribution coming from the uncoated graphite sample carrier and carbon foam insulation.

The seed fibers were mounted approximately vertically in the gas stream, so that all a-face and m-face surfaces (excluding the 2mm portion residing in mounting holes in the graphite holding carrier – left side photo of Fig. 5) are exposed to identical growth conditions in the gas stream. The fibers and carrier immediately following a prolonged (8-hour) growth are shown on the right photo of Figure 5. The small yellow crystals visible on the post-growth carrier, and some regions of the fibers, are 3C-SiC that undesirably nucleated during the growth.

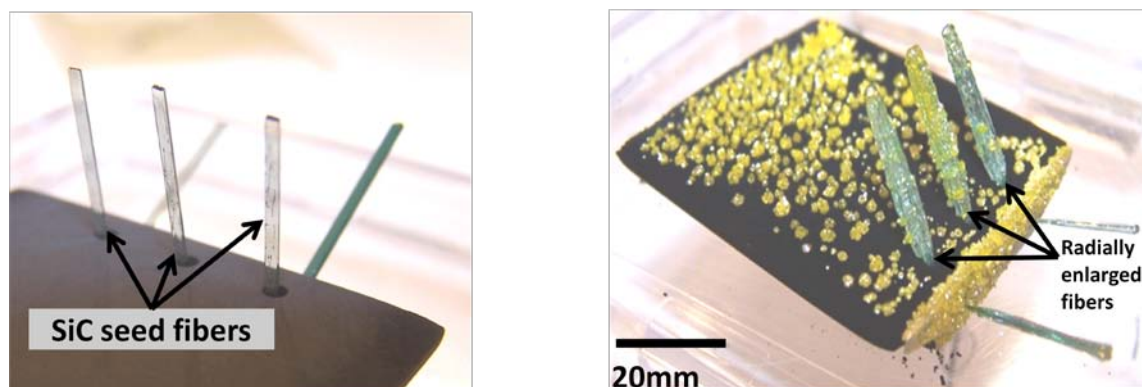


Figure 5: (Left) Pre-growth image of the slivers mounted on the uncoated graphite carrier. (Right) Post growth results for the 8- hour growth. Yellow 3C-SiC decorates the surface of the post-growth graphite carrier.

SEM examination of the 5-hour (left) and 8-hour (right) radial enlargement growth runs are shown in Figure 6. These images show significant radial growth enlargement occurred on both a-face and m-face surfaces of the crystals. As expected, growth facets consistent with the hexagonal SiC crystal structure evolve as the crystal is expanded by radial growth, thus transforming the cross-section from starting rectangular shape (white dashed lines) towards hexagonal geometry. The growth rate is therefore dependent on crystallographic direction. For the 8-hour crystal on the right of Figure 6, a maximum effective growth rate of about $180\mu\text{m}/\text{hour}$ was obtained. This experimentally achieved radial growth rate is sufficient for use in a full LTC process as described in US Patent 7,449,065. The total radial enlargement of the 8-hour Fiber 2 crystal in the m-direction is about 1.5 mm. This crystal has several locations where 3C-SiC has nucleated and negatively impacted the growth morphology, particularly near the end where growth occurs on the small silicon-face tip of the seed. It is proposed that carbon particulates coming from the uncoated graphite carrier contributed to the formation of the 3C-SiC. Further process optimization, including use of carbide-coated sample carriers, is expected to suppress parasitic 3C-SiC nucleation as this experimental work further progresses towards realizing much larger (~ 0.5 cm diameter initial project milestone) radially-grown SiC crystals. A large number of morphological steps/mini-facets are present on the as-grown surface of both fibers. The fact that the 8-hour fiber has evolved some smooth-facet regions (near in the center of the length) that suggest these features might be smoothed out as thicker radial crystals are grown.

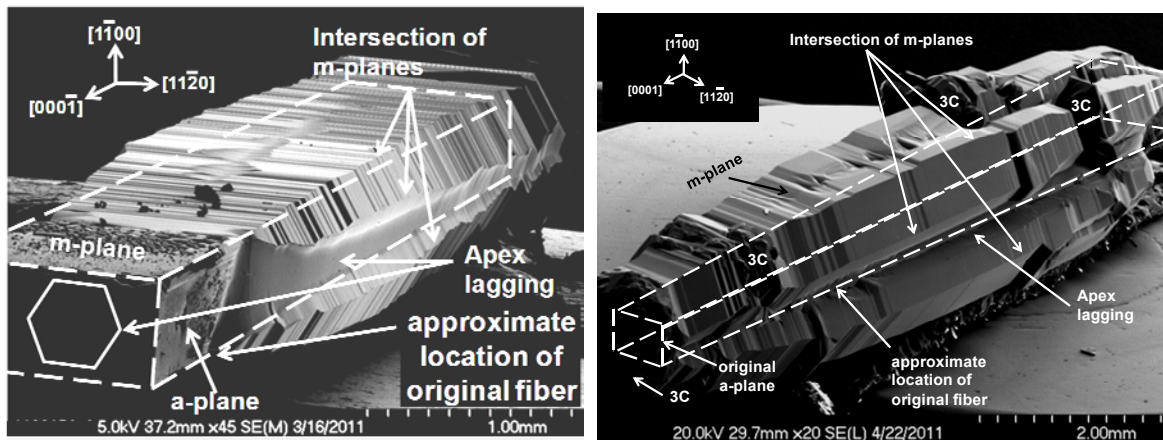


Figure 6. SEM images of radially expanded SiC crystals following (left) 5-hour and (right) 8-hour epitaxial growth.

Both crystals shown in Figure 6 underwent synchrotron white beam x-ray topography (SWBXT) analysis by Prof. Dudley's group at Stony Brook University. Such X-ray analysis enables spatial mapping of crystal structure (polytype), crystallographic defects and strain in SiC crystals. Figure 7 shows one of the topographic images collected on the 8-hour Fiber 2. For regions free of 3C-SiC nucleation, the radially grown epilayer was found to exactly replicate the seed crystal structure and was largely free of strain. As desired, the X-ray analysis did not find evidence of additional defect formation in the homoepitaxially grown regions of the crystal.

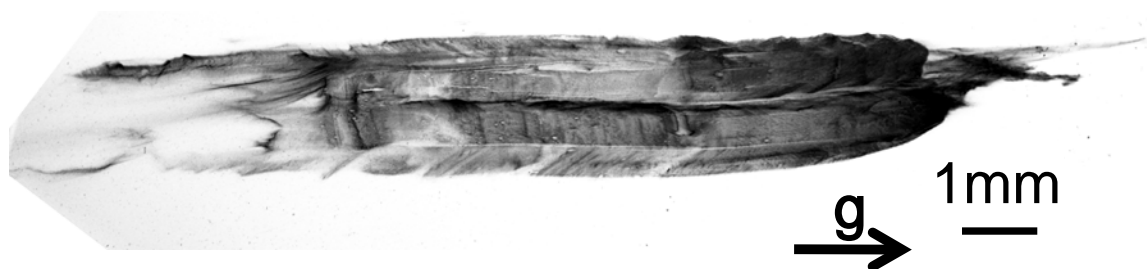


Figure 7. SWBXT image of 8-hour Fiber 2 crystal. The central faceted sections where no 3C-SiC has nucleated are epitaxial with the substrate and are of high crystalline quality and low strain.

It must be noted that on August 12, 2011 the RF induction generator subsystem of the NASA Glenn SiC epitaxial growth system suffered a major failure with resulting heaving damage (Figure 8). The damage was so extensive that the manufacturer is refusing to warranty its on-going repair of the unit. NASA Glenn has now contracted for the purchase of a new RF induction heating system at cost just under \$100K with an anticipated delivery date of January 30, 2012. The repaired hardware is expected to return to NASA Glenn in November 2011. Present plan is to resume LTC radial epitaxial growth experiments using the repaired unit (if possible) until the new heating system arrives and can be installed. Thus this setback has delayed attempts to realize DOE milestone experiment (realization of 0.5 cm diameter boule) at least 6 months.

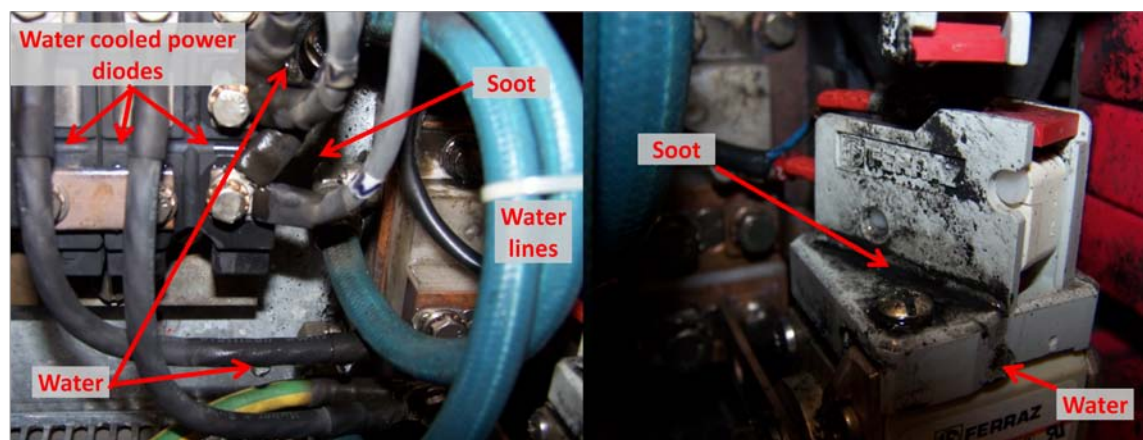


Figure 8. Photos documenting heavy damage (soot, water) to inside of failed RF induction generator subsystem of NASA Glenn SiC epitaxial growth system. All LTC radial growth work is delayed until heating system is repaired or replaced.

Conclusion

Over the past year NASA Glenn has successfully initiated experimental studies of the two critical (previously un-attempted) “fiber” and “radial” growth processes needed to realize Large Tapered Crystal (LTC) SiC boules. Significant understanding was gained and progress made toward project technical goals, including first experimental implementation of single-crystal SiC growth via Solvent-LHFZ technique as well as demonstration of radial epitaxial expansion at commercially viable growth rate $> 100 \mu\text{m}/\text{hour}$. However, given failed hardware and difficult remaining technical challenges, it is unlikely that quantitative crystal size metrics will be achieved by the end of the NASA-DOE agreement schedule (December 2011). Further work and funding beyond this date will be necessary to achieve complete LTC feasibility demonstration goals/milestones.

If successfully implemented, LTC boules promise to greatly improve the cost and quality of wide bandgap wafers that will become the basis for realizing much more advanced high-power semiconductor switches. These devices in turn offer high-impact benefits to power conversion/management systems including utility power transmission and electric/hybrid vehicles.

Publications

A. A. Woodworth, P. G. Neudeck, A. Sayir, D.J. Spry, A. J. Trunek and J. A. Powell, *SiC Growth by Solvent-Laser Heated Floating Zone*, International Conference on Silicon Carbide and Related Materials, Cleveland, OH, September 11-16, 2011, Submitted.

A.J. Trunek, P.G. Neudeck, A.A. Woodworth, J. A. Powell, D.J. Spry, B. Raghathamachar, and M. Dudley, *Lateral Growth Expansion of 4H/6H-SiC a/m-plane Pseudo Fiber Crystals by Hot Wall CVD Epitaxy*, International Conference on Silicon Carbide and Related Materials, Cleveland, OH, September 11-16, 2011 Submitted.

References

- [1] F. Ritzert and L Westfall, “Laser Heated Floating Zone Production of Single Crystal Fibers” NASA Technical Memorandum 4732 (1996)
- [2] L. B. Griffiths and A. I. Mlavsky, “Growth of α -SiC Single Crystals from Chromium Solution”, J. Electrochem. Soc., **111**, 805 (1964).
- [3] T Yoshikawa, S Kawanishi and T Tanaka, Fundamental Study for Solvent Growth of Silicon Carbide Utilizing Fe-Si Melt, International Conference on Advanced Structural and Functional Materials Design 2008, Journal of Physics: Conference Series 165 (2009) 012022.
- [4] H. B. Wahlen and Harry W. Knop, Jr., “The Spectral Emissivity of Iron and Cobalt”, Phys. Rev., 74, (1948) 687-689
- [5] M.R. Null and W.W. Lozier, “Measurement of Reflectance and Emissivity of Graphite at Arc Temperature with a Carbon Arc Image Furnace”, J. Appl. Phys., 29, (1958) 1605

Patents

- 2. None this period. This project is based upon development of US Patent 7,449,065 Awarded 11 November 2008.

3. Electric Motors Research and Technology Development

3.1 A New Class of Switched Reluctance Motors Without Permanent Magnets

Principal Investigator: Tim Burress

Oak Ridge National Laboratory

National Transportation Research Center

2360 Cherahala Boulevard

Knoxville, TN 37932

Voice: 865-946-1216; Fax: 865-946-1262; E-mail: burresta@ornl.gov

DOE Technology Development Manager: Susan A. Rogers

Voice: 202-586-8997; Fax: 202-586-1600; E-mail: Susan.Rogers@ee.doe.gov

ORNL Program Manager: Mitch Olszewski

Voice: 865-946-1350; Fax: 865-946-1262; E-mail: olszewskim@ornl.gov

Objectives

- Overall Objectives
 - Develop, design, build, and test an unconventional traction drive that
 - has no permanent magnet (PM) material;
 - has lower torque ripple and acoustic noise than that of a conventional switched reluctance motor (SRM); and
 - maintains the low cost, simplicity, and power density of the conventional SRM.
 - Obtain operational characteristics for finalized design and compare with targets:
 - power density: 5 kW/L (2015 DOE target),
 - specific power: 1.3 kW/kg (2015 DOE target), and
 - cost between \$7/kW and \$4.7/kW (2015 and 2020 targets, respectively).
- FY 2011 Objectives
 - Construct prototype.
 - Characterize prototype machine parameters.
 - Develop and prepare drive/controller hardware and software.
 - Conduct comprehensive motor testing in dynamometer test cell to determine performance, efficiency, torque ripple, and acoustic noise characteristics.

Approach

- Select preferred design approach for novel switched reluctance (SR) machine.
 - Analyze basic feasibility of various novel SR machine designs.
 - Conduct finite element analysis (FEA) to obtain motor characteristics.
 - Develop preliminary novel control schemes.
 - Simulate final designs with basic dynamic model.
 - Obtain estimated capabilities of torque and power as a function of speed.
 - Choose preferred design approach based on preliminary cost assessments, FEA, and dynamic simulation results.
- Perform detailed design and simulation of selected design approach.
 - Conduct structural, thermal, and acoustic noise modeling.

- Adjust design approach as necessary.
- Investigate potential to apply air-gap enhancements.
- Carry out comprehensive dynamic simulations.
- Refine novel control algorithm and investigate potential to apply other novel control techniques.
- Obtain accurate capabilities of torque and power as a function of speed
- Build and test SRM prototype and novel control technique.
 - Determine power density, specific power, and cost based on results from dynamometer tests.

Major Accomplishments

- Developed unconventional SR machine design.
- Verified through simulations that the design meets 2015 performance targets with less than 5% torque ripple.
- Developed custom software to accomplish various tasks.
 - Two universal dynamic simulators.
 - Parametric: efficient means to optimize control and design parameters.
 - FEA: capable of conducting dynamic electromagnetic and structural simulations.
 - Automated FEA based geometric optimization.
 - Complex multivariable, multiobjective optimization of control waveforms as a function of speed and torque.
- Achieved near-zero torque ripple for low and moderate torque levels (up to 150 Nm).
- Developed iterative self-learning pseudo-flux observer-based control algorithm.
 - Capable of tracking/producing abstract current waveforms.
- Tested machine up to 5,000 rpm.
 - Results lower than expected, but accounting for steel degradation, results are close to simulations.

Future Direction

- This project will not be funded by the DOE Vehicle Technologies Program beyond FY 2011, but several potential prospects exist for the continuation of this work.

Technical Discussion

Background

Because of the high and unpredictable cost and availability of rare earth PMs, which are used in most hybrid vehicle applications today, many automotive manufacturers have a common interest in the use of electric machines which do not use these materials. Although PM motors are not easily surpassed with respect to efficiency and power density, other competitive motor technologies exist which can have lower cost per power rating (dollars/kilowatt). Of the alternative motor technologies, the SRM offers the simplest rotor configuration, which is advantageous in terms of material cost, manufacturing cost, speed capability, and reliability. The highly nonlinear behavior and unusual control methods associated with the SRM require the use of sophisticated and computationally intensive software programs to fully optimize its design and operation. Therefore, the SRM is a relatively young motor technology, in terms of research and development, as opposed to other technologies such as the induction motor. Two primary drawbacks of the SRM are the level of torque ripple and the acoustic noise inherently associated with the SRM's doubly salient stator and rotor geometry. The intent of this project is to apply novel design techniques that significantly reduce torque ripple and acoustic noise while maintaining the intrinsic benefits of the SRM.

Existing torque ripple and acoustic noise reduction techniques typically incur significant compromises of things such as peak torque, torque–power density, material/manufacturing costs, and/or design complexity. A conventional SRM with eight stator teeth and six rotor teeth is shown in Fig. 1(a). If the

rotor is assumed to be rotating clockwise, the two stator teeth without a superimposed yellow “X” are the only stator teeth that would have excited windings if a conventional control scheme were used. That is, only two (25%) of the eight stator teeth are active during this instant. As the rotor position continues to increase in the clockwise direction, coils of two additional stator teeth are excited, and thus 50% of the stator teeth are active at that instant. However, this condition is maintained only for a short duration, and only 25% of the stator teeth are active beyond this short duration, giving a low average of active stator teeth.

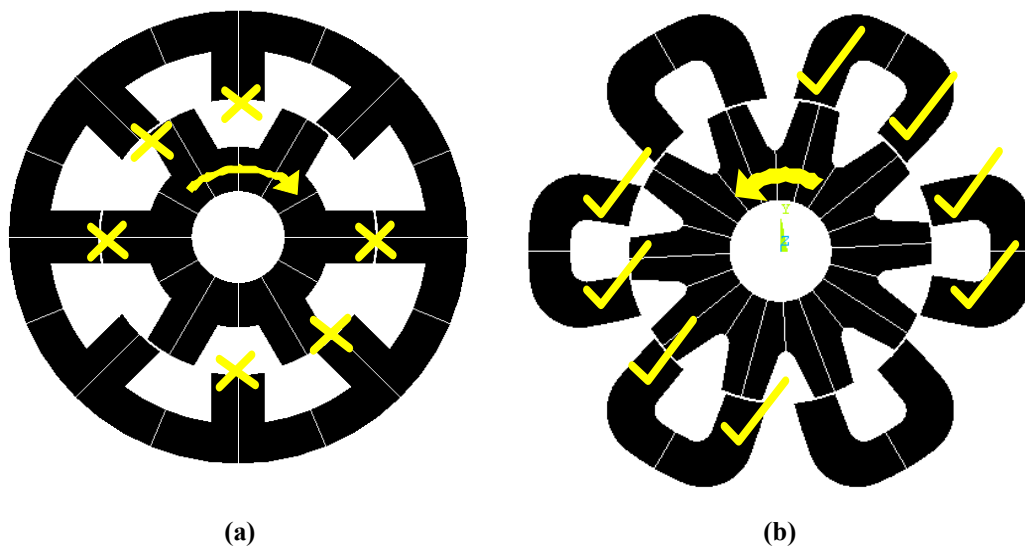


Fig. 1. Active stator teeth of (a) a conventional SRM and (b) an unconventional SRM.

After observing the low amount of active air-gap area within the conventional SRM, it seemed that novel concepts could be used to increase the average number of active stator teeth that are producing productive torque to more readily distribute the torque production and thereby reduce torque ripple. Because the fundamental means in which torque is produced in an SRM relies on the magnetic saliency of the stator and rotor, it can be difficult to increase the number of active stator teeth without compromising the reluctance ratio between aligned and unaligned rotor positions. This is a result of introducing stator and/or rotor teeth within a closer proximity of each other, thereby promoting detrimental flux leakage through undesired paths, which typically decreases the overall torque capability of the machine. Therefore, the proposed general approach uses isolated multiple flux paths (IMFPs) to carry out the tasks mentioned above while seeking to minimize counterproductive flux flow by means of magnetic path isolation. Because the permeability of steel approaches that of air as magnetic saturation increases in the steel, it is not possible to have completely isolated magnetic paths in this type of application, particularly since the SRM often operates in the saturation region for applications requiring high power density. Therefore, these types of hardware approaches must be incorporated carefully in such a way that the natural operation and control of the motor inhibits the detrimental tendencies of leakage and undesired flux paths.

In FY 2009, a wide variety of designs which use this technique were developed and analyzed for feasibility. Based on comparisons of estimated performance, size, cost, and manufacturability, the most feasible geometry was chosen to be the focus of FY 2010 development efforts. As shown in Fig. 1(b), 8 of 12 stator teeth are typically active at the indicated rotor position for counterclockwise motoring operation. As the rotor continues to rotate, only 4 of 12 stator teeth are active for a brief period of time and then 8 of 12 stator teeth are active again. Therefore, on average, at least 50% of the stator teeth are active in this unconventional SRM versus roughly 33% in a conventional SRM. While many more

characteristics should be considered in making a direct comparison, this quick observation reveals the potential of the design to facilitate greater overlap of torque production among the phases compared with a conventional SRM.

Dynamic Simulators

To have the capability to fully assess the overall impact of the variation of a range of design parameters, two separate universal dynamic simulators were developed. The simulators are universal in the sense that they can simulate various motor designs, even other types of motors, with slight modification to the simulator. An FEA based simulator was developed for design optimization such that most of the design parameters are variable and the corresponding design geometry, mesh, boundary conditions, and constraints are generated in an automated manner. This simulator is well suited for integration with other types of analyses such as integrated structural and thermal FEA. The other simulator is similar in nature, but is better suited for control optimization and uses a differential equation based machine model developed by ORNL.

Extensive efforts were made to ensure that the impacts of saturation, mutual coupling, and other interactions between phases were fully realized. It is common for designers to neglect these phenomena, but the acknowledgement of these aspects is particularly important for this unconventional design approach. Both simulators have the capability to work in various modes such as current, torque, or speed regulated operation so that the simulation is conducted as if the design were in actual operation in a vehicle. Fig. 2 shows a graphical user interface (GUI) that was developed to provide an effective way to operate the dynamic simulators and generate and edit waveforms which are supplied and returned from the simulator code.

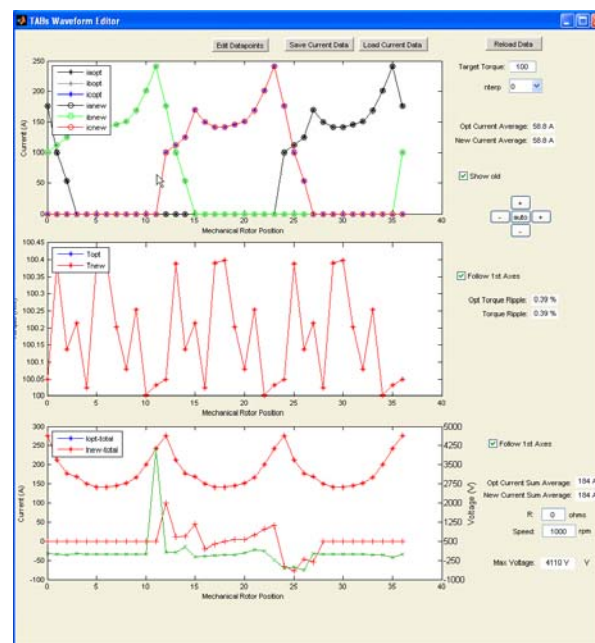


Fig. 2. GUI developed to operate dynamic simulators.

Control Algorithm Development

The dynamic equation based simulator is particularly useful for optimizing control conditions such as maximum torque per amp, minimum torque ripple, and maximum efficiency. A considerable amount of effort was devoted to the development of control optimization codes for operation with near-zero torque ripple. Since torque is a function of three currents and position, the currents at each position can be

chosen to meet the desired torque reference, provided that current and voltage constraints are not violated. Therefore, this approach requires dynamic modeling to ensure that the required voltage does not exceed the amount available from the dc link. The resulting problem is nonlinear multivariable, multiobjective optimization with nonlinear constraints. Attempts were made to use optimization algorithms including various genetic and neural networking techniques, but computational times were tremendous and there was difficulty in obtaining globally optimal solutions, as local solutions were often presented despite the use of a global algorithm. Therefore, ORNL developed an algorithm termed the “brute-force” method, based on the unconventional manner in which the problem is approached using this method. The method involves the automated generation of an initial solution for the desired conditions followed by development of a series of solutions that fall within the given constraints. At this point, the brute-force method finds the optimal solution and verifies that it is a global solution, or another iteration is commenced. It is estimated that about 10,000 lines of code were written to carry out this task in which recursive functionality is used to explore solution regions. The overall result is a collection of reference waveforms for points throughout the entire operation region.

Solutions obtained from the brute-force method were analyzed with the dynamic equation based simulator, with the results for less than 5% torque ripple conditions indicated by the blue trace in Fig. 3. Torque ripple can be defined in various ways, and in this case, it is based on the quadratic mean of the ripple divided by the average torque multiplied by 100. This method was used as opposed to using single values such as the maximum and minimum torque, which do not fully incorporate all aspects of the torque waveform. For example, a torque spike with very short duration could be present in the torque waveform, and the latter torque ripple calculation would be greatly affected although the inertia of the system would most likely render the spike to be minimally consequential. A torque level of about 170 Newton meters (Nm) is achievable at low speeds with a torque ripple level of 5%. At 4,000 rpm, the machine is capable of producing 125 Nm, which is a power level of 52.4 kW, with a torque ripple of only 5%. Calculations which include copper and iron losses indicate that the efficiency of the motor under these conditions is about 94.5%. As speed increases, the power capability decreases if the torque ripple is limited to 5%. But at higher speeds, it may be possible to alleviate the torque ripple constraints based on the increased momentum associated with these speeds.

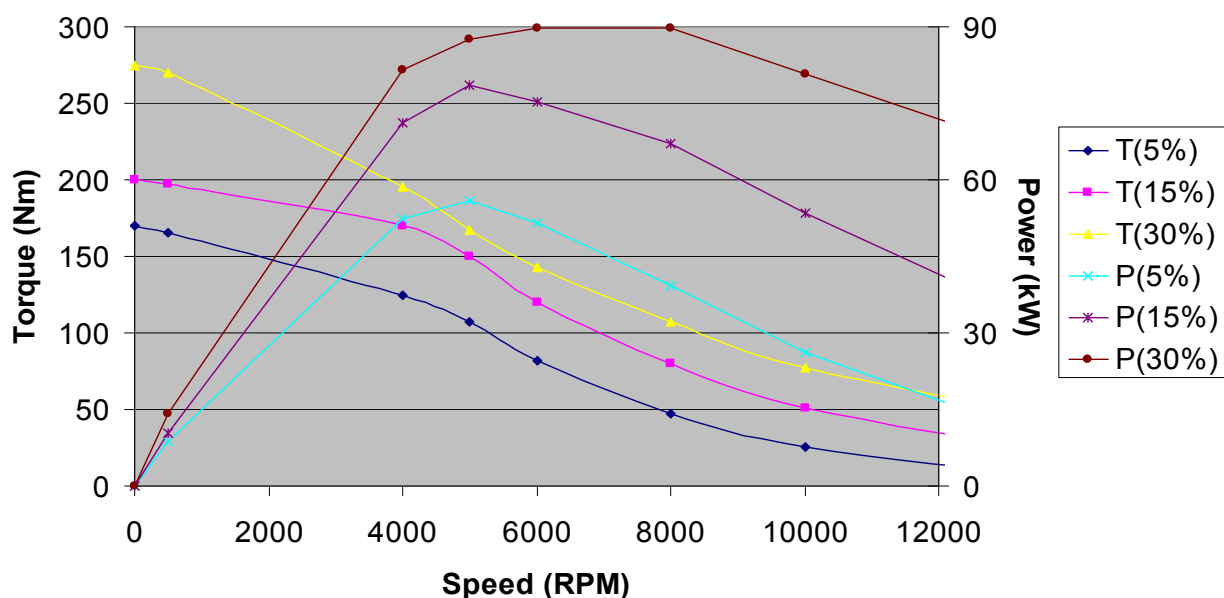


Fig. 3. Torque and power versus speed.

Continuous conduction control can greatly increase the output power of an SRM at moderate and high rotor speeds as a higher amount of current is applied in the torque production region (for the motoring operation mode). This is achieved by not requiring the current in each stator tooth to reach zero during each electrical cycle. Because current is not zero when the rotor rotates beyond the alignment position, negative torque is applied to the shaft, and thus this control mode does not operate with utmost efficiency, but it can greatly increase the power capability of the machine. This is particularly relevant to vehicle propulsion applications, wherein the average required power is relatively low for normal driving conditions and only short durations of high power demand are required for situations such as passing other vehicles or merging with high-speed traffic. However, there may be issues associated with acoustic noise during this type of operation.

The additional traces shown in Fig. 3 represent the torque and power capabilities of the machine with torque ripple percentages that are greater than 5%. Simulations indicate that the machine can produce about 75 kW at 8,000 rpm with a torque ripple of 20% and more than 90 kW at 8,000 rpm with a torque ripple of 30%. Simulations also show that the machine is capable of operating beyond 15,000 rpm. The size of the machine used in these simulations matches that of the second generation Prius, with roughly a 10 in. stator outer diameter and a 3.3 in. stack length. This particular design is well suited for an application similar to that of the primary motor of the Camry hybrid electric vehicle (HEV), where a gear reducer is used to increase the torque capability while the high speed operation results in improved power density. These simulation results indicate that this design approach could potentially offer a competitive alternative to PM machines in HEVs.

Structural, Modal, and Acoustic Assessments

Mechanical analyses were conducted to perform design optimization and validation in terms of structural integrity and minimal acoustic signature. Force vector results from electromagnetic FEA studies were used to establish proper loading conditions and boundary conditions for these mechanical FEA studies. As peak loading conditions were applied, stress analyses were conducted on the components within the assembly. As structural improvements were incorporated into the design in response to these studies, the impacts upon the electromagnetic characteristics were assessed in separate analyses, as necessary.

Advantages of IMFP Design

In unconventional IMFP SRMs, air or other nonmagnetic materials provide magnetic isolation between segments which would otherwise have a direct path in which flux traverses. Fig. 4 shows examples of the flux paths for a conventional 12-8 (12 stator poles and 8 rotor poles) SRM [4(a)] and an unconventional 12-10 SRM [4(b)]. The flux path of the conventional 12-8 SRM, indicated in light orange, travels an angular distance of 90° through the stator back-iron (yoke) from pole to pole. The unconventional IMFP 12-10 uses short, localized flux paths (also indicated in light orange).

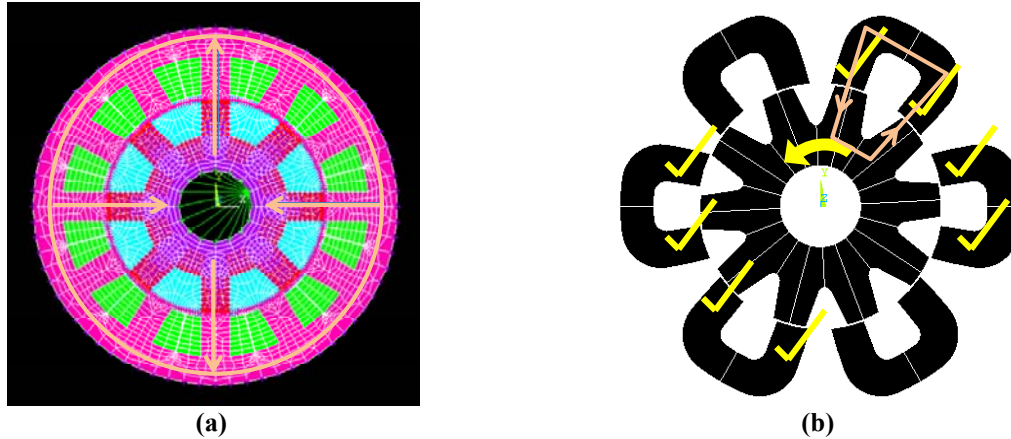


Fig. 4. Flux paths in (a) conventional 12-8 and (b) unconventional IMFP 12-10 SRMs.

Three major loss components in electric machines are hysteresis, eddy current, and copper losses. Hysteresis and eddy current losses are roughly proportional to the length of the flux path. Therefore, the IMFP has a noticeable advantage over conventional designs because the flux path length is much shorter. Furthermore, hysteresis loss (heat) is generated from molecular friction when magnetic particles in the steel are subject to a reversal of magnetic field. For certain IMFP configurations, such as the 12-10, there is essentially no flux reversal in the stator pieces. This is a significant advantage when compared with conventional flux reversal frequencies that are 3 or more times the electrical frequency because all phases share the same back-iron. Additionally, SRMs in general have a smaller amount of wasted copper at the end-turns because the phase windings do not overlap each other and thus can have lower copper (I^2R) losses than what is typical for PM or induction machines with distributed windings.

Conventional winding arrangements in SRMs consist of single coils individually wrapped around each stator tooth, as shown in Fig. 5. This winding arrangement can be used on the unconventional IMFP 12-10 (and other IMFP arrangements), with a coil wrapped around each of the 12 stator teeth. In this case, each pair of coils on the U-shaped stator pieces is typically connected in series, and these can be connected in series or parallel with other coils in the same phase. However, the segmented pieces of the IMFP provide another option for coil placement. A coil can be “yoke-wound” on each stator piece, as indicated in Fig. 6. The coil can be strategically wound such that the impact upon the radial size of the machine is minimal. This is achieved by allowing the conductors of the outermost portion of the coil to spread wide across the outermost arc of the stator pieces. It can be assumed that area “A1” and area “A2” (Fig. 6) should be about equal, and because the arc of A2 is much greater than the arc of A1, the radial width of the outermost coil is much smaller.

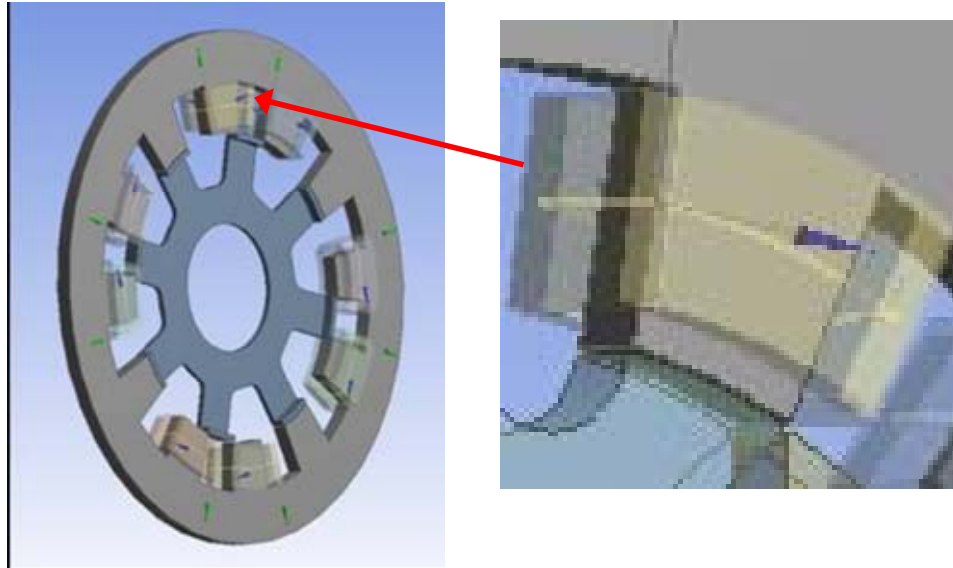


Fig. 5. Conventional SRM tooth winding.

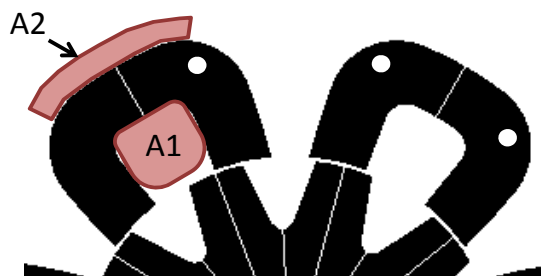


Fig. 6. Yoke-wound IMFP 12-10 SRM.

Although the significance of the transition from conventional tooth-wound coils to yoke-wound coils seems minimal, there are many advantages that can be gained from this transition.

1. Improved heat transfer. Copper has a thermal conductivity that is about 40 times higher than steel, and thus the wire on the outer arc of the pieces can interface with a cooling infrastructure. Normally, the heat in motors has to travel through the steel before reaching a heat exchanging interface (often aluminum for hybrid vehicles). For the IMFP, heat generated by copper losses has a good thermal conduction path directly to the heat exchanger. Note that because the windings are not a solid piece of copper, but actually insulated copper wires, the observed benefit will not be 40 times higher. Removal of heat is essential for obtaining high power densities—which is important for vehicle applications, among many other applications. Therefore, this improvement of heat transfer leads to improved power densities and specific powers as higher output power can be obtained with an equivalently sized motor.
2. Wider stator and rotor teeth. The stator teeth can be much wider because the conductors are not located outside of the teeth on the U-shaped pieces. This allows for the torque production from each phase to be more broad, increasing the overlap of torque production among phases. This can also increase the overall torque, and facilitates the reduction of torque ripple and opens up more opportunities to reduce acoustic noise from a controller/software standpoint. The rotor teeth would

also likely be wider as the stator teeth are wider. Therefore, the teeth in the motor are more mechanically substantial and will not vibrate and create acoustic noise as much as thin teeth would.

3. Higher fill factor. More conductors can be located in the middle of the “U” because two coils do not share this volume. Because the yoke-wound approach has one single coil, the issue of winding two coils in place or installing two prewound coils onto the stator teeth is avoided. These latter approaches require compromises on fill factor. Additionally, high voltage applications may require the two coils to be separated with insulation material to keep the coils electrically isolated and mechanically protected from vibration. And ultimately, fill factor is also a key factor in obtaining high power density and/or specific power.
4. Facilitation of acoustic noise damping techniques. Because the space between the U-shaped stator pieces is void, there is opportunity to incorporate noise damping countermeasures into this void. For example, an epoxy or rubber-like substance could be inserted between the pieces to dampen the noise, which may allow some the acoustic energy to be dissipated in the damping compound as opposed to being transmitted through the chassis/support structure.
5. Other ways to use void between stator pieces. Other unexplored uses of the void between the U-shaped pieces include the integration of coolant passages (air or liquid), addition of separate coils, use of non-rare-earth magnets to counteract leakage, and location of power electronics/controls.
6. Winding manufacturability. The U-shaped stator pieces can be wound before they are installed in the motor, and they can be wound directly by simply “chucking” the pieces such that they can be rotated while wire is wrapped around them. This method was used during the fabrication of the prototype. The tooth-wound approach allows for the stator pieces to be wound before they are installed in the motor, but the coils would typically be prewound and then slid onto the stator teeth. Finally, the tooth-wound approach requires the interconnection of the two separate coils on each stator piece, while this is avoided with the yoke-wound technique.

Fabrication and Assembly of IMFP SRM

High tolerance parts for the IMFP SRM were fabricated externally by tool shops and lamination manufacturers. Figure 7(a) shows the SRM assembly with star-shaped end bells, a stator containment ring with integrated cooling channels, end plates, a stainless steel shaft, and custom swaging tool. The swaging tool was used to simultaneously compress the rotor laminations and fold a rigid retention lip to hold the laminations in place. Rotor and stator laminations are shown in Fig. 7(b), where the stainless steel shaft with a 2 in. outer diameter is also visible. With a rotor outer diameter of about 6 in. and stator outer diameter of about 10 in., the lamination dimensions are similar to that of Toyota designs. The laminations were combined into a 3.0 in. stack, which is shorter than the 2004 Prius stack length of 3.3 in. and slightly longer than the 2007 Camry stack length of 2.8 in. Both rotor and stator laminations are 0.014 in. thick and are made of nonoriented M19 steel with a C5 coating for electrical insulation.

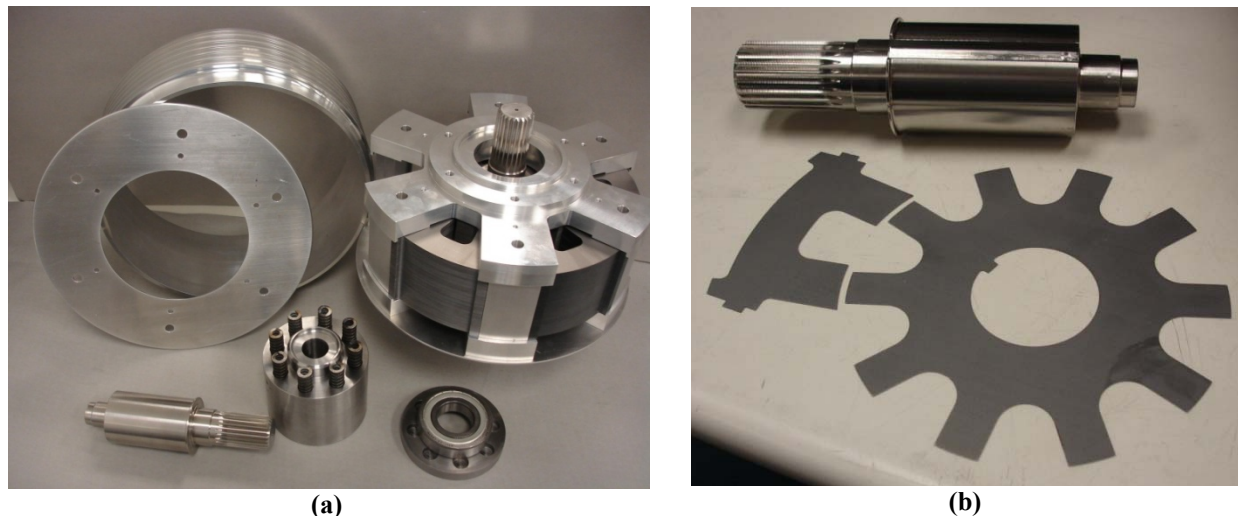


Fig. 7. High tolerance parts for the IMFP SRM: (a) fabricated parts and (b) stator and rotor laminations with rotor shaft.

A custom in-house winding system was developed to clamp, hold, and rotate the stator piece and compress the windings to improve fill factor and form it to mate with the stator containment ring. The first batch of stator windings incurred some hi-pot test failures, and the stator pieces were rewound with special care at sharp bending radii. Mylar was used as a slot liner, with 0.005 in. and 0.010 in. thick pieces being applied, depending on the location. The windings were vacuum impregnated with a variant of Dolph's thermal-setting varnish. Opposing stator coils, shown in Fig. 8(a), were connected in series with two coils per phase. These could have been connected in parallel, and other possibilities include the use of switchable windings to obtain high torques at low speed and to extend the speed range of the machine.

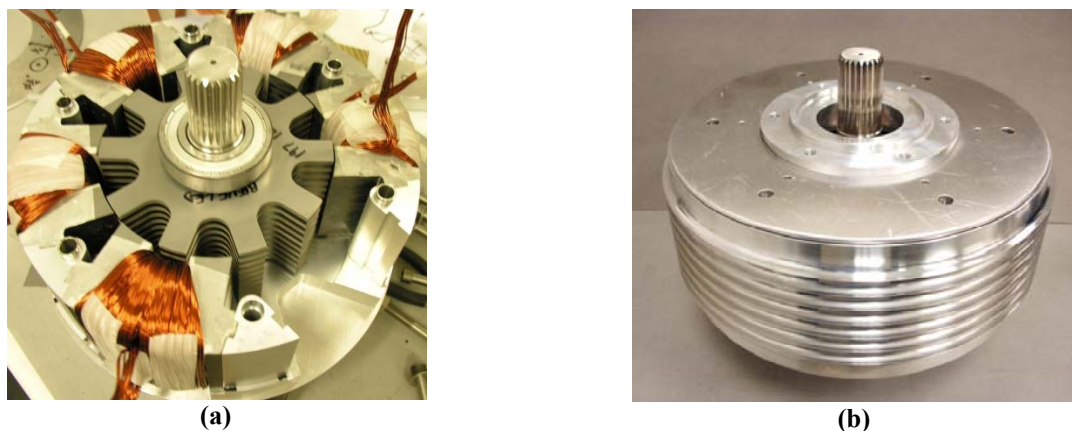


Fig. 8. IMFP SRM final assembly: (a) winding installation and (b) finished IMFP SRM.

Characterization

Control optimization software developed by ORNL uses machine parameters to determine optimal control conditions throughout the entire torque and speed range. These machine parameters (namely torque and flux linkages) vary as a function of rotor position and three independent currents. With the need to collect 1,500 data points which include many high-current situations, a system was developed to automatically step and lock the rotor in desired positions as sequences of current combinations were applied to the windings. This system required a substantial amount of time to develop, but was crucial in obtaining motor parameters without experiencing over-temperature conditions. Figure 9 shows locked rotor torque measurements for single phase excitation plotted against position. These measurements are significantly

lower than what simulations indicated. A clear comparison can be made by computing a ratio of simulated locked rotor torque over measured locked rotor torque. This ratio is plotted versus dc current in Fig. 10 for single phase (pink trace) and multiple phase (yellow trace) excitation. This graph indicates that the measured torque-per-current ratio is relatively close to simulated values for very low currents, but the ratio decreases significantly with increasing current. At 200 A, the measured torque values are 25% and 35% lower than simulated torque capabilities for multiple phase and single phase excitation, respectively. These results suggest that the steel starts magnetically saturating at a much lower current level than simulations indicate. Premature saturation results in lower torque capability and ultimately lower efficiency. Locked rotor simulations are simple and usually accurate as there is no impact from eddy current, hysteresis, and I^2R losses. These results were verified with multiple FEA software packages, and therefore, it can be reasonably assumed that the quality of the steel laminations is inferior.

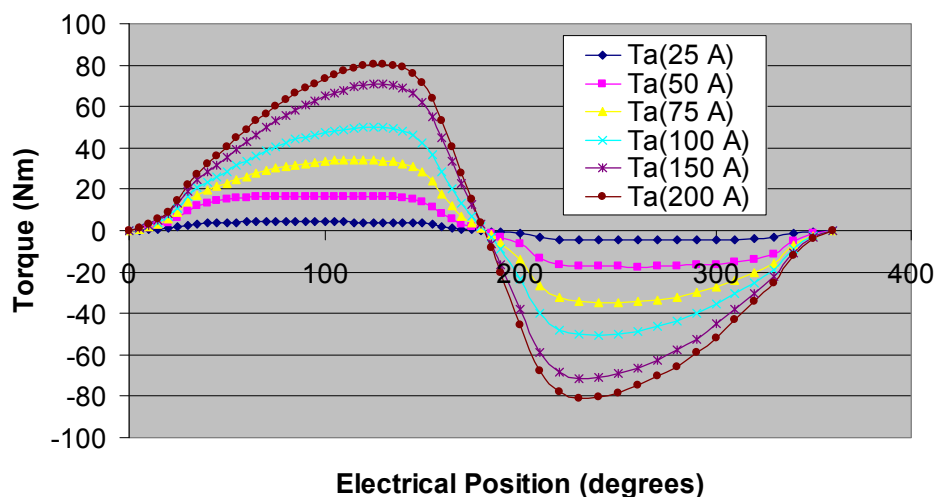


Fig. 9. Single phase locked rotor torque.

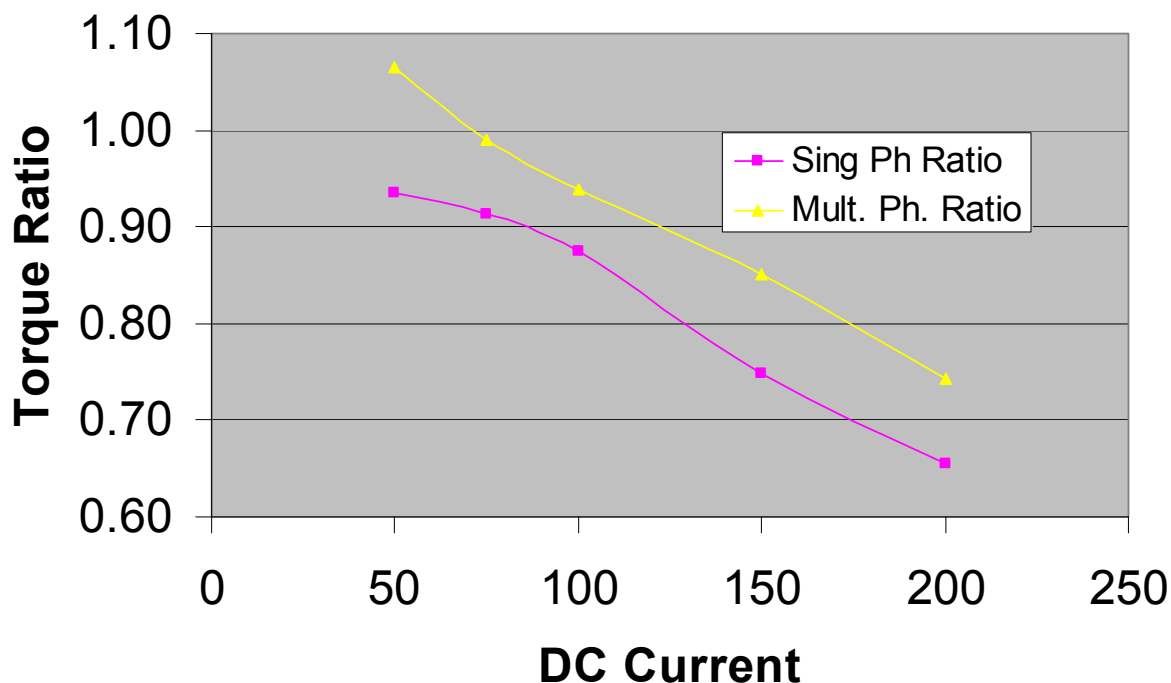
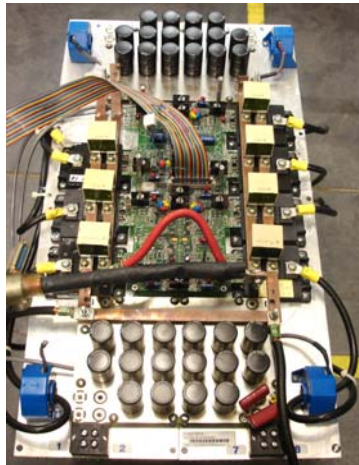


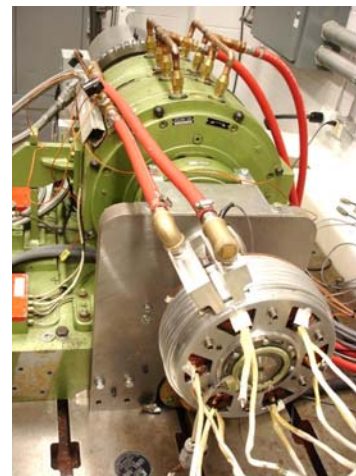
Fig. 10. Ratio of simulated/measured locked rotor torque.

Drive/Controls Implementation and Test Results

The inverter drive shown in Fig. 11(a) was developed on a previous project for a four phase 8-6 SRM and was used to drive the three phase IMFP 12-10 SRM. A face-mounting system was used where the IMFP SRM was face-mounted to a torque meter and the torque meter was face-mounted to the dynamometer, as shown in Fig. 11(b). The circuit diagram in Fig. 12(a) depicts two IGBTs and two diodes per phase, which is the same as a conventional inverter except the diodes are not antiparallel diodes. Several switching schemes are available, but an interleaved switching technique was used which is capable of applying $+V_{dc}$ and $-V_{dc}$ (when rectifying) as well as a zero volt loop which alternates between upper and lower IGBTs, thereby dispersing heat generation. Additionally, the effective switching frequency in the winding is 2 times that of the individual IGBT switching frequency, which facilitates improved current control and reduced acoustic noise. A comprehensive control system console, shown in Fig. 12(b), was developed to allow convenient manipulation of various control parameters. Original control methods involved a conventional current feedback loop with proportional-integral-derivative (PID) regulation. To mitigate torque ripple, optimal current profiles typically have significant transients which are difficult for a conventional PID current loop to track. In addition to transient references, the influence of electromagnetic interference, current transducer bandwidth, and position measurement resolution are also factors in the performance of the current loop. Therefore, a self-learning pseudo-flux-observer control algorithm was developed to more readily anticipate and generate the appropriate control signals needed to track the optimal current profile. The uppermost and middle graphs visible in the control console shown in Fig. 12(b) show successful tracking of a demanding current profile.



(a)



(b)

Fig. 11. Test setup: (a) inverter used to drive the IMFP SRM and (b) dynamometer installation.

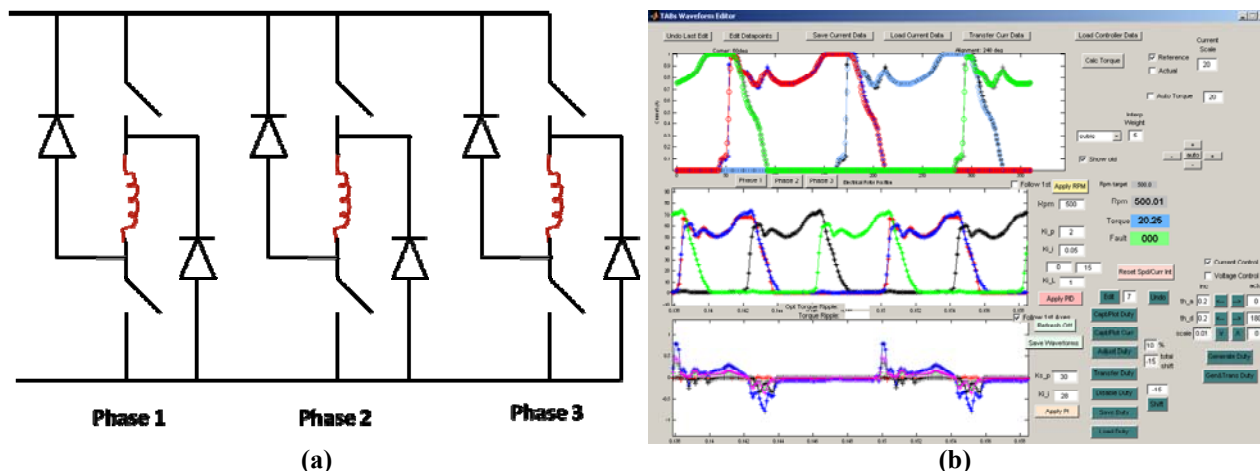


Fig. 12. Drive controls: (a) converter diagram and (b) control console.

The motor was designed for operation with a dc link voltage of 650 V, but tests were limited to 400 V to ensure that potential failures did not occur as time limitations became eminent. For the same reasons, phase currents were limited to 200 Arms and rotational speed was limited to 5,000 rpm. An ethylene-glycol coolant temperature regulator was used to maintain the coolant temperature at 65°C during most of the tests. An efficiency map is shown in Fig. 13, with portions above 5,000 rpm being extrapolated. Motor efficiency is comparable to many benchmarked PM machines for low to moderate loads and low speeds (less than 750 rpm) and reaches 90% at 3,500 rpm with a peak efficiency measurement of 93%. However, efficiency values are relatively low between 1,000 and 3,000 rpm in comparison with most PM machines, which is no surprise when considering the low torque-per-current that was observed in locked rotor tests. Peak torque and peak power curves for 400 V are shown in Fig. 14, with a peak power level of 23.4 kW at 3,000 rpm. Also shown in Fig. 14 are peak torque and power curves for 650 V, which were extrapolated from 400 V operational data. The curves indicate that the motor can produce a power level of about 38 kW. Torque-ripple levels at these peak power conditions reached about 15% to 20%, which is much higher than simulations indicated. This is also a detriment that was likely caused by inferior electrical steel properties. Because the torque-per-current was observed to be about 0.75 of the simulated locked rotor torque, peak power capability with the expected steel quality can be roughly estimated to be 38 kW times a factor of 1/0.75, which is 50.7 kW.

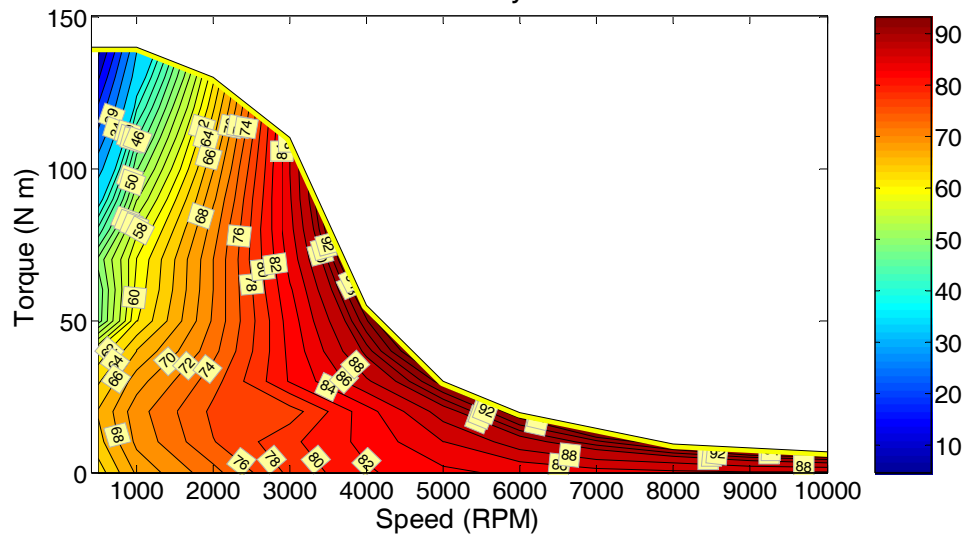


Fig. 13. Motor efficiency measurements.

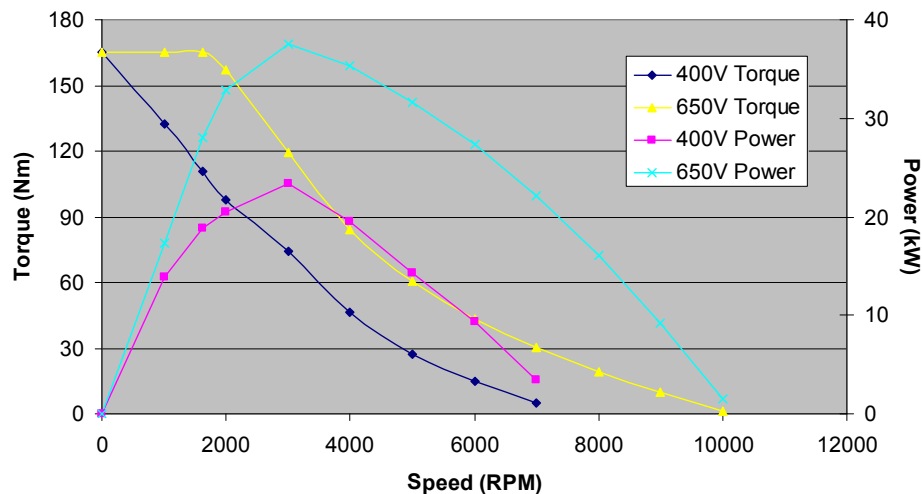


Fig. 14. Motor torque and power capability.

Using the measured and estimated power levels previously discussed, power densities and specific power values were generated using a volume of 8.5 L and a mass of 36 kg (Table 1). While 400 V power capabilities result in low power densities and specific power, estimated 650 V capabilities put the design close to DOE 2015 targets. If estimations with improved steel are used (50.7 kW), DOE 2015 targets are surpassed and DOE 2020 power density is surpassed. In Table 2, a similar comparison is made with systems that have been benchmarked at ORNL. Tested power densities at 400 V compare closely with the 2011 Hyundai Sonata, and expected 650 V power densities fall short of 2010 Prius power densities, whereas anticipated improved steel estimations place the power density and specific power above the 2010 Prius. The SRM has the advantage of reduced end-turn volume, but the axial length of the motor may need to be increased to modify the structure to mitigate potential eddy current impacts upon efficiency.

Table 1. Comparison of ORNL IMFP SRM power density and specific power with DOE targets

| Parameter | ORNL IMFP 400 V SRM (23.4 kW) | ORNL IMFP 650 V SRM (38 kW) | ORNL IMFP 650 V SRM (50.7 kW) (estimation with improved steel) | DOE 2015 targets | DOE 2020 targets |
|-------------------------------|-------------------------------------|-----------------------------------|--|---------------------|---------------------|
| Peak power density, kW/L | 2.8 | 4.5 | 6.0 | 5.0 | 5.7 |
| Peak specific power, kW/kg | 0.7 | 1.1 | 1.4 | 1.3 | 1.6 |

Table 2. Comparison of ORNL IMFP SRM power density and specific power with benchmarked systems

| Parameter | ORNL IMFP SRM 400V, (23.4 kW) | ORNL IMFP SRM 650V, (38 kW) | ORNL IMFP SRM 650V, (50.7 kW) (estimation with improved steel) | 2011 Sonata (30 kW) | 2010 Prius (60 kW) | 2006 Honda Accord (12 kW) | 2004 Prius (50 kW) |
|-------------------------------|--|--------------------------------------|---|---------------------------|-----------------------|------------------------------------|-----------------------|
| Peak power density, kW/L | 2.8 | 4.5 | 6.0 | 3.0 | 4.8 | 1.5 | 3.3 |
| Peak specific power, kW/kg | 0.7 | 1.1 | 1.4 | 1.1 | 1.6 | 0.5 | 1.1 |

Conclusion

- Created design optimization tool for SRMs.
 - Automated geometric optimization, meshing, and application of boundary conditions.
 - Interfaced with existing FEA software package.
- Generated control optimization software.
 - Parameterized dynamic nonlinear three phase modeler.
 - Optimizes with respect to speed and torque ripple.
- Achieved encouraging simulation results.
 - 52.4 kW (125 Nm at 4,000 rpm) with 5% torque ripple and 93% efficiency.
 - 75 kW at 8,000 rpm with 20% torque ripple.
 - 90 kW at 8,000 rpm with 30% torque ripple using continuous conduction.
 - Stress and modal analyses verified design feasibility in qualitative acoustic noise assessments.
- Tested machine up to 5,000 rpm.
 - Results lower than expected, but accounting for steel degradation, results are close to simulations and address DOE targets.
 - Torque ripple improved, but still not to desired level observed in simulations.

Patents

T. Burress and C. Ayers, *Isolated Multiple Flux Path Reluctance Motors with Yoke-Wound Coils and Wedge Supports*, Serial number 61/509,213, filed 7/19/2011, patent pending.

Publications

None.

3.2 Novel Flux Coupling Machine without Permanent Magnets

Principal Investigator: John Hsu

Oak Ridge National Laboratory

National Transportation Research Center

2360 Cherahala Boulevard

Knoxville, TN 37932

Voice: 865-946-1325; Fax: 865-946-1262; E-mail: hsujs@ornl.gov

DOE Technology Development Manager: Susan A. Rogers

Voice: 202-586-8997; Fax: 202-586-1600; E-mail: Susan.Rogers@ee.doe.gov

ORNL Program Manager: Mitch Olszewski

Voice: 865-946-1350; Fax: 865-946-1262; E-mail: olszewskim@ornl.gov

Objectives

- Research the feasibility of an electric motor, without permanent magnets (PMs), that has the potential to replace the interior PM (IPM) motor in hybrid electric vehicles and plug-in hybrid electric vehicles.
- Create a novel flux coupling machine (NFC-machine) with the following characteristics.
 - Is brushless.
 - Contains no rotor windings.
 - Has no PM material.
 - Is an adjustable field synchronous machine.
 - Retains both rotor-excitation torque and reluctance torque productions.
- Produce a motor that meets or comes close to DOE's 2020 motor targets for cost, weight, volume, and efficiency.

Approach

- Based on the FY 2010 identification of the advantages and weaknesses of the most advanced IPM motors available in the market today,
 - develop and fabricate a prototype motor that retains the advantages of IPM motors without the use of rare earth PMs and
 - overcome the disadvantages such as the nonadjustable field, low permissible temperature, and the low power factor at peak power of the IPM machines.

Major Accomplishments

- Completed engineering drawings that were based on the results of a significant number of electromagnetic and mechanical simulations.
- Completed prototype NFC-motor parts machining, fabrication, and assembly.
- Completed locked rotor test on the NFC-machine prototype.
 - Confirmed that the novel NFC-machine concept is a workable concept.
 - Full testing scheduled to be completed during FY 2012 (scheduling issues with the Dyne cells prevented completion by the end of September 2011).
- Completed study on the power factor of IPM motors during the period the prototype motor was fabricated and machined.
- Based on the power factor study of the IPM motor, determined the technical approach for better power factor of the NFC-machine was feasible (discussed in detail later in this report).

Future Direction

- DOE funding for this project ended this fiscal year. Any issue observed from the full test will be recorded and used as we seek industry partners to bring this novel achievement to the market.

Technical Discussion

The prototype NFC-motor is shown in Fig. 1. Its overall size based on the active materials (13.6 L) is about the same as the Toyota Camry motor (13.9 L).

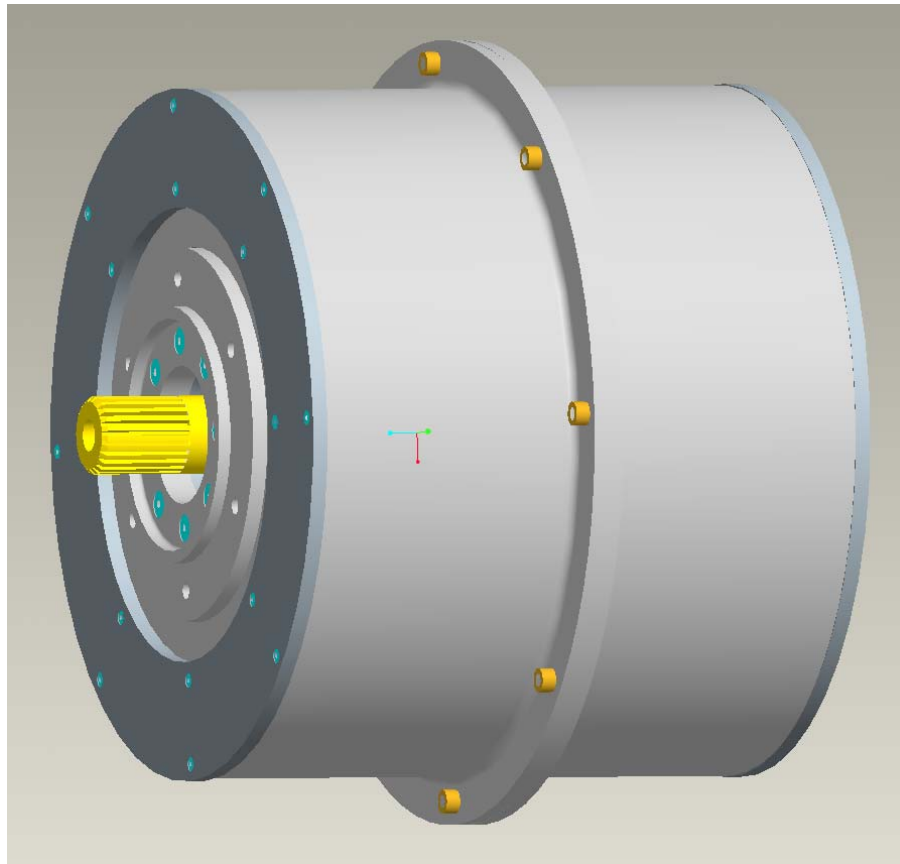


Fig. 1. Prototype NFC-motor.

Locked-Rotor Tests

Figure 2 shows the results of the locked rotor torque versus load angle tests for the prototype NFC-motor at 100 Stator winding currents with field excitation currents changed from 0 A to 6 A. The torque curves do not go up much when the field excitation current exceeds 3 A. This indicates that the magnetic saturation becomes significant at higher field excitation currents.

Figure 3 shows the results of similar tests, under similar conditions, for the Toyota Camry IPM motor. The prototype NFC-motor's peak torque of 86 Nm at 100 A stator winding current (with 6 A field excitation current) shown in Fig. 2 compares favorably with the peak torque of 85 Nm at 100 A shown in Fig. 3 for the Toyota Camry IPM motor.

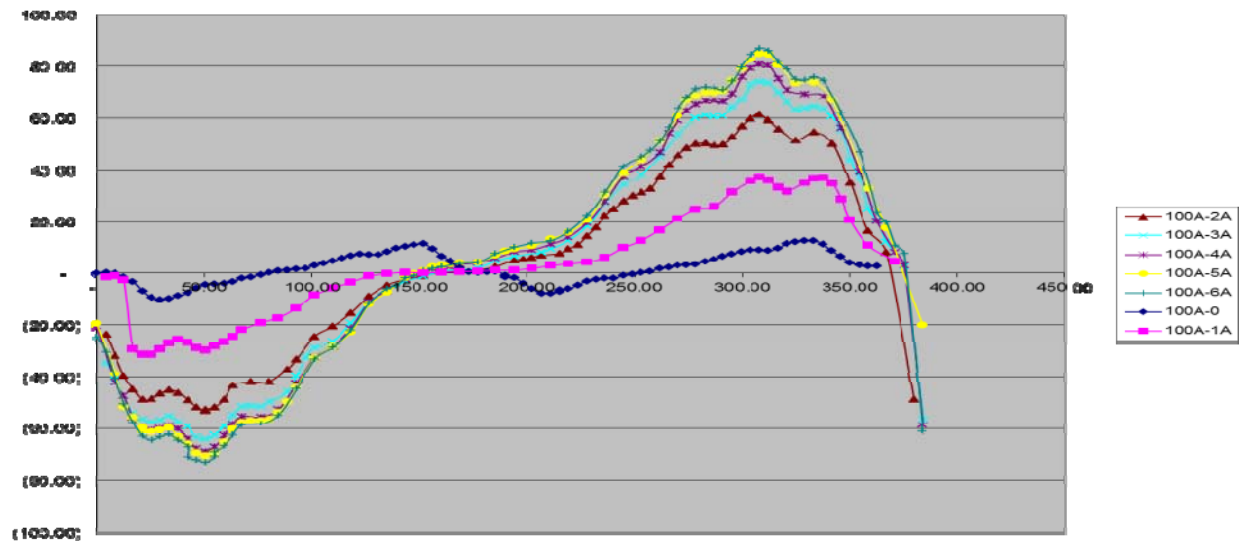


Fig. 2. Results of locked rotor torque versus load angle tests at 100 A stator current with field excitation currents changed from 0 A to 6 A.

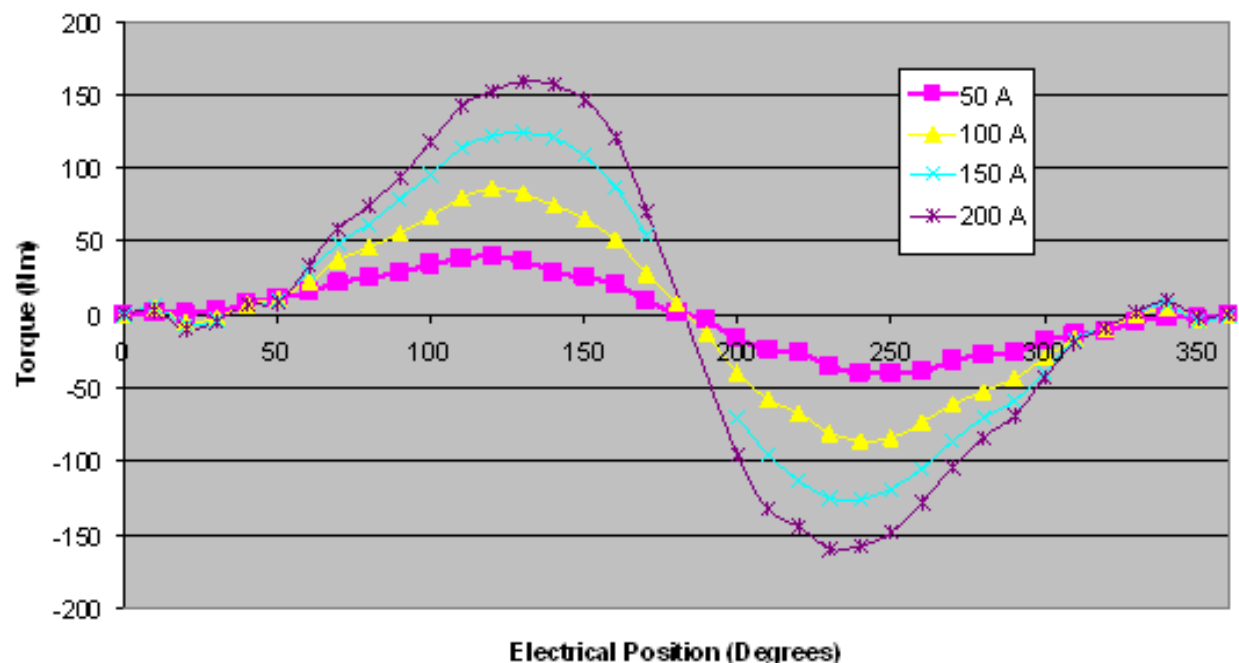


Fig. 3. Results of locked rotor torque versus load angle tests of Toyota Camry IPM motor.

Figure 4 shows the results of locked rotor torque versus load angle tests of the prototype NFC-motor at 150 A stator current with field excitation current at 0, 3, and 6 A. As this figure shows, the peak torque at 6 A excitation current is 106 Nm. For the Camry motor the peak locked rotor torque shown in Fig. 3 at 150 A stator winding current is 122 Nm. Based on this comparison, the NFC-motor saturates more rapidly than the Camry motor.

Comparing Figs. 2 and 4, the increase of the excitation current seems to be more effective for the additional torque when the stator winding current goes up.

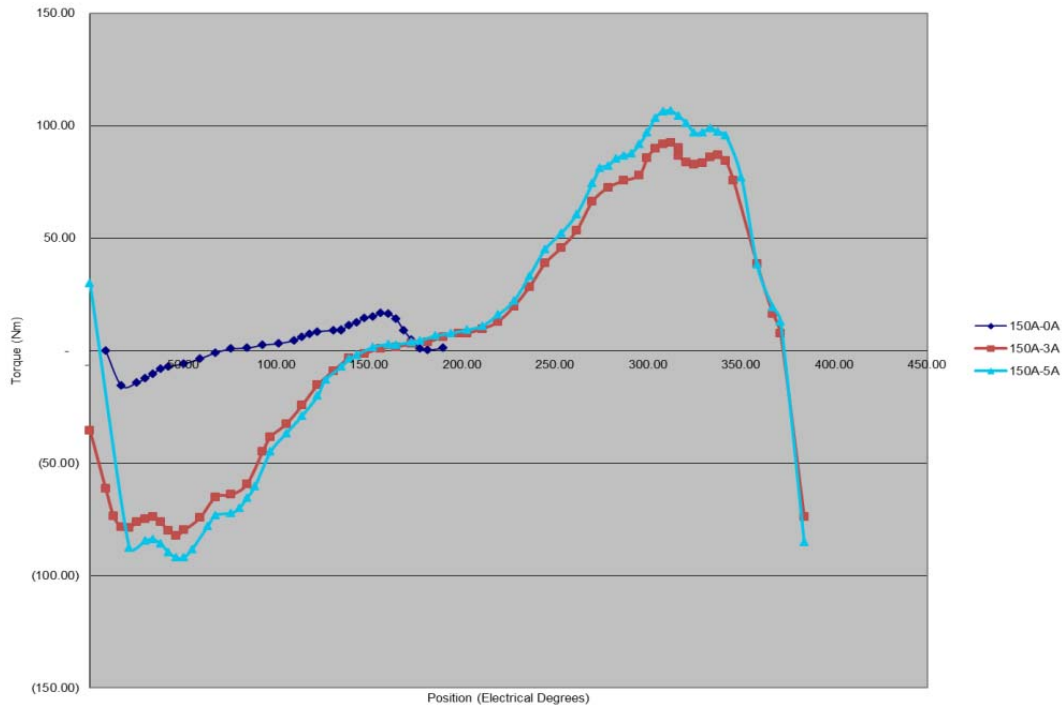


Fig. 4. Prototype NFC-motor tested locked rotor torques versus load angle at 150 A stator current with field excitation current at 0, 3, and 6 A.

Tests conducted at 240 A stator winding current and 8 A field excitation current give 132 Nm locked rotor torque. This is proportionally lower than the 160 Nm predicted in the theoretical performance simulation shown in Fig. 5. However, this magnetic saturation problem can be overcome in future designs.

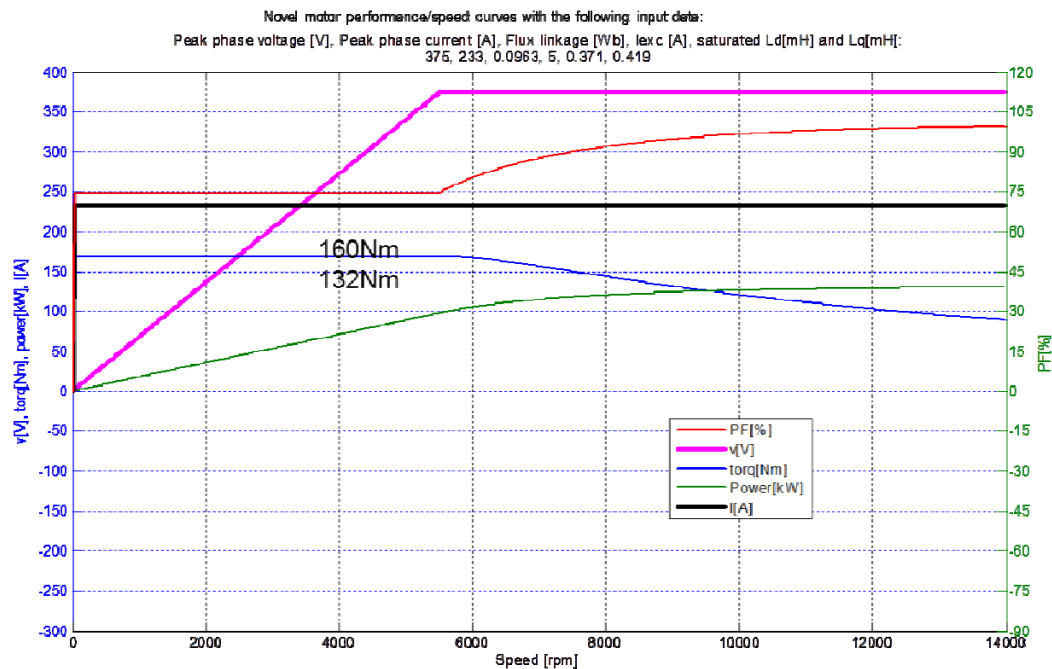


Fig. 5. Simulated prototype NFC-motor performance versus speed.

Study on Power Factor of IPM Motors for Guiding Arrangement of NFC-Machine Reluctance Poles

The Toyota Camry and Lexus motors are IPM motors. Figure 6 shows the direct (d) and quadrature (q) axes of their rotor laminations. The d-axis flux of any of these IPM motors has to go through rare earth PMs that have a low permeability value roughly equal to the permeability of air. Therefore this d-axis flux path is difficult for the flux created by the stator winding current to go through as compared to the q-axis flux path without the blocking from the PM. The basic knowledge for power factors of wound-field synchronous machines can be viewed from [1]. Additional information on the Toyota Camry and Lexus motors can be found in references [2] and [3].

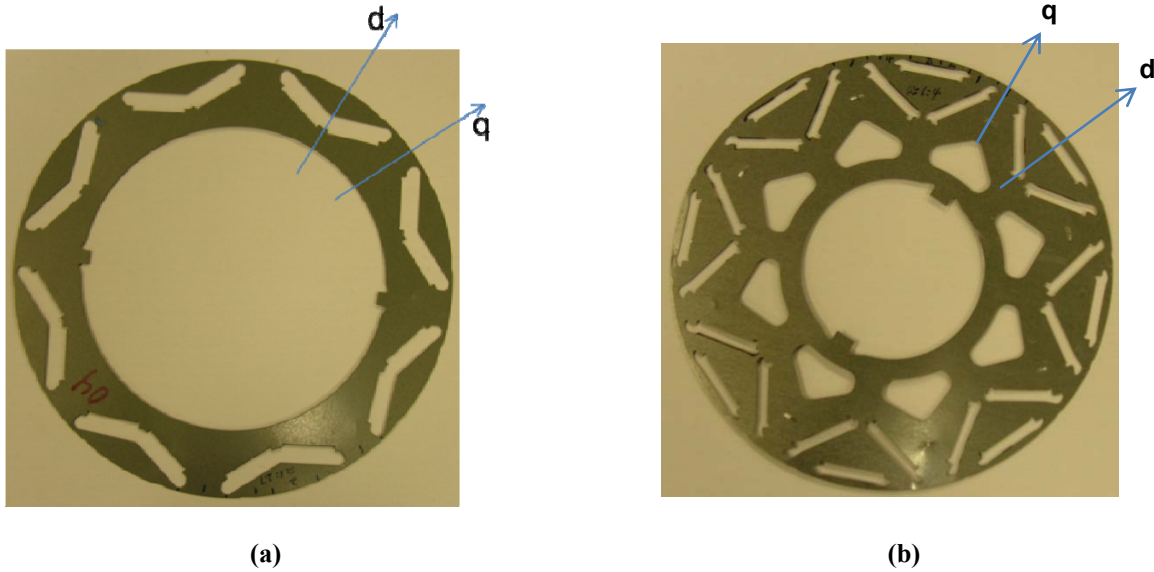


Fig. 6. Locations of rotor direct (d) and quadrature (q) axes of typical IPM motors:
(a) Toyota Camry and (b) Lexus.

Based on the definition of inductance, L , that is the ratio of the flux linkage of the stator winding divided by the stator winding current, the inductance of the stator winding for the d-axis flux, L_d , is lower than that of the q-axis. The mathematical expression for the comparison of inductance values of the rare earth IPM motors is as follows:

$$L_d < L_q . \quad (1)$$

Low power factor at peak power of IPM motors. Some test reports indicate that the power factor at peak power of IPM motors can be as low as 0.45. The reason is that the IPM peak torque versus load angle, δ , is changed greatly according to the motor torque equation:

$$\text{Power} = 3 \frac{V E}{\omega L_d} \sin \delta + 3V^2 \frac{(L_d - L_q)}{2\omega(L_d L_q)} \sin 2\delta . \quad (2)$$

When $L_d < L_q$, the second term of Eq. (2) becomes negative; the negative $\sin 2\delta$ term makes the peak torque located at δ greater than 90° . The corresponding peak torque versus load angle, δ , is shown in Fig. 7. These curves are taken from previous testing performed on the 2004 Prius. They show that the reluctance torque is about 70% of the PM torque.

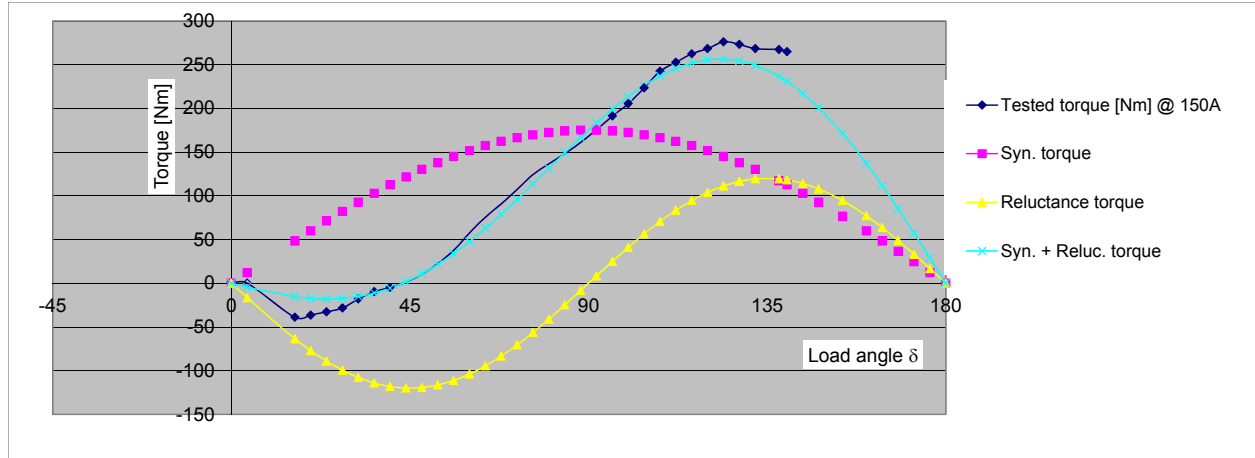


Fig. 7. When $L_d < L_q$, peak torque (or peak power) is at load angle, δ , greater than 90° .

The stator winding voltage phasor, V , must be balanced with the phasor sum of the back-electromotive force (emf), E , and reactance voltage drops, $V_{\text{reactance drops}}$, in the stator winding. The phasor of the back-emf, E , is lagging behind the winding voltage, V , by δ degrees. This results in the diagram of the voltage phasors shown by the darker plots for the $L_d < L_q$ case in Fig. 8.

From the phasor of the reactance voltage drop, $V_{\text{reactance drops}}$, the stator winding current, I , for $L_d < L_q$ can be seen to be roughly 90° lagging. The power factor angle, ϕ , can be obtained from the diagram. The power factor angle, ϕ , is large, causing the power factor, $\cos(\phi)$, to be low at peak powers for rare earth IPM motors.

Reluctance Poles Arrangements for U-Machines

Because there is no PM in the rotor of the NFC-machine to block the flux produced by the stator winding current, the NFC-machine can be designed for either the $L_d < L_q$ case or for the $L_d > L_q$ case.

When the option of an $L_d > L_q$ design is selected, the corresponding $L_d > L_q$ peak torque (or peak power) is at a load angle, δ , less than 90° as shown in Fig. 9.

The assessment of power factor at peak power is shown by the lighter plots in Fig. 8. The angle between the motor winding voltage, V , and the motor winding current, I , for $L_d > L_q$ is significantly less than the IPM $L_d < L_q$ case; hence a higher power factor at peak power can be obtained.

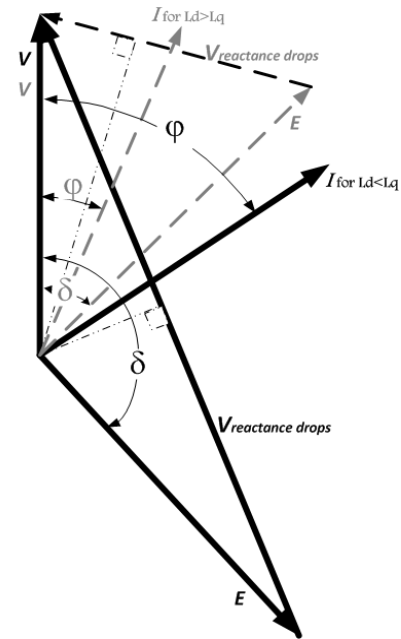


Fig. 8. Phasor diagrams for (a) the $L_d < L_q$ case (darker plots) and (b) the $L_d > L_q$ case (lighter plots).

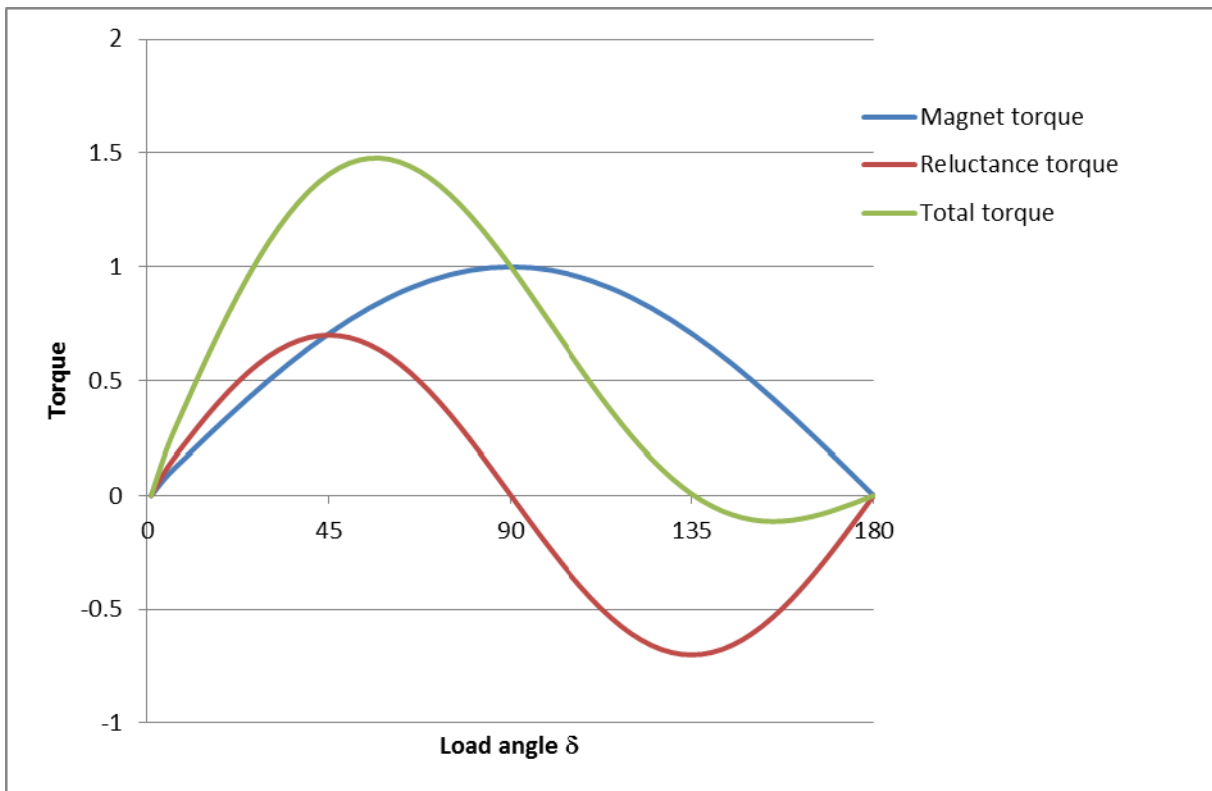


Fig. 9. When $L_d > L_q$, peak torque (or peak power) is at a load angle, δ , less than 90° .

Conclusion

- This DOE project has created a new topology for a motor without PMs, brushes, or rotor windings. Additionally, the machine contains adjustable windings.
- Initial tests confirm the practical validity of the novel flux coupling concept.
- Adjustable field excitation of the NFC-machine can improve the power factor and consequently lower motor and inverter currents.
- The magnetic saturation shows up earlier than the simulation predicts; however, this saturation problem can be overcome in future designs.
- In view of the rapid cost increase of rare earth PMs, the NFC-machine without PMs may reduce cost per kilowatt of the vehicle drive motors by 75% or more.
- The NFC-machine can operate at higher temperatures because there is no PM related temperature limitation.
- Integration of the NFC-machine and the current source inverter may further lower the drive system cost.

Patents

1. J. S. Hsu, ID-2505, *Combined Electric Machine and Current Source Inverter Drive System*, serial number 61/417,906, filed 11/30/2010.
2. J. S. Hsu, ID-2522, *Multilevel Windings*, serial number 61/433,546, filed 1/18/2011.
3. J. S. Hsu, ID-2670, *Arc Suppression for Reactive-Circuit Switches* filed 2011.

Publications

1. Internal and DOE review meeting publications only.

References

1. A. E. Fitzgerald, Charles Kingsley, Jr., and Stephen D. Umans, *Electric Machinery*, McGraw-Hill Book Company, Fourth Edition, 1983.
2. T. A. Burress, C. L. Coomer, S. L. Campbell, L. E. Seiber, L. D. Marlino, R. H. Staunton, and J. P. Cunningham, *Evaluation of the 2007 Toyota Camry Hybrid Synergy Drive System*, ORNL/TM-2007/190, January 2008 (Revised April 2008).
3. T. A. Burress, C. L. Coomer, S. L. Campbell, A. A. Wereszczak, J. P. Cunningham, L. D. Marlino, L. E. Seiber, and H. T. Lin, *Evaluation of the 2008 LEXUS LS Hybrid Synergy Drive System*, ORNL/TM-2008/185, January 2009.

3.3 Motor Packaging with Consideration of Electromagnetic and Material Characteristics

Principal Investigator: John M. Miller

Oak Ridge National Laboratory

National Transportation Research Center

2360 Cherahala Boulevard

Knoxville, TN 37932

Voice: 865-946-1469; Fax: 865-946-1262; E-mail: millerjm@ornl.gov

DOE Technology Development Manager: Susan A. Rogers

Voice: 202-586-8997; Fax: 202-586-1600; E-mail: Susan.Rogers@ee.doe.gov

ORNL Program Manager: Mitch Olszewski

Voice: 865-946-1350; Fax: 865-946-1262; E-mail: olszewskim@ornl.gov

Objectives

Motor continuous power ratings become increasingly important as traction drives become more electrified. Motor packages need to be developed to satisfy the requirement for increased continuous power, including consideration of electromagnetic effects and new material characteristics. In light of this, for FY 2011 the key objectives were as follows.

- Characterize a state-of-the-art (SOA) interior permanent magnet (IPM) electric machine for use as the baseline comparator.
- Establish the technology trajectory of the baseline IPM based on designs from the last 7 years.
- Develop a complete model of the baseline IPM, including fully characterized electromagnetic parameters.
 - Assess its leakage inductance for future alternative winding design comparisons.
 - Compare performance to laboratory measurements.
- Develop a thermal model, including material characteristics, of the baseline IPM and compare results to laboratory measurements.

Approach

- Use the 2010 Prius 60 kW IPM traction motor benchmarking data [1] and available dynamometer mapping point data to construct an equivalent circuit model of the baseline machine.
- Assess the electromagnetic and material characteristics of the baseline IPM as a means for improving motor continuous power rating (complements National Renewable Energy Laboratory motor cooling project).
- Establish technology trajectory of SOA IPM designs through comprehensive review of ORNL archived benchmarking reports [1, 2]. Apply the design comparisons to the overall objective of this project to identify areas for future exploitation to improve continuous power rating relative to peak power.
- Develop a thermal model of the baseline IPM using material characteristics, and compare simulation results to ORNL dynamometer thermal rise test data.
- Establish directional guidelines based on FY 2011 project electric-magnetic-thermal results for use in a follow-on FY 2012 prototype IPM design project having a goal to deliver higher continuous power. The work is supported by ORNL materials specialists in lamination steels (shear rolled, graded silicon, other) and thermal materials (epoxy composites, others).
- Assess alternative winding designs suitable for FY 2012 design program.

Major Accomplishments

- Analyzed ORNL benchmarking data on the 2010 Prius IPM, and extracted key parameters for development of an electrical equivalent d-q axis circuit model. The main reluctance torque production mechanisms obtained from the saturation dependent inductances $L_{qds}(I_s)$ resulted in a high accuracy torque prediction model.
- Developed a computer model for the lamination material reluctivity to be used in the magnetic equivalent circuit (MEC) model and simulation.
- Developed the baseline IPM technology trajectory showing highly optimized magnetic flux, electric matching of machine to source voltage, and virtually constant power loss of stator copper for the 7 years of products evaluated. The implication is that the IPM supporting thermal management system evolved little over the interim.
- Developed a thermal model of the baseline IPM, and validated it against ORNL benchmarking data. The thermal model provides ORNL researchers a finite element analytical model for predicting IPM copper, lamination iron, and rotor magnet dissipation mechanisms.
- Established directional guidelines for the FY 2012 machine design improvement to demonstrate higher continuous power rating.

Future Directions

- During FY 2012 initiate design alternatives for the baseline IPM rotor and stator laminations to decrease magnetic loss. Perform detailed deformation sequences on shear rolled lamination steel for higher GOSS (grain oriented silicon steel) texture and lower losses to transverse and rotational flux. Include in the design and simulation work the material properties of new composite epoxy and other thermal management materials.
- Fabricate testable prototypes of the FY 2012 IPM design, and validate improved continuous power rating based on new lamination steel, improved conductor and winding design, and thermal management materials.
- Fabricate one stator with new lamination steel, and compare performance to baseline IPM.
- During FY 2013 perform fabrication and testing of thermal materials.

Technical Discussion

Development of Baseline IPM Electrical Model

The 2010 Prius [Toyota Motor Company (TMC)] traction motor rated at 60 kW (Fig. 1) was selected as the baseline machine because it represents a SOA IPM technology according to ORNL benchmarking data. Essential electrical parameters were extracted from the dynamometer test data so that a comprehensive electrical model could be compiled for future use as a comparator for alternative magnetic and thermal materials and for performance comparisons. Dynamometer testing data were taken using the TMC production inverter power stage and ORNL's inverter controller. A point of interest regarding TMC's IPM designs is that all have been 48 slot, eight pole, and three phase using 0.3 mm lamination steel but various rotor permanent magnet (PM) designs from straight (2003) and single "V" to one double V in the 2008 Lexus hybrid.

Table 1 summarizes the electromagnetic design of the baseline IPM, a 2010 Prius traction motor rated at 60 kW; 13,500 rpm; and 205 Nm. Based on the electromagnetic mass (22.74 kg), the specific power of this design is: $SP = 2.64 \text{ kW/kg}$ and compares very favorably with the DOE 2020 target of 1.6 kW/kg.

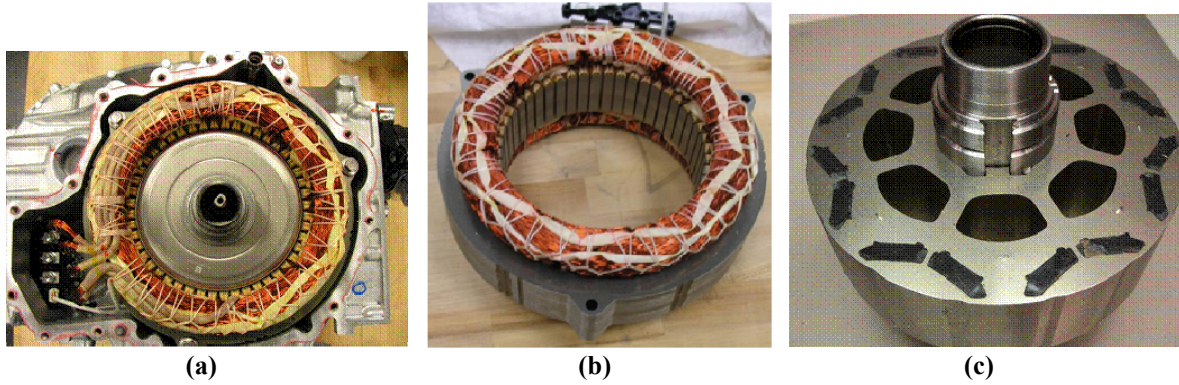


Fig. 1. 2010 Prius traction motor: (a) assembly, (b) stator, and (c) rotor.

Table 1. Dimensional data on the baseline IPM^a

| ODs (mm) | IDs (mm) | Gap (mm) | ODr (mm) | Stator stack (mm) | Rotor stack (mm) | Stator mass (kg) | Stator copper (kg) | Rotor mass (kg) | PM mass (kg) |
|-------------|-------------|-------------|-------------|-------------------------|------------------------|------------------------|--------------------------|-----------------------|-----------------|
| 264 | 162.4 | 0.73 | 160.4 | 50.8 | 50.165 | 10.36 | 4.9 | 6.7 | 0.78 |

^aAbbreviations: ODs = outer diameter-stator, IDs = inner diameter-stator, and ODr = outer diameter-rotor.

ORNL benchmarking data taken on the baseline IPM [1] provided sufficient test data for a convenient characterization and mapping point (5,000, 60) for a speed of 5,000 rpm and continuous torque of 60 Nm. This mapping point was selected because it represents the 30 kW continuous operating power at rated voltage and is also the point of highest efficiency of this IPM, as demonstrated in Table 2. The power factor (PF) angle at this mapping point was 35.88° , giving $\text{PF} = 0.81$, a relatively low value but realistic for the IPM at this load condition.

Table 2. Measured data from dynamometer test

| U_{dc} (V _{dc}) | I_{dc} (A _{dc}) | P_e (kW) | P_m (kW) | U_{an} (V _{rms}) | I_{an} (A _{rms}) | m (Nm) | n (rpm) | η (#) |
|--------------------------------|--------------------------------|---------------|---------------|---------------------------------|---------------------------------|-------------|--------------|---------------|
| 652.4 | 50.8 | 32.9 | 31.4 | 310 | 43 | 60 | 5,000 | 0.954 |

In operation the IPM stator current vector, I_s , is placed along the maximum torque per ampere line, which for this machine is at the torque angle listed in Table 3. In addition to the torque angle, γ (angle of current relative to q-axis), the IPM will operate with a stator voltage vector that satisfies the machine reactance at this speed. The resulting power angle, δ (angle of stator voltage vector relative to the q-axis), is such that $\delta = \gamma + \theta$.

Table 3. IPM angles needed to construct phasor diagram at mapping point

| Torque angle (γ) | PF angle (θ) | Power angle (δ) | Phase displacement (a) | Electrical angle (θ_e) |
|------------------------------|--------------------------|-----------------------------|---------------------------|------------------------------------|
| 33.34° | 35.88° | 88.06° | $2\pi/3$ radian | $\omega_e t$ |

The relationship of the inverter drive voltage limit, U_s ; current limit, I_s ; and electromagnetic torque are conveniently shown as circle diagrams. The circle diagram for the SOA baseline IPM is shown in Fig. 2, where the current circle represents the full extent of current vector control over the d-q plane. A segment of the torque hyperbolae and the speed dependent voltage ellipses for three different operating speeds, the mapping point at 5,000 rpm and higher speed ellipses for 9,000 and 13,000 rpm, are also plotted on this

same scale. The fact that the inverter runs out of voltage control and/or current as speed increases is very evident from the figure. In fact, referring to the maximum current circle diagram one can see that the controller would follow a maximum torque per ampere trajectory down the I_s vector until that vector falls inside the voltage ellipse for that speed, thereby satisfying both the inverter voltage and current limit.

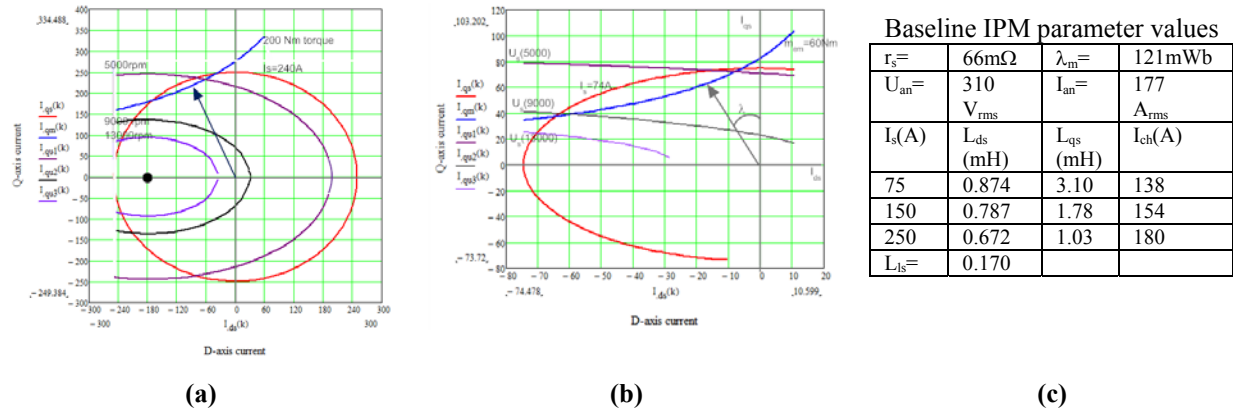


Fig. 2. Baseline IPM circle diagrams: (a) maximum capability and (b) situation at mapping point. The table, (c), shows the extracted parameter values for the baseline IPM.

The IPM characteristic current, I_{ch} , is shown as the solid circle in these diagrams. The parameter table in Fig. 2 highlights the fact that for nonlinear magnetics the characteristic current is a function of loading and moves away from the origin with increasing stator current, but inside the maximum controllable stator current circle. This is very important because as long as the IPM characteristic current remains within the inverter maximum current rating, it will not be damaged under inverter faults such as loss of gating signals at high speed resulting in uncontrolled generation mode. As shown in Fig. 2, the baseline SOA IPM always has its characteristic current well within the current circle and voltage ellipse, even at the highest operating speed.

Figure 3 summarizes the baseline IPM modeling work showing the resultant phasor diagram at the mapping point (5,000, 60) at a phase current of 43 A_{rms}, phase voltage of 310 V_{rms}, and power of 32 kW. The diagram also illustrates some interesting controller behavior in the power angle magnitude, which, being a few degrees larger than what is needed, could potentially improve the PF at this operating point. The modeled torque is nearly the same as the measured.

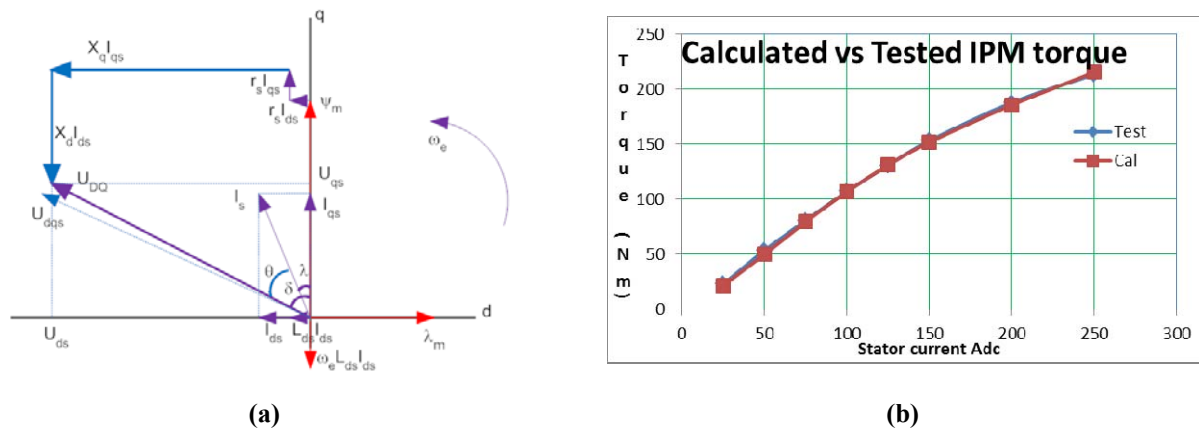


Fig. 3. Summary of modeling work: (a) SOA IPM phasor diagram at (5,000 rpm, 60 Nm) and (b) measured vs estimated torque.

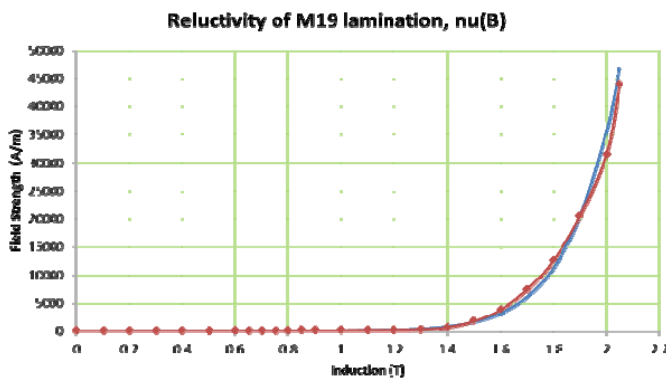
The electrical model concludes with a summary of the synchronous inductance variations with stator current loading and the modeled versus calculated electromagnetic torque of this IPM. Table 4 summarizes the findings and shows that calculated electromagnetic torque using the d-q axis inductances that are functions of stator current agrees very well with laboratory measured torque.

Table 4. SOA IPM calculated torque and inductance parameter versus stator current

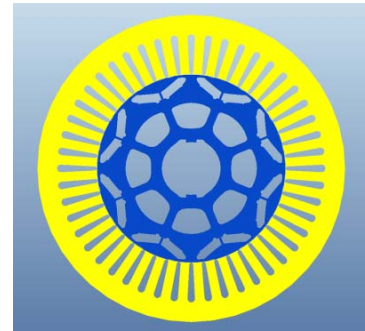
| I_s (A _{dc}) | $m_{em\ meas}$ (Nm) | $m_{em\ cal}$ (Nm) | $L_{ds}^*(I_s)$ (mH) | $L_{qs}^*(I_s)$ (mH) |
|-----------------------------|------------------------|-----------------------|-------------------------|-------------------------|
| 25 | 23 | 21.8 | 0.93 | 4.73 |
| 50 | 53.7 | 50.2 | 0.9 | 3.815 |
| 75 | 80.8 | 79.6 | 0.874 | 3.104 |
| 100 | 107.3 | 107.1 | 0.845 | 2.55 |
| 125 | 131 | 131.2 | 0.816 | 2.118 |
| 150 | 153.2 | 152 | 0.787 | 1.783 |
| 200 | 188 | 185.9 | 0.73 | 1.317 |
| 250 | 213.6 | 215.4 | 0.672 | 1.035 |

Development of Baseline IPM Magnetic Model

Motor packaging work is not complete without an assessment of the flux path material utilization. This turns out to a very useful approach from which the electrical model behavior can be better understood (e.g., why the synchronous inductances exhibit the nonlinearities noted in Table 4). This essentially boils down to the particular machine design specification and material characteristics for low silicon, nonoriented, lamination steel. Lamination steel magnetization is inverse modeled using reluctivity (ν) rather than permeability to iteratively determine the magnetic field strength in the machine element as a function of flux density, $H(B) = \nu(B)$. Using the popular M19 motor grade steel (JFE35JN250) as the baseline case, it was found that a simple power law expression resulted in a very good fit of the steel intensive variable, its magnetic field strength as a function of extensive variable, and flux density. Figure 4(a) illustrates the fit of $\nu(B)$ to the manufacturer's data (diamond markers). The fit is excellent, especially in the highly nonlinear knee region where the IPM mainly operates.



(a)



(b)

Fig. 4. Reluctivity model of (a) lamination steel and (b) lamination design.

An MEC model was developed to identify the main contributors to the nonlinearity in machine inductances and also to find those areas in which the majority of the permanent magnet and armature

reaction magnetomotive forces (mmfs) were consumed. Figure 5 summarizes the MEC model in both its simulation and physical context.

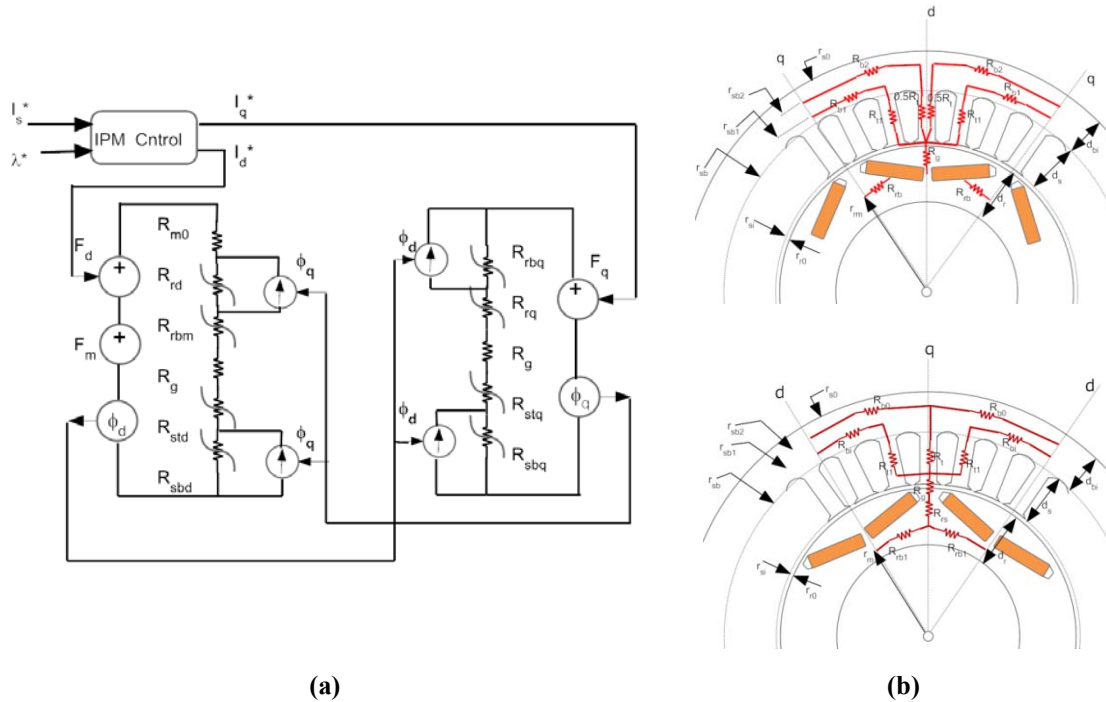


Fig. 5. MEC model of the baseline IPM: (a) circuit simulation model and (b) magnetic element model.

Another purpose for the MEC model was to better understand the rotor magnet V configuration being aligned with and tangent to the d-axis and q-axis flux contours. Finite element analysis (FEA) with the rotor magnet pockets redefined as lamination steel confirmed this—the V is indeed oriented in this manner, having the magnet slabs orthogonal to d-axis flux and tangent to q-axis flux as shown graphically in Fig. 6. Figure 7 shows the corresponding MEC model derived d-axis and q-axis mmf distributions with stator current loading in the various regimes of the IPM (i.e., the stator and rotor steel, the air gap, and the magnet cavities). The MEC model accounts for PM leakage flux in rotor posts and bridges as 9.5% of its mmf and 14% of its flux per magnet or twice that per pole (i.e., 28% leakage flux on each pole). This is in very good agreement with FEA showing 26% flux leakage via posts and bridges in each pole. PM leakage flux in IPMs is a concern given the fact that hybrid vehicle grade NdFeB magnets have 20%–25% Nd and 6%–9% Dy content at 2011 prices of \$275/kg and \$920/kg, respectively.

It is clear from the MEC model that the IPM rotor saturates most in both d-axis and q-axis; therefore it is the dominant factor in setting the magnetizing inductance variation with stator current. Because of the magnet pockets the variation in $L_{ds}(I_s)$ is much shallower than for the mostly iron q-axis flux path.

IPM Technology Trajectory and Evaluation Areas

This project explored the technology trajectory of the TMC IPM electric machines developed for its hybrid vehicle products in the Prius, Camry, and Lexus vehicle lines. Our findings are that little has changed in the electromagnetic design of these IPMs over the course of the past decade. This is understandable for serial production automotive components as running changes can be very expensive. In light of this, TMC has remained with a three phase, eight pole, 48-slot basic design. Related work on electric machines indicates that eight pole designs do indeed represent a more optimal choice. Table 5

summarizes the salient points of the technology trajectory mapping. In this analysis the electric machine design trends are shown in terms not only of power and torque rating but also of basic attributes such as stator bore to stator stack ratio (OD_s/h) and air gap radius (r_g). Stator bore diameter to stator stack ratio is a fundamental electric machine metric. Another important electric machine metric is aspect ratio that defines the relative deviation from unity of the ratio of stack to pole pitch. Most fundamental of all is the ability of an electromagnetic design to develop a high level of rotor surface shear force (N) per unit mass (kg) termed specific force, SF. SF is fundamental since the lever arm contribution of air gap radius needed to determine torque is eliminated from the metric. The key metrics used in technology trajectory mapping are shaded in Table 5.

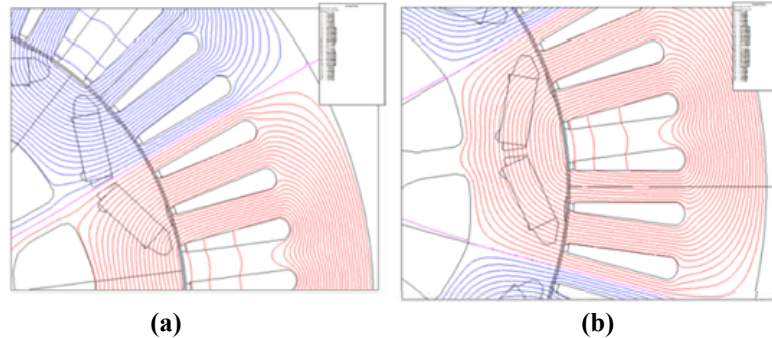


Fig. 6. PM placement relative to the d- and q-axes ($I_s = 100$ A):
(a) FEA for d-axis; (b) FEA for q-axis.

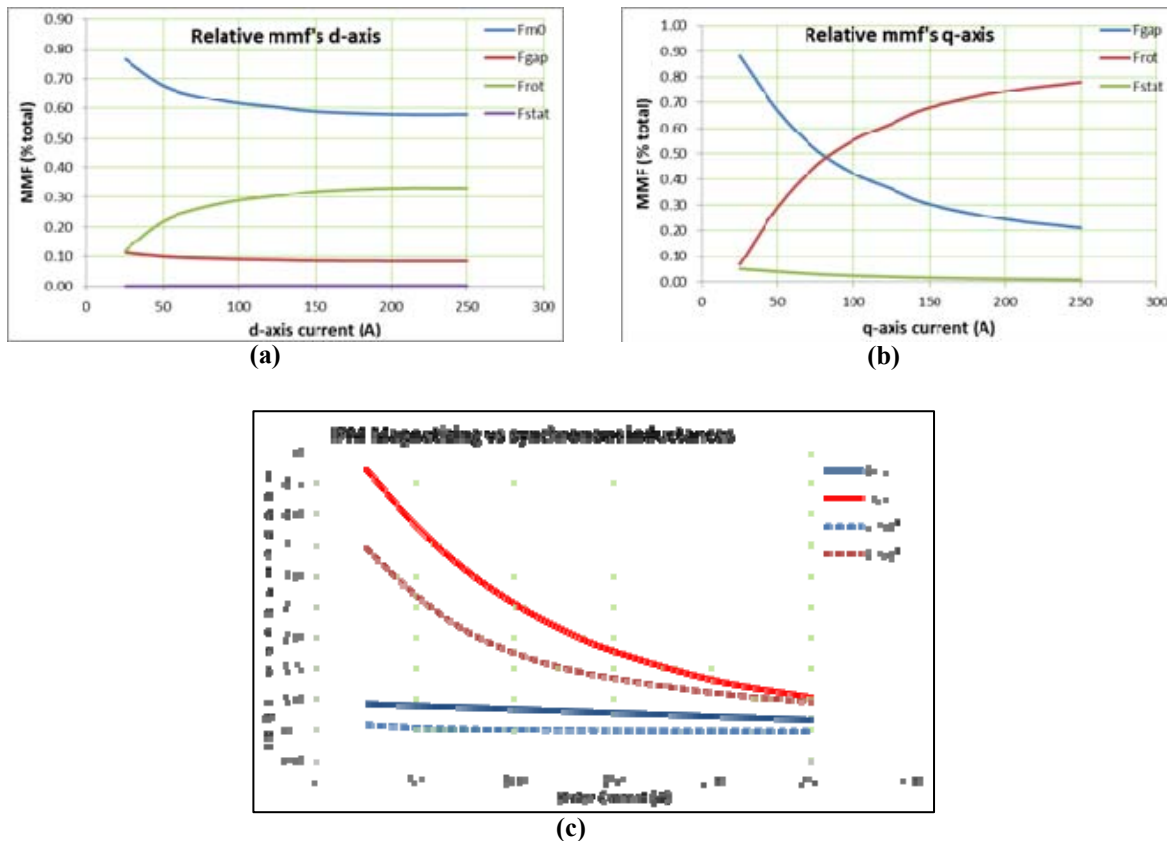


Fig. 7. Mmf distribution breakdown for (a) d-axis and (b) q-axis and (c) inductance comparison for the machine inductance electrical model vs the MEC model.

Table 5. SOA IPM calculated torque and inductance parameter versus stator current

| Attribute | Unit | Model | | | |
|---|---------------|------------|------------|------------|------------|
| | | 2004 Prius | 2007 Camry | 2008 Lexus | 2010 Prius |
| Peak power, P_{pk} | kW | 50 | 70 (105) | 110 (165) | 60 |
| Peak torque, m^{pk} | Nm | 400 | 270 | 300 | 205 |
| Stator bore: OD_s/h | # | 1.92 | 2.64 | 0.95 | 3.16 |
| Mid-gap radius, r_g | mm | 80.98 | 80.98 | 65.44 | 80.47 |
| Aspect, $\gamma_s = \frac{h}{\tau_p}$ | # | 1.32 | 0.95 | 1.35 | 0.77 |
| Gap flux: $\bar{B}_g = \frac{\Phi}{\tau_p h}$ | T | 0.446 | 0.453 | 0.434 | 0.442 |
| SF | N/kg | 136.8 | 123.3 | 149.4 | 112.3 |
| Current density, J_{Cu} | A_{ms}/mm^2 | 26.25 | 17.05 | 16.29 | 27.35 |
| Copper, P_{Cu} | kW | 6.47 | 6.97 | 6.24 | 6.65 |
| Inverter switches, J_{Si} | A_{pk}/cm^2 | 94.7 | 124.7 | 131.6 | 109.7 |

The first of the key metrics is aspect ratio or stack/pole pitch, from which the TMC designs can be seen to vary about unity for the production years evaluated (i.e., $h/\tau_p=1.0$). This in itself is of considerable value as the IPM designs tend to a square aspect ratio, which is a known design criterion for both performance and efficiency. The next key metric is average air gap flux density, which tends to be nearly constant over all the electric machines evaluated, with less than $\pm 2.2\%$ variation. This is an extremely small variation over the applications and machine power ratings being evaluated. Therefore, an interim conclusion on trajectory is that aspect ratio and average air gap flux are essentially constant. This is not the case for the SF metric, which varies from 112 N/kg to about 150 N/kg. An SF value of 110 to 120 N/kg is typical of the best induction and variable reluctance electric machines. The real benefit of the high energy permanent magnets used is the capacity of these IPMs to reach SF values of 137 to 150 N/kg, truly high performance.

The remaining three metrics relate to the thermal management system and the power inverter. The first of these thermal metrics is the current density in the copper (J_{Cu}), which not surprisingly aligns with the winding scheme of S-P-P-S going left to right on this table row (P=parallel, S=series). The two series wound stators have the highest current density at maximum loading, while the two parallel wound stators have the lowest peak current density. However, the total copper losses (P_{Cu}) in the machines studied are very nearly identical. This may be intentional on TMC's part and a capacity limitation of their vehicle thermal management system.

The final metric considers the current density in the power inverter semiconductor switches that appears to follow a criterion of $J_{Si}=115 + 14\%/-17\% A/cm^2$ for the insulated gate bipolar transistors in use. The correlation with switch current density, if there is any, appears to be with machine SF generation. But that is more coincidence than anything else. A plausible explanation may be taken from the mission requirements of the IPMs studied: (1) Prius is designed for moderate driving, an urban dynamometer driving schedule; (2) Camry is designed for more performance; and (3) Lexus is a premium brand designed for the US06 drive cycle and aggressive driving. Following that rationale, the power converter switch current density number is in proper alignment with vehicle mission requirements.

The main conclusions to be drawn from this trajectory mapping are that few changes have taken place at the electromagnetic level and basically no changes at the materials level over the last 7 years. This puts emphasis on this program's technical direction that advancements on electric machines now must occur at the materials level, specifically focusing on lower loss and inexpensive lamination steel and thermal

compounds. Therefore, when the program moves into its second year in FY 2012, the focus will be on lamination steel and thermal materials using the 2010 Prius IPM as the baseline comparator. The following section summarizes work to date on the baseline electric machine thermal model.

Development of baseline IPM thermal model

Thermal analysis and modeling is based on Fourier's law of heat transfer. Heat transfer in the dynamic state involves a generation rate, an outflow, and storage over any volume under consideration. Our interest is higher efficiency during continuous operating mode, which means the heat generation is balanced by conduction and convection mechanisms so that Fourier's law becomes the vector Poisson's equation. Thermal FEA essentially solves the vector Poisson equation in each mesh element's volume:

$$q_g + \nabla \cdot (k \nabla T) = \rho c_p \frac{\partial T}{\partial t} \quad (W/m^3); \quad Q = h_c A_s \delta T \quad (W),$$

where, $k [=] \frac{W}{mK}$; $\rho [=] \frac{kg}{m^3}$; $c_p [=] \frac{J}{mK}$; $h_c [=] \frac{W}{m^2K}$; $Q [=] W$. And in steady state, $\nabla^2 T = -\frac{q_g}{k}$ the vector Poisson equation is solved in the analysis software Flux2D.

Figure 8 illustrates the IPM pole area and slot model for analysis of iron and copper loss. The slot area is lined with Nomex paper (10 mil), and the equivalent copper conductor area is modeled according to the number-in-hand (NIH) winding pattern and coil turns (N_c) showing representative magnet wire insulation content suited to a 220°C rated wire.

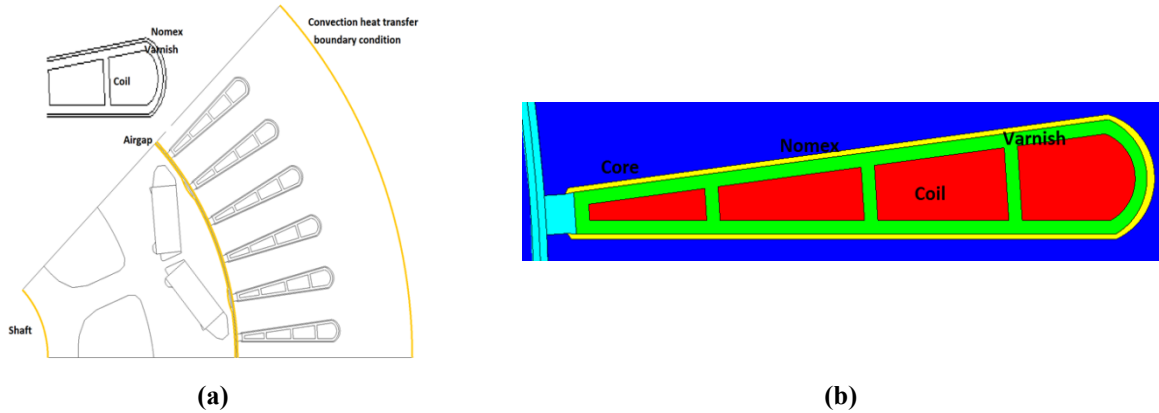


Fig. 8. One-eighth model pole area (a) and slot model (b) used for thermal analysis of the baseline machine.

The heat source, q_g , consists of the lamination core plus copper loss. Heat conduction in this two-dimensional (2D) analysis consists mainly of the core, coil, and insulating material paths. A convection coefficient is applied to the rotor at the mapping point condition (5,000 rpm, 60 Nm) given $I_s = 43 A_{rms}$ applied to the stator windings. A constant thermal conduction boundary condition is applied at the rotor shaft, and a constant convection coefficient is applied at the stator OD. The simulation was then run and the stator OD boundary condition modified until the simulated temperature rise was in agreement with laboratory test data. The boundary condition $155 W/m^2K < h_c < 200 W/m^2K$ resulted in good agreement between simulation and measurement.

Copper loss is computed as the Joule heating due to phase current flow in the winding conductors, corrected for temperature as $R_{ph} = 77(1 + 0.00393(100 - 21^\circ C)) = 100.9 m\Omega$ at $T=100^\circ C$ and the corresponding power dissipation as $P_{cu} = 3 \times I_s^2 \times R_{ph} = 559.7 W$.

Lamination steel core loss is computed using the Bertotti formula (Fig. 9), a modified Steinmetz relation that includes the usual hysteresis component ($\propto f$) and eddy current contribution ($\propto f^{3/2}$) plus an additional eddy current term containing material properties $\sigma = 5.96 \times 10^7 (\Omega\text{m})^{-1}$, $d = 0.3 \text{ mm}$, $p = 7,700 \text{ kg/m}^3$ and k_h is the coefficient of hysteresis loss and k_e is the coefficient of additional eddy current loss. At the mapping point the core loss heat generation turns out to be $P_{\text{core}} = 421 \text{ W}$ determined using the following where M_s is the stator core mass in kilograms:

$$P_{\text{core}} = \left\{ k_h B_m^2 f + \frac{\pi^2 \sigma d^2}{6\rho} (B_m f)^2 + k_e (B_m f)^{3/2} \right\} M_s (W) .$$

At the mapping point the IPM mechanical shaft power, $P_m = 31 \text{ kW}$ at $\eta = 96\%$, implies a power dissipation, $P_d = 1292 \text{ W}$ [using $P_d = ((1-\eta)/\eta)P_m$]. The net result then is that $P_d = P_{\text{cu}} + P_{\text{fe}} + P_{\text{mech}} \rightarrow P_{\text{mech}} = 1,292 - 559.7 - 421 = 311.3 \text{ W}$ for bearing friction, windage friction, and stray losses. Stray load losses are not well quantified at this point but can be partitioned into friction components along with error in copper and core loss due to harmonics, skin effects, and proximity effects.

Summarizing the thermal model performance at the stated mapping point results in the heating shown in Fig. 10 when the rotor convection coefficient, h_c , is $65 \text{ W/m}^2\text{K}$, and the stator OD boundary condition, h_c , is $155 \text{ W/m}^2\text{K}$. After 32 minutes the stator temperature has equilibrated to a final value of $T_{\text{copper}} = 141^\circ\text{C}$.

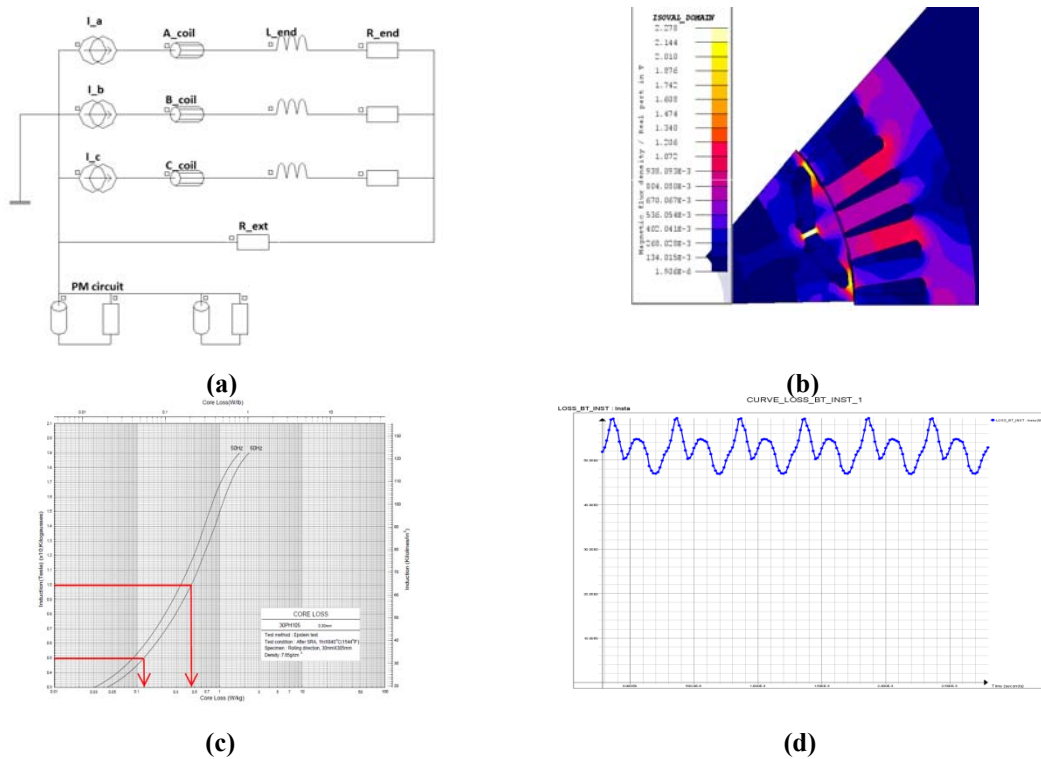


Fig. 9. Derivation of core loss coefficients for Bertotti formula: (a) per pole electrical model, (b) corresponding pole flux density plot, (c) material characteristics, and (d) resultant core loss.

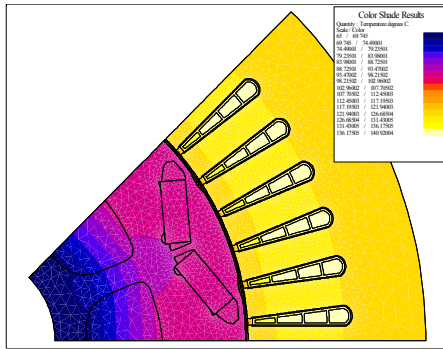
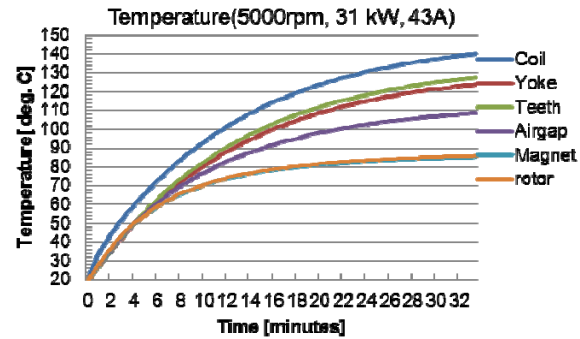


Fig. 10. Thermal model result at mapping point after 32 min.



Benchmarking data is not available at the selected IPM mapping point but is available at a power level of 25 kW (3,000 rpm, 79.6Nm) and $I_s = 54A_{rms}$. Measured stator coil temperature at this power level was 134°C at 34 min given a power dissipation in the machine of 1,275 W. Simulation at this same point showed a stator coil temperature of 138°C at 34 min into the test as summarized in Fig. 11. At this test point the rotor convection coefficient $h_c = 65 \text{ W/m}^2\text{K}$ and stator OD boundary condition were reset to $h_c = 180 \text{ W/m}^2\text{K}$ to match the test data. This adjustment is needed in 2D simulation.

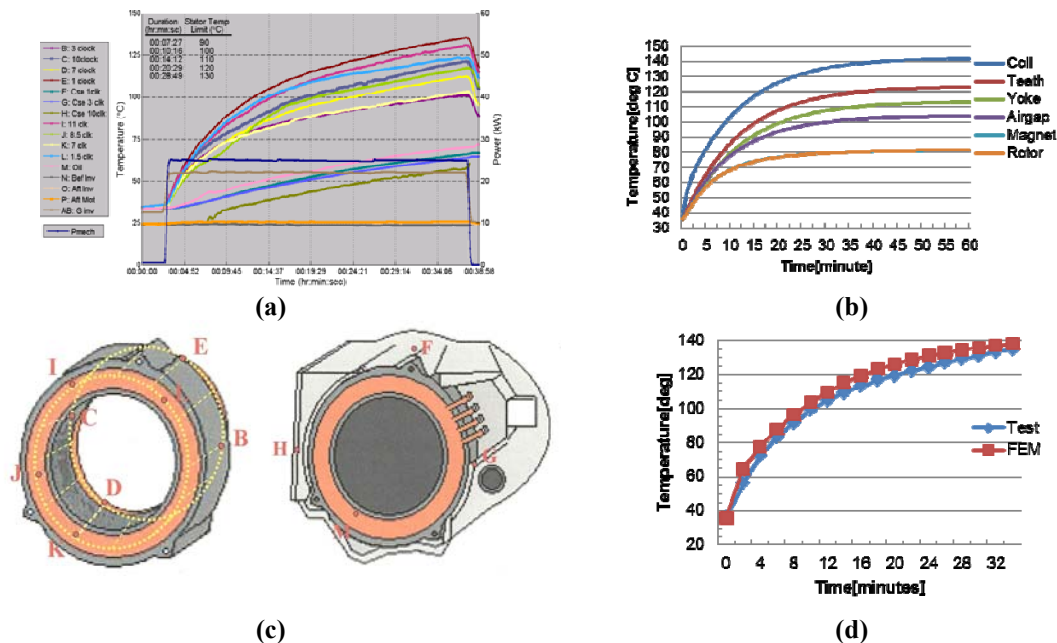


Fig. 11. Thermal model result at tested point after 34 min: (a) measured temperatures, (b) simulated temperatures, (c) thermocouple locations, and (d) comparison to test data.

The thermal evaluations are ongoing and will be extended to remove the stator OD boundary constraint on heat conduction by replacing this with the actual lamination stack to aluminum case with coolant jacket. The thermal analysis will also need to be three dimensional (3D) because end turn and rotor windage contribute significantly to heat rejection.

Electromagnetic and Thermal Mapping for Material Improvements

The mapping activities in this program are focused on identification of material improvements that will enhance the continuous power rating of the traction motor. In the program work this year that meant a focus on performance at the mapping point (5,000 rpm, 60 Nm). To understand the lamination steel needs

in terms of its crystal structure, or GOSS texture, the stator lamination flux density is computed as a vector trajectory over a rotor pole pair. The (x,y) components of the flux vector are shown in Fig. 12 at five evaluation points in the lamination steel.

Flux vector plots for 90 mechanical degrees of rotation show flat to shallow ellipse patterns where the flux essentially pulsates in magnitude with fixed or nearly fixed spatial direction. This happens in the center of the teeth and at the stator OD in the back iron. At the base of each tooth and base of the slot in the back iron the situation is very different, with the flux vector showing a strong circular polarization. The flux pattern at the tip of the stator tooth was very surprising, exhibiting a strong pulsating character with superimposed 540° of circular polarization at each magnetic polarity.

During FY 2012 the program will continue from this point and build a magnetothermal coupling model to better quantify the core losses. This will be a level of refinement beyond the Flux2D Bertotti evaluation within each mesh element. The essentials of this approach are to compute the material loss for each component of the flux vector as shown in Fig. 13(a) in matrix form with reluctivity tensor. This is illustrated graphically in Figs. 13(a) and 13(b), where the flux density vector and its attendant field strength are shown.

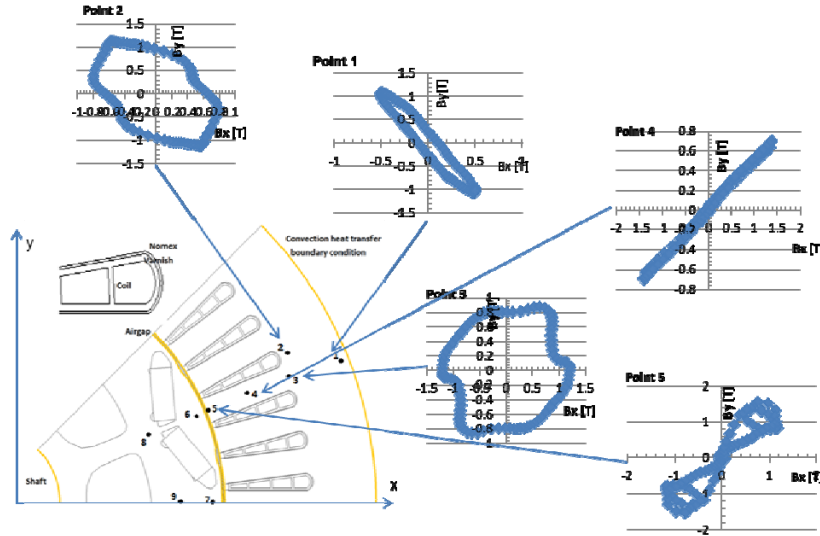


Fig. 12. Flux vector at representative points in the IPM stator.

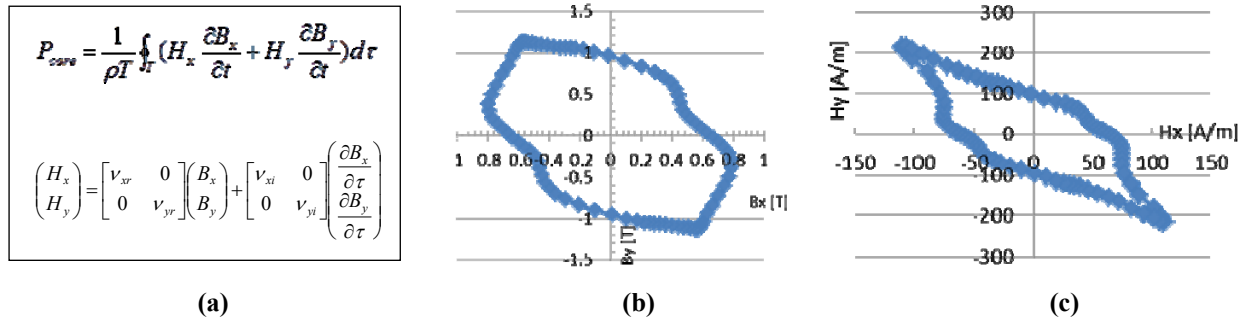


Fig. 13. Illustration of the magnetothermal coupling method: (a) calculation of material loss for flux vector, (b) flux density locus at point 2, and (c) magnetic field intensity at point 2.

As the project moves into FY 2012, the pressing materials question for new lamination steel and its processing is to determine whether its crystal structure can be zonally oriented so that aligned, transverse, and circular polarized flux will contribute minimal losses. The first round of inquiry into this question will consist of deformation sequences in the steel processing stage, including evaluating the benefits of the shear rolling process and annealing steps. The FY 2012 project will also explore electroslog casting (ESC) as a means to obtain body centered cubic (bcc) crystal structure of $\langle 100 \rangle$ aligned axis and $\langle 100 \rangle$ in transverse axis. There will also be an investigation of alternative conductor designs such as Mitsubishi's rectangular magnet wire.

Electric-Magnetic-Thermal Directional Guidelines for IPM Optimization

During FY 2011 the baseline IPM was also evaluated for thermal performance enhancement using epoxy matrix composite (EMC) materials for stator winding potting. Investigation focused on EMCs with thermal conductivities ranging from 0.5 to 20 W/mK. The baseline IPM was loaded at the maximum copper power dissipation of 6.65 kW and the structure simulated for thermal profiles in steady state. Figure 14 illustrates three representative simulation runs with thermal conductivity, K , such that $0.2 < K < 20$ W/mK. Our interest in thermal materials is motivated by the desire to improve heat conduction, and higher K -factor materials have higher thermal diffusivity, D , that in turn contributes to reduced thermal time constant, τ_{th} . The relationships are $D = \frac{K}{\rho c_p}$; $\tau_{th} = \frac{\rho c_p}{K} S_A$, where ρ = density, c_p = specific heat, and S_A = active area.

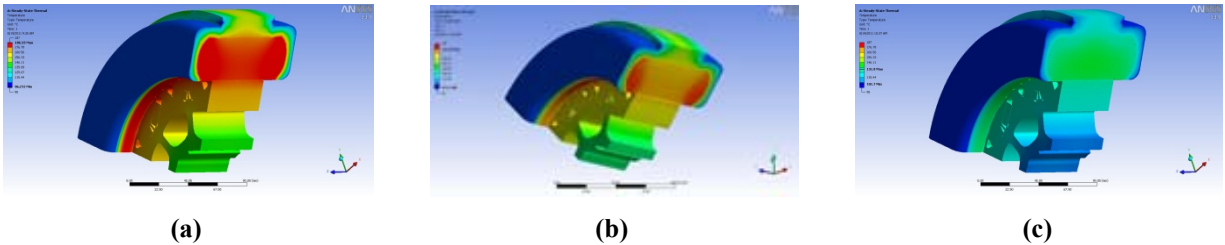


Fig. 14. Illustration of IPM thermal profiles of EMC potted windings ($P_d = 6.65$ kW and $T_{coolant} = 105^\circ\text{C}$): (a) $K = 0.5$, (b) $K = 2$, and (c) $K = 20$.

For the $K = 0.5$ case [Fig. 14(a)], the end winding potting temperature is 96°C and core temperature at the end winding sides is 186°C . For the $K = 2.0$ case [Fig. 14(b)], the end winding potting temperature is 97°C and core temperature at the end winding sides is 174°C . For the $K = 20$ case [Fig. 14(c)], the end winding potting temperature is 101.7°C and core temperature at the end winding sides is 131.9°C . The key finding here is that for the same coolant temperature of 105°C , the higher the thermal conductivity, K , the higher the end turn temperature is and the lower the stator core temperature at the end turn sides. The implication is that the higher the thermal conductivity of the EMC material, the more uniform the overall stator temperature becomes. Reviewing the sequence of thermographs, it is also apparent that the EMC properties affect magnet temperature.

Conclusion

During its first year, this project has made significant progress toward meeting the objectives set out during the FY 2011 kickoff. The overarching objective of this motor packaging work was to develop an electromagnetic model for the baseline IPM and to evaluate the benefits possible from improved magnetic steel and thermal materials. This has been accomplished and the results presented in this report. The stage is therefore set to build on this modeling and materials work for quantitative evaluation in FY 2012, specifically in the evaluation of efficiency improvement potential from novel core steel processing

methods and the inclusion of modern thermal potting materials. The key objectives met include the following.

- Completed characterization of the TMC 2010 Prius traction drive motor, a 60 kW IPM design. The key finding is that torque saturation occurs due to reduction in reluctance torque with stator current—diminished L_{qs} - L_{ds} magnitude because of q-axis saturation.
- Completed technology trajectory by mapping the design changes introduced by TMC into its hybrid vehicle product line traction motors. The period of evaluation covered 2003 to 2010 and Prius, Camry, and Lexus models. The bottom line is that fine tuning adjustments were made to winding designs (series and parallel), rotor magnet configuration (straight, single V, and double V, but no U shapes), and overall OD to stack ratio. Essentially no material changes were made, and TMC elected to stay with a proven P = eight pole, m = three phase, Q_s = 48 slot design using $t_{lam} = 0.3$ mm thickness. Some insights included the fact that all the designs evaluated maintained near 0.44 T on average mid-gap flux density, an aspect ratio that is nearly square, and use of multiple round conductor bundles (NIH), contributing to skin effect cut-in frequencies greater than 13 kHz.
- Completed building the IPM model based on characterization of winding resistance, synchronous inductance versus current, magnet flux linkage, and assessment of end turn leakage inductance. Using the model parameters, the simulated torque versus current was shown to very accurately match laboratory measured torque (obtained from FY 2010 benchmarking at ORNL).
- Completed an initial thermal model based on material characteristics, and defined what the stator boundary conditions needed to be to match characterization data temperature measurements. However, only initial evaluations of coolant jacket performance were obtained because the thermal model was done in 2D FEA and 3D FEA is needed to resolve the end winding dissipation via automatic transmission fluid splash. The project did include 3D FEA thermal modeling of the benefits of EMC as a guide for FY 2012 materials development.

During FY 2012 the focus of the Motor Packaging with Consideration of Electromagnetic and Material Characteristics project will be on material characterization and design suitable for the IPM stator, specifically the evaluation of both shear roll processing of lamination steel for bcc crystal orientation in rolling and transverse directions so that local core loss contributions due to radial, circumferential, and circular polarized flux are minimized. The FY 2012 work will also investigate high silicon content ESC for suitability for an IPM. One IPM stator will be fabricated, wound, and tested for comparison to the baseline IPM performance. Thermal materials such as EMC will continue to be modeled and evaluated, but because of budget restrictions, prototype builds and evaluation will not take place until FY 2013.

Patents

New project; none to date.

Publications

1. J. M. Miller, “New Materials and Processes Lead Way to PEV Traction Motor Efficiency Improvement,” presented at the Wisconsin Electric Machines and Power Electronics Consortium (WEMPEC) 30th Annual Review Meeting, University of Wisconsin-Madison, May 18–19, 2011.

References

1. T. Burrell, *Evaluation of the 2010 Toyota Prius Hybrid Synergy Drive System*, ORNL/TM-2010/253, Oak Ridge National Laboratory, March 2011.
2. C. Ayers, *Evaluation of 2004 Toyota Prius Hybrid Electric Drive System*, ORNL/TM-2004/247, Oak Ridge National Laboratory, November 2004.

3. E. C. Lovelace, T. M. Jahns, and J. H. Lang, "A Saturating Lumped-Parameter Model for an Interior PM Synchronous Machine," *IEEE Transactions on Industry Applications*, Vol. 38(3), pp. 645–650, May/June 2002.
4. E. C. Lovelace, T. M. Jahns, J. Wei, T. Keim, J. H. Lang, D. D. Wentzloff, P. J. McCleer, F. Leonardi, and J. M. Miller, "Design and Experimental Verification of a Direct-drive Interior PM Synchronous Machine Using a Saturable Lumped-Parameter Model," *IEEE 37th Industry Applications Society Annual Meeting*, Pittsburgh, Pennsylvania, October 13–18, 2002, pp. 2486–2492.
5. M. A. Rahman, T. A. Little, and G. R. Slemon, "Analytical Models for Interior-Type Permanent Magnet Synchronous Motors," *IEEE Transactions on Magnetics*, Vol. Mag-21(5), pp. 1741–1743, September 1985.
6. N. Bianchi and S. Bolognani, "Magnetic Models of Saturated Interior Permanent Magnet Motors based on Finite Element Analysis," in *Proceedings of the IEEE 33rd Industry Applications Society Annual Meeting*, St. Louis, Missouri, October 12–15, 1998, pp. 27–34.
7. M. A. Rahman, P. Zhou, D. Lin, and M. F. Rahman, "Measurement of Parameters for Interior Permanent Magnet Motors," in *Proceedings of the IEEE Power and Energy Society General Meeting*, Calgary, Alberta, Canada, July 26–30, 2009, pp. 1–4.
8. P. Zhou, D. Lin, G. Wimmer, N. Lambert, and Z. J. Cendes, "Determination of d-q Axis Parameters of Interior Permanent Magnet Machine," *IEEE Transactions on Magnetics*, Vol. 46(8), pp. 3125–3128, August 2010.
9. E. C. Barnes, "An Experimental Study of Induction Machine End-turn Leakage Reactance," *AIEE Transactions*, Vol. 70, pp. 671–679, 1951.
10. R. D. Findlay, N. Stranges, and D. K. MacKay, "Losses Due to Rotational Flux in Three Phase Induction Motors," *IEEE Transactions on Energy Conversion*, Vol. 9(3), pp. 543–549, September 1994.
11. W. A. Pluta, "Specific Total Loss Components Under Axial Magnetization in Electrical Steel Sheets with Different Degree of Goss Texture," *IEEE Transactions on Magnetics*, Vol. 44(11), pp. 3832–3835, November 2008.
12. J. R. Brauer, "Magnetic Diffusion Times for Infusion and Effusion in Nonlinear Steel Slabs and Cylinders," *IEEE Transactions on Magnetics*, Vol. 43(7), pp. 3181–3188, July 2007.
13. ASTM International (ASTM), *Standard Test Method for Alternating Current Magnetic Properties of Materials Using the Wattmeter-Ammeter-Voltmeter Method, 100 to 10,000 Hz and 25-cm Epstein Frame*, A 348/A 348M-05, ASTM: West Conshohocken, Pennsylvania, 1991.
14. Bo yang, *Development of Thermal Models for Permanent-Magnet Traction Motors*, MS thesis, Royal Institute of Technology, Stockholm, Sweden, July 2009.
15. Sami Ruoho et.al., "Temperature Dependence of Resistivity of Sintered Rare-Earth Permanent-Magnet Materials," *IEEE Transactions on Magnetics*, Vol. 46(1), pp.15–20, January 2010.
16. Heesung Yoon, Inhyun Kim, Pan Seok Shin, and Chang Seop Koh, "Finite Element Implementation of a Generalized Chua-Type Vector Hysteresis Model and Application to Iron Loss Analysis of Three-Phase Transformer," *IEEE Transactions on Magnetics*, Vol. 47(5), pp. 1122–1125, May 2011.
17. W. L. Soong, *Thermal Analysis of Electrical Machines: Lumped-Circuit, FE Analysis and Testing*, Power Engineering Briefing Note Series, PEBN 6, University of Adelaide, School of Electrical and Electronic Engineering, Australia, May 20, 2008, pp. 21–22 (available online at <http://www.eleceng.adelaide.edu.au/research/power/pebn>).
18. Wojciech A. Pluta, "Specific Total Loss Components Under Axial Magnetization in Electrical Steel Sheets with Different Degree of Goss Texture," *IEEE Transactions on Magnetics*, Vol. 44(11), pp. 3832–3835, November 2008.

3.4 Permanent Magnet Development for Automotive Traction Motors

Principal Investigator: Iver E. Anderson

Division of Materials Sciences and Engineering

Ames Laboratory, Iowa State University

Ames, IA 50011

Voice: 515- 294-9791; Fax: (515) 294-8727; E-mail: andersoni@ameslab.gov

DOE Technology Development Manager: Susan A. Rogers

Voice: 202-586-8997; Fax: 202-586-1600; E-mail: Susan.Rogers@ee.doe.gov

DOE Technology Manager (Propulsion Materials): Jerry L. Gibbs

(202) 586-1182; fax: (202) 586-1600; e-mail: jerry.gibbs@ee.doe.gov

Objectives

- Develop the materials and processes needed to fabricate high performance permanent magnets (PM) that can be used for advanced traction drive motors with an internal PM rotor design to meet APEEM goals for enhanced performance at elevated temperature (180-200°C) and reduced cost.
- Anisotropic magnets should be developed to satisfy the need for magnets with maximum magnetic energy density and minimum content of valuable materials. If possible, improved magnet forming processes and mechanical properties also should be developed to further reduce manufacturing costs and extend lifetime in service.
- While magnet materials meeting the technical specifications are most readily achieved using rare earth (RE) permanent magnets, the market factors of rising RE demand/cost and near total foreign control of RE supplies dictate that in the long term, alternative non-RE magnets must be developed.

Approach

This program consists of two major thrust areas.

- Continue investigation of ***RE anisotropic*** permanent magnets, as recommended in an industry expert study, placing effort on generating anisotropic particulate for bonded magnets and on novel processing of sintered RE permanent magnets, exploiting the improved high temperature tolerance of the Ames mixed rare earth (MRE)-Fe-B alloys.
- Develop aligned microstructures in MRE-Fe-B magnet alloy particulate with little or no Dy content, preferably by controlled rapid solidification as a low cost route to make large gains in bonded magnet strength and reduced magnet cost for simplified motor manufacturing.
- Further develop anisotropic sintered permanent magnets from micron-sized single crystal particles of MRE-Fe-B alloys using pressure-driven liquid phase sintering with intrinsic or extrinsic sintering additives for fully dense magnets of the highest magnetic strength, aiming for greatly reduced Dy content.
 - It should be noted that techniques being developed to produce anisotropic RE magnets probably can be used in the second thrust area, as well.
- New high strength ***non-RE anisotropic*** permanent magnets will be developed that meet the requirements for advanced interior PM electric traction motors. The investigation will involve theory and modeling efforts, as well as experimental synthesis of magnet compounds and prototype magnet fabrication and characterization.
- Development of non-RE anisotropic permanent magnets will include attempts to improve on known systems, e.g., Alnico, by gaining enhanced knowledge of coercivity mechanisms with more sensitive

characterization techniques and by innovative processing to improve coercivity using greater control of microstructure.

- Non-RE anisotropic permanent magnets also will be pursued with help from theory and modeling, seeking to discover new phases based on Fe-Co with beneficial intrinsic properties, i.e., high Curie temperature, magnetization and magnetic anisotropy.
- If the new non-RE permanent magnet phases have insufficient magnetic properties as single-phase magnets, increased properties will be sought with further extrinsic manipulation, including use a soft magnetic second phase to produce enhanced exchange coupling.
 - It should be noted that this task area is extremely high risk, but if successful it will revolutionize the cost structure of permanent magnet motors and reduce the reliance on foreign controlled commodities for hybrid and electric vehicle production.

Major Accomplishments

- For RE magnets, a large Dy reduction was enabled by targeted diffusion (at 900°C) of DyF₃ “paint” to the interior microstructure in anisotropic sintered MRE_{2.5}(Fe, Co)₁₄B magnets, where MRE = [Nd_{0.45}(Y₃Dy₁)_{0.55}], which achieved an energy product, (BH)_{max}, of 31.4MGOe and a coercivity, H_{ci}, of 15 kOe, both at ambient temperature, and a temperature coefficient of H_{ci}, β, of -0.5%/°C, all equivalent to commercial Nd-based Nd₂Fe₁₄B magnets that are used in drive motors for 200°C operation (EH grade, containing 8-10% Dy), but by using only 5.3wt.% Dy or about 45% less Dy for large magnet cost decrease.
- In development of particulate for anisotropic bonded MRE_{2.2}Fe₁₄B_{1.1} magnets without Dy, where MRE = [Y_{0.55}Nd_{0.45}], highly aligned columnar solidification patterns resulted from a novel Ag micro-alloying (<1at.%Ag) effect that achieved strong and unique texture control in ribbon samples that were melt spun at low speed (5m/s), producing an anisotropic particulate that was crushed for epoxy bonding and testing, but further microstructure scale refinement and texture design is needed before this concept is tailored for bonded magnets that can achieve suitable coercivity levels.
- In our search for non-RE permanent magnets, a genetic algorithm (GA) method was adapted to enable computational phase diagram exploration for alloys based on Fe-Co, speeding up by at least 1000 times the search for candidate chemical compositions with desirable structures and properties. Using only a shared computer cluster at Ames, an initial structure search of Fe-Co alloys successfully predicted structures at a specific range of compositions that have energies lower (more favorable) than those proposed in the literature, but further GA searching of Fe-Co-X systems for enhanced crystalline anisotropy will require the increased capabilities of a dedicated cluster and DOE supercomputer facilities, e.g., at ORNL.
- As a tool for rapid structural analysis in our “beyond RE magnets” (BREM) thrust, a multiple sample staging system was developed at the DOE synchrotron X-ray source at Stanford Synchrotron Research Laboratory and demonstrated by characterization of thin film samples from a Fe-Co-W combinatorial “library” of compositions, determining that an upper W content of about 15 at.% is set in this system by the onset of dominant amorphous phase formation.
- In the portion of the BREM thrust devoted to improvement of existing Alnico magnets, a series of density functional theory (DFT) calculations predicted that the magnetic anisotropy of Fe-Co layers at the interface of Fe-Co precipitates and the NiAl matrix phase is increased by two orders of magnitude, indicating that a significant coercivity benefit could result from reducing the spinodal spacing to far less than the typical 50 nm. TEM studies of commercial Alnico 5-7 magnets indicated that the chemical partitioning of Fe and Co in the NiAl matrix phase is far from complete, with about 30-40 at.% Fe-Co measured in this region, suggesting a further direction for microstructure improvement that can benefit the magnetic properties.

Future Directions

- Continue focused work on improved processing of ***RE anisotropic*** permanent magnets, stepping up studies on innovative processing of sintered RE permanent magnets and on direct solidification processing of anisotropic particulate for bonded magnets, exploiting the improved high temperature tolerance of the Ames mixed rare earth (MRE)-Fe-B alloys with little or no Dy content.
 - Focus on development of anisotropic sintered MRE magnets using pressure assisted sintering with extrinsic additives to permit greatly reduced temperatures for full consolidation, exploring additive alloy design to diminish or eliminate Dy use.
 - Enhance development of micro-alloying for direct solidification of MRE magnet alloy without Dy to refine spacing of aligned columnar microstructure in resulting ribbons and accentuate magneto-crystalline anisotropy in precursor particulate for bonded microcrystalline magnets.
- Enhance the theory side of the effort to develop new high strength ***non-RE anisotropic*** permanent magnets that meet the requirements for advanced interior PM electric traction motors based on the critical need for compositional clarification of experimental directions. This will follow a compressed down-selection of promising magnet alloy compositions that is planned for early in FY2012. In general, it is critical that the investigation maintains close collaboration of theory and modeling efforts, of experimental magnet material synthesis work, and of detailed characterization studies on the new materials.
 - Refine and implement genetic algorithm calculations for rapid theoretical investigation of potential new phases in Fe-Co and Fe-Co-X alloys, starting with (by priority) W, Hf and Zr on a new dedicated cluster and on external supercomputer resources.
 - Focus density functional theory calculations on for Fe_mT_n , Co_mT_n , and $(\text{Fe-Co})_m\text{T}_n$, starting with (by priority) T=W, Hf, Zr, Mo, Ta, and Nb, to look for the most promising ternary compositions and use theory to investigate anti-phase boundaries and twinning effects on coercivity with small dedicated cluster computer.
 - Employ combinatorial synthesis experiments to explore limited composition ranges of $(\text{Fe-Co})_m\text{T}_n$, where T = Hf, Zr, Ta, and Nb, as well as any follow-up work needed on W and Mo, to look for the most promising ternary compositions, with detailed feedback from characterization efforts to enable effective screening of these systems.
 - Extend cluster deposition experiments to explore specific compositions of $(\text{Fe-Co})_m\text{T}_n$, starting with T=W and Hf to try promising new ternary compositions in highly metastable nano-particle configurations, where detailed characterization by TEM, XRD, and magnetometers will assist in search for promising M_s , K_1 and H_a values.
 - Develop chemical synthesis and self-assembly methodologies for limited composition ranges of Fe_mT_n , Co_mT_n , and $(\text{Fe-Co})_m\text{T}_n$, starting with W, Hf, and Zr, to gain understanding of the processing parameters for promising binary and ternary compositions in these nano-particle configurations. Desirable layered structures also will be developed as a step toward preparation of enhanced exchange coupled magnets.
 - Begin development of bulk magnet fabrication approaches to support the eventual need for full magnet sample testing of $(\text{Fe-Co})_m\text{T}_n$ alloys.
 - Utilize detailed characterization results for commercial Alnico as starting point for theoretical analysis of degree of improvement possible in this magnet family.
 - Implement initial theoretical analysis of a possible coercivity enhancement method in Alnico by microstructure control experiments, intending to refine precipitation size and spacing and to enhance solute segregation. Also, begin theoretical and experimental studies of Vicalloy system to determine potential for increased coercivity.
 - Conduct Annual Workshop (Nov. 2011---completed) and Spring Workshop (May 2012).

Technical Discussion

Accomplishments in Rare Earth Anisotropic ($R_2Fe_{14}B$ -type) Magnet Research

Dy Reduction in Anisotropic Sintered RE Magnets: Especially for temperatures above 120°C, the magnetic properties of isotropic MRE-based magnets are superior to those of current commercially available isotropic Nd-based magnets. Recently, grain-aligned sintered MRE-based magnets were developed with a maximum energy product $(BH)_{\max}$ above 25 MGOe, compared to the 12 MGOe of the MRE isotropic magnets. However, the sintered anisotropic MRE magnets exhibited a far stronger (undesirable) temperature dependence for the coercivity (i.e. higher β absolute value), similar to Nd-based magnets. An improved β value may be obtained by adding heavy rare earth elements such as Dy to the bulk magnet alloy to achieve higher magnetic anisotropy of the 2:14:1 phase to increase coercivity, but in the current commercial environment, this would add unacceptable high cost. It is known that the interface between the matrix phase and grain boundaries of the 2:14:1 grains in sintered magnets provides the nucleation sites for magnetization reversal, resulting in a low coercivity. Thus, we decided to attempt the targeted introduction of Dy at the grain boundary regions to strengthen magnetic anisotropy of the localized interfacial 2:14:1 phase regions and to more effectively improve coercivity of our MRE-based magnets with a significantly reduced Dy addition.

Based on this concept, Dy was introduced as a segregant into $MRE_2(Fe, Co)_{14}B$ magnets by using DyF_3 powder in two different methods, since this type of Dy addition can be less costly and much less susceptible to oxidation during processing. One method is referred to as a grain boundary diffusion treatment, where finished sintered magnets with a thickness of 1.5mm were coated with DyF_3 powder (from an ethyl alcohol-based paint) and heated to 900°C to promote Dy diffusion along grain boundaries and into grain exteriors, producing “diffusion” magnets. Another method is that the magnet alloy powder is blended with DyF_3 powder and then made into sintered magnets by conventional methods, producing “blended” magnets. In this conventional method, ingots with an initial composition of $[Nd_{0.45}(Y_3Dy_1)_{1/(r+1)*0.55}]_{2.6}Fe_{bal}Co_{0.7}B$ were prepared by arc melting in an Ar atmosphere. The alloy ingots were then free-jet melt spun on a Cu wheel at a low wheel speed of about 2 m/s to obtain strip cast flakes. The strip cast flakes were subjected to hydrogen decrepitation (HD) treatment and milled into powders using conventional ball milling. The powders were aligned with a magnetic field of 1.8T, pressed and finally sintered in vacuum at 1050-1080°C for 2-4h to obtain a “baseline” magnet. In addition, the magnet alloy powder for making baseline magnets was blended with 5wt.% DyF_3 powder before ball milling and sintered/aligned to make blended magnets.

Magnetic properties were measured using a Quantum Design MPMS SQUID magnetometer with a maximum field of 5.0 T. As illustrated in the second quadrant of the hysteresis loop that is shown in Fig. 1, processing improvements raised $(BH)_{\max}$ @ RT of anisotropic sintered $MRE_{2.5}(Fe, Co)_{14}B$ “baseline” magnets from 25.6 to 32.7 MGOe, very similar to the ambient temperature energy product of industrial sintered magnets that are currently used for hybrid electric vehicles. The Dy addition to diffusion enhanced magnets raised H_{ci} to 15 kOe with $(BH)_{\max}$ maintained at 31.4 MGOe. The blended Dy addition to MRE magnets (5wt% DyF_3) also raised H_{ci} to 17.8 kOe, but the $(BH)_{\max}$ was reduced to 25.4MGOe, due to a considerable reduction of remanence.

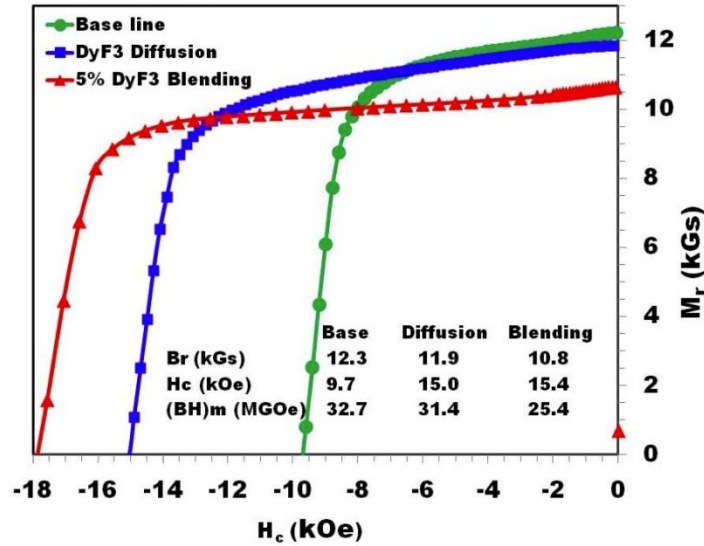


Figure 1. Summary of data from the second quadrant of the hysteresis loop for baseline, diffusion, and blended samples of MRE-(Fe-Co)-B, showing the effect of DyF₃ additions.

High temperature magnetic properties were measured by a vibrating sample magnetometer (VSM) with a field of 9.0T. The effect of coercivity on the temperature coefficients of coercivity in the temperature range of 27 to 127°C is shown in Fig. 2. For comparison, the magnetic properties of commercial Neomax magnets (from their data sheets) are also included in the figure. It is seen that the temperature coefficient of coercivity decreases with increasing coercivity. However, these magnets need quite different coercivities in order to achieve the same acceptable β value, for example 0.5%/°C. The commercial Neomax magnets require a coercivity above 30 kOe, while the MRE magnets modified by DyF₃ blending and diffusion needed only 16 and 15 kOe, respectively. This means that the blending and diffusion modified MRE magnets need a lower amount of Dy to achieve the same thermal stability as Nd-based Neomax magnets, and that initial magnetization of Neomax magnets that are mounted in a soft magnetic (Fe-Si) rotor is more difficult.

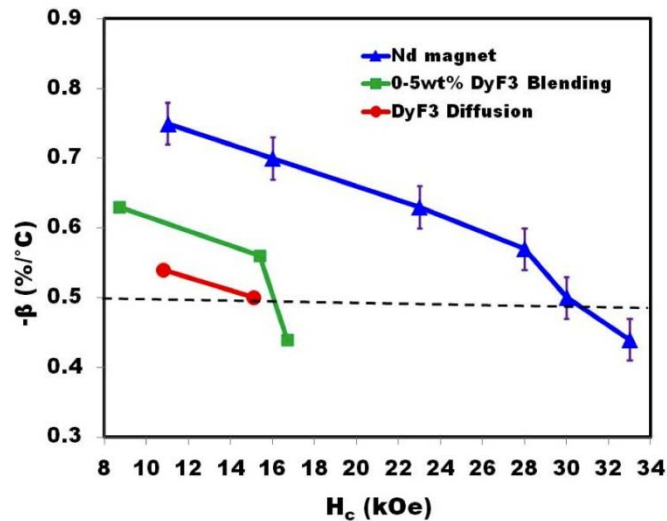


Figure 2. Summary of the effect of coercivity on the temperature coefficients of coercivity in the DyF₃ modified MRE magnet alloys for temperature range of 27 to 127°C, compared to data for commercial Neomax magnets.

Actually, Dy content vs. β value (seen in Fig. 3) clearly shows this fact. The Dy contents of the diffusion magnets were calculated according to the weight gain before and after diffusion treatment. The Dy contents of Nd-based magnets were estimated according to the data from published references, including product information on Neomax magnets. It is seen from Fig.3 that the diffusion or blending modified MRE magnets with the same β value always require a lower amount of Dy than the Nd-based magnets. For example, the total Dy concentration in the MRE-based diffusion magnets with a β value of $-0.5\%/^{\circ}\text{C}$ was 5.3 wt%, while typical commercial Nd-based magnets that achieved such a useful β value needed about 10 wt% Dy.

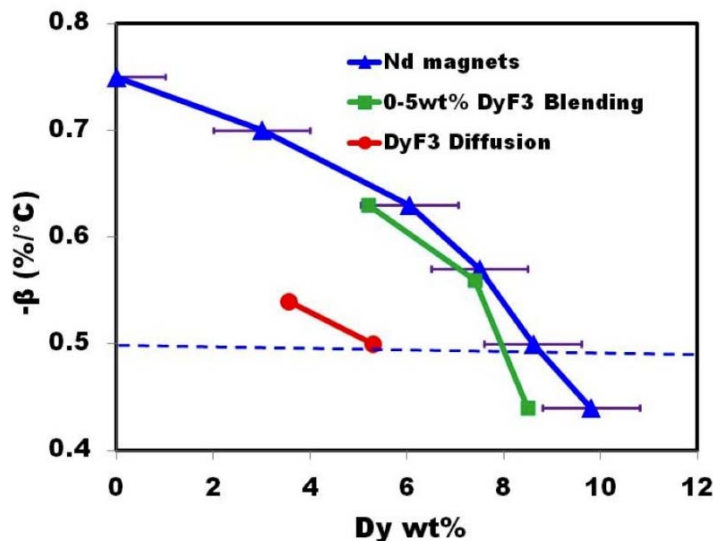


Figure 3. Summary of Dy content vs. β value, as further analysis of the data in Fig. 2.

These results indicate that the intrinsic temperature compensation effect contributed by the $\text{MRE}_2\text{Fe}_{14}\text{B}$ magnet alloy (containing Y and Dy, along with Nd) offers a significant advantage for high temperature operation, especially with DyF_3 diffusion modification of the sintered $\text{MRE}_2\text{Fe}_{14}\text{B}$ magnets. Thus, anisotropic sintered $\text{MRE}_{2.5}(\text{Fe}, \text{Co})_{14}\text{B}$ magnets achieved an energy product, $(\text{BH})_{\text{max}}$, of 31.4 MGOe and a coercivity, H_{ci} , of 15 kOe, both at ambient temperature, and a temperature coefficient of H_{ci} , β , of $-0.5\%/^{\circ}\text{C}$. These characteristics are competitive with commercial Nd-based $\text{Nd}_2\text{Fe}_{14}\text{B}$ magnets that are used in drive motors for 200°C operation (EH grade, containing 8-10% Dy), but by using only 5.3wt.% Dy or about 45% less Dy for a large magnet cost decrease. For further advantage, new work will be started on DyF_3 diffusion magnets in a lower Dy version of MRE magnet alloy with a 6:1 ratio of Y:Dy, based on our earlier observations with isotropic magnets.

Aligned Particulate for Anisotropic Bonded RE Magnets: Control of microstructure and texture is of critical importance in forming rare earth (RE)-iron-boron particulate suitable for anisotropic bonded permanent magnets in order to obtain the highest performance from these alloys. Particulate for these applications must be able to maintain coercivity as well as having a large enough particle size to avoid excessive oxidation. Especially in the case of polymer-bonded magnets, anisotropic magnets would have a great advantage over current isotropic bonded magnets, up to 4X the maximum energy product. In this study, the selected approach to controlling grain size, while maintaining texture, is through stabilization and refinement of directional growth in melt-spun ribbons. To obtain suitable anisotropic particulate from these melt-spun ribbons, a mild crushing would be needed, followed by bonding with a polymer (or an alternative extrinsic binder phase) under an imposed magnetic field.

One avenue to obtain suitable directional growth in melt-spun ribbons was studied previously by Kramer et al.^{2,3} who determined the mechanism by which Nd-Fe-B ribbons that were melt-spun at low wheel speed (e.g. $\sim 5\text{-}10\text{ m/s}$) developed a $\langle 001 \rangle$ texture¹ on the free surface. This observation could not be

directly exploited for the current study because there was often a final zone of coarse dendrites on the free surface and there was no obvious means to refine significantly the spacing of the columnar dendrites, which would be needed for anisotropic bonded magnets. However, we hypothesized that this refinement might be achieved by using a segregating (highly insoluble) additive, e.g., Ag, at the proper concentration to introduce instability in the Fe-rich liquid interface, promoting growth of a finer, textured structure. Moreover, the Nd-based 2-14-1 magnetic phase ($\text{Nd}_2\text{Fe}_{14}\text{B}$) is known to have poor high temperature magnetic properties. Fortunately, suitable MRE alloy particulate for isotropic polymer-bonded magnets for use at high temperatures (up to 200°C) previously was developed (in this project) through the addition of yttrium and a heavy rare earth element, i.e. Dy^2 , but concerns over price and availability of heavy rare earths have led us to experiment on Dy-free MRE alloys to see if a simple MRE of Y-Nd would provide sufficient high temperature magnetic properties. Thus, varying concentrations of Ag (0.3-1.7 at.%Ag) were added to melt-spun ribbons (produced with a 5 m/s wheel speed) of a base composition of $(\text{Y}_{0.55}\text{Nd}_{0.45})_{2.2}\text{Fe}_{14}\text{B}_{1.1}$.

In samples containing no Ag, significant variation in microstructure exists with some regions displaying a columnar microstructure, but Fig. 4a shows a more typical microstructure. Along the wheel surface of these ribbons, a fine, equiaxed region exists (labeled “1” in Fig. 4a), but as growth proceeds a columnar region forms that is quickly interrupted by either large equiaxed grains (labeled “4” in Fig. 1a), or fine dendritic regions characterized by a large degree of secondary arm branching (labeled “5” in Fig. 4a). The bright phase in this micrograph corresponds to the RE-rich intergranular phase observed in typical sintered magnets. In all ribbons containing Ag, a layer of fine equiaxed grains, approximately $20\mu\text{m}$ thick, was present near the wheel surface (identified in Fig.4b of the ribbon with 0.6 at. % Ag by the arrow labeled “1”). Projecting out of this region, columnar dendrites of $\text{MRE}_2\text{Fe}_{14}\text{B}$, extend through the thickness of the ribbon (denoted by the arrow labeled “2” in Fig. 4b). Alloys where $x \geq 0.1$ (0.6 at. % Ag) displayed a fine secondary phase, enriched in Ag and Nd (the bright spots labeled “3” in Figs. 4b), dispersed along the boundaries of the columns. Energy dispersive spectroscopy (EDS) of a TEM sample (not shown) indicated that this phase is likely a 2:1 (Ag:RE) intermetallic compound, with approximately 80% of the RE as Nd, with the remainder Y. This composition is consistent with a study of Nd-Fe-Ag equilibrium by Takeda et al. The morphology and distribution of the Ag_2RE phase indicated that the phase likely coarsened during cooling. In the sample with 0.3 at. % Ag (not shown), a more continuous RE-rich film coated the columnar dendrites, similar to the intergranular phase observed in sintered Nd-Fe-B magnets.

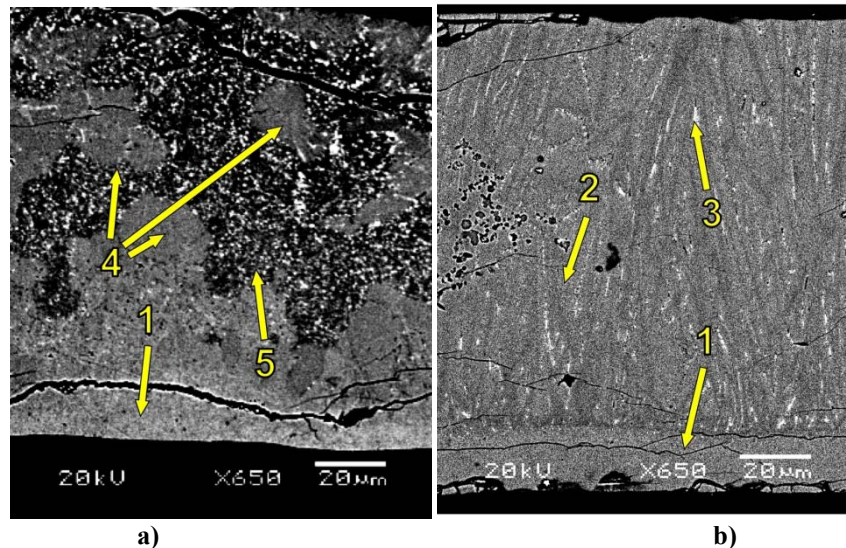


Figure 4 - Cross section BSE micrographs of $(\text{Y}_{0.55}\text{Nd}_{0.45})_{2.2}\text{Fe}_{14}\text{B}_{1.1}\text{Ag}_x$ ribbon melt-spun at 5 m/s, where x is a) 0.0, and b) 0.1 in at.%. Arrows point to features described in the text.

Average center-to-center column spacing was determined using a line-intercept method. This was plotted as a function of distance from the equiaxed/columnar grain interface (where columnar growth initiates) to determine the degree to which columnar growth is stabilized and refined (Fig. 5). All cases show a fine grain spacing ($\sim 2 \mu\text{m}$) near the interface between the equiaxed zone and the start of directional growth. The spacing slowly increases through the thickness of the ribbon. In the Ag-containing alloys, the concentration of Ag seems to have some effect on the stability of spacing of the columns, with 0.10 wt.%Ag (0.6 at.%) as the most stable. However, an average error of $\pm 1.2 \mu\text{m}$ adds uncertainty to this finding. In the case without silver, the columnar structure breaks down and grain spacing increases drastically as the columnar grains give way to larger, equiaxed ones.

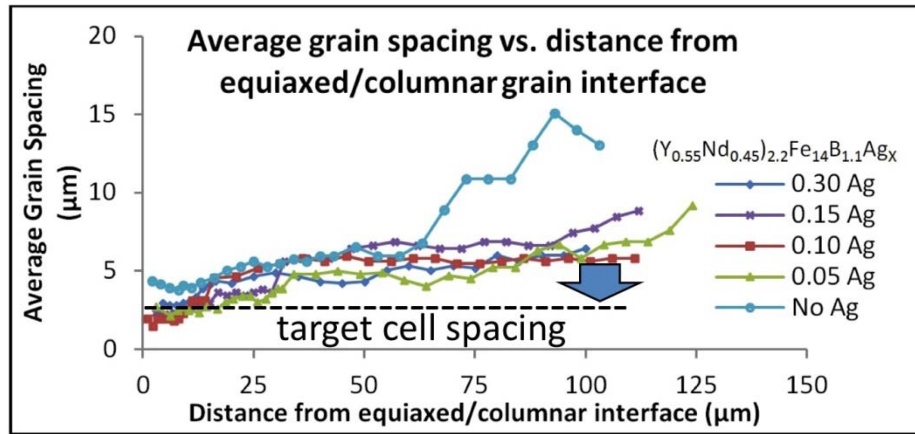


Figure 5. Summary of average center-to-center column spacing from line-intercept method in all ribbon alloys studied vs. distance from the equiaxed/columnar grain interface, where the labeled Ag contents are in wt.%.

It was determined that Ag stabilized through-thickness columnar growth in the ribbons with additions as small as 0.3 at. %, but the Ag also produced a unique texture in the ribbons, compared to alloys with no Ag added. In MRE-Fe-B ribbons without Ag (see Fig. 6a), a strong $\langle 00 \rangle$ texture was observed in the X-ray diffraction (XRD) patterns at the free surface, consistent with the Kramer^{2,3} mechanism. In all Ag-containing ribbons (0.6 at.%Ag shown in Fig 6b), the observed texture is canted to both the c- and a-axes, but the mechanism for this change is unclear.

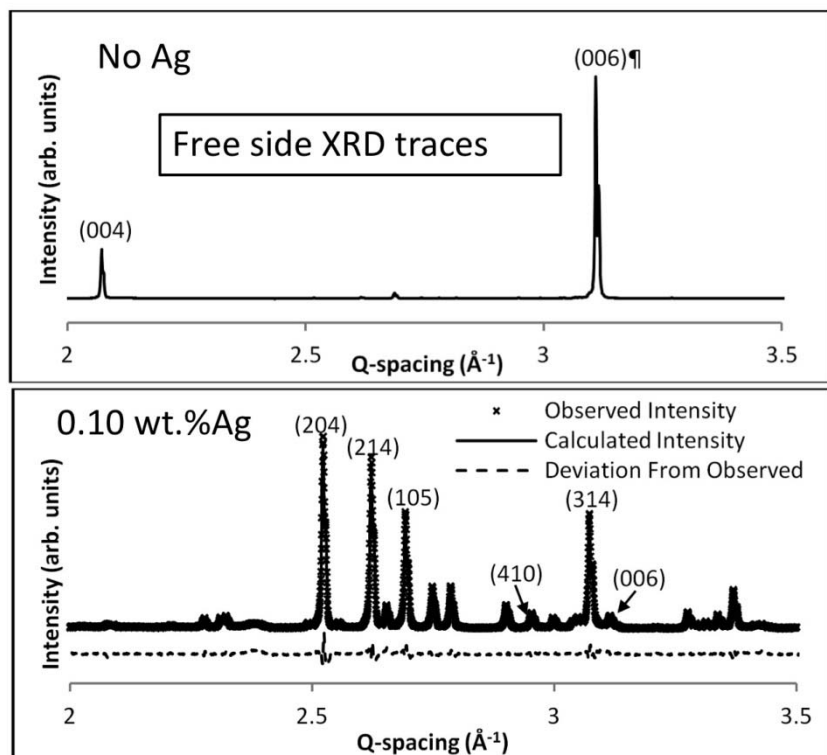


Figure 6. Comparison of the XRD patterns for a) a ribbon without Ag (top), and b) a ribbon with 0.6 at.% Ag (bottom).

The addition of Ag to RE-Fe-B alloys provided significant modification to the microstructure and growth observed and a columnar structure was stabilized through nearly the entire thickness of the ribbon. The spacing of these columns increased gradually as growth proceeded and this trend seemed to vary slightly with Ag concentration. The Ag also altered the texture in the ribbons, indicating a disruption in the normal $\text{RE}_2\text{Fe}_{14}\text{B}/\alpha\text{-Fe}$ templating mechanism⁴ for Ag-free magnet alloy ribbons melt-spun at low wheel speeds. While the novel texture obtained is not a single crystalline orientation (as desired for ease in optimum alignment), improved understanding of the new solidification sequence could lead to additional refinement (to the level indicated in Fig 5) and texture design, producing suitable coercivity levels in ribbons that could be crushed to form fragmented particulate for anisotropic bonded magnets fabrication.

Accomplishments in Beyond Rare Earth Magnets (BREM) Research

Genetic Algorithm for Rapid Computational Prediction of Magnet Materials: Computational materials discovery now is being applied to the pursuit of superior permanent magnetic (PM) materials that do not contain rare earth (RE) elements, which are quickly rising in global strategic importance. Ames has developed computational algorithms and codes to perform supercomputer assisted phase diagram exploration and materials structure prediction and discovery, especially for iron-based alloys. This breakthrough speeds up the search process by at least 1000 times, making it possible to perform accelerated computational studies to identify candidate chemical compositions and structures that have desirable properties.

Ames' algorithm development represents a new paradigm to accelerate the discovery process. This computational approach is effectively coupled with a strong experimental synthesis effort in the Beyond Rare Earth Magnets (BREM) partnership, supplying mutual feedback to greatly speed up the materials

discovery process far beyond trial and error methods. The algorithms, code, and experience gained in this effort will be directly applicable to other accelerated materials discovery efforts as well.

Using the shared cluster computer available at Ames Laboratory, an initial structure search for Fe-Co binary alloys has successfully predicted structures at a range of compositions that have energies lower than those structures proposed in the literature (see Fig. 7). With the help of peta-scale computing power from Oak Ridge National Laboratory, for example, that should become available with further code development and demonstration, we hope to be able to explore much larger structural space, including Fe-Co-X alloys for enhanced crystalline anisotropy. We are confident that many new promising structures of Fe-based compounds can be discovered from these calculations to guide experimental design and synthesis of new non-RE permanent magnets.

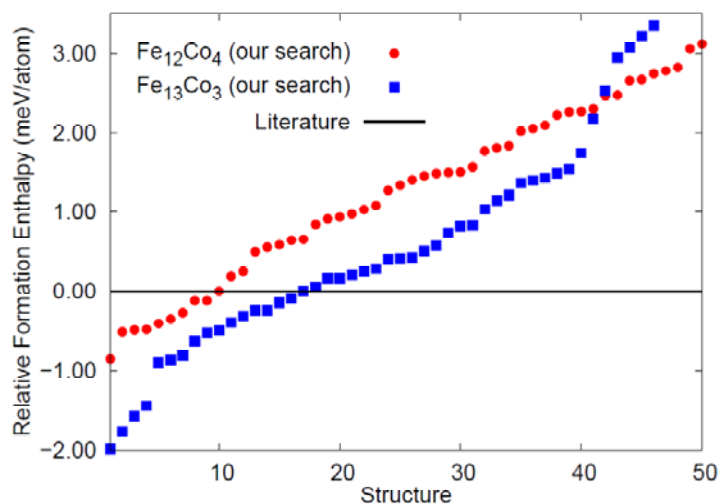


Figure 7. Structures of Fe₁₂Co₄ and Fe₁₃Co₃ obtained from our genetic algorithm search with energies lower than that of the best structures proposed in the literature.

Rapid Crystal Structure and Phase Composition Mapping: The BREM Characterization group (I. Takeuchi and M. Kramer) was successful in getting a Program User Proposal awarded at Stanford Synchrotron Research Laboratory (SSRL), a DOE User Facility, to develop a versatile instrument for systematically carrying out micro-diffraction for high-throughput studies. The instrument will allow us to perform rapid scanning of composition using energy dispersive spectroscopy (EDS) and crystal structure using micron resolution X-ray diffraction (XRD), thus providing rapid elemental and phase mapping on a variety of thin film and bulk samples. The instrument will be able to perform moderately high temperature (up to 1200°C) annealing in a controlled environment (inert, oxidizing and vacuum) with programmable heating rates to obtain complete composition and phase analysis of a multiple sample array in a single experiment. The sample holder will be flexible so as to hold combinatorial thin film libraries and diffusion multi-couples that cover multi-component phase diagram regions. Combined with other rapid characterization methods, this instrument will allow quick navigation of phase space to search for novel compounds with enhanced magnetic properties. The next critical step will be the development of software to analyze the large amount of data obtained, enabling easy visualization and searching of the database that is generated.

In February of 2011, we carried out preliminary experiments at SSRL using a vacuum lamp heating set up, and it was verified that in situ annealing and phase mapping experiments could be performed (Fig. 8). The system studied was a ternary Fe-Co-W thin film combinatorial “library.” The library, composed of an array of discrete “tiles”, was formed by co-sputtering from separate Fe, Co, Fe-50W, and Co-50W (in at.%) sources onto a 10 cm Si/SiO₂ wafer. Most of the tile regions in the as-deposited films were amorphous material so the sample was externally annealed at 600°C. The XRD mapping showed that there were clear structural changes between samples with less than about 15%W. The low W regions were crystalline bcc-Fe (Fig. 9) and had higher magnetization and coercivity (from separate mapping experiments) than the mostly amorphous regions that were richer in W (Fig. 10). In the future, we plan to heat these samples in situ.

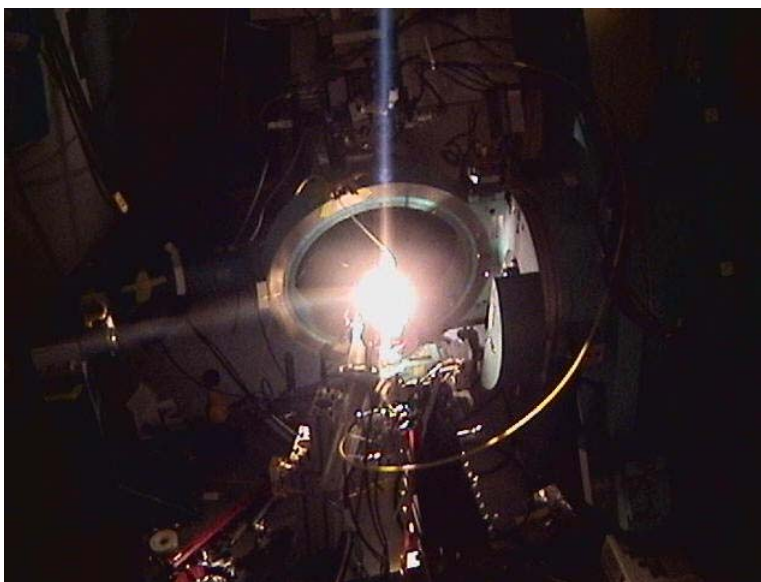


Figure 8. Photograph of prototype system in-use for high throughput chemical and structural phase mapping at SSRL.

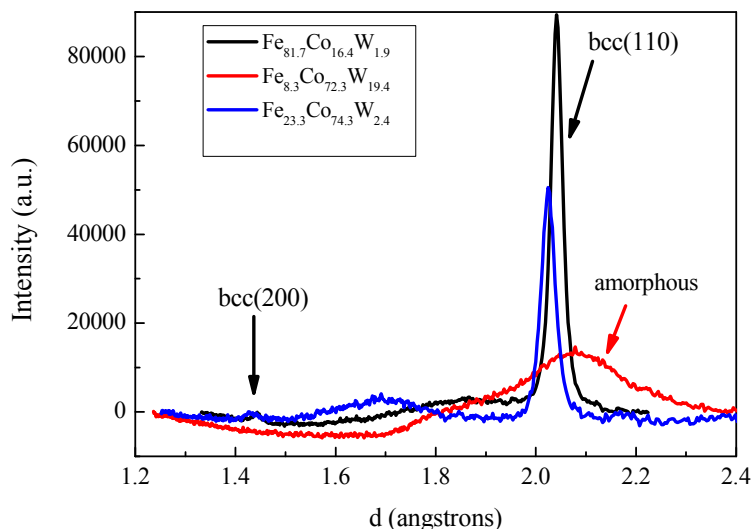


Figure 9. Portion of XRD traces from 3 tiles with different compositions in the Fe-Co-W library, providing evidence for the onset of amorphous phase formation at enriched W content.

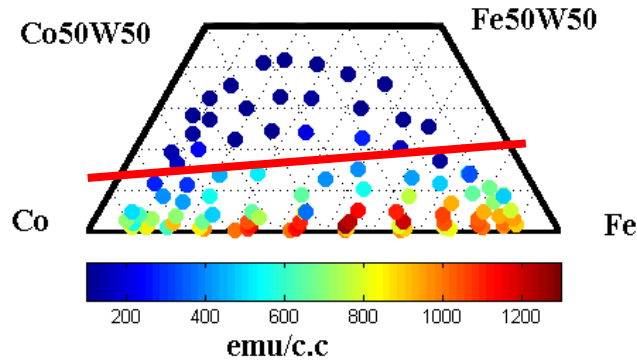


Figure 10. Magnetization measurements on the same library showing that the region of high magnetization and coercivity (not shown) is in the region of less than 15 at.% W.

Improvements to Alnico Magnets: Of the commercially viable non-RE magnets, ALNICO has the highest remanent magnetization however it is severely limited by its low coercivity. This is due to the fact that the anisotropy in ALNICO is a result of shape anisotropy of the magnetic phase, Fe-Co, and an essentially nonmagnetic phase, NiAl (Figure 11). Commercial ALNICO magnets have coercivities approaching the limit of shape anisotropy so that improvements will be dependent on our ability to add other forms of anisotropy such as surface anisotropy.

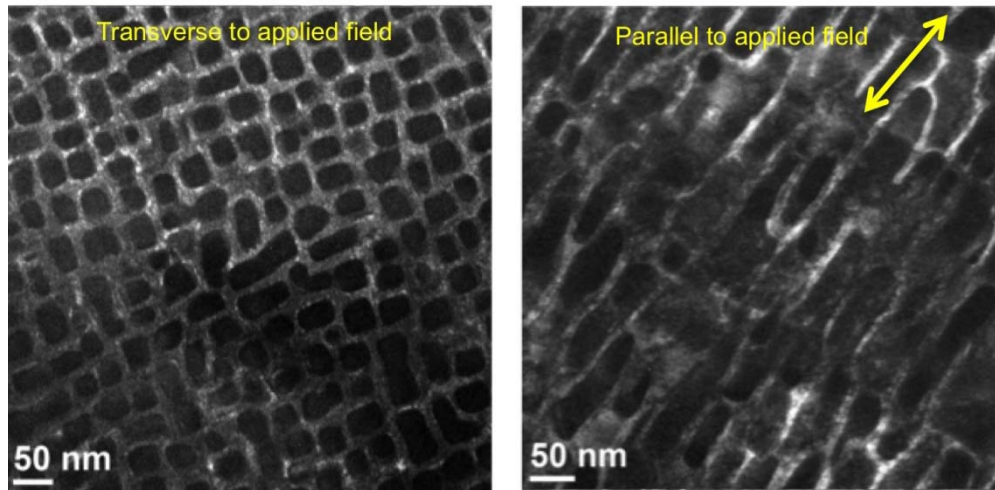


Figure 11. TEM dark field images of Arnold Alnico 5-7 magnet microstructure with Fe-Co precipitates (dark) in a NiAl matrix (light).

Using density functional theory (DFT) we have predicted that the magnetic anisotropy of Fe-Co layers at the interface of Fe-Co precipitates and the NiAl matrix phase is increased by two orders of magnitude over that of the bulk (Figure 12). This suggests that both improving the sharpness of the interface and increasing the interfacial area should lead to increasing the coercivity of the magnets. Current studies have focused on characterizing the interface structure and chemistry.

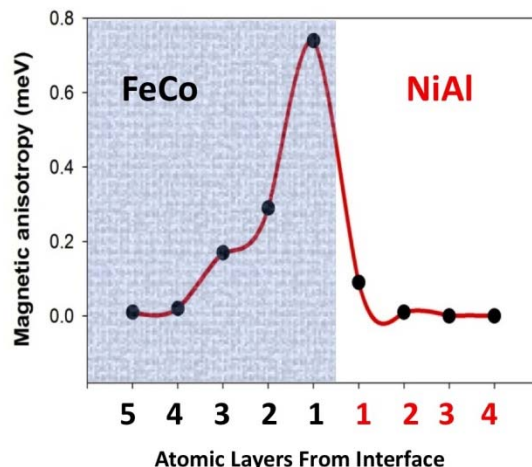


Figure 12. Density functional theory (DFT) calculations predict that anisotropy of Fe-Co layers at the Fe-Co/NiAl interface is increased by two orders of magnitude.

TEM studies of commercial ALNICO 5-7 magnets (Fig. 13) indicated that the chemical partitioning of Fe and Co in the NiAl matrix phase is far from complete, with about 30-40 at.% Fe-Co measured in this region compared to an equilibrium value of less than 10% according to the published phase diagrams. This suggests improving the sharpness of the chemical partitioning of the spinodal can greatly improve the magnetic properties. In order to refine our knowledge of the spinodal kinetics, further characterization of ALNICO alloys with various heat treatments are planned using atom probe tomography (APT).

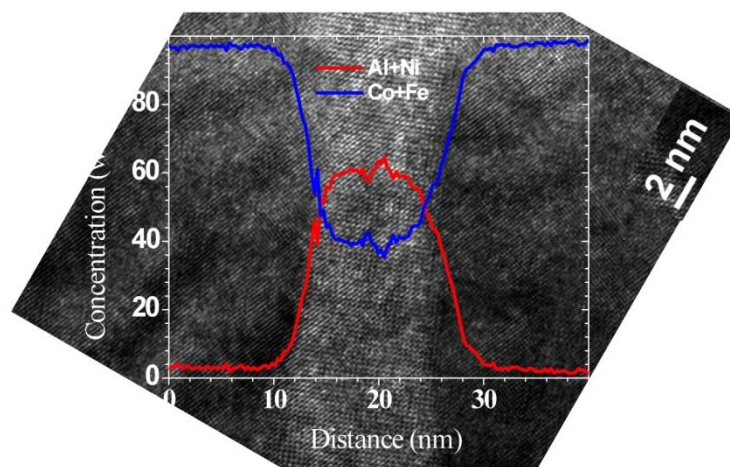


Figure 13. Representative EDS line scan (in the TEM) across the cubic NiAl interface between two bcc Fe-Co precipitates, showing concentration in at. %.

In order to increase the interfacial area, the spinodal spacing must be reduced to far less than the typical 50 nm. Theoretically, it should be possible to adjust the spinodal spacing by adjusting the heat treatment schedule for the decomposition and experimental studies are expected to verify this. Changes in the heat treatment are also expected to alter the concentration profiles of Fe and Co in the ALNICO.

Conclusions

For RE magnets, a large Dy reduction was enabled by targeted diffusion (at 900°C) of DyF₃ “paint” to the interior microstructure in anisotropic sintered MRE_{2.5}(Fe, Co)₁₄B magnets. This work achieved an energy product, (BH)_{max}, of 31.4 MGOe and a coercivity, H_{ci}, of 15 kOe, both at ambient temperature, and a temperature coefficient of H_{ci}, β, of -0.5%/°C. These magnetic properties are all equivalent to commercial Nd-based Nd₂Fe₁₄B magnets that are used in drive motors for 200°C operation, containing 8-10% Dy. Our diffusion method for targeted enhancement of Dy additions used only 5.3wt.% Dy or about 45% less Dy, which could enable a large magnet cost decrease. In development of particulate for anisotropic bonded MRE_{2.2}Fe₁₄B_{1.1} magnets without Dy, highly aligned columnar solidification patterns resulted from a novel Ag micro-alloying (<1at.%Ag) effect. A strong and unique texture was achieved in these ribbon samples. In a demonstration of the concept, mild crushing produced an anisotropic particulate that was bonded with epoxy and tested, but further microstructure scale refinement and texture design is needed before such magnets that can achieve suitable coercivity levels.

In our search for non-RE permanent magnets, a genetic algorithm (GA) method was adapted to enable computational phase diagram exploration for alloys based on Fe-Co, speeding up by at least 1000 times the search for candidate chemical compositions with desirable structures and properties. Using only a shared computer cluster at Ames, an initial structure search of Fe-Co alloys successfully predicted structures at a specific range of compositions that have energies lower (more favorable) than those proposed in the literature, but further GA searching of Fe-Co-X systems for enhanced crystalline anisotropy will require the increased capabilities of a dedicated cluster and DOE supercomputer facilities, e.g., at ORNL. As an experimental tool for rapid structural analysis in our “beyond RE magnets” (BREM) thrust, a multiple sample staging system was developed at the DOE synchrotron X-ray source at Stanford Synchrotron Research Laboratory and demonstrated by characterization of thin film samples from a Fe-Co-W combinatorial “library” of compositions. It was determined that an upper W content of about 15 at.% exists in this system for the onset of dominant amorphous phase formation.

For improvement of existing Alnico magnets, a series of density functional theory (DFT) calculations predicted that the magnetic anisotropy of Fe-Co layers at the interface of Fe-Co precipitates and the NiAl matrix phase is increased by two orders of magnitude. These results indicated that a significant coercivity benefit could result from reducing the spinodal spacing to far less than the typical 50 nm. TEM studies of commercial Alnico 5-7 magnets indicated that the chemical partitioning of Fe and Co in the NiAl matrix phase is far from complete, with about 30-40 at.% Fe-Co measured in this region, suggesting a further direction for microstructure improvement that can benefit the magnetic properties.

Publications

1. W. Tang, Y. Q. Wu, N. T. Oster, K. W. Dennis, M. J. Kramer, I. E. Anderson, and R. W. McCallum, *Improved energy product in grained aligned and sintered MRE₂Fe₁₄B magnets MRE=Y+Dy+Nd*, *J. Appl. Phys.*, 107, 09A728 (2010).
2. R. Skomski, V. Sharma, B. Balamurugan, J. E. Shield, A. Kashyap, and D. J. Sellmyer, *Anisotropy of Doped Transition-Metal Magnets*, Proc. REPM'10, Eds.: S. Kobe and P. McGuinness, Jozef Stefan Institute, Ljubljana, pp. 55-60, 2010.
3. P. Manchanda, P. Kumar, V. Sharma, A. Kashyap, R. Skomski, and D. J. Sellmyer, *Proximity Moment and Anisotropy in Fe-Rich Thin Films*, Proc. REPM'10, Eds.: S. Kobe and P. McGuinness, Jozef Stefan Institute, Ljubljana, pp. 157-160, 2010.
4. V. Sharma, P. Manchanda, R. Skomski, D.J. Sellmyer, and A. Kashyap, *Anisotropy of Heavy Transition Metal Dopants in Co*, *J. Appl. Phys.* **109**, 07A727 (1-3) (2011).

5. Kashyap, R. Skomski, P. Manchanda, J.E. Shield, and D.J. Sellmyer, *Layered Transition-Metal Permanent-Magnet Structures*, J. Appl. Phys. **109**, 07A714 (1-3) (2011).
6. R. Skomski, A. Kashyap, A. Enders, *Is the Magnetic Anisotropy Proportional to the Orbital Moment?*, J. Appl. Phys. **109**, 07E143 (2011).

References

1. D. Dadon, Y. Gefen, and M. Dariel, "The texture of melt spun Fe₇₆Nd₁₆B₈ ribbons," *Magnetics, IEEE Transactions on*, vol. 23, pp. 3605-3606, 1987.
2. M. J. Kramer, N. Yang, R. W. McCallum, K. W. Dennis, and L. H. Lewis, "In situ determination of Nd-Fe-B crystallization pathways," *J. Appl. Physics*, vol. 91, pp. 8156-8158, 2002.
3. M. J. Kramer, L. H. Lewis, L. M. Fabietti et al., "Solidification, microstructural refinement and magnetism in Nd₂Fe₁₄B," *Journal of Magnetism and Magnetic Materials* **241** (1), 144-155 (2002).

Patents

1. R. W. McCallum, Y-W. Xu, I. E. Anderson, K. W. Dennis, and M. J. Kramer, U.S. Patent Application (PCT) filed November 18, 2002, "Permanent Magnet Alloy with Improved High Temperature Performance," under examination.

3.5 Scalable, Low-Cost, High Performance IPM Motor for Hybrid Vehicles

Principal Investigator: Ayman EL-Refaie

General Electric Global Research Center

1 Research Circle.

Niskayuna, NY 12309

Voice: 518-387-6660; Fax: 518-387-6675; E-mail: elrefaie@research.ge.com

Materials Tasks Leader: Francis Johnson

General Electric Global Research Center

1 Research Circle.

Niskayuna, NY 12309

Voice: 518-387- 5087; Fax: 518-387-6232; E-mail: johnsonf@research.ge.com

DOE Technology Development Manager: Susan A. Rogers

Voice: 202-586-8997; Fax: 202-586-1600; E-mail: Susan.Rogers@ee.doe.gov

GE Program Manager: Ayman EL-Refaie

Voice: 518-387-6660; Fax: 518-387-6675; E-mail: elrefaie@research.ge.com

Objectives

Electric drive systems, which include electric machines and power electronics, are a key enabling technology for advanced vehicle propulsion systems that reduce the petroleum dependence of the transportation sector. To have significant effect, electric drive technologies must be economical in terms of cost, weight, and size while meeting performance and reliability expectations.

The objective of the GE Global Research “Scalable Low-Cost, High-Performance IPM Motor for Hybrid Vehicles” program is to develop a higher power density IPM motor at a lower cost. Successful completion of this program will accelerate the introduction of hybrid electric vehicles into the U.S. road vehicle fleet and bring the added benefits of reduced fuel consumption and environmental impacts.

(A) Motor Development

- Develop advanced motor concepts including electromagnetic, mechanical, and thermal concepts.
- Build proof-of-principle machines to verify the design process as well retire the key risks.
- Design and build 55kW/30kW machines that meet the DoE specifications
- Develop cost model to estimate the advanced IPM motor based on 100000 units/year
- Investigate the scalability of the developed concepts by building and testing a 120kW/65kW machine

(B) Materials Development

- Demonstrate scalable processing of high resistivity permanent magnet and determine cost advantage

Approach

(A) Motor Development

- Simplified stator windings will reduce end-turn length and losses, together with motor mass and volume and manufacturing cost.
- Advanced rotor concepts to achieve higher power density as well as meeting the high-speed requirement.

- Advanced scalable thermal management schemes for both the stator and the rotor to meet the required set of specifications.

(B) Materials Development

- Scale-up to kilogram scale of high resistivity permanent magnets at domestic permanent magnet producer.

Major Accomplishments**(A) Motor Development**

- 2 rotor & 2 stator EM concepts developed & analyzed in detail
- Scalable rotor and stator cooling concepts selected to meet performance, simplicity and scalability requirements
- Highest-performance EM concepts selected for proof-of-principle motors build.
- First proof-of-principle motor built and fully tested
- Second proof-of-principle machine (different rotor structure) is built and fully tested
- Third and final 30kW/55kWpk machine built and fully tested
- DoE to witness the testing on November 2011
- Development of cost model is almost finalized (fine tuning is still needed)

(B) Materials Development

- Achieved kilogram scale production of $\text{Nd}_{15}\text{Fe}_{77}\text{B}$ permanent magnet powder for scaled processing
- Identified insulating layer compositions whose densification behavior approaches that of NdFeB with minimal reaction with NdFeB

Future Direction**(A) Motor Development**

- Finish the building and testing of the third 30/55 kW machine
- Verification testing to be witnessed by the DoE

(B) Materials Development

- Tune sintering behavior of insulation phase to match NdFeB
- Identify insulating phase composition with lowest raw material costs
- Demonstrate kg scale production of high-resistivity magnet at external vendor

Technical Discussion**(A) Motor Development**

After building and fully-testing the two proof-of-principle (PoP) motors, one of them was down-selected for further development. The test setup has to be upgraded to be able to test the motor with 105°C coolant inlet temperature including chillers that control the temperature of EWG and transmission fluid at 105°C as well as special flow meters. The updated test setup is shown in Fig.1. Table I summarizes the key test equipment and their key features.

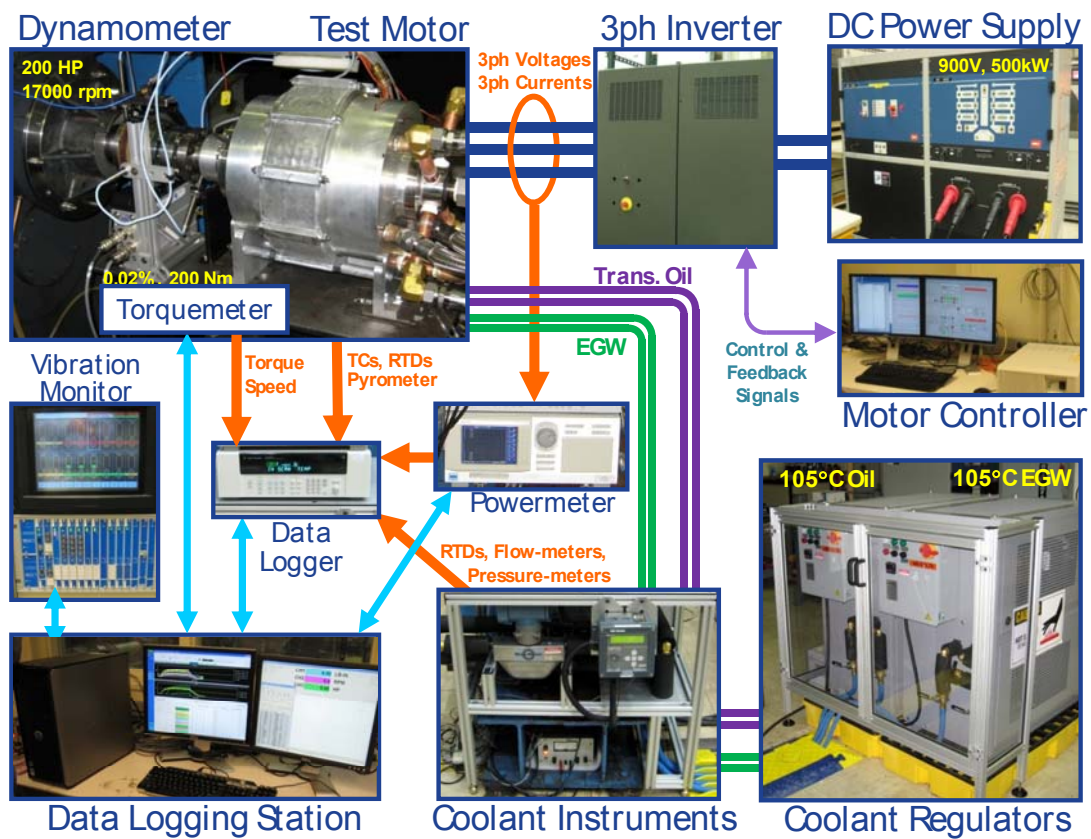


Fig. 1. Upgraded test setup to be able to test the motor at 105oC coolant inlet temperature

Table I: List of key test equipment and their key features

| Items | Equipment | Features/ Details |
|---|---|--|
| Dynamometer | 200HP GE DC motor & drive Step-up gear box (6.43x) | <ul style="list-style-type: none"> • Speed & torque regulation • Over torque / Over speed |
| Inverter | Custom IGBT inverter | <ul style="list-style-type: none"> • Short circuit protection • Over voltage protection brake |
| Controller | dSPACE control platform | <ul style="list-style-type: none"> • Over speed protection • Over current protection |
| Data Acquisition & Monitoring System | Agilent 34980A | <ul style="list-style-type: none"> • Motor Thermal Monitoring > 40 TCs Rotor temperature using pyrometry • Coolant Monitoring (EGW & Oil) 5 TCs for Calorimetry 2 Flowmeters 5 Pressure transducers |
| Electric Power Measurement | Yokogawa WT1600 | <ul style="list-style-type: none"> • 0.1% Accuracy |
| Mechanical Power Measurement | HBM T12 | <ul style="list-style-type: none"> • 0.02% Accuracy |
| Vibration Monitoring | Bently Nevada | <ul style="list-style-type: none"> • Excessive vibration protection |

The third and final motor is shown in Fig. 3 while the back emf at 100°C and 1000 rpm is shown in Fig. 4. Third machine has been optimized to meet the 35kg mass requirement as well as the 105°C coolant inlet temperatures. Machine back emf closely matches predictions. Table II summarizes the machine's measured performance vs. specifications. It can be seen that the motor meets many of the key challenging specifications.

The machine efficiency map is shown in Fig. 5 while the power factor map is shown in Fig. 6. It can be seen that the machine has a very high efficiency over a wide range of operation. Fig. 7 shows the machine measured torque at 1 rpm and 60°C. It can be seen that the peak-peak torque ripple is ~4.2% which is less than the 5% requirement.

Fig. 8 shows the measured peak power at various temperatures while Fig. 9 shows the measured temperatures during 20 seconds of peak power. Both figures show that the motor meets the peak power requirement without exceeding the thermal limit.

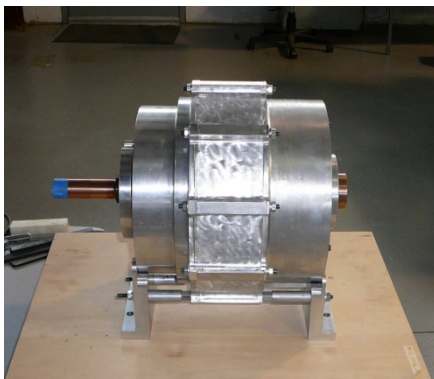


Fig.3 Third machine optimized to meet 35 Kg and 105°C coolant inlet temperature

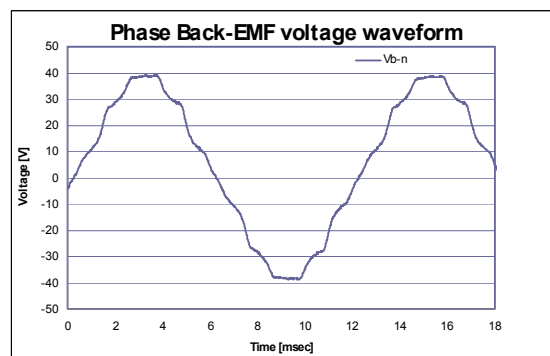
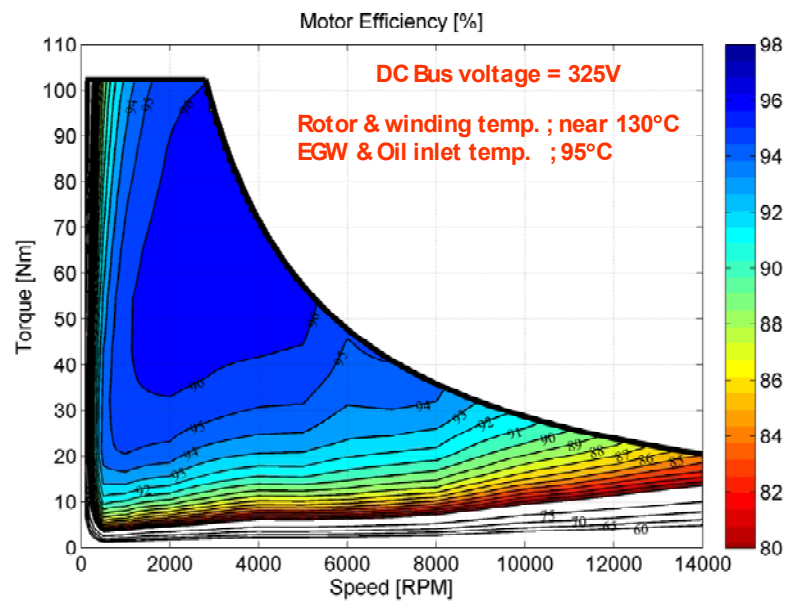


Fig. 4 Third machine back emf at 100°C and 1000 rpm

Table II: Comparison of machine measured performance vs. specifications

| Items | Specification | Status and Result |
|---|--|--|
| Max. Speed | 14,000rpm | Verified |
| Peak Power | 55kW @20% speed for 18sec | 57.2 kW @2800rpm @30°C 54.2 kW @2800rpm @105°C (20 sec verified) |
| Maximum Current | 400Arms | Verified |
| Cont. Power | 30kW @20~100% speed @Vdc=325 | Verified (95°C coolant inlet temperature) |
| Efficiency | >95% @10~100% speed @20% rated torque | > 94% @10~20% speed > 90% @~ 9000 rpm > 85% @~ 14000 rpm |
| Operating Voltage | 200~450V (325V nominal) | 325V and 450V operation verified 200V test pending |
| Back EMF | <600Vpk line-to-line @100% speed | < 950Vpk line-to-line @14000 rpm |
| Torque Pulsation | <5% of Peak Torque @any speed | 4.2% of Peak Torque @rated torque 1 rpm |
| Characteristic Current | < Maximum Current | 185Arms |
| Weight | ≤35kg | Refer to slides covering weights and volumes |
| Volume | ≤9.7L | Refer to slides covering weights and volumes |
| Cost @100k | ≤\$275 | Refer to slide covering cost estimate |
| Ambient (outside housing) Operating Temperature | -40~140°C | Pending (expected not to be a challenge) |
| Coolant inlet | 105°C, <10LPM, 2psi drop, <20psi inlet | EGW ; 95°C, 10LPM, 3psi Transmission oil ; 95°C, 6LPM, 7psi (By lowering the flow rate, 2 psi expected to be met. Additional tests planned to quantify this) |
| Minimum isolation impedance-phase terminal to GND | 1Mohm | >100Gohm @500V |

**Fig. 5 Third machine efficiency map**

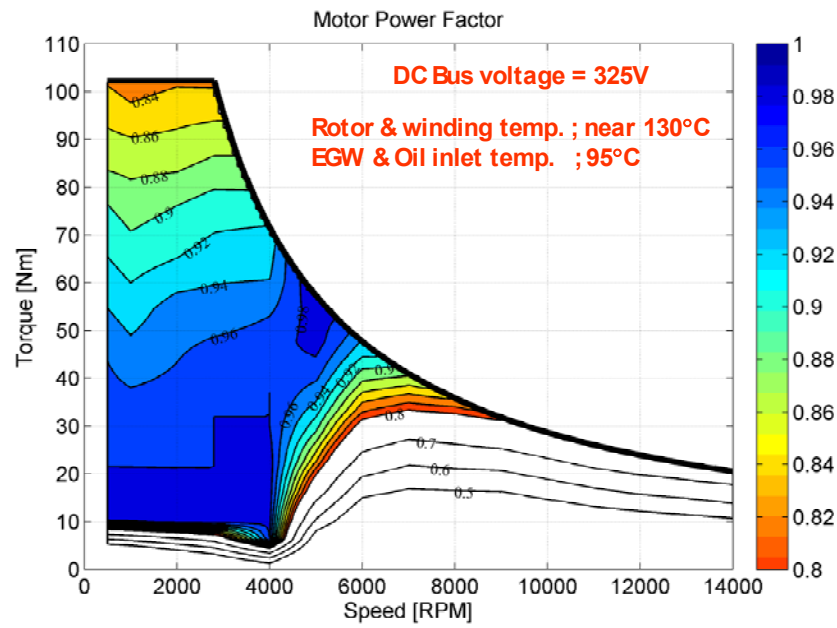


Fig. 6 Third machine power factor map

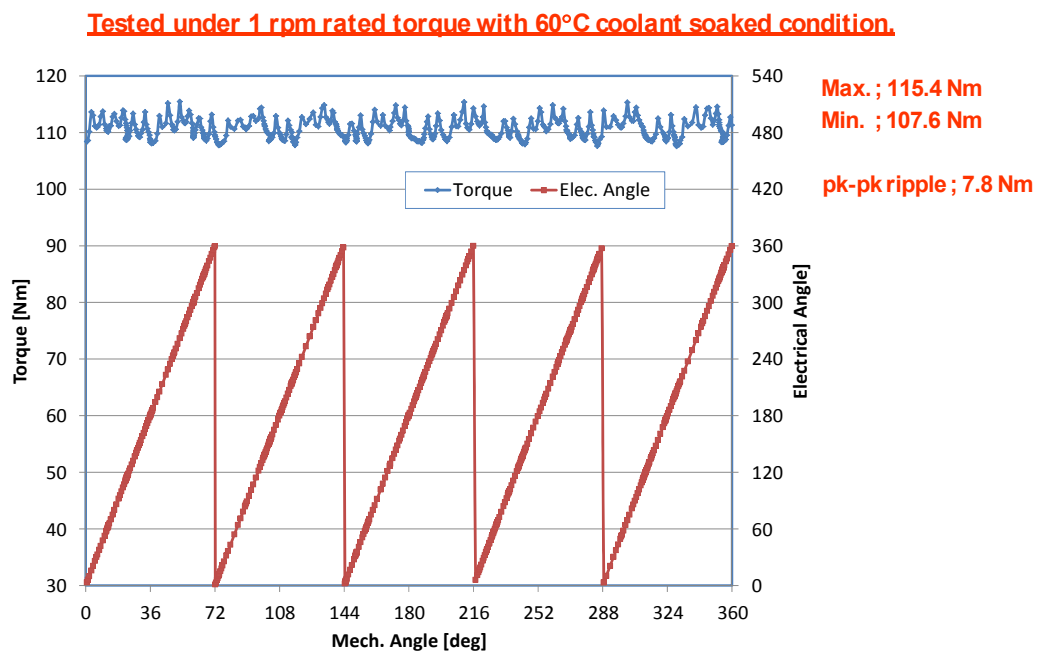


Fig. 7 Third machine measured torque ripple

| Test Data | | | | | | | | | | | |
|-------------|---------------|-------------|--------------|---------|-----------|---------|------------|------------|-----------|-------|-----------|
| Motor Temp. | Coolant Temp. | Speed [RPM] | Torque [N-m] | Pm [kW] | Pmot [kW] | Eff [%] | Vph [Vrms] | Vll [Vrms] | Iph [Ams] | PF | Loss [kW] |
| 30°C | 25°C | 2800 | 195.2 | 57.24 | 63.06 | 90.8 | 111.6 | 193.3 | 404.0 | 0.466 | 5.82 |
| 95°C | 95°C | 2800 | 185.3 | 54.33 | 60.75 | 89.4 | 109.7 | 190.0 | 404.0 | 0.457 | 6.41 |
| 105°C | 95°C | 2800 | 184.8 | 54.19 | 60.80 | 89.1 | 111.5 | 193.1 | 404.0 | 0.450 | 6.61 |

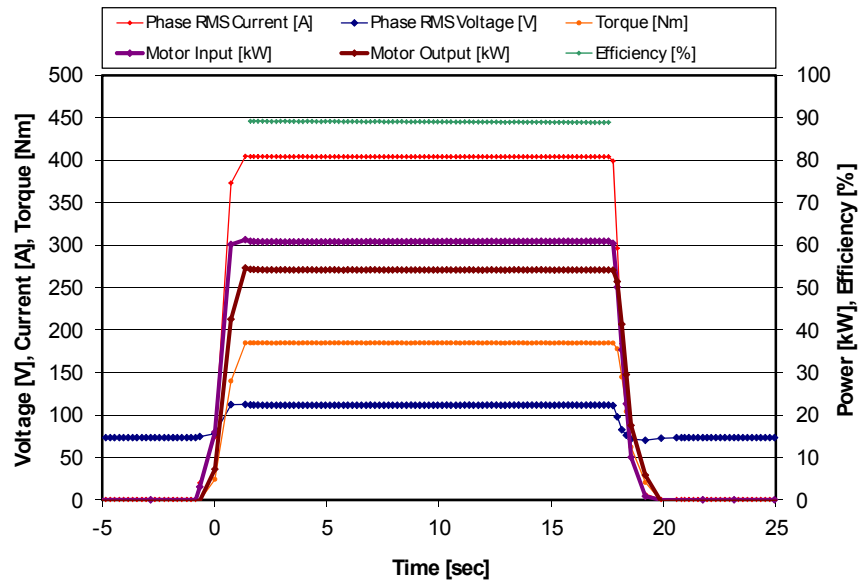


Fig. 8 Third machine measured peak power

Peak Power applied for 20 sec at 2800 rpm with 95C coolant.

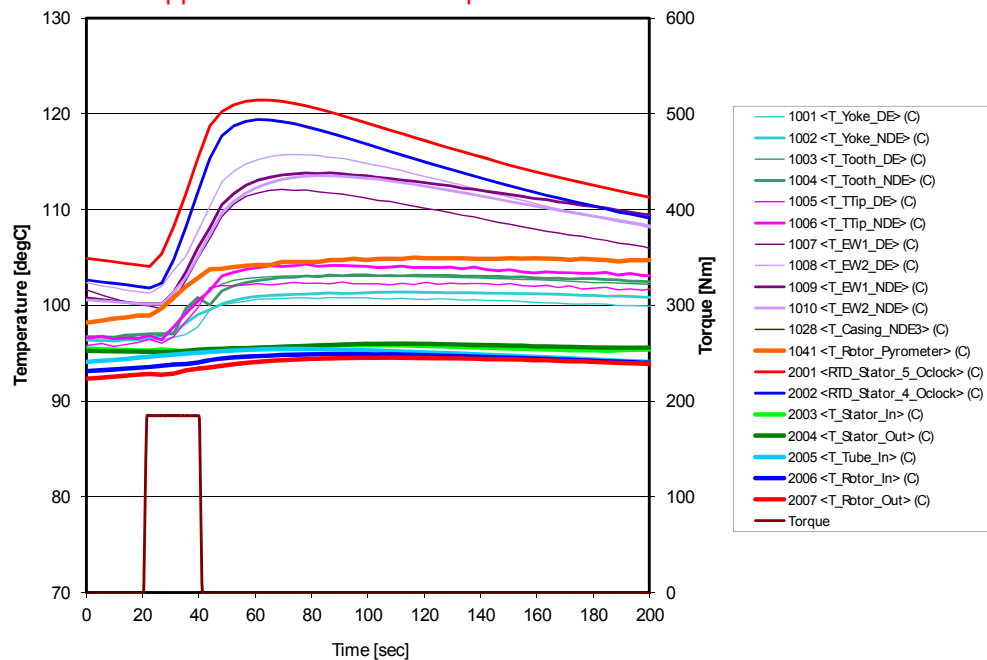


Fig. 9 Third machine measured temperature during peak power

Fig. 10 shows the measured machine performance during heat runs at 30 kW. Fig.11 shows the temperature rise in various parts of the machine at various speeds during heat runs. Fig. 12 shows the measured temperature during a heat run at 30 kW and 2800 rpm while Fig. 13 shows the corresponding results at 14000 rpm. All these results confirm that the machine is capable of producing a 30 kW continuous power at 105°C over the entire speed range without exceeding the thermal limit of 180°C.

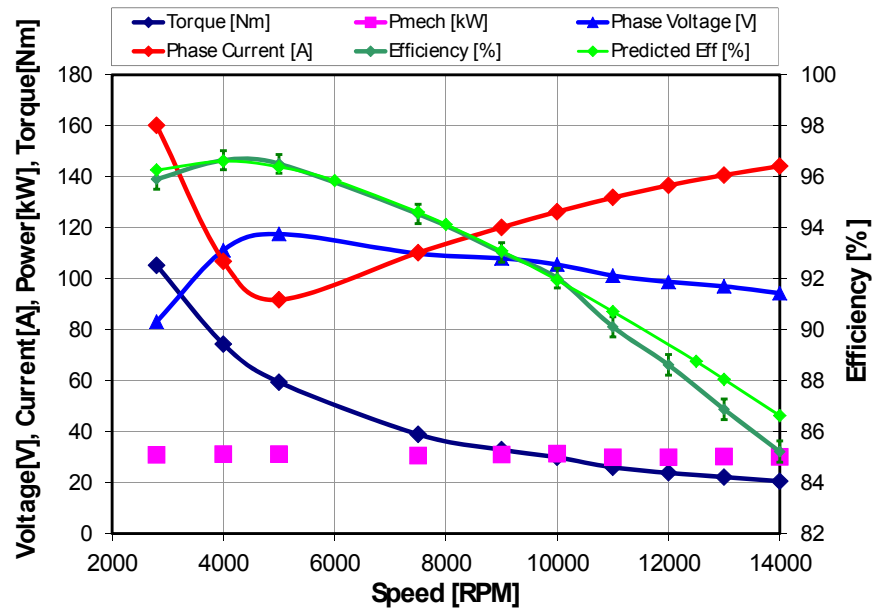


Fig. 10 Third machine measured performance during heat runs

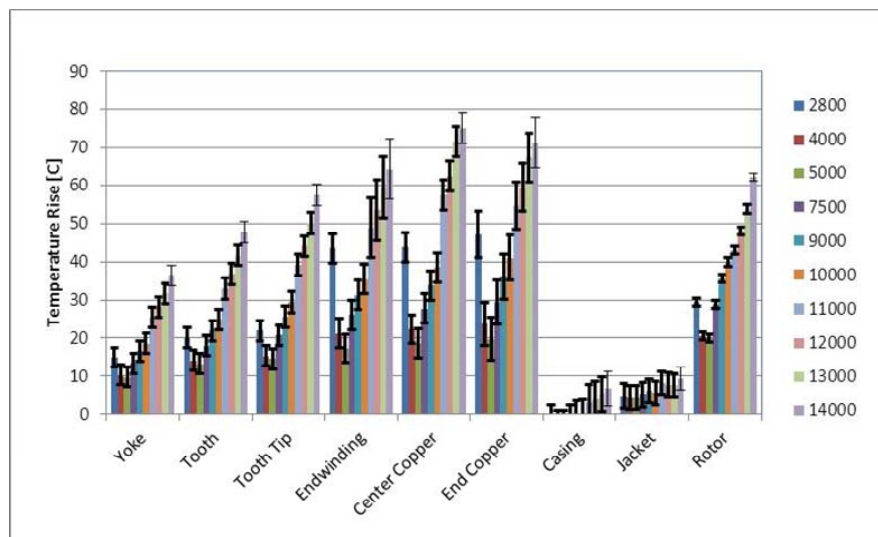


Fig. 11 Third machine measured temperature rises at 30kW at various speeds

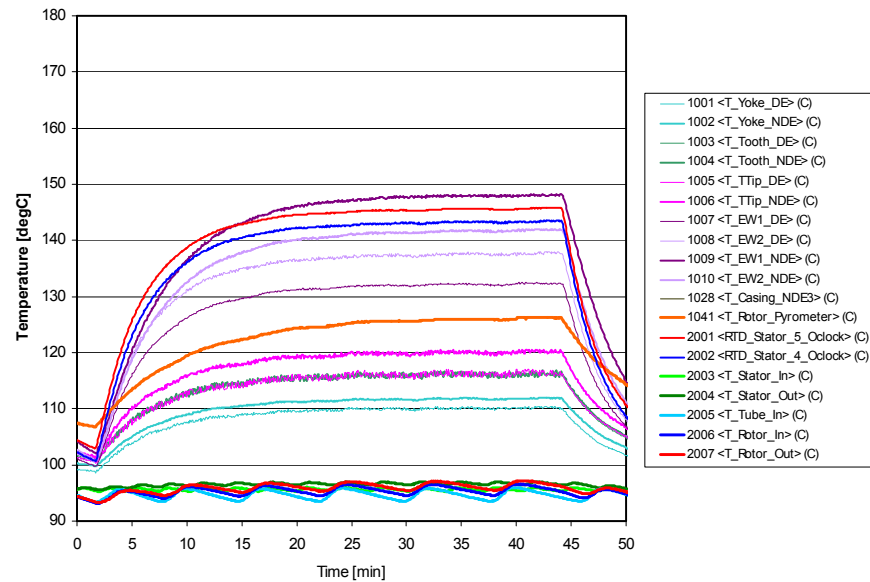


Fig. 12 Third machine measured temperatures during heat run at 30 kW and 2800 rpm

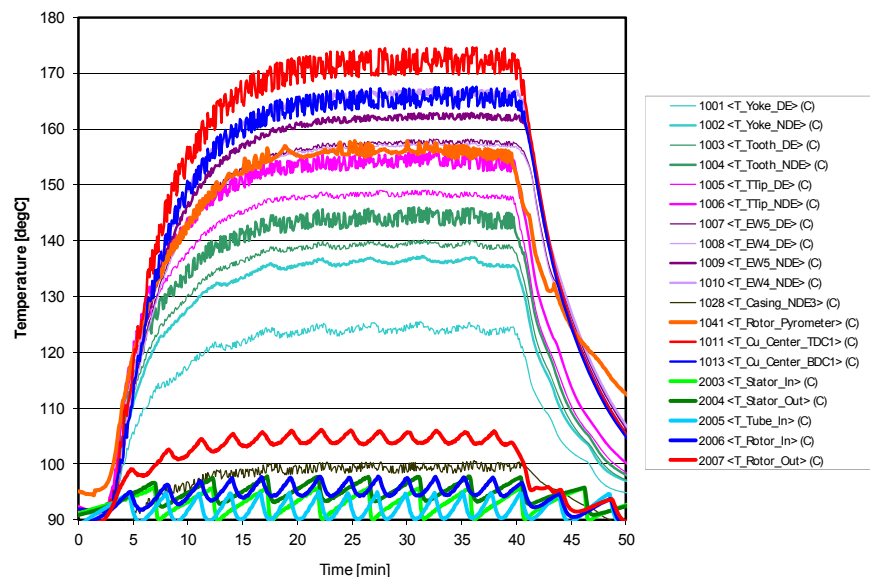


Fig. 13 Third machine measured temperatures during heat run at 30 kW and 14000 rpm

(B) Materials Development

High resistivity magnet microstructure

Multiphase layered composite permanent magnets have been developed that display an effective resistivity 3X that of sintered NdFeB (the resistivity of sintered NdFeB is $150 \mu\Omega\text{-cm}$). Magnet loss reduction is achieved by the insulating phase in the composite impeding the flow of eddy currents in the magnet structure. The insulating phase is introduced into the composite structure by co-sintering with NdFeB magnet powder, enabling a manufacturing cost reduction by avoiding the need for machining and assembling segmented permanent magnets.

Magnet powder production

In the previous year a baseline composition of $\text{Nd}_{15}\text{Fe}_{77}\text{B}_8$ (atomic %) was chosen as the magnet powder for developing the high resistivity magnet compositions. This composition is well known and is in the public domain (Harris et al, 1985). Its physical properties and processing behavior are similar to high performance NdFeB compositions that are proprietary to permanent magnet producers. Pilot production of several kilograms of precursor material, with particle sizes from 1 to 3 μm was performed at GE Global Research. This material was used for scaled processing of high resistivity composite NdFeB magnets both at an external vendor (Electron Energy Corporation) and within GE Global Research.

Insulating phase development

Screening of candidate compositions for the insulating phase considers several factors, including:

- 1) Electrical resistivity of at least 2000 times that of NdFeB
- 2) Raw material cost comparable to NdFeB
- 3) Densification rate during sintering matched to NdFeB
- 4) Not infiltrated/completely de-oxidized through reaction with NdFeB
- 5) CTE match with NdFeB when cooling from the sintering process

These criteria enabled the selection of a set of insulating phase mixtures whose sintering behavior could be tuned to match that of NdFeB. The densification behavior was systematically explored using dilatometry and sintering trials. The electrical behavior was verified using four point probe resistance measurements and the microstructure was probed with scanning electron microscopy. 33 insulating phase compositions were screened with variation of composition, volume fraction ratios, and powder processing conditions. A mixture of oxides and fluorides that was ball milled, freeze granulated, and calcined was found to have densification behavior close to NdFeB. Since the match is not exact vertical cracks appear in the interlayers as stress is relieved during densification. Fig. 14 shows the microstructure of a permanent magnet with an insulating insulator sintered between two layers of NdFeB. Despite the presence of cracks these interlayers were shown to be capable of electrically isolating the NdFeB layers.

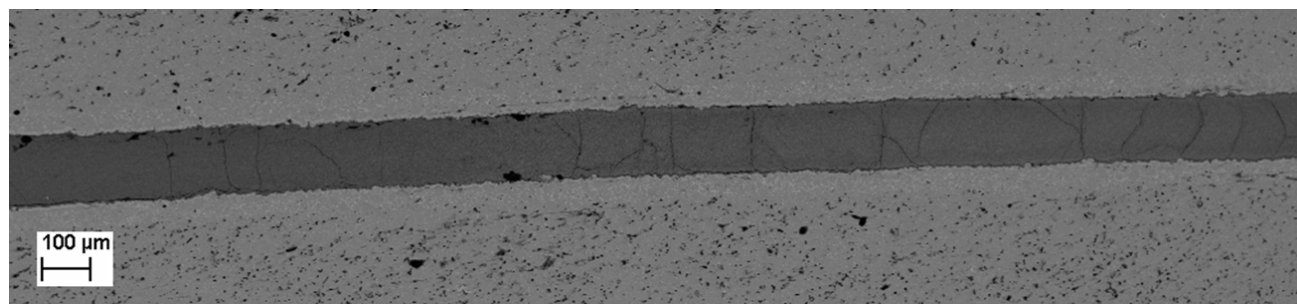


Fig. 14. Insulating interlayer (dark region) between two layers of sintered NdFeB permanent magnet material.

Scaled processing of high resistivity permanent magnets

A purchase order was issued to an external vendor to manufacture aligned and sintered magnets in a multilayer structure to specification provided by GE and with raw materials provided by GE. Two lots of NdFeB powder, cast and milled at GE, and two lots of insulating material, were provided by GE to the vendor.

The vendor processed a total of 1 kilogram of material as 10 magnets of 100 gram mass each. Fig. 15 displays a Demagnetization curve on the material after sintering and annealing. The vendor was able to produce a fully dense and aligned magnet. The energy product was less than expected due to a lower than expected value of intrinsic coercivity. The source of the lower than expected coercivity is believed to be caused by variability in composition and particle size of the magnet powder produced by the small scale

process used to produce it. Commercially produced powder produced by conventional jet-milling processes will have the ability needed to achieve higher energy products. Commercial powder was not used in this effort as it was not found to be available in lot sizes less than several hundred kilograms.

The multilayer magnets produced by the vendor demonstrated that the sintering and alignment procedures can be used in kilogram scale production. However, waviness of the insulating interlayer was observed, as well as electrical shorting across the layer. This indicated that the die filling and loading procedure required more development to improve the yield of electrically insulating magnets. Rather than continue work at the vendor it was decided to refine these procedures at GE Global Research

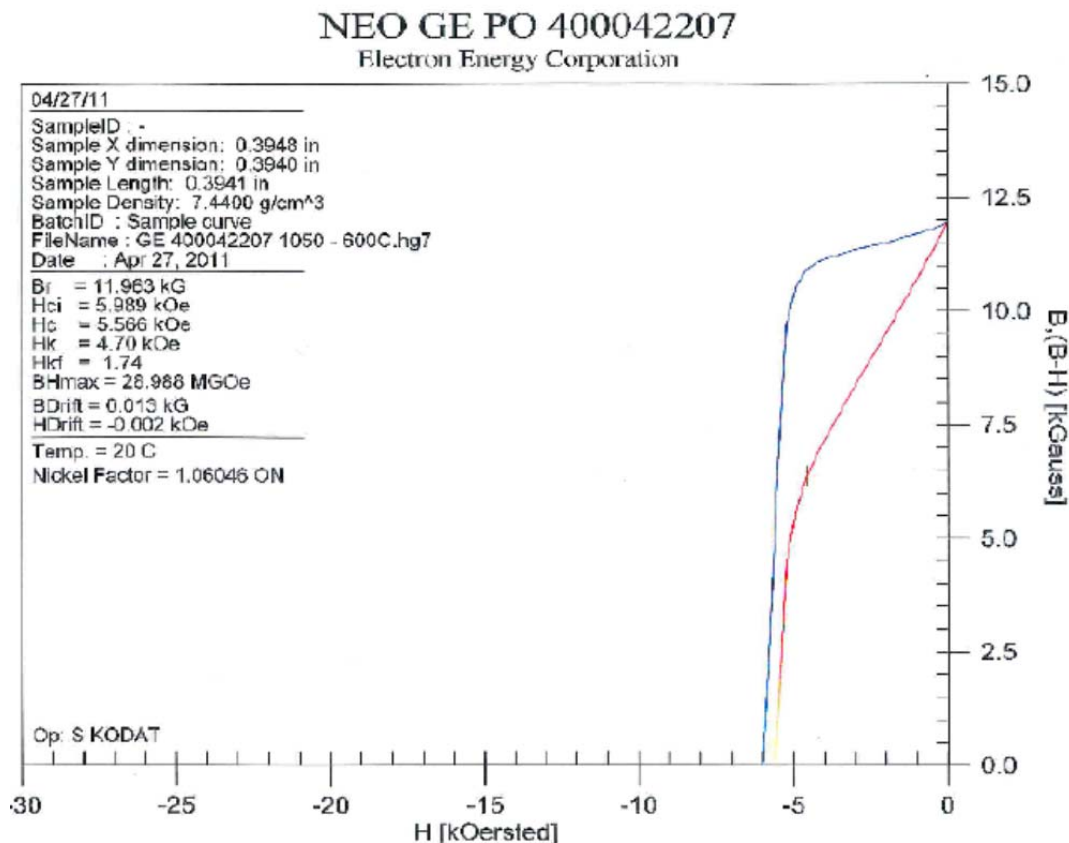


Fig.15. Demagnetization curve of NdFeB magnet composition provided by GE and aligned and sintered at the external vendor. A lower than expected coercivity led to a lower than desired energy product. Fig. 16 shows a 20 gram multilayer magnet produced at GE Global Research. Unaligned magnets were initially attempted to simplify processing. An improved die filling and loading procedure has improved the uniformity and decreased the waviness of the insulating interlayers. Interlayer shorting was still observed but yield was improved compared to the magnets produced at the external vendor.

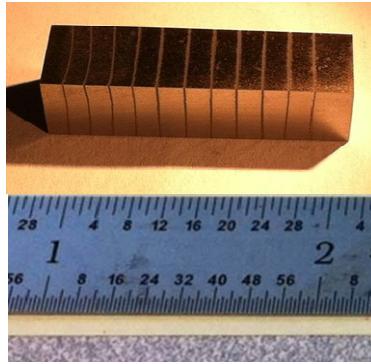


Fig. 16. 20 gram multilayer NdFeB magnet. The sample was unaligned and fully sintered.

Fig. shows a set of 100 gram unaligned multilayer magnets produced at GE Global Research. The interlayer spacing was set to yield the increased effective resistivity specified for the motor designed in this project. Fig. shows 100 gram multilayer magnets that are aligned and sintered. Cracks were observed in one face of the sintered magnets due to differential cooling. Fig. is a demagnetization curve measured on aligned and sintered material produced at GE. The energy product and coercivity are similar to those produced at an external vendor.

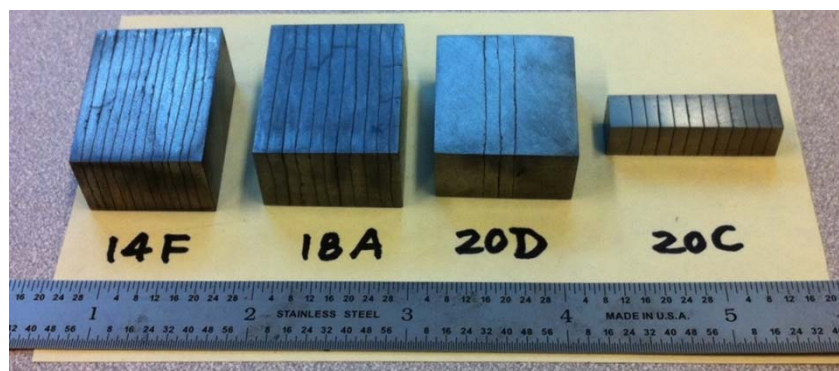


Fig. 17. Left three magnets are 100 gram unaligned, sintered multilayer magnets processed at GE Global Research. The right magnet is a 20 gram sample similar to that presented in Fig. .

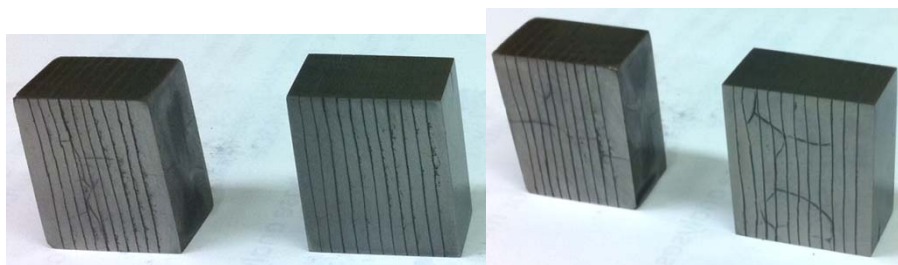


Fig. 18. Aligned, uncoated magnets with cracks in one side

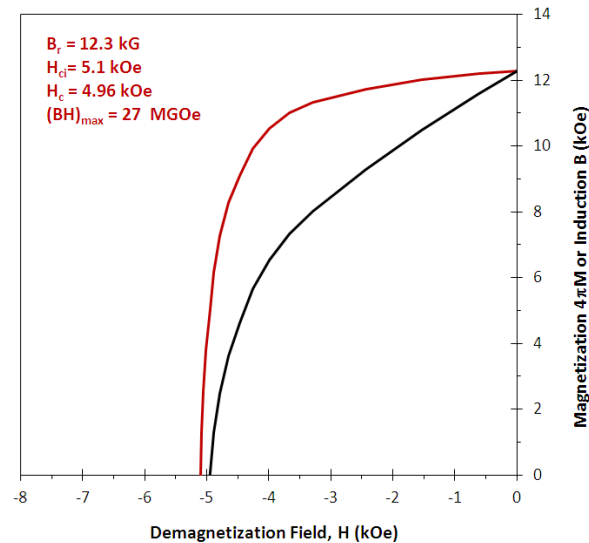


Fig. 19. Demagnetization curve of aligned and sintered NdFeB magnets processed at GE Global Research

The aligned and sintered, multilayer magnets were found to have several issues that must be solved in follow-on work that would bring these magnets into production at a cost lower than segmented magnets:

1. Low yield of insulating layer resistivity. Presently only 20-30% of the interlayers are measured to be fully insulating. Further development in die loading procedures, particularly aimed at preventing “smearing” of the layers at the die wall, should mitigate this effect.
2. The powder handling device must be engineered to fill the magnet dies with two powders
3. Magnet cracking is a known issue faced by conventionally magnet sintering and can be mitigated by refined temperature control during the sintering process
4. Delamination of the multilayer magnets was observed after exposure to air for time periods greater than four weeks. The cause was traced to absorption of humidity by the insulating material. Coating of the multilayer magnets with the same anticorrosion coatings presently used in production NdFeB magnets should mitigate this issue.
5. Magnet machining and grinding must be performed with non-aqueous lubricants as the interlayer compounds may be hygroscopic.

The raw material cost of the insulating interlayer material was estimated to be \$75/kg as of the end of 2010, comparable to the Dy-containing high temperature magnet compositions being used in these motor applications. It should be noted that the recent fluctuations in the cost of rare earth elements makes it very difficult to estimate future raw material prices. Estimation of the processing cost is difficult due to the uncertainties regarding the die loading procedure needed to incorporate the insulating interlayers into the magnet. Additionally, the need to machine the sintered multilayer magnets in non-aqueous lubricants is a departure from conventional magnets processing techniques and may increase processing cost.

Conclusion

Motor Development

- Significant progress made since last year
- Two advanced proof-of-principle machines were built. Both were fully tested
- Major risks including spinning the novel rotor concept at 14000 rpm have been retired
- Test results closely match predictions. This provides confidence in design process

- Alternate rotor materials identified to enhance thermal management and efficiency capabilities of the final 30kW/55kWpk machine
- Final 55kWpk/30kW machine designed and built and fully tested
- More than 12 US patent applications filed to date

Materials

- A multiphase permanent magnet microstructure has been developed that exhibits high effective resistivity by component magnetic and insulating phases in a multilayer geometry.
- Insulating phases with densification behaviors approaching that of NdFeB have been identified and laboratory scale multilayer magnets have been produced.
- Kilogram scale production of NdFeB powder has been achieved to support scaled magnet synthesis at a domestic permanent magnet producer
- Multiple sintered high resistivity magnets of ≈ 100 gram mass have been produced. The best attainable yield of insulating interlayers is presently 20-30%.
- Delamination of interlayers can be avoided by coating the sintered magnets with the same anticorrosive coatings used in production magnets as well as by machining the magnets in a non-aqueous lubricant such as mineral oil.
- Maximum achieved energy product is 27 MGOe due to insufficient control of composition and grain size distribution resulting in low coercivity.
- Yield and coercivity can be improved with further process optimization.
- The raw material cost of the multilayer magnets is comparable to the Dy-containing NdFeB compositions presently used in high performance motors.
- Processing cost estimates are uncertain due to further development needed in the die loading and filling procedure needed to increase the yield insulating interlayers beyond 30%.

Publications

1. William D. Gerstler, Eric J. Ruggiero, Farshad Ghasripoor, Ayman El-Refaie, H. Peter De Bock, Xiaochun Shen and James P. Alexander, “ A Liquid-Cooled Rotor for High Density Electric Machines”, 47th AIAA/ASME/SAE/ASEE Joint Propulsion Conference & Exhibit, 31 Jul - 3 Aug 2011, San Diego, CA
2. Patel Reddy, A.M. El-Refaie , kum-Kang Huh, Jagadeesh Tangudu, and Thomas Jahns “Comparison of Interior and Surface PM Machines Equipped with Fractional-Slot Concentrated-Windings for Hybrid Traction Applications”, 2011 IEEE Energy Conversion Congress and Exposition ECCE 2011, September 17-22, Phoenix, AZ, USA
3. Patel Reddy, A.M. El-Refaie, kum-Kang Huh, “Effect of Number of Layers on Performance of Fractional-Slot Concentrated-Windings Interior Permanent Magnet Machines”, 2011 IEEE 8th International Conference on Power Electronics ECCE Asia ,May 30-June 3, 2011,Jeju, Korea
4. A.M. El-Refaie, “Motors/Generators for Traction/Propulsion Applications”, 2011 International Electrical Machines and Drives Conference IEMDC 2011, May. 15-18, Niagara Falls, ON, Canada
5. Francis Johnson, Satish Prabhakaran, Ayman El-Refaie, “The requirements of soft magnetic materials for industrial applications”, 2011 TMS Annual Meeting & Exhibition, Magnetic Materials for Energy Applications Symposium, February 27 - March 3, 2011 • San Diego
6. Ayman M. EL-Refaie, James P. Alexander, Steven. Galioto, Manoj R. Shah, Kum-Kang Huh, William D. Gerstler, Jagadeesh Tangudu, and Thomas M. Jahns, “Scalable, Low-Cost, High Performance IPM Motor for Hybrid Vehicles”, 2010 International Conference of Electrical Machines ICEM 2010, Sept.. 6-9, Rome, Italy

7. A.M. El-Refaie, Manoj Shah, J.P. Alexander, S. Galitoto, Kum-Kang Huh, W.D. Gerstler, "Rotor End Losses in Multi-Phase Fractional-Slot Concentrated-Winding Permanent Magnet Synchronous Machines", 2010 Energy Conversion Congress and Exposition ECCE 2010, Sept. 12-16, Atlanta, GA
8. Jagadeesh Tangudu, Thomas M. Jahns, A.M. El-Refaie, "Core Loss Prediction Using Magnetic Circuit Model for Fractional-Slot Concentrated-Winding Interior Permanent Magnet Machines", 2010 Energy Conversion Congress and Exposition ECCE 2010, Sept. 12-16, Atlanta, GA
9. Jagadeesh Tangudu, Thomas M. Jahns, A.M. El-Refaie, "Unsaturated and Saturated Saliency Trends in Fractional-Slot Concentrated-Winding Interior Permanent Magnet Machines", 2010 Energy Conversion Congress and Exposition ECCE 2010, Sept. 12-16, Atlanta, GA
10. Konrad Weeber, Manoj Shah, Kiruba Haran, Ayman EL-Refaie, Ronghai Qu, Chales Stephens, and Steven Galimoto, "Advanced Permanent Magnet Machines for a Wide Range of Industrial Applications", 2010 IEEE PES General Meeting, July 26-29, Minneapolis, USA.
11. Manoj Shah, A.M. El-Refaie, "End Effects in Multi-Phase Fractional-Slot Concentrated-Winding Surface Permanent Magnet Synchronous Machines", 2009 Energy Conversion Congress and Exposition ECCE 2009, Sept. 20-24, San Jose, CA
12. Jagadeesh Tangudu, Thomas M. Jahns, A.M. El-Refaie, Z.Q. Zhu, "Segregation of Torque Components in Fractional-Slot Concentrated-Winding Interior Permanent Magnet Machines Using Frozen Permeability", 2009 Energy Conversion Congress and Exposition ECCE 2009, Sept. 20-24, San Jose, CA
13. Jagadeesh Tangudu, Thomas M. Jahns, A.M. El-Refaie, Z.Q. Zhu, "Lumped Parameter Magnetic Circuit Model for Fractional-Slot Concentrated-Winding Interior Permanent Magnet Machines", 2009 Energy Conversion Congress and Exposition ECCE 2009, Sept. 20-24, San Jose, CA

References

1. "EVALUATION OF THE 2007 TOYOTA CAMRY HYBRID SYNERGY DRIVE SYSTEM"
<http://www.osti.gov/bridge/servlets/purl/928684-rRNS3/928684.pdf>
2. Ashby, M.F., "Materials Selection in Mechanical Design, Second Edition," Butterworth-Heinemann, 1999.
3. Sagawa, M., Hirosawa, S., Yamamoto, H., Fujimura, S., and Matsuura, Y., "Nd-Fe-B Permanent Magnet Materials," Japan. J. Appl. Phys., 26 [6] 785-800 (1987).
4. Harris, I.R., Noble, C., Bailey, T., "The hydrogen decrepitation of an Nd₁₅Fe₇₇B₈ magnetic alloy," J. of the Less-Common Metals, 106, L1-L4 (1985).
5. T. M. Jahns, G. B. Kliman, and T. W. Neuman, "Interior Permanent-Magnet Synchronous Motors for Adjustable-Speed Drives," IEEE Trans. Industry Applications, vol. IA-22, pp. 738-747, 1986.
6. B. Sneyers, D. W. Novotny, and T. A. Lipo, "Field Weakening in Buried Permanent Magnet Ac Motor Drives," IEEE Trans. Industry Applications, vol. 21, pp. 398-407, 1985.
7. T. M. Jahns, "Flux-Weakening Regime Operation of an Interior Permanent Magnet Synchronous Motor Drive," IEEE Trans. Industry Applications, vol. 23, pp. 681-689, 1987.
8. T. Sebastian and G. R. Slemon, "Operating Limits of Inverter-Driven Permanent Magnet Motor Drives," IEEE Trans. Industry Applications, vol. 23, pp. 327-333, 1987.
9. A. K. Adnanes and T. M. Udeland, "Optimum Torque Performance in PMSM Drives Above Rated Speed," Rec. of IEEE Industry Applications Society Annual Meeting, vol. 1, pp. 169-175, October 1991.

10. W. Soong, T.J.E. Miller, "Field Weakening Performance of Brushless Synchronous AC Motor Drives", IEE Proceedings-Electric Power Applications, vol. 141, no. 6, November 1994, pp. 331-340.
11. T. M. Jahns and V. Caliskan, "Uncontrolled Generator Operation of Interior PM Synchronous Machines Following High-Speed Inverter Shutdown," IEEE Trans. Industry Applications, vol. 35, pp. 1347-1357, November/December 1999.
12. A. G. Jack, B. C. Mecrow, P. G. Dickinson, D. Stephenson, J. S. Burdess, N. Fawcett, and J. T. Evans, "Permanent Magnet Machines with Powdered Iron Cores and Pressed Windings," IEEE Trans. Industry Applications, vol. 36, pp. 1077-1084, July/August 2000.
13. P.M. Staunton, et.al., "PM Motor Parametric Design Analyses for a Hybrid Electric Vehicle Traction Drive Application" Oak Ridge National Lab Technical Report, ORNL/TM-2004/217, Septemeber 2004, submitted to Energy Efficiency and Renewable Energy FreedomCAR vehicle Technologies Team
14. P.J. Otaduy, and W.C. Johnson, "The Role of Reluctance in PM Motors" Oak Ridge National Lab Technical Report, ORNL/TM-2005/86, June 2005, submitted to Energy Efficiency and Renewable Energy FreedomCAR vehicle Technologies Team
15. P.J. Otaduy, and J.W. McKeever, "Modeling Reluctance-Assited PM Motors" Oak Ridge National Lab Technical Report, ORNL/TM-2005/185, January 2006, submitted to Energy Efficiency and Renewable Energy FreedomCAR vehicle Technologies Team
16. R.H. Wiles, C.L. Coomer, and J. S. Hsu, "Interior Permanent Magnet Reluctance Machine with Brushless Field Excitation" Oak Ridge National Lab Technical Report, ORNL/TM-2005/222, October 2005, submitted to Energy Efficiency and Renewable Energy FreedomCAR vehicle Technologies Team
17. R.H. Staunton, C.W. Ayers, L.D. Marlino, J.N. Chiasson and T. A. Burrese, "Evaluation of 2004 Toyota Prius Hybrid Electric Drive System" Oak Ridge National Lab Technical Report, ORNL/TM-2006/423, May 2006, submitted to Energy Efficiency and Renewable Energy FreedomCAR vehicle Technologies Team
18. J.M. Bailey, and J.W. McKeever, "Fractional-Slot Surface Mounted PM Motors with Concentrated Windings for HEV Traction Drives" Oak Ridge National Lab Technical Report, ORNL/TM-2005/183, October 2005, submitted to Energy Efficiency and Renewable Energy FreedomCAR vehicle Technologies Team
19. J.M. Bailey, and J.W. McKeever, "Control of Surface Mounted Permanent Magnet Motors with Special Application to Fractional-Slot Motors with Concentrated Windings" Oak Ridge National Lab Technical Report, ORNL/TM-2005/184, December 2005, submitted to Energy Efficiency and Renewable Energy FreedomCAR vehicle Technologies Team
20. A.M. EL-Refaie, and T.M. Jahns, "Application of Bi-State Magnetic Material to an Automotive IPM Starter/Alternator Machine", IEEE Transactions on Energy Conversion, Volume: 20, Issue:1, March 2005, Pages:71 - 79.
21. A.M. EL-Refaie, R. Manzke, and T.M. Jahns, " Application of Bi-State Magnetic Material to Automotive Offset-Coupled IPM Starter/Alternator Machine", IEEE Transactions on Industry Applications , Volume: 40 , Issue: 3 , May-June 2004, Pages:717 - 725.
22. A.M. EL-Refaie, and T.M. Jahns, "Optimal Flux Weakening in Surface PM Machines Using Concentrated Windings", IEEE Trans. Industry Applications, vol. 41, no. 3, May-Jun 2005, pp. 790-800.

23. A.M. EL-Refaie, T.M. Jahns, and D.W. Novotny, "Analysis of Surface Permanent Magnet Machines Equipped with Concentrated Windings", IEEE Trans. Energy Conversion, vol. 21, Mar. 2005, pp. 34-43.
24. A.M. EL-Refaie, and T.M. Jahns, P.J. McCleer, and J.W. McKeever, "Experimental Verification of Optimal Flux Weakening in Surface PM Machines Using Concentrated Windings", IEEE Trans. Industry Applications, vol. 42, March-April 2006, pp. 443-453.
25. J. Cros, P. Viarouge, "Synthesis of High Performance PM Motors with Concentrated Windings", IEEE Trans. Energy Conversion, vol. 17, June 2002, pp. 248-253.
26. F. Magnussen, C. Sadarangani, "Winding Factors and Joule Losses of Permanent Magnet Machines with Concentrated Windings", in Proc. of 2003 IEEE Intl. Elec. Mach. and Drives Conf. (IEMDC'03), vol.1, Madison, WI, pp. 333-339, June 2003.
27. Z.Q. Zhu, D. Howe, "Influence of Design Parameters on Cogging Torque in Permanent Magnet Machines", IEEE Trans. Energy Conversion, vol. 15, no. 4, December 2000, pp. 407-412.
28. E. C. Lovelace, T. M. Jahns, and J. H. Lang, "A Saturating Lumped-Parameter Model For an Interior PM Synchronous Machine," IEEE Trans. Industry Applications, vol. 38, pp. 645-650, May-June 2002.
29. E. C. Lovelace, T. M. Jahns, and J. H. Lang, "Impact of Saturation and Inverter Cost on Interior PM Synchronous Machine Drive Optimization," IEEE Trans. Industry Applications, vol. 36, pp. 723-729, May-June 2000.
30. E. C. Lovelace, "Optimization of a Magnetically Saturable Interior PM Synchronous Machine Drive," PhD Thesis in Dept. of Elec. Eng. & Comp. Sci. Cambridge, MA: MIT, 2000.
31. E. C. Lovelace, T. M. Jahns, T. A. Keim, and J. H. Lang, "Mechanical Design Considerations for Conventionally-Laminated IPM Synchronous Machine Rotors," Proc. of IEEE Intl. Conf. on Elec. Mach. & Drives (IEMDC'01), pp. 163-169, Cambridge, MA, June 2001.
32. K. T. Lowe, C.W. Ayers, and J. S. Hsu, "Floating Refrigerant Loop Based on R-134a Refrigerant Cooling of High-Heat Flux Cooling" Oak Ridge National Lab Technical Report, ORNL/TM-2005/223, September 2005, submitted to Energy Efficiency and Renewable Energy FreedomCAR vehicle Technologies Team

Patents

1. US7994668B2 "COOLING SYSTEM FOR ROTATING MACHINE", August 9, 2011
2. US8004140 "DOVETAIL SPOKE INTERNAL PERMANENT MAGNET MACHINE", August 23, 2011
3. US8018110 "HIGH SPEED INTERNAL PERMANENT MAGNET MACHINE and method of manufacturing the same", September 13, 2011

4. Traction Drive Systems Research and Technology Development

4.1 Benchmarking of Competitive Technologies

Principal Investigator: Tim Burress

Oak Ridge National Laboratory

National Transportation Research Center

2360 Cherahala Boulevard

Knoxville, TN 37932

Voice: 865-946-1216; Fax: 865-946-1262; E-mail: burresta@ornl.gov

DOE Technology Development Manager: Susan A. Rogers

Voice: 202-586-8997; Fax: 202-586-1600; E-mail: Susan.Rogers@ee.doe.gov

ORNL Program Manager: Mitch Olszewski

Voice: 865-946-1350; Fax: 865-946-1262; E-mail: olszewskim@ornl.gov

Objectives

- Provide status of nondomestic hybrid electric vehicle (HEV) technologies through assessment of design, packaging, fabrication, and performance during comprehensive evaluations.
 - Compare results with other EV technologies.
 - Distribute findings in open literature.
- Support U.S. DRIVE program planning and assist in guiding research efforts.
 - Confirm validity of the program technology targets.
 - Provide insight for program direction.
- Produce a technical basis that aids in modeling/designing.
- Foster collaborations with the Electrical and Electronics Technical Team (EETT) and the Vehicle Systems Analysis Technical Team (VSATT).
 - Identify unique electric machine/inverter/converter/drive-train technologies.
 - Ascertain what additional testing is needed to support research and development (R&D).

Approach

- Choose vehicle subsystem.
 - Evaluate potential benchmarking value of various HEVs.
 - Consult with original equipment manufacturers as to which system is most beneficial.
- Perform system level tear down.
 - Determine volume, weight, specific power, and power density.
 - Assess design and packaging improvements.
 - Conduct tests upon magnets and capacitors.
- Prepare components for experimental evaluation.
 - Develop interface and control algorithm.
 - Design and fabricate hardware necessary to conduct tests.
 - Instrument subsystems with measurement devices.
- Evaluate hybrid subsystems.
 - Determine peak and continuous operation capabilities.
 - Evaluate efficiencies of subsystems.

— Analyze thermal data to determine assorted characteristics.

Major Accomplishments

- Selected and procured the 2011 Hyundai Sonata because it is the first hybrid to be sold in the United States by Hyundai Motor Company, which in 2010 ranked 4th in the world in motor vehicle production volume.
- Conducted design/packaging studies of the 2011 Hyundai Sonata power control unit (PCU), hybrid starter-generator (HSG), and primary motor, which revealed a wide range of design characteristics and R&D efforts that differ considerably from that of Toyota hybrids.
- Bypassed the 2011 Hyundai Sonata motor inverter controls to allow full control over testing conditions while using the Sonata's insulated gate bipolar transistor (IGBT) driver board to ensure consistent inverter operation.
- Assessed mass, volume, power density, and specific power of Sonata hybrid subsystems.
- Evaluated efficiency, performance, and other operational characteristics of the 2011 Sonata subsystems.
- Communicated effectively with EETT and VSATT to aid in discerning project direction, test plan, and test results.

Future Direction

- Continue benchmarking efforts with a focus on technologies of interest to DOE, EETT, and VSATT.
- Incorporate approaches similar to that of previous benchmarking studies while working to suit the universal need for standardized testing conditions.

Technical Discussion

The 2011 Hyundai Sonata hybrid is the first hybrid to be added to Hyundai's product line, and the Sonata's hybrid drive train is also used in the 2011 Kia Optima hybrid. Although the vehicle was scheduled to be released in the fall of 2010, release dates were delayed several times and sales began in select metropolitan areas in January of 2011. ORNL obtained parts in the February–April timeframe even though the vehicle was not available at the local dealership. Parts arrived with February production dates stamped upon them. Hyundai refers to their drive system as the “Hybrid Blue Drive,” and it includes a 30 kW primary permanent magnet (PM) motor and an 8.5 kW HSG. The PCU, shown in Fig. 1, includes inverters for these two motors as well as a converter which steps the 270 V hybrid battery voltage level down to the standard 12 V supply level. Overall, the hybrid subassemblies include more off-the-shelf components than hybrids made by Toyota and Honda. A comparison of the 2010 Toyota Prius, 2007 Toyota Camry, and 2011 Hyundai Sonata PCUs is shown in Fig. 1, with total masses and volumes of 13.0 kg and 16.2 L, 17.4 kg and 11.7 L, and 11.8 kg and 10.6 L, respectively. Although the Sonata PCU is shorter, dc and three phase interconnects make it slightly wider than the Prius and Camry PCUs. It should be noted that the combined motor and generator inverter power capabilities of the Sonata (38.5 kW) are much lower than the Prius (~90 kW) and Camry (~120 kW). Also note that there is not a converter which boosts the hybrid battery voltage in the Sonata, as there is in the 2010 Prius PCU (but not the Camry).

As indicated in the left portion of Fig. 2, the 270 V to 12 V dc-dc converter is located in the uppermost compartment of the Sonata PCU. The HSG and primary motor inverters and their periphery are located in the lowest compartment of the PCU. A cast aluminum serpentine heat exchanger/cold plate with cooling fins is integrated into the chassis of the lower compartment, and this is sealed with the nearly flat surface of the upper compartment. An ethylene glycol cooling loop (separate from the engine cooling loop) flows through the PCU and HSG, with a reservoir and pressure relief cap located on top of the PCU, which is visible in Fig. 2. The three phase interconnects for the HSG and primary motor are also shown in Fig. 2.

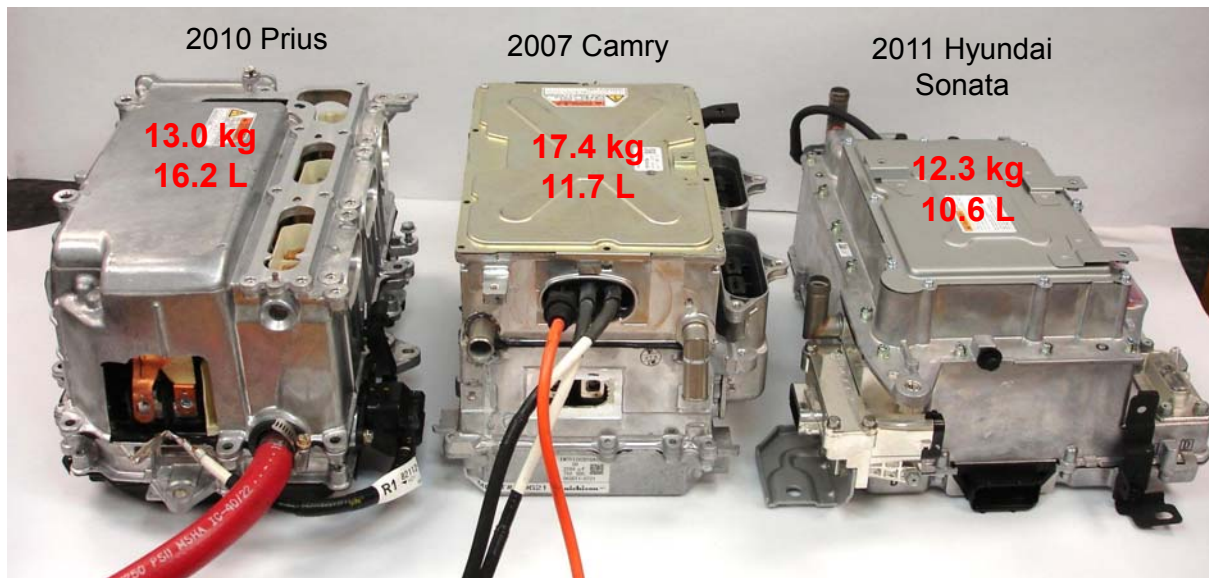


Fig. 1. Comparison of 2010 Prius, 2007 Camry, and 2011 Hyundai Sonata PCUs.

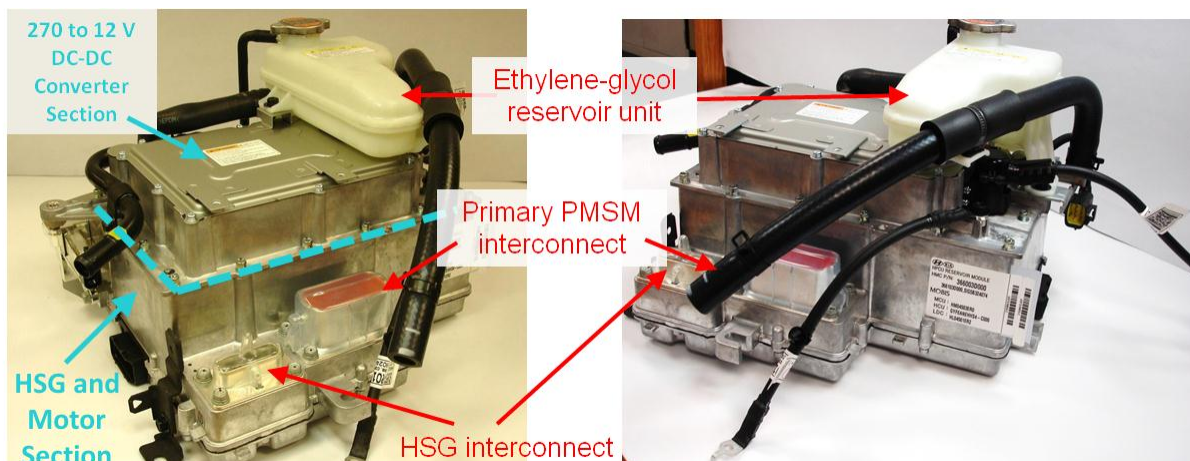


Fig. 2. 2011 Hyundai Sonata PCU.

Most of the components in the bottom compartment of the PCU, visible in Fig. 3, are mounted upside down when the PCU is installed in the vehicle. This allows the 270–12V converter and the inverters to share the cast aluminum heat sink. Two power and communication connectors are located on the bottom sides of the PCU, and the 270 V battery interconnect (with safety interlock pins) is also near the bottom of the PCU. One of the power and communication connectors is mounted to a board labeled “Inverter MCU,” which does not connect or interface with any other components in the PCU. It is possible that this is the control board for the three phase oil pump, which is discussed later in this report. The larger board visible in Fig. 3 is also labeled “Inverter MCU” and serves as the control and power regulation board for the HSG and primary motor inverters. As indicated, several well-known integrated circuits are used for the controls, power supply, and feedback. Tamagawa chips, observed in all PCUs benchmarked thus far, are used to supply and decode resolver signals to provide position feedback from the HSG and primary motor.

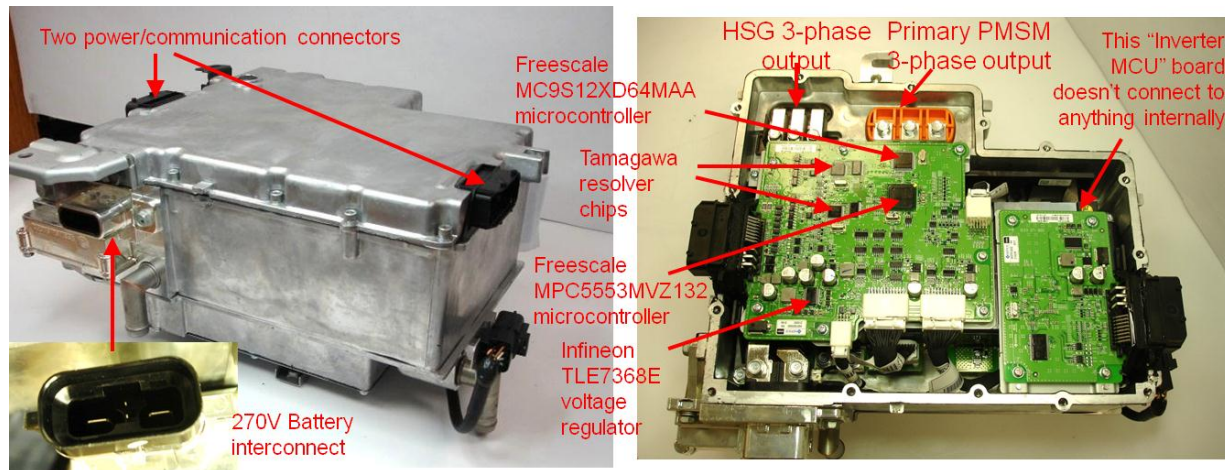


Fig. 3. Bottom compartment of 2011 Hyundai Sonata PCU.

A substantial shielding plate, seen in Fig. 4, is located below the control boards and the main capacitor to mitigate influence of electromagnetic interference (EMI) generated by IGBT switching transients, which could cause significant issues in control circuitry and ultimately system operation. The main capacitor module includes a 600 V, 680 μF capacitor and two additional integrated 0.28 μF capacitors and has a total mass of 1.72 kg and volume of 0.96 L. The 2010 Prius capacitor module is rated at 750 V and 888 μF , with a mass and volume of 1.79 kg and 1.45 L. One of the 0.28 μF capacitors is connected to the PCU chassis and the other is connected to the dc link. Bus bars are integrated into the Sonata's capacitor module, which connects the 270 V interconnect to the two power electronics modules, and a dc-link bleed resistor is mounted on the side of the module. An x-ray image of the capacitor, shown in Fig. 5, indicates that eight capacitor cells are used to form the 680 μF capacitor.

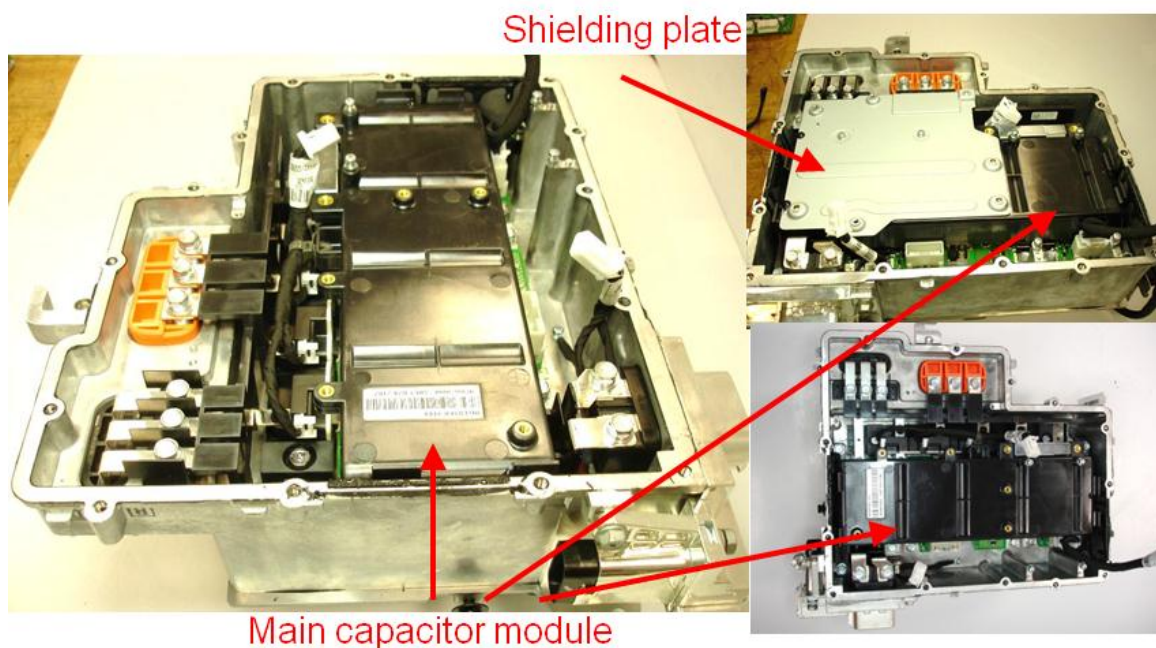


Fig. 4. Bottom compartment of 2011 Hyundai Sonata PCU with control boards removed.

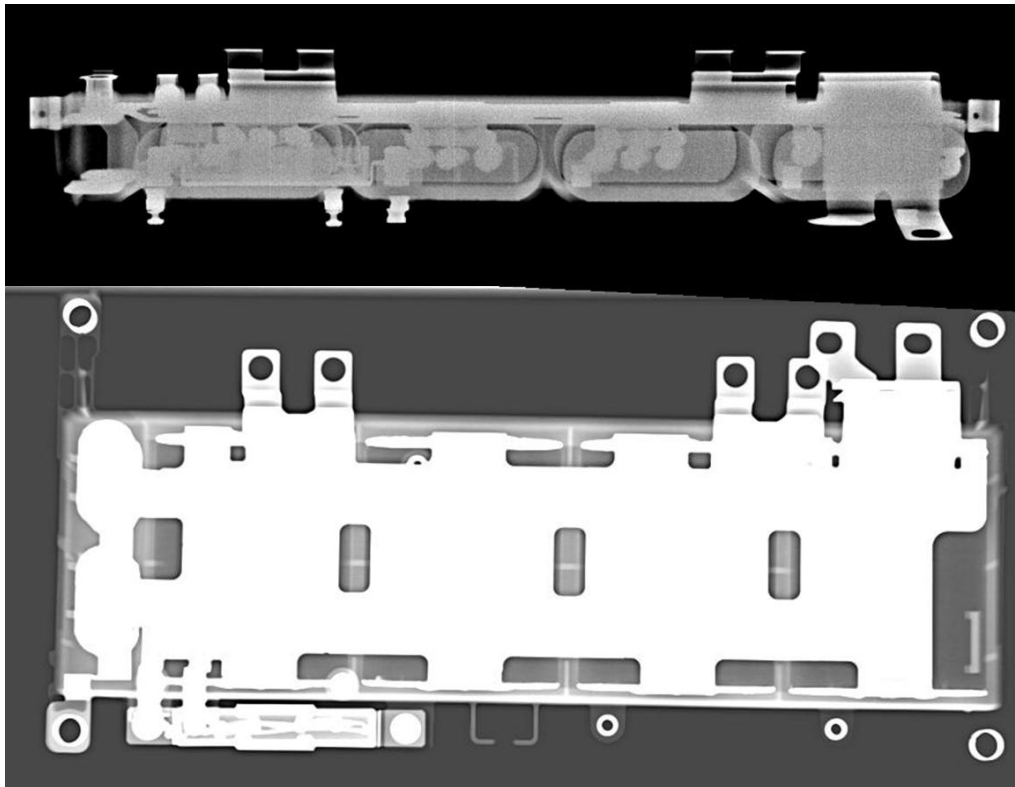


Fig. 5. Main capacitor of 2011 Hyundai Sonata PCU.

After the main capacitor module is removed (Fig. 6), the power electronics modules (PEMs) and driver boards for the HSG and primary motor are accessible. A bus bar infrastructure is used for both three phase inverter outputs and includes two LEM HAH1DR-500S-SP1 500 A current transducers for the primary motor and two LEM HAH1DR-300S-SP1 300 A current transducers for the HSG. It is interesting to note that despite the significant difference between the HSG and primary motor power ratings (8.5 kW versus 30 kW, respectively), the size and packaging of the PEMs are identical. A closer look at a PEM is given in Fig. 7, where specific components of the driver board are indicated. The white modules are labeled “HIG-FeB1” and are identical in appearance to Infineon’s HybridPack1 PEMs. With the gate driver board and thin white plastic plate removed, the IGBTs and diodes of the HSG and primary motor PEMs are visible in Fig. 8. Dimensions of the IGBTs and diodes are shown in millimeters, and the motor IGBTs and diodes are 1.85 and 1.88 times larger than the HSG IGBTs and diodes, respectively. Note that the ratio of power ratings is $30 \text{ kW}/8.5 \text{ kW} = 3.53$, indicating that the generator IGBTs and diodes are likely oversized. There are 12 IGBTs and 12 diodes in each PEM with cross-sectional areas of silicon of about 960.2 mm^2 and $1,194.5 \text{ mm}^2$ for the HSG and primary motor, respectively, with a total of $2,154.7 \text{ mm}^2$ for both PEMs. Only one buffer is used for two parallel IGBTs, and they also share the same gate signal trace. This may entail imbalance between IGBT activity due to the slight impedance discrepancy between each IGBT and the buffer output. Three surface-mounted thermistors are located near the outer edge of the PEM. Only the centermost thermistor is monitored for over-temperature conditions.

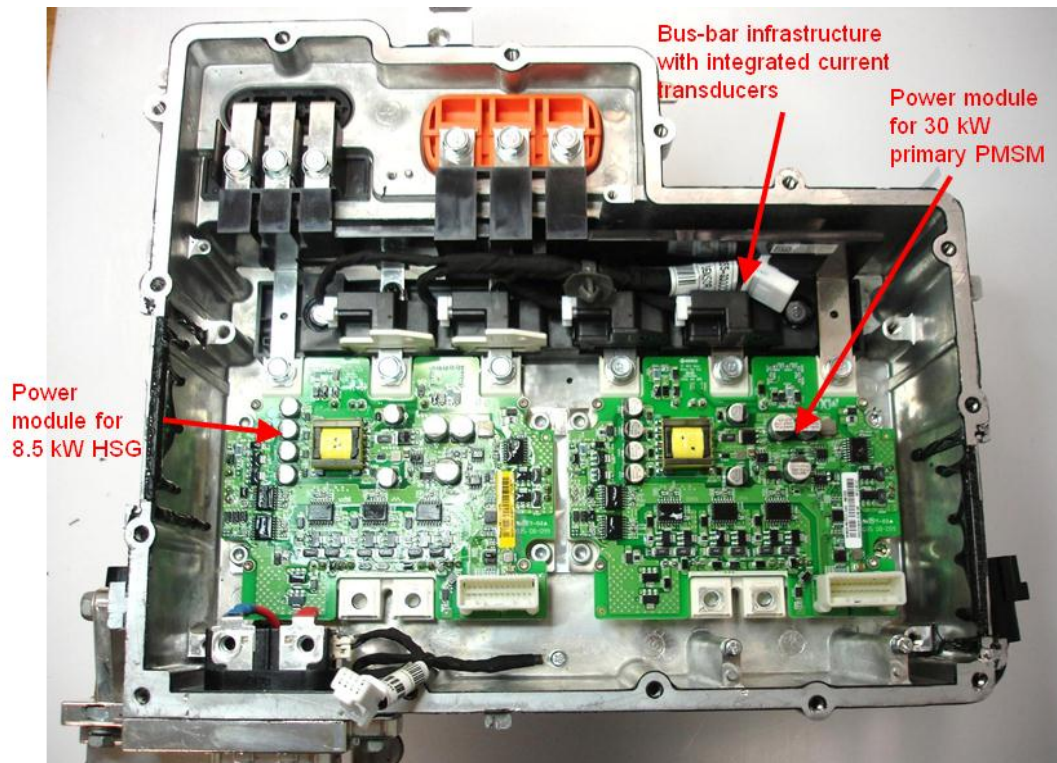


Fig. 6. Bottom compartment of 2011 Hyundai Sonata PCU with main capacitor removed.

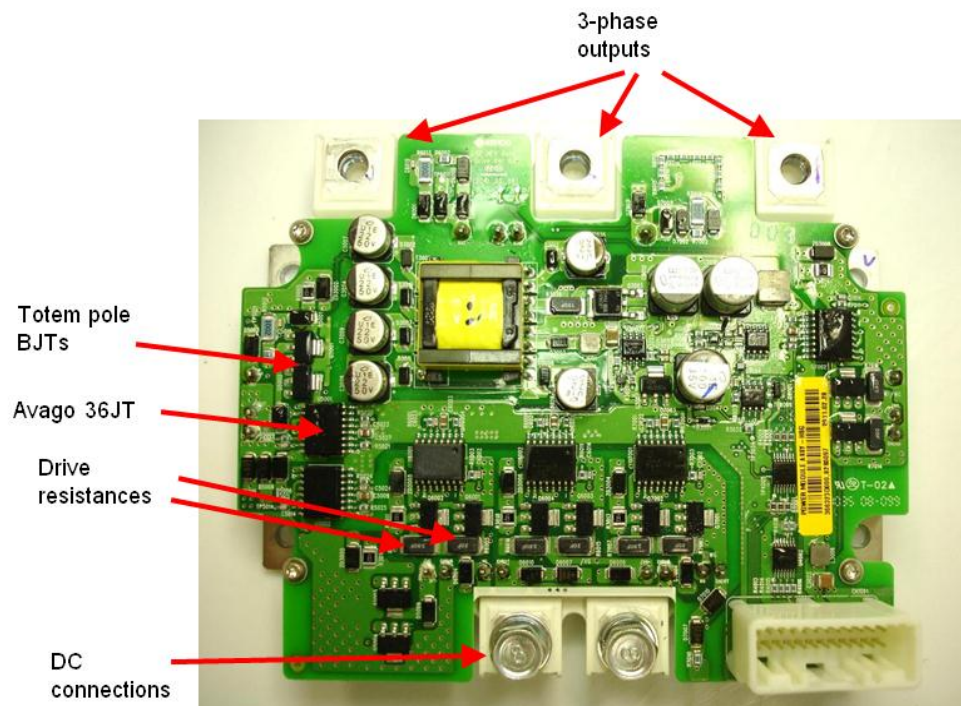


Fig. 7. 2011 Hyundai Sonata PEM with driver board.

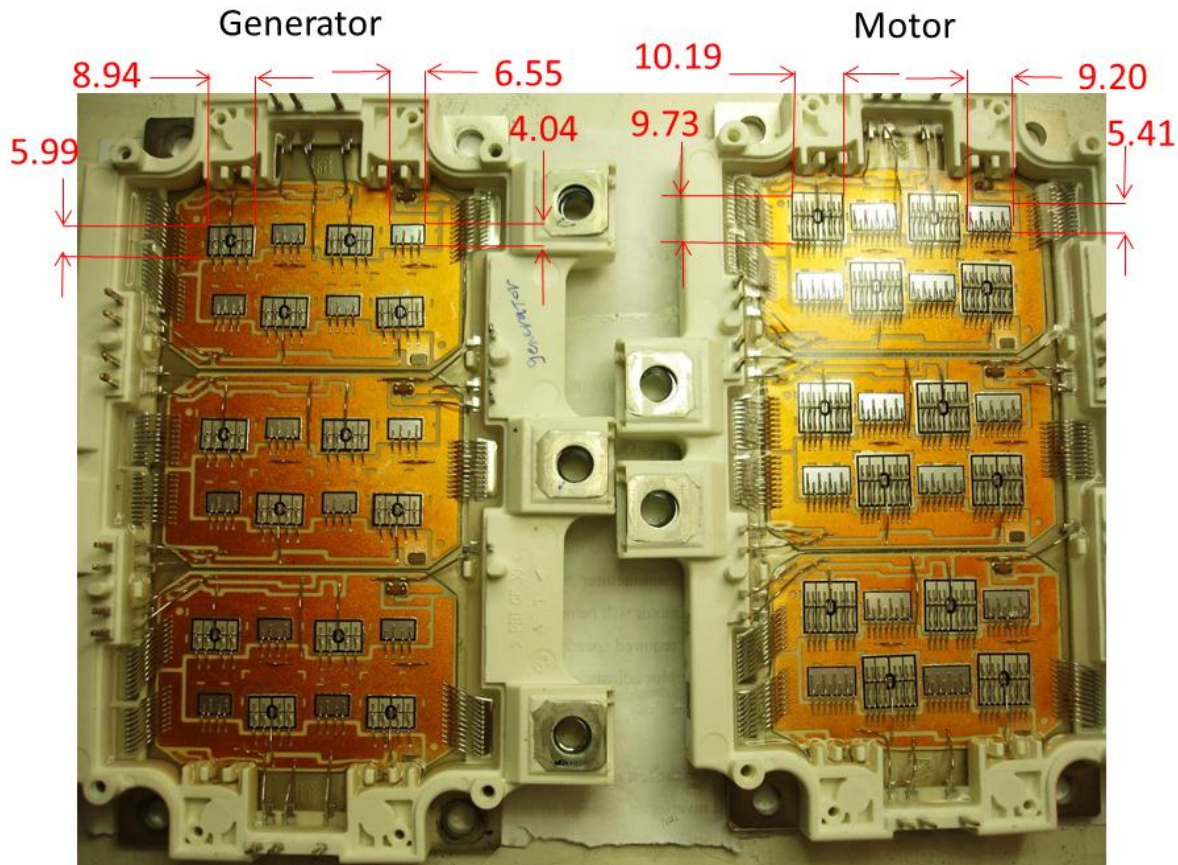


Fig. 8. 2011 Hyundai Sonata PEM with driver board removed.

The 2011 Hyundai Sonata hybrid drive system includes an HSG which is similar in size to a conventional alternator. The HSG is also connected to the engine crankshaft pulley like a conventional alternator, yet the belt is more substantial than most standard belts. Some U.S. made hybrids have a similar starter-alternator arrangement, yet it is operated on the 12 V system which is likely inferior to the Sonata's 270 V HSG system in terms of efficiency, power density, and specific power. With a power rating of 8.5 kW, the HSG is a three phase interior PM (IPM) machine that can develop 43 Nm of torque to absorb energy from the engine to recharge the 270 V battery and to start the engine for cold starts and in-driving restarts (e.g., so the engine can be stopped when the vehicle is at rest). The stator, shown in Fig. 9, has 36 stator slots which form six poles, and the distributed windings have a thermistor installed to prevent overheating. A resolver with relatively small outer diameter is used for position feedback, and it has a 12-pole stator and a rotor with three lobes. The stator is enclosed in a water jacket in which ethylene glycol is circulated as it travels from the coolant inlet port to the coolant outlet port. There is not a significant separator between the coolant inlet and outlet ports (both of which are visible in Fig. 10), so it seems that the angle of the inlet is intended to project the coolant in such a manner that the coolant does not bypass the loop around the HSG. As the HSG was disassembled, a seal for the water jacket with preexisting damage was discovered. Details will be discussed in a later section of this report.

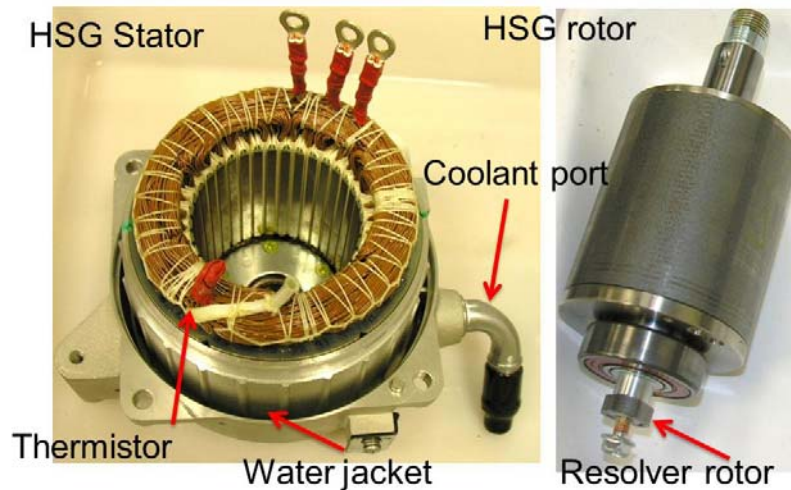


Fig. 9. 2011 Hyundai Sonata HSG.

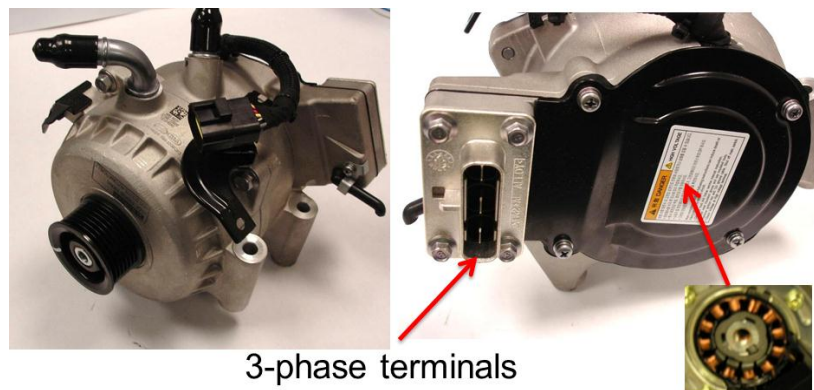


Fig. 10. 2011 Hyundai Sonata HSG.

The 2011 Hyundai Sonata hybrid drivetrain includes a six speed automatic transmission (AT) which is similar in shape and size to most front wheel drive transmissions, which is reasonable as Hyundai also offers various non-hybrid versions of the Sonata. As received, the total mass of the transmission-transaxle (shown in Fig. 11) was 117.2 kg, which is slightly higher than that of the 2007 Camry at 108 kg. A 30 kW IPM machine is located inside the assembly, which also houses, among many things, a mechanical gear pump, drive gears, differential gears, etc. As shown in Fig. 12, a relatively large oil pump is located on the side of the transmission. This three phase PM-machine-driven pump may be necessary because (unlike the conventional AT) a clutch is located between the engine and the six speed transmission (and the internal mechanical pump), and thus the engine cannot help develop the hydraulic pressure needed to shift gear states if, for example, it is turned off at a stop light. Note that the primary electric motor essentially resides where a torque converter would normally be located, which is right at the transmission-engine interface. The torque converter aids in developing hydraulic pressure in a conventional AT. Three-phase terminals for the oil pump and the primary electric motor are indicated in Fig. 12. Substantial oil lines, also indicated in Fig. 12, are used to supply oil to actively cool the motor. As previously mentioned, the primary motor resides near the engine interface, and this section of the motor has been removed and is viewed from the rear in Fig. 13. This 30 kW motor can produce 205 Nm, with an approximate corner speed of 1,400 rpm. The stator has 24 concentrated windings with each stator

tooth being a separate piece but interlocked with its neighboring stator teeth (as shown in the left portion of Fig. 13). The rotor, shown in Fig. 14, has 16 poles, and in general, the stator and rotor laminations are nearly identical to that of Honda hybrid motor designs. A Honda Accord hybrid motor rotor lamination is shown in the bottom right portion of Fig. 14 for comparison. However, one considerable difference is the method of clutch integration into the center of the rotor. While the primary electric motor is always connected to the input of the six speed AT, a clutch located in the center of the rotor allows for the engine to be disengaged and stopped when the vehicle is stopped or operating in electric-only mode. Hyundai claims that the Sonata hybrid can operate up to 62 mph in electric-only mode. This is one advantage of this design over Toyota's Hybrid Synergy Drive system in which the primary electric motor is connected to the drive wheel through a fixed gear ratio.

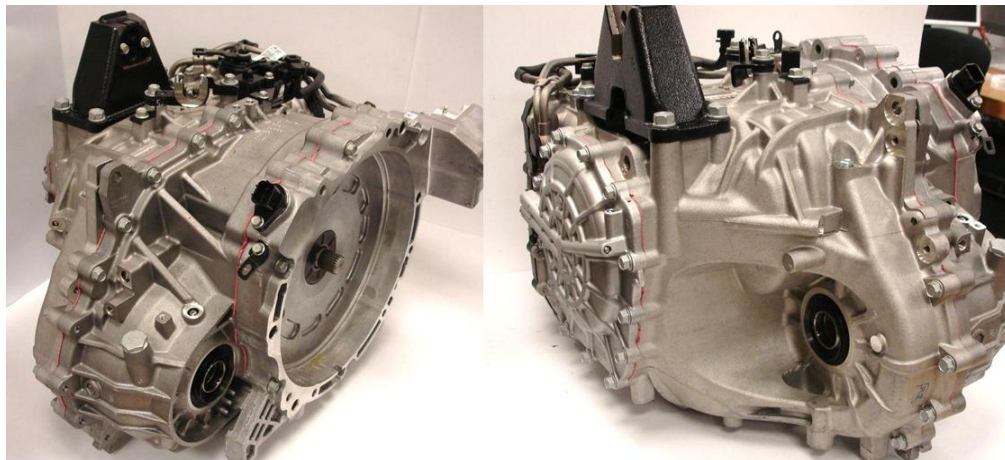


Fig. 11. 2011 Hyundai Sonata transmission-transaxle.

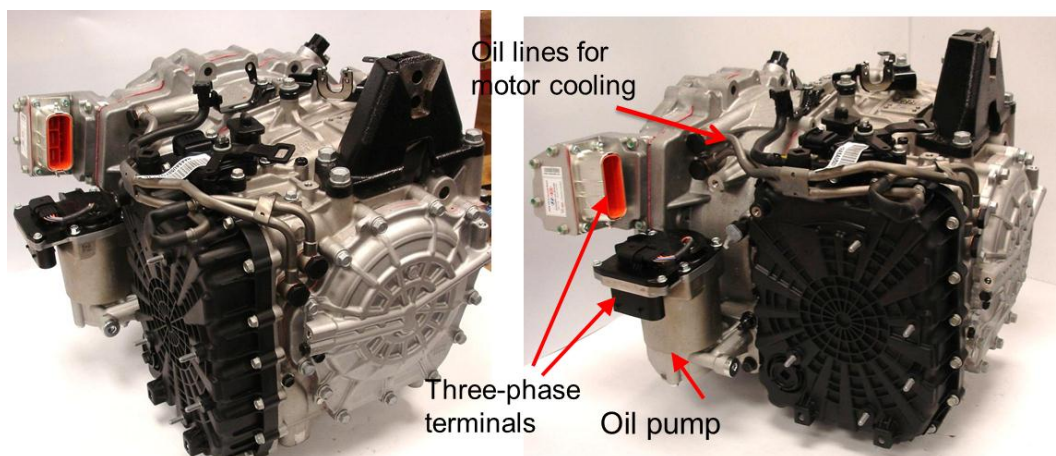


Fig. 12. 2011 Hyundai Sonata transmission-transaxle.

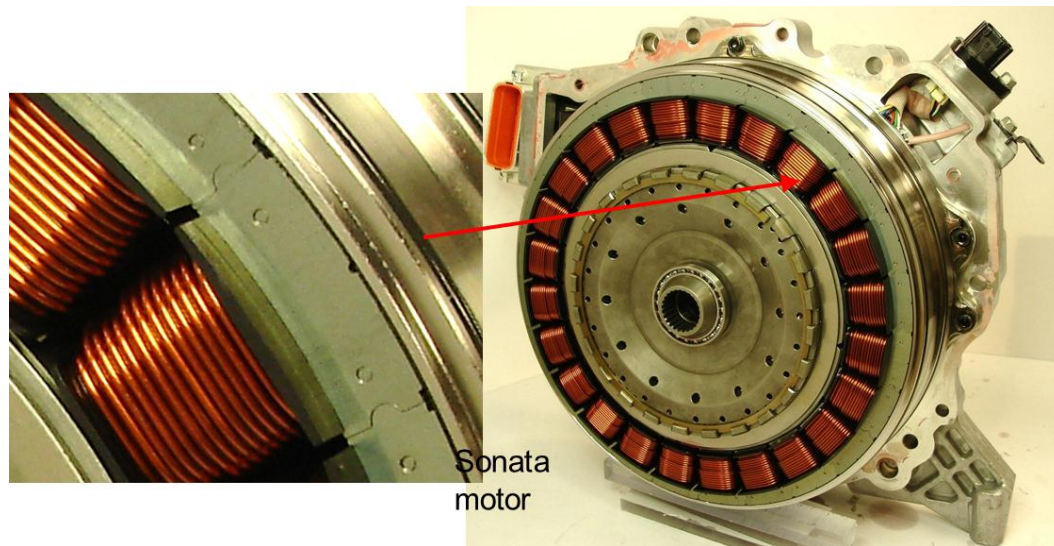


Fig. 13. 2011 Hyundai Sonata motor.

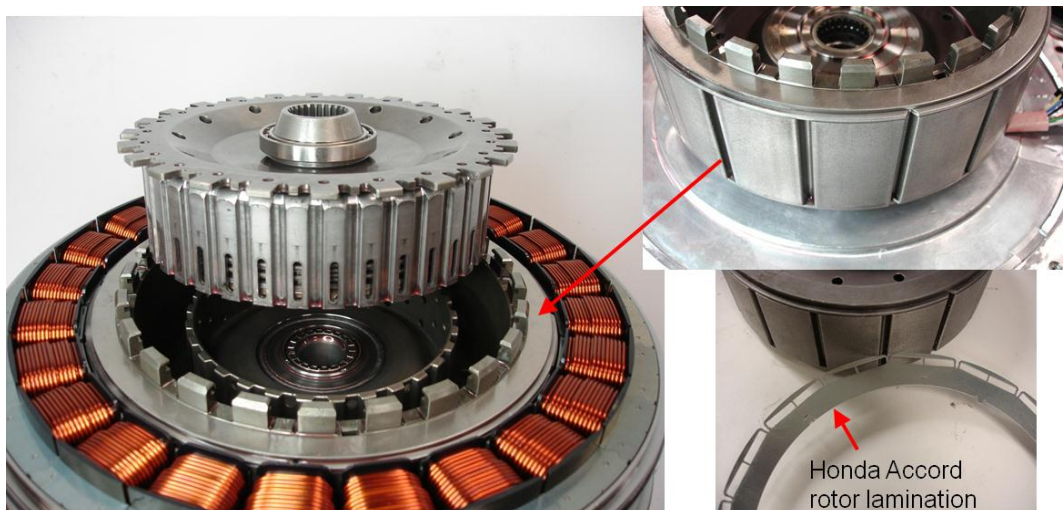


Fig. 14. 2011 Hyundai Sonata motor.

Hydraulic pressure for the integrated clutch is provided by a port (shown in the upper left portion of Fig. 15), which is located in the center of the main transmission shaft. Also shown in Fig. 15 is the basic functionality of the motor cooling system. The previously mentioned oil lines serve as a supply and drain for the oil inlet and oil outlet labeled in Fig. 15. Two very large o-rings are located around the outer diameter of the stator. These o-rings form a seal with the chassis, and thus oil can be circulated around the entire perimeter of the motor stator before it exits the channel formed by the o-rings. While transmission oil is not the best transfer medium, this provides uniform cooling and mitigates potential thermal imbalances.

After removing the next section of the transmission, the mechanical oil pump, drive gears, and differential gear are visible, as shown in Fig. 16(a). Figure 16(b) is a view from the back of the transmission with the rear plate removed. The compound multiple planetary gear system in the forefront of the image carries out most of the functionalities of the six speed transmission. As shown in Fig. 17, a seal from the HSG and a seal for the differential gear output shaft were both damaged when the Sonata parts arrived. The HSG seal was pinched and likely maintained a proper seal when it was discovered.

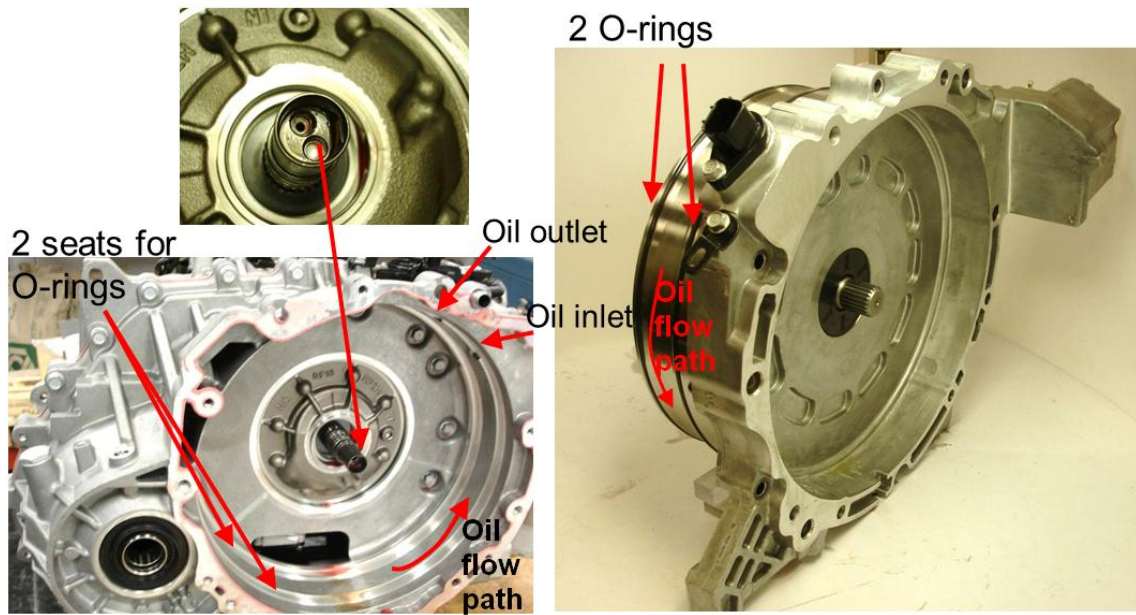


Fig. 15. 2011 Hyundai Sonata motor cooling system and hydraulic supply for clutch (upper left).

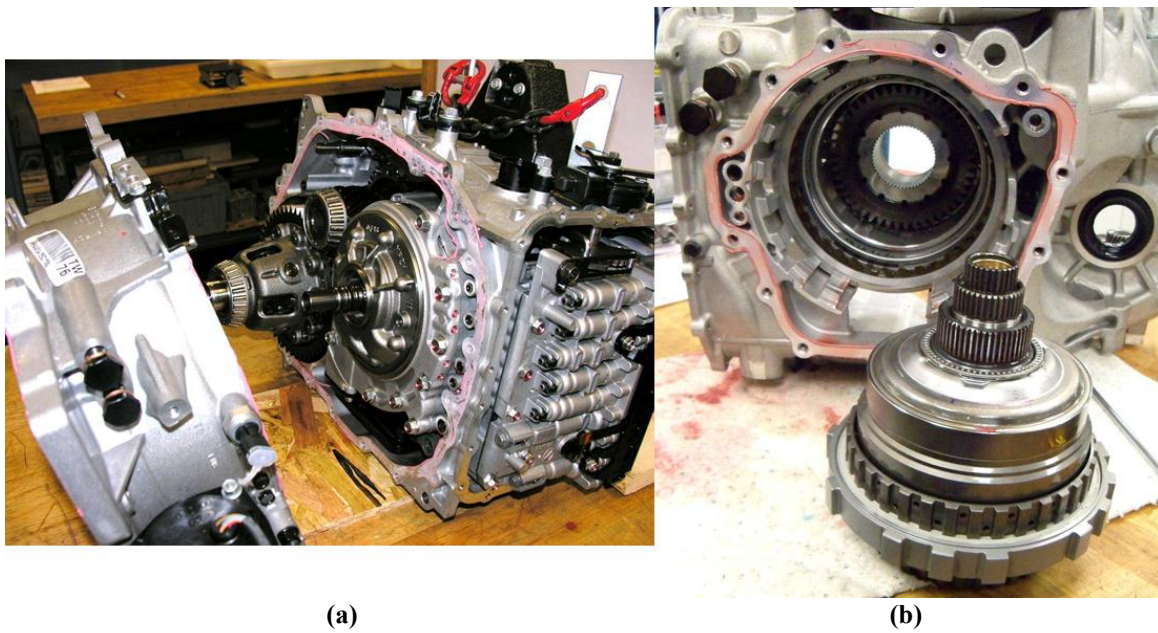


Fig. 16. 2011 Hyundai Sonata: (a) transaxle and (b) view from the back of the transmission showing the compound multiple planetary gear system.

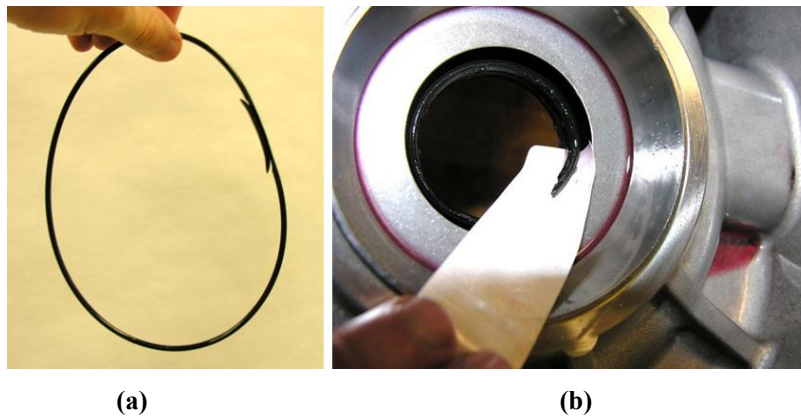


Fig. 17. Damaged seals from (a) HSG and (b) transaxle differential shaft output (right).

In preparation for testing the Sonata subsystems in a dynamometer test cell, a mounting plate was designed and fabricated to access the output shaft of the primary electric motor while also providing proper mechanical support, cooling, and lubrication. The first section of the transmission-transaxle was mounted to the custom plate, with the engine-transmission bolt pattern facing away from the plate and unused as a clutch disengages the engine input from the electric motor. While seemingly simple, the design of the plate involved a complex design process which included high tolerance guidance and alignment mechanisms and bearing support and lubrication. As shown in Fig. 18(a), the stator was instrumented with thermocouples to monitor coil, core, oil port, and case temperatures during tests. Coil, core, and case thermocouples were strategically located to observe potential thermal gradient based on proximity to the oil inlet and outlet. Current transducers and voltage taps were installed on the input of the inverter and the output of the inverter. The Sonata motor and custom ORNL support plate were face-mounted to a Himmelstein torque transducer to measure mechanical power, and the torque transducer was mounted to the dynamometer [Fig. 18(b)]. Figure 19 shows back-electromotive force (emf) test results compared with those for the 2006 Honda Accord. At about 3,750 rpm, the line to neutral RMS voltage measurement reaches 120 V, which is roughly the maximum ac voltage output capability of the inverter with a 270 V dc link. Thus, operation above this speed will certainly require field weakening techniques. This characteristic is common among other hybrid systems, and optimal control of previously tested motors typically involved field weakening at relatively low speeds.

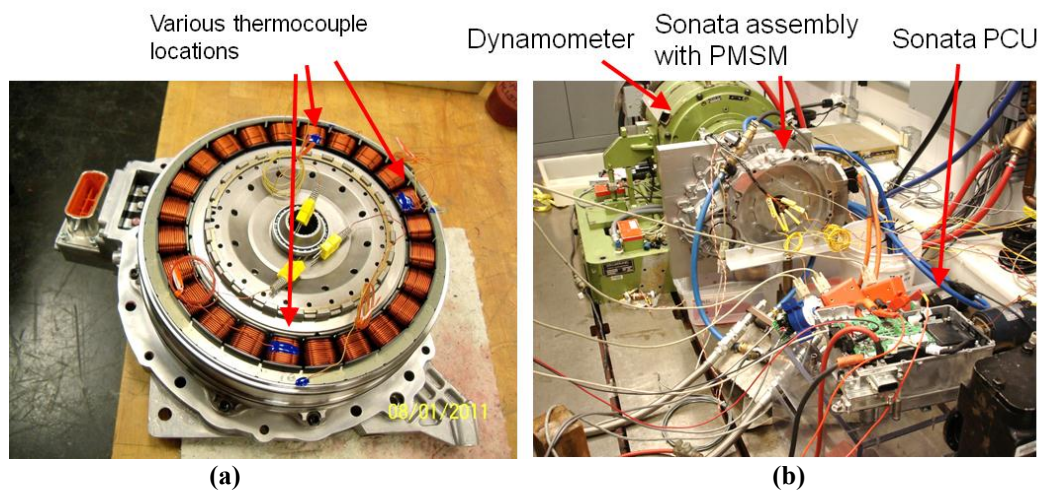


Fig. 18. Test setup showing (a) thermocouple installation locations and (b) dynamometer setup.

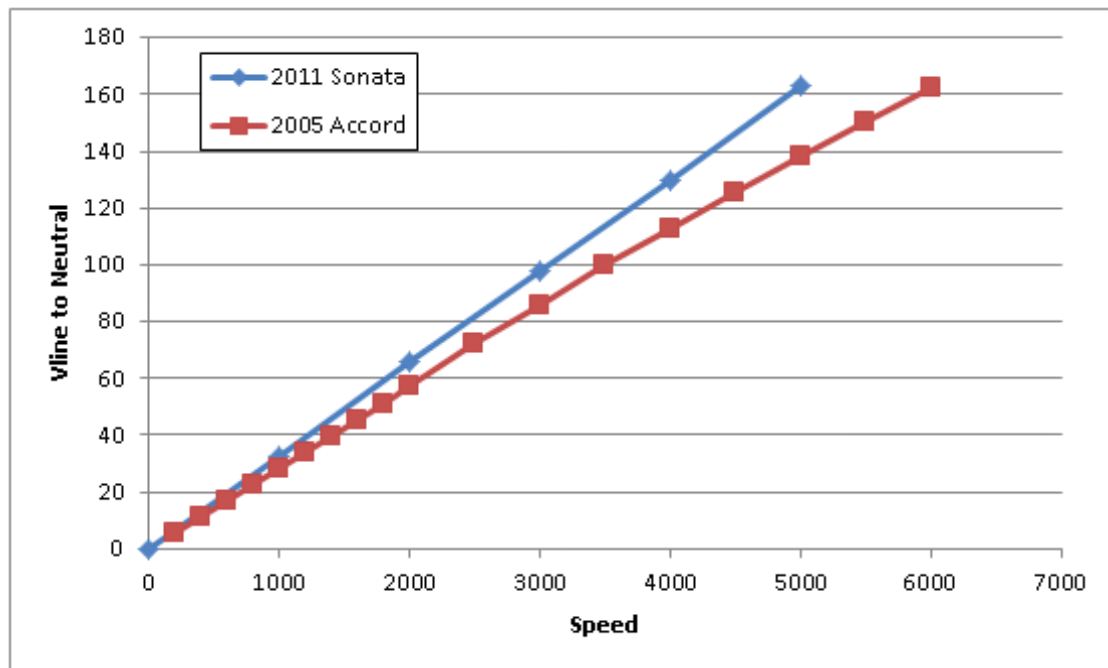


Fig. 19. Back-emf versus speed for 2011 Hyundai Sonata and 2006 Honda Accord motor.

Locked rotor torque measurements were made as the positive terminal of a dc supply was connected to phase “a” and the negative terminal of a dc supply was connected to phases “b” and “c” (in parallel). These tests were conducted as various current levels were applied and the rotor was incrementally locked in positions over a full electrical cycle. The results, shown in Fig. 20, indicate that like the 2006 Accord, the total torque does not include a considerable reluctance component in comparison with Toyota’s designs. This is expected based on the layout of the magnets observed in Fig. 14. However, in comparison with the 2006 Accord, the locked rotor torque profile of the 2011 Sonata is much smoother. Peak torque values for each current level were selected and plotted versus current in Fig. 21. The results indicate that about 300 A dc was required to produce the published peak torque of 205 Nm. Figure 21 also indicates that the torque-per-current ratio of the motor remains approximately linear even up to 250 A and shows slight indications of saturation at 300 A. This is quite different from Toyota designs, which begin to operate in saturation at much lower current levels. Low speed efficiency mapping has been completed. Efficiency testing will be completed early in FY 2012. Fairly high efficiencies have been observed at low speeds. For example, at 500 rpm and 50 Nm, inverter and motor efficiencies were 92% and 93%, respectively, which is higher than most of the previously benchmarked systems in this operation region.

A comparison of power density (PD) and specific power (SP) for various systems benchmarked at ORNL is given in Table 1. The 2011 Sonata motor PD and specific power SP are more than 2 times those of the 2006 Accord motor (which has a similar topology). This is largely due to the increase of the dc-link voltage from the Accord’s 144 V to the Sonata’s 270 V. These PD and SP values are comparable to those of the 2004 Prius, even though the 2004 Prius uses a 500 V dc link. High speed ratings and a 650 V dc link provide high PD and SP values for recent Toyota designs. Inverter PD and SP values of the 2011 Sonata improved greatly over the 2006 Accord inverter. Increased dc-link voltage contributes to this improvement of PD and SP in the Sonata. The 2006 Accord has a large air cooled heat sink, whereas the Sonata uses an ethylene glycol cooling loop. Toyota motor inverters have two values each for PD and SP: one that includes the boost converter and one that does not. When the boost converter is included in the motor inverter PD and SP calculations, the 2011 Sonata surpasses all systems except the 2008 LS 600h. When the boost converter is not included in these calculations, the Sonata motor inverter PD and SP values are comparable to those for the 2004 Prius.

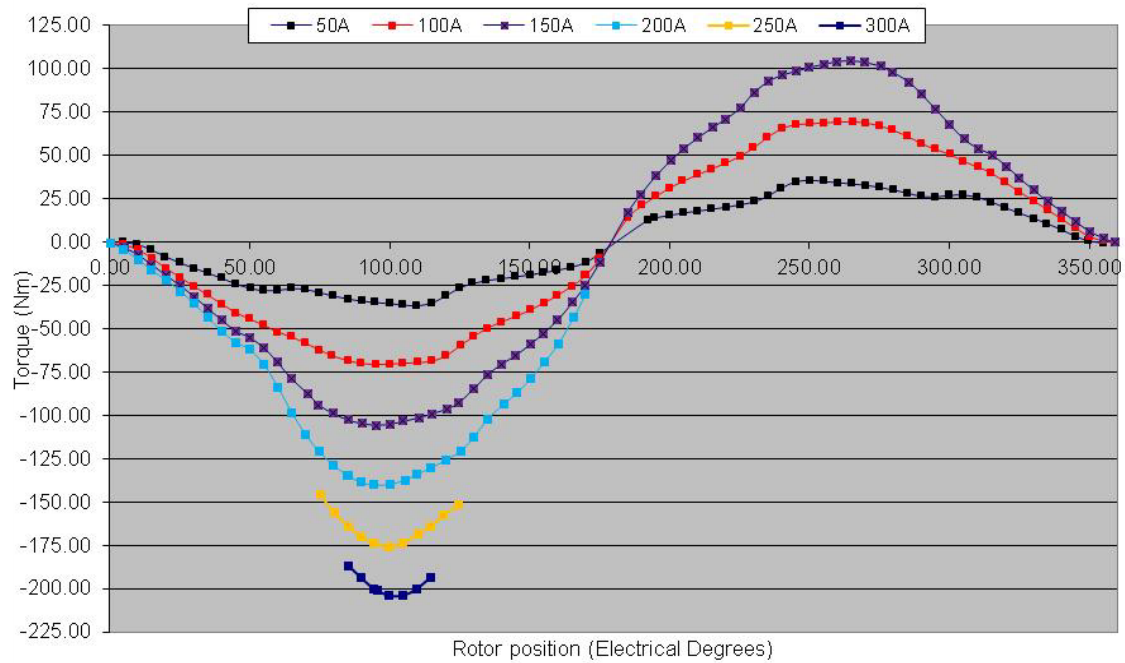


Fig. 20. Locked rotor torque versus position for the 2011 Hyundai Sonata motor.

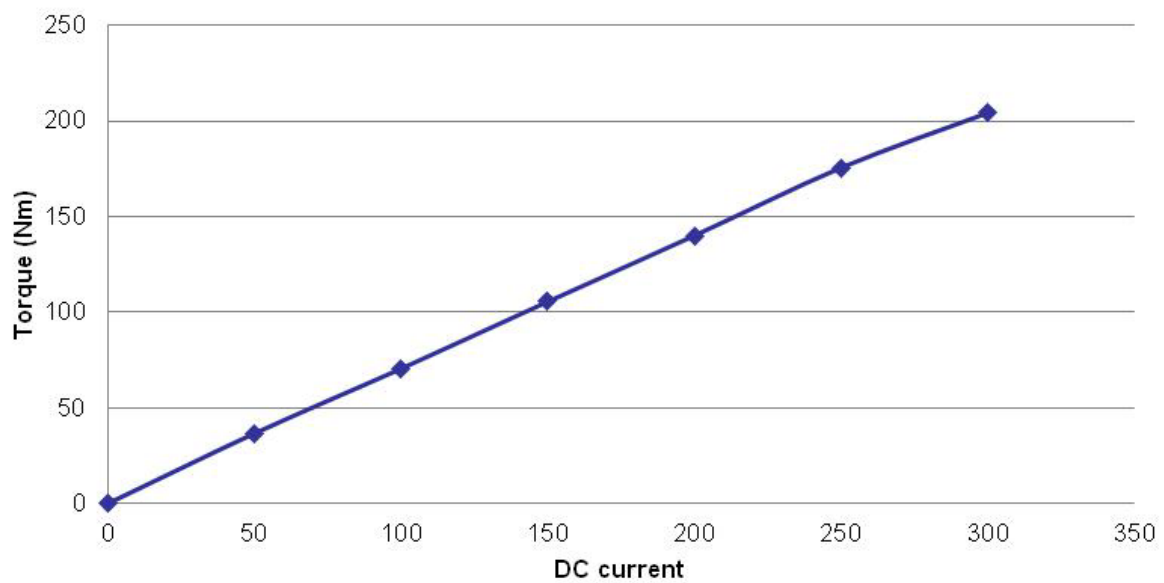


Fig. 21. Peak locked rotor torque versus current for the 2011 Hyundai Sonata motor.

Table 1. Comparison of specific power and power density for various HEV components

| Component and parameter | 2011 Sonata (30 kW) | 2010 Prius (60 kW) | 2008 LS600h Lexus (110 kW) | 2007 Camry (70 kW) | 2006 Honda Accord (12 kW) | 2004 Prius (50 kW) |
|---|------------------------------------|-------------------------------|---|-----------------------------------|--|-------------------------------|
| Motor | | | | | | |
| Peak power density, kW/L | 3.0 | 4.8 | 6.6 | 5.9 | 1.5 | 3.3 |
| Peak specific power, kW/kg | 1.1 | 1.6 | 2.5 | 1.7 | 0.5 | 1.1 |
| Inverter —excluding generator inverter (parenthetical values do not include boost converter mass/volume) | | | | | | |
| Peak power density, kW/L | 7.3 | 5.9 (11.1) | 10.6 (17.2) | 7.4 (11.7) | 2.9 | 4.5 (7.4) |
| Peak specific power, kW/kg | 6.9 | 6.9 (16.7) | 7.7 (14.9) | 5.0 (9.3) | 2.4 | 3.8 (6.2) |

Conclusion

1. The 2011 Hyundai Sonata hybrid and 2011 Kia Optima hybrids share the same drivetrain.
2. Overall PCU slightly smaller than Toyota PCUs even though combined generator and motor power is only 38.5 kW versus ~90 kW for the 2010 Prius.
3. PCU has many off-the-shelf components including what appears to be Infineon's HybridPack1 PEMs.
4. PEMs are the same size for 8.5 kW HSG versus 30 kW motor, indicating potential for improved power density.
5. The HSG and PCU share ethylene glycol coolant loop.
6. The HSG is similar in size to alternator but has much higher power rating and efficiency because it uses a 270 V system (as opposed to 12 V).
7. The HSG is cooled with a water jacket, and the primary motor has a dedicated oil path around the stator for cooling.
8. The stator and rotor lamination design approach appears to be the same as the 2006 Accord, but with different design parameters
9. Integrated clutch in motor rotor required significant engineering effort.
10. The motor barely operates in saturation at peak torque.
11. Efficiencies measured at low speeds are favorable (e.g., 92% inverter and 93% motor efficiency measured at 500 rpm and 50 Nm).

Patents

None.

Publications

None.

References

1. T. A. Burress, et al., *Evaluation of the 2010 Toyota Prius Hybrid Synergy Drive System*, ORNL/TM-2010/253 Oak Ridge National Laboratory, 2011.
2. T. A. Burress, et al., *Evaluation of the 2007 Toyota Camry Hybrid Synergy Drive System*, ORNL/TM-2007-190, Oak Ridge National Laboratory, 2007.
3. T. A. Burress, et al., *Evaluation of the 2008 Lexus LS600h Hybrid Synergy Drive System*, ORNL/TM-2008/185, Oak Ridge National Laboratory, 2008.

4.2 High Power Density Integrated Traction Machine Drive

Principal Investigator: Fred Wang

Oak Ridge National Laboratory

National Transportation Research Center

2360 Cherahala Boulevard

Knoxville, TN 37932

Voice: 865-946-012; Fax: 865-946-1262; E-mail: wangf@ornl.gov

DOE Technology Development Manager: Susan A. Rogers

Voice: 202-586-8997; Fax: 202-586-1600; E-mail: Susan.Rogers@ee.doe.gov

ORNL Program Manager: Mitch Olszewski

Voice: 865-946-1350; Fax: 865-946-1262; E-mail: olszewskim@ornl.gov

Objectives

- The overall objective is to develop a reliable, fault-tolerant, integrated modular motor drive (IMMD) that is capable of operating at 200°C junction and 150°C ambient temperatures.
- For FY 2011, the objectives are
 - to develop a demonstrator version of the IMMD with fault-tolerant controller using the most promising configuration to verify performance characteristics including power density and distributed control and
 - to develop the 10 kW phase leg power modules needed for implementing the full power IMMD. The modules should be based on low cost silicon and can operate at an ambient temperature of 150°C, with junction temperature up to 200°C.

Approach

- Analyze alternative fault-tolerant machine and controller configurations to identify the most promising candidates for future demonstration in prototype hardware.
- Apply the results of the initial analysis to design and build a preliminary 10 kW demonstrator integrated traction drive in FY 2011 followed by a full-scale 55 kW (peak) prototype unit in FY 2012 and FY 2013.
- Evaluate the ruggedness of the selected silicon insulated gate bipolar transistor (IGBT) for operation at 200°C considering latch-up immunity, short circuit capability, and dynamic avalanche capability.
- Design and fabricate a 10 kW phase leg module, aiming for 200°C junction temperature operation. Test the electrical and thermal characteristics of the high temperature power module.

Major Accomplishments

- Designed, built, and tested a 10 kW, six phase, 10-pole permanent magnet (PM) machine that is serving as a concept demonstrator in preparation for developing a full-scale 55 kW prototype IMMD unit.
- Developed a modular IMMD power converter that conforms to the dimensions of the 10 kW concept demo PM machine, providing a testbed for implementing the IMMD distributed control software.
- Tested ruggedness of selected IGBT at various temperatures, concluding that the device has good latch-up immunity and adequate short circuit capability for operation at 200°C.

- Designed and fabricated a 10 kW phase leg power module, and tested its electrical and thermal characteristics up to 200°C.
- Designed the gate driver boards and main board for the IGBT phase leg modules with which the continuous test is conducted with liquid cooling up to 10 kW.

Future Direction

- This project will not be funded by the DOE Vehicle Technologies Program beyond FY 2011.

Technical Discussion

Demonstrator IMMD Machine and Test Results

10 kW IMMD Machine

Based on the results of the IMMD analytical machine study completed in FY 2010, a six phase, 10-pole surface PM (SPM) machine was selected for further development during FY 2011 [1]. A 10 kW demonstrator SPM machine with the target six phase, 10-pole configuration [2-4] was built to verify key concepts before moving forward with the planned 55 kW version. To save both time and financial resources, a new stator was designed for an existing SPM rotor that was available at the University of Wisconsin (UW)-Madison. The only significant complication that had to be addressed was that the active length of the existing 10-pole SPM rotor is significantly longer than necessary because it was originally designed for a machine with a higher power rating. As a result, the rotor in the demonstrator 10 kW IMMD machine has 25 mm of rotor overhang on each side of the new stator stack. Although not ideal because of additional losses that the overhanging rotor magnets induce in the stator, this approach was adopted because it is consistent with the concept demonstration objectives for FY 2011.

New stator windings using multistrand, twisted magnet wire were designed to maintain the nominal dc bus voltage level at 325 V. Figure 1(a) shows the new demonstrator machine placed in its mounting fixture and 1(b) a cross-sectional view of the machine. Initial testing of the demonstrator machine is being carried out using a three phase inverter to measure the machine parameters and performance characteristics; Fig. 1(c) shows both parallel and series winding configurations that are being used during this initial testing. Table 1 provides a summary of machine dimensions, construction features, and rated operating conditions.

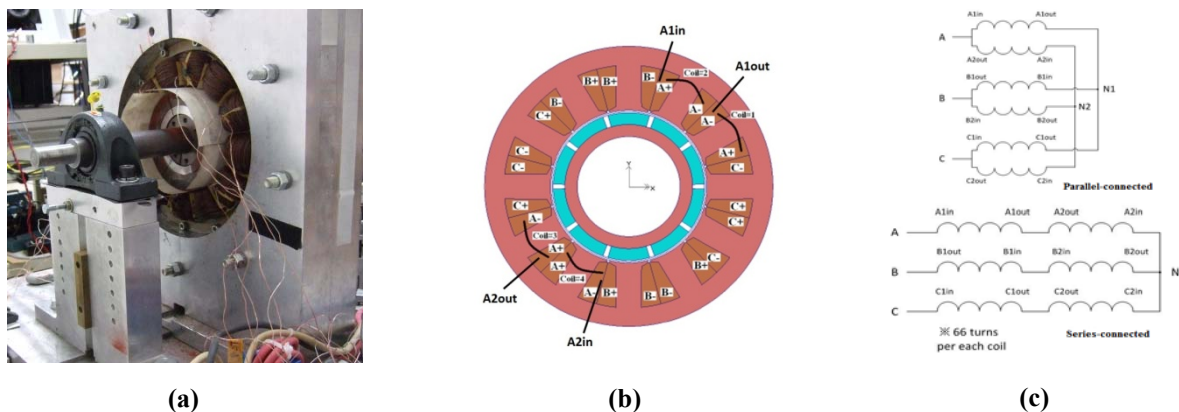


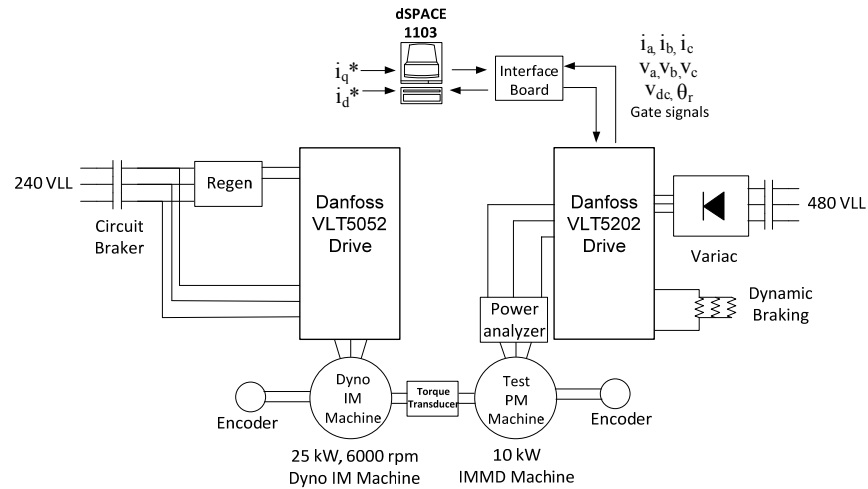
Fig. 1. 10 kW demonstrator IMMD machine (a) mounted in an open-frame fixture, (b) machine cross-section, and (c) three-phase parallel and series winding connections for the six phase machine.

Table 1. Demonstrator 10 kW machine dimensions and key design variables

| Parameter | Value | Parameter | Value |
|---|------------|--|------------------------|
| Stator OD (mm) | 280 | Rated torque and speed (Nm/rpm) | 34.3/2,800 |
| Rotor OD (mm) | 142 | Peak torque and current (Nm/A _{rms}) | 61.4/28.5 |
| Stator active axial length (mm) | 25 | Number of turns per coil | 66 |
| Rotor active axial length (mm) | 75 | Number of strands per turn | 20 |
| Maximum speed (rpm) | 14,000 | Wire gauge (AWG) | 24 |
| Rated current/voltage (six phase configuration basis) (A _{rms} /V _{rms}) | 14.2/132.7 | Wire configuration | Transposed magnet wire |

Dynamometer Test Configuration

A dynamometer with a 25 kW induction load machine rated at 6,000 rpm was selected for the demonstrator machine testing at UW-Madison. A Danfoss VLT-5202 three phase, adjustable-speed drive is used to excite the six phase demonstrator PM machine using both the series or parallel winding configurations shown in Fig. 1(c). The drive receives its gating signals from a dSPACE controller used as a rapid prototyping system. A block diagram of the dynamometer configuration is shown in Fig. 2.

**Fig. 2. Dynamometer test configuration for testing the 10 kW machine.**

The dSPACE controller is programmed with a high performance synchronous-frame current regulator that makes it convenient to independently control the d-axis and q-axis currents, which, in turn, determine the torque developed by the demonstrator machine. The phase currents and voltages, dc link voltage, shaft torque, and thermocouple temperatures are measured and recorded during steady-state operating conditions. In addition, a three phase power analyzer is used to measure the terminal electrical performance of the machine including both real power input and power factor.

Demonstrator Machine Measured and Predicted Parameters

One of the first tests was to measure the machine's open-circuit back-electromotive force (emf) waveforms to determine its magnet flux linkage value in comparison to predictions. Figure 3(a) shows a comparison of the measured and finite element (FE) predicted back-emf voltage waveforms at 500 rpm. The frequency spectrum component amplitudes for the two back-emf waveforms are compared in Fig. 3(b), and plots of the fundamental component amplitudes of the back-emf voltage and magnet flux linkage as a function of rotor speed are provided in Fig. 3(c). The back-emf waveform is dominated by its

fundamental component, and this is expected because of the fractional-slot concentrated winding design. The measured experimental back-emf amplitudes are only 0.7% lower than the predicted values at 20°C. As indicated in Fig. 3(c), the magnet flux linkage is nearly constant with changes in the rotor speed.

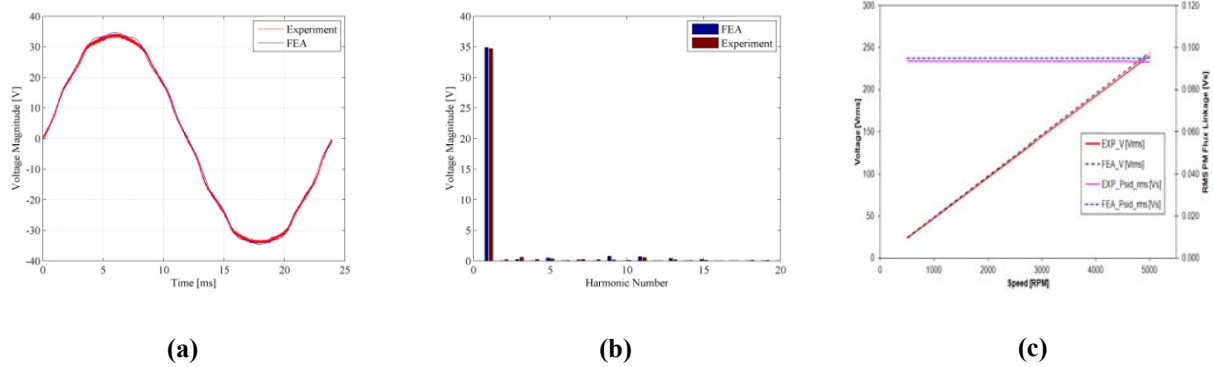


Fig. 3. Back-emf waveforms: (a) comparison of measured and FE predicted phase back-EMF waveforms for the parallel-connected IMMD machine at 500 rpm and 20°C, (b) frequency spectrum of back-emf waveforms at 500 rpm, and (c) measured and predicted back-emf and magnet flux linkage fundamental amplitudes vs speed at 20°C.

Static tests were carried out to measure the key machine parameters to populate the machine equivalent circuit. Table 2 presents a comparison of the measured and FE predicted machine parameters. The agreement between the predicted and measured machine parameters is generally very good.

Table 2. Comparison of measured and FE predicted machine parameters

| Parameter | R_s (m Ω) | λ_{pm_rms} (V-s) | L_d (mH) | L_q (mH) |
|-----------------|---------------------|---------------------------|------------|------------|
| Measured value | 53.3 | 0.0936 | n/a | 1.17 |
| Predicted value | 51.4 | 0.0949 | n/a | 1.35 |

Demonstrator Machine Load Tests

Machine testing has been carried out under loaded conditions to investigate the performance characteristics of the demonstrator 10 kW machine. Figure 4 provides plots of measured waveforms for operating conditions of $i_q = 20$ A (peak) and $i_d = 0$ A at 1,000 rpm. This operating point corresponds to about 50% of rated torque for this machine. Table 3 provides a comparison of the predicted and measured performance characteristics with these same i_q and i_d current commands at both 1,000 rpm and 2,800 rpm. Again, the agreement between the measured and predicted machine performance is generally very good.

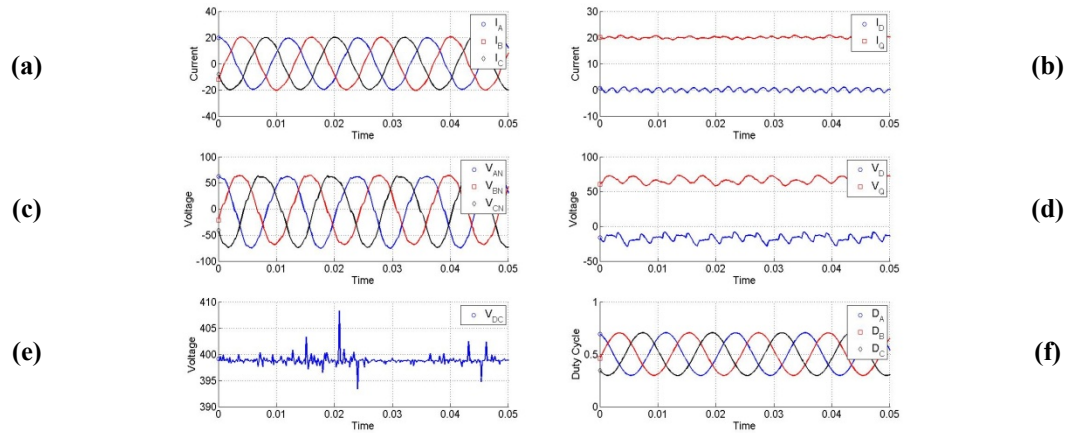


Fig. 4. Steady-state loaded machine operation with $i_q = 20$ A and $i_d = 0$ A at 1,000 rpm.

Graphs from top left: (a) phase currents; (b) synchronous frame currents, i_d , and i_q ; (c) filtered phase voltages; (d) filtered synchronous frame voltages, v_d , and v_q ; (e) dc bus voltage, v_{dc} ; and (f) commanded duty cycle.

Table 3. Comparison of measured and predicted machine performance for $i_q = 20$ A and $i_d = 0$ A

| Speed | 1,000 RPM | | 2,800 RPM | |
|------------------------|-------------|------------|-------------|------------|
| | FE analysis | Experiment | FE analysis | Experiment |
| Phase current [A peak] | 20 | 19.4 | 20 | 20.1 |
| Phase voltage [V peak] | 72.0 | 68.3 | 194.8 | 192.0 |
| Power factor | 0.981 | 0.974 | 0.927 | 0.921 |
| Output torque [Nm] | 17.2 | 16.1 | 17.2 | 16.6 |
| Efficiency [%] | 85.2 | 87.4 | 92.0 | 90.8 |

Demonstrator IMMD Power Converter and Controller

Power Converter Configuration

Although the initial testing of the demonstrator 10 kW machine described in the preceding section is being carried out using a commercial three phase inverter drive, a demonstrator power converter that incorporates the IMMD principles [5] was also developed during FY 2011 to demonstrate key concepts during this phase of the project while establishing a design that can be easily upgraded to the full-scale 30 kW (55 kW peak) prototype unit scheduled for development during the next phase of this project. This power converter has been designed to consist of six separate phase modules that incorporate the power switches, gate drives, current sensor, and controller in each phase module. A view of this new power converter configuration is provided in Fig. 5(a), which shows that the phase modules have been shaped to conform to the dimensions of the six stator core segments corresponding to the six machine phases. Hardware selection for this power converter was carried out to balance costs, availability, and high temperature operation [6].

Fig. 5(b) provides a more detailed solid-model view of one phase module in the new power converter showing that it consists of a four-layer PC board that has a dc link film capacitor mounted on it and a smaller PC board that has the two phase leg IGBTs soldered to it. The IGBT subassembly uses a high current eight-pin connector that makes it easy to connect and disconnect IGBTs from the main converter module board without soldering. This design achieves a power density of about 9 kW/L for the complete power converter while operating with 105°C water-ethylene glycol (WEG) coolant.

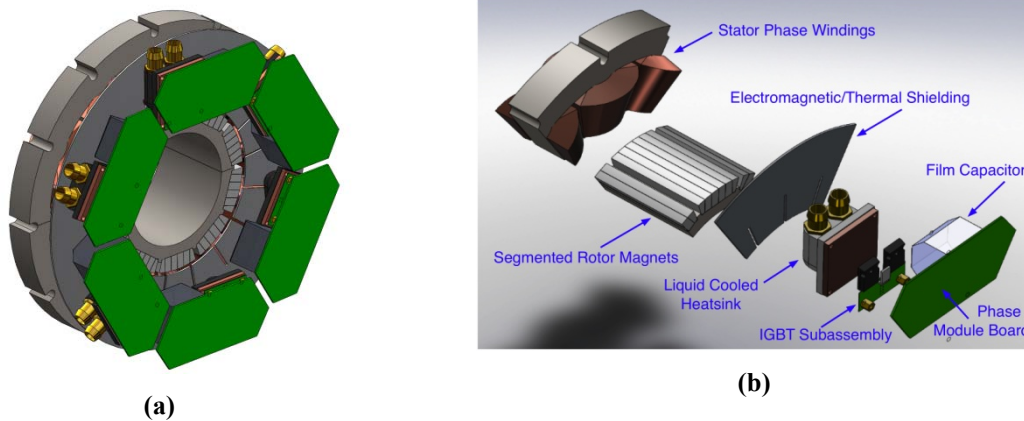


Fig. 5. Demonstrator 10 kW IMMD highlighting new six phase power converter configuration showing (a) complete power converter mounted on machine and (b) individual phase module.

The power switches for the 10 kW demonstrator are off-the-shelf IGBTs in TO-247 packages that have the power-handling capability and thermal performance needed for the 10kW power level. The IGBT subassembly is designed so that the IGBTs can be mounted on either liquid-cooled heatsink assemblies (as shown in Fig. 6) or air-cooled heat sinks, depending on the application. The adoption of the pin connector for the IGBT subassembly makes it straightforward to replace these commercial IGBTs with the new 200°C-rated power modules that are being developed as part of this project if they become available for testing in this demonstrator power converter in the future.

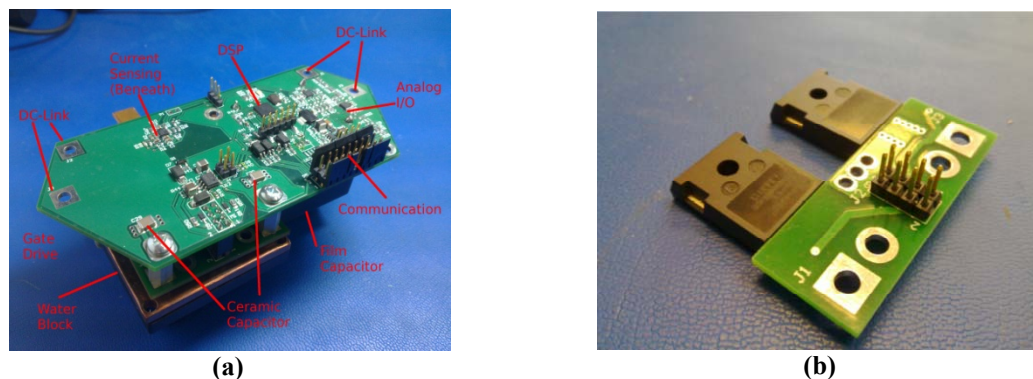


Fig. 6. Photos of new power converter hardware showing (a) complete phase module including film capacitor, IGBT subassembly, and water-cooled heat sink and (b) close-up view of IGBT subassembly.

Figure 7 shows the power circuit schematic for the demonstrator 10 kW IMMD. It shows that the six power converter phase modules are actually broken into two groups of three phases, with each group exciting a separate balanced wye-connected “star” set of stator windings. To improve the fault tolerance of the drive, the neutral points of the two star windings are not connected to each other [7].

A ring-and-star bus configuration with multiple layers of capacitance closely coupled to the switching nodes was adopted for the capacitors and dc bus structure for the IMMD. To this end, all IGBT half-bridges are decoupled directly at their power terminals by ceramic capacitors with large current-handling abilities and very low parasitics that help absorb switching transient energy in the megahertz range. Each module also has a 20 μF metalized film capacitor for bulk capacitance. Metalized film capacitors were chosen instead of electrolytics to increase the capacitor temperature limit to 125°C.

These film capacitors provide a total drive capacitance of 120 μF that is similar in value to several commercial drives with closely coupled high performance film capacitors. The power bus interconnections for the modules are provided by the bottom two layers of the main power converter board, which helps reduce power bus inductance and provides good decoupling for very high frequency noise.

Controller Configuration

Figure 8 shows the control architecture selected for implementing the IMMD's distributed control algorithm. Each phase is equipped with a dedicated digital signal processor that takes in analog measurements of current for its own phase as well as two adjacent phases. This information is then used to determine the complex current vector for the torque controller. Each phase controller is also provided the signals from a shaft encoder to determine rotor position. The neutral voltage for each phase is sensed and used to determine whether there are faults in any other phase winding of the star.

The drive commands, system status, and controller trim values are shared over a controller area network (CAN) bus between the phase modules and a user interface. Saturation of the CAN bus with critical control loop communications is avoided by using analog signals for sharing the current measurements.

The software architecture for each phase is modified from a standard field-oriented three phase drive for this distributed control algorithm. The control software uses the sensed currents and encoder position to regulate a complex current vector for each phase and assumes that the other phase controllers are doing the same. Fault tolerance is achieved externally to this loop as an error-checking function. Special attention is being devoted to designing the controller architecture to incorporate as many opportunities for enhancing the IMMD's fault tolerance as possible.



Fig. 7. Power circuit schematic for demonstrator 10 kW IMMD drive.



Fig. 8. Controller architecture for demonstrator 10 kW IMMD drive.

The dsPIC33 digital signal controller manufactured by Microchip was selected for implementing this control architecture. One of the attractive features of this processor is that it is available in a space-saving quad-flat, no-leads package and rated for operation at 140°C.

Si IGBT Ruggedness Evaluation at 200 °C

IGBTs are widely used in hard-switching applications where they are required to turn on or off rated current with full bus voltage across the terminals and also survive during malfunctions of systems such as short circuit conditions. To withstand the high stress conditions, these power devices are required to have robust safe operating areas. When temperature increases, the latch-up current is decreased because the current gains of the NPN and PNP transistors within an IGBT increase [8–9]. The static avalanche breakdown voltage increases with the temperature. However, the dynamic avalanche breakdown due to a current filament formation could deteriorate with high temperatures, which elevate the filament temperature before the self-heating [10–12]. In addition, the short circuit capability is also an important issue related to device ruggedness in high temperature operation, especially in practical motor drive applications [13–15].

To ensure the safe and reliable operation of the IGBT at 200°C, the high temperature IGBT ruggedness has to be verified by testing the safe operating area limits. The trench-gate field-stop IGBT with soft, fast recovery antiparallel diode from Infineon (IKW40N120H3) to be used in the IMMD power module was selected for ruggedness evaluation at high temperatures.

Latch-Up Immunity

“Latch-up” means the IGBT is tied to a state of continuous current conduction and gate voltage has no influence on output collector current. Today’s commercial IGBTs have good latch-up immunity with latch-up suppressed designs. At high temperature operation, however, the latch-up current is decreased because the current gains of the NPN and PNP transistors increase.

Because of this, the following experiment was conducted to evaluate the latch-up immunity of the IGBT in extreme conditions. The gate voltage, V_{GE} was increased from 15 V to 30 V to prevent the IGBT from saturation at a low current level. The gate resistance was reduced from 12 Ω to 3 Ω to increase the turn-off speed. Also the ambient temperature was increased to 250°C. As shown in Fig. 9, the IGBT turned off the current of 300 A with a small gate resistance (3 Ω) at 250°C. These experimental results demonstrated that the IGBT shows very good latch-up immunity even at very high temperatures.

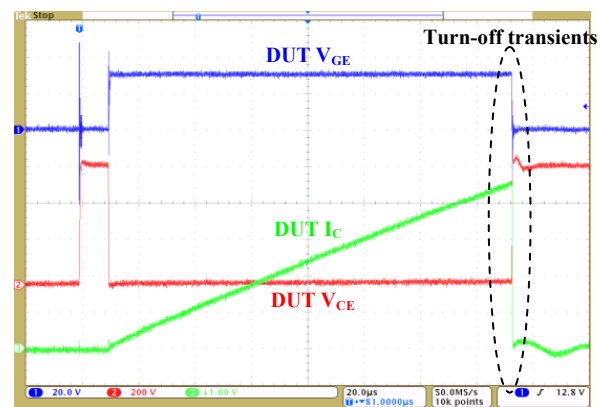


Fig. 9. Latch-up immunity evaluation in extreme conditions: gate voltage, $V_{GE} = 30$ V; gate resistance, $R_G = 3$ Ω ; and ambient temperature, $T = 250$ °C.

Short Circuit Capability

Short circuit capability is important especially for motor drive applications. When operating at high temperatures, the short circuit energy and short circuit withstand time are reduced due to the higher initial temperature. Therefore, for IGBT operation at the elevated temperature of 200°C, short circuit capability needed experimental evaluation.

Experiments were conducted to evaluate the short circuit capability of a trench-gate field stop IGBT operating at 200°C. Figure 10 shows the short circuit waveforms under hard switching fault condition at

25°C. In Fig. 10(a), the short circuit pulse is 32 μs . The device is turned off safely without destruction. In Fig. 10(b), the short circuit pulse is extended to 38 μs . The device looks as if it has safely turned off but destruction happens at 86 μs after the turn-off. A similar failure is reported in [13, 14]. At 200°C, the critical short circuit time is reduced to 22 μs .

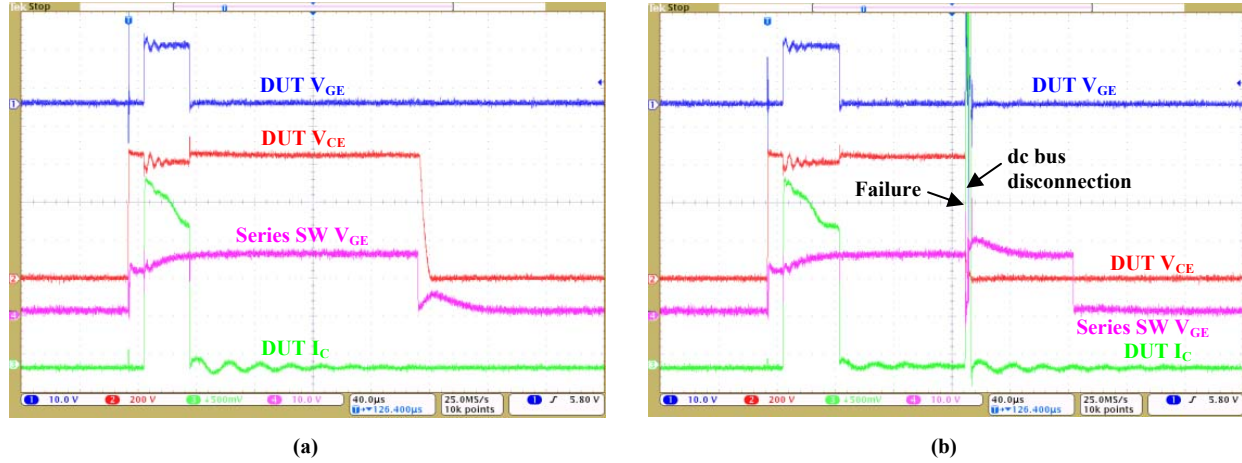


Fig. 10. Short circuit failure by thermal runaway at 25°C: (a) IGBT is turned off safely when short circuit pulse of 32 μs is applied at 25°C; (b) IGBT is destroyed at 86 μs after turn-off.

The short circuit pulse of 38 μs is destroyed at 25°C.

Experimental results showed that the 1,200 V, 40 A field stop IGBT experiences short circuit failure by thermal runaway during the off state due to the high temperature leakage current caused by heat spreading after short circuit turn-off. The critical short circuit time is reduced to 22 μs when operating at 200°C compared with 32 μs at 25°C, but it is still adequate for protection.

Dynamic Avalanche Capability

During turn-off transients of IGBT, the high di/dt can cause the voltage to spike as a result of parasitic inductance. When the threshold electric field is reached with both voltage and current presented in the IGBT structure, the dynamic avalanche occurs [12].

A large stray inductance of 1.25 μH was used in the test circuit to evaluate the turn-off capability of the IGBT at various temperatures. Figure 11 shows the turn-off transients of the device under test (DUT) with various dc bus voltages. The dc bus voltage, V_{DC} , is increased from 600 V to 850 V in increments of 50 V while the current, I_C , is maintained at 40 A. In normal conditions, the voltage spike increases with higher dc bus voltage. In Fig. 11, however, it is observed that the voltage spike of V_{CE} is suppressed to 1,350 V when various dc bus voltages are applied, which means the dynamic avalanche occurs in the DUT. With V_{DC} increasing, the avalanche sustaining time increases to 70 ns until the DUT fails.

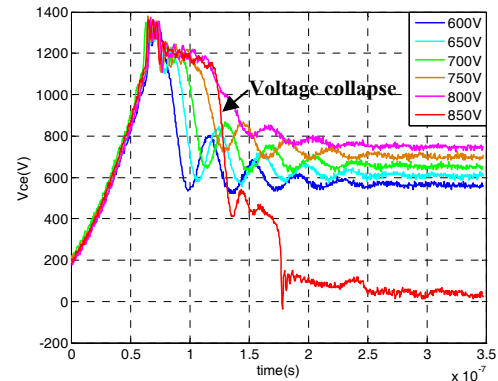


Fig. 11. V_{CE} voltage at turn-off with various V_{DC} applied when IGBT enters the dynamic avalanche mode at 25°C.

The avalanche capability of the DUT was further evaluated at 200°C where the avalanche sustaining time was reduced to 35 ns. These experimental results show that the 1,200 V IGBT under test has insufficient

avalanche capability and is very sensitive to overvoltage. It should not be operated exceeding the rated voltage in any cases from 25°C to 200°C.

Silicon IGBT Phase Leg Module for Operation at 200°C

This part of the report discusses suitable packaging and cooling for silicon IGBTs to achieve high temperature capability, high density, good thermal characteristics, and low cost.

IGBT Module Packaging Design

Wire-bonding technology was adopted for the design of the 10 kW phase leg power module. Two silicon IGBTs and two silicon diode dies from Infineon with maximum ratings of 1,200 V, 50 A, and 175°C were selected. A 10 mil aluminum wire with a maximum current rating of 22 A [16] was selected for wire bonding. Au80Sn20 solder was used for the die attachment, with optimized thickness of 200µm. Figure 12 shows the fabricated power module.

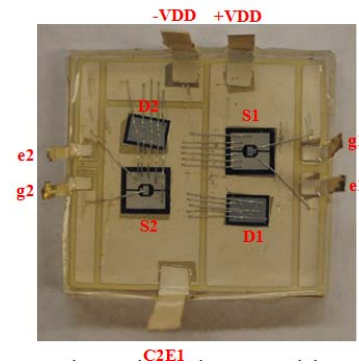


Fig. 12. Fabricated 10 kW power module.

IGBT Module Static Characterization

The static characterization of the fabricated power module was conducted with the curve tracer. Figure 13 shows the output characteristics of the IGBT at various temperatures. Figure 14 shows the leakage current at 650 V as a function of junction temperature. The leakage current is 3.98 mA at 200°C, which is smaller than that of the discrete device we characterized before (16.8 mA at 200°C).

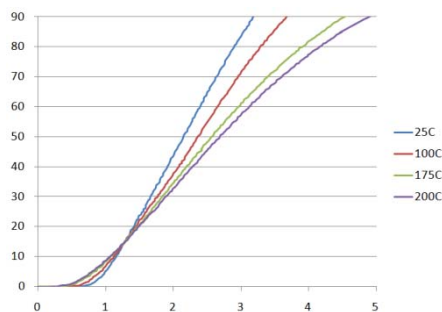


Fig. 13. Output characteristics of silicon IGBT module at various temperatures.

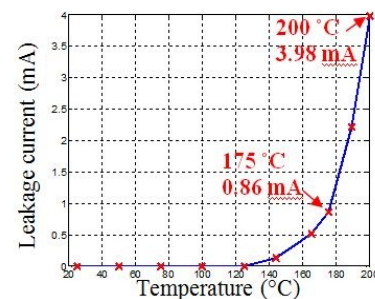


Fig. 14. Leakage current at 650 V as a function of junction temperature.

IGBT Module Switching Characterization

With the designed gate driver board and switching test board, the switching waveforms of the designed IGBT modules were tested and the switching losses estimated. Figure 15 shows the turn-on and turn-off waveforms at different temperatures, all at 650 Vdc and 70 A load current.

Figure 15 shows that the turn-on and turn-off time of the designed IGBT module increases with temperature, leading to higher switching loss for the IGBT module at higher temperatures. Furthermore, the reverse recovery of the diode is also worse at higher temperatures, also resulting in extra losses. The loss comparison is shown in Table 4.

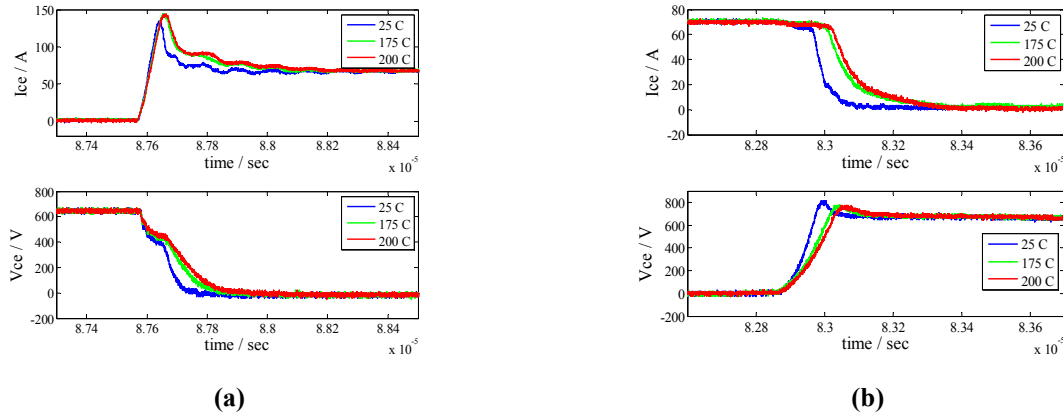


Fig. 15. Switching waveform comparison for designed IGBT phase leg module:
(a) turn-on transients; (b) turn-off transients.

Table 4. Switching loss comparison (650 Vdc, 70 A case)

| | Turn-on loss (mJ) | Turn-off loss (mJ) | Reverse recovery loss (mJ) |
|-------|-------------------|--------------------|----------------------------|
| 25°C | 3.9 | 3.2 | 1.2 |
| 175°C | 6.7 | 6.1 | 2.8 |
| 200°C | 7.2 | 6.5 | 3.2 |

IGBT Module Loss Calculation

Based on the static characterization of the 10 kW power module, the losses were calculated with the switching frequency at 12 kHz and compared with those of a phase leg composed of discrete devices. As shown in Fig. 16, the fabricated module has smaller leakage current loss, but larger conduction loss and reverse recovery loss compared to the discrete devices phase leg. The total losses of the two are close. The total loss for the 10 kW phase leg composed of the discrete devices is 245.73 W, and the efficiency is 97.54%. The total loss for the power module is 248.33 W, and the efficiency is 97.52%.

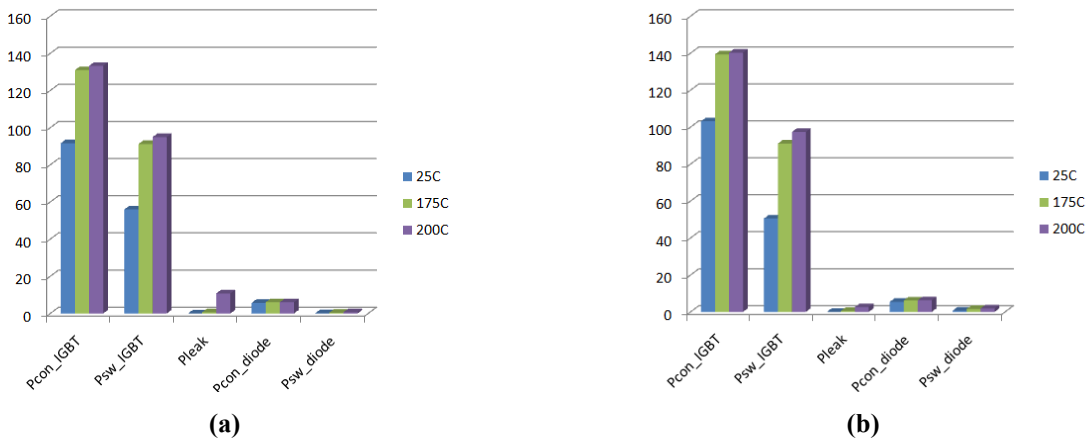


Fig. 16. Power losses in (a) a phase leg composed of discrete devices and
(b) the fabricated phase leg power module ($f_s=12$ kHz).

IGBT Module Thermal Performance Evaluation

The thermal management system is one of the key challenges in the motor drive. In today's vehicles, the inverter and motor use different cooling loops and coolants. One objective of this project is to use a single liquid cooling loop and coolant for both the inverter and motor. A two-pass-tube cold plate from Aavid Thermalloy was used for the baseline design of the cooling system. A 105°C WEG coolant with a flow rate of 2.5 GPM is used to cool the module.

Comsol was used to characterize the thermal performance of the proposed package and cooling system. Figure 17 shows the cooling performance of the packaging design. The maximum IGBT junction temperature is 193.6°C. The thermal resistance is 0.738°C/W.

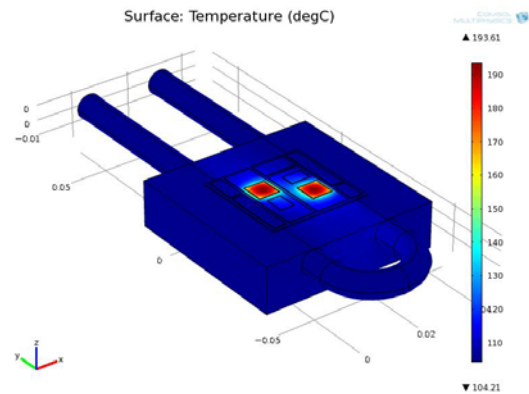


Fig. 17. Cooling performance of the packaging design.

Experiments were also conducted to evaluate the thermal performance. In the experiments, the junction temperature was measured using the electrical parameters of the device. The forward voltage drop of the IGBT was used as the temperature-sensitive parameter. The losses were generated with a heating pulse. The thermal resistance measured was 1.417°C/W, significantly larger than the simulation results of 0.738°C/W. The increased thermal resistance is mainly caused by the attachment layer between the power module and the cold plate, which needs to be improved in future work.

Design Approach for System-Level Electrical Architecture and Continuous Power Test

To test the designed IGBT phase leg module, gate-driver circuit, switching test (double-pulse-test) circuit, and main converter circuit are designed. To simplify the design and test, a flexible system-level electrical architecture that can accommodate both commercial IGBT modules and custom built modules was used. Figure 18 shows the gate driver board used for the custom IGBT modules.

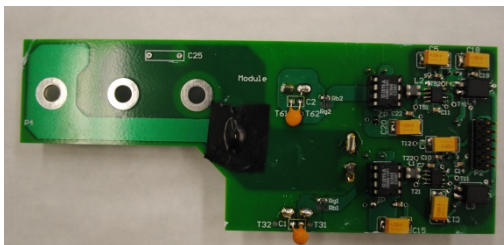


Fig. 18. Gate driver board for custom IGBT modules.

After the loss estimation and thermal design, a continuous power test for the custom IGBT phase leg module was conducted to verify the performance of the module in the converter. The test circuit, which is run as a buck converter, with the component parameters is shown in Fig. 19. With dc voltage of 650 V and duty cycle of 0.85, the converter runs with 10 kW output power and 12 kHz switching frequency. Liquid cooling is applied to the converter at a 2.5 GPM flow rate. Liquid at 25°C was used for preliminary evaluation due to the limitations of the fabricated module thermal performance.

Experimental results are shown in Fig. 20, with the V_{CE} and V_{GE} of bottom IGBT, load voltage, and inductor current. This test verified the 10 kW power conversion capability of the designed IGBT module.

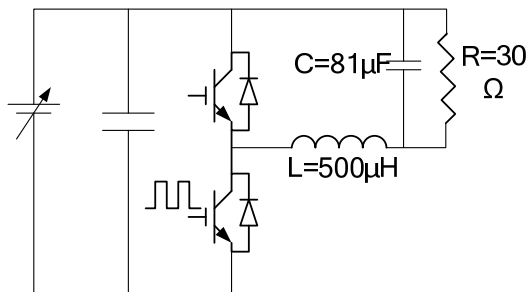


Fig. 19 Circuit for continuous test.

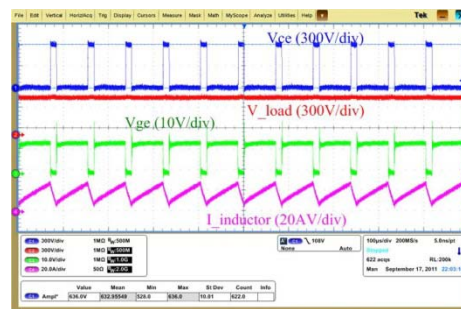


Fig. 20. Experimental results for 10 kW phase leg power module.

Conclusion

Significant progress has been made during FY 2011 toward demonstrating the key concepts associated with the integrated traction drive system. A 10 kW demonstrator version of the six phase, 10-pole SPM machine has been successfully fabricated and tested using a commercial three phase inverter for the initial tests. The matches between the predicted and measured machine parameters and torque production characteristics are very good, raising confidence in the machine modeling tools. A demonstrator version of the six phase modular power converter has also been developed for mounting immediately adjacent to the machine stator end windings. Each phase module includes a half-bridge IGBT power stage for exciting the associated phase winding and a dedicated controller chip and current sensor for controlling the phase excitation. The preferred heterarchical control architecture has been implemented to achieve the desired high levels of fault tolerance. According to this architecture, the loss of any one of the controllers does not affect the remaining five healthy controllers, providing the basis for achieving robust control of the integrated traction drive.

The silicon IGBT ruggedness operating at high temperatures was evaluated with a safe operating area test circuit, showing that the selected IGBT has good latch-up immunity and decreased but still adequate short circuit capability at 200°C. The IGBT has limited avalanche capability from 25°C to 200°C, so the rated voltage should not be exceeded in any cases. The 10 kW power module was designed and fabricated, and the electrical and thermal characteristics were tested. Compared to the discrete device tested in FY 2010, the module has smaller leakage current but large on-state voltage drop and reverse recovery current. The total losses of the two are very close. The thermal resistance of the fabricated power module is larger than the simulation results, caused by poor attachment between module and cold plate, which will be improved in future work. A continuous power test has been completed for the phase leg module. The module can work for 10 kW output power with 12 kHz switching frequency with the 25°C liquid cooling.

Patents

None.

Publications

1. G. Choi, Z. Xu, M. Li, S. Gupta, T. M. Jahns, F. Wang, N. A. Duffie, and L. Marilino, "Development of integrated modular motor drive for traction applications," *SAE International Journal of Engines*, vol. 4(1), pp. 286–300, June 2011.
2. Z. Xu, M. Li, F. Wang, and Z. Liang, "Investigation of Si IGBT operation at 200 °C for traction applications," in *IEEE Energy Conversion Congress and Expo (ECCE)*, 2011, pp. 2397–2404.
3. Z. Xu, and F. Wang, "Experimental investigation of Si IGBT short circuit capability at 200°C," *IEEE APEC*, 2012, submitted.

4. Z. Xu, M. Li, P. Ning, F. Wang, and Z. Liang, "Si IGBT phase-leg module packaging and cooling design for operation at 200 °C in hybrid electrical vehicle applications," *IEEE APEC*, 2012, submitted.

References

1. G. Choi and T. M. Jahns, *Update on High Power Density Fractional Slot Concentrated Winding Modular PM Machine Design*, Integrated Modular Motor Drive Project Report, University of Wisconsin-Madison, April 2010.
2. A. M. EL-Refaie, *High Speed Operation of PM Machines*, PhD thesis, University of Wisconsin-Madison, 2005.
3. A. M. EL-Refaie and T. M. Jahns, "Comparison of synchronous PM machine types for wide constant-power speed range operation," in *Proc. IEEE IAS Annu. Meeting*, 2005, pp. 1015–1022.
4. J. K. Tangudu and T. M. Jahns, "Comparison of interior PM machines with concentrated and distributed stator windings for traction applications," in *Proc. of 2011 IEEE Vehicle Power and Propulsion Conference (VPPC'11)*, 2011.
5. N. R. Brown, T. M. Jahns, and R. D. Lorenz, "Power converter design for an integrated modular motor drive," in *Rec. of 2007 IEEE Industry Applications Society Annual Meeting (IAS'07)*, 2007, pp. 1322–1328.
6. C. Buttay, D. Planson, B. Allard, D. Bergogne, P. Bevilacqua, C. Joubert, M. Lazar, C. Martin, H. Morel, D. Tournier, and C. Raynaud, "State of the art of high temperature power electronics," presented at *Microtherm 2009*, 2009, pp. 1–10.
7. B. A. Welchko, T. A. Lipo, T. M. Jahns, and S. E. Schultz, "Fault tolerance three-phase ac motor drive topologies: A comparison of features, cost, limitations," *IEEE Trans. Power Electron.*, vol. 19(4), pp. 1108–1116, July 2004.
8. A. Bhalla, S. Shekhawat, J. Gladish, J. Yedinak, and G. Dolny, "IGBT Behavior During Desat Detection and Short Circuit Fault Protection," in *Proc. IEEE ISPSD*, 1998, pp. 245–248.
9. A. Muller, F. Pfirsch, and D. Silber, "Trench IGBT Behaviour near to Latch-up Conditions," in *Proc. IEEE ISPSD*, 2005, pp. 255–258.
10. M. Trivedi and K. Shenai, "Failure Mechanisms of IGBTs under Short-Circuit and Clamped Inductive Switching Stress," *IEEE Trans. on Power Electronics*, vol. 14(1), pp. 108–116, January 1999.
11. K. H. Oh, Y. C. Kim, K. H. Lee, and C. M. Yun, "Investigation of Short-Circuit Failure Limited by Dynamic-Avalanche Capability in 600-V Punchthrough IGBTs," *IEEE Trans. on Device and Materials Reliability*, vol. 6(1), pp. 2–8, March 2006.
12. C. C. Shen, A. R. Hefner, D. W. Berning, and J. B. Bernstein, "Failure Dynamics of the IGBT during Turn-off for Unclamped Inductive Loading Conditions," *IEEE Trans. on Industry Applications*, vol. 36(2), pp. 614–624, March/April 2000.
13. M. Otsuki, Y. Onozawa, M. Kirisawa, H. Kanemaru, K. Yoshihara, and Y. Seki, "Investigation on the Short-Circuit Capability of 1200V Trench Gate Field-Stop IGBTs," in *Proc. IEEE ISPSD*, 2002, pp. 281–284.
14. A. Benmansour, S. Azzopardia, J. C. Martina, and E. Woirgarda, "Failure Mechanism of Trench IGBT under Short-circuit after Turn-off," *Microelectronics and Reliability*, vol. 46, no. 9-11, pp. 1778–1783, Sept.–Nov. 2006.
15. C. Abbate, G. Busatto, and F. Iannuzzo, "IGBT RBSOA non-destructive testing methods Analysis and discussion", *Microelectronics Reliability*, vol. 50, no. 9-11, pp. 1731-1737, Sept. –Nov. 2010.
16. W. W. Sheng and R. P. Colino, *Power Electronic Modules: Design and Manufacture*, CRC press, Boca Raton, 2005.

4.3 Novel Packaging to Reduce Stray Inductance in Power Electronics

Principal Investigator: Leon M. Tolbert

Oak Ridge National Laboratory

National Transportation Research Center

2360 Cherahala Boulevard

Knoxville, TN 37932

Voice: 865-946-1332; Fax: 865-946-1262; E-mail: tolbertlm@ornl.gov

DOE Technology Development Manager: Susan A. Rogers

Voice: 202-586-8997; Fax: 202-586-1600; E-mail: Susan.Rogers@ee.doe.gov

ORNL Program Manager: Mitch Olszewski

Voice: 865-946-1350; Fax: 865-946-1262; E-mail: olszewskim@ornl.gov

Objectives

- Package devices in large power modules such that stray inductance is reduced.
- Reduce the stress on the insulated gate bipolar transistors (IGBTs) in hybrid electric vehicle (HEV) traction drives and dc-dc converters so that the IGBTs can work at higher power ratings and/or have better reliability and longer lifetimes.
- Reduce the distortion in output voltage.
- Improve reliability of converters.

Approach

- Layout design of phase leg module using P-cell and N-cell technique (i.e., series connection of IGBT and diode instead of antiparallel connection of IGBT and diode).
- Perform electromagnetic-field simulation of the package to extract the parasitics using Ansoft Q3D extractor.
- Perform circuit simulation for switching characterization with package parasitics.
- Use impedance analyzer to measure the parasitics in a prototype phase leg module.
- Use double pulse testing to experimentally test the switching behavior of the phase leg module.

Major Accomplishments

- Fabricated prototypes of the power modules.
- Obtained steady state characteristics for and measured the parasitics (stray inductance and resistance) of the modules.
- Built experimental setup for the double pulse test. Several methods were used to improve the accuracy of the measurement. The experimental results show 11 V lower overshoot voltage during IGBT turn-off in the proposed module than in the conventional module as a result of the reduction of the module stray inductance.
- Applied the novel switching cell concept in a multichip module (two chips in parallel for an individual switch position). The proposed layout and a conventional layout were designed in ANSYS Q3D Extractor.
- Studied switching characteristics under module inductance using Saber simulation.
- Fabricated modules for the multichip module, and measured the stray inductance in the modules experimentally.
-

Future Direction

- This project will not be funded by the DOE Vehicle Technologies Program beyond FY 2011.

Technical Discussion

In FY 2010, the module layout was designed and the parasitics were extracted using Q3D Extractor. Switching characterization was carried out using Saber simulation. The next step, which was the main work for FY 2011, was to fabricate the proposed module, measure the stray inductance, and build an experimental setup to verify the simulation.

Parasitics Measurement

Because an IGBT is a normally off device, the commutation loop is not conducting by nature. Thus, the inductance should be measured part by part. However, because the inductance is so small (a few nanohenries), it is difficult to obtain an accurate measurement of the individual stray inductances. Also, it does not take the coupling effect between the pieces into account. In the Q3D simulation, the devices are set to copper to get a conductive commutation loop. Actually, this has the same effect as if the devices were set to conductor and the wires bonded directly to the direct bonded copper (DBC) substrate. Therefore, modules without devices were fabricated and the wires were bonded directly to the DBC. To measure the commutation loop formed by S1 and D2, the wires were bonded directly to the DBC where S1 and D2 seat, as shown in Fig. 1(a). The conducting trace actually is from terminal C1 through the DBC copper trace to S1 and through a group of bonding wires to the DBC, where the output terminal seats, and then through another set of wires to D2 and from D2 through another group of wires to the negative terminal E2.

Taking the same method, commutation Loop 2 in the conventional phase leg and commutation Loop 1 and Loop 2 in the proposed phase leg were fabricated as shown in Figs. 1(b), (c), and (d). Basically, they are the etched DBC patterns with wires which are bonded to the position of the devices that should conduct in the commutation loop. The commutation loops are made conductive this way and the stray inductance is measured.

Another concern is the measuring equipment. Because the inductance is very small, Agilent precision impedance analyzer 4294A was used. It has a wide measurement frequency range: from 40 Hz to 110 MHz. Meanwhile, using the correct probe fixture is also critical in this measurement. The commonly used alligator probe is not proper in this condition. The wires with the alligator probe introduce parasitics that are comparable to the one under test. Thus a pin probe was used; the shape of the probe is fixed. The parasitics with this probe is small and can be completely compensated using calibration.

Table 1 compares results of the measurement and simulation. The measurement value should compare with the ac simulation results because ac excitation is used in measurement.

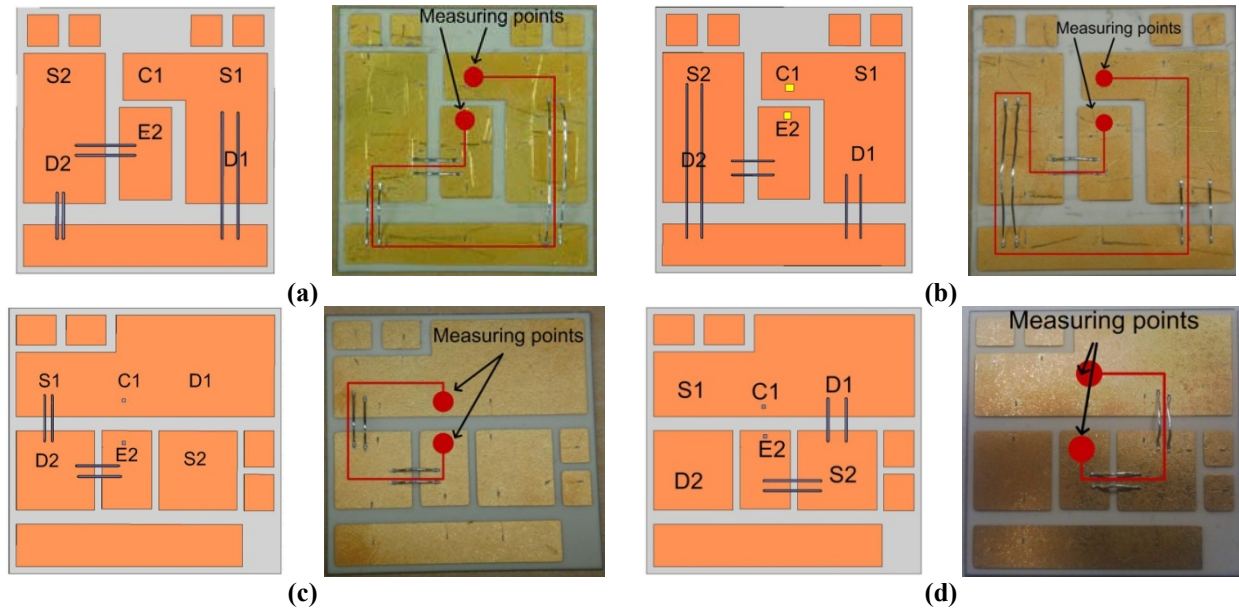


Fig. 1. DBC pattern with bonding wires designed for parasitic measurement: (a) conventional module Loop 1, (b) conventional module Loop 2, (c) proposed module Loop 1, and (d) proposed module Loop 2.

Table 1. Comparison of stray inductance measurement and simulation

| | | Simulation results (nH) | Measurement results (nH) |
|---------------------|--------|-------------------------|--------------------------|
| Conventional module | Loop 1 | 20.5 | 25 |
| | Loop 2 | 20.3 | 21 |
| Proposed module | Loop 1 | 7.2 | 6.5 |
| | Loop 2 | 8.6 | 6.0 |

Switching Characterization

Double Pulse Tester

Switching characterization can be conducted with only two pulses instead of a practical converter. The first pulse is used to charge the load inductor to the testing current, and then the device under test (DUT) is turned off. As a result, the turn-off characteristic can be captured. After a few microseconds the device is turned back on, and its turn-on characteristic is obtained. Figure 2 shows the double pulse tester (DPT) printed circuit board. A 450 V, 1,000 μF electrolytic capacitor is soldered at the back of the board. Three low inductance 300 nH film capacitors and twenty 100 nH ceramic capacitors together work as decoupling capacitors. A shunt resistor is used to measure current. The power module is attached at the back of the board. Also, the gate drive circuit is on the same board and close to the gate terminal of the power module. BNC (Bayonet-Neill-Concelman) connectors are used for accurate voltage measurement.

The DPT circuit parameters and testing condition are shown in Table 2. A large electrolytic capacitor is necessary as energy storage. Actually, a large part of the load current draws from this capacitor as there is usually a long cable connected from the dc voltage source and impedance is much higher. During switching transitions, the dc source and C_{bulk} will not be able to provide adequate energy quickly enough due to high values of equivalent series resistance (ESR) and equivalent series inductance (ESL), leading to large ringing of the voltage across the positive and negative buses. Decoupling capacitors with low ESR and ESL must be added to provide a low impedance path for the transient current. Film and ceramic capacitors, which have low ESR and ESL, were selected for this purpose. Paralleling of the decoupling capacitor is also useful, to reduce the ESR and ESL of the decoupling capacitors themselves.

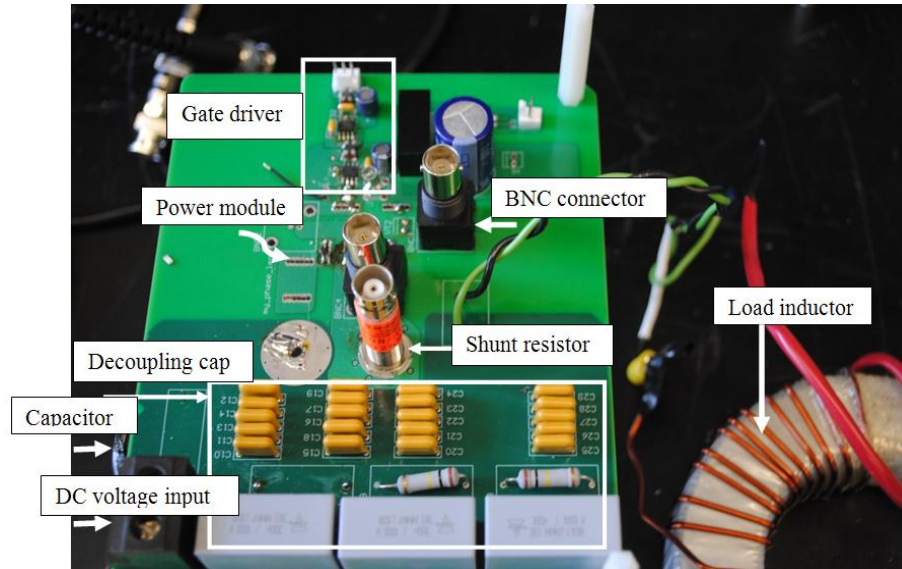


Fig. 2. Printed circuit board of DPT.

Table 2. Circuit Parameters

| Parameters | Value/Rating |
|---|-----------------------------|
| dc electrolytic capacitor C_{bulk} | 1,000 μF , 450 V |
| dc decoupling capacitors C_{dec} | 2.9 μF |
| Gate resistor | 3 Ω |
| IGBT 5SMY 12J1280 | 1,200 V, 75 A |
| Diode 5SLY12F1200 | 1,200 V, 75 A |
| Load inductor | 47 μH |
| dc link voltage | 300 V |
| Testing current | 75 A |

The current measured here is IGBT current, I_C . During transition, the current slope is very sharp (from the datasheet of the ABB IGBT, the rise time is 50 ns while the fall time is 75 ns). This equals a frequency of $f = 0.5 / t_r = 5 \text{ MHz}$. Typically a frequency margin of 5 times is maintained, so the current sensor should have a bandwidth of at least 25 MHz. A coaxial shunt resistor was selected as the current sensor. The connection to the oscilloscope was through a coaxial cable, which eliminates the probe connection. The voltage across the resistor has to be less than 10 V as there is no attenuation for the coaxial cable. This voltage was directly connected to the oscilloscope. In this experiment the testing current was 75 A; during reverse recovery, the current can be as high as 150 A. The resistance should be less than 0.06 Ω . A 0.025 Ω shunt resistor from T&M research was selected for this experiment. The bandwidth is 1,200 MHz, and the power rating is 3 mJ.

The input impedance of the voltage probe can be modeled as a capacitor of around 10 nF and a resistor of 10 M Ω in parallel. The ground lead of the voltage probe introduces stray inductance, which forms an LC resonant circuit with the input capacitor. If a step voltage is applied at the probe, high frequency resonance can occur. Then the detected voltage is not the step voltage itself but the resonance at the capacitor. This phenomenon is obvious when measuring high dv/dt . For accurate voltage measurement in this experiment, the grounding leads were removed and tip adaptors were used. When measuring gate voltage using P6139, a tip adaptor, Tek 131 5031 00, is used. The high voltage probe has a different tip to BNC adaptor, Tek 013 0291 01. Then a BNC jack is used on the printed circuit board. The use of a tip adaptor eliminates the grounding lead, which reduces the stray inductance in the probe.

IGBT Die Voltage Measurement

In the past, any voltage measurement was from the terminals of the module or device; however, that will not work in this case because it does not take the voltage drop of the module stray inductance into account, and one of the purposes of this project is to compare the difference of the voltage drop of the stray inductance for different layout techniques. Therefore, the voltage that should be measured here is the true stress on the IGBT die.

As part of this research, a new method was proposed to measure the die voltage. Two wires are attached to the collector and emitter side of the die. Then the wires are twisted and connected to the board, where the BNC connector and adapter are used to connect to the oscilloscope. As shown in Fig. 3(a), one wire is soldered to the DBC near the IGBT die under test to get the collector signal of point A. Because the top emitter pad cannot be soldered, the other wire is soldered to the auxiliary emitter for the gate signal, point B in Fig. 3(a). Attention should be paid here that there are two groups of bonding wires connected out from the emitter side of the die, power emitter, and auxiliary emitter. Because the gate drive current is very small, point B can represent the voltage of the IGBT emitter because the voltage drop associated with this small current through the bonding wires is negligible.

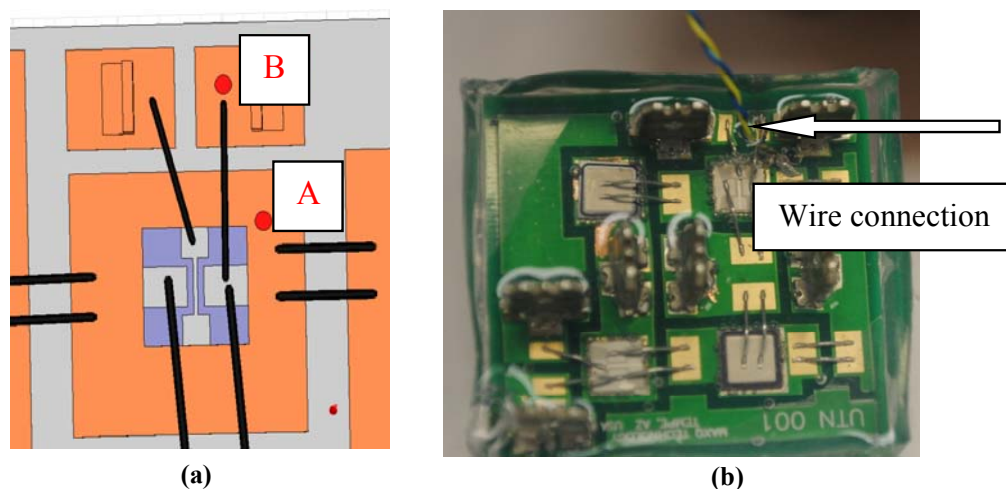


Fig. 3. Module with wire connection from IGBT die: (a) wire soldering schematic and (b) photo of finished module.

Using the method described above, the voltage was measured across the IGBT die. At the same time, voltage across the terminals was also measured, as shown in Fig. 4. Taking the measurement for the conventional module as an example, the voltage across the IGBT die is 392 V, while the voltage at the terminal is 376 V, which indicates that there is a 16 V voltage drop across the module stray inductance. It is the same for the proposed module measurement, but because the module stray inductance in the proposed module is reduced, the difference is only 10 V.

Experimental Results

The turn-off current and voltage waveforms for both the conventional and proposed modules are shown in Fig. 5. At the test condition of 300 V and 75 A, the overshoot voltage in the conventional module [Fig. 5(a)] was higher than that in the proposed module [Fig. 5(b)]. It is clear in these two figures that the overshoot voltage is 92 V and 81 V, respectively, for the conventional and the proposed modules.

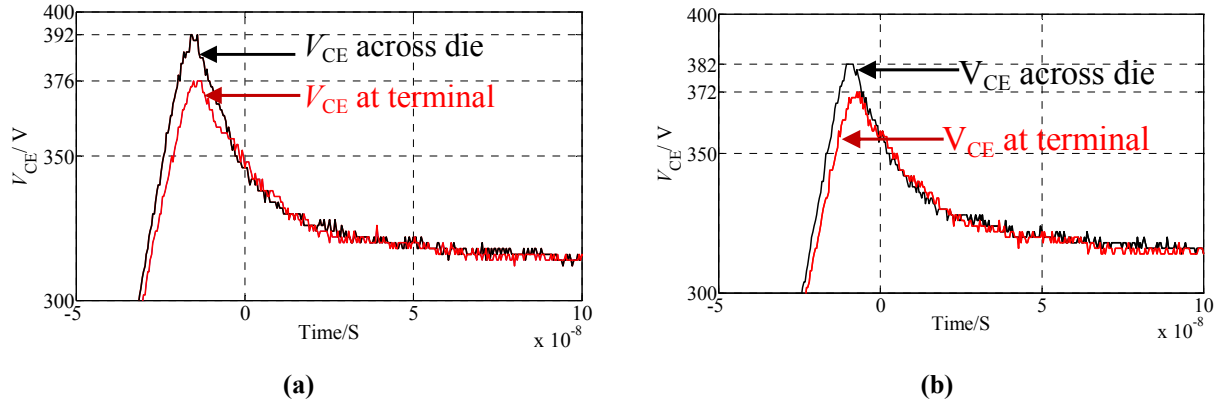


Fig. 4. Enlarged waveform of turn-off voltage of IGBT die at different measuring points:
(a) conventional module and (b) proposed module.

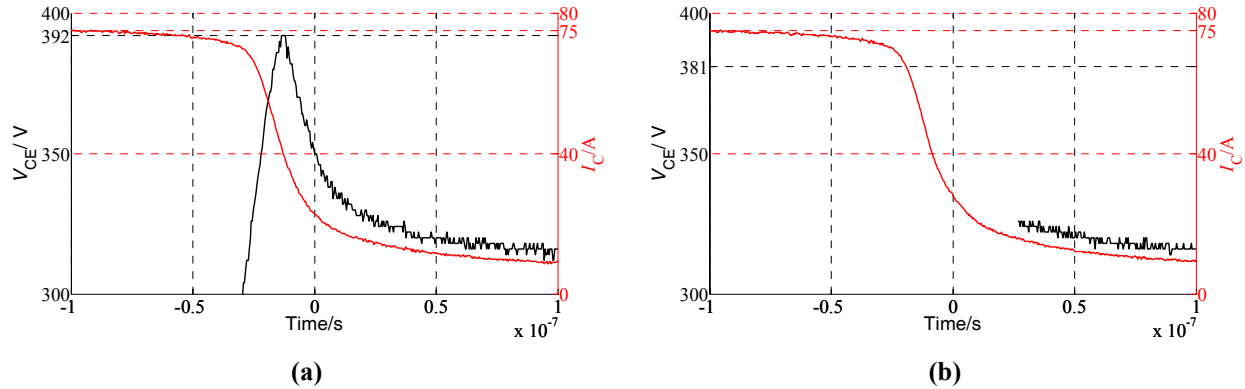


Fig. 5. Voltage overshoot during turn-off for (a) conventional module and (b) proposed module.

The turn-off current slope was also calculated (Fig. 6). The slope in the conventional module was 2,550 A/ μ s, while in the proposed module it was 2,650 A/ μ s. The reduction of stray inductance can accelerate the switching speed.

During turn-on, the space charge stored in the depletion region because of the large reverse-bias voltage is removed by the forward current. Then the excess-carrier distribution in the drift region grows. As the forward current grows in time, there is an increasingly large voltage drop across the drift region because there is no conductivity modulation of the region until the space charge layer is discharged to its thermal equilibrium value at around 40 V. This voltage is measured at the module terminals; therefore it also includes the voltage drop at the module stray inductance. It is difficult to separate the two parts.

The switching loss is calculated using the math function on the oscilloscope. To get an accurate measurement of the loss, synchronization of the voltage (channel one) and current signal (channel 2) is necessary. The propagation delay of the high voltage probe P5100, which is 14.9 ns, can be detected automatically by the scope. The propagation delay of the current channel was 7.4 ns. First, the voltage and current are multiplied using math function and saved to R1. Then the R1 signal is integrated as the red waveform (Fig. 7). The energy increase from cursor “a” to cursor “b” is the turn-off loss. In the conventional module it was 3.16 mJ, and in the proposed module it was 3.10 mJ.

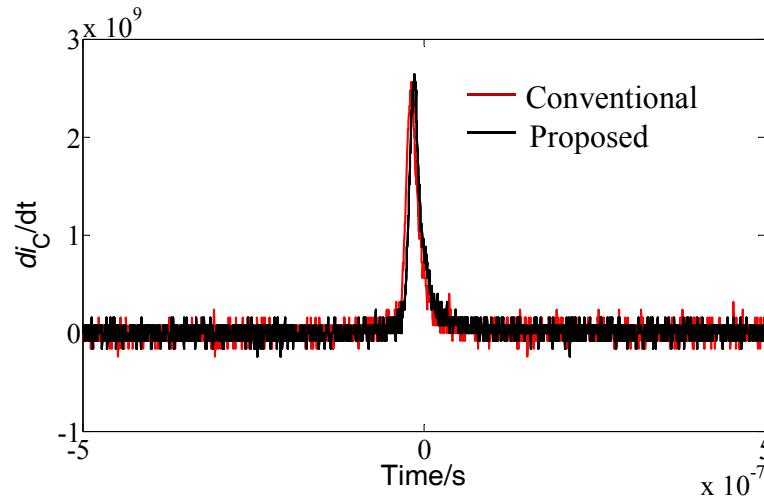


Fig. 6. Slope of the turn-off current.

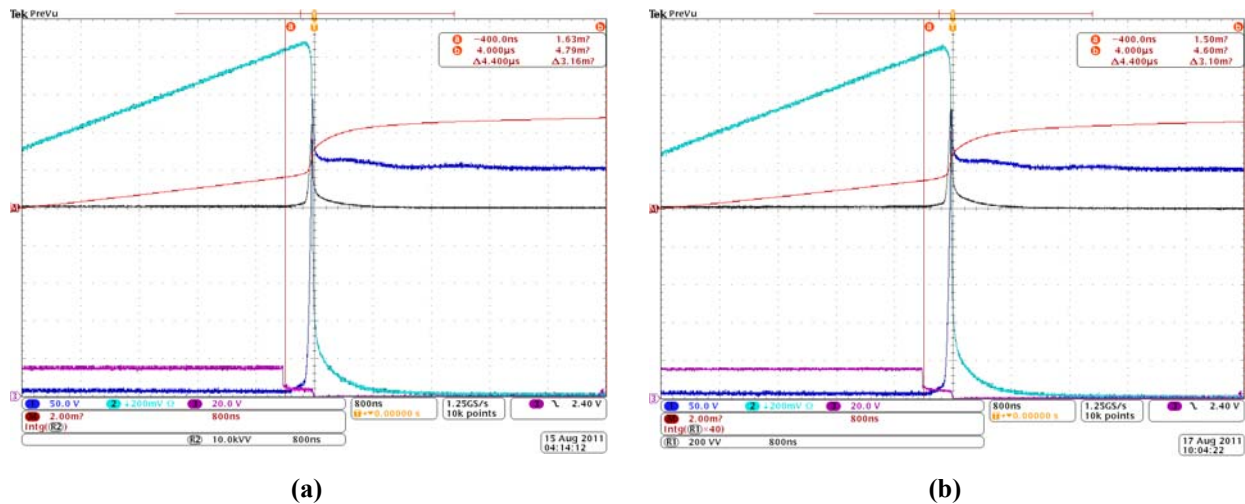


Fig. 7. Turn-off loss calculation for (a) conventional module and (b) proposed module.

Using Novel Switching Cells in IGBT Module with Paralleled Chips

In mid or high power areas, such as HEVs, many IGBTs and diode chips are connected in parallel inside the module to increase the current capability. In the packaging of multichip IGBT modules, except reducing loop stray inductance, another concern is the mismatch of the parameters of the two paralleled loops. More uniform parasitics and dice characteristics in the module offer more even distribution of current and commutation voltage conditions between chips, which helps to keep the components inside the module at similar temperatures, enables better use of silicon, and minimizes potential early wear out failures due to degradation over module lifetime. Power modules with two devices in parallel were studied using a conventional layout designed according to a commercial module and a multichip module designed using the P-cell–N-cell concept. Parasitics were extracted for both modules, and Saber simulation was conducted for the electrical characteristics under different parasitics.

Layout Design of Multichip Power Modules

A commercial module from a hybrid electrical vehicle 3 was used for the conventional layout [Fig. 8(a)]. The antiparalleled IGBT and diode form the upper and lower cells. The upper cell is in one piece of the DBC, while the lower cell is in another.

The parasitic model of the commercial multichip power module is shown in Fig. 8(b). The parasitic model is based on the physical layout. The parasitic inductance was extracted piece by piece. The commutation loop inductance can be calculated by adding them together, which is 24 nH for one of the die and 25.4 nH for the second die. The mismatch of the inductance is 1.4 nH. The parasitic resistance was also extracted. Because the resistance doesn't affect transient behavior much but does affect the steady state current distribution, the resistance was extracted under the condition of dc excitation. The resistances of the paralleled upper branch are 1.0 m Ω and 1.1 m Ω for each of the two die; while in the two lower branches, they are 0.9 m Ω and 1.0 m Ω respectively.

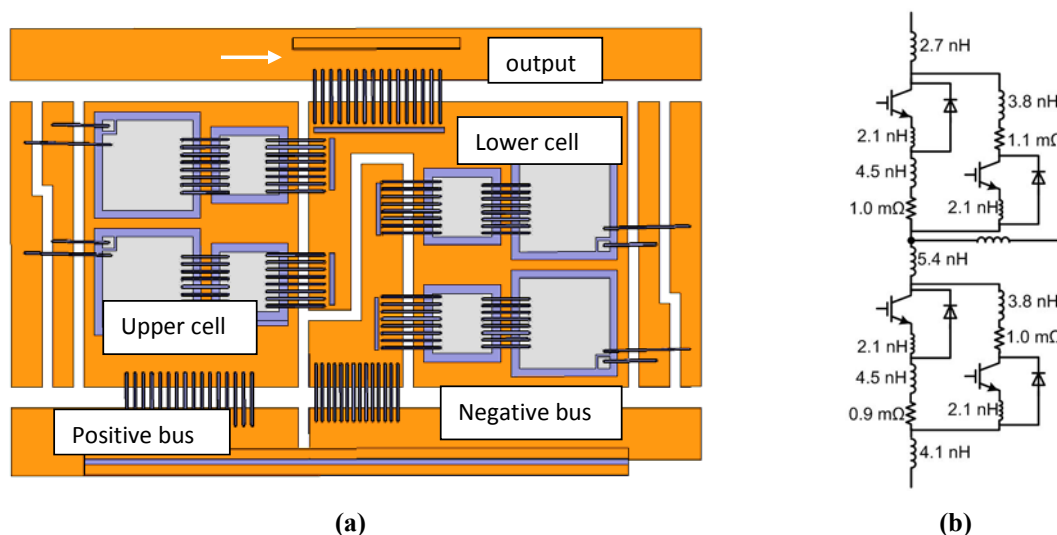


Fig. 8. Commercial IGBT module showing (a) layout with paralleled dice and (b) parasitics extraction.

Another layout using P-cell and N-cell was also designed [Fig. 9(a)]. In this design, the commuting IGBTs and diodes, identified as P-cell or N-cell, are arranged together. The parasitics was modeled differently from the conventional module, as shown in Fig. 9(b). In this arrangement, the stray inductance has been reduced to some extent. In P-cell the loop inductances were 14.2 nH and 24.3 nH, respectively, for the two die; in N-cell the loop inductances were 21.4 nH and 16.5 nH, respectively, for the two die. The dc resistance was also extracted and is reflected in the model. It is worthwhile to point out that the resistance is between the output and positive or negative bus. For example, if the IGBTs in P-cell are conducting, the paths are shown in Fig. 9 as the white and black lines. From the layout, it can be seen that the two conducting paths have similar lengths. Therefore, the resistance in the paralleled branches, about 1 m Ω , is similar.

Comparing the two layouts, it can be concluded that, in general, the proposed method has short commutation loops for some branches; however, the length of each paralleled loop is different, and this creates inductance mismatch. The mismatch can become serious as the paralleled branches increase. The conventional layout has similar loop length for each parallel loop, although the stray inductance value is at the level of the largest in the proposed layout. As for dc resistance, the two layouts have similar values and there is no mismatch either design. The effect during the transient activity is discussed in the next section.

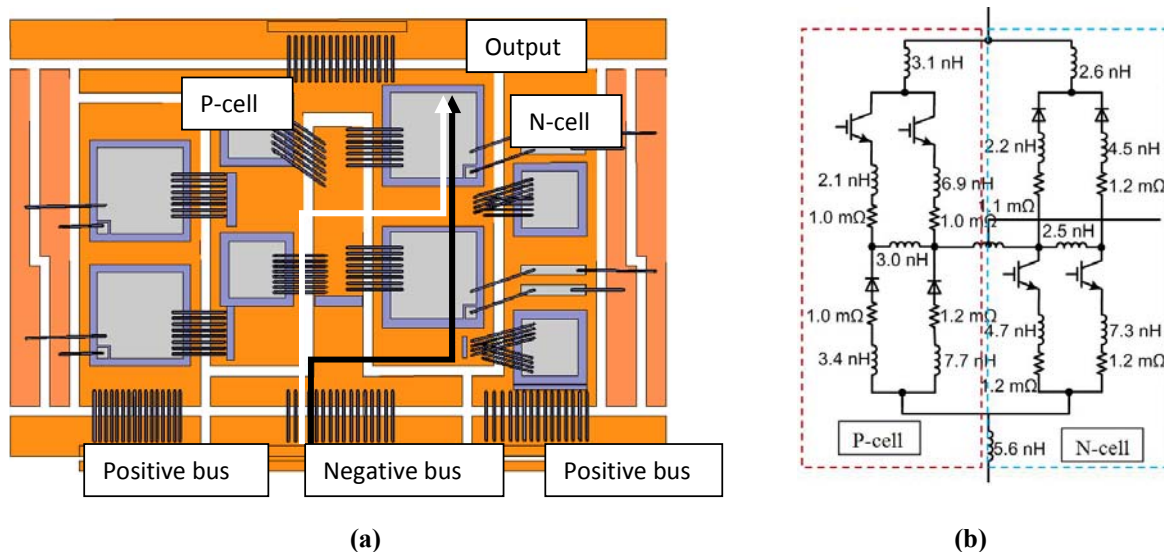


Fig. 9. Novel IGBT module: (a) layout showing switching cells and (b) parasitics extraction.

Electrical Evaluation of Switching Characteristics of Multichip Module

To study the switching behavior of the multichip modules under different parasitics, a DPT with detailed module parasitics was built in Synopsys Saber.

The transient voltages and currents on the IGBTs and diodes are shown in Figs. 10, 11, and 12. In each figure, there are four waveforms, which are the two paralleled devices in two layouts. The green and orange lines are from the conventional design, and the blue and purple lines are for the proposed layout. The turn-off voltages on the IGBTs are shown in Fig. 10. The overshoot voltage is higher in the conventional layout. The reason is that there is some common stray inductance between the upper and lower cells; the whole current 150 A flows through this path and the voltage drop is thus higher. In the proposed layout, the two paralleled paths and their parasitics are relatively separated. The turn-off voltage in the two paralleled devices in the proposed module is not the same, caused by the mismatch of the parasitic inductance of the two loops. Although it is not serious, it might cause loss mismatch in the long run. This compromises the benefit of the proposed layout.

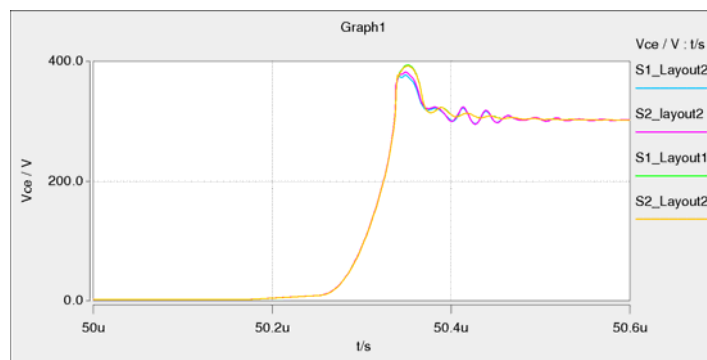


Fig. 10. Turn-off voltages of IGBTs.

Figure 11 shows the turn-on currents of the IGBTs. The currents peak because the reverse recovery is higher, and the oscillation after turn-on is more severe in the conventional module. However, as expected there is some mismatch for the transient current in the proposed module.

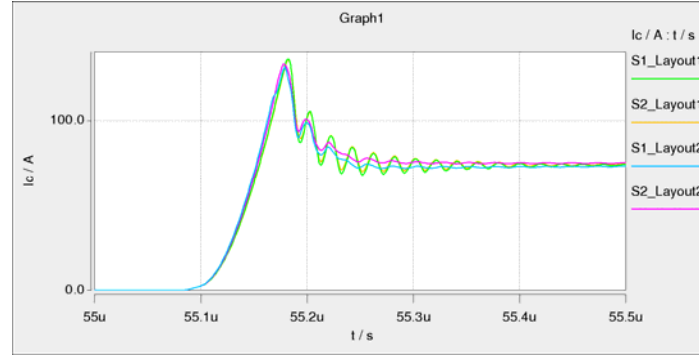


Fig. 11. Turn-on currents of IGBTs.

Figure 12 shows the turn-on currents of the diodes. It can be seen that the diode currents are significantly affected by the stray inductance. Therefore, the mismatch between the two devices in the proposed layout is around 25 A. Because the two paralleled loops in the conventional module are not identical, there is also some mismatch in this module.

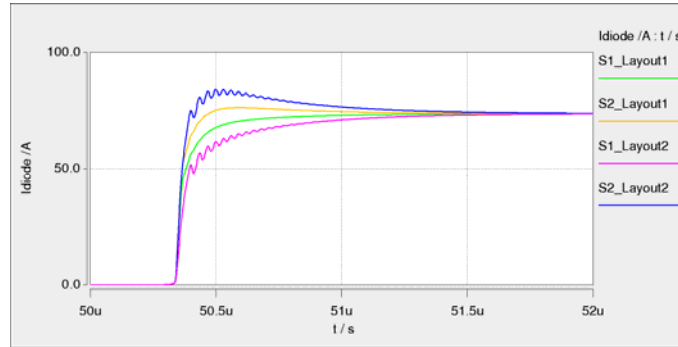


Fig. 12. Turn-on currents of diodes.

Measurement of the Parasitics in the Multichip Modules

Figure 13 shows different commutation loops in the conventional layout design. To ease the measurement, the bus bars have been removed and only the substrate inductance is taken into account. It should be mentioned that the identified loops are not exactly the current path. For example, in Fig. 13(a), the current which goes through IGBT A, does not exactly pass diode B. It would be more accurate to model the module inductance as shown in Fig. 13(b); however, it is not realistic to measure the stray inductance part to part in practice. Figures 13(a) and (b) show the two paralleled paths, Loop 1 and Loop 2, that are formed by devices A, B and C, D. Figures 13(c) and (d) show the other two paralleled loops, Loop 3 and Loop 4.

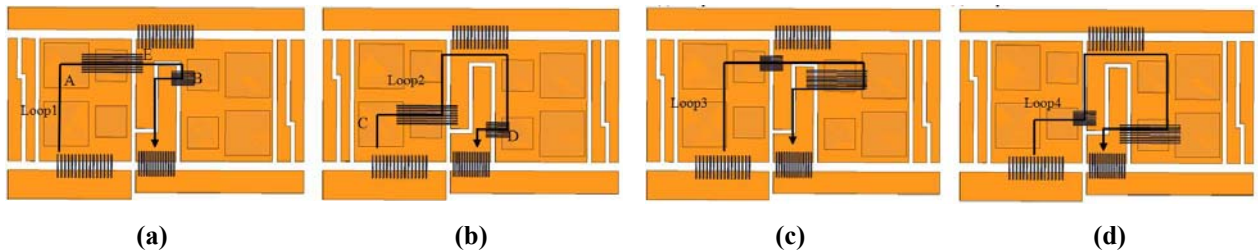


Fig. 13. Commutation loops in the conventional layout: (a) Loop 1, (b) Loop 2, (c) Loop 3, and (d) Loop 4.

Figure 14 shows the different loops in the proposed layout design. The four figures (a), (b), (c), and (d) represent the four commutation loops. It is obvious that in this design the two paralleled loops, for example Loop 1 in (a) and Loop 2 in (b), have different covered areas, and therefore the stray inductance for the two loops is different. It is the same thing for the two paralleled loops in N-cell, as shown in Figures 14(c) and 14(d).

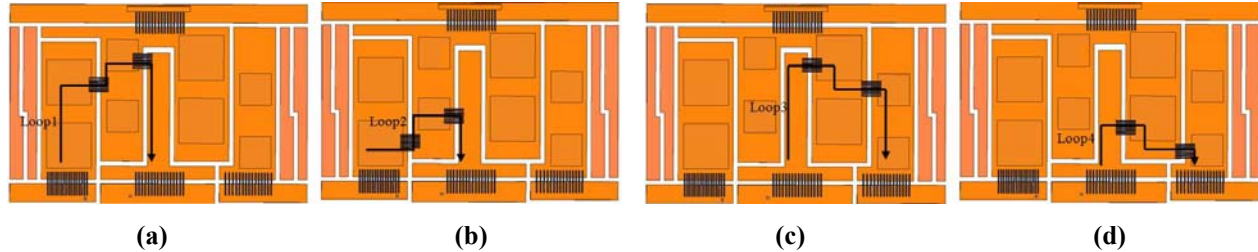


Fig. 14. Commutation loops in the proposed layout: (a) Loop 1, (b) Loop 2, (c) Loop 3, and (d) Loop 4.

For measurement, the two designed substrate patterns were etched and the wires bonded. Figure 15(a) shows Loop 1 of the conventional design, and Fig. 15(b) shows the longer loop, Loop 1, and the shorter loop, Loop 4, for the proposed design. Table 3 compares the results for the detailed simulation and measurement of inductance.



Fig. 15. Fabricated commutation loops for (a) the conventional design and (b) the proposed design.

Table 3. Comparison of the inductance value simulation and measurement results

| | Conventional layout (nH) | | Proposed layout (nH) | |
|--------|--------------------------|-------------|----------------------|-------------|
| | Simulation | Measurement | Simulation | Measurement |
| Loop 1 | 23.4 | 22.2 | 21.8 | 18.6 |
| Loop 2 | 21.6 | 20.1 | 13.0 | 11.8 |
| Loop 3 | 21.3 | 19.8 | 20.5 | 17.9 |
| Loop 4 | 22.0 | 20.2 | 13.5 | 12.7 |

Conclusion

The project for FY 2011 mainly focused on measurement of the stray inductance inside the power module and the experimental work on characterizing the switching performance of the power module. The measurement results of the stray inductance agree with the simulation results; the commutation loop inductances in the proposed layout design are smaller than in the conventional layout. The experimental setup for a DPT was built. Several methods were used to improve the accuracy of the measurement. To measure the voltage drop on the stray inductance, two wires were attached as close as possible to the collector and emitter of the IGBT die. Voltage was measured both across the die and across the module

terminal. There is a difference of more than 10 V for the two measurements, which shows the effectiveness of this method. The experimental results show an 11 V lower overshoot voltage during IGBT turn-off in the proposed module than in the conventional module, which results from the reduction of the module stray inductance.

A novel switching cell concept was applied in a multichip (two parallel devices) module. The proposed layout and a conventional layout were designed in Q3D Extractor. Under this layout design, the dc buses are arranged at one side of the module; this causes the proposed layout to have a disadvantage of uneven loop inductance. Although the loop inductance can be reduced, the effect is not significant. The mismatch in the parasitics causes imbalance in the switching voltage and current of the paralleled branches. The current dice metallization is made in a certain pattern: the collector of the IGBT and the cathode of the diode are made of silver alloy for solder attachment; the emitter of the IGBT and the anode of the diode are made of aluminum alloy for wire bonding. This requires the two devices in P-cell and N-cell to be arranged on separate DBC substrates, which takes more substrate area. This shows that additional effort is needed to ensure the stray inductance is even for paralleled die in a module.

Patents

None.

Publications

1. S. Li, L. M. Tolbert, F. Wang, and F. Peng, "Reduction of Stray Inductance in Power Electronic Modules Using Basic Switching Cells," in *Proc. IEEE Energy Conversion Congress and Exposition*, 2010, pp. 2686–2691.
2. S. Li, L. M. Tolbert, F. Wang, and F. Peng, "P-cell and N-cell based IGBT module: Layout design, parasitic extraction, and experimental verification," in *Proc. IEEE Applied Power Electronics Conference and Exposition*, 2011, pp. 372–378.

References

1. J. Witcher, *Methodology for Switching Characterization of Power Devices and Modules*, M.S. thesis, Dept. Electrical Eng., Virginia Polytechnic Institute and State University, Blacksburg, Virginia, 2002.
2. L. Schnur, G. Debled, S. Dewar, and J. Marous, "Low Inductance, Explosion Robust IGBT Modules in High Power Inverter Applications," in *Proc. IEEE Industry Applications Conference*, 1998, pp. 1056–1060.
3. T. A. Burress, R. H. Staunton, and C. L. Coomer, *Evaluation of the 2007 TOYOTA Camry Hybrid Synergy Drive System*, ORNL/TM-2007/190, 2007.

4.4 Integration of Novel Flux Coupling Motor and Current Source Inverter

Principal Investigator: John Hsu

Oak Ridge National Laboratory

National Transportation Research Center

2360 Cherahala Boulevard

Knoxville, TN 37932

Voice: 865-946-1325; Fax: 865-946-1262; E-mail: hsujs@ornl.gov

DOE Technology Development Manager: Susan A. Rogers

Voice: 202-586-8997; Fax: 202-586-1600; E-mail: Susan.Rogers@ee.doe.gov

ORNL Program Manager: Mitch Olszewski

Voice: 865-946-1350; Fax: 865-946-1262; E-mail: olszewskim@ornl.gov

Objectives

- Produce an integrated motor and inverter assembly that marries two ORNL technologies, the novel flux coupling motor (NFC-motor) and the current source inverter (CSI), to eliminate the inductor in the CSI topology.

Approach

- Design an excitation core that can take high frequency.
- Fabricate prototype core and coil for test.
- Test the prototype core with inverter.
- Find out the pros and cons from test.
- Repeat the loop for improvement until the goal is reach.

Major Accomplishments

- Validated the concept of the integration of the NFC-motor and the CSI through laboratory tests.
- Determined through test that the efficiency needs to be improved.

Future Direction

- Identify the source of the losses associated with the winding and the soft-iron-wire core of the NFC-motor.
- Simulate potential improvements.
- Fabricate and test the improvements for the integration.
- Repeat the loop for improvement until the goal is reached.

Technical Discussion

The CSI [1–7] circuit diagram is shown in Fig. 1. It does not have the huge dc link capacitor bank of the voltage source inverter but has an additional inductor, L_{dc} . A CSI prototype is shown in Fig. 2.

Figure 3 shows the prototype NFC-motor. It contains two stationary excitation cores that produce dc excitation flux to the rotor.

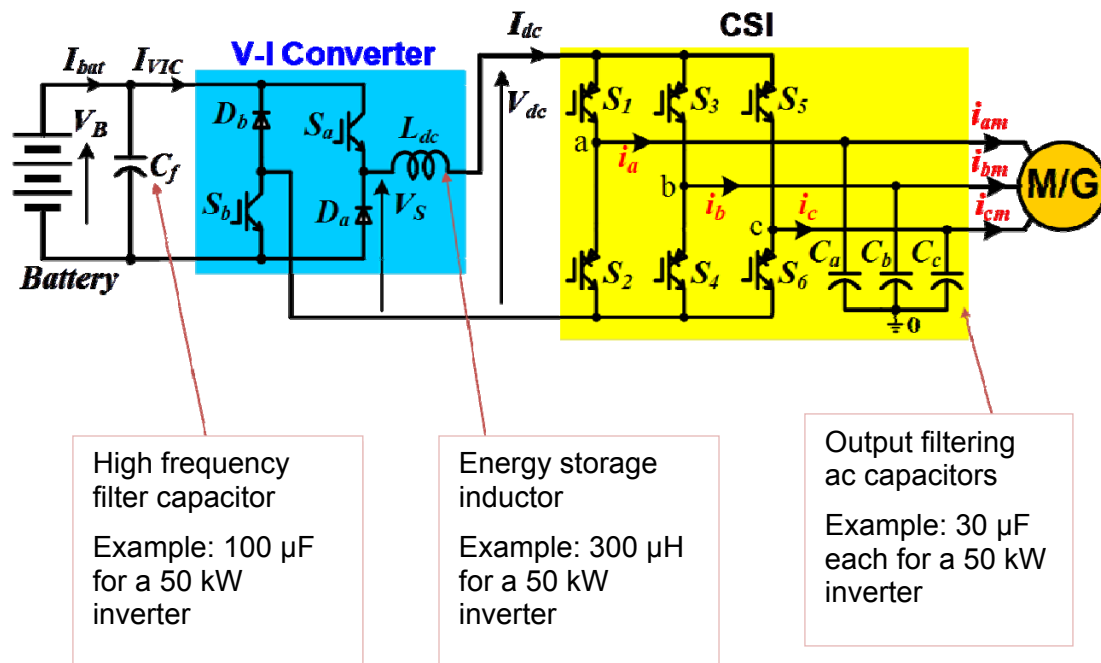


Fig. 1. CSI circuit diagram.

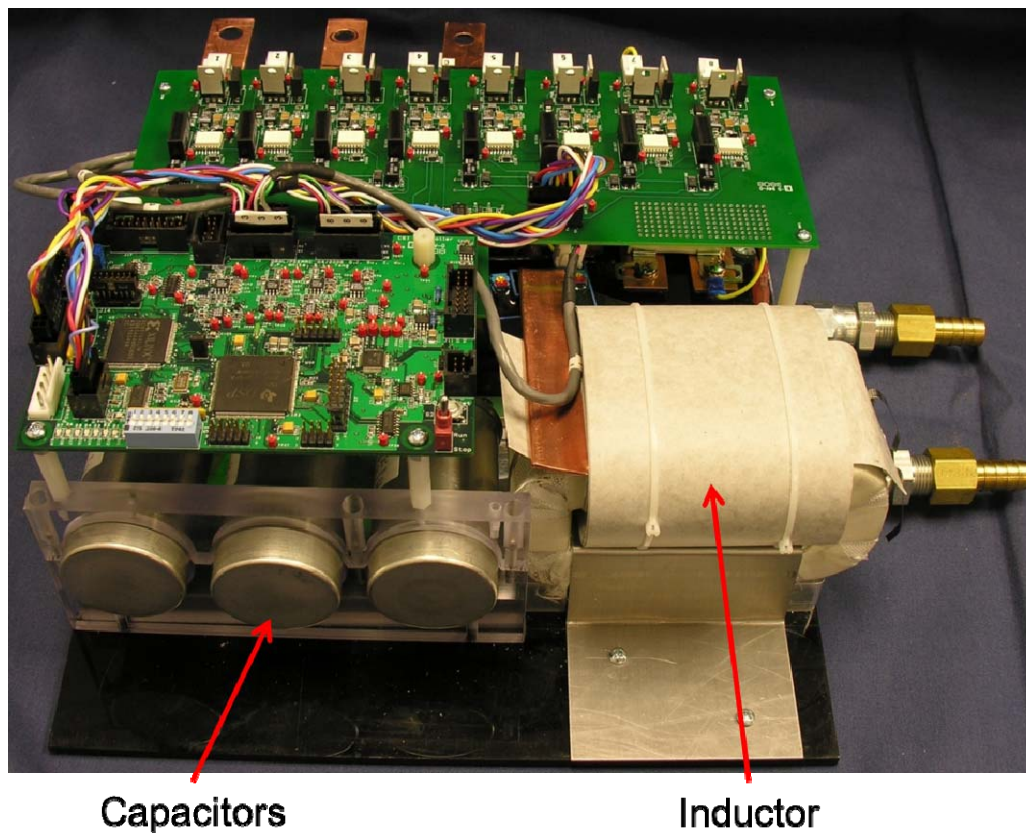


Fig. 2. CSI prototype.

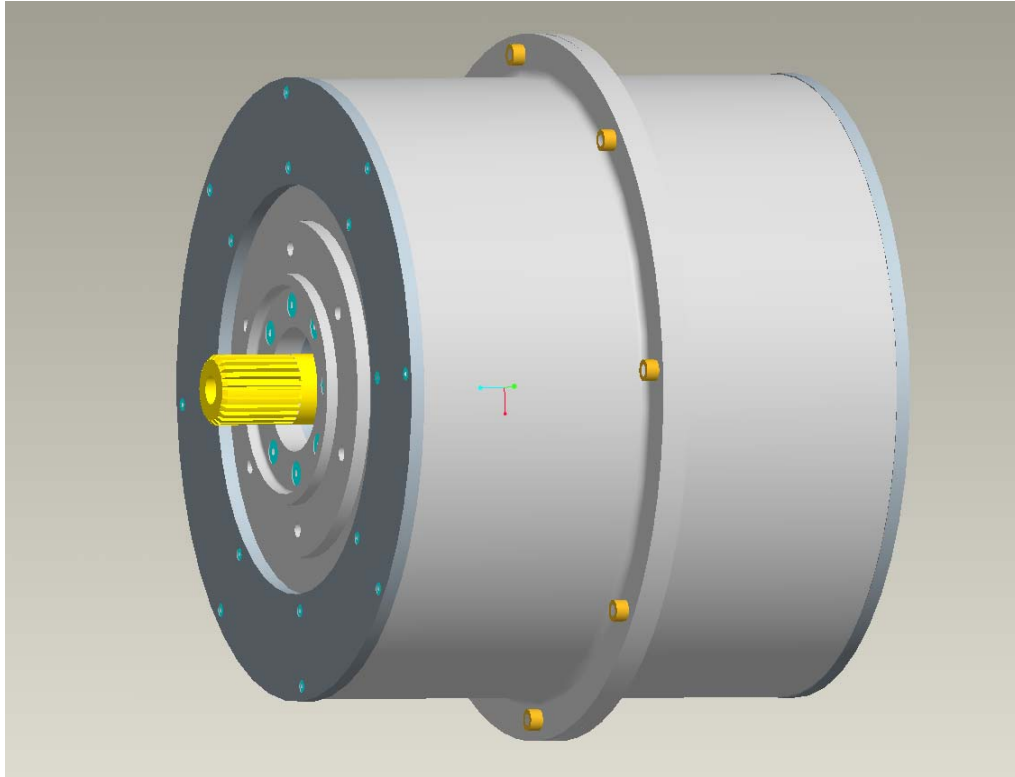


Fig. 3. Prototype NFC-motor.

Figure 4 shows the experimental setup used to determine the feasibility of using the excitation coils of the motor to eliminate the CSI inductor. It includes an excitation core that is made of thin, soft iron wires coated with thin surface insulation. The reason to use the thin, soft iron wires for the excitation core is to reduce the core loss associated with the high frequency current component in the inductor.

Figures 5 and 6 show the results for the tests with the old inductor of the CSI prototype and with the NFC-motor excitation coil functioning as the inductor. The test traces of the input current (100 A/div), two output voltages (500 V/div), two output currents (50 A/div), and input voltage (500 V/div) for the two cases show very little difference. This validates the concept of integration of the NFC machine and the CSI.

Figure 7 shows the power electronic system (excluding load) efficiency curves with different dc bus inductors (measured with a PZ4000 power meter) versus the modulation index. The V_{dc2} and V_{dc} used for the modulation index are shown in Fig. 8. Three efficiency curves are shown, corresponding to the following scenarios: (1) the old inductor of the CSI used, (2) the old inductor of the CSI replaced by the new wound core of the NFC-motor, and (3) an additional short-circuit coil ("SC ring" in the figure) placed on top of the new wound core. The efficiency curves indicate that the efficiencies for either of the two NFC-CSI integration scenarios described [(2) or (3) above] are low and need to be increased before this concept would be acceptable for commercial products.

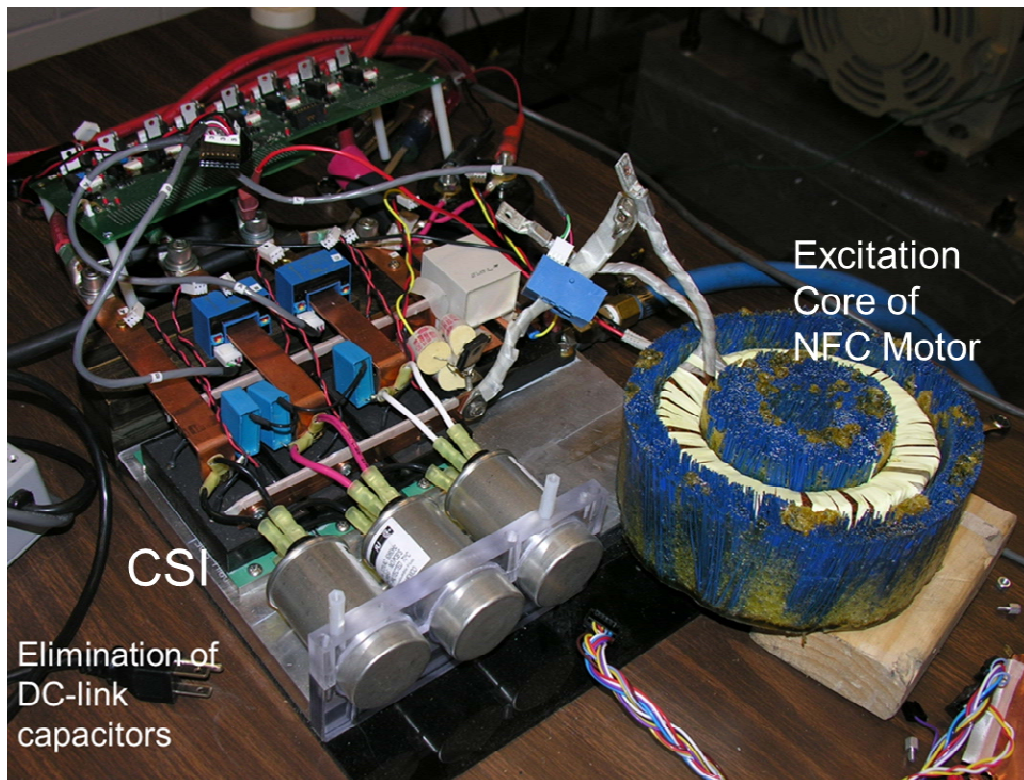


Fig. 4. Experimental setup for integration of NFC-motor and CSI.

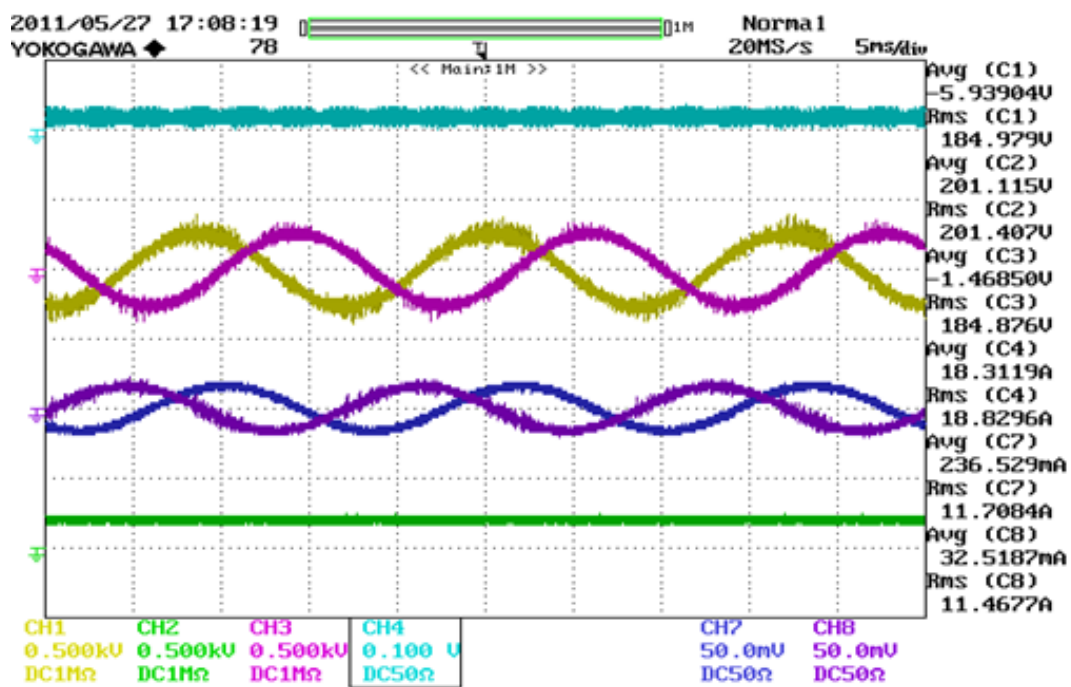


Fig. 5. Test of old inductor under the following conditions: input current (100 A/div), two output voltages (500 V/div), two output currents (50 A/div), and input voltage (500 V/div).

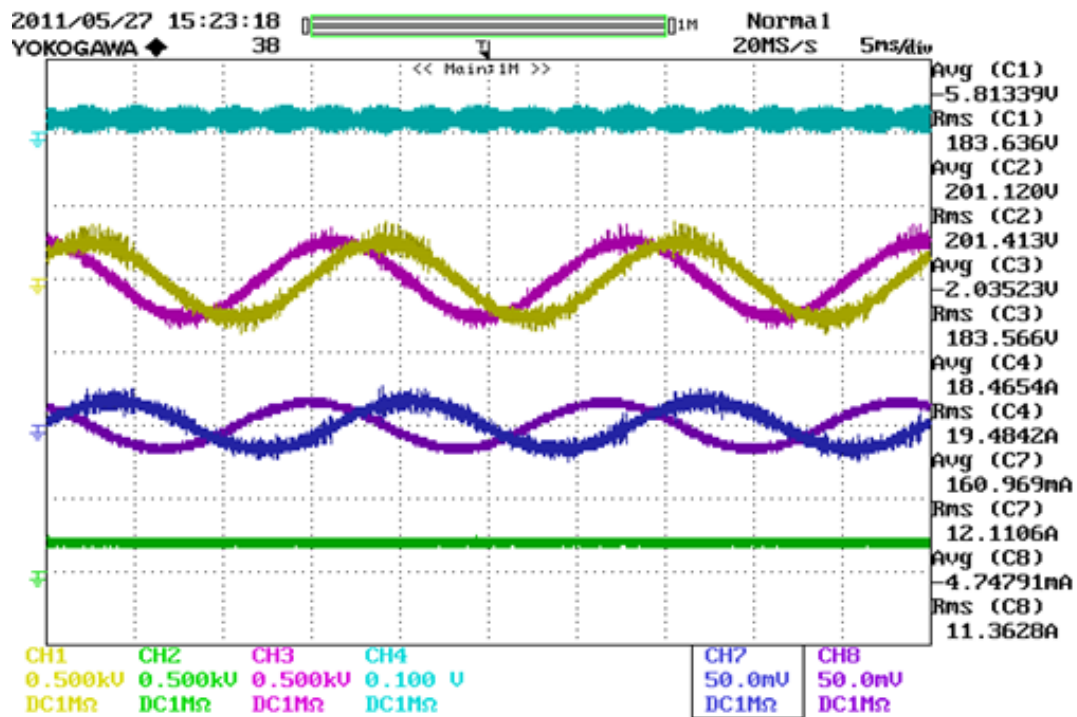


Fig. 6. Test of NFC-motor excitation inductor under the following conditions: input current (100 A/div), two output voltages (500 V/div), two output currents (50 A/div), and input voltage (500 V/div).

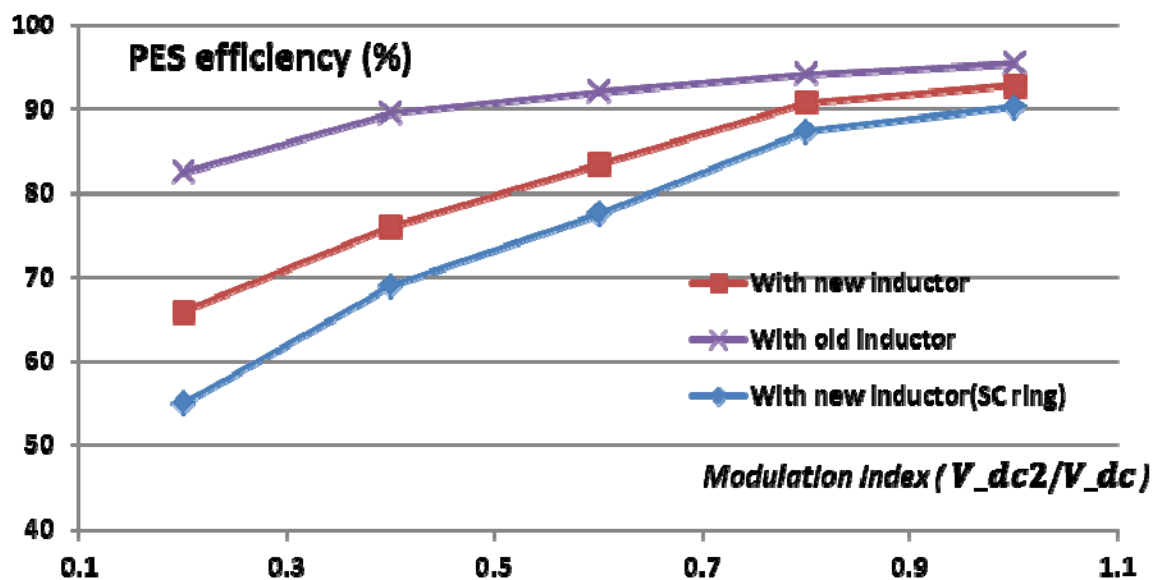


Fig. 7. Power electronic system (PES) efficiency (excluding load) with different dc bus inductors (measured with a PZ4000 power meter).

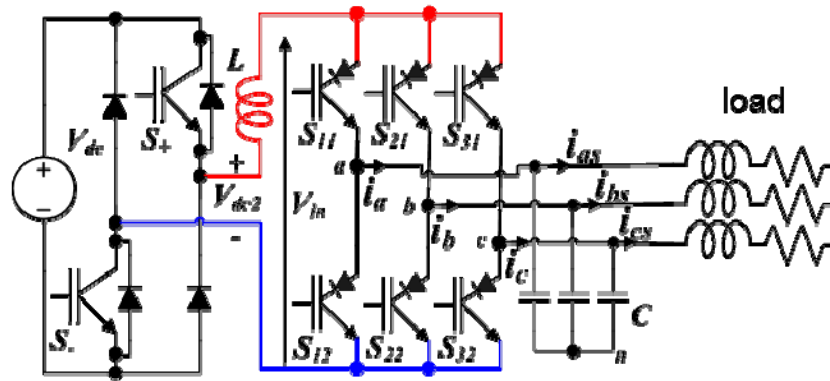


Fig. 8. Locations of V_{dc2} and V_{dc} .

Conclusion

The concept of integration of the NFC machine and the CSI has been validated through test. Low efficiency numbers indicate further work is needed for acceptable performance.

Patents

None.

Publications

Internal and DOE review meeting publications only.

References

1. A. E. Fitzgerald, Charles Kingsley, Jr., and Stephen D. Umans, *Electric Machinery*, McGraw-Hill Book Company, Fourth Edition, 1983.
2. T. A. Burruss, C. L. Coomer, S. L. Campbell, L. E. Seiber, L. D. Marlino, R. H. Staunton, and J. P. Cunningham, *Evaluation of the 2007 Toyota Camry Hybrid Synergy Drive System*, ORNL/TM-2007/190, Revised: April 2008, Publication Date: January 2008.
3. T. A. Burruss, C. L. Coomer, S. L. Campbell, A. A. Wereszczak, J. P. Cunningham, L. D. Marlino, L. E. Seiber, and H. T. Lin, *Evaluation of the 2008 LEXUS LS Hybrid Synergy Drive System*, ORNL/TM-2008/185, January 2009.
4. Gui-Jia Su, L. Tang, and Z. Wu, "Extended Constant-Torque and Constant-Power Speed Range Control of Permanent Magnet Machine Using a Current Source Inverter," in *Proceedings of the 2009 Vehicle Power and Propulsion Conference (VPPC 2009)*, Dearborn Michigan, September 7–11, 2009 pp. 109–115.
5. L. Tang and Gui-Jia Su, "Boost Mode Test of a Current-Source-Inverter-Fed Permanent Magnet Synchronous Motor Drive for Automotive Applications," in *Proceedings of the Twelfth IEEE Workshop on Control and Modeling for Power Electronics (COMPEL 2010)*, Boulder, Colorado, June 2010.
6. L. Tang and Gui-Jia Su, "Novel Current Angle Control of a Current Source Inverter Fed Permanent Magnet Synchronous Motor Drive for Automotive Applications," in *Proceedings of the 2011 Energy Conversion Congress Expo (ECCE2011)*, Phoenix, Arizona, September 2011.
7. Gui-Jia Su and L. Tang, "Current Source Inverter Based Traction Drive for EV Battery Charging Applications," in *Proceedings of the 2011 Vehicle Power and Propulsion Conference (VPPC 2011)*, Chicago, Illinois, September 2011.

4.5 Advanced Integrated Electric Traction System

Principal Investigator: Greg S. Smith

Organization: General Motors

3050 Lomita Blvd

Torrance, CA 90505

Phone: (310) 257-3812

E-mail: gregory.3.smith@gm.com

DOE Technology Development Manager: Susan A. Rogers

Voice: 202-586-8997; Fax: 202-586-1600; E-mail: Susan.Rogers@ee.doe.gov

Objectives

- Develop and demonstrate advanced technologies for an integrated ETS capable of 55kW peak power for 18 seconds and 30kW of continuous power.
- The ETS is to cost no more than \$660 (55kW at \$12/kW) to produce in quantities of 100,000 units per year, should have a total weight less than 46kg, and have a volume less than 16 liters with a nominal 105°C coolant and >93% efficiency.
- The cost target for the optional Bi-Directional AC/DC Converter is \$375.

Approach

- Develop accurate system specifications to reduce cost and increase reliability of system.
- Increase motor power density to reduce cost, less material needed for same power.
- Board centric power electronics to increase flexibility to adapt to vehicle applications, simplify manufacturing process, while improving electrical performance.
- Power module, improve design with new switched with on-chip current and temperature sense, reduced packaging inductance, and improved joint.
- Dc bus capacitor design to eliminate housing, minimize potting and bus structure to reduce cost by eliminating non value added material and increase flexibility of scaling capacitance

Major Accomplishments

- Built, demonstrated, and verified through test Electric Traction System that met all DOE 2010 objectives and met DOE 2015 objectives for specific power and power density
 - Build
 - Inverter, two open units for electrical evaluation and controls development and ten complete units for environmental stress screening, electromagnetic interference and electrical traction system testing
 - Motor, three axial inserted and two radial inserted
 - Testing
 - Environmental Stress Screening
 - Full characterization, temperature, vibration, voltage, and current
 - Electromagnetic
 - Dyne - Temperature, voltage and current, and system efficiency
 - Technology Learning's
 - Every new technology/component when placed into a system create new engineering problems that must be addressed
 - Power module
 - Capacitor and heavy copper board

- DC bridge
- Motor build processes for five phase both axial and radial inserted
- Built, demonstrated, and tested bi-directional charger

Future Direction

- Project has been completed, but learning's have been incorporated into production product developments

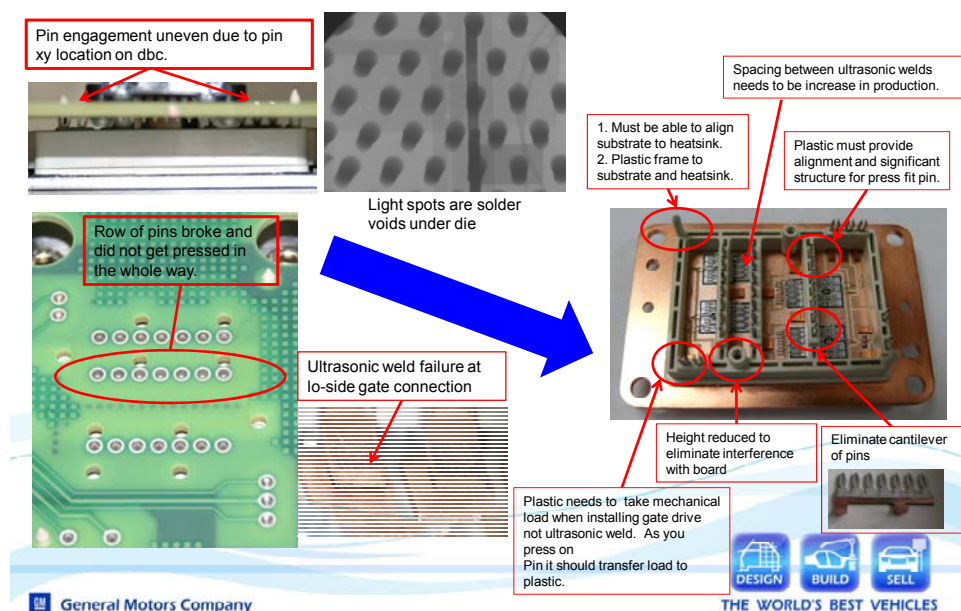
Technical Discussion

This cooperative development project develops an Advanced Integrated Electric Traction System. This program is divided into two phases: a research phase and a development and demonstration phase. The research phase is for experimentation and evaluation of technologies and manufacturing processes. The development and demonstration phase utilized the learning's from the research phase to design, built, and test an Electric Traction System and a bi-directional Charger. The focus of FY11 was the completion of the unit build, testing, analysis of test results, and verification of unit performance to DOE objectives.

Testing was done individually and then finally as a system. This began the process of characterization of the units and the technology that it represents. The purpose was to identify and understand design and manufacturing issues excited by automotive environment and performance requirements. Tests that were performed were Electrical Bench, ESS, EMI, Dyne, and Vibration. Identified issues were root caused and verified. Considerable time and effort was needed to accomplish the testing and experimentation to identify and verify the root cause of failures. The following issues were identified on the inverter:

1. Power Module production inconsistencies: frame and pin alignment, ultrasonic welds, solder voiding, and press fit pin support during insertion.

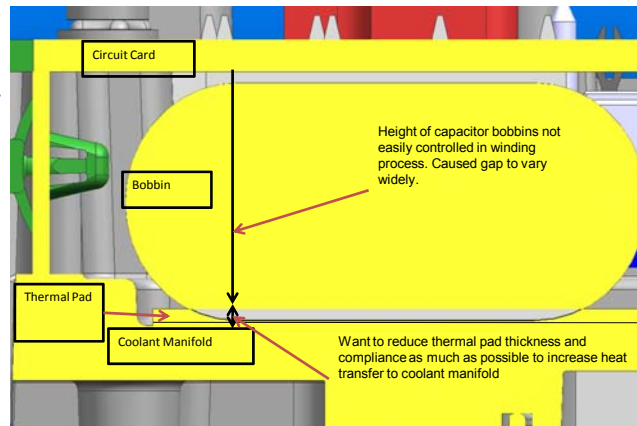
Power Module Learning's



2. Capacitor variation of bobbin size, causing thermal interface issues to coolant.

Capacitor Learning's

- Capacitor
 - Variation in bobbin diameter greater than expected
 - Soldering of capacitor to heavy copper board difficult

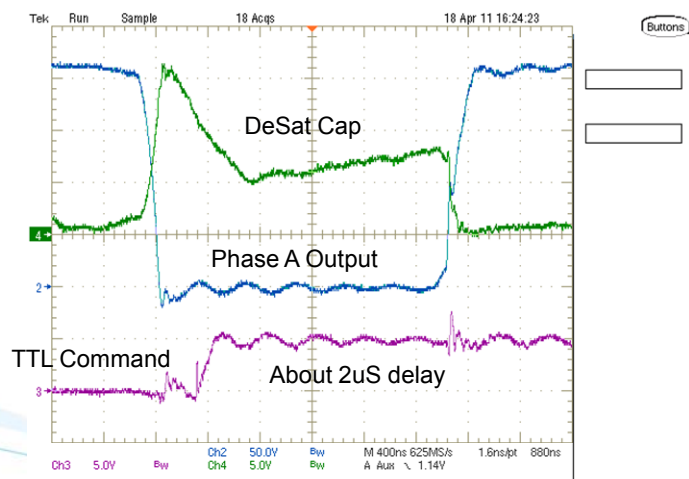


General Motors Company

DESIGN BUILD SELL
THE WORLD'S BEST VEHICLES

3. Heavy Copper Board device soldering, difficulty in consistence and quality of joint.
4. Gate drive IC and circuit, poor turn on and off and common ground plane.

Gate Driver Desat Signals



General Motors Company

DESIGN BUILD SELL
THE WORLD'S BEST VEHICLES

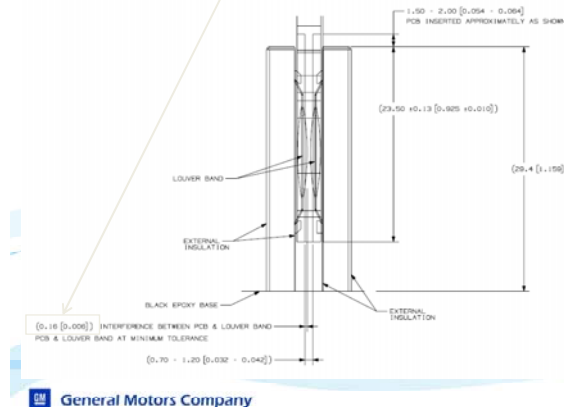
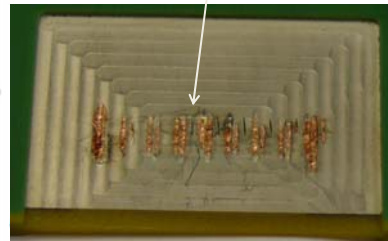
5. DC Bridge bus bar, poor contact from lack of spring compression

DC Bridge Failure

- DC Bridge was manufactured to print
- Interface design was called out correctly, but bus bar supplier did not follow spring suppliers compression spec for high current (0.3-0.5mm compression, vs. 0.16mm at min interference)



•Lack of compression in louvered contact led to arcing between circuit card and busbar contact

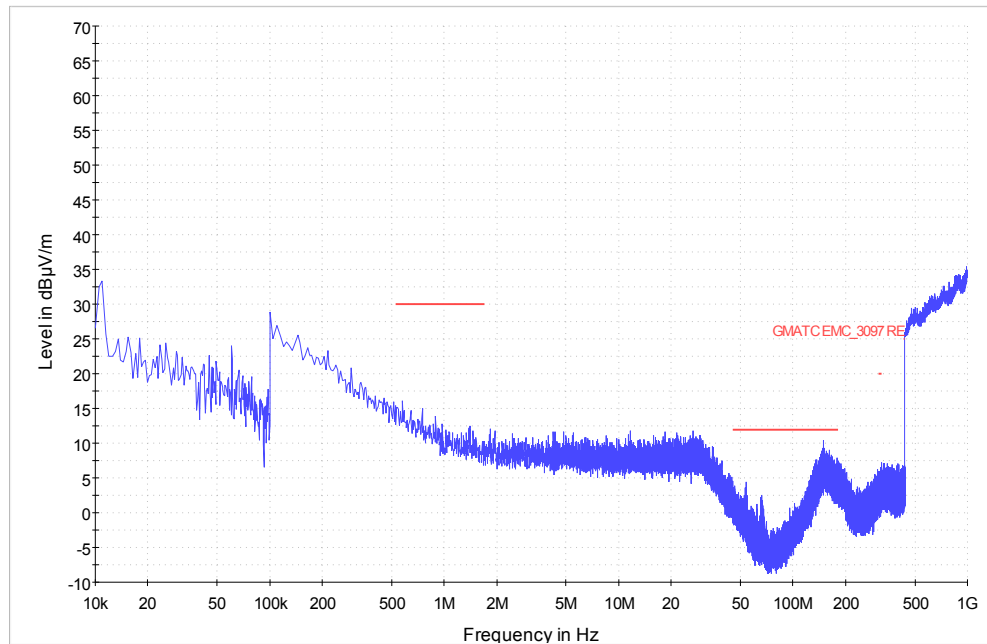


The bi-directional converter had power module failures caused by manufacturing defects requiring new process and quality standards to be implemented. The bar wound motor had significant manufacturing processes issues in coil forming and insertion, and coil welding. 5-Phase motor has a higher slot count and number of conductors than a conventional 3-Phase motor causing the increased complexity of the manufacturing processes. Additionally motor test data was correlated to simulation data and identified higher than expected leakage inductance. Through investigation, analysis and experimentation it was determined that longer than expected end turns accounted for the higher leakage inductance. If manufacturing processes can be improved allowing for a reduction in end turn length motor performance will be as originally predicted. All the identified issues have been communicated to suppliers and are being incorporated into the supplier's production design offering.

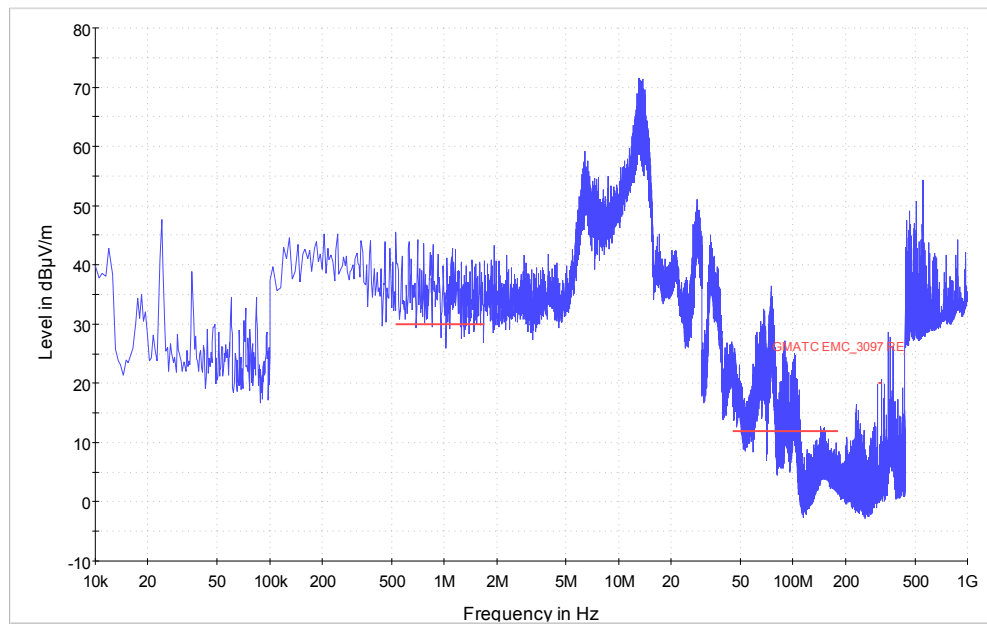
EMI testing was done in March '11. Tests that were performed were to determine the radiated and conducted emissions of the ETS. The following tests were performed:

1. RE GMW 3097 – AIETS in wakeup and drive modes
2. CE GMW 3097 – LISN on 12 V + and 12 V return lines
3. CE with current probe – Measure common mode current on all external cables

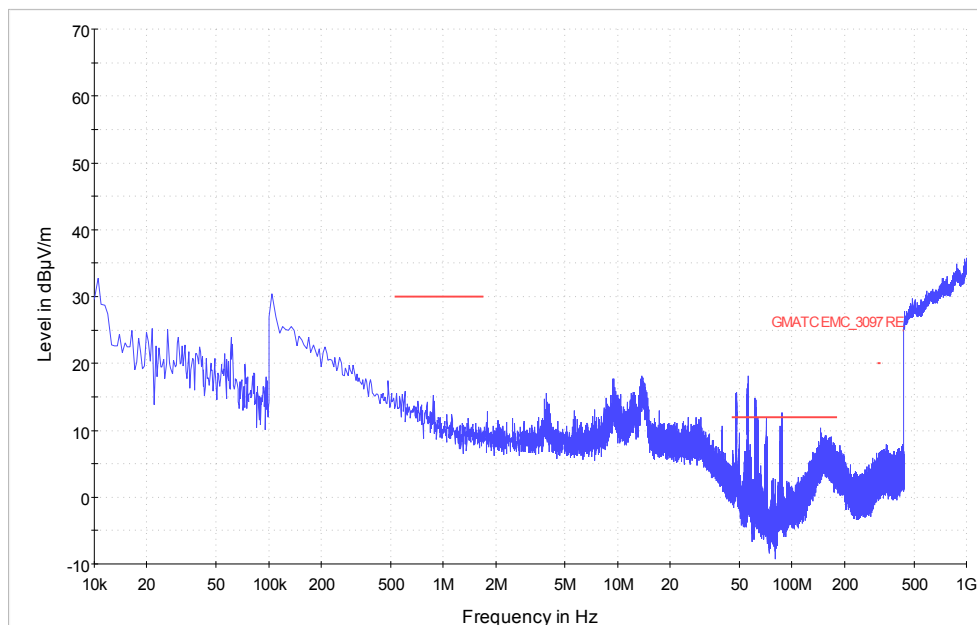
Results show, see below, that the ETS is not passing RE GMW3097, passing CE GMW3097, and CE with Current Probe shows IGBT switching noise being conducted on each external cable and through the output driveshaft. Reduction in EMI emissions was determined could be accomplished through a re-layout of the Bia's supply to meet GM EMI requirements.



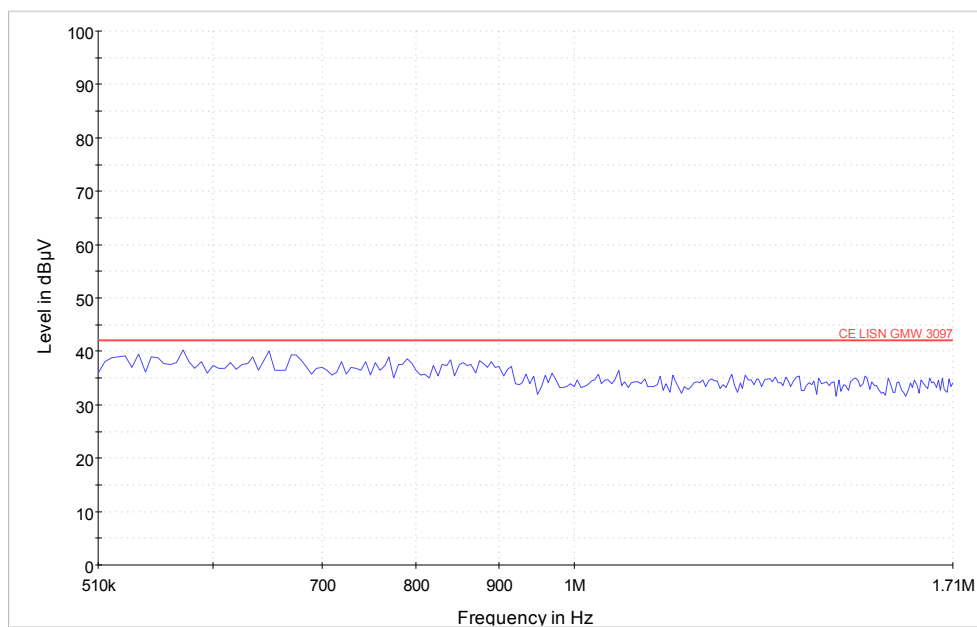
RE DOE 5-PHASE AIETS
CHAMBER AMBIENT
07MAR11



RE DOE 5-PHASE AIETS
300 HVDC & 12V - ENABLED
DRIVE MODE-ENABLED; 1KRPM
08MAR11



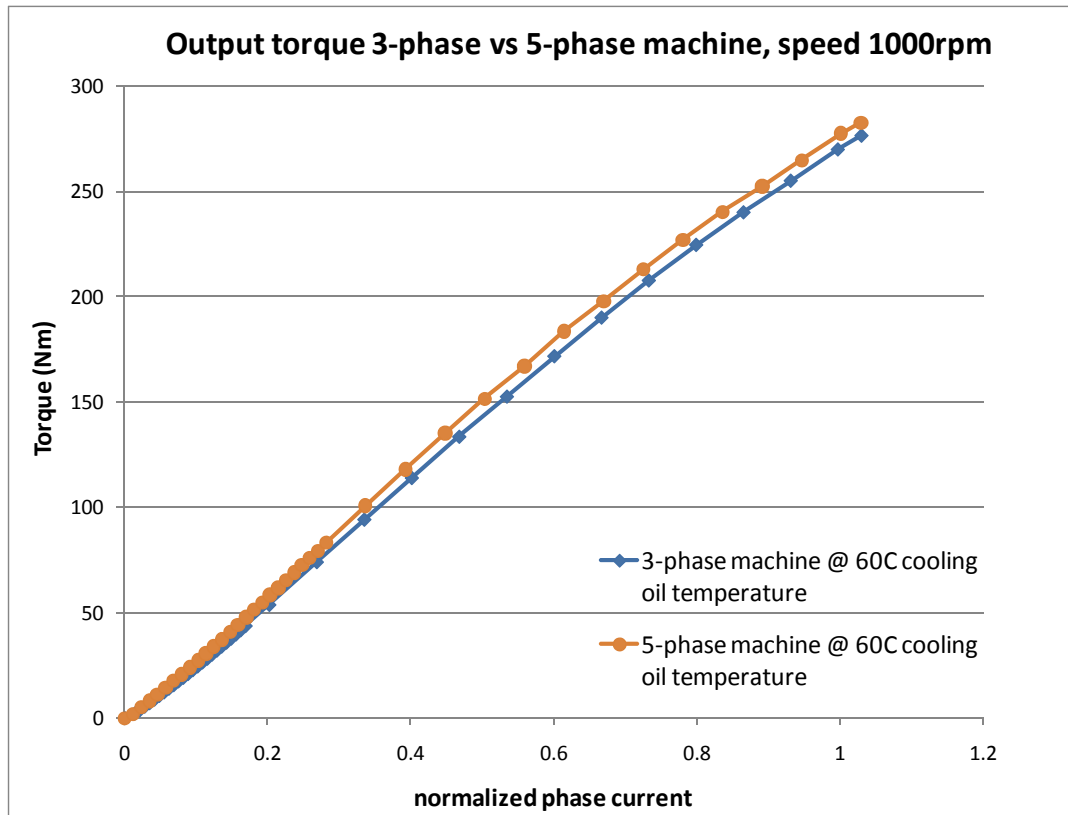
RE DOE 5-PHASE AIETS
 300 HVDC - ENABLED
 SIGNAL HARNESS CONNECTED
 07MAR11

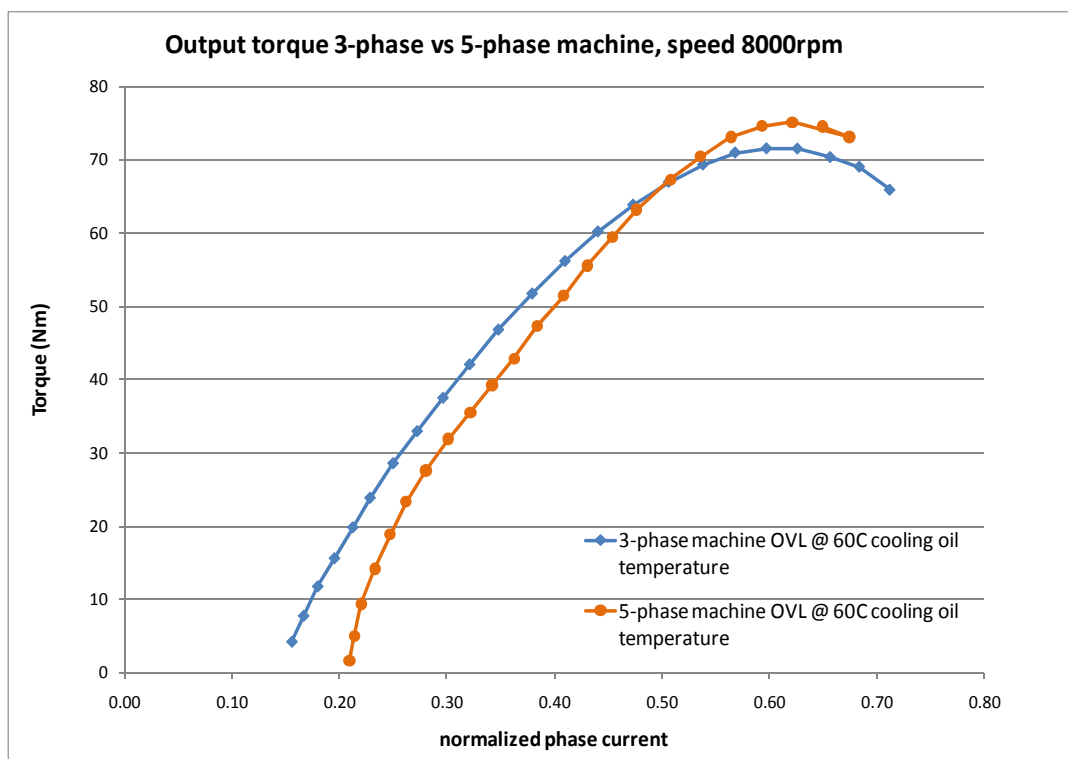
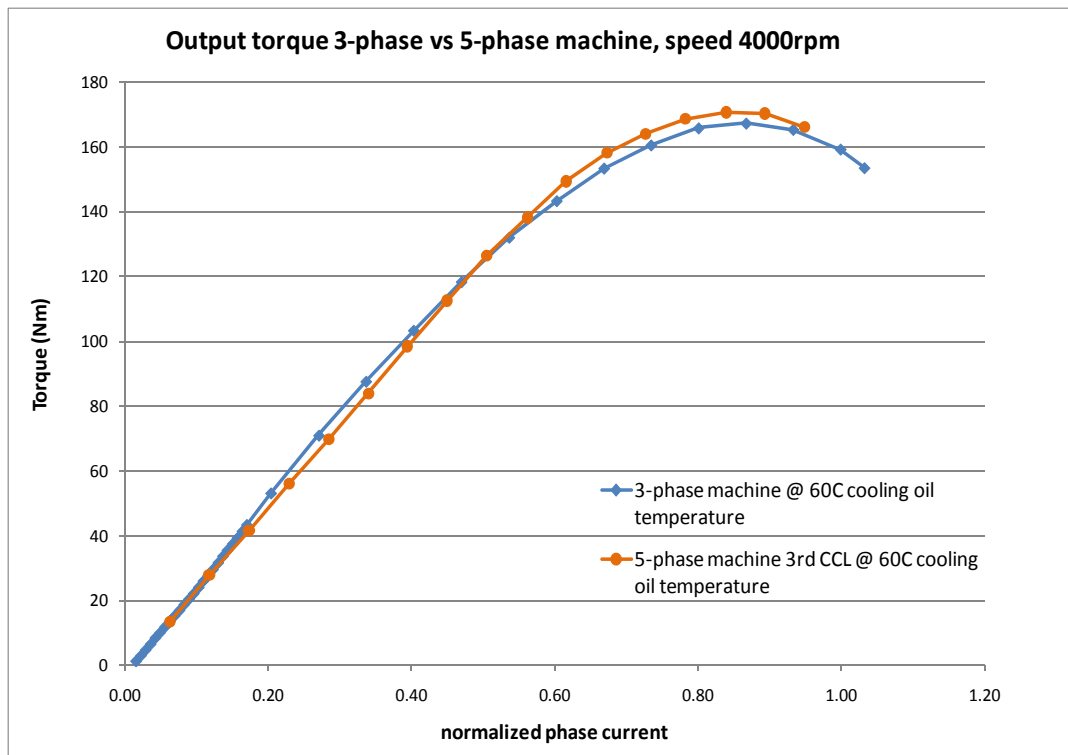


CE LISN B+ DOE 5-PHASE AIETS
 300 HVDC & 12V - ENABLED
 DRIVE MODE-ENABLED; 1KRPM
 08MAR11

The integration of the motor and inverter into an ETS was done in March 2011. Dyne testing up to this point on the traction system was done with the motor and inverter not integrated so full instrumentation

could be used. System efficiency, continuous and peak power, and hot and cold testing was done. Measured data from dyne tests are shown below and were verified during government witness testing in May 2011.





ETS performance testing correlated to predicted performance from simulation when taking into account the motor high leakage inductance. Test data from 5-Phase machine shows higher peak torque/power than 3-phase machine, in particular in the field-weakening region, but the gain of the tested 5-phase machine is not significant because of the leakage inductance. Efficiency measurements showed that the

3-Phase machine was higher than the 5-Phase machine, however, 5-Phase has again the potential to match or have higher machine efficiency than 3-Phase if leakage inductance is reduced. Leakage inductance can be reduced by decreasing the motor end turn length by improving current manufacturing processes which is achievable.

Conclusion

This project developed an ETS that met DOE 2010 objectives and met specific power and power density 2015 requirements at 105°C. Full automotive characterization testing was performed to assess viability of technology for production application. Additionally unit verification testing was done with DOE representatives present. Challenges in the areas of cost and system efficiency remain daunting to meet all the 2015 DOE objectives. Cost reduction will require greater specific application component development to be done. Higher efficiency will greatly depend on improvement in motor winding production processes and the development of new switch technology.

Publications

1. Program Kickoff October 30, 2007
2. PEEM FY'08 Kickoff November 6, 2007
3. 2008 Merit Review February 27, 2008
4. AIETS Phase 1 Review July 17, 2008
5. PEEM FY'09 Kickoff November 18, 2008
6. 2009 Merit Review May 22, 2009
7. PEEM FY'10 Kickoff October 27, 2009
8. 2010 Merit Review June 10, 2010
9. PEEM FY'11 Kickoff November 17, 2010
10. 2011 Merit Review May 11, 2011

Patents

| | TITLE | STAT | PS |
|----|--|-------------|----------|
| 1 | Dual Leg Inverter Drive System with Anti-polarity Phase Connections | FILED | P-008046 |
| 2 | Sensor Mount Assemblies and Sensor Assemblies | FILED | P-005081 |
| 3 | Hermetic plastic overmolding of substrate | FILED | P-005080 |
| 4 | Method of Fast Approximation of Peak Summed Fundamental and Third Harmonic Voltages in Multi-Phase Electric Machine Inverter | FILED | P-009261 |
| 5 | Optimum Current Commands for speed transition from Constant Torque to Field-weakening region for Multiphase Machine using FEA | TOOL/METHOD | P-011616 |
| 6 | Method to Calculate Optimum Current Commands for Multiphase Machine using FEA | TOOL/METHOD | P-011615 |
| 7 | Method of Injecting 5th Harmonic Voltage to Maximize 5-phase Machine Power in Field-Weakening region | TOOL/METHOD | P-010017 |
| 8 | Control Algorithm for 2 machines with 1 inverter | FILED | P-007520 |
| 9 | Boost inverter with 2 machines | FILED | P-007521 |
| 10 | Plastic lead frame with distributed-force substrate support | FILED | P-005033 |
| 11 | Direct IGBT Die Y-Capacitors to Control Electromagnetic Compatibility | FILED | P-007055 |
| 12 | Over-modulation Strategy for 5-phase Machine | FILED | P-010699 |
| 13 | Low Inductance Busbar Assembly | ISSUED | P-005609 |
| 14 | Methods, Systems and Apparatus For Controlling Third Harmonic Voltage When Operating A Multi-Phase Machine in an Overmodulation Region | FILED | P-013479 |

| | TITLE | STAT | PS |
|----|---|-------------|----------|
| 15 | Compensation Strategy for Bidirectional Matrix Converter Nonlinearities | FILED | P-013487 |
| 16 | Adaptive Compensation Strategy for Bidirectional Matrix Converter Nonlinearities | FILED | P-013491 |
| 17 | Methods, Systems and Apparatus for Adjusting Duty Cycle of Pulse Width Modulated (PWM) Waveforms | FILED | P-013482 |
| 18 | Method to Enhance THD and PFC in Single Phase ac/dc Boost Converter | FILED | P-013488 |
| 19 | Soft Start-Up for High Power AC – DC Charger/Inverter | FILED | P-013476 |
| 20 | Bidirectional Matrix Converter Battery Charger Control Strategy | FILED | P-013485 |
| 21 | Surface Enhancement Utilizing Boundary Layers with Indirect Jet Impingement | FILED | P-006123 |
| 22 | Current Control with Voltage Loop to Obtain Optimum 3rd Harmonic and Fundamental Current Commands for Multiphase Machines in the Field-weakening region | TOOL/METHOD | P-010015 |
| 23 | Crossed, overlapped power module bus structure | FILED | P-005578 |
| 24 | Electrical System for Pulse-Width Modulated Control of a Power Inverter Using Phase-Shifted Carrier Signals and Related Operating Methods | FILED | P-005286 |
| 25 | Fractional slot multiphase machines with open slots allow preformed/combined coils insertion from inner diameter, weldings reduction, decrease weldings failure, eliminate weld-end twisting/bending steps, eliminate costly/complex twisting/bending tooling a | FILED | P-009713 |
| 26 | Inverter Gate Drive PCB Inner Core High Current Access | FILED | P-010684 |
| 27 | Electromagnetic Interference Filter for Automotive Electrical Systems | FILED | P-010022 |
| 28 | Power Module Assemblies with Staggered Coolant Channels | FILED | P-010063 |
| 29 | Systems and Methods for Deactivating A Matrix Converter | FILED | P-010773 |
| 30 | Hairpin winding configuration for fractional slot multiphase machines | FILED | P-009322 |
| 31 | PWM strategy to minimize DC-link current ripple | FILED | P-011617 |
| 32 | Three Modes PWM Control Strategy for AC/DC Matrix Converter | FILED | P-005203 |
| 33 | Systems and Methods for Bi-Directional Energy Delivery with Galvanic Isolation | FILED | P-006564 |
| 34 | A DC Bus Capacitor of an Electrical Converter System | FILED | P-014442 |
| 35 | Maximum Voltage usage for Multiphase Machines in Field-weakening region | FILED | P-010014 |
| 36 | Voltage Control Method to Obtain Optimum 3rd Harmonic and Fundamental Current Commands for Multiphase Machines in the Field-weakening region | TOOL/METHOD | P-010013 |
| 37 | Integrated, High Performance, Low Inductance Power Inverter Module | FILED | P-010203 |
| 38 | Battery Pack Filter to Control Electromagnetic Compatibility | FILED | P-007072 |
| 39 | BIOS Extensions to Control Multiple Motors with Single-Motor Application Code | FILED | P-010747 |
| 40 | Copper and Core Losses separation for Multiphase machines | TOOL/METHOD | P-016841 |
| 41 | PWM Voltage Compensation | PURSUE | P-016838 |
| 42 | Method to Obtain Optimum 3rd Harmonic and Fundamental Current Commands in the Constant Torque Region for Multiphase Machines | TOOL/METHOD | P-010011 |
| 43 | Calibration Method for Bidirectional Matrix Converter Forced Commutation | TOOL/METHOD | P-016840 |
| 44 | Finite Element Analysis Calculation and Postprocessing Tool for 5- and 6-phase IPM machines | TOOL/METHOD | P-009323 |

5. Thermal Management Research and Technology Development

5.1 Air Cooling Technology for Power Electronics Thermal Management

Principal Investigator: Jason A Lustbader

National Renewable Energy Laboratory

Center for Transportation Technologies and Systems

1617 Cole Blvd. MS 1633

Golden, CO 80401

Voice: 303-275-4443; Fax: 303-275-4415; E-mail: Jason.Lustbader@nrel.gov

DOE Technology Development Manager: Susan A. Rogers

Voice: 202-586-8997; Fax: 202-586-1600; E-mail: Susan.Rogers@ee.doe.gov

Objectives

- Develop air-cooled thermal management system solutions that help meet DOE's 2015 technical targets by 2014
- Develop and demonstrate commercially viable, low-cost air-cooling solutions for a range of vehicle applications and assess their potential for reducing the cost and complexity of the power electronics cooling system.
- Enable heat rejection directly to ambient air, simplifying the system by eliminating liquid coolant loops, thereby improving weight, volume, cost, and reliability

Approach

- Use a system-level approach that addresses the cooling technology, package mechanical design, balance of system, and vehicle application requirements.
- Research each of these areas in depth and apply findings to develop effective system-level designs.
- Develop experimental and analytical/numerical tools and processes that facilitate high-quality and rapid research results.
- Work closely with industry, university, and national laboratory partners to ensure relevant and viable solutions.

Major Accomplishments

- Applied system-level analysis to an inverter for both air-cooled and liquid-cooled approaches. This analysis showed that by using an allowable junction temperature of 200°C or 150°C plus the use of an advanced spreader, the air-cooled system is able to match the power density of the liquid-cooled approach. It also showed that equal or higher electric current per silicon area could be achieved. This feasibility study demonstrates that there are several possible pathways for successful air-cooled thermal design.
- Improved the Air Cooling Characterization Platform and used it to study steady jet and synthetic jet heat transfer. The synthetic jet was found to have up to a 40% improvement in Nusselt number for the same Reynolds number. For the synthetic jet, the best heat transfer was observed at $H/D_h = 10$. A correlation was also developed that accurately describes the steady jet performance.
- Proposed the introduction of a dynamic Reynolds number and demonstrated that it collapses the synthetic jet Nusselt number to the steady jet Nusselt number. This indicates that the heat transfer coefficient is not only a function of the Reynolds number, but also a function of the changing rate of velocity.

- Conceptualized and modeled a new heat exchanger design that could be applicable to air-cooled or liquid-cooled systems. The design was submitted for a non-provisional patent.

Future Direction

- Expand fundamental heat transfer research to high temperature and high power target. Investigate a range of advanced cooling technologies, including jets, heat spreaders, fins, and other surface enhancement methods.
- Develop balance-of-system and inverter system-level testing capabilities. Use new test capabilities to characterize fan performance and predict balance-of-system trade-offs.
- Collaborate closely with Oak Ridge National Laboratory using both experimental and modeling capabilities, develop a high temperature air-cooled inverter thermal management concept. Experimentally demonstrate initial prototype thermal management design at the module level.
- Use system-level analysis to understand air-cooled inverter trade-offs at the vehicle level.

Technical Discussion

Approach

The objective of NREL's Air-Cooling Technology for Power Electronics Thermal Management project is to assess, develop, and apply air-cooling technology to improve power electronics thermal control design and influence industry's products, thereby enhancing system performance to meet DOE technical targets for weight, volume, cost, and reliability. With the notable exception of the low-power Honda Insight, commercially available hybrid vehicles use liquid-cooled power electronic systems. All the heat from a vehicle, however, must ultimately be rejected to air. For liquid-cooled systems, heat from the power electronics is transferred to a water-ethylene glycol coolant via a heat exchanger and then pumped to a separate, remote liquid-to-air heat exchanger where the heat is rejected to air. This research effort seeks to develop the necessary heat transfer technology and system-level understanding to eliminate the intermediate liquid-cooling loop and transfer heat directly to the air. The relative merits of air-cooled, high-heat-flux automotive power electronic thermal management systems will be quantified, evaluated, and demonstrated under steady state and transient conditions.

Effectively and viably accomplishing these goals requires an air-cooled system thermal design understanding and approach. As shown in Figure 2, this project will analytically and experimentally address each aspect of the system: heat transfer cooling technology, power electronics package thermal design, balance of system (prime movers, ducting, etc.), and their interconnected interactions. It is also critical to account for and understand the effects of constraints and inputs into the air-cooled thermal management system: thermal environment, device type, and vehicle context. The thermal environment constraints have a direct impact on the driving temperature difference available for air-cooled heat transfer and can vary depending on design targets and system location in a vehicle. Under-hood temperatures are approximately 100°C –140°C and are therefore unsuitable for cooling. External ambient air at 30°C –45°C is highly suitable for cooling, and some additional benefit can be gained from using cabin air, but it must be balanced with the added parasitic load. The device type will determine both the maximum junction temperature and efficiency and thus influences the maximum allowable package surface temperature and heat load. Advanced power semiconductors, such as silicon carbide and gallium nitride, have the potential to greatly expand the air-cooling feasibility range by increasing the allowable junction temperature from 125°C to 200°C or higher while possibly improving efficiency. Vehicle context determines the power electronics duty cycle, affecting the total heat rejection needs and also imposing constraints on the system volume and weight. Understanding the in-vehicle demands on the power electronics systems will allow for modulated designs to meet cooling needs, reducing system overdesign and minimizing parasitic losses.

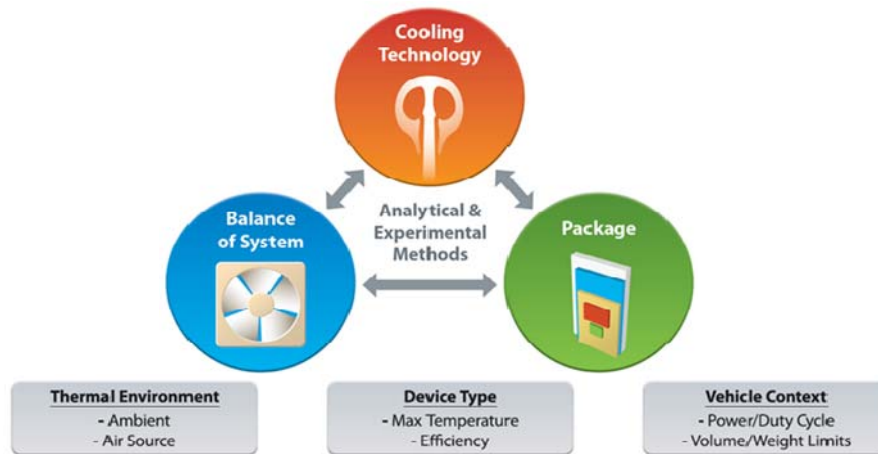


Figure 2. Power electronics air-cooled thermal management system research and design approach

To move ideas from concept to implementation, four levels of research, development, and demonstration will be used: novel cooling technology fundamental heat transfer, system-level heat transfer and balance of system, inverter-level application, and vehicle-level demonstration with partners (Figure 3). This process will both ensure that each level of complexity assists in achieving the overall objectives and will serve to screen ideas so that only the best approaches pass to the next level.

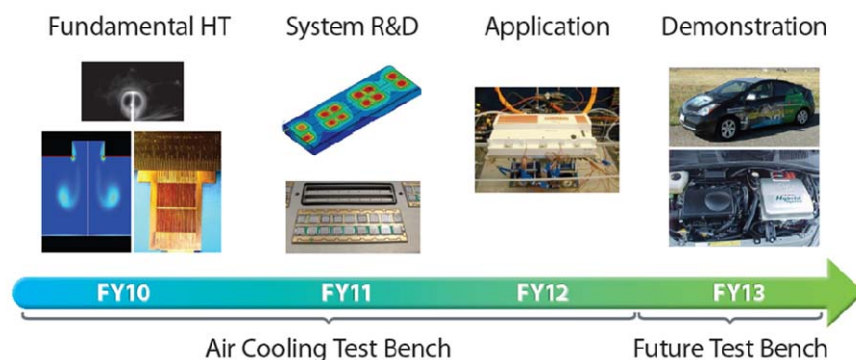


Figure 3. Air-cooling system research, development, and demonstration approach

System-Level Analysis

A high-level system analysis software program was developed in MATLAB in FY10 and expanded in FY11. The model captures interactions of the three thermal management system components and their inputs from Figure 2. This tool can be used to explore the design space and match cooling technology, thermal package designs, and the balance of system with vehicle application requirements. These results will relate high-level Advanced Power Electronics and Electric Motors (APEEM) specification goals or targets to thermal management system improvements. The system analysis inputs include application specification (electrical and vehicle description), cooling technology, package mechanical design, and balance of system. Further details can be found in FY10 Air-Cooling Technology for Power Electronics [1].

After being improved and expanded, this analysis approach was applied to an example air-cooled and liquid-cooled three-phase inverter. The goal of this analysis was to compare the air- and liquid-cooled approaches and investigate the effect of junction temperature and an advanced spreader plate concept on

performance. For both cases the inverter performance was modeled at 450 VDC, 400 Arms, and a 0.5 power factor. The power factor provides a 3-to-1 heating ratio between the IGBT and diode, representing a motoring condition. The capacitor size was assumed to be 59.5 kW/L (10.53 $\mu\text{F}/\text{kW}$ and 1.596e-3 L/ μF).

The air-cooled inverter configuration is shown in Figure 4. In this configuration, air is blown from the side and across the short length of the inverter, Figure 4a. The semiconductors are mounted to a spreading plate, and the fins are mounted to this. Figure 4b shows one leg of the inverter. The red box indicates the minimum thermal symmetry unit, 1/6 of one inverter leg, modeled using finite element analysis, shown in Figure 4c.

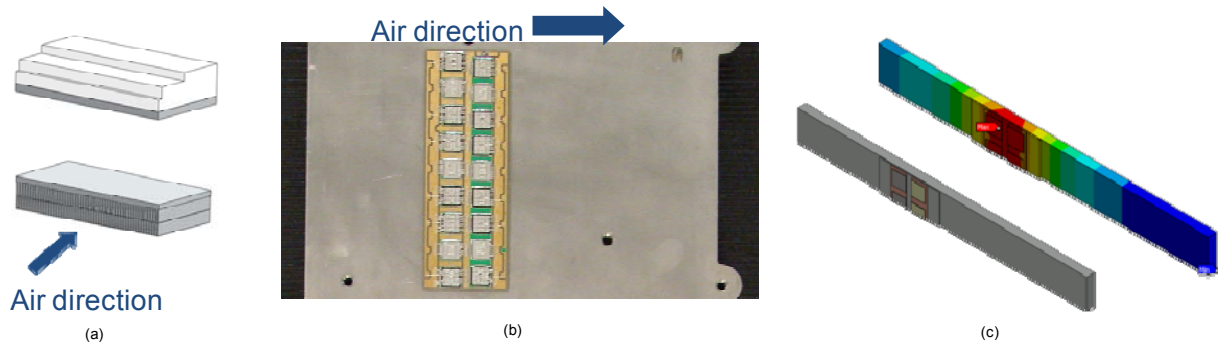


Figure 4. Air-Cooled example inverter (a) fin orientation (b) one leg of inverter (b) thermal model

The liquid-cooled inverter, Figure 5, has ethylene glycol water flowing across pin fins located directly below the mounted semiconductors. The red box in Figure 5a indicates one of the inverter leg cooling regions. In this case, the smallest thermal symmetry is 1/12 of one inverter leg, as show in Figure 5b. The thermal model is shown in Figure 5c.

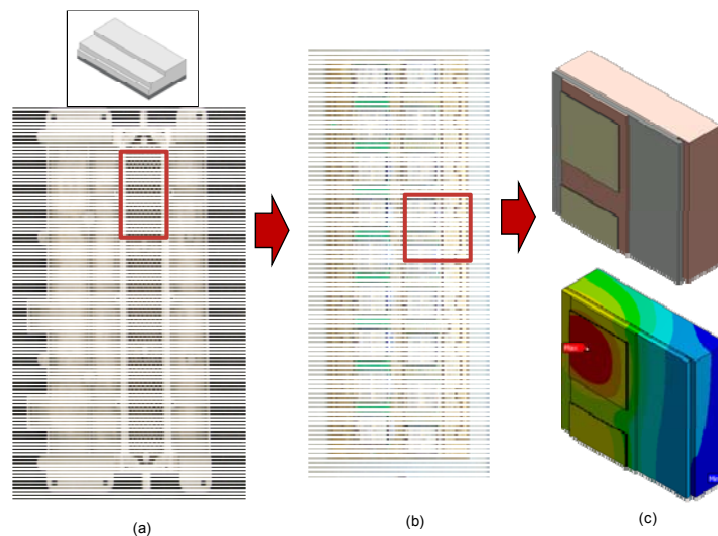


Figure 5. Liquid-cooled inverter example (a) fin configuration, (b) on leg of the inverter, (c) thermal model

The models agreed well with specification sheet performance data where comparison was possible. Figure 5 shows the air-cooled inverter's predicted electrical power capabilities for different heat exchanger performance. The blue band indicates example fin cooling performance range using air. The

intersection of the cooling performance and the inverter scenario lines indicate viable cooling regimes. The black lines show baseline inverter performance for increasing maximum junction temperature. Increasing allowable junction temperature from 125°C to 200°C substantially increases the allowable inverter power. The red lines show the potential performance improvement of using an advanced spreader concept that reduces the spreading resistance. With this design, the advanced spreader achieves approximately the equivalent of a 50°C rise in allowable junction temperature.

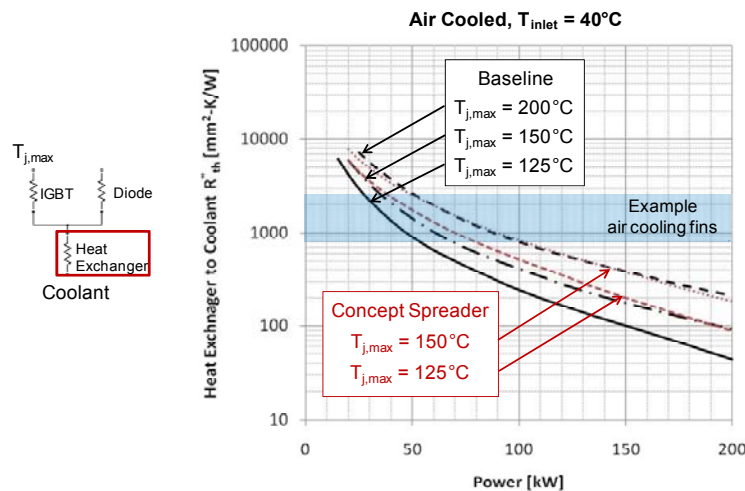


Figure 6. Air-cooled example inverter performance with advanced technology

As shown in Figure 7, the baseline liquid-cooled system significantly outperforms the air-cooled system, as expected. The relative performance of the air-cooled system improves with increasing allowable junction temperature and/or use of the improved concept spreader. At an allowable junction temperature of 200 °C or 150 °C plus the use of the advanced spreader, the air-cooled system is able to match the power density of the liquid-cooled approach (Figure 7a). Insufficient information is available about this system to directly estimate cost. However, the power per silicon area can be a good indicator for cost. Figure 6b shows that the air-cooled system using advanced technology can meet or exceed the power per total IGBT area of the liquid cooled system.

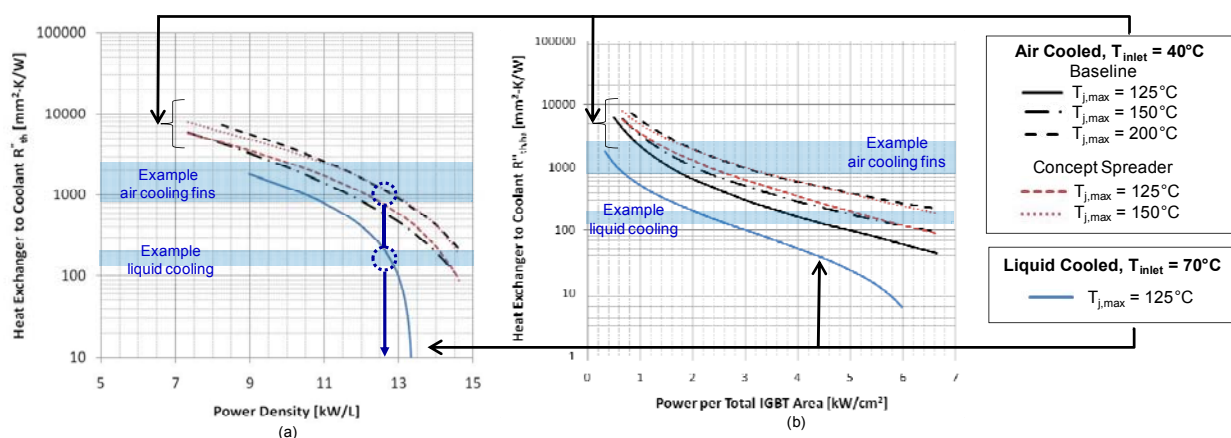


Figure 7. Air-cooled and liquid-cooled inverter performance:
(a) power density (b) power per total IGBT (silicon) area

Cooling Technology

Improving convective heat transfer from a surface for a fixed driving temperature difference requires improving the heat transfer coefficient and/or increasing the wetted surface area. This must be achieved, however, without increased parasitic losses caused by either increased pressure loss or additional work requirements. For electronics cooling, it is also critical to maximize the available driving temperature at the surface by minimizing the temperature drop from the **semiconductors** to the wetted surface where it can be rejected. The focus of the cooling technology work is to research and develop innovative approaches to achieve these goals. Possible ways of accomplishing this are to use jets. A synthetic jet is a type of fully pulsatile jet that results from the formation and interaction of vortex rings [2]. A synthetic jet can be created by the application of a threshold periodic pressure gradient across an orifice. With each cycle, a shear layer forms at the orifice edge and rolls up into a vortex ring that travels downstream due to its self-induced velocity. Both steady and synthetic jets were experimentally studied using the Air Cooling Technology Characterization Platform and their performance compared.

Experimental Setup

The updated Air Cooling Technology Characterization Platform is shown in Figure 8. Compressed air was supplied to a desiccant dryer to remove moisture. The air was dried to a dew point of -20°C or lower. It was then passed through a $5\mu\text{m}$ particulate filter and regulated to a constant 68 to 137 kPa. This regulated pressure served as the source air for a mass flow controller, Sierra model C100L, which provided a range of flow from $3.3\text{ cm}^3/\text{s}$ to $166\text{ cm}^3/\text{s}$. The air then passed through a plate heat exchanger for optional temperature control. Next, a laminar flow element (LFE), CME model 10 ($0\text{--}166\text{ cm}^3/\text{s}$) was used for more accurate measurement of the actual air flow rate. This more accurate measurement was then used to adjust the upstream mass flow controller set point. The air was then supplied to a settling chamber where a honeycomb structure followed by two spaced screens straightened the flow and reduced turbulence prior to entering the nozzle. The air then exited the nozzle and impinged on the heat transfer target. The nozzle and target were placed within a Plexiglas enclosure to minimize the effect of ambient air motion in the laboratory. Heat transfer measurements were fully automated and controlled by a computer and a National Instruments data acquisition system.



Figure 8. Schematic and photograph of the steady jet experimental setup: (1) compressed air, (2) desiccant dryer, (3) filter/regulator, (4) mass flow controller, (5) plate heat exchanger, (6) recirculating bath, (7) laminar flow element, (8) settling chamber, (9) nozzle, (10) heater target, (11) heater power supply, (12) isolation box

Steady jet nozzles were fabricated using a rapid prototyping process. The nozzles are 60 mm long, each with one of four different exiting aspect ratio (x/y), including: $1\text{ mm} \times 4\text{ mm}$, $1\text{ mm} \times 8\text{ mm}$, $1\text{ mm} \times 12\text{ mm}$, and $1\text{ mm} \times 15\text{ mm}$. The steady jet nozzle design with exiting aspect ratio of $1\text{ mm} \times 8\text{ mm}$ is shown in Figure 9. The nozzles are designed to attach to the settling chamber base plate, using an O-ring to prevent air leakage.

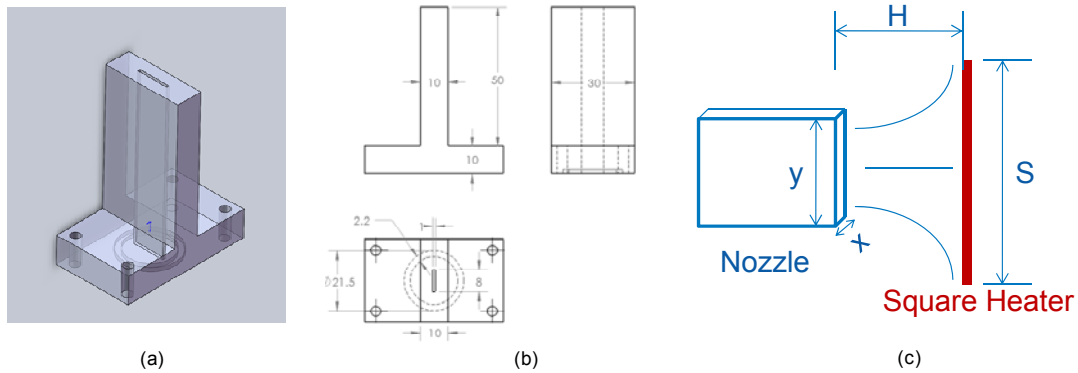


Figure 9. Steady jet nozzle design, 1×8 mm (a) drawing (b) dimensions (c) operational schematic

The synthetic jets used in this study (shown in Figure 10) were provided by General Electric Global Research Center. They have two piezoelectric actuators, bonded together with an elastomeric material applied along the entire perimeter, except the orifice. The disks are then energized with an alternating power source to actuate at a frequency in the range of 100 to 600 Hz to alternately intake and expel air through the orifice. The lower frequency limit represents the experimentally found lowest operating frequency at which the jets start to move enough air to improve heat transfer. The present synthetic jets have a fundamental frequency of around 600 Hz, where the disk displacement and the exit velocity reach their peak values. Any further increase in the frequency results in reduced cooling efficiency and increased power consumption. Therefore, focus in this study was given to 100–600 Hz range. In this work, a signal generator (HP 33120A) provided a sinusoidal wave with the desired frequency and voltage, which was amplified by a power amplifier (Alpine MRP-T220) and a transformer (Radio Shack 273-1512B) before being applied to the synthetic jet. The actual power applied to synthetic jet was monitored by a Yokogawa DL850 ScopeCorder.

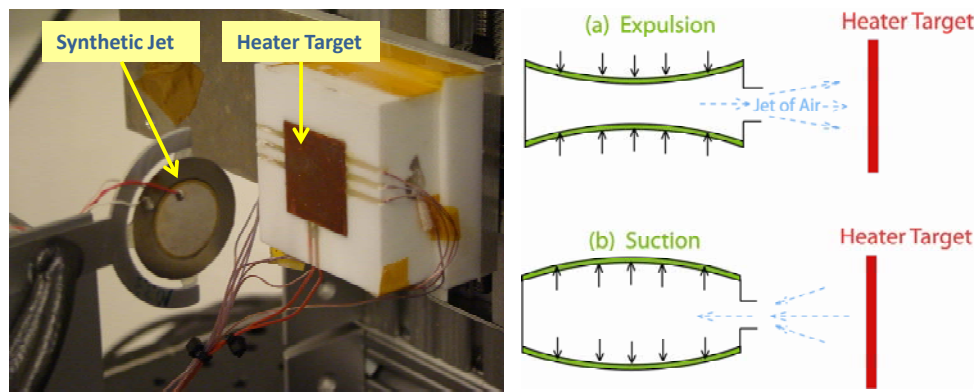


Figure 10. Close-up view of synthetic jet experimental setup and typical operation of a synthetic jet

Heat transfer was measured with a target heater assembly and a guard heater assembly (Figure 11). The copper heat transfer surface measured $25.4 \text{ mm} \times 25.4 \text{ mm} \times 1 \text{ mm}$. A 10 watt Kapton flexible heater (Omega KHLV-101/10) was attached to the back of the copper surface. A 0.5 mm thick aluminum sheet with the same cross-sectional dimensions was then attached to the back of the heater. These heater layers were adhered together with Arctic Silver conductive epoxy to form the target assembly. The assembly was then embedded in a Teflon block with the copper measurement surface flush with the exposed Teflon

surface. A non-conductive epoxy was used to hold the target assembly in the Teflon. Three thermocouples were attached along the target diagonal using epoxy in machined grooves cut in the backside of the copper plate. Thermocouples were also added in grooves to the back of the aluminum plate and the Teflon to check the heater temperature and help determine steady-state conditions. The heater was powered using a DC power supply (Agilent N8700/5700). The target copper surface was controlled to 57°C above the ambient air. The target position was accurately controlled by stages.

The guard heater was used to support the measurement of heat loss to the target Teflon block. The guard heater was composed of three layers: a 10 watt Kapton flexible heater (Omega KHLV-101/10), a 25.4 mm × 25.4 mm × 1 mm thick copper sheet, and a Kapton heat flux sensor (Omega HFS-3). Three thermocouples were attached along the copper plate diagonal using epoxy in machined grooves cut in the backside of the copper plate.

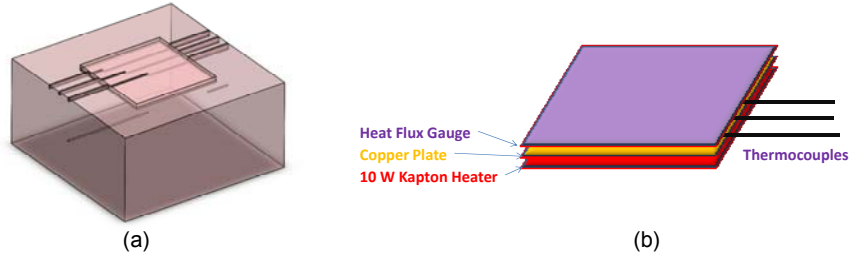


Figure 11. (a) Target heater assembly (b) guard heat assembly

It took two steps to acquire the heat transfer on the vertical copper heater target. The first step was to measure the total target heater power consumption (Q_{total}). The second step was to measure the heat loss (Q_{loss}) through the Teflon block. This was done by eliminating the heat flux on the copper heat transfer surface using a guard heater, which was attached to the vertical copper heat transfer surface. During the test, the guard heater was heated and stabilized to achieve zero heat flux between the copper heat transfer surface and the guard heater. The target heater power was recorded as the heat loss.

The heat transfer on the copper surface ($Q_{surface}$) is calculated as:

$$Q_{surface} = Q_{total} - Q_{loss} \quad (1)$$

The average heat transfer coefficient on the copper surface is calculated as:

$$h_{Average} = \frac{Q_{surface}}{A \cdot (T_s - T_{air})} \quad (2)$$

The Nusselt (Nu) number is calculated as:

$$Nu_{Average} = \frac{h_{Average} \cdot D_h}{k} \quad (3)$$

where D_h is the jet nozzle hydraulic diameter (m), and k is the air thermal conductivity (W/m-K).

Jet exit velocity measurements were taken using a TSI IFA300 constant temperature hot wire anemometer system with a TSI 1250A single-axis hotwire probe. The sensing element length was 1.27 mm with a diameter of 3.8 μm . The sensor was parallel to the long axis of the nozzle exit and to the nozzle surface. Measurement position was controlled with automated stages with a minimum step of 0.004 inches. The hotwire was calibrated prior to each test day using a TSI 1128 velocity calibrator. The standoff distance was less than 1mm. The centerline velocities were used for comparison. A typical velocity profile for the synthetic jet is shown in Figure 12.

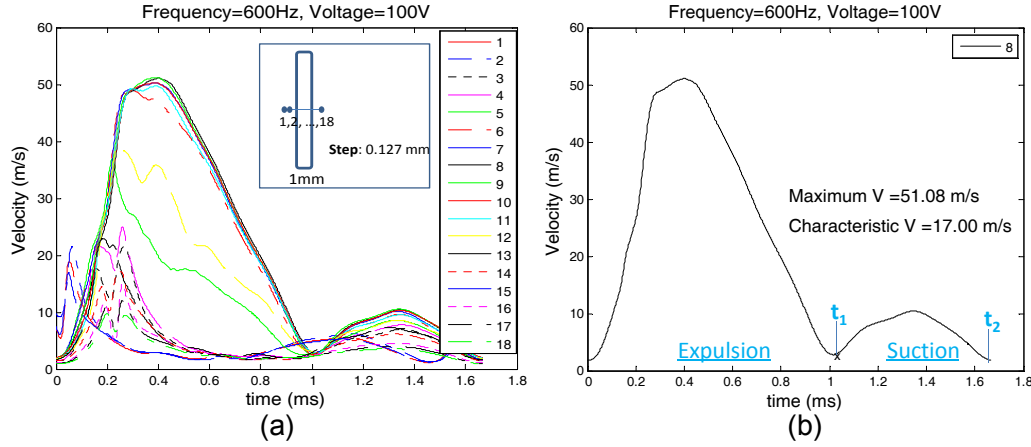


Figure 12. Instantaneous jet exit velocities for 1mm \times 8 mm jet at 100V and 600 Hz

During the suction mode, velocity is much lower than during expulsion. Since only the expulsion stroke will contribute to cooling from the target surface, the suction stroke is excluded from the characteristic Reynolds number. The characteristic synthetic jet velocity is defined as:

$$V_{SynJet} = \frac{1}{t_2} \int_0^{t_1} V(t) dt \quad (4)$$

Major sources of uncertainty for the experiments were identified as the heat losses through the heater holder, temperature measurements, heater power, and velocity measurements. As mentioned before, separate heat loss experiments were performed for the heaters to quantify the heat losses through the substrate. This was done with a guard heater. During the data reduction, the heat loss, measured with a guarded heater test, was subtracted from total power supplied into the heater. Another source of uncertainty was the T-type thermocouple measurements. Thermocouples were calibrated using an isothermal bath and reference probe, achieving a U_{95} uncertainty of 0.1°C.

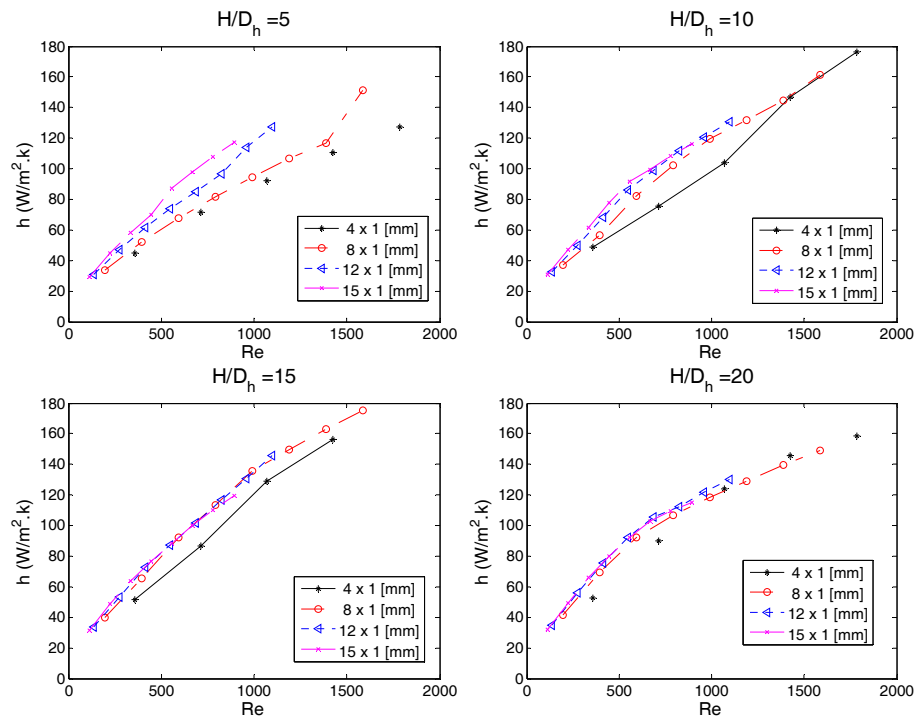
Table 3 summarizes the uncertainties calculated based on the procedures given in [3]. The largest uncertainty is found to be in the average Nu number calculation due to the propagation of uncertainties from power measurements, velocity measurement, and nozzle size measurement. Uncertainty in the velocity measurement is strongly influenced by the hotwire placement at the jet exit. The synthetic jet and steady jet systems did not have a better resolution than ± 0.1 mm. Fluid properties for Nusselt and Reynolds numbers were calculated using average measured temperatures and uncertainties were propagated.

Table 3: Uncertainties in the Experimental Measurements

| | |
|---|------|
| T-type thermocouples [$^{\circ}\text{C}$] | 0.1% |
| Heater power measurement [W] | 1.1% |
| Jet exit velocity (m/s) | 2% |
| Hydraulic diameter [mm] | 4.5% |
| Average Nu number | 5% |
| Re number | 6% |
| Heat transfer coefficient | 1.5% |

Steady Jet Heat Transfer

Experiments were conducted using four different nozzles ($1\text{ mm} \times 4\text{ mm}$; $1\text{ mm} \times 8\text{ mm}$; $1\text{ mm} \times 12\text{ mm}$; $1\text{ mm} \times 15\text{ mm}$) at four nozzle-to-plate surface distances ($H/D_h = 5, 10, 15, 20$). Figure 13 shows the variation of the averaged heat transfer coefficient as a function of Re number and nozzle geometry at each H/D_h . Generally speaking, heat transfer coefficient increases with Re number and nozzle size. For $H/D_h = 5$, nozzle geometry has significant impact on heat transfer coefficient. The impact of nozzle geometry diminishes with increasing H/D_h . For $H/D_h \geq 10$, the heat transfer coefficient is insensitive to nozzle geometry if “y” (Figure 9) is larger than 8 mm. The nozzle measuring $1\text{ mm} \times 4\text{ mm}$ exhibits the lowest heat transfer coefficient at all H/D_h values because of lower mass air flow under the same Re number.

**Figure 13. Variation of heat transfer coefficient with Re, nozzle geometry, and nozzle-to-plate spacing**

For large nozzle-to-plate spacing ($H/D_h \geq 10$) and $y/x \geq 8$, heat transfer coefficient is insensitive to both nozzle geometry and nozzle-to-plate surface distance. The correlation for the average heat transfer coefficient ($y/x \geq 8$, $H/D_h \geq 10$, $Re < 1600$) has the following form:

$$h_{ave} = 1.35 * Re^{0.655} \quad (5)$$

The averaged Nu number can be calculated as:

$$Nu_{ave} = 1.35 * Re^{0.655} \frac{D_h}{k_f} \quad (6)$$

Figure 14 compares the Nu number calculated using Equation 6 with the experimental results. The differences are within $\pm 15\%$, which means the correlation represents the heat transfer characteristics in the tested ranges.

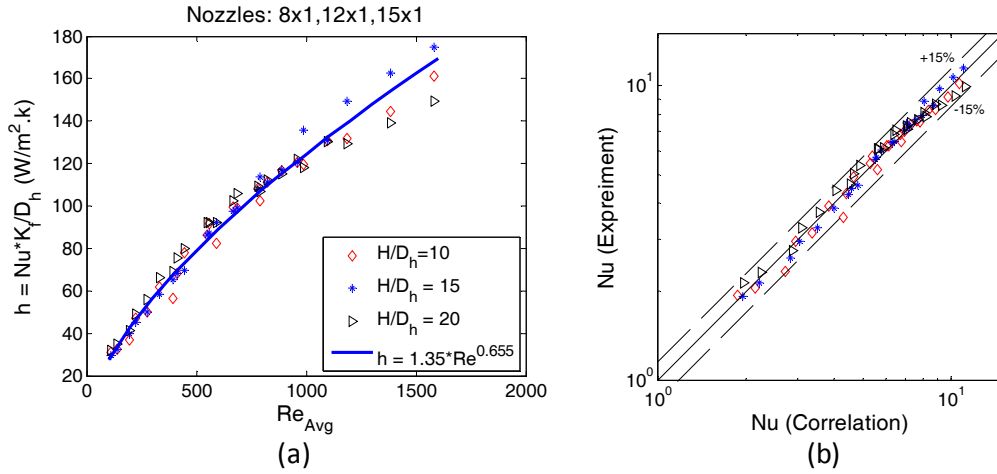


Figure 14: Correlations compared to data (a) heat transfer coefficient (b) Nusselt

For small nozzle-to-plate spacing ($H/D_h = 5$), nozzle geometry has significant impact on the average heat transfer coefficient. Figure 15 shows the variation of the average Nu number with Reynolds number and nozzle exit geometry. The average Nu number for $H/D_h = 5$ have the following form:

$$Nu_{ave} = 0.0784 * Re^m \left(\frac{H}{D_h} \right)^{-0.15} \cdot \left[a + b \cdot \frac{y}{S} + c \cdot \left(\frac{y}{S} \right)^2 \right] \quad (7)$$

where

$$m = 0.695 - \left[\left(\frac{S}{4 \cdot x} \right) + \left(\frac{H}{2 \cdot x} \right)^{1.33} + 3.06 \right]^{-1},$$

S is the width of the heat transfer surface, x is the nozzle width, and y is the nozzle length, as shown in Figure 9c.

The correlation was developed by adopting the correlation recommended by Choo *et al.* [4] and replacing the Re number exponent term (m) recommended by Martin [5]. A second order polynomial term is included to represent the effect of nozzle geometry. Constants a, b, and c are solved in least-square sense based on the experimental data, where $a = 0.826$, $b = 0.928$, $c = 0.742$.

Figure 15 also shows the Nu number predicted by Equation 7. The correlation of the average Nu number matches well with the experimental results to within $\pm 10\%$, as shown in Figure 15.

Synthetic Jet Heat Transfer

In this study, only a $1 \text{ mm} \times 8 \text{ mm}$ synthetic jet was studied. Figure 16 shows the variation of Nu number with synthetic jet Reynolds number and frequency. The steady jet Nusselt numbers are also included in the figure for comparison. For small nozzle-to-plate spacing ($H/D_h = 5$), Nu number tends to increase with jet frequency. Compared to the steady jet, the synthetic jet provided a higher Nu number. A Nu number increase as high as 40% was observed at the same Reynolds number. At a large nozzle-to-plate spacing ($H/D_h \geq 10$), jet frequency has little impact on Nu number. The difference between synthetic and steady jet tends to diminish with increasing H/D_h . At $H/D_h = 10$, the Nu numbers of the synthetic jet are about 30% higher than that of the steady jet, which reduced to 20% at $H/D_h = 15$ and 15% at $H/D_h = 20$. This is not surprising, as the dynamic feature of the synthetic jet tends to dissipate with increasing distance between nozzle and heater surface. For synthetic jet, the best heat transfer performance was observed at $H/D_h = 10$.

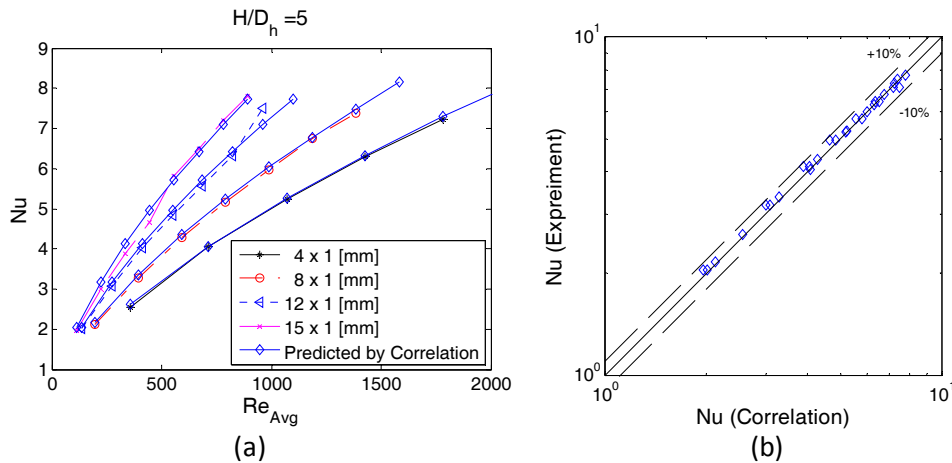


Figure 15. Variation of Nu number with Re and nozzle geometry at $H/D_h = 5$ (a) correlation and data (b) correlation error

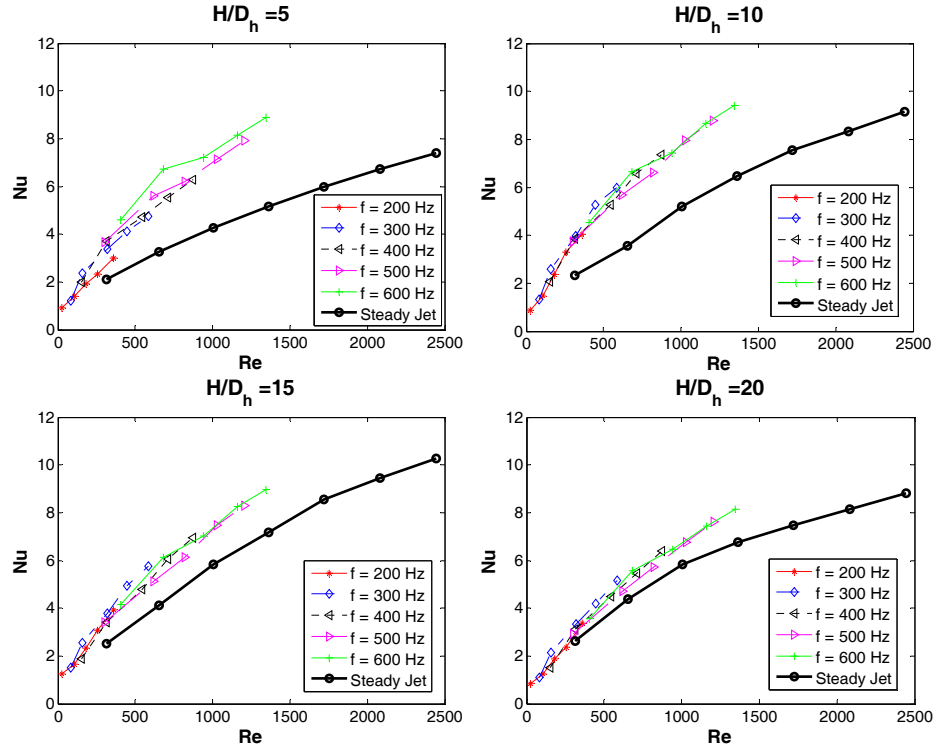


Figure 16. Variation of Nu number with Re and nozzle frequency (nozzle: 1 mm × 8 mm)

Correlating Steady Jet and Synthetic Jet Heat Transfer

Zeng *et al.* [6] conducted dimensional analysis on unsteady convective heat transfer in the internal combustion engine (ICE) intake manifold. Based on the analysis, Zeng used a dynamic correction term and introduced dynamic Reynolds number to develop the unsteady heat transfer models for heat transfer process in the ICE intake manifold. The same analysis can be applied to the impingement heat transfer on a vertical surface.

The time averaged momentum equation for the unsteady boundary layer can be written as:

$$\frac{\partial \bar{u}}{\partial t} + \bar{u} \frac{\partial \bar{u}}{\partial x} + \bar{v} \frac{\partial \bar{u}}{\partial y} = \nu \frac{\partial^2 \bar{u}}{\partial y^2} \quad (8)$$

Normalizing Equation 8 using the following dimensionless variables:

$$\begin{aligned} u^* &= \bar{u} / U, v^* = \bar{v} / U, \text{ where } U = U(t) \\ u^* &= x / L, v^* = y / L \\ t^* &= t / (L^2 / \alpha) = \text{Fourier number} \end{aligned}$$

the normalized momentum equation can be expressed as:

$$\left[\frac{L}{U^2} \frac{dU}{dt} \right] u^* + \frac{1}{\text{Re} \cdot \text{Pr}} \frac{\partial u^*}{\partial t^*} + u^* \frac{\partial u^*}{\partial x^*} + v^* \frac{\partial u^*}{\partial y^*} = \frac{1}{\text{Re}} \frac{\partial^2 u^*}{\partial y^{*2}} \quad (9)$$

In addition to Reynolds and Prandtl number, a third dimensionless variable which is related to the unsteady boundary layer is introduced as:

$$\Pi = \frac{L}{U^2} \frac{dU}{dt} = \frac{\rho \frac{dU}{dt}}{\rho U \frac{U}{L}} = \frac{\text{temporal gradient of inertial force}}{\text{spatial gradient of inertial force}} \quad (10)$$

Zeng *et al.* [6] introduced dynamic velocity using the dimensionless variable defined as:

$$U_{dyn} = U \left[1 + C \frac{L}{U^2} \frac{dU}{dt} \right] \quad (11)$$

where C is a calibration constant determined experimentally.

The analysis above was conducted based on the air velocity near the heat transfer surface. In this study, however, the velocity was measured at the nozzle exit. Here, a fourth dimensionless correction term was introduced to represent the dynamic velocity dissipation impacted by the nozzle-to-plate surface distance. For jet impingement heat transfer, the authors introduced a modified dynamic velocity as:

$$U_{dyn} = U \left[1 + C_1 \frac{D_h}{V_{SynJet}^2} \left(\frac{dV}{dt} \right)_{\max} \left(\frac{H}{D_h} \right)^{C_2} \right] \quad (12)$$

where $\left(\frac{dV}{dt} \right)_{\max}$ is the maximum changing rate of velocity, C_1 and C_2 are constants determined based on the experimental data to give the best agreement between the steady jet and synthetic jet heat transfer coefficient. The result shows that C_2 is very close to 1. To simplify the unsteady correction term, C_2 is selected to be equal to 1 and C_1 is recalculated. The following correlation best represent the dynamic Reynolds number:

$$\text{Re}_{dyn} = \text{Re} \left[1 + 1.262 e^4 \cdot \frac{D_h}{V_{SynJet}^2} \cdot \left(\frac{dV}{dt} \right)_{\max} \cdot \frac{H}{D_h} \right] \quad (13)$$

Figure 17 shows the variation of Nu number with dynamic Re number for both synthetic jet and steady jet. By introducing the dynamic correction term, the synthetic jet Nu number collapses to the steady jet Nu number. This indicates that the heat transfer coefficient is not only a function of Reynolds number, but also a function of the changing rate of velocity

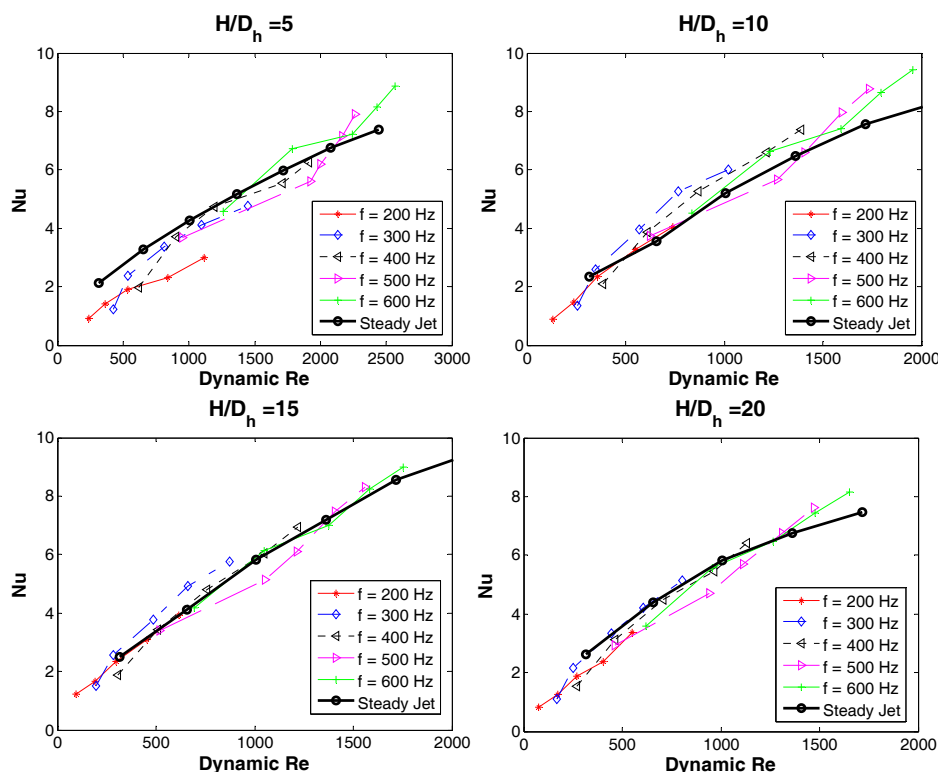


Figure 17: Variation of Nu number with dynamic Re number

Conclusion

Significant progress was made toward the project's objective to develop and apply air-cooling technology to improve power electronics thermal control design and influence industry, thereby enhancing system performance to meet DOE technical targets for weight, volume, cost, and reliability.

The high-level system analysis method was improved and applied to air- and liquid-cooled inverters. This analysis shows that by using an allowable junction temperature of 200 °C or 150 °C plus the use of an advanced spreader, the air-cooled system is able to match the power density of the liquid-cooled approach. It also showed that equal or higher electric current per silicon area could be achieved. This feasibility study demonstrates that there are several possible pathways for successful air-cooled thermal design.

The Air-Cooling Technology Characterization Platform was improved and used to measure the heat transfer performance of both steady and synthetic jets. Steady jet correlations were developed that accurately predict the experimental data. The synthetic jet exhibited better heat transfer performance than the steady jet over the entire regime tested with up to a 40% increase in Nu number for the same Re. A dynamic Reynolds number for synthetic jets was proposed and shown to collapse the data to the steady jet Nu number. This indicates that the heat transfer coefficient is not only a function of Reynolds number, but also a function of the changing rate of velocity. In addition to improved heat transfer, synthetic jets are more self contained and do not require a remote prime mover or ducting.

A new heat exchanger design that could be applicable to air-cooled or liquid-cooled systems was also conceptualized, modeled, and submitted for a non-provisional patent. The work done in FY11 laid the foundation for the research and development of advanced and effective air-cooled power electronics systems in FY12.

Publications

1. Lustbader, J.; Bennion, K.; King, C.; Krishnan, G.; Narumanchi, S. SAE World Congress: “System Level Approach to Air-Cooled Power Electronics Thermal Management” SAE World Congress, Detroit, MI, April 12-14, 2011, Presentation.
2. ITherm: “Comparison of Synthetic Jets and Steady Jets for Cooling Electronics Components” Co-authored with GE. (planned – draft complete)

Acknowledgements

- Susan Rogers and Steven Boyd, DOE Technology Development Manager for Power Electronics and Electrical Machines
- Coauthors: Kevin Bennion and Xin He (NREL)
- Thanks to: Mehmet Arik and Rajdeep Sharma (GE GRC). Charlie King and Sreekant Narumanchi (NREL)

References

1. Lustbader, J., Bennion, K., Krishnan, G. 2010, “Air-Cooling Technology for Power Electronics,” FY2010 DOE Annual Progress Report for Advanced Power Electronics and Electric Machines.
2. Glezer, A. and Amitay, M. “Synthetic Jets.” *Annual Review of Fluid Mechanics*; Vol. 34, 2002; pp. 503-529.
3. Dieck, R.H.; Steele, W.G.; Osolobe, G. “Test Uncertainty.” *ASME PTC 19.1*. New York, NY: American Society of Mechanical Engineers, 2005.
4. Choo, K.S.; Youn, Y.J.; Kim, S.J.; Lee, D. H. “Heat Transfer Characteristics of a Micro-Scale Impinging Slot Jet.” *Int. J. Heat Mass Trans*; Vol. 52, 2009; pp. 3169-3175.
5. Martin, H. “Heat and Mass transfer Between Impinging Gas Jets and Solid Surfaces.” J. P. Hartnett, J.P. and Irvine, Jr., T.F., eds. *Advances in Heat Transfer* Vol. 13, New York, NY: Academic Press, 1977.
6. Zeng, P. and Assanis, D.N. “Unsteady Convective Heat Transfer Modeling and Application to Engine Intake Manifolds.” Proceeding of IMECE 2004, 2004 ASME International Mechanical Engineering Congress and RD&D Expo, Nov. 13-19, 2004, Anaheim, CA, IMECE 2004-60068.

Patents

1. Bennion, K.; Lustbader, J, Non-provisional patent application for integrated module heat exchanger. NREL ROI-11-74. Submitted September 30, 2011
2. Bharathan, D.; Kelly, K.; Bennion, K.; Narumanchi, S. U.S. Non-Provisional Patent Application. “Fluid-cooled heat sink with improved fin areas and efficiencies for use in cooling various devices.” Number S-117593. 2011.

5.2 Thermal Performance and Reliability of Bonded Interfaces

Principal Investigator (PI): Sreekant Narumanchi

Co-PI: Douglas DeVoto

National Renewable Energy Laboratory

1617 Cole Blvd MS 1633

Golden, CO 80401

Voice: 303-275-4062; Fax: 303-275-4415; E-mail: sreekant.narumanchi@nrel.gov

DOE Technology Development Manager: Susan A. Rogers

Voice: 202-586-8997; Fax: 202-586-1600; E-mail: Susan.Rogers@ee.doe.gov

Objectives

In automotive power electronics packages (e.g., insulated gate bipolar transistor [IGBT] packages), conventional thermal interface materials (TIMs) pose a bottleneck to heat removal. Due to advantages from heat transfer and packaging standpoints, there is an industry trend towards high-thermal-performance bonded interfaces. However, due to coefficient of thermal expansion (CTE) mismatches between materials/layers and the resultant thermomechanical stresses, these interfaces are susceptible to fatigue, resulting in defects that pose a problem from a reliability standpoint. These defects, such as cracks, voids, or delaminations, manifest themselves in increased thermal resistance in the package, which again is a bottleneck to heat removal. Hence, the overall objective of this project is to investigate and improve the thermal performance and reliability of emerging bonded interface materials (BIMs) for power electronics packaging applications. Specifically, the objectives for FY2011 were:

- Establish capabilities at the National Renewable Energy Laboratory (NREL) for synthesis and characterization of thermal performance and reliability of bonded interfaces for power electronics packages.
- In conjunction with partners, synthesize large-area bonded interfaces between direct-bond-copper (DBC) substrates and copper base plates for BIMs based on lead-based solder, thermoplastics with embedded carbon fibers, and silver sintered materials.
- Initiate finite element modeling of plastic work density in the BIMs with the intent of establishing curves of experimental cycles-to-failure versus the plastic work density in the BIMs.

Approach

- Establish various bonded interfaces between 50.8 mm x 50.8 mm cross-sectional area DBC and copper base plate samples. These interfaces are based on lead-based solder (as a baseline), sintered silver (based on micrometer-sized particles), and thermoplastics with embedded carbon fibers. Also, synthesize direct-bond-aluminum (DBA) to aluminum base plate bonded interfaces in FY2012.
- Perform thermal shock and thermal cycling on these samples (going from -40°C to 150°C) according to the Joint Electron Device Engineering Council (JEDEC) standards for up to 2,000 cycles as an upper limit. Monitor thermal resistance, perform acoustic microscopy and high-potential tests on these samples after select number of thermal cycles.
- Perform mechanical tests on the select bonded interface samples to obtain information on stress versus strain relationship for the bonded material. In conjunction with modeling, this will ultimately help in establishing strain energy density versus cycles to failure curves for the different bonded interfaces.
- Change synthesis parameters to obtain improved thermal performance and reliability for the emerging/novel bonded interfaces under investigation.

Major Accomplishments

- We acquired the C-mode scanning acoustic microscope (C-SAM), laser profilometer as well as a shear tester from XYZTEC. The acoustic microscope helps in quantitative examination of the quality of the bonded interfaces, the laser profilometer helps in determining camber and surface flatness of the bonded samples, and the XYZTEC tester helps in determining shear strength of the bonds as well as in establishing stress-strain constitutive relations for the BIMs.
- Bonded interfaces were established between 50.8 mm x 50.8 mm cross-sectional area DBC and copper base plate samples for lead-based solder, thermoplastics with embedded carbon fibers, and silver sintered materials. Initial thermal cycling (up to 100 cycles) was performed on these samples.
- Initial results suggested that good quality bonds between the DBC and base plates were obtained with the thermoplastics.

Future Direction

The following activities are envisioned for this project for FY2012 and potentially FY2013.

- Due to issues with delamination as well as cracking of the DBCs (based on aluminum nitride [AlN] ceramic), a decision was made to acquire silicon nitride (Si_3N_4) – based substrates in early FY2012 with the same 50.8 mm x 50.8 mm cross-sectional area. Bonds between these new active metal bonding (AMB) substrates and copper base plates will be established for the 3 materials mentioned previously.
- Due to strong industry interest, also acquire DBAs and aluminum base plates with the same cross-sectional area as mentioned above, and establish bonded interfaces between the DBAs and aluminum base plates.
- Establish the shear strength and stress-strain constitutive relations for the three BIMs.
- Synthesize and characterize the various bonded interfaces mentioned in the Approach section. In conjunction with modeling [finite element analysis (FEA)] and incorporating suitable constitutive models for the BIMs, obtain information on cycles-to-failure for these interfaces.
- Characterize the degradation in thermal resistance of the BIMs with increasing number of thermal cycles.

Technical Discussion

In a power electronics module, a semiconductor chip/die is typically attached by a BIM such as solder to a DBC. The DBC is composed of a ceramic substrate bounded by copper layers on either side and provides electrical isolation. This DBC is then mounted on to a base plate or directly to a heat sink, typically made of copper or aluminum, via another BIM. A cross-section of a typical power electronics package is shown in Figure 1 [1].

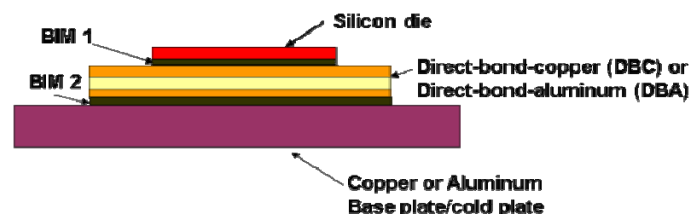


Figure 18. A typical power electronics package

A CTE mismatch between the ceramic substrate and the copper base plate can cause crack initiation and propagation in the joining solder layer. Lead-based solders have predominantly been used in the

electronics packaging industry; however, Restriction of Hazardous Substances compliance necessitates the need for lead-free solutions. Initially, the industry focused on various SAC (tin, silver, and copper) compositions as a suitable lead-free alternative, with Innolot (SnAg3.8Cu0.7Bi3.0Sb1.4Ni0.2) proving to be a promising solution [2, 3]. Research found that varying the composition of silver and copper content in the solders would help minimize creep strain. Overall, reliability under temperature cycling continues to be a concern with lead-free solders. To provide greater thermomechanical reliability under temperature cycling and to allow for higher temperature applications, sintered silver material has also emerged as a promising bonding solution in power electronics packages [4, 5]. However, to reduce processing/synthesis temperatures to below 300°C, up to 30 MPa of pressure must be applied to the package, causing a higher complexity in the production process and more stringent flatness specifications of the substrates. Hence, alternative bonding techniques are being developed to increase the thermomechanical reliability of this joint through the use of newer materials, such as thermoplastics with embedded micrometer-sized carbon fibers. Little information is available on the thermal performance and reliability of large-area attaches based on the more recently developed thermoplastic materials.

Prior work at NREL [1, 6] focused on establishing a consistent and high-accuracy database, via the ASTM steady-state approach [7], on the thermal performance of conventional as well as emerging TIMs. The conventional materials included greases, gels, phase-change materials, and filler pads. It was concluded that the tested conventional materials could not meet the thermal performance specification of 5-mm²K/W thermal resistance for a 100-μm bondline thickness. For a number of power electronics packaging stack-ups, the TIM stops being a bottleneck to heat removal when its resistance is on the order of 5 mm²K/W, which is the reason why it is a target. In addition, practical power electronics packaging configurations and manufacturing constraints dictate that the TIM has to fill gaps on the order of 100 μm. Due to the promise of BIMs [8–12], work at NREL is now focused on assessing their thermal performance and reliability. Conclusions on thermal performance and reliability from this effort are intended to directly assist the incorporation of these materials into automotive power electronic designs. This report focuses on thermoplastic (polyamide) adhesive with embedded near-vertical aligned carbon fibers (8- to 10-μm diameter), sintered silver based on micrometer-sized silver particles, and lead-based solder as a baseline. The sample synthesis, characterization plan, and results are described below.

Materials and Sample Synthesis

The assembly consists of a 5-mm-thick copper base plate attached to a 1.235-mm-thick DBC substrate (0.635-mm-thick AlN with 0.3-mm-thick Cu foil on either side of AlN, 50.8 mm x 50.8 mm cross-sectional area footprint) via the bonding material. Before assembly, the copper layers in the DBC substrate and the copper base plate were electroplated with 0.2-μm-thick and 5-μm-thick layers of silver, respectively, to improve adhesion with the bonding material. An assembled sample is shown in Figure 2.

We developed a tabletop hot press for synthesizing test samples, as shown in Figure 3. Two hot plates are positioned on either side of the sample to be bonded and are embedded with five 250-W cartridge heaters. Three heaters are inserted in the top hot plate and two in the bottom hot plate. A temperature controller adjusts the power of the heaters based upon the temperature measurement by a thermocouple located in the bottom hot plate. The test sample and hot plates are placed between layers of mica and cold plates (Figure 3), and then inserted into an arbor press [13]. Glycol-water (50%–50% mixture by volume) coolant is circulated within the cold plates to isolate the high bonding temperatures from the hydraulic piston and fluid. A screw jack is also placed between the hydraulic piston and top cold plate to provide fine adjustment to the applied bonding pressure. The pressure of the hydraulic fluid is electronically monitored to determine the force applied to the sample under bonding.

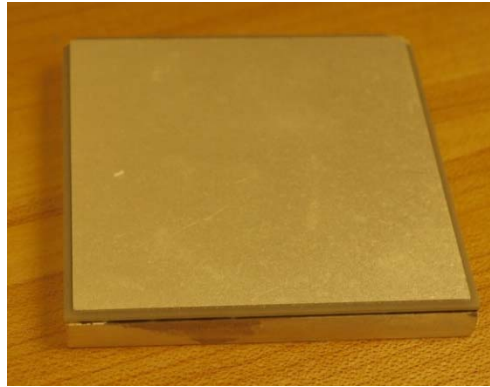


Figure 19. Representative DBC/base plate assembly (Photo credit: Doug DeVoto, NREL)

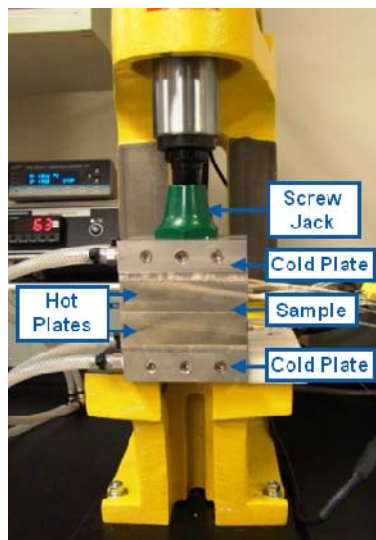


Figure 20. NREL hot press (Photo credit: Doug DeVoto, NREL)

The thermoplastic HM-2, manufactured by Btech Corporation, was placed between the DBC/base plate assembly and subjected to a pressure of 689.5 kPa and a temperature of 190°C. Once the temperature was reached, the assembly was allowed to cool down to room temperature while maintaining the pressure. Figure 4 shows a representative scanning electron microscopy (SEM) image, which shows the 8- to 10- μm -diameter carbon fibers embedded in the polyamide/thermoplastic adhesive. As a baseline, a lead-based (Sn63Pb37) bond was also synthesized between the DBC/base plate assembly. Bonded interfaces based on micrometer-sized sintered silver particles were also synthesized. The synthesis of bonded samples based on lead-based solder and sintered silver materials were performed by Virginia Tech.

For synthesis of the lead-solder-based samples, a 50.8- μm stainless-steel stencil was raised to 101.6 μm with Kapton tape and placed over the base plate. The stencil pattern had 9-mm x 9-mm square openings with 1-mm separations. The assembled sample passed through a Sikama reflow oven following the recommended profile as shown in Figure 5. The reflow profile had a maximum temperature of 225°C.

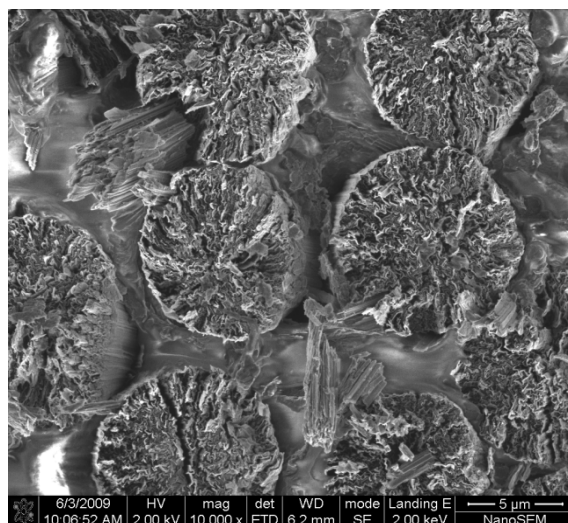


Figure 4. SEM image showing carbon fibers embedded in the polyamide/thermoplastic (Btech HM-2)
(Photo credit: Bobby To, NREL)

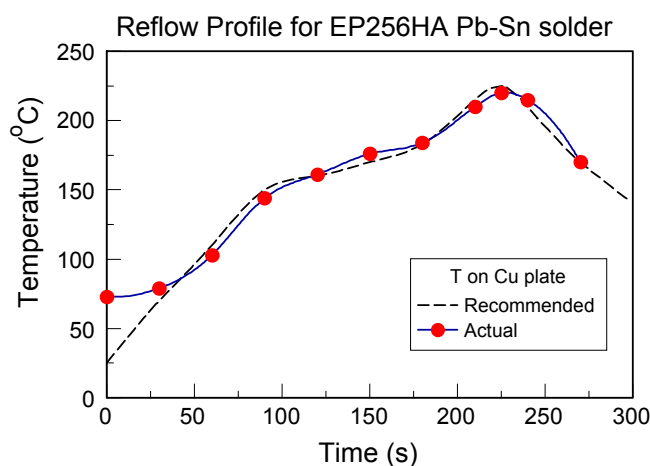


Figure 5. Reflow profile for lead-based solder

For the samples with bonded interfaces based on sintered silver, two layers of paste were applied with a 50.8- μm stencil, and each layer was dried after application at 80°C for 30 minutes. The binder was burned off for 2 hours at 250°C, and then the assembly was heated to 280°C and underwent 30 MPa of pressure for 30 minutes. High bonding temperatures and pressures caused cracking within the AlN layer, and poor adhesion at the edges was revealed in the C-SAM images (Figure 6). Cracking of the AlN occurred in most of the samples with the sintered silver bonded interface. However, there were a couple of samples in which the AlN did not crack. These select samples will be cycled to determine the quality of the bonded interface after cycling. Overall, due to the quality issues with the AlN-based DBC, the bonding procedure for sintered silver material will be repeated with Si_3N_4 -based DBC substrates in FY2012.

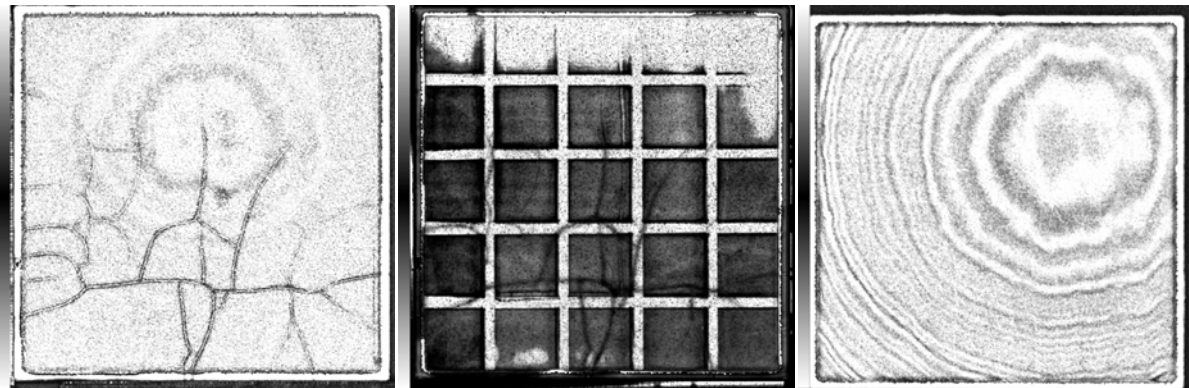


Figure 6. C-SAM images showing cracks in the AlN layer (left image), the sintered silver bonded interface layer (middle image) and a different sample in which the AlN layer is not cracked (right image) (Photo credit: Doug DeVoto, NREL)

Material Characterization

Degradation (e.g., cracks, voids, and delaminations) of the bonded interface can be non-destructively detected by several measurement techniques. After defect initiation, the thermal and electrical performance of the sample assembly degrades. Samples were measured for initial performance and then subsequently tested after a few thermal cycles.

We have previously developed a steady-state thermal resistance tester [6] based on ASTM test method D5470 [7]. The test setup, shown in Figure 7, consists of an aluminum hot plate with embedded cartridge heaters and an aluminum cold plate with silicone oil circulating through it. Between the hot and cold plates are copper spreader blocks and copper metering blocks with embedded resistance temperature detectors (right side of Figure 7). A layer of thermal grease with 25- μm glass beads was applied to the surfaces of the metering blocks to ensure a consistent and known thermal resistance between the blocks and the sample under test.

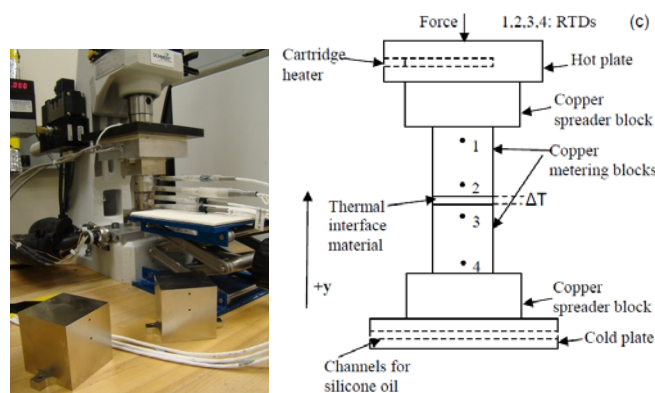


Figure 7. Steady-state thermal resistance tester shown with 50.8-mm square metering blocks (left) and as a schematic (right) (Photo credit: Doug DeVoto, NREL)

In addition to steady-state thermal resistance measurements, the electrical resistance of the AlN insulation layer was also measured. In a high-potential (hipot) test, a high voltage is applied to an electronic device's current-carrying components. The quality of the insulation in the device is determined by measuring the presence of a leakage current. Leakage current indicates that dielectric breakdown in the insulation layer has occurred [14]. We constructed a dielectric resistance tester based on the hipot testing process to detect

when a crack in the AlN within the DBC/base plate assembly has developed. A custom fixture contacts the top and bottom sides of a test sample and applies a test voltage of 2.0 kV, which is sufficient voltage to cause an arc in the air through a defect/crack in the 0.635-mm-thick AlN layer. Measurement of the leakage current from an arc indicates that damage has occurred within the AlN layer in the sample. The dielectric tester is surrounded by an acrylic safety enclosure to protect the operator from the high voltages used during sample examination. The fixture and enclosure are shown in Figure 8.



Figure 8. Dielectric resistance tester (Photo credit: Doug DeVoto, NREL)

Additional non-destructive investigation of the test samples includes the detection of cracks, voids, and delaminations by a C-SAM. The microscope emits ultrasound waves with frequencies ranging from 5 MHz to 400 MHz into a sample suspended in water. The strength of the signal reflected back to the microscope's transducer from an interface within a sample depends on the relationship between the acoustic impedances of the two materials forming the interface. A crack, void, or delamination will create a solid-to-air interface, the presence of which will cause a strong reflection to be detected by the microscope's transducer.

Initial Sample Performance

The thermal resistance of each sample prior to any thermal cycling was characterized in the steady-state thermal resistance tester. The values listed in Table 1 signify the total thermal resistance between the metering blocks in the tester, including the resistance of the bonded DBC/base plate sample and the 25- μ m thermal grease layers on both sides of the sample.

Table 4. ASTM Thermal Resistance of Samples ($\text{mm}^2\text{K/W}$)

| Sample Number | 1 | 2 | 3 | 4 | 5 |
|---------------|------|------|------|------|------|
| Sn63Pb37 | 44.6 | 41.2 | 41.0 | 41.3 | 40.4 |
| Btech HM-2 | 49.6 | 58.5 | 56.5 | 56.5 | - |

Differences in thermal conductivity of the materials as well as voiding in the interface during the bonding process possibly account for the performance variation. Due to camber in the samples after synthesis, it is also likely that the grease thickness between the metering blocks and the samples during the thermal resistance measurements may be more than 25 μ m. We are currently determining the grease thickness more accurately by measuring each sample's camber with a laser profilometer.

CTE mismatches within the samples cause stresses to build up in the AlN layer during the cool down from the synthesis temperature to room temperature. These stresses can be sufficient to cause cracking within the ceramic/AlN, leading to failure of the layer's electrical insulating properties. Each sample was

placed in the dielectric resistance tester, and a voltage of 2.0 kV was applied for 20 seconds. The sample successfully passed the test if no current was measured over the analysis period. A failure indicated an internal crack within the AlN layer. The results of the dielectric resistance testing are shown in Table 2. The results show that the Sn-Pb and thermoplastic bonding process posed no issues for the ceramic layer.

Table 5. Dielectric Resistance Test Results

| Sample Number | 1 | 2 | 3 | 4 | 5 |
|---------------|------|------|------|------|------|
| Sn63Pb37 | Pass | Pass | Pass | Pass | Pass |
| Btech HM-2 | Pass | Pass | Pass | Pass | Pass |

Acoustic imaging of the samples highlights initial defects created during the bonding process. While the thermoplastic exhibited a uniform bond between the base plate and DBC, a low percentage of voiding (less than 5%) was found in the Sn-Pb samples. This could be minimized by using a vacuum solder reflow unit instead of the current non-vacuum hot press. Images of both the Btech thermoplastic sample and the Sn-Pb sample are shown in Figure 9. The higher contrast image of the Sn-Pb sample highlights the voided regions as light-colored areas.

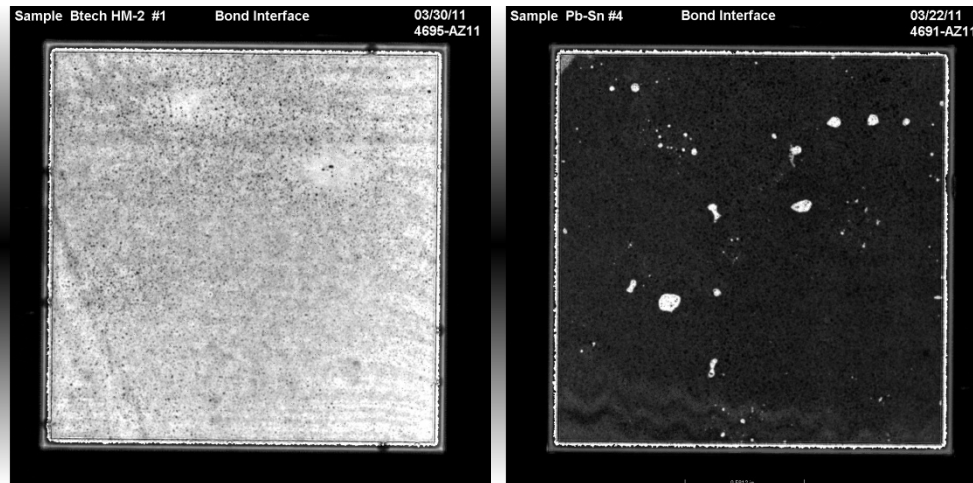


Figure 9. C-SAM images of a Btech thermoplastic sample (left) and Sn-Pb sample (right) at the bonded interface after synthesis (Photo credit: Doug DeVoto, NREL)

Bonded Interface Condition After Thermal Cycling

After initial characterization of the test samples, conditions must be applied to create thermally induced stresses, leading to cracking, voiding, or delamination failures. Generally, there are three types of thermal duty cycles that can be used to create thermally induced stresses: a temperature cycle, a thermal shock cycle, and a power cycle. A temperature cycle specifies the temperatures to which a sample under test will be exposed, the durations of exposure, and the rate of change of temperature when the sample under test is brought to a new temperature set point. A thermal shock cycle is similar to a temperature cycle, but consists of rapid changes in the ambient temperature. Finally, a power cycle is created by heat dissipation in an actual electronic device to create realistic heat flow patterns and temperature distributions in a sample under test. Because the lifetimes of samples are too long to be tested in real time, an accelerated temperature cycling test procedure is employed to bring testing times down to a reasonable duration. We initiated cycling of the samples between -40°C and 150°C, a common temperature range for electronics testing, to evaluate the quality of the bonded interfaces [15–18]. A soak, or dwell, time of 10 minutes at the maximum and minimum temperatures is prescribed for solder fatigue and creep testing of

interconnections [15]. Ramp rates for thermal cycling must be sufficiently low to avoid transient thermal gradients in the test samples; therefore, ramp rates were in the 10°C/min range.

The chamber used for the thermal cycling of the samples is shown in Figure 10 along with the cycling profile. The temperature profile shows the intended profile, while the sample profile shows the representative temperature in the sample (two base plates sandwiched together with the thermocouple in between to monitor the temperature) measured by a thermocouple during the temperature cycling.

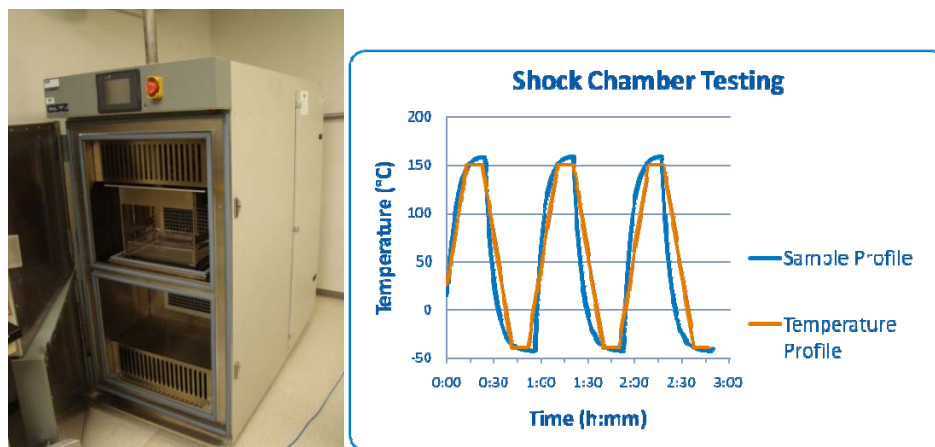


Figure 10. Thermal shock chamber (left) and the cycling profile (bottom)
(Photo credit: Doug DeVoto, NREL)

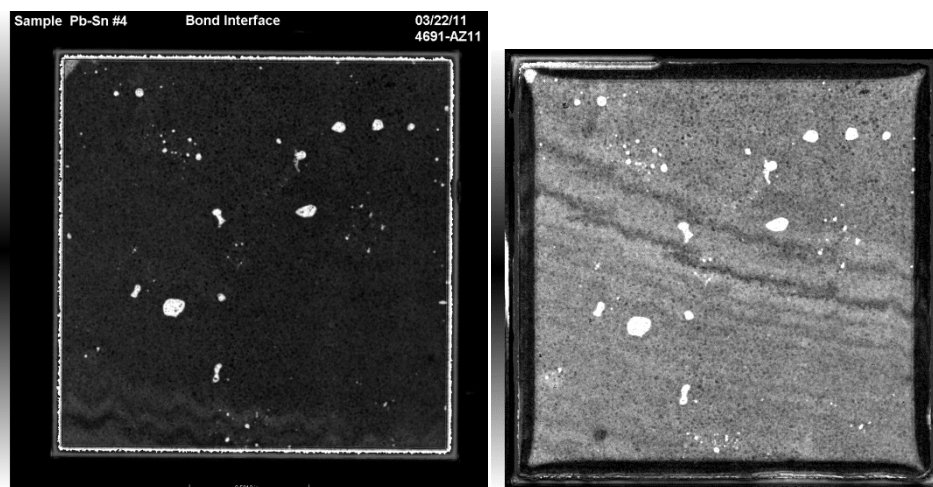


Figure 11. C-SAM images of Sn-Pb samples before cycling (left) and after 100 thermal cycles

Figures 11 and 12 show the C-SAM images of the interfaces based on the Sn-Pb solder and the Btech HM-2 thermoplastic material, respectively, before and after thermal cycling. Results are shown after only a few thermal cycles because the DBC itself was delaminating (i.e., the Cu was delaminating from the AlN). Fairly severe DBC delamination was observed after 100 thermal cycles. The thermal cycling tests were stopped after 100 cycles because DBC delamination prevents an assessment of the quality of the bonded interfaces. However, the C-SAM images of the bonded interface after a few cycles (Figures 11 and 12), in conjunction with the hipot test results as well as thermal resistance measurements, indicate that the interfaces based on these two materials presented are of a reasonably good quality. Similar to the

sintered silver material, bonding for both the Sn-Pb and thermoplastic material will be repeated on a DBC/base plate assembly with the DBC based on Si_3N_4 .

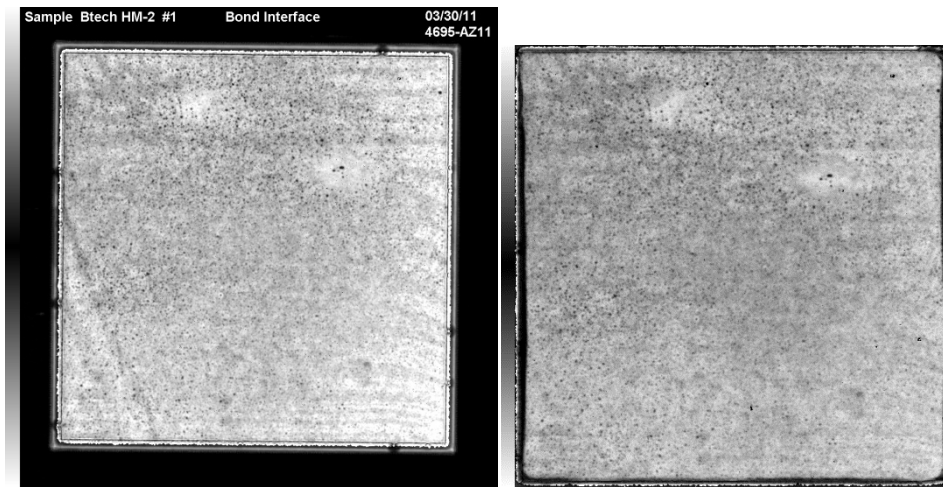


Figure 12. C-sam images of btech samples before (left) and after 20 thermal cycles (right)

Modeling of Plastic Work Density in the BIMs

There is a link between the thermal cycles-to-failure (with failure defined in an appropriate/suitable way) and the plastic work density of the BIM. The intent of this work is to establish curves for experimentally determined cycles-to-failure to the plastic work density obtained from FEA for the different BIMs.

This FEA analysis was performed in ANSYS, and the simulation domain is shown in Figure 13. It consists of 50.8 mm x 50.8 mm cross-sectional area composed of a copper base plate, a lead-based solder (63Sn-37Pb) BIM, and a DBC based on AlN (layers are similar to Figure 1 except there is no silicon die and die-attach solder). Due to the complex nature of the viscoplastic BIM, the solution time can be intensive [17]. Symmetry conditions were utilized to generate a quarter package geometry, which reduces the solution time without loss of any relevant/valuable information (Figure 13). The vertex on the bottom corner of the base plate in the center of the package was fixed. This was done under the assumption that the center of the package/assembly sees zero displacement or deformation as the materials expand and contract under temperature variations.

The model was subjected to an accelerated temperature cycle. First, the sample temperature came down from the reflow temperature (150°C in this example) to room temperature (22°C), and then the temperatures cycled between 150°C to -40°C with 10-minute temperature dwells and 10°C/min ramp rates (Figure 14). Four temperature cycles were simulated to reduce the solution time of the problem. The analysis assumed there was no temperature variation throughout the domain during thermal cycling, so analysis was performed at increasing increments of constant temperature.

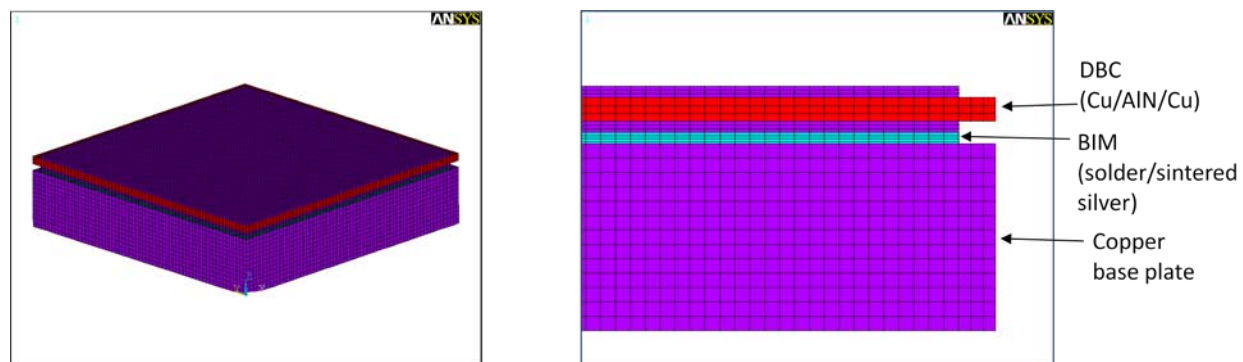


Figure 13. Quarter symmetry model (left) and layers in the bonded assembly (right)

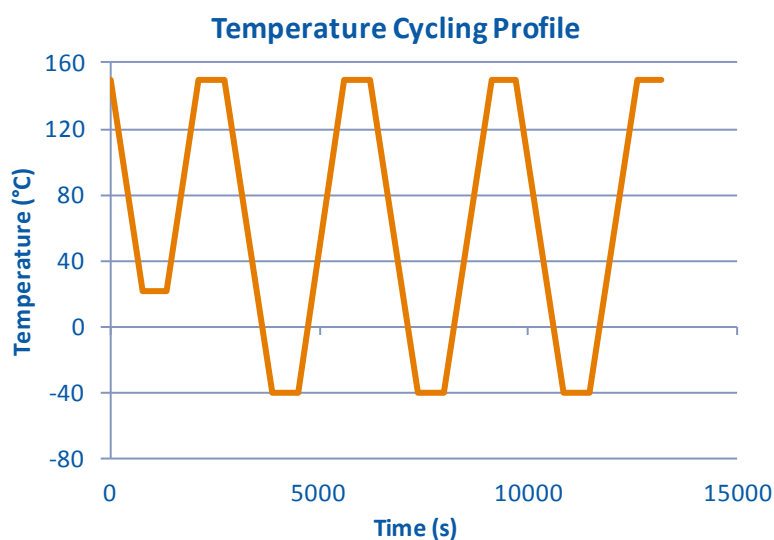


Figure 14. Temperature cycling profile of the DBC/base plate bonded assembly

Copper and AlN materials exhibit temperature-dependent properties that are defined in the script for the FEA [18]. The viscoplastic material properties are assigned to the lead-based solder BIM, and the Anand model [19] is used to describe the stress-strain constitutive relationship for the solder. As a result of the mismatch in CTE, interfacial stresses are generated at various temperatures. The viscoplastic nature of the BIM causes the material to undergo plastic deformation with every thermal cycle. Plastic strain energy density is calculated as an average over a prescribed volume because the edge elements undergo a greater amount of plastic strain than the elements closer to the center. As mentioned previously, joint/bond failure directly correlates to the strain energy density (plastic work) within the material [19]. Therefore, volume-averaged plastic work can be used a metric that relates to the reliability of the bonded assembly.

Plastic work is computed using ANSYS Mechanical. The results illustrate that the region of highest plastic strain occurs at the corner of the solder layer (Figure 15). The maximum plastic work occurs at the interface between the BIM and the base plate at the corner of the solder joint (Figure 16). The corner at the interface between the solder and the DBC is also selected for plastic work analysis. Values for plastic work are significantly less at the DBC/solder interface than at the solder/base plate interface (Figure 17). A specified corner region of the solder joint is the third location at which the plastic work is evaluated. This region takes the solder elements/volumes across the joint thickness into consideration instead of only

the elements/volumes at the interfaces. These calculations over a volume/element spread over the joint thickness are more applicable to reliability and failure predictions because the plastic work correlates to a larger volume instead of a localized point. As seen in the graph, the corner plastic work analysis fits in between the two extremes of the nodal analyses and therefore gives a better interpretation of joint failure (Figure 17).

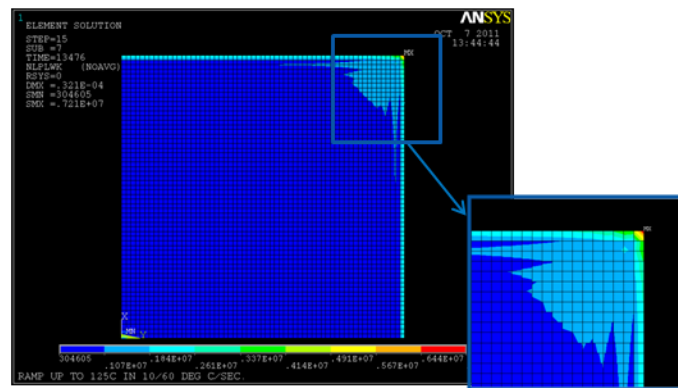


Figure 15. Plastic work at the corner of the solder joint layer (view is of the solder/base plate interface)

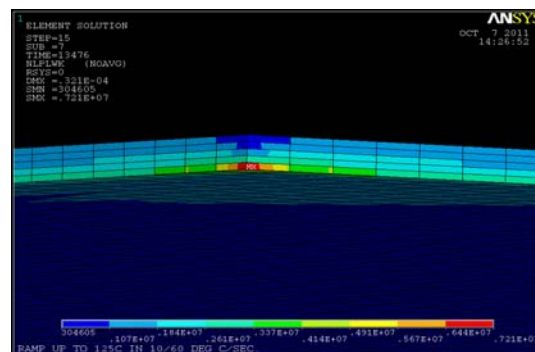


Figure 16. Plastic work in the BIM

Parallel computing on multiple cores was utilized to generate the numerical results. Various run times were evaluated using a simplified model to run on different number of cores. Variations of one, two, four, and eight cores were tested, and eight cores produced the fastest solution times. However, speed-up in simulation time exhibited an asymptotic behavior, with the speed-up in solution time starting to level off at four cores.

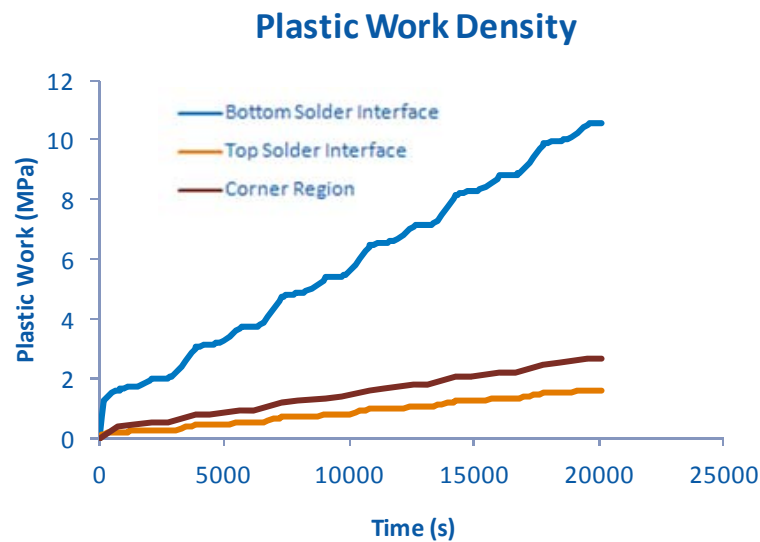


Figure 17. Plastic work values over time in the solder joint

The next phase of the work is to experimentally determine the stress-strain constitutive relations for the BIMs (lead-based solder, sintered silver, thermoplastics) and develop appropriate constants for the Anand model to feed into the FEA. Appropriate Anand models for the BIMs would help determine generate graphs similar to Figure 17 for the plastic work density for the different BIMs. These plastic work densities will then be linked to the experimental number of thermal cycles-to-failure.

Conclusion

We have implemented a consistent framework to establish the thermal performance and reliability of large-area bonded joints based on novel/emerging materials such as thermoplastics with embedded carbon fibers and silver sintered materials as compared to lead-based solder. These large-area attachments are currently being considered in state-of-the-art power electronics packages for hybrid and electric vehicle applications. Initial results for bond quality suggest that thermoplastics with embedded fibers could be a promising alternative to lead-based solders.

Significant quality issues were encountered with the AlN-based DBCs in terms of delamination after a few thermal cycles as well as cracking of the AlN under high temperature and pressure for the synthesis of the sintered silver bonded interfaces. This necessitated consideration of Si_3N_4 -based DBCs. A detailed plan for synthesis and characterization of bonded interfaces between DBC (Si_3N_4) and copper base plate is currently under implementation. Bonded interfaces between DBA/aluminum base plate will also be synthesized and characterized to cater to the strong industry interest.

Modeling of plastic work density for the lead-solder BIM bonded between the DBC and copper base plate was performed using the Anand model parameters for the solder BIM from the literature. The results appear reasonable and will be leveraged in the efforts to generate experimental cycles-to-failure versus plastic work density (obtained from modeling) curves for the different BIMs of interest.

Publications

1. Narumanchi, S., DeVoto, D., Mihalic, M., Popp, T., and McCluskey, P. (2011). "Thermal performance and reliability of large-area bonded interfaces in power electronics packages," IMECE2011-65399, *Proceedings of the 2011 ASME Mechanical Engineering Congress & Exposition*, November 2011, Denver, CO.

Acknowledgments

The authors would like to acknowledge the support provided by Susan Rogers and Steven Boyd, technology development managers for Advanced Power Electronics and Electric Motors, Vehicle Technologies Program, U.S. Department of Energy Office of Energy Efficiency and Renewable Energy. The contributions of Mark Mihalic, Tim Popp, and Patrick McCluskey (NREL) to the project are acknowledged. The authors would also like to acknowledge Jay Browne (Btech Corporation) for providing the HM-2 thermoplastic films, as well as G.-Q. Lu and Jesus Calata (Virginia Tech) for providing the lead-based solder and sintered silver bonded samples.

Nomenclature

| | |
|-------|--|
| AlN | aluminum nitride |
| Ag | silver |
| ASTM | ASTM International |
| BIM | bonded interface material |
| C-SAM | C-mode scanning acoustic microscope |
| CTE | Coefficient of thermal expansion |
| Cu | copper |
| DBA | direct-bond-aluminum |
| DBC | direct-bond-copper |
| Hipot | high-potential |
| HM-2 | thermoplastic adhesive with embedded carbon fibers |
| IGBT | insulated gate bipolar transistor |
| Pb | lead |
| SAC | solder composed of tin, silver and copper |
| SEM | scanning electron microscopy |
| Sn | tin |
| TIM | thermal interface material |

References

1. Narumanchi, S., 2008, 2009, *Thermal Interface Materials for Power Electronics Applications*, NREL Technical Report MP43970, September 2008; NREL Technical Report, September 2009.
2. Dudek, R., Faust, W., Ratchev, R., Roellig, M., Albrecht, H., Michel, B., 2008, "Thermal Test- and Field Cycling Induced Degradation and its FE-based Prediction for Different SAC Solders," 11th Intersociety Conference on Thermal and Thermomechanical Phenomena in Electronic Systems, ITherm 2008, pp.668–675.
3. Wang, Q., Johnson, W., Ma, H., Gale, W. F., Lindahl, D., 2005, "Properties of Lead Free Solder Alloys as a Function of Composition Variation," Proceedings ECWC 10 at IPC Printed Circuits Expo, SEMA Council APEX and Designers Summit 05, pp. 02-6–02-6-13.
4. Schulze, E., Mertens, C., Lindemann, A., 2009, "Low Temperature Joining Technique – a Solution for Automotive Power Electronics," 2009 Power Conversion, Intelligent Motion (PCIM), Nuremberg, Germany.

5. Schulze, E., Mertens, C., Lindemann, A., 2010, "Pure Low Temperature Joining Technique Power Module for Automotive Production Needs," 6th International Conference on Integrated Power Electronics Systems (CIPS), Nuremberg, Germany.
6. Narumanchi, S., Mihalic, M., Kelly, K., Eesley, G., 2008, "Thermal Interface Materials for Power Electronics Applications," Proceedings of the IThERM Conference, Orlando, FL, May 28–31, 2008, pp. 395–404.
7. American Society for Testing and Materials, 2005, ASTM Standard D5470-01.
8. Chuang, R. W., Lee, C. C., 2002, "Silver-Indium joints produced at low temperature for high temperature devices," IEEE Transactions on Components and Packaging Technologies, **25**, (3), pp. 453–458.
9. McCluskey, P., Quintero, P. O., 2007, "High temperature lead-free attach reliability," Proceedings of InterPACK 2007, IPACK2007-33457, Vancouver, British Columbia, Canada, July 8–12, 2007.
10. Wu, R., McCluskey, F. P., 2007, "Reliability of indium solder for cold temperature packaging," Proceedings of InterPACK 2007, IPACK2007-31456, Vancouver, British Columbia, Canada, July 8–12, 2007.
11. Lu, G-Q., Zhao, M., Lei, G., Calata, J. N., Chen, X., Luo, S., 2009, "Emerging lead-free, high-temperature die-attach technology enabled by low-temperature sintering of nanoscale silver pastes," 2009 International Conference on Electronic Packaging Technology & High Density Packaging (ICEPT-HDP), pp. 461–466.
12. Lei, T. G., Calata, J. N., Lu, G-Q., Chen, X., Luo, S., 2010, "Low-temperature sintering of nanoscale silver paste for attaching large-area ($>100 \text{ mm}^2$) chips," IEEE Transactions on Components and Packaging Technology, **33**, (1), pp. 98–104.
13. Enerpac, 2011, "Arbor, c-clamp and bench frame presses," <http://www.enerpac.com/en-US/products/presses/arbor-c-clamp-and-bench-frame-presses>. Accessed May 2011.
14. Associated Research, Inc., "Exploring the Necessity of the Hot Hipot Test," <http://www.asresearch.com/events-training/pdfs/HotHipot.pdf>. Accessed May 2011
15. JEDEC Solid State Technology Association, 2009, "JESD22-A104D Temperature Cycling."
16. Vandevelde, B., Gonzalez, M., Limaye, P., Ratchev, P., Beyne, E., 2007, "Thermal cycling reliability of SnAgCu and SnPb solder joints: A comparison for several IC-packages," Microelectronics Reliability, **47**, pp. 259–265.
17. Aoki, Y., Tsujie, I., Nagai, T., 2007, "The effect of ramp rate on temperature cycle fatigue in solder joints," Espec Technology Report, pp. 4–13.
18. Lu, G-Q., Calata, J. N., Lei, G., Chen, X., 2007, "Low-temperature and Pressureless Sintering Technology for High-performance and High-temperature Interconnection of Semiconductor Devices," 2007 International Conference on Thermal, Mechanical and Multi-Physics Simulation Experiments in Microelectronics and Micro-Systems, EuroSime, pp. 1–5.
19. Zahn, B. A., 2002, "Finite Element Based Solder Joint Fatigue Life Predictions for a Same Die Stacked Chip Scale Ball Grid Array Package," ChipPAC Inc.
20. Lau, L., Pao, Y., 1997, *Solder Joint Reliability of BGA, CSP, Flip Chip, and Fine Pitch SMT Assemblies*. The McGraw Hill Company, pp. 115–120.
21. Darveaux, R., "Effect of Simulation Methodology on Solder Joint Crack Growth Correlation," Proceeding of 50th Electronic Components & Technology Conference, May 2000, pp. 1048–1058.

5.3 Light-Weight, Single-Phase Liquid-Cooled Heat Exchanger/Cold Plate

Principal Investigator (PI): Sreekant Narumanchi

National Renewable Energy Laboratory

1617 Cole Blvd MS 1633

Golden, CO 80401

Voice: 303-275-4062; Fax: 303-275-4415; E-mail: sreekant.narumanchi@nrel.gov

DOE Technology Development Manager: Susan A. Rogers

Voice: 202-586-8997; Fax: 202-586-1600; E-mail: Susan.Rogers@ee.doe.gov

Objectives

Reducing cost and increasing power density and specific power are some of the key objectives of the U.S. Department of Energy (DOE) Advanced Power Electronics and Electrical Motors (APEEM) program to meet the 2015 and 2020 program targets and to help increase market penetration of electric-drive vehicles. The overall objective of this project is to design, develop, characterize and demonstrate a light-weight, low-cost, inverter-scale (based on the UQM inverter) single-phase liquid-cooled [with water-ethylene glycol (WEG), (50%-50% mixture by volume) coolant] heat exchanger/cold plate, which is a significant improvement over conventional channel-flow-based heat exchangers. The specific objectives for FY2011 were:

- Design the heat exchanger based on impinging jets in conjunction with microfinned/enhanced surfaces on the copper base plate and a plastic fluid manifold using finite-element analyses (FEA) as well as computational fluid dynamics (CFD) modeling.
- Characterize the thermal performance of the channel-flow-based heat exchanger via the transient thermal tester.
- Initiate characterization of the reliability of jet impingement.

The objectives for FY2012 are:

- Fabricate prototype heat exchangers and characterize thermal performance via experiments on the transient thermal tester as well as utilizing the dynamometer.
- Complete characterization of reliability of jet impingement on plain surface as well as on microfinned surfaces.

Approach

- Using CFD, design a heat exchanger based on impinging jets of WEG in conjunction with microfinned surfaces and a fluid-manifold made of automotive-grade glass-fiber reinforced nylon plastic. Through modeling, demonstrate improvements in thermal performance for the new heat exchangers as compared to the baseline channel-flow-based heat exchanger.
- Fabricate the prototypes using mass-manufacturing techniques (e.g., casting, injection molding) to yield the lowest cost.
- Characterize the thermal performance of the new heat exchangers (one based on impingement on a plain surface and another based on impingement on a microfinned surface) using the transient thermal tester, which helps simulate steady-state heating of the insulated-gate-bipolar transistors (IGBTs) and diodes. Compare and demonstrate improvements in performance for the new heat exchangers with respect to the baseline and also compare experimental data to results previously obtained through modeling.

- Characterize thermal performance of the heat exchangers using a dynamometer to simulate a real-world thermal load profile. Compare thermal performance of the new heat exchangers with the baseline.
- Comprehensively characterize the reliability of long-term WEG jet impingement on microfinned surfaces, impingement on direct-bond-copper (DBC) and direct-bond-aluminum (DBA) with nickel and gold coatings, as well as impingement on copper base plates with nickel coating.

Major Accomplishments

- Established collaborations with UQM and Wolverine Tube, Inc. and obtained a commercially available inverter from UQM.
- Completed design of the new heat exchangers using FEA and CFD modeling. These heat exchangers were designed to be a replacement for the baseline heat exchanger on the UQM inverter.
- Completed experiments with the transient thermal tester to characterize the thermal performance of the baseline channel-flow-based heat exchanger. Obtained good correlation between CFD results and experimental data on the baseline heat exchanger.
- Though modeling, demonstrated improvements in thermal resistance, coefficient-of-performance (COP), power density and specific power for the new heat exchangers with respect to the baseline.
- Initiated experiments to characterize the reliability of jet impingement on the microfinned/ enhanced surfaces through observations of the surface and jet nozzle conditions under a microscope, measurement of weight of both the nozzle and the target surface with the microfins, as well as periodic characterization of thermal performance of the target surface. The key result was that the thermal performance of the microfinned surface did not degrade after 90 days of nearly-continuous impingement.

Future Direction

The following activities will be performed in FY2012:

- Complete and finalize the design of the heat exchangers and build the prototypes. The first prototype will be built without any microfinned surfaces on the copper base plate (i.e., jets impinge on the plain copper base plate).
- Characterize thermal performance of the new heat exchanger using the transient thermal tester and compare results with the baseline as well as the modeling results from FY2011. If results are in accordance with expectations from modeling, proceed with building the second prototype heat exchanger with jets impinging on the copper base plate with the microfinned surface.
- Characterize the thermal performance of the second prototype heat exchanger, which incorporates the microfinned surfaces.
- Continue characterization of reliability of WEG jet impingement on microfinned surfaces, as well as metalized/coated DBAs/DBCs and copper base plates.

Technical Discussion

Single-phase liquid jets have been studied extensively in the literature [1-4]. These studies include experiments, theoretical analyses, and numerical simulations. Different configurations of impinging jets have been studied, including single free-surface jets [5], multiple free-surface jets [6-8], single submerged jets [5, 9, 10], multiple submerged jets [6, 9], and confined single submerged jets [3, 11-13]. Both planar and circular jets have been studied. In the context of electronic cooling, a large number of experimental correlations have been developed for the local and average heat transfer coefficients on the surface of the simulated chip [1-3]. Most of the simulated chips are either $10 \times 10 \text{ mm}^2$ or $12.7 \times 12.7 \text{ mm}^2$. Air jets have also been studied extensively [9]. Some of the non-dimensional heat transfer correlations developed from studies on air jets [9] can be applied to liquid jets also. Researchers have explored the impact of a

vast array of parameters—such as jet velocity, jet diameter, impact angle, nozzle-to-chip spacing, nozzle-to-nozzle spacing, turbulence levels, nozzle shapes, nozzle length, jet pulsations, jet confinement, chip-surface enhancement, and fluid properties—on the chip-surface heat transfer coefficients. All these are covered in detail in comprehensive reviews [1-3, 9].

Moreover, studies have demonstrated that jet impingement heat transfer can be further enhanced through the use of surface roughening techniques for both liquid and air [14-17] jets. Gabour and Lienhard [16] investigated the impact of surface roughness on jet impingement heat transfer. Their results demonstrated that stagnation point heat transfer increases with increasing roughness with the roughest surface producing 50% greater heat transfer as compared to the baseline surface. Moreover, the roughness enhancement increased with increasing Reynolds numbers. The enhancement was associated with the roughness structures protruding through the thermal boundary layer within the stagnation zone. Sullivan et al. [17] also reported enhancement using roughened heat sources in the submerged jet configuration. In this study [17], the heat transfer enhancements of the roughened surfaces were associated with mechanisms occurring within the wall jet region. It was speculated that roughened surfaces increased heat transfer by advancing transition to turbulent flow and by disrupting the viscous sublayer within the turbulent region. The heat transfer performance, on a 12.7-mm-diameter copper target surface, of a number of enhanced surface configurations were presented in [18]. This study [18] demonstrated the superior performance of the configuration of submerged/flooded jets impinging on a microfinned surface with respect to impingement on a plain surface as well as impingement on a number of other enhanced surfaces. These results were also noteworthy because of the feasibility of the submerged/flooded jet configuration for practical applications [19, 20].

In automotive power electronics, it is important to reduce cost, increase power density and specific power (Figure 1) to help make electric drive vehicles more cost-effective and increase their market acceptance and penetration. Figure 1 shows that while cost remains the most stringent target, improvements are required for power density and specific power also when high-temperature coolant is considered. Traditionally, channel flow-based cold plates using a WEG mixture (50-50% by volume) are widely used in a majority of hybrid electric vehicles for cooling power electronics components. In this work, we present a novel cold plate/heat exchanger based on impinging jets (using WEG), enhanced surfaces, and light-weight, low-cost plastic material for the fluid manifold. Modeling results (CFD) are presented that demonstrate improvements in thermal performance and power density and reduction in weight for this new heat exchanger as compared to the baseline heat exchanger within the context of a commercial inverter for hybrid/electric vehicle applications. Some validations of the modeling results with experimental data for the baseline channel-flow-based cold plate are also presented.

Heat Exchanger Design

The UQM inverter framework within which we intend to prove the concepts in this work is shown in Figure 2. Figure 2 also shows the inverter scale heat exchanger with the three Powerex power modules mounted on top. The schematic in the middle of Figure 2 also illustrates the concept, which involves impingement of WEG jets on the copper base plate. The back of the base plate has the microfinned surfaces on which the impingement occurs. Table 1 shows the different layers in each of the power modules along with their thermal resistance, while Table 2 shows the properties of the WEG coolant used in the conjugate heat transfer CFD simulations performed in ANSYS Fluent. A couple of design iterations were performed to bring the pressure drop in the new heat exchanger design closer to the pressure drop in the baseline channel-flow-based heat exchanger. The first step was to perform heat transfer and pressure drop experiments on the inverter with the baseline heat exchanger and compare experimental data with CFD modeling results. This helped get confidence in the CFD modeling in the baseline heat exchanger and also established the modeling results for the baseline against which the modeling results for the jet-based heat exchanger would be compared. The validation of CFD modeling for the baseline channel-flow-based heat exchanger is described next.

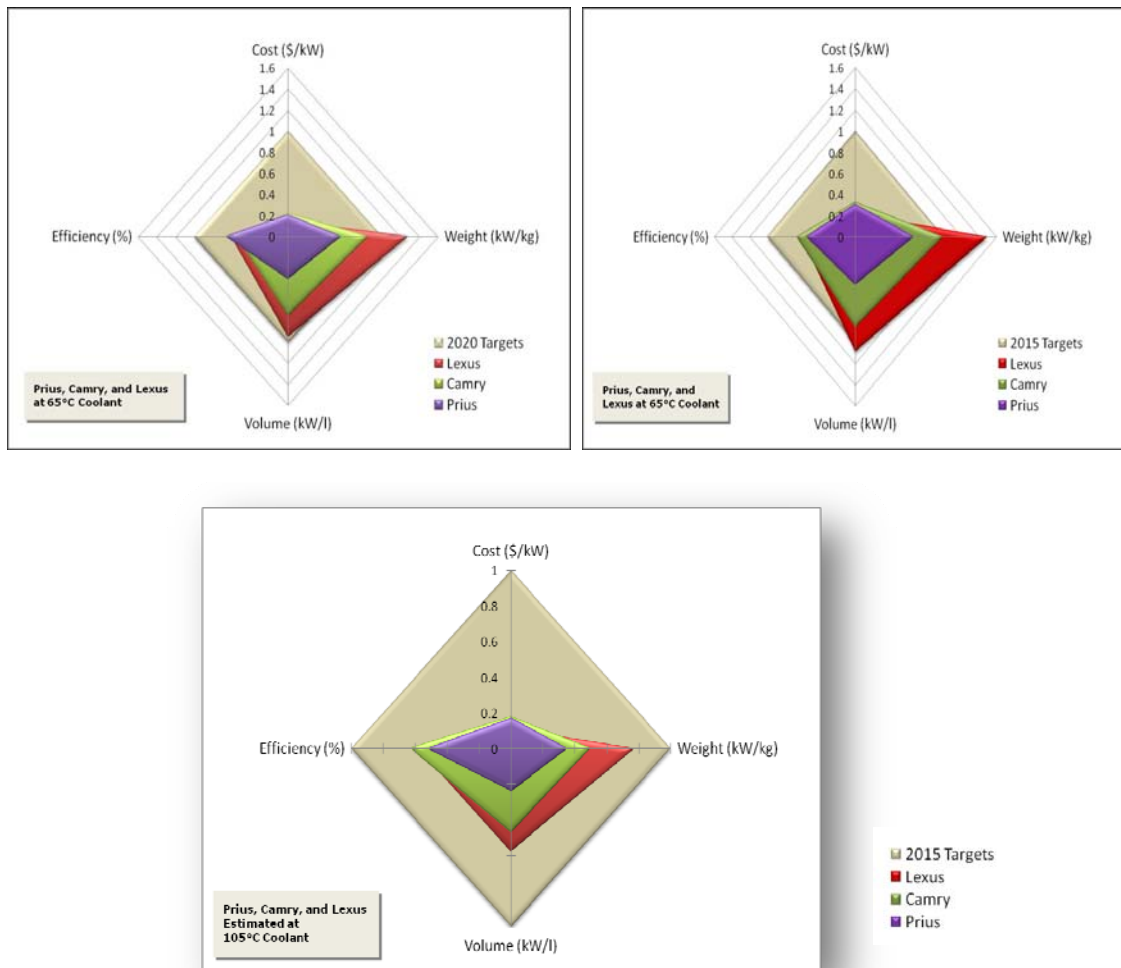


Figure 1. APEEM technical targets for cost, power density, and specific power; 2015 targets for 65°C coolant (top left), 2020 targets for 65°C coolant (top right), and 2015 targets for 105°C coolant (bottom)

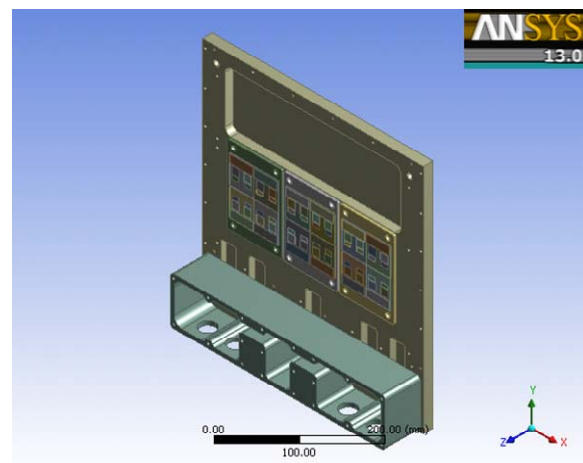
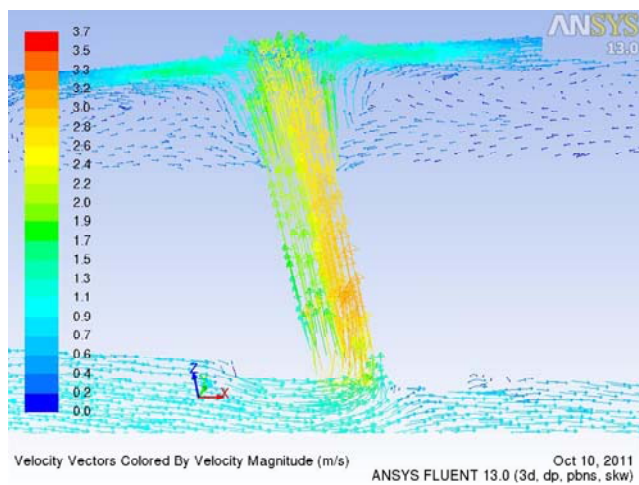
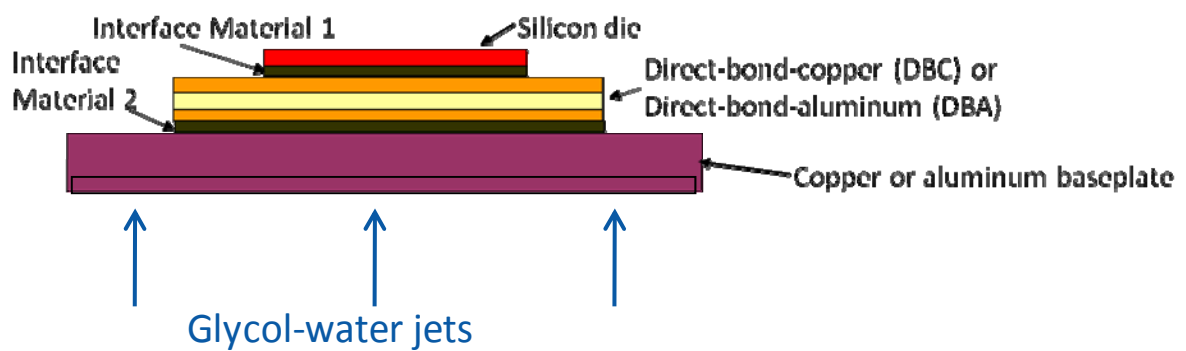


Figure 2. UQM inverter (top), impinging jets in conjunction with enhanced surfaces (middle), a single impinging jet (bottom left), and the inverter heat exchanger with three power modules (bottom right)

Table 1. Different Layers in the Package Stack-Up and Their Thermal Resistance

| Layers | Thermal resistance (mm ² K/W) |
|----------------------------|--|
| Silicon | 2.9 |
| Solder | 1.3 |
| DBC | 5.8 |
| Solder | 2.6 |
| Cu base plate | 1.0 |
| Thermal interface material | 16.3 |

Table 2. Properties of the Water-Ethylene Glycol Mixture (50%-50% by Volume) Coolant at 70°C.

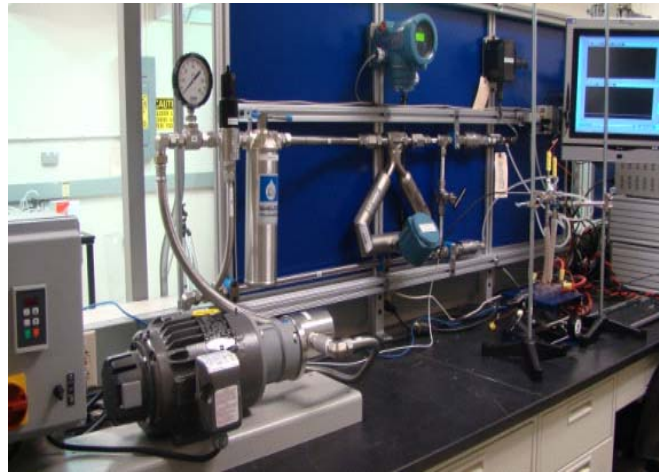
| Property | Value |
|----------------------------|-----------|
| Density, kg/m ³ | 1,034 |
| Specific heat, J/kgK | 3,512.7 |
| Thermal conductivity, W/mK | 0.42 |
| Dynamic viscosity, kg/ms | 0.0012925 |

Validation of CFD modeling for the baseline heat exchanger

Using direct-current power supplies in conjunction with the transient thermal tester (T3Ster), 105.3 W of heat was dissipated across four diodes in parallel in the center power module of the UQM inverter. WEG coolant at 70°C was used in the baseline channel-flow-based heat exchanger. The diode temperatures reached steady state and were measured using T3Ster. The coolant loop on which the experiments were performed is shown in Figure 3. The resistance (primarily thickness) of the grease between the copper base plate and the aluminum heat sink is an unknown and was used as a parameter in the CFD modeling to match temperature results from the modeling to the experimental quantity for the 1.667E-04 m³/s flow rate case in Table 3. After this, the parameters of the package were kept fixed and flow rate was changed to 0.336E-04 m³/s. From Table 3, it can be inferred that the modeling results for the pressure drop and temperature follow the trend in the experimental data at the different flow rates quite well. This gives confidence in the CFD modeling framework as a design tool. In the CFD modeling, the pressure drop across the connectors is not accounted for, which could be the reason for the discrepancy in CFD results for pressure drop with respect to the experimental pressure drop, especially at the elevated flow rate. For fluid flow, the k-omega turbulence model was used. The approximate Reynolds number for the flows is expected to be in the range of 8,000 – 43,000 based on the hydraulic diameter of the channels. The k-omega turbulence model has been shown to yield a very good match between CFD results and experimental data for impinging jet configurations [20]. Hence, for consistency, this model was used for both the channel flow as well as impinging jet configurations in this work. Per the stipulations of the k-omega model, the mesh in the boundary layer (interface between solid/fluid) was fine enough to keep wall y+ close to 1. Up to 20 million cells/control volumes were used in the simulations, and the modeling results for both pressure drop and temperature are expected to be mesh-independent to within 5%. Parallel processing was utilized very extensively and up to 16 cores were employed for the simulations.

Table 3. Comparison between Experimental and CFD Results for the Baseline Heat Exchanger

| Flow rate (m ³ /s) | Pressure drop (Pa) | | Average temperature in diodes (°C) | |
|-------------------------------|--------------------|--------|------------------------------------|------|
| | Experimental | CFD | Experimental | CFD |
| 0.336E-04 | 1,076 | 1,079 | 84.9 | 84.0 |
| 1.667E-04 | 19,374 | 16,988 | 82.8 | 82.9 |

**Figure 3. WEG loop**

Performance of the new heat exchanger designs predicted by modeling

In this section, we present the results for the performance of the new heat exchanger designs as compared to the baseline heat exchanger. In this case study, we dissipated 2.5 kW of heat spread over the 24 IGBTs (72 W each IGBT) and 24 diodes (33 W) in three power modules of the UQM inverter. It is worth emphasizing again that the impinging jet design is as shown in Figure 2. One case involves impingement on a plain surface, while another case involves simulating the effect of the microfinned surface on enhancing the heat transfer rates obtained from the impinging jets based on information gained from prior experimental data [18]. The coolant properties used in the simulations are similar to those presented in Table 2, and the thermal resistance numbers presented in Table 4 are computed based on the volume average temperature of four diodes in the center module of the UQM inverter (similar to the previous section) as $R_{th, ja} = (T_{4diodes, avg} - T_{coolant})/q_{4diodes}$, where $T_{4diodes, avg}$ is the volume average temperature of the four diodes mentioned above, $T_{coolant}$ is 70°C, and $q_{4diodes}$ is the total heat dissipation in the four diodes (132 W in this case study). Table 4 shows that the pressure drop with the impinging jet configuration for 1.667E-04 m³/s flow rate is similar to the pressure drop for the baseline channel-flow-based heat exchanger at the same flow rate. This implies that parasitic power (product of flow rate and pressure drop) will be approximately the same between the two cases. The mean jet velocity in the nozzles for the jet impingement case is about 2.3 m/s, which is similar to the mean velocities in the channels for the baseline heat exchanger.

Table 4. Performance comparison based on CFD modeling results for baseline and new heat exchangers.

| Parameter | Baseline (channel flow) | Jets impinging on plain surface | Jets impinging on microfinned surface |
|--------------------------------------|----------------------------|------------------------------------|---|
| ΔP (Pa) | 16,858 | 17,458 | 17,458 |
| $R_{th,ja}$ (K/W) | 0.294 | 0.191 | 0.166 |
| Isothermality ($^{\circ}\text{C}$) | 2.7 | 0.3 | 0.15 |

Table 4 shows that the thermal resistance with respect to the baseline case decreases by 34% and 44%, respectively, for the heat exchanger with impinging jets on a plain copper base plate surface and the heat exchanger with impinging jets on the microfinned surface. In addition, the temperature uniformity within the four diodes is within 2.7°C for the baseline case, 0.3°C for the case with impinging jets on the plain surface, and 0.15°C for the case with impinging jets on the microfinned surface. Hence, these results demonstrate significant thermal enhancements for the jet-based designs as compared to the baseline case both from a thermal resistance and a temperature uniformity standpoint.

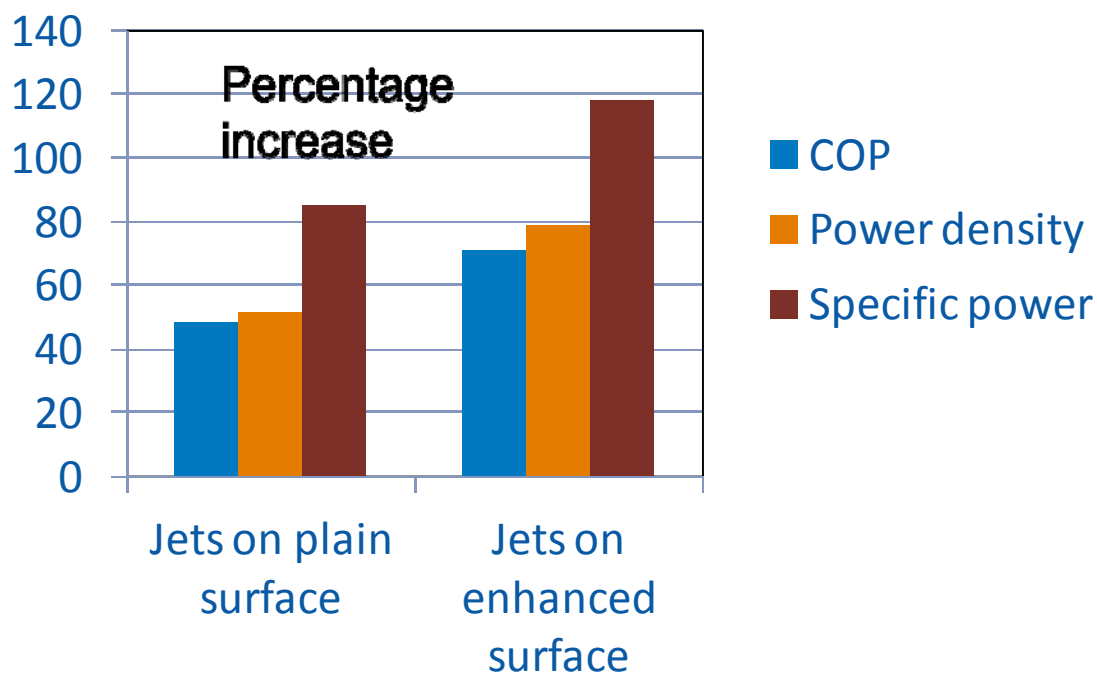
**Figure 4. Percentage increase in performance metrics for new heat exchangers as compared to the baseline.**

Figure 4 shows the percent increase in COP, power density, and specific power for the jet-based designs as compared to the baseline. The COP is computed as the ratio of thermal conductance (inverse of thermal resistance) divided by the parasitic power. Since the percent differences with respect to the baseline are of interest here, the specific units for the quantities are not important. Figure 4 shows that at the inverter

scale, increases of up to 71%, 79%, and 118% can be obtained in COP, power density, and power density, respectively. The specific power increases are different from the power density because of the decrease in mass of the new heat exchanger manifold by almost 2.9 kg (up to 50% reduction with respect to the baseline) through the use of automotive grade glass-fiber reinforced nylon/plastic.

We are in the process of estimating the cost of the new heat exchanger design. Through the use of low-cost mass-manufacturing techniques such as casting and injection-molding, we anticipate that the cost of the new heat exchanger will be competitive (if not lower) with respect to the baseline aluminum channel flow-based heat exchanger.

Experimental reliability assessment of jet impingement

We initiated a series of experiments to address questions related to long-term reliability of jet impingement. Figure 5 shows the impingement configuration. A jet nozzle with a 1.4-mm diameter is placed 6 mm away from the target surface, which has the microfinned surfaces as shown at time $t=0$ for both samples W1 and W2 in Figure 5. Continuous jet impingement at 2 m/s (sample W2) and 7 m/s (sample W1) on the 12.7-mm-diameter copper target surface with the microfinned surfaces was initiated.

The impingement was interrupted periodically (every 30 days) to perform thermal performance characterization on the target surfaces. There is evidence of oxidation on the target surface for both samples W1 and W2. There are three aspects that are worth mentioning. First, these impingement experiments were performed in an open-loop system, which implies there is sufficient supply of air and in turn oxygen. This helps promote the oxidation that is seen in Figure 5. Automotive systems are likely to be closed loop, pressurized systems with much lower/minimal air/oxygen supply, and it is likely that oxidation will be much more limited. Second, a pure 50%-50% mixture by volume WEG coolant was used in this impingement study. Automotive systems usually have corrosion suppressants added to the WEG mixture, which may suppress/prevent oxidation/corrosion. Third, perhaps a thin nickel coating (2 to 3 μm) on the microfinned surfaces could also help/prevent oxidation.

The heat transfer performance of the target surfaces was tested every 30 days to detect any degradation in thermal performance with respect to the performance at time $t=0$ (prior to any prolonged impingement). Figure 6 plots the heat transfer coefficients/rates on the microfinned target surface as a function of the jet impingement velocity for both sample W1, which was exposed to prolonged jet impingement at 7 m/s, and W2, which was exposed to prolonged jet impingement at 2 m/s. The heat transfer characterization tests were conducted at time $t=0$, $t=30$ days, $t=60$ days, and $t=90$ days. Results indicate that the thermal performance was within the 95% confidence interval, which means that the thermal performance of the microfinned surfaces did not degrade noticeably after 90 days of continuous impingement. The current plan is to continue impingement for another 7 months for a total impingement duration of 10 months. The rationale is that for an inverter heat exchanger that is operational for 2 hours per day for 10 years, the total operation time is 7,300 hours, which equates to approximately 10 months of continuous operation. It is difficult to simulate in-field use exactly; however, the results presented here are important and give some confidence in the reliability of the jet impingement configuration.

In addition to impingement on the microfinned surfaces, we also plan to perform jet impingement on DBC and DBA with appropriate metallization (nickel coating followed by gold coating), as well as a simulated copper base plate with a nickel coating. Some other plans in FY2012 include using automotive grade antifreeze coolant for the impingement as well as performing the impingement at elevated coolant temperatures (70°C to 75°C as opposed to 35°C for the current/ongoing long-term impingement experiments). Modifications to the test loop that will enable all these experiments is currently underway, and these tests will be initiated approximately in the middle of FY2012.

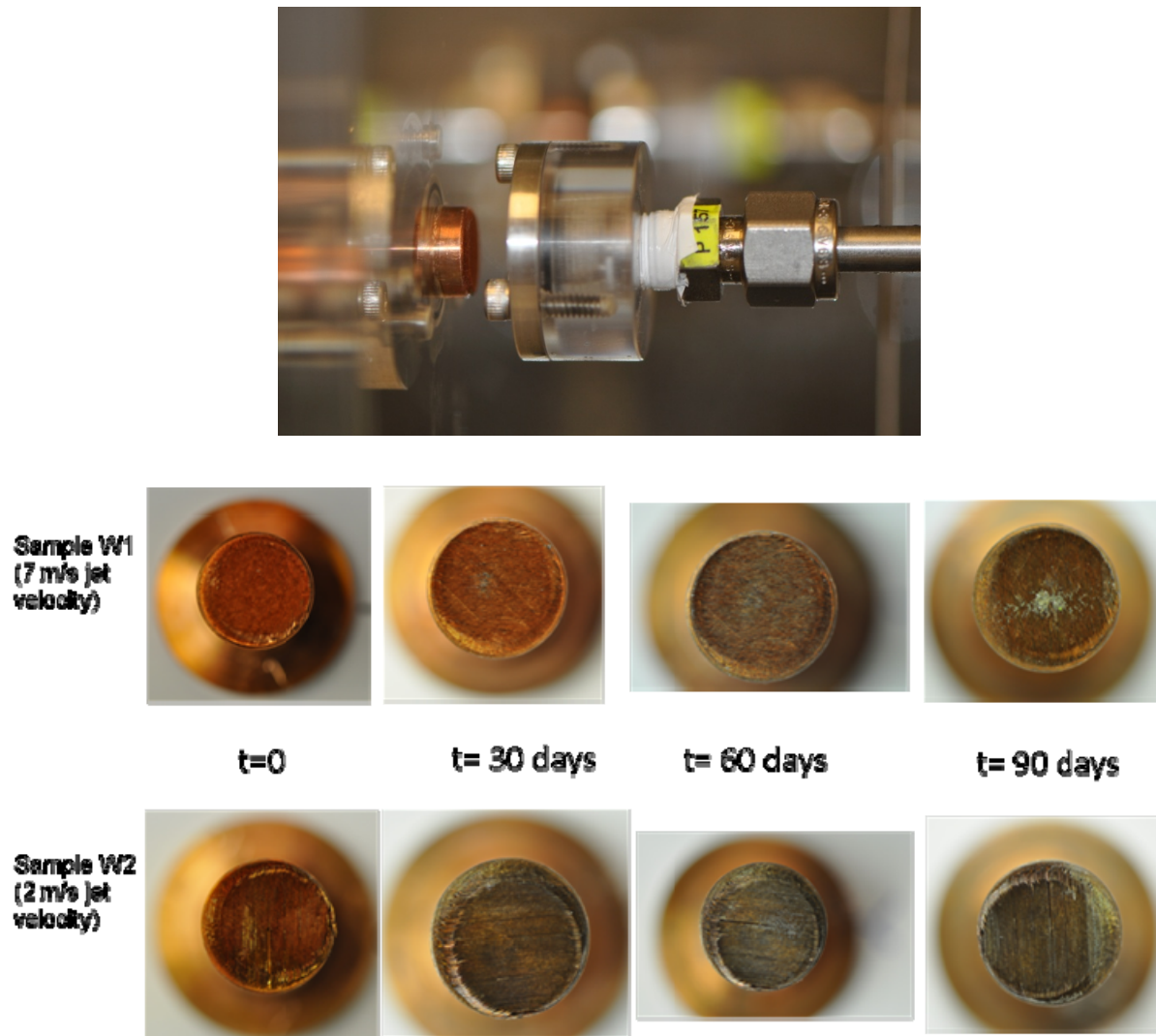


Figure 5. Impingement configuration (top); sample W1 with continuous WEG jet impingement at 7 m/s and photographs after select number of days (middle row); sample W2 with continuous WEG jet impingement at 2 m/s and photographs after select number of days (bottom row)

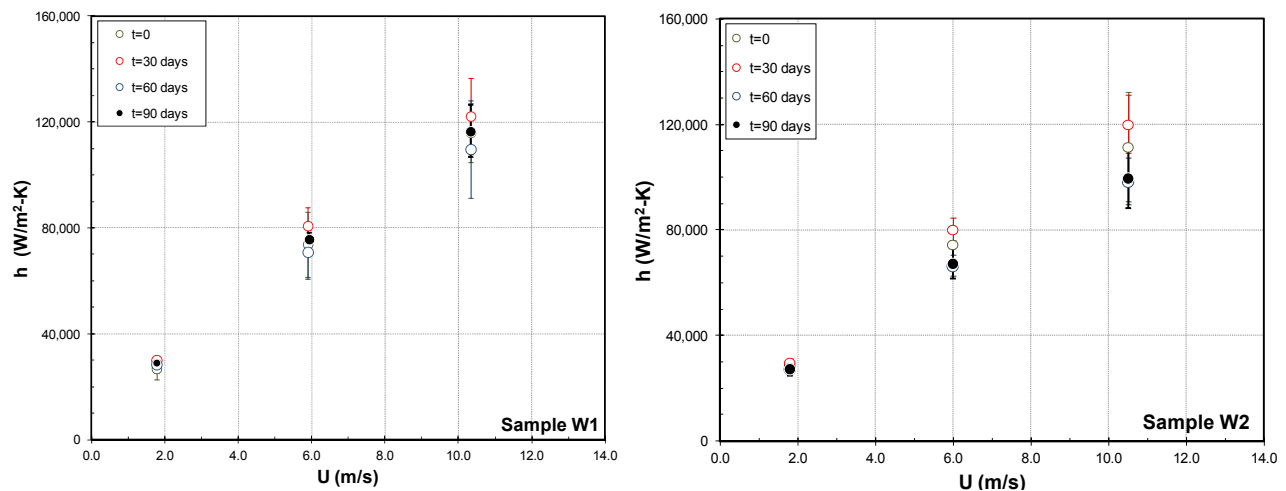


Figure 6. Heat transfer rates/coefficients on the microfinned target surface as a function of impingement jet velocity for sample W1 (left) and sample W2 (right).

In addition to the thermal performance characterization over time, we also measured the mass of the copper blocks with the microfinned surfaces over time, as well as the jet nozzle mass and nozzle diameter over time. The sample and nozzle masses over time are shown in Figure 7. The mass scale was changed after the $t=60$ days time period; therefore, the results at $t=90$ days are not shown because they cannot be compared to the results from the earlier time period. Overall results indicate that the masses of the samples and the nozzles do not change noticeably after 60 days of continuous impingement. Figure 8 shows the nozzle orifice diameter over time and again illustrates that the diameter does not change noticeably over time.

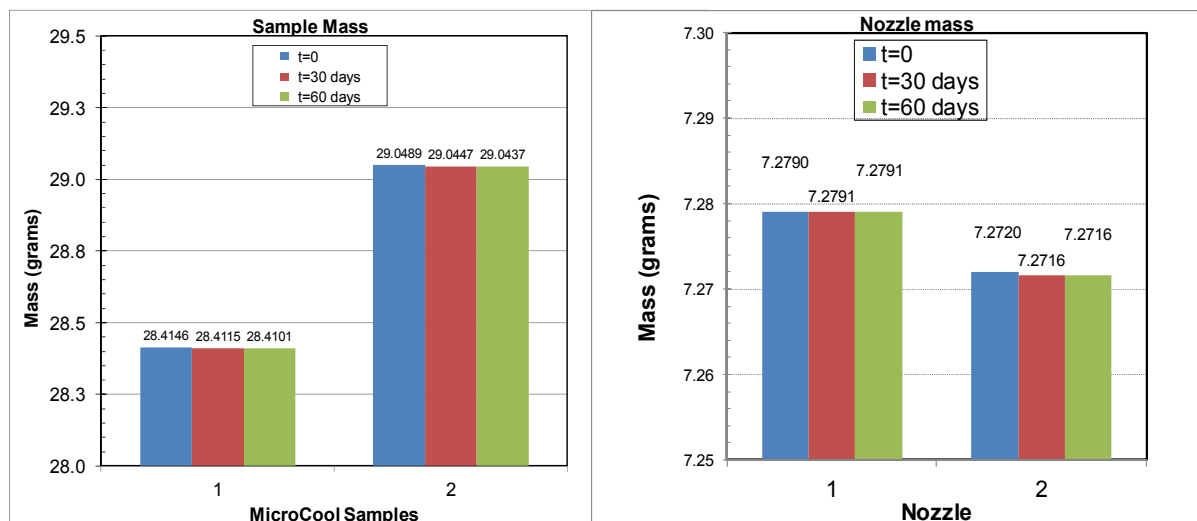


Figure 7. Mass of the copper blocks with the microfinned surfaces as a function of time-of-exposure to impingement (left). Jet nozzle mass as function of duration of jet impingement (right).

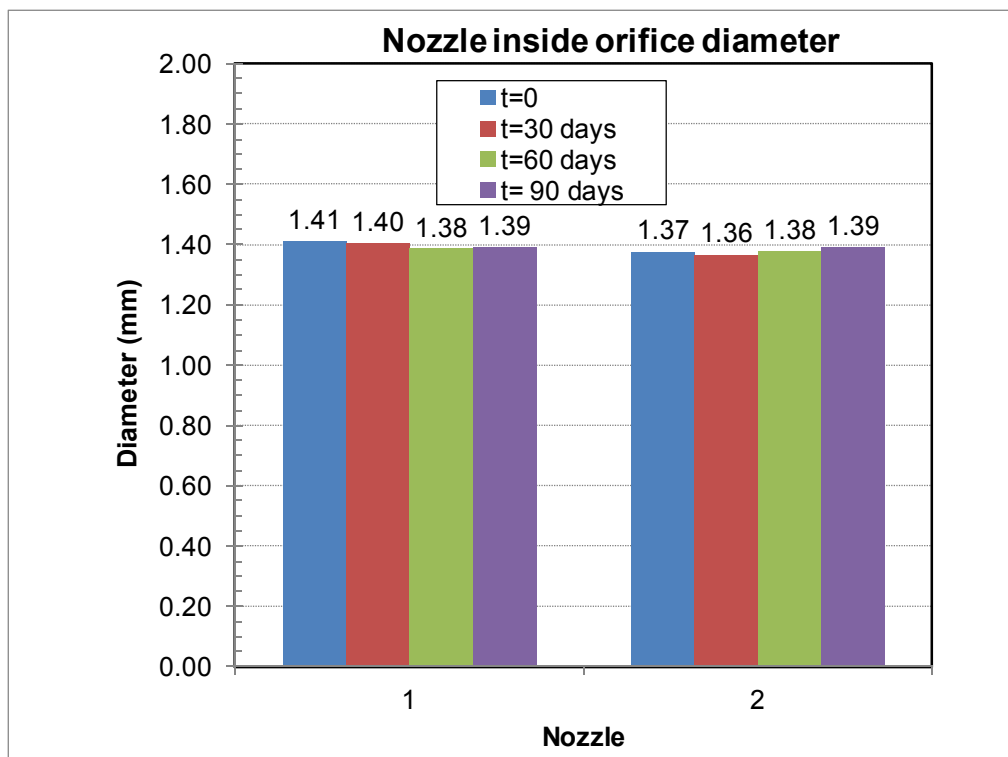


Figure 8. Jet nozzle orifice diameter as a function of duration of jet impingement

Overall, it appears from the results to date that after 90 days of nearly continuous impingement, the thermal performance of the microfinned surfaces has not degraded.

Conclusion

Through detailed modeling and design, we are on track to achieve up to 71% increase in COP, 79% increase in power density, and 118% increase in specific power for the new heat exchanger as compared to the baseline channel-flow configuration. The cost is likely to be competitive with respect to the baseline. While these results are obtained within the framework of this specific UQM inverter, we believe these results should scale (to various extents) in other inverter configurations as well. The experiments to date on the characterization of reliability have shown that nearly continuous impingement for 90 days does not degrade the thermal performance of the microfinned surfaces.

Through thermal management, this project is addressing some of the key aspects related to power density, specific power, cost, and reliability. The results obtained to date look promising, and the next phase in FY2012 is experimental demonstration of the performance in inverter-scale hardware.

Acknowledgments

The authors would like to acknowledge the support provided by Susan Rogers and Steven Boyd, technology development managers for Advanced Power Electronics and Electric Motors, Vehicle Technologies Program, U.S. Department of Energy Office of Energy Efficiency and Renewable Energy. The contributions of Mark Mihalic, Gilbert Moreno, and Kevin Bennion (NREL) to the project are acknowledged. The authors would also like to acknowledge Jon Lutz (UQM) for providing very useful information on the UQM inverter, as well as Sy-Jenq Loong (Wolverine Tube Inc.) for providing samples with the microfinned surface enhancements.

Nomenclature

| | |
|--------|---|
| APEEM | Advanced Power Electronics and Electrical Motors |
| CFD | computational fluid dynamics |
| COP | coefficient of performance |
| Cu | copper |
| DBA | direct-bond-aluminum |
| DBC | direct-bond-copper |
| FEA | finite element analysis |
| IGBT | insulated gate bipolar transistor |
| R | thermal resistance, K/W |
| T | temperature, °C |
| T3Ster | transient thermal tester |
| WEG | water-ethylene glycol coolant (50%-50% mixture by volume) |

Greek

ΔP pressure drop (Pa)

Subscripts

avg average

th, ja junction-to-coolant

Patents

NREL Record of Invention, ROI-12-00004, Light-weight, Low-cost, High Thermal Performance, Heat Exchanger/Cold Plate.

References

1. Webb, B.W., Ma, C.-F., 1995, "Single-phase liquid jet impingement heat transfer," *Advances in Heat Transfer*, **26**, pp. 105-217.
2. Lienhard, J.H., 1995, "Liquid jet impingement," *Annual Review of Heat Transfer*, pp. 199-270.
3. Garimella, S.V., 2000, "Heat Transfer and flow fields in confined jet impingement," *Annual Review of Heat Transfer*, pp. 413-494.
4. Narumanchi, S.V.J., Amon, C.H., Murthy, J.Y., 2003, "Influence of pulsating submerged liquid jets on chip-level thermal phenomena," *ASME Journal of Electronic Packaging*, **125**, pp. 354-361.
5. Womac, D.J., Ramadhyani, S., Incropera, F.P., 1993, "Correlating equations for impingement cooling of small heat sources with single circular liquid jets," *ASME Journal of Heat Transfer*, **115**, pp. 106-115.
6. Womac, D.J., Incropera, F.P., Ramadhyani, S., 1994, "Correlating equations for impingement cooling of small heat sources with multiple circular liquid jets," *ASME Journal of Heat Transfer*, **116**, pp. 482-486.
7. Pan, Y., Webb, B.W., 1994, "Heat transfer characteristics of arrays of free-surface liquid jets," *General Papers in Heat and Mass Transfer, Insulation and Turbomachinery*, ASME, **HTD - Vol. 271**, pp. 23-28.
8. Yonehara, N., Ito, I., *Cooling characteristics of impinging multiple water jets on a horizontal plane*. 1982, Tech. Report - Kansai University. p. 267-281.

9. Martin, H., 1977, "Heat and mass transfer between impinging gas jets and solid surfaces," *Advances in Heat Transfer*, **13**, pp. 1-60.
10. Wadsworth, D.C., Mudawar, I., 1990, "Cooling of a multichip electronic module by means of confined two-dimensional jets of dielectric liquid," *ASME Journal of Heat Transfer*, **112**, pp. 891-898.
11. Garimella, S.V., Rice, R.A., 1995, "Confined and submerged liquid jet impingement heat transfer," *ASME Journal of Heat Transfer*, **117**, pp. 871-877.
12. Garimella, S.V., Nenaydykh, B., 1996, "Nozzle-geometry effects in liquid jet impingement heat transfer," *International Journal of Heat and Mass Transfer*, **39**(14), pp. 2915-2923.
13. Li, C.-Y., Garimella, S.V., 2001, "Prandtl-number effects and generalized correlations for confined and submerged jet impingement," *International Journal of Heat and Mass Transfer*, **44**, pp. 3471-3480.
14. Incropera, F.P., 1999, *Liquid Cooling of Electronic Devices by Single-Phase Convection*, John Wiley & Sons, Inc.
15. Beitelmal, A.H., Saad, M.A., Patel, C.D., 2000, "Effects of Surface Roughness on the Average Heat Transfer of an Impinging Air Jet," *International Communications in Heat and Mass Transfer*, **27**(1), pp. 1-12.
16. Gabour, L.A., Lienhard, J. H.V., 1994, "Wall Roughness Effects on Stagnation-Point Heat Transfer beneath an Impinging Liquid Jet," *Journal of Heat Transfer*, **116**(1), pp. 81-87.
17. Sullivan, P.F., Ramadhyani, S., Incropera, F.P., 1992, "Use of Smooth and Roughened Spreader Plates to Enhance Impingement Cooling of Small Heat Sources with Single Circular Liquid Jets," San Diego, CA, USA, 206-2, pp. 103-110.
18. Moreno, G., 2010, "Characterization and development of advanced heat transfer technologies," FY2010 DOE Thermal Management of Advanced Power Electronics and Electrical Motors Annual Report.
19. Hassani, V., Vlahinos, A., Bharathan, D., 2007, "Low Thermal Resistance Power Module Assembly," United States Patent Number 7190581.
20. Narumanchi, S.V.J., Hassani, V., Bharathan, D., 2005, *Modeling single phase and boiling liquid jet impingement cooling in power electronics*, NREL Technical Report, NREL/TP-540-38787, <http://www.nrel.gov/docs/fy06osti/38787.pdf>.

5.4 Integrated Vehicle Thermal Management – Combining Fluid Loops on Electric Drive Vehicles

Principal Investigator: John Rugh

National Renewable Energy Laboratory

Center for Transportation Technologies and Systems

1617 Cole Blvd. MS 1633

Golden, CO 80401

Voice: 303-275-4413; Fax: 303-275-4415; E-mail: john.rugh@nrel.gov

DOE Technology Development Manager: Susan A. Rogers

Voice: 202-586-8997; Fax: 202-586-1600; E-mail: Susan.Rogers@ee.doe.gov

Objectives

- Work with industry partners to research the synergistic benefits of combining thermal management systems in vehicles with electric powertrains
 - Improve plug-in hybrid electric vehicles (PHEV) and electric vehicle (EV) performance (reduced weight, aerodynamic drag, and parasitic loads)
 - Reduce cost and volume
 - Improve battery life

Approach

- Develop a 1-D (lumped mass, uniform flow) thermal model using commercial software to assess the benefits of integrated vehicle thermal management and identify research opportunities
- Combine with vehicle performance/cost and battery life models
- Identify the synergistic benefits from combining cooling systems
 - Select the most promising combined thermal management system concepts and perform a detailed performance assessment with production-feasible component data
- Assess technical feasibility of combining fluid loops
 - Vehicle performance impact
 - Battery life impact

Major Accomplishments

- Leveraged previous U.S. Department of Energy (DOE) development of a battery life model, vehicle cost/performance model, and lumped parameter motor thermal model
- High quality data provided by Visteon formed the basis of the detailed KULI component models
- Using KULI thermal software, built the A/C, cabin, power electronics cooling loop, and battery cooling loop models
 - Validated the models with test data when available
 - Simulated a full thermal management system in an EV
 - Results followed expected trends

Future Direction

- Work closely with industry partners to assess the most promising concepts through bench testing
- Refine and improve the 1-D thermal model as required

- Assess new concepts for combining cooling loops

Technical Discussion

Background

Electric drive vehicles (EDVs) [e.g., hybrid electric vehicles (HEVs), PHEVs, fuel cell vehicles, and EVs] must provide cooling to protect powertrain-related subsystems, including the power electronics, electric motor, and energy storage system (ESS). In addition, climate control is required for passenger compartment comfort and safety (e.g., demisting and defrosting), and if there is an internal combustion engine, engine thermal management is necessary.

Advanced power electronics and electric motor (APEEM) components commonly use a dedicated cooling loop in today's HEVs. In the future, the cooling demands will only increase with the transition to more electrically dominant powertrains. Combining the APEEM cooling loop with other vehicle thermal management systems could reduce cost and complexity while providing the opportunity to manage the average and peak heat loads from multiple vehicle systems.

Lithium (Li)-ion batteries operate best at temperatures that are comfortable to the human body, around 10°C to 30°C. At lower temperatures, power output is reduced. At higher temperatures, battery life is reduced. In a hot environment, the goals of battery thermal management are to lower the average and peak cell temperatures to within an acceptable range. In hot climates, active cooling of the battery is desirable during driving, charging, and even during standby while the vehicle is parked outdoors.

To reduce the total system cost of the vehicle, it is desirable to combine some of the multiple cooling loops while maintaining vehicle performance and reliability. In selecting approaches for combining thermal management systems, two high-level requirements were considered. The first is the need for a similar coolant temperature specification for different systems. The second requirement is the ability to manage the misalignment of peak component heat loads in an integrated system. The heat load for combined thermal management systems should be less than the sum of the peak heat loads from each of the individual systems. Different components experience peak heat loads at different times depending on their use, which leads to an overall decrease in the net heat exchanger weight and area.

Past efforts looking at combining cooling loops include work by Ap et al. [1], who proposed a low-temperature liquid water-ethylene glycol (WEG) coolant loop for the air conditioning (A/C) condenser, charge air cooler, and fuel cooler. They concluded that 60°C coolant to the liquid-to-refrigerant condenser ensured adequate A/C performance. This project intends to extend the work by Ap et al. [1] to investigate combined cooling systems for vehicles with electric drive systems.

The combined cooling loops research focuses on reducing vehicle cost and improving battery life. The pathways investigated in this analysis look at combining the cooling systems for the power electronics and electric motor with other vehicle cooling systems evaluated by Bennion and Thornton [2] and enabling technologies for vehicle cabin thermal preconditioning or standby ESS thermal management [3]. NREL's research focuses on the following combined thermal management approaches as applied to EDVs: a low-temperature WEG fluid loop that integrates the power electronics, electric motor, cabin heating, ventilation and air conditioning (HVAC), and ESS where the ESS is cooled with:

- Air from the vehicle cabin
- A dedicated evaporator
- A secondary loop cooling system.

Approach

NREL developed a modeling process to assess integrated cooling loops in EDVs. The initial analysis focused on EVs. Once the EV analysis is completed, NREL will investigate PHEVs, which add engine cooling, oil cooling, variable engine control strategies, and the exhaust system.

There are three main parts to the modeling process: the vehicle cost/performance model, the thermal model, and the battery life model. The vehicle cost/performance model simulates an EV over a drive cycle. An output of the model is the time-dependent heat generated in the APEEM and ESS components. These data are used as an input to the thermal model. KULI software [4] was used to build a model of the thermal systems of an EV, including the passenger compartment, APEEM, and ESS. The thermal model calculates the temperatures of the components and the power required by the various cooling systems, including the fans, blowers, pumps, and A/C compressor. The power consumption profile is then used in the vehicle cost/performance model, and a new heat generation calculated. If the heat generation is significantly different from the initial run, it is input into the KULI thermal model again, and the cycle is repeated. An overview of the analysis flow is shown in Figure 1.

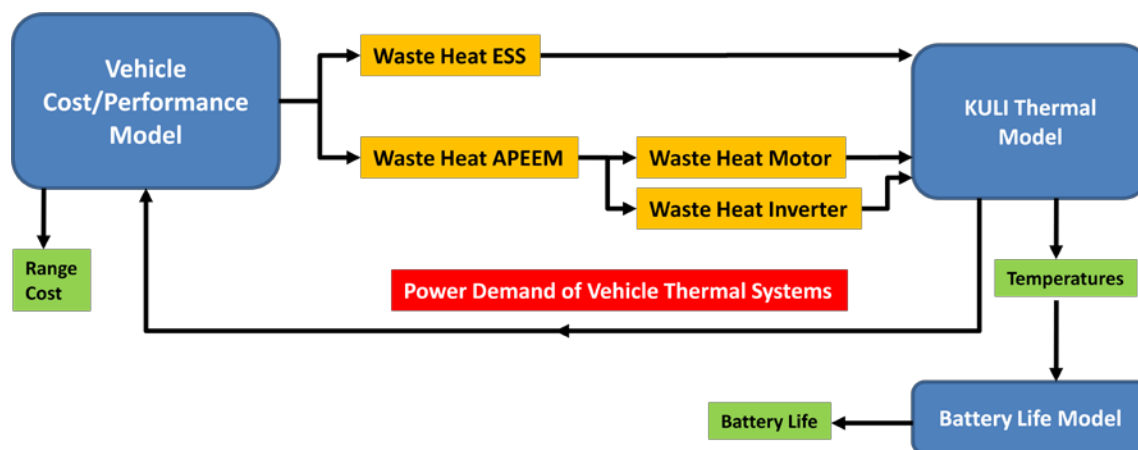


Figure 1. EV integrated vehicle thermal management analysis flow diagram

The vehicle cost/performance model calculates the range at a fixed cost. For example, if combining thermal systems reduces cost, the vehicle model increases the battery size to maintain constant cost with an extended vehicle range. If combining cooling loops results in lower required power, then there is more electric power and energy for propulsion and the range is improved for the same cost.

The battery life model operates on a 10- to 15-year time scale while the KULI thermal model and vehicle cost/performance model operate on a 10- to 20-minute time scale. Therefore, in the battery life model, a composite 24-hour temperature profile for the battery is created based on assumptions about when during the day the vehicle is driven, parked + charging, or parked + standby. The composite battery temperature profile is then used to calculate average values for battery degradation rate constants. The resistance growth and remaining capacity of the battery, assuming 10 years of continuous exposure to this composite battery temperature profile, is calculated.

Air conditioning component model

The components modeled in this effort represent a production A/C system for a model year 2008 mid-sized vehicle. Using actual dimensions, pressure drop, and heat transfer data, each component was built in the KULI model. The compressor used in the validation runs was a belt-driven, piston type, with a displacement of 213 cc. For the EV passenger compartment cooldown simulations, an electrically driven 33-cc scroll compressor was used. Heat was rejected to the air as the refrigerant phase changes from a

vapor to a liquid in the condenser. The condenser was a two-pass design with 16-mm tubes and an external receiver-dryer (R/D). Liquid refrigerant exited the condenser and flowed into a 325-cc R/D where liquid and any remaining vapor were separated, allowing only liquid to exit. The R/D also removed any moisture. From the R/D, the liquid refrigerant continued to the Thermal eXpansion Valve (TXV), where it expanded and cooled significantly. Finally, refrigerant boiled as it absorbed heat in the evaporator, a 45-mm-deep plate-fin core with four end-tanks.

A/C system KULI model

The KULI model of the A/C system was composed of a compressor, condenser, receiver/dryer, TXV, and evaporator. To ensure that each of the A/C components was modeled properly, a KULI model was written for each component, where the component of interest was the only element in an open cooling circuit. The model was given inputs from the component calorimeter data for various operating points with the intent of obtaining the corresponding outputs for each operating point. Once a satisfactory comparison was made between the calorimeter data and the model's results, the component was inserted into the A/C system model.

Passenger compartment KULI model

The advanced passenger compartment model that comes with KULI was used. The cabin dimensions, interior volume, and material properties were used to model a small U.S. sedan that the National Renewable Energy Laboratory (NREL) tested in Golden, Colorado. To tune the three critical KULI cabin heat transfer resistances, a simulation was run using the environmental conditions that occurred during the NREL thermal soak and cool-down test. The global horizontal solar irradiance (average 870 W/m²) and ambient temperature (average 22.3°C) profiles were used for the simulated 2-hour soak and the 21-minute drive. The vent temperature was set to the measured profile, and the flow rate was determined by supplier data. The exterior velocity profile was set to approximate real vehicle speeds, and the HVAC blower setting was reduced from high to medium 13 minutes after the start of cooldown. The three KULI cabin heat transfer resistances were adjusted so the model temperatures approximated the test data. Figure 2 shows that the average cabin air temperature during the soak and cooldown matched the test data fairly well.

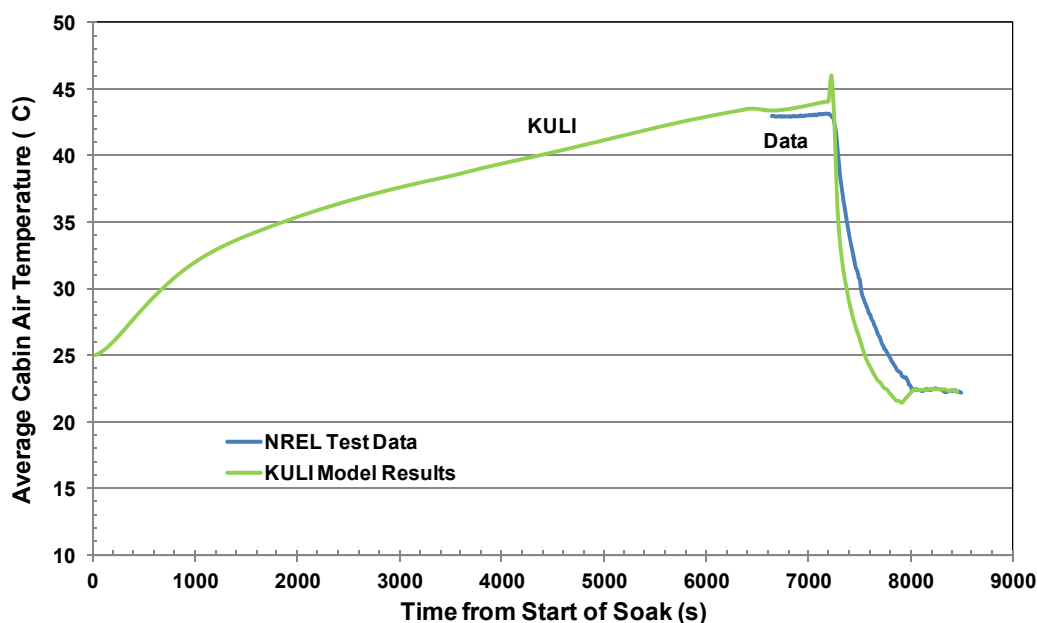


Figure 2. Comparison of passenger compartment average air temperature for the KULI model and test data

The cabin model was then combined with the A/C system model described in the previous section. A proportional-integral-derivative (PID) controller was added to prevent evaporator icing early in the cooldown as well as passenger compartment overcooling later in the cooldown.

Power electronics and electric machine KULI model

As seen in Figure 1, the vehicle performance model outputs an overall heat load for the APEEM system. To properly model the cooling of the APEEM components, the heat load must be divided between the individual components that make up the APEEM system. For an EV, it was assumed that the APEEM system consisted of an inverter to convert the direct-current power that is supplied by the battery to three-phase alternating-current power to run an electric motor. A combined heat load for the inverter and motor was provided from the vehicle performance model, and the individual inverter and motor heat loads were estimated assuming that the heat loss within the inverter was always half of the heat loss in the motor. A more accurate heat loss model of the individual inverter and motor heat could be incorporated into the model. The heat loads for the inverter and motor were used in the KULI model to determine the temperatures of the cooling system, inverter, and motor.

The temperature constraints placed upon the model included a maximum allowable coolant temperature of 70°C [5,6] into the power electronics and the maximum motor end winding temperature. While class H insulation for motor windings is rated for 180°C [7], a lower limit of 130°C [8] for the motor windings was imposed on the model to be consistent with other published results.

The motor thermal characteristics were approximated by a first-order, lumped parameter, thermal spreadsheet model based on data for a motor cooled with a water jacket surrounding the stator [8]. The spreadsheet model approximated the transient thermal resistance between the end winding of the motor and the cooling fluid from the steady-state thermal resistance (R_{th}) and an overall effective thermal capacitance (C_{th}). The temperature response of the lumped model was determined according to equation 1 [9] for a first-order system where Q_m is the motor heat load, θ_0 is the initial winding temperature, $\theta(t)$ is the transient temperature response and t is time.

$$\theta(t) = R_{th}Q_m + (\theta_0 - R_{th}Q_m)e^{-t/R_{th}C_{th}} \quad (1)$$

The results were compared with data for the reference motor to determine R_{th} and C_{th} . The R_{th} and C_{th} values were finally converted into an effective heat transfer coefficient, effective cooling area, motor mass, and motor specific heat to supply the KULI model with the necessary input values.

The inverter temperature was not simulated in the KULI model because of the smaller thermal mass of the inverter as compared with the motor. Instead, all the heat loss of the inverter was assumed to go into the coolant fluid. As long as the coolant temperature into the inverter remained below the maximum allowable coolant temperature, it was assumed that the inverter could operate within its temperature limits.

A model of a baseline WEG cooling system was then built into KULI. Pump and engine cooling radiator data from Visteon were used to build the individual KULI components. The radiator was scaled to the size of the Japanese version of the Mitsubishi iMiEV. The heat added to the cooling loop from the inverter and motor APEEM components was rejected to the environment (air) by the radiator.

Energy storage system KULI thermal and life models

The KULI battery thermal model considered the cells in the pack to be a single, lumped thermal mass. Cell-internal heat generation rate, a function of drive cycle and vehicle design, was determined from separate vehicle simulations. Two additional mass nodes in the battery model represent the battery jacket

and case. The jacket node was thermally connected to the WEG cooling loop, while the battery case node accounted for a passive cooling path for thermal conduction through the battery case and convection to the outside environment. In the initial simulations discussed in this report, we assumed a Nissan Leaf-sized 24-kWh Li-ion battery with a mass of 246 kg.

Two models of a baseline ESS WEG cooling system were then built in KULI. Pump and engine cooling radiator data from Visteon were used to build the individual KULI component models. One system model had a refrigerant to WEG heat exchanger (chiller) to remove energy from the WEG cooling system. This model was used in high ambient temperature simulations to quickly reduce the temperature of the battery cells. The second model used a low temperature radiator to remove heat energy from the WEG. This model was used in moderate environments. Software challenges prevented a single cooling loop model with the chiller and radiator in separate branches and the flow controlled with valves.

NREL's battery life model calculated performance fade due to battery temperature exposure and duty-cycle. For light-duty passenger vehicles under moderate duty cycles, calendar degradation (rather than cycling degradation) may control whether the battery will last for the 10- to 15-year life of the vehicle. Laboratory calendar aging tests typically show Li-ion battery performance falls off with the square root of time due to corrosion reactions that occur at electrode surfaces inside the cell. The battery calendar life model describes battery relative resistance growth, R , and relative capacity fade, Q , as:

$$R = 1 + a t^{1/2} \quad (2)$$

$$Q = 1 - b t^{1/2} \quad (3)$$

Rate constants a and b were made temperature-dependent using the Arrhenius equation:

$$n = n_{ref} \exp \left[\frac{-E_n}{R_{gc}} \left(\frac{1}{T} - \frac{1}{T_{ref}} \right) \right] \quad \text{where } n = a \text{ or } b \quad (4)$$

In equation 4, R_{gc} is the universal gas constant, and the reference temperature is $T_{ref}=293.15$ K. Activation energies E_a and E_b and reference rate constants a_{ref} and b_{ref} were fit to calendar-life aging data for the nickel-cobalt-aluminum/graphite Li-ion chemistry [10].

Vehicle performance model

The vehicle performance model, used to predict range and fuel use, captured the critical parameters needed for this analysis. It calculated the power to overcome drag, acceleration, ascent, rolling resistance, and inertia over specified drive cycles. The model included vehicle components such as the battery, electric motor, and engine. These components were modeled at a level that matched well with detailed component models included in vehicle simulation software such as Autonomie. The components were combined in the most common architectures, including conventional vehicles and EDVs. The model accounted for auxiliary loads, regenerative braking, and energy management strategies.

To gain confidence in the model, component sizes and vehicle characteristics were entered into the model for a variety of vehicles. As seen in Figure 3, the model predicted the fuel economy within 10%. The electrical efficiency was defined as the electrical energy consumption per mile. While Nissan Leaf data were not available for constant speeds, the vehicle performance model prediction matched the U.S. Environmental Protection Agency's (EPA's) city/highway rating of 0.34 kWh/mi.

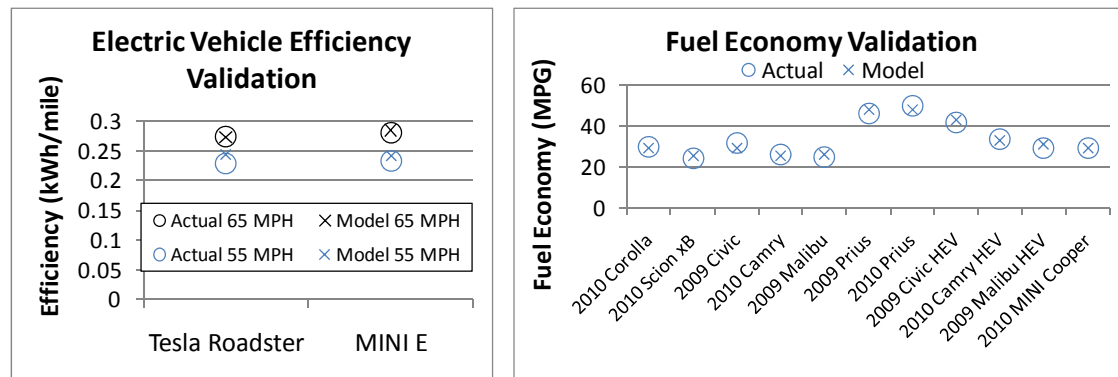


Figure 3. Vehicle validation data – electrical efficiency and fuel economy

A model of a Nissan Leaf was used to generate heat loss profiles for the APEEM components and ESS over the EPA FTP, Highway, and US06 drive cycles. Figure 4 shows the APEEM and battery heat loss over the US06. This heat load was used in the KULI model of the APEEM and ESS cooling loops.

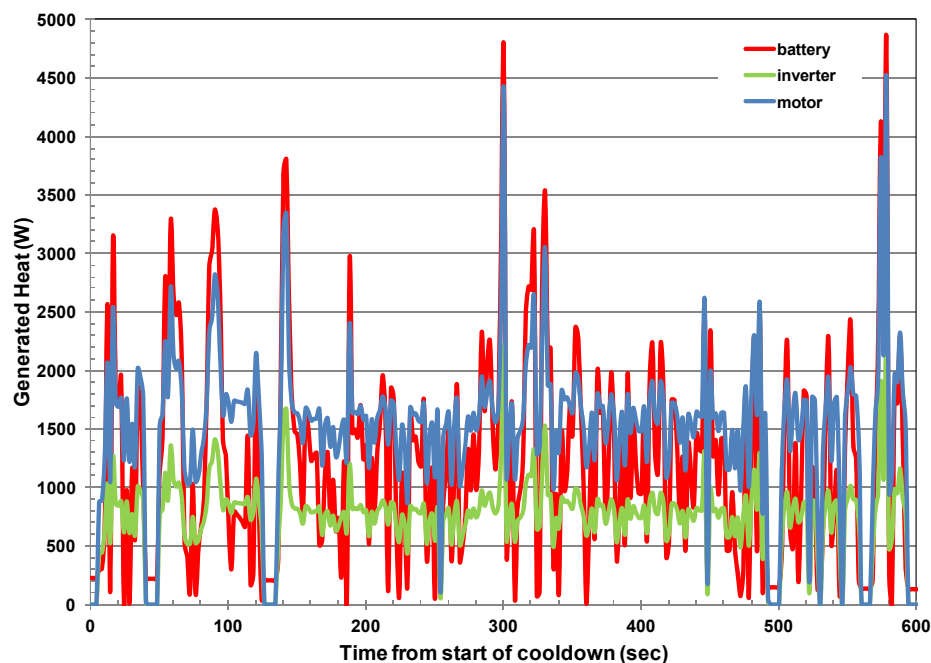


Figure 4. Heat generated in the APEEM and ESS components of a Nissan Leaf over the US06 drive cycle

Results

The KULI A/C model system was run at three steady-state operating points. These steady-state bench data, obtained in Visteon environmental chambers, were used to validate the system model. For these validation runs, the 213-cc compressor was used. At the 35°C, high blower setting, and 48.3 km/hr (30 mph) vehicle speed, the pressure drops produced by the model for each of the components were within 24 kPa (3.5 psi) of the Visteon data. The temperatures of the components were also consistent with the Visteon data with some slight fluctuations at the compressor outlet (Figure 5). Simulations with 45°C

ambient, high HVAC blower speed and 35°C ambient, medium HVAC blower speed conditions were also run. The evaporator heat transfer for the non-cycling runs exceeded the Visteon data by approximately 480 W while the compressor work matched well. Overall, the A/C model matched the data to enable comparison of combined cooling loop configurations with a baseline configuration.

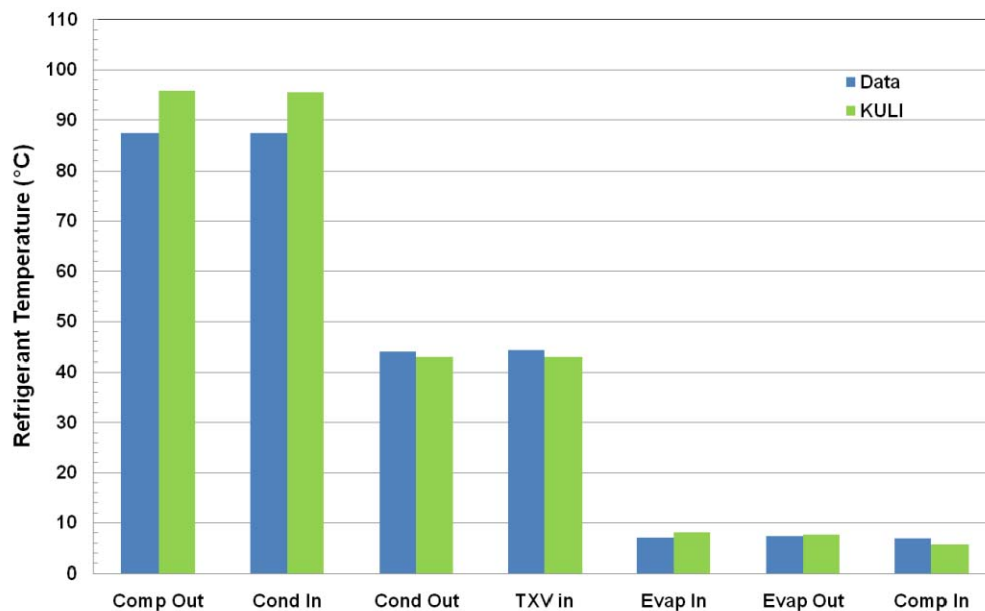


Figure 5. Refrigerant system temperatures for 35°C, high blower speed

After the A/C system was validated with bench data, it was combined with the small sedan cabin model to approximate a small EV. A 33-cc scroll compressor was used with its rotational speed determined by a PID controller. The control parameters were set to obtain a 3°C evaporator air temperature and 20.6°C cabin air temperature. A solar load of 850 W/m² was applied, and the cabin interior temperatures were initialized to 20°C above ambient. The blower was set to high (0.136 kg/s) with only outside air (0% recirculation).

After separately testing the ESS and APEEM cooling loop models, they were combined with the A/C and cabin models. In this baseline vehicle simulation, the ESS cooling loop was connected to the A/C system through the chiller while the APEEM cooling loop remained standalone. On the air side, the low temperature radiator (blue in Figure 6) of the APEEM cooling loop impacted the A/C condenser (green in Figure 6) by virtue of its upstream location. A constant air mass flow of 0.796 kg/s was applied to the air side of a low temperature radiator and condenser.

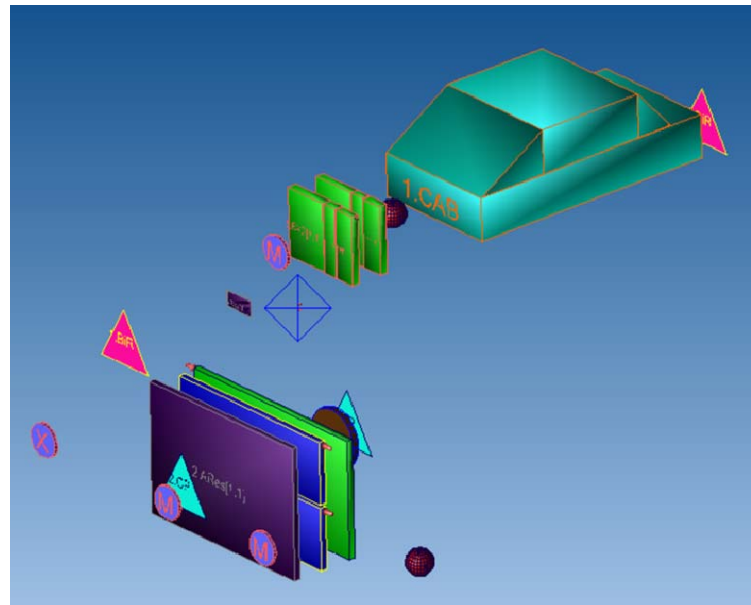


Figure 6. Air-side configuration of the baseline vehicle model

A series of runs were conducted at 45°C, 35°C, and 25°C ambient temperatures to assess the performance of the thermal management systems in the baseline model. Figure 7 shows the evaporator exit air temperature did not reach the 3°C antifreeze control setpoint during the 10-minute drive cycle for the 45°C and 35°C ambient conditions. For the 25°C ambient condition, the evaporator air reached its 3°C control in 20 seconds. The cabin air temperature (Figure 8) did not reach its control setpoint of 20.6°C in any of the cases due to the short drive cycle and initial hot soak interior temperature.

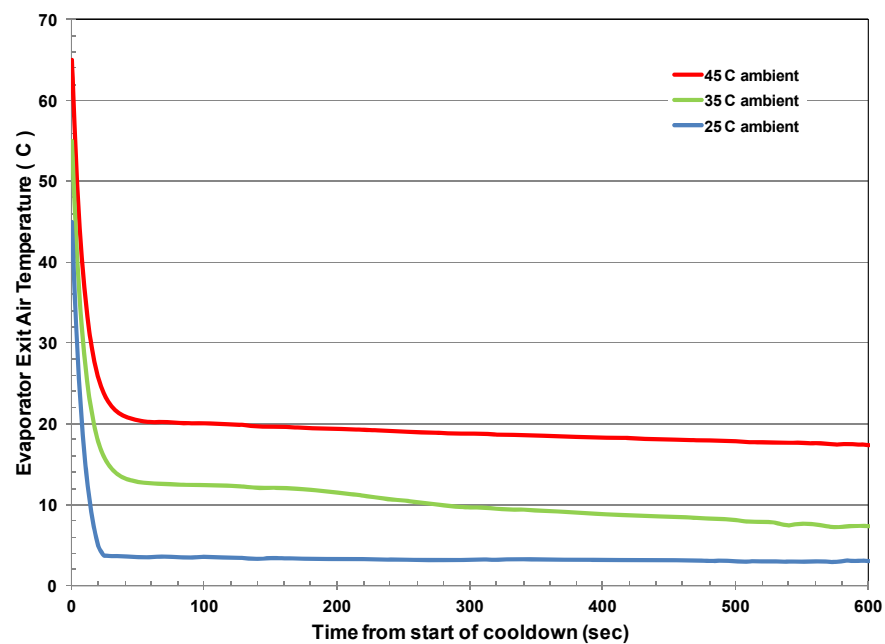


Figure 7. Evaporator exit air temperature over the US06 drive cycle for the chiller configuration

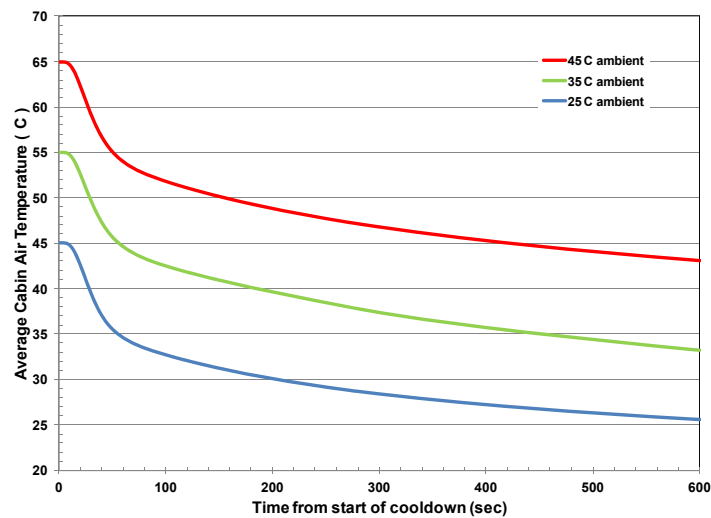


Figure 8. Cabin air temperature over the US06 drive cycle for the chiller configuration

The APEEM cooling loop initial component temperatures were set to ambient temperature. A pump speed of 5,000 rpm resulted in a 50/50 WEG flow rate of 5 L/min. The heat generation for the motor and inverter over the US06 drive cycle was determined by the vehicle performance model. Figure 9 shows the motor temperature approached 65°C for the hottest environment. The inlet fluid temperature was 52°C for this case. Based on the author's experience, these temperatures were reasonable although the flow rate was slightly lower than typical.

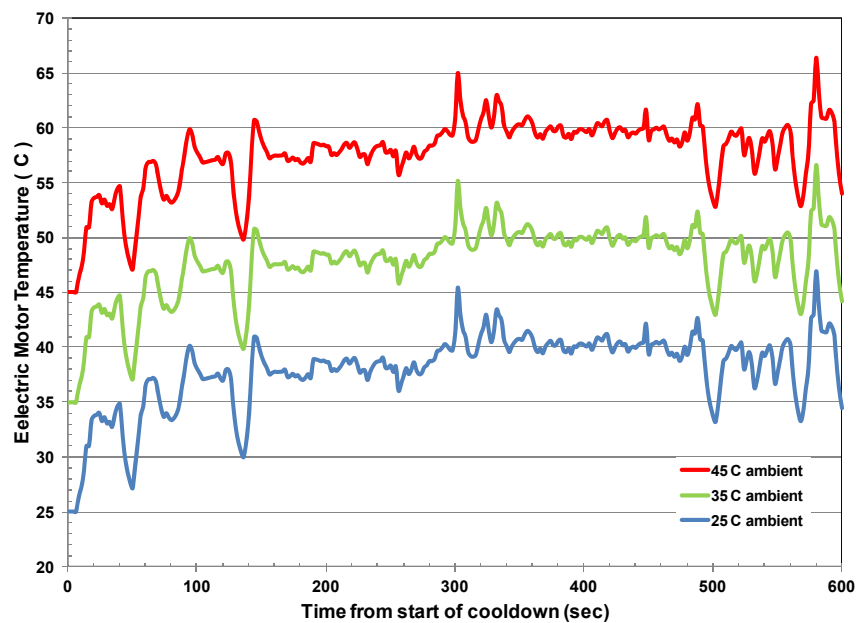


Figure 9. Electric motor temperature over the US06 drive cycle for the chiller configuration

The ESS cooling loop initial component temperatures were set to 1.5°C above ambient temperature. The pump speed was controlled by a PID controller with setpoints designed to maintain the battery cell temperature at 26.5°C. Figure 10 shows the cell temperature for the 45°C ambient run never cooled to the setpoint while the cell temperatures for the 35°C ambient run attained the 26.5°C setpoint at the end of the run. A maximum 50/50 WEG flow rate of 4 L/min was attained at the beginning of the 45°C and 35°C runs. For the 25°C run, the battery did not require as much WEG flow because the cells started the drive cycle at the control temperature.

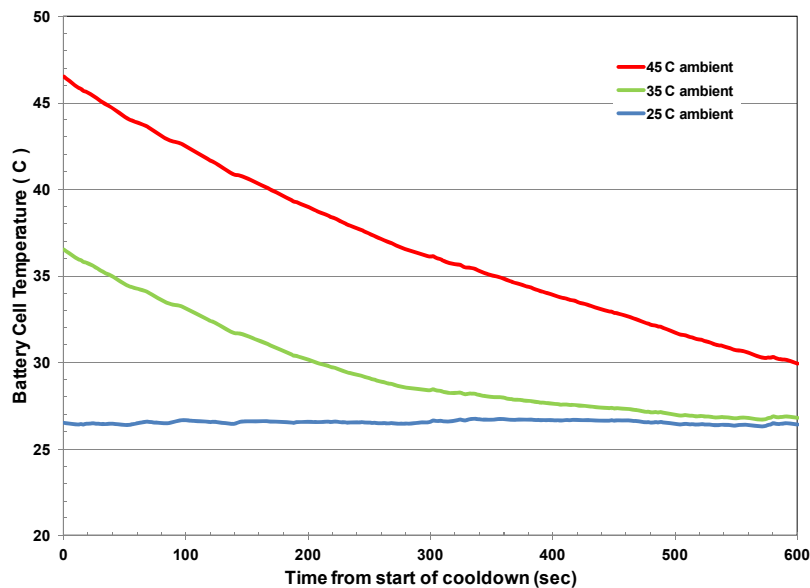


Figure 10. Battery cell temperature over the US06 drive cycle for the chiller configuration

The combined thermal management power consumption included the A/C compressor, ESS pump, APEEM pump, A/C blower, and condenser fan. Figure 11 shows a 5-kW power consumption for the 45°C case while the 25°C case resulted in a 1.6-kW load. In the 25°C ambient case, the drop in power 20 seconds into the run was due to the A/C evaporator exit air temperature reaching its antifreeze control setpoint and the compressor rpm dropping.

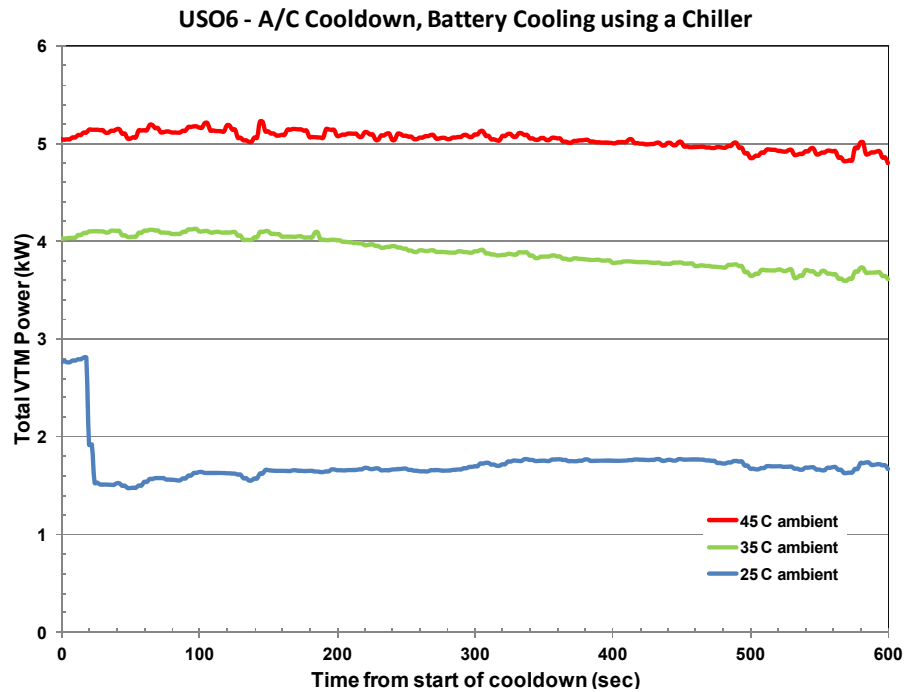


Figure 11. Total vehicle thermal management power over the US06 drive cycle for the chiller configuration

For the 25°C ambient case, the second baseline vehicle thermal management configuration, which includes a low temperature radiator in the ESS cooling loop, was run. Figure 12 shows the cell temperatures were higher for this case because the low temperature radiator was less efficient at removing heat than the chiller. The benefit of the low temperature radiator was less power consumption compared to the chiller as shown in Figure 13

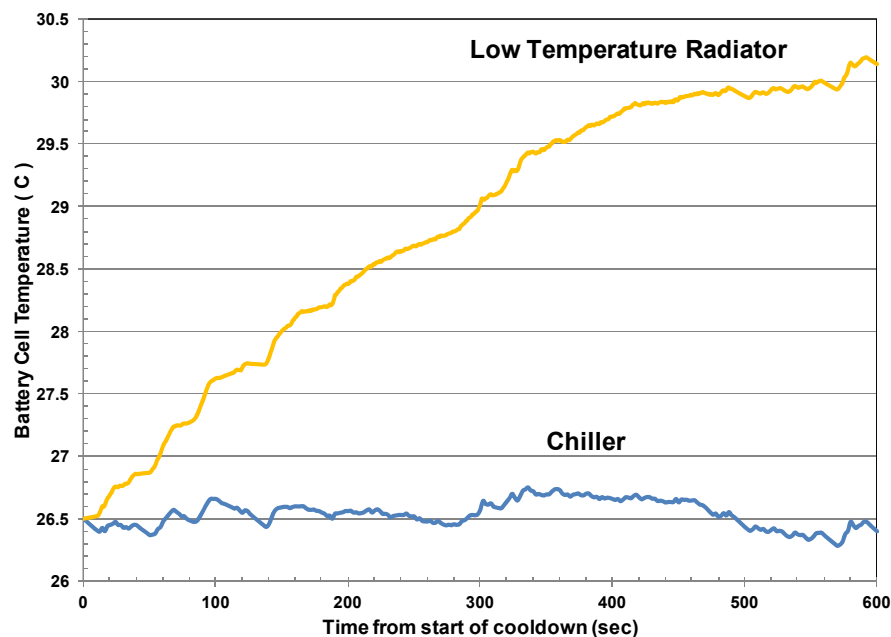


Figure 12. Battery cell temperature over the US06 drive cycle for 35°C ambient

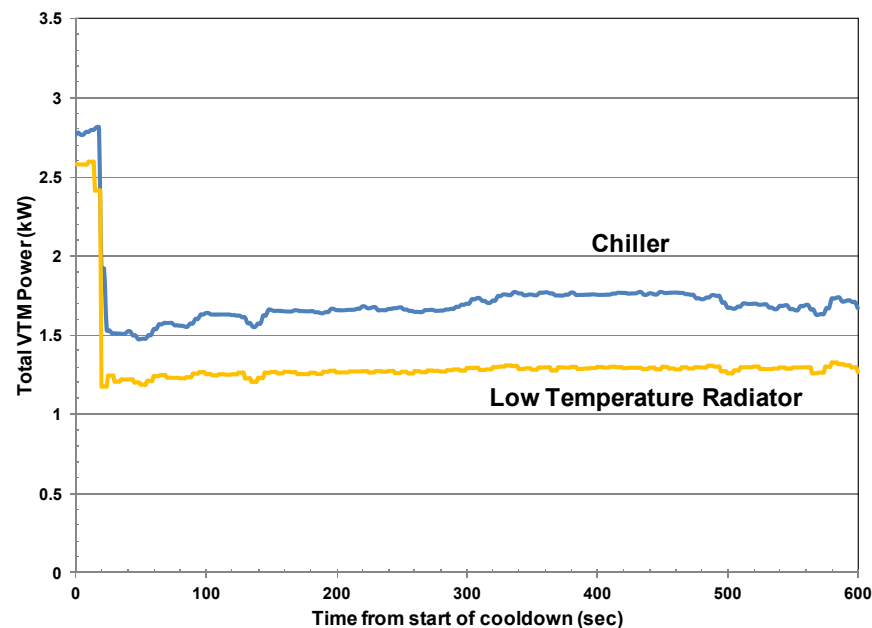


Figure 13. Total vehicle thermal management power over the US06 drive cycle for 35°C ambient

Figure 14 illustrates the competing demands of battery cooling and occupant comfort. For the 35°C ambient temperature case, the chiller capacity used to cool the battery was initially 4 kW, while the evaporator capacity used to cool the passenger compartment was initially 3.2 kW. For this configuration, more of the cooling capacity initially went to cooling the battery. This is apparent in the resulting temperatures. Figure 10 shows the battery cells cooled to 26.5°C in 10 minutes while the passenger compartment was still above 33°C at the end of the run (Figure 8). This vehicle-level challenge will be critical for EDVs as automotive engineers trade battery temperature and life against occupant comfort in some operating conditions.

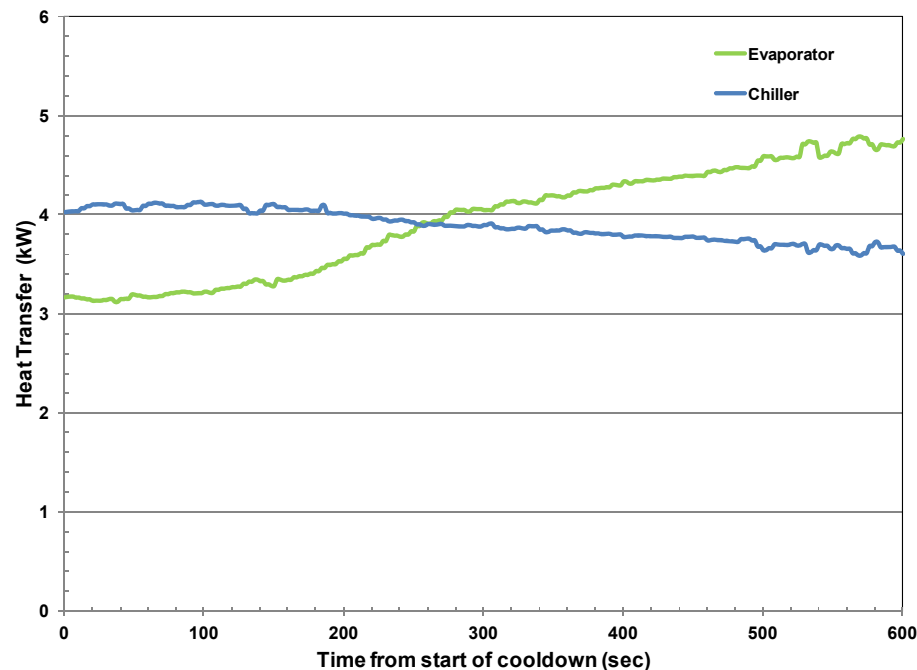


Figure 14. Evaporator and chiller capacity over the US06 drive cycle for 35°C ambient

Conclusion

A modeling process was developed to assess the synergistic benefits of combining cooling loops in vehicles with electric powertrains. Visteon provided high-quality component data to form the basis of the models. Using KULI software, an A/C model was built and validated with test data. After a model of a small sedan cabin was built and tuned, it was combined with the A/C model and produced reasonable cool-down performance. APEEM and ESS cooling loops were built and produced typical temperatures and flow rates. These models were combined with the A/C and cabin models to form a baseline vehicle thermal model. The baseline vehicle model was run at three ambient conditions. As the ambient temperature dropped, the required thermal management power dropped as temperatures approached the desired values.

The next step is to link the KULI model and the vehicle cost/performance and battery life models and assess strategies for combining cooling loops. This type of vehicle-level analysis is critical for assessing potential cost reductions and performance improvements due to combined cooling systems in EDVs. The potential benefits are unknown and need to be quantified. Reducing EDV cost and improving performance would increase consumer acceptance and incorporation of vehicles with electric powertrains.

Publications

1. Rugh, J.P.; Bennion, K.; Brooker, A.; Langewisch, J.; Smith, K.; and Meyer, J. (2011) "PHEV/EV Integrated Vehicle Thermal Management - Development of a KULI Model to Assess Combined Cooling Loops," *Proceedings of the 10th Vehicle Thermal Management Systems Conference*, May 15-19, 2011, Gaydon Warwickshire, UK, Institution of Mechanical Engineers.

References

1. Ap, N-S., Guerrero, P., Jouanny, P., Potier, M., Genoist, J., Thuez, J., “UltimateCooling™ New Cooling System Concept Using the Same Coolant to Cool All Vehicle Fluids,” 2003 Vehicle Thermal Management Systems Conference (VTMS6), IMechE C599/010/2003, May 2003.
2. Bennion, K., Thornton, M., “Integrated Vehicle Thermal Management for Advanced Vehicle Propulsion Technologies,” SAE Paper 2010-01-0836, 2010.
3. Barnitt, R., Brooker, A., Ramroth, L., Rugh, J., Smith, K., “Analysis of Off-Board Powered Thermal Preconditioning in Electric Drive Vehicles,” 25th World Battery, Hybrid and Fuel Cell Electric Vehicle Symposium & Exhibition, Shenzhen, China, November 2010.
4. KULI Energy Management Simulation Software, Version 8.0-1.02, Engineering Center Steyr GmbH & Co KG, <http://www.kuli.at/>, accessed November 16, 2010.
5. Hsu, J., Staunton, R., Starke, M., *Barriers to the Application of High-Temperature Coolants in Hybrid Electric Vehicles*, Oak Ridge National Laboratory Technical Report, ORNL/TM-2006/514, 2006.
6. Vehicle Technologies Program Plans and Roadmaps. “Electrical and Electronics Technical Team Roadmap,” December 2010, http://www1.eere.energy.gov/vehiclesandfuels/pdfs/program/eett_roadmap_12-7-10.pdf, accessed February 28, 2011.
7. Lipo, T., *Introduction to AC Machine Design*, 3rd Edition, Madison: University of Wisconsin. 2007.
8. Lindström, J., “Thermal Model of a Permanent-Magnet Motor for a Hybrid Electric Vehicle,” Department of Electric Power Engineering, Chalmers University of Technology, Göteborg, Sweden, 1999.
9. Figliola, R., Beasley, D., *Theory and Design for Mechanical Measurements, 2nd Edition*, New York,: John Wiley and Sons. 1995.
10. Smith, K., Markel, T., Pesaran, A., “PHEV Battery Trade-off Study and Standby Thermal Control,” 26th International Battery Seminar & Exhibit, Fort Lauderdale, FL, March, 2009.
11. Simpson, A., “Cost-Benefit Analysis of Plug-In Hybrid Electric Vehicle Technology,” 22nd International Battery, Hybrid and Fuel Cell Electric Vehicle Symposium and Exhibition (EVS-22), Yokohama, Japan, October 23-28, 2006.

5.5 Electric Motor Thermal Management

Principal Investigator: Kevin Bennion

National Renewable Energy Laboratory

1617 Cole Blvd.

Golden, CO 80401-3305

Voice: 303-275-4447; Fax: 303-275-4415; E-mail: Kevin.Bennion@nrel.gov

DOE Technology Development Manager: Susan A. Rogers

Voice: 202-586-8997; Fax: 202-586-1600; E-mail: Susan.Rogers@ee.doe.gov

Objectives

As part of its work for the U.S. Department of Energy's (DOE) Vehicle Technologies Program (VTP), Advanced Power Electronics and Electric Motors' (APEEM) thermal management activity seeks to develop electronic and electric machine technology that meets specific research and technical development targets. Meeting these targets is necessary in order to achieve widespread commercialization of eco-friendly advanced vehicle technologies, which include hybrid electric, plug-in hybrid electric, electric, and fuel cell vehicles. By commercializing these advanced vehicle technologies, the United States can reduce the amount of petroleum used in transportation.

While researchers strive to achieve smaller component volumes, lower costs, and lower weights without sacrificing performance or reliability, specifically focusing on thermal management provides an important way to improve the cost, weight, volume, and robustness of electric drive systems. For this reason, the APEEM activity has developed an active research and development effort to improve the thermal management of electric drive systems.

Thermal management for electric motors will only become more important as the automotive industry continues its transition to more electrically dominant vehicle propulsion systems. Currently, thermal constraints are one of the primary limitations on how electric motors ultimately perform, and as thermal management improves, there will be a direct trade-off between its performance and the sizing of electric motors to operate within the thermal constraints.

The goal of this research project is to characterize the current state of thermal management technologies for electric traction-drive motors and quantify the impact of thermal management on the performance of electric motors. The ultimate goal is to identify areas for improvement and knowledge gaps that would benefit from additional research. The research objectives are summarized as follows:

- Establish a foundation on which to evaluate potential improvements to electric motor thermal management
- Quantify opportunities for improving cooling technologies for electric motors
- Link thermal improvements to their impact on APEEM targets to prioritize future research
- Increase publically available information to support thermal management of electric motors.

Approach

The approach for FY 11 expanded on past power electronics cooling efforts in the Thermal Systems Integration focus area. By applying an integrated systems approach to this work, it is possible to cascade higher level program targets, specifications, and constraints to application specific thermal performance targets. Also, a systems approach enables linking improvements in cooling technologies to their impact on higher level application specific program targets. This process is illustrated in Figure 1, below. The

approach for FY11 focused on integrating five main areas, each of which will be described in more detail in the technical discussion:

- application technical specifications
- package mechanical design
- thermal design targets
- cooling technology selection
- cooling technology balance of system

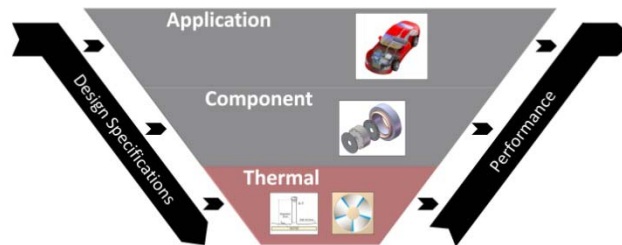


Figure 21: Thermal System Integration Approach

Major Accomplishments

While the key FY11 accomplishments are explained in more detail in the technical description, section, they can be summarized as creating:

- a preliminary loss model to evaluate loss distributions within the electric motor for different operating conditions
- thermal property data of motor lamination materials with industry input
- analytical and 3-D (three-dimensional) finite element analysis (FEA) models for determining effective composite material conductivity as applied specifically to motor slot windings
- a stator thermal model validated against published data
- a parameter sensitivity study of thermal design factors for motor stator cooling
- initial oil cooling hardware test designs
- collaboration with the VTP cross-cut project “Integrated Vehicle Thermal Management—Combining Fluid Loops on Electric Drive Vehicles” involving Energy Storage, Vehicle Systems, and APEEM.

Future Direction

Future work will focus on package mechanical design, cooling technology selection, and thermal design targets. Specifically, efforts in FY12 will focus on:

- completing thermal property testing of lamination materials and measurement of lamination contact resistances
- completing permanent magnet thermal sensitivity analysis to identify areas of thermal improvement common to alternative permanent magnet motor configurations
- completing fundamental heat transfer experiments with oil jets impinging on flat target
- initiating oil jet durability experiments for winding insulation.

Technical Discussion

The ability to remove heat from the electric motor poses one of the major constraints on a motor designer's ability to achieve higher motor power density values. For this reason, with support from DOE, the National Renewable Energy Laboratory (NREL) began working to identify opportunities for improving thermal management of electric motors that are used in electrified vehicle traction drives. To support this effort, NREL partnered with the University of Wisconsin—Madison because of their recognized expertise in designing and analyzing electric motors. In addition to working with the University of Wisconsin, NREL sought input from representatives from the electric motor industry.

An overall thermal design depends on a number of factors that influence the system's performance and cooling design. These factors include

- application technical specifications
- package mechanical design
- cooling technology selection
- cooling technology balance of system.

Combined, these four factors impact the thermal design targets of the specific application as shown in Figure 2, below, and discussed below.

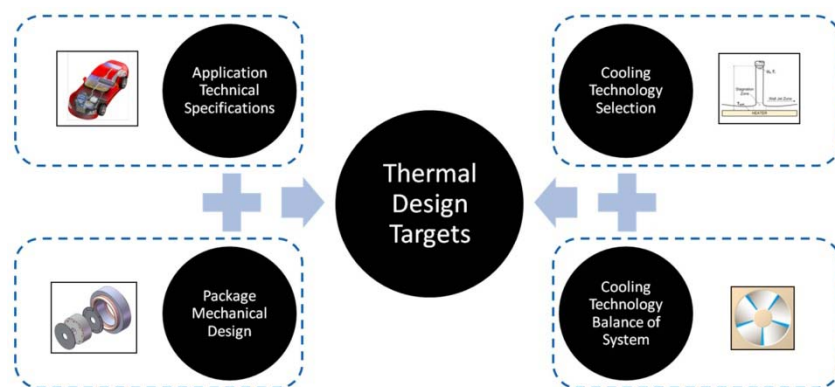


Figure 22: Motor cooling focus areas and thermal system integration

Application Technical Specifications

The application technical specifications determine an electric motor's operating conditions, temperature constraints, power level, and efficiency. These factors determine the constraints placed on a thermal management system and the heat loads that must be managed. The researchers selected three methods to estimate the thermal loads which included literature searches, benchmark data from Oak Ridge National Laboratory (ORNL), and loss estimation methods developed by the University of Wisconsin. The university's loss estimation methods to analyze the heat load distribution within an electric motor are summarized below.

The purpose of estimating the motor losses was to create a simplified and computationally fast analytical loss model, that could provide input to a lumped parameter thermal equivalent circuit or a finite element analysis (FEA) thermal model. This modeling approach uses segregated lumped loss data generated by

electromagnetic FEA over a range of current magnitudes and current angle conditions, at a fixed reference speed, near the middle of the motor's operating envelope. Researchers can then use the calculated core loss data for the machine to predict the losses throughout the machine's full operating envelope. The resulting model uses a combination of physics-based formulas and interpolation that is based on a condensed set of two-dimensional data tables to predict losses for any operating point corresponding to speed, torque, and temperature.

The computational effort required to evaluate this model is comparable to the effort required to estimate loss for iron and copper based on the assumption of linear iron with only the fundamental frequency component of magnetic flux. The advantage of the proposed approach using physics-based formulas to extrapolate FE-based loss data is that it maintains most of the accuracy of detailed FEA modeling but is much faster. This approach also accounts for losses due to saturation, time and spatial harmonics, and the eddy current losses in rotor magnets. The lumped loss components researchers evaluated for this thermal model includes:

- stator winding (copper) losses in the stator slots and end turns
- stator back-iron (yoke) losses
- stator tooth iron losses
- stator tooth-tip iron losses
- rotor losses, including rotor iron losses and magnet losses due to eddy currents.

The *Introduction to AC Machine Design* [1] addresses some other mechanical loss components such as friction and windage losses, but researchers did not incorporate either friction or windage losses into this thermal model. However, researchers did use the lumped loss extrapolation method to account for other loss contributions such as stray load losses [1] caused by harmonics aggravated by slotting effects, even though these can be difficult to calculate using analytical methods.

Researchers pre-calculated reference data tables during post-processing of electromagnetic FEA results in order to determine the iron and magnet loss values as functions of current and current angle at a reference frequency. They also extrapolated losses at other operating points and operating frequencies according to Equation 1 in which $P_{IronTotal}$ is the total lumped iron loss for a specific component evaluated at frequency f_e in watts at the same current and current angle, where f_{ref} is the reference frequency for the pre-calculated data, $P_{IronHys}$ is the reference iron hysteresis loss, and P_{IronEC} is the reference iron eddy-current loss. Both $P_{IronHys}$ and P_{IronEC} are obtained from a lookup table for a given current magnitude and current angle. Researchers also used this approach to estimate the losses in the IPM machine magnets, except that they calculated the magnet losses as scaled eddy-current losses only, without the hysteresis loss component:

$$P_{IronTotal} = P_{IronHys} \left(\frac{f_e}{f_{ref}} \right) + P_{IronEC} \left(\frac{f_e}{f_{ref}} \right)^2 \quad (1)$$

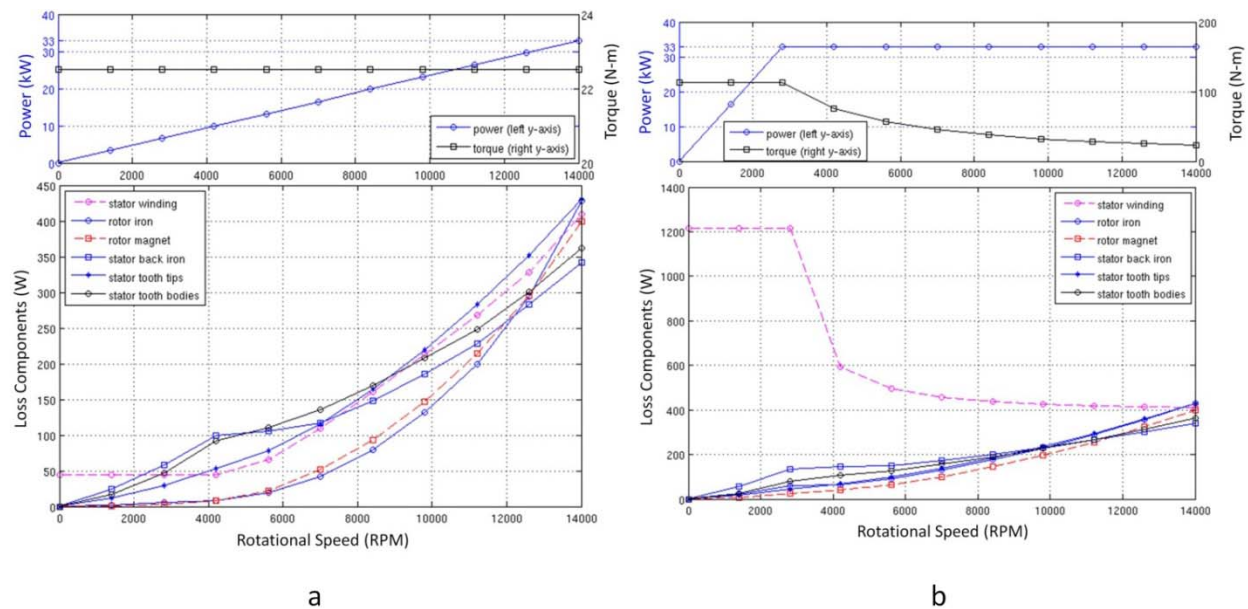


Figure 23: (a) Top graph—power and torque vs. speed for constant 22.51 N-m torque; bottom graph—lumped loss component amplitudes vs. speed for given torque vs. speed conditions; (b) Top graph—power and torque vs. speed for high constant torque (<2,800 rpm) and continuous power limit (>2,800 rpm); bottom graph—lumped loss component amplitudes vs. speed for given torque vs. speed conditions.

The copper winding resistance is calculated as a function of the number of wire strands, the wire cross sectional area, the wire length, the wire electrical resistivity, and the wire temperature. The model developed for this research was for a Litz wire winding that suppresses the onset of high-frequency copper losses that are known as proximity losses. To extend this type of loss analysis to windings that have stronger frequency dependencies due to high-speed proximity losses, the winding loss model can include correction coefficients for frequency.

Figure 3 compares the estimated losses applied to a 33 kW continuous power interior permanent magnet motor that has a maximum speed of 14,000 RPM. Figure 3(a) shows the loss distribution that occurs while operating at a constant torque (approximately 20% of rated torque) over the motor's speed range. Figure 3(b) shows the loss distribution at the continuous power limit of 33 kW from 2,800 to 14,000 rpm and at high torque below 2,800 rpm. The differences observed in the relative magnitudes of the different lumped loss components plotted in these figures highlight the importance of estimating each loss component individually. Their relative magnitudes vary significantly, and a motor's power and torque-limiting thermal hot spot at one operating point is likely to be different from the limiting hot spot at another operating point. For example, Figure 3(b) shows that the machine losses are heavily concentrated in the stator windings at high torque and low speed, but the losses are increasingly dominated by the combined total iron losses at high speed. When the individual iron loss components are added, the combined result is significant. The adopted loss estimation technique does have some limitations, including:

- The increase in iron losses due to pulse width modulation (PWM) effects is not accounted for in these calculations. If needed, a correction for the PWM-related increase in iron losses compared to the fundamental component iron loss alone could be introduced [2], [3].
- Proximity losses in the windings are not calculated. Proximity effects can be important in some special high-performance machines that operate at high speeds when the stators are wound with

standard magnet wire or bar windings. Future versions of this model could be modified to include high-frequency losses by modeling the resistances to include a winding resistance component that varies as a function of frequency.

- Iron losses in the present model are not compensated for temperature variations.

Package Mechanical Design

The Package Mechanical Design represents the physical geometry, materials, and interfaces that affect a motor's heat spreading capability. Depending on the motor design and the selected cooling technology, the thermal limiting feature may be caused by internal thermal interfaces or low thermal conductivity materials. In order to create an effective thermal model for an electric motor, appropriate thermal properties must be known. Public literature provides some information about this, and the work during FY11 increased the amount of publically available information related to material thermal properties for electric motors. APEEM's material analysis work on motor lamination steels and slot windings also contributed to other efforts to develop FEA thermal models for electric motors.

Lamination Steel Testing

During literature searches conducted during FY10, researchers established that public literature had only limited information on bulk lamination thermal properties for specific materials and the thermal effects of lamination stack contacts. For this reason, efforts were made during FY11 to measure thermal properties related to bulk lamination materials and the effect of thermal contact resistance between laminations. A range of lamination materials were selected with industry input to represent a range of thicknesses as listed in Table 1, below.

Table 6: Selected lamination materials and nominal thickness, as provided by supplier

| Electrical Steel Grade | Surface Insulation | Nominal Thickness (mm) |
|-------------------------------|---------------------------|-------------------------------|
| M19 (24 Gauge) | C-5 | 0.635 |
| M19 (26 Gauge) | C-5 | 0.470 |
| M19 (29 Gauge) | C-5 | 0.356 |
| HF-10 | C-5 | 0.260 |
| ARNON 7 | C-5 | 0.178 |
| ARNON 5 | C-5 | 0.127 |

Figure 4 shows the initial thermal property test results. Figure 4(a) shows the effective through-stack thermal conductivity through a stack of ten laminations. The most notable result of these test results is the significant (>10x) reduction in thermal conductivity relative to the bulk material, shown in Figure 4(b). The results for bulk material thermal conductivity shown in Figure 4(b) and specific heat in Figure 4(c) are preliminary, but initial results are comparable to public information of thermal conductivity for general electrical steels [1], [4–6] and specific heat of carbon and electrical steels [6], [7].

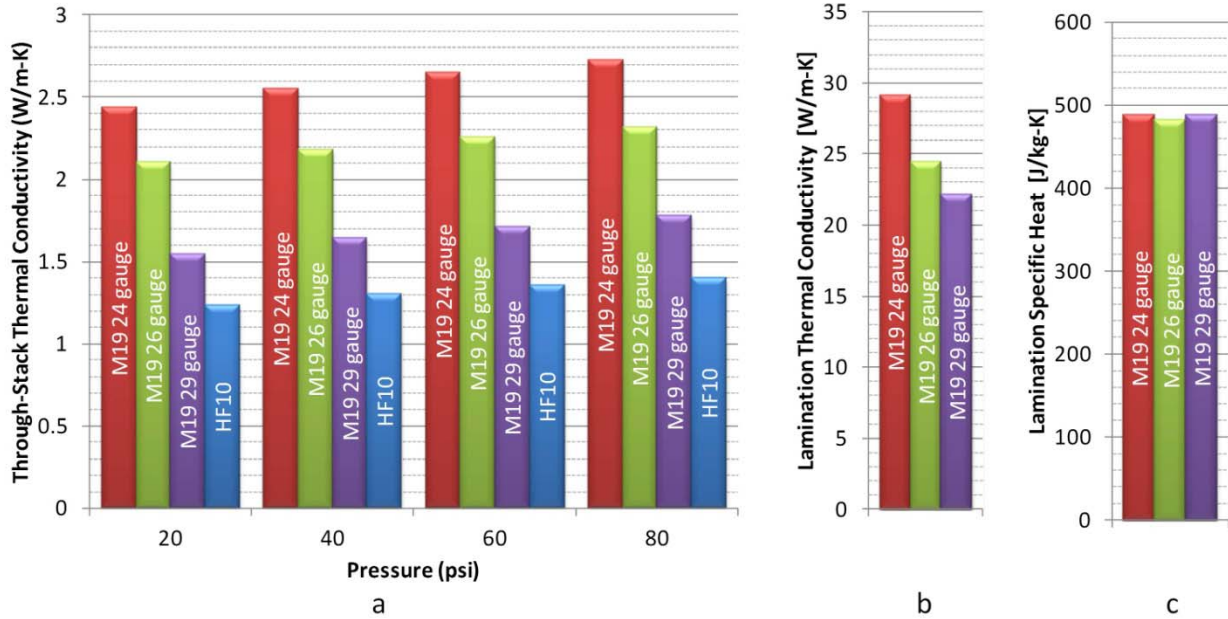


Figure 24: (a) Through-stack effective thermal conductivity of a stack consisting of 10 laminations; (b) Preliminary data for bulk lamination material thermal conductivity; (c) Preliminary data for bulk lamination material specific heat

Slot Winding Effective Thermal Properties

In addition to the lamination material, another critical element to thermal models of electric motors includes the thermal properties of the slot materials. It is impractical to model the stator windings with each individual component (wire, insulation, slot filler). For this reason efforts have been made in the literature to evaluate the effective thermal properties of the slot winding [8], [9].

In the past, work included efforts to quantify the effective material properties in-plane and out-of-plane (parallel to wires). For example Jih lists a common method for approximating the axial, or out-of-plane, thermal conductivity of a bundle of wires [8]. The axial, or out-of-plane, conductivity depends on the ratio of the areas of each material and can be solved analytically. In-plane conductivity depends on the wire configuration and cannot be solved exactly analytically. Because of this, two general configurations were considered in the past: open pack (Figure 5[a]) and closed pack (Figure 5[b]). H. Kanzaki evaluated a three-component (wire, insulation, filler) configuration for the open pack winding configuration as shown in Figure 5(a) [9]. However, for the closed pack configuration, Kanzaki gives a two-component approximation, in which the wire insulation and the epoxy filler are incorporated together to simplify the derived expressions [9]. For both cases, Kanzaki stated that the analytic expressions results were slightly lower than FEA thermal models. The reason for this artifact will be examined in greater detail in the following sections

Efforts in FY11 focused on building on this previously published analysis. FEA thermal models were constructed within the ANSYS computer simulation model, and validated against analytically derived expressions. The goals for this analysis included:

- Expanding on analytical expressions for calculating in-plane effective thermal conductivity
- Obtaining effective properties for the stator windings that can be used in larger scale electric motor thermal models

- Developing a modeling approach for complex winding structures in which multi-dimensional heat spreading effects are critical.

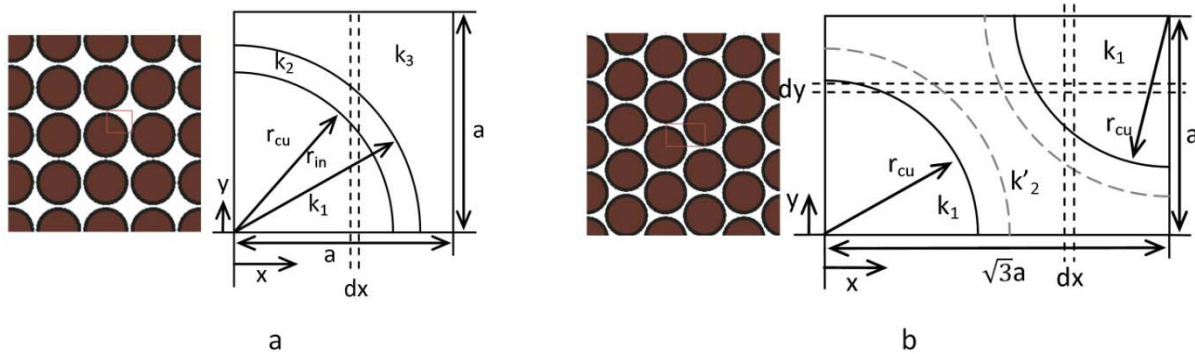


Figure 25: (a) Open package winding configuration; (b) Closed pack winding configuration

The researchers used two approaches to accomplish the above objectives. The first involved developing new analytical expressions for the in-plane thermal conductivity of the open and closed configurations as shown in Figure 5. However, for the closed configuration, they expanded the model to a three-component model to include the wire, insulation, and epoxy filler material. The second approach involved creating flexible parametric finite element analysis models within ANSYS for the configurations shown in Figure 5.

As expected, the FEA results in the axial direction match the analytic expression exactly and the in-plane results are slightly higher than Kanzaki's approach [9]. A comparison of the in-plane thermal conductivity results are shown in Figure 6(a), below. For the open pack configuration, the resistive model exactly matches the method Kanzaki proposed and is omitted from the graph. For the closed pack configuration, the three-component resistive model ("Analytical Model") shows a very small improvement over the two-component ("Kanzaki et al.") model for high fill factors as shown in Figure 6(a).

Figures 6(b) and 6(c) explain the higher effective in-plane thermal conductivity of the FEA model. Figure 6(b) shows the heat flow paths when the FEA model forces the heat to flow in one direction. The result of this constraint on the heat flow is seen in Figure 6(a), and the "FEA polarized" model matches the analytical model results. However, when the constraint is removed and heat is allowed to flow normally (Figure 6(c)), the result is an increase in the effective in-plane thermal conductivity of the slot winding. The results demonstrate the effectiveness of the FEA modeling approach, and show it will prove useful when looking at winding structures in which the multi-dimensional heat flow is significant.

Although the developed three-component resistive model produces longer and apparently more complex equations than Kanzaki's proposed approach, the derivation process is highly systematic and can be applied to any compound system provided that the internal boundaries in that system can be described mathematically. Any software package capable of numeric integration (MATLAB was used in this case) can be used to integrate the resulting expression. This approach can also be used to provide a survey of estimates for a wide range of material properties allowing the more time-consuming FEA to be applied to points requiring additional analysis.

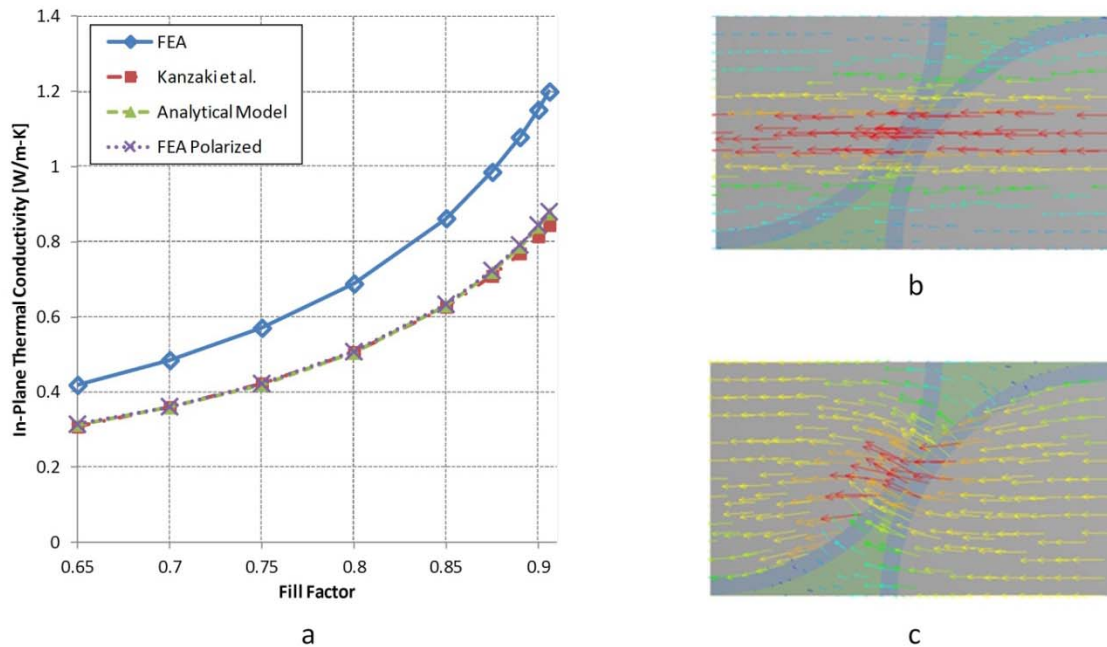


**Figure 26: (a) Comparison of in-plane thermal conductivity models;
 (b) Polarized FEA thermal model showing heat flow in one direction;
 (c) Standard FEA model showing preferred heat flow paths**

Once confidence has been established in the FEA model's ability to accurately model the windings, it is possible to explore the effects of various changes on the effective properties of the stator windings. To simplify the model, the thickness of the coating is determined as a function of the conductor diameter using a curve fit for Polyurethane-180, heavy build data from MWS Wire Industries website for AWG 16-26 [10]. The material properties used for the analysis match those used by Jih [8] and are listed in Table 2.

Table 7: Slot winding material properties

| Material | Conductivity (W/m-K) |
|----------------------|----------------------|
| Copper | 389 |
| Wire Coating (Mylar) | 0.155 |
| Slot Filling Epoxy | 0.11 |

A script was written in MATLAB to drive ANSYS with various combinations of parameters that would allow hundreds of data points to be collected in a relatively short timeframe. Samples of the results are shown in Figure 7, below. Figure 7(a) compares the in-plane thermal conductivity over a range of wire sizes and fill factors assuming an ideal fill condition with no voids in the filler material. Figure 7(b) shows the effective axial thermal conductivity for the same input variables. Although the figure does not reflect this, researchers also investigated the effect of air voids in the epoxy by varying the conductivity of the epoxy filler from its nominal value to a lower limit equivalent to the thermal conductivity of air. The impact of the epoxy fill values on axial conductivity was negligible. The in-plane thermal conductivity showed a maximum of a 36% reduction in the in-plane thermal conductivity when the fill factor was at its maximum.

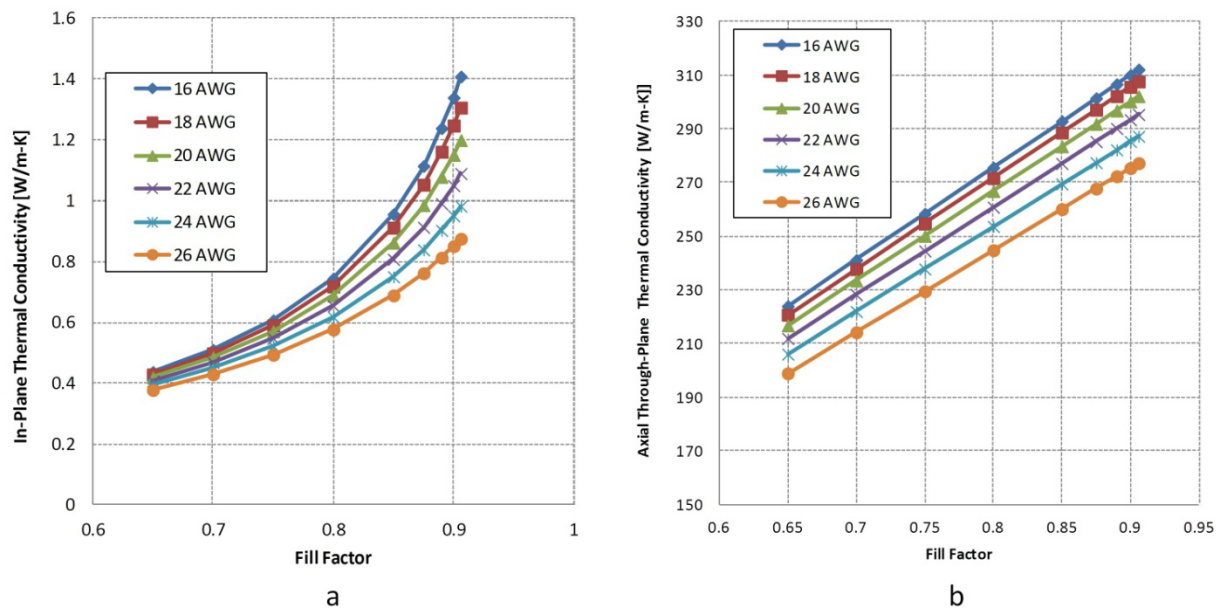


Figure 27: (a) In-plane effective thermal conductivity for closed pack winding configuration; (b) Axial, or through-plane, effective thermal conductivity for closed pack winding configuration

Thermal Design Targets

The purpose for the thermal design targets box in Figure 2 is to link application specifications and the mechanical package to thermal design targets and cooling technologies. The result helps identify which thermal improvements have the most impact on motor performance and APEEM program targets. For FY11, the goal was to determine the sensitivity of the total motor/system's thermal performance to changes or uncertainty in elements related to motor cooling. To perform this analysis, researchers constructed an FEA model for a permanent magnet motor stator described by Lindström [11]. They then compared these model results against published data, and once they established confidence in the model, they performed a parameter study using the previously described MATLAB-based script and graphical user interface (GUI).

The full stator model was constructed in SolidWorks and converted to a symmetrically sliced parametric FEA thermal model in ANSYS, as shown in Figure 8(a) and 8(b). The material properties applied to the thermal FEA model are listed in Table 3. Researchers applied the yoke-case contact effective thermal conductivity to a 1 mm thick section with an equivalent thermal resistance as the derived case-yoke contact thermal resistance. Converting the contact resistance into an effective thermal conductivity made it easier to include it as a variable in the sensitivity studies of material thermal conductivities within the machine because the conversion kept units across the varying parameters consistent. Also, treating the yoke-case contact as an effective thermal conductivity also provided a more effective method to parameterize the yoke-case contact resistance within ANSYS. When researchers checked their approach for modeling the contact resistance by comparing model results with a pure contact resistance and the 1 mm effective thermal conductivity, they saw no significant difference in the temperature results.

The comparison of the model thermal results against the published measurement data is shown in Figure 8(c), below. The temperatures within the motor sections vary by location. For this reason, it was necessary to create scripts within ANSYS to extract statistics related to temperatures within the motor

stator sections. Figure 8(c) compares the maximum, minimum, and average temperatures for the slot winding sides and end windings. The data from Lindström falls within the ranges verifying that the motor thermal model was generating results that were within expected values.

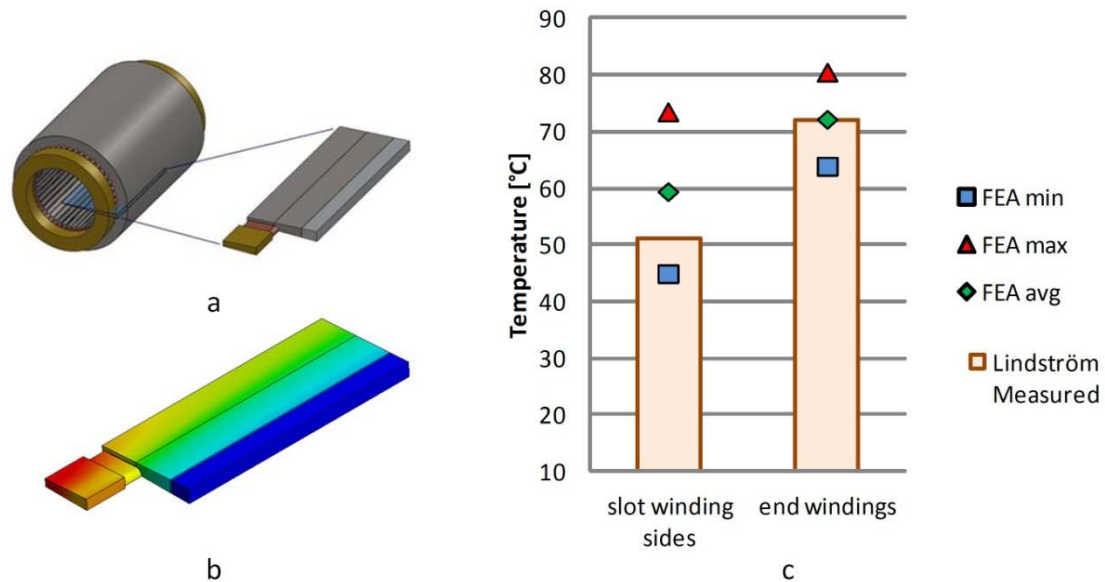


Figure 28: (a) Full stator geometry and sliced section for FEA thermal model; (b) Sample FEA thermal model temperature distribution; (c) Comparison of FEA model results against published temperature data

Table 8: Baseline thermal FEA model material properties

| Material | Conductivity (W/m-K) | Source |
|---------------------------------------|-----------------------|--|
| Insulation paper liner | 0.144 | [8] |
| Yoke-case contact | 1.17 | Applied to 1mm thick section with equivalent thermal resistance |
| Stator radial / angular / axial | 22.17 / 22.17 / 2.02 | Based on preliminary lamination thermal property measurements at NREL |
| Slot Winding radial / angular / axial | 1.2 / 1.2 / 302.2 | FEA data for 20AWG closed-pack with max fill factor and 100% epoxy goodness (no voids) |
| End Winding radial / angular / axial | 0.764 / 201.7 / 101.2 | Adjusted from FEA data for 20AWG closed pack with max fill factor and 0% epoxy goodness (100% air voids) |

Once confidence was established in the motor FEA thermal model, researchers initiated a sensitivity study to identify areas that would most impact thermal performance. Identifying areas of greatest impact provided information on what material properties need more focus in the motor model. In addition, the sensitivity study highlighted potential areas where thermal performance could be improved in an electric motor. The thermal sensitivity study incorporated a large number of potential design factors, including material thermal conductivity properties, heat loading distribution, cooling location, and cooling performance. Due to the large number of parameters, a MATLAB script and GUI interface were created to drive batch runs of ANSYS while handling common problems or interruptions that might occur while running unattended so that no data would be lost. The script enabled quick setup and unattended runs of more than 1,200 ANSYS simulations for this study.

The first step in the parameter sensitivity study altered a component's thermal conductivity by $\pm 20\%$ and measured the effect on the thermal resistance between the location of maximum temperature in the winding to the ambient coolant temperature ($R_{th,wa}$). Values are swept over a broad range of convection coefficients representing different levels of cooling effectiveness. An example of one of these plots is shown in Figure 9, below. As mentioned previously, since all other values are in terms of thermal conductivity, the stator-case or yoke-case contact resistance was replaced with a 1 mm thick strip with an appropriate thermal conductivity. Figure 9 also reflects the sensitivity to different heat loading distributions within the stator. Different winding loss to iron core loss heat distributions were evaluated including 60:40 (baseline distribution), 50:50, and 40:60. The different distributions are seen in Figure 9 and the variation in heat load did not appear to significantly impact the results for this specific application. The axial direction of the material properties is aligned with the motor axis or shaft.

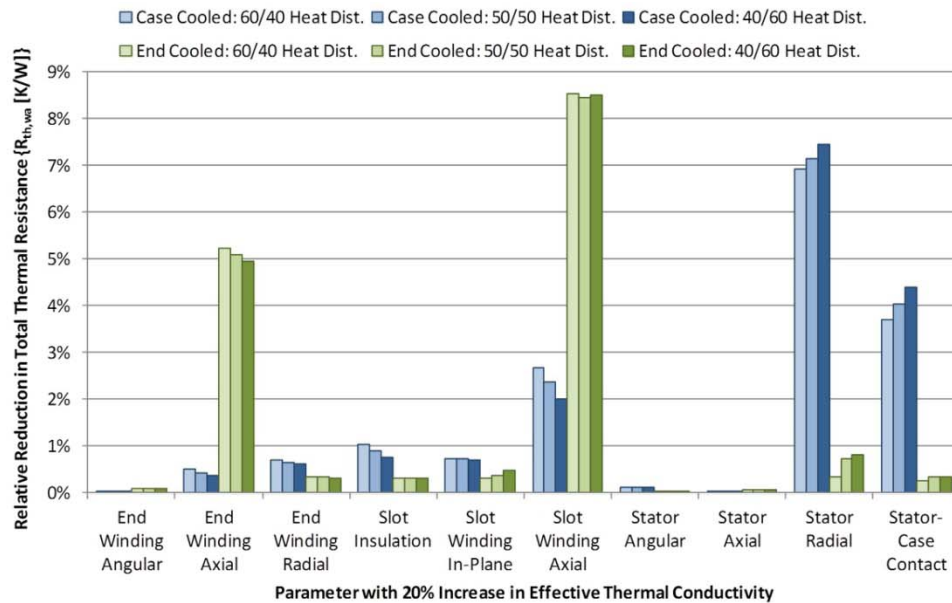
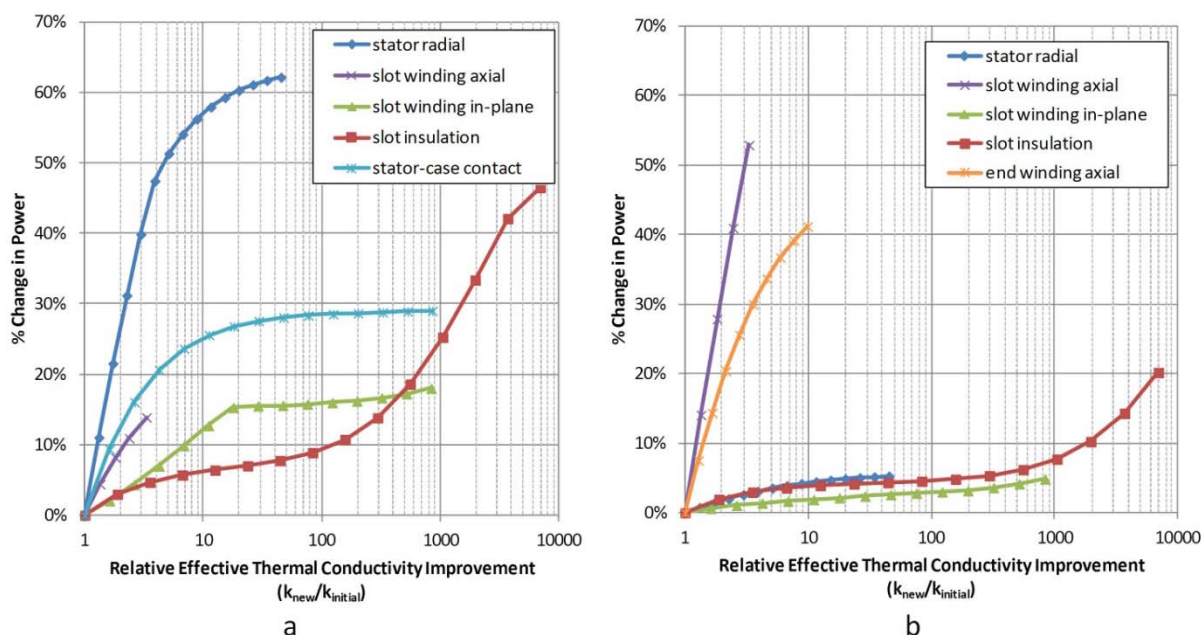


Figure 29: Parameter sensitivity analysis for 20% increase in component thermal conductivity. The impact is measured in terms of the reduction in the total thermal resistance between the peak winding temperature and the ambient coolant temperature. Multiple heat load distributions from winding losses to core losses are included with 60/40 as the baseline case provided by Lindström.

The parameter sensitivity plot above shows that there are a few key components that have thermal conductivity impacts on total thermal resistance. For the case cooled configuration, it is the axial slot winding, stator radial, and the yoke-case contact. For end winding cooled configuration, the axial slot winding and axial end winding effective thermal conductivity appeared to be the most significant factors. Although not as impactful in this analysis, the slot liner insulation also has an effect, especially for the case cooled condition.

Figure 9 identified design factors that have a significant effect on a total system's thermal performance. As with the APEEM activity, it is important to translate the thermal performance benefit into the impact on a program's overall targets concerning power. Figure 10, below, shows that for the highlighted materials, there is a percent increase in power for a given relative improvement in effective thermal conductivity. The graph compares the relative change in thermal conductivity of each component to the relative change in available power as each component's thermal conductivity increases. The upper limits

are not intended to represent the practical limit, but instead illustrate the effects as the thermal conductivity improves. The steepness of the slope in the lines in Figure 10 agrees with the parameter sensitivity study (Figure 9). Researchers also repeated the analysis for the case cooled and end winding cooled conditions. The results shown in Figures 9 and 10 are plotted for a single heat exchanger performance value ($R''_{th,ha} = 31.6 \text{ mm}^2\text{-K/W}$ in Figure 11) in which the impact of improved heat exchanger performance diminishes. The heat exchanger performance value was selected in order to better study the effects of the motor mechanical package or heat spreading capabilities.



**Figure 30: (a) Change in available power output vs. relative increase in component thermal conductivity for case cooled configuration;
(b) Change in available power output vs. relative increase in component thermal conductivity for end-winding cooled configuration.**

A full discussion of the sensitivity analysis for the case cooled and end winding cooled motor conditions is beyond the scope of this summary report. A more complete discussion is scheduled to be published at a conference later in FY12. However, it is possible to share some of the unexpected results from the sensitivity analysis, including:

- The slot liner material did not have as large of a relative impact on the total thermal performance as was initially expected. This may be attributed to the thinness of the layer and the effect of other low conductivity materials in the motor. Also, the FEA model does not account for the contact resistance between the slot insulation and the laminations, which could include air voids. A more detailed description of the slot and slot liner thermal properties is provided by Speer [12] and Kylander [13].
- Another unexpected result was the relatively low impact of the slot winding in-plane effective thermal conductivity. This may be due to the narrow width of the slot.

Cooling Technology Selection

The purpose for the Cooling Technology Selection box in Figure 2 is to demonstrate the alternative methods for cooling an electric motor. Thermal management of an electric motor depends on integrating cooling technology performance and the mechanical package thermal design, which includes material selection and thermal interfaces.

The impact of cooling technology selection is illustrated in Figure 11, which shows a system's total thermal resistance between the winding peak temperature and the ambient or coolant temperature ($R_{th,wa}$) versus the cooling technology heat exchanger cooling performance ($R_{th,ha}''$). Two cooling conditions are shown. The first, shown by the blue line, applies the cooling to the outer case of the motor, while the second condition applies cooling to the end windings. Improving the heat exchanger's cooling performance causes the total system performance ($R_{th,wa}$) to follow the curve to the left. As expected, the total thermal performance will decrease initially, but as the heat exchanger performance continues to improve (lower $R_{th,ha}''$), the effect on total thermal performance gradually decreases. As shown in Figure 11, the location where the total system thermal performance flattens out depends on where the cooling technology is located. The internal structure of the package mechanical design also affects the shape and location of the system's thermal performance curves. Analyzing the total thermal performance using this method can help select appropriate cooling locations, technologies, and mechanical thermal structure designs to achieve the desired thermal performance.

During FY10, researchers performed a summary of cooling methods for automotive electric traction drive motors. One of the common methods for cooling electric motors uses transmission oil for cooling [14–16]. During FY11, researchers determined that public literature had insufficient information about the performance of oil cooling for electric motors. An effort was made to design and initiate work to develop a test setup to perform experiments that could better characterize the heat transfer performance of oil jets and their durability impact on winding insulation. This experimental work will be a primary focus for FY12, and will provide valuable data to characterize where oil cooling performance falls relative to graphs such as Figure 11.

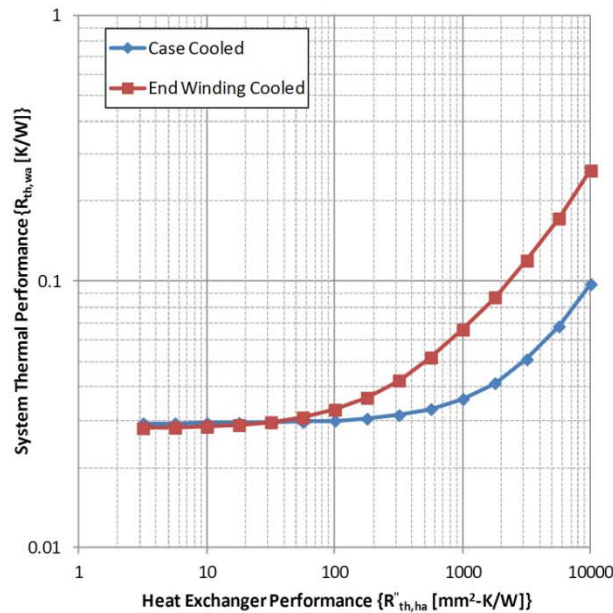


Figure 31: Impact of cooling performance and location on total system thermal resistance from FEA thermal model of permanent magnet motor described by Lindström [11]

Cooling Technology Balance of System

The cooling technology balance of system box in Figure 2 helps connect the work on motor thermal management to constraints placed on the motor cooling system. These constraints include fluid flow rate, coolant inlet temperatures, maximum allowable coolant temperatures, and parasitic power or pressure drop limitations. While not the primary focus of efforts in FY11, researchers did work on two of these areas during FY11. First, they performed a high level survey of available coolant flow rates and temperatures. Second, they worked to coordinate their efforts with other work being undertaken in the VTP to ensure consistent assumptions relative to cooling technology balance of system parameters.

A survey of commercially available automotive traction drive motors is listed in Table 4, and shows ranges of flow rates and temperature limits for water ethylene glycol and automatic transmission fluid. This list is not intended to be comprehensive, but instead indicates limitations related to flow and temperature. Data obtained through benchmarking efforts at ORNL showed oil flow rates between 1.5 and 6.5 L/min for a single oil nozzle on the 2008 Lexus LS 600H [15]. As described in the report, the oil pump serves two oil nozzles. Assuming equivalent flow for each nozzle, this leads to total oil flow rates between 3 and 13 L/min, which is in line with ranges shown in Table 4. Additional sources of flow and temperature constraints can be found in the Electrical and Electronics Technical Team Roadmap [17].

Table 9: Selection of coolant flow and temperature ranges of commercially available traction motors

| Cooling Method | Flow Rates | Coolant Inlet Temperatures |
|------------------------------|----------------------------------|----------------------------|
| Automatic Transmission Fluid | 5-10 (up to 30 for higher power) | 70-90 |
| Water Ethylene Glycol | 8-10 | 55-70 |

The collaboration with other areas within the VTP included the cross-cut project “Integrated Vehicle Thermal Management—Combining Fluid Loops on Electric Drive Vehicles,” which covers APEEM,

Energy Storage System (ESS), and Vehicle Systems Analysis (VSA) areas. Work was performed to support APEEM integration into the vehicle thermal analysis flow model, and ongoing efforts include collaborating to investigate approaches to integrate APEEM cooling with other vehicle thermal management systems. Additional details are available in the report and in a publication presented at the 10th Vehicle Thermal Management Systems Conference in 2011 [18].

Conclusion

The goal of this research project is to improve thermal management of electric machines to impact the achievable continuous power density so that it can meet the needs of more electrically dominant vehicle applications. Work during FY11 focused on establishing a foundation on which to evaluate opportunities for improved thermal management of electric motors. The work focused on the four critical areas of application technical specifications, package mechanical design, cooling technology selection, and cooling technology balance of system. The four factors combine to impact the thermal design targets of the specific application as shown in Figure 2. The key accomplishments included:

- Developing methods to approximate loss distributions within the electric motor for different operating conditions
- Performing thermal property testing of motor lamination materials with industry input
- Developing analytical and 3-D finite element analysis models for determining effective conductivity of motor slot windings
- Building a stator thermal model validated against published data
- Performing parameter sensitivity studies of thermal design factors for motor stator cooling
- Initiating oil cooling hardware test capabilities
- Collaborating with Vehicle Technologies Program (VTP) cross-cut project “Integrated Vehicle Thermal Management—Combining Fluid Loops on Electric Drive Vehicles” involving energy storage, vehicle systems, and APEEM.

Future work will focus on completing testing on the thermal properties of lamination materials and measuring lamination contact resistances. The results will support modeling activities and contribute to public information supporting improved motor cooling. Additional modeling work will complete thermal sensitivity analysis studies to identify areas of thermal improvement common to alternative permanent magnet motor configurations. Finally, during FY12, there will be a transition from modeling and analysis to experimental work in order to complete fundamental heat transfer experiments with oil jets and to initiate oil jet durability experiments for winding insulation.

Acknowledgements

Team Members: Justin Cousineau, Douglas DeVoto, Gilbert Moreno, and Mark Mihalic (NREL)
Thomas M. Jahns and Seth McElhinney (University of Wisconsin—Madison)

References

1. T. A. Lipo, *Introduction to AC machine design*, 3rd ed. Wisconsin Power Electronics Research Center, University of Wisconsin, 2007.
2. A. Boglietti, A. Cavagnino, and A. M. Knight, “Isolating the Impact of PWM Modulation on Motor Iron Losses,” in *IEEE Industry Applications Society Annual Meeting, 2008. IAS '08*, 2008, pp. 1-7.
3. A. Boglietti, A. Cavagnino, D. M. Ionel, M. Popescu, D. A. Staton, and S. Vaschetto, “A General Model to Predict the Iron Losses in PWM Inverter-Fed Induction Motors,” *IEEE Transactions on Industry Applications*, vol. 46, no. 5, pp. 1882-1890, Oct. 2010.

4. D. Staton, A. Boglietti, and A. Cavagnino, "Solving the More Difficult Aspects of Electric Motor Thermal Analysis in Small and Medium Size Industrial Induction Motors," *IEEE Transactions on Energy Conversion*, vol. 20, no. 3, pp. 620- 628, Sep. 2005.
5. H. A. Toliyat and G. B. Kliman, *Handbook of electric motors*, 2nd ed. CRC Press, 2004.
6. J. R. Hendershot and T. J. E. Miller, *Design of brushless permanent-magnet motors*. Magna Physics Pub., 1994.
7. F. Incropera and D. DeWitt, *Fundamentals of Heat and Mass Transfer*, 4th ed. John Wiley & Sons, 1981.
8. E. Jih, K. Chen, T. Abraham, and V. Siddapureddy, "Thermal Management for the HEV Liquid-Cooled Electric Machine," in *Vehicle Thermal Management Systems Conference & Exposition*, Nashville, TN, 2001, vol. 2001-01-1713.
9. H. Kanzaki, K. Sato, and M. Kumagai, "Study of an estimation method for predicting the equivalent thermal conductivity of an electric coil," *Heat Transfer - Japanese Research*, vol. 21, no. 2, pp. 123-138, 1992.
10. "MWS Wire Industries - Magnet Wire Specifications." [Online]. Available: <http://www.mwswire.com/awgsearch1.asp>. [Accessed: 12-Oct-2011].
11. J. Lindström, "Thermal Model of a Permanent-Magnet Motor for a Hybrid Electric Vehicle," Chalmers University of Technology, Goteborg, Sweden, 1999.
12. D. R. Speer, "Thermal conductivity improvements for electric motors," in *Electrical Insulation Conference, 1997, and Electrical Manufacturing & Coil Winding Conference. Proceedings, 1997*, pp. 723-725.
13. G. Kylander, "Thermal Modeling of Small Cage Induction Motors," Chalmers University of Technology, Goteborg, Sweden, 1995.
14. T. Burress et al., "Evaluation of the 2007 Toyota Camry Hybrid Synergy Drive System." Oak Ridge National Laboratory. ORNL/TM-2007/190, Apr-2008.
15. T. Burress et al., "Evaluation of the 2008 Lexus LS 600H Hybrid Synergy Drive System." Oak Ridge National Laboratory. ORNL/TM-2008/185, Jan-2009.
16. T. Burress et al., "Evaluation of the 2010 Toyota Prius Hybrid Synergy Drive System." Oak Ridge National Laboratory. ORNL/TM-2010/253, 01-Mar-2011.
17. "Electrical and Electronics Technical Team Roadmap." [Online]. Available: http://www1.eere.energy.gov/vehiclesandfuels/pdfs/program/eett_roadmap_12-7-10.pdf. [Accessed: 11-Oct-2011].
18. J. Rugh, K. Bennion, A. Brooker, J. Langewisch, K. Smith, and J. Meyer, "PHEV/EV Integrated Vehicle Thermal Management - Development of a KULI Model to Assess Combined Cooling Loops," in *10th Vehicle Thermal Management Systems Conference*, Gaydon Warwickshire, UK, 2011.

5.6 Physics of Failure of Electrical Interconnects

Principal Investigator: Douglas DeVoto

Co-Investigator: Tim Popp

National Renewable Energy Laboratory

Center for Transportation Technologies and Systems

1617 Cole Blvd MS 1633

Golden, CO 80401

Voice: 303-275-4256; Fax: 303-275-4415; E-mail: Douglas.DeVoto@nrel.gov

DOE Technology Development Manager: Susan A. Rogers

Voice: 202-586-8997; Fax: 202-586-1600; E-mail: Susan.Rogers@ee.doe.gov

Objectives

In automotive power electronics modules, standard packaging technologies have limited the advancement of insulated gate bipolar transistor (IGBT)-based power modules toward designs that promise higher performance and reliability. Increased power densities and larger temperature swings reduce lifetimes for traditional bond wire interconnects. Replacement of wire bonds can be accomplished with a transition to ribbon bonding technology. The ribbon bond process promises a reduction in bonding time, lower loop heights and corresponding less heel fatigue, and higher current densities than wire bonds. However as a newer technology, ribbon bond failure mechanisms are not as well understood and thus do not have an accurate lifetime estimate. The objective of this research is to investigate and improve the reliability of alternative interconnect technologies to wire bonds, beginning with ribbon bonding. The objectives for FY11 were to:

- Establish capabilities for synthesis and characterization of bond strength of ribbon interconnects for power electronics packages.
- Establish industry collaborations.
- Establish a testing procedure for evaluating the reliability of ribbon interconnects under a variety of accelerated thermal, power, and humidity conditions.
- Review wire bond physics of failure (PoF) models and determine their validity for ribbon bond geometry.

Approach

- Establish sample packages that incorporate ribbon interconnect technology under a variety of material and geometry selections.
 - Perform mechanical tests on the ribbon bond interconnects to obtain information on initial bond strength and strength after accelerated testing conditions.
 - Perform thermal elevation, thermal cycling, combination power and thermal cycling, and high humidity testing to accelerate failure mechanisms within ribbon interconnects. Monitor electrical resistance of interconnects after a select number of cycles and perform destructive mechanical tests and cross-sectioning after the completion of accelerated testing.
 - Update wire bond PoF models to provide ribbon interconnect lifetime estimation.
16. Assess the performance and reliability advantages of transitioning from wire to ribbon bond technology.

Major Accomplishments

- Established capabilities at NREL for accelerated testing and mechanical evaluation of ribbon bond interconnects.
- Finalized ribbon layout geometry and obtained direct bond copper (DBC) substrates.
- Selected industry partners for the supply of ribbon material and the bonding process.
- Generated finite element analysis (FEA) models to predict heel stresses within wire and ribbon bonds.

Future Direction

- The following activities are envisioned for this project for FY2012 and FY2013:
- Complete accelerated testing of ribbon interconnects technology.
- In conjunction with physics of failure models, obtain estimates for cycles to failure.
- Expand accelerated testing and reliability models to include additional interconnect technologies, such as planar interconnects and flexfoil.

Technical Discussion

Introduction

The expansion of hybrid electric vehicles in the automotive market has led to increased performance demands on power electronics modules. The trend toward higher power densities, current levels, and operating temperatures has resulted in a situation where traditional packaging designs cannot meet the industry's reliability needs. Figure 1 shows an example of a power electronics package with wire bonds, die (IGBT or diode) substrate, baseplate, and heat sink components.

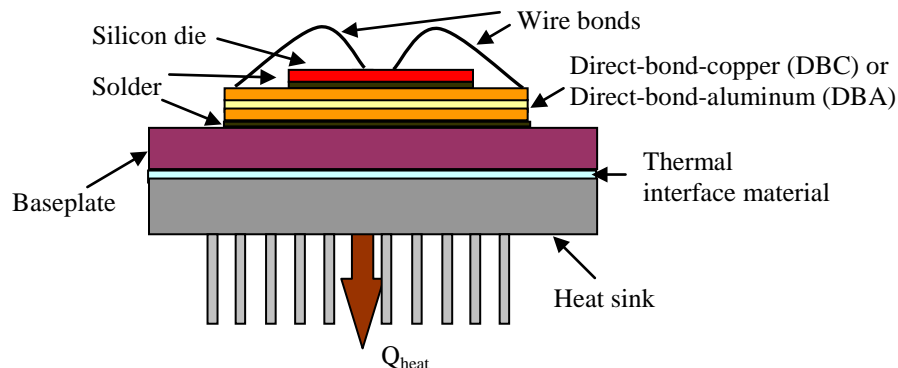


Figure 1. Traditional power electronics package

Wire bonding technology is used to electrically connect dies to each other, to the top copper layer of the DBC, or to lead frames. Gold, copper, and aluminum have traditionally been used as the material for the wire, with each having tradeoffs in cost, current carrying capability, and mechanical strength [1]. For most common applications, aluminum has replaced gold and copper for its lower cost, but copper may still be selected in power module designs with high current requirements. In addition to material selection, the maximum current a wire can carry is dependent on its length and diameter. Wire sizes typically range between 250-500 μm in diameter. Operating current levels are kept lower than that needed for fusing of the wire caused by ohmic self-heating [2]. Heating from within the wire as well as from the silicon dice creates large temperature fluctuations during operation. These temperature variations combine with CTE mismatches between the wire material and the silicon dice to cause failure in the heel of the wire through flexure fatigue as well as bond wire liftoff. Analytical models have been developed for both failure mechanisms to estimate the mean number of cycles to failure.

For high-current power modules, limiting the diameter of a bond wire to 500 μm has required multiple wires to be bonded in parallel. Adding additional parallel wires is limited by a substrate's bond pad area and increases the time and cost of bonding. These limitations have generated interest in replacing wire bonds with ribbon bonding technology. Three aluminum wire bonds with diameters of 400 μm can be replaced by one ribbon bond with a cross section of 2,000 μm x 200 μm [3]. The single ribbon requires a bond width of 2 mm while the three wire bonds require a width of 2.5 mm. Bonding times for both technologies remain the same (300 ms per bond); therefore, the ribbon bonding time for a package can be reduced. For the same span distance, a ribbon bond requires a lower loop height than a wire bond. This helps to reduce heel stress and ultimately flexure fatigue. Minimizing heel stress is necessary as desired IGBT operating junction temperatures continue to rise to 175°C or higher [4]. However, due to the ribbon's larger geometry, higher bonding energies and forces are required and bond pad contact areas become larger. Damage initiated during the bonding process could become more likely under ribbon bonding, and coefficient of thermal expansion mismatches between the interconnect material and silicon devices could cause failure under thermal cycling conditions.

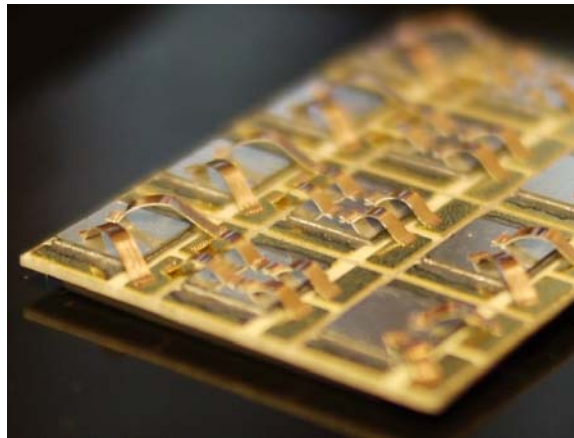


Figure 2. Ribbon bonds

Due to the variety of failure mechanisms in a power electronics module, NREL is expanding its reliability research that began with bonded interface materials to focus additionally on interconnect technologies. While the performance and reliability of conventional wire bonding is well understood, lifetime uncertainties of newer interconnect technologies remain a barrier for those novel processes to be utilized by industry. NREL is now focused on providing a comprehensive reliability assessment of alternative interconnect technologies to wire bonds, beginning with ribbon bonding. Ribbon bonds will be attached to a substrate under a variety of materials and geometries, and then subjected to accelerated test conditions that will highlight the same failure mechanisms found under normal operating conditions. Unique ideas to ribbon bonding will be evaluated, first with the selection of an aluminum-clad copper ribbon that allows the aluminum to be easily bonded to silicon die surfaces while providing the improved electrical performance of copper [5]. The ribbon's rectangular cross-section geometry makes twisting to create forced angles more difficult than with wire bonding; therefore, bonds with several forced angles will be attached to substrate samples [6]. The proposal to attach multiple ribbons over the same bond pad location will be explored as a stacked bonding technique [7]. In conjunction with accelerated testing, physics of failure models based on wire bond geometry will be validated for ribbon bonds.

Materials and Sample Synthesis

NREL has chosen several ribbon materials under various geometries for accelerated testing. The variations are as follows:

- Material – Aluminum (Al) and aluminum-clad copper (Al/Cu) ribbon
- Ribbon cross section – Two cross sections suitable for current levels within a power module were chosen to be 2,000 μm x 200 μm and 1,000 μm x 100 μm
- Ribbon span – 10 mm and 20 mm spans selected with corresponding loop heights
- Number of stitches – Single and double
- Ribbon stacking – Stacking one ribbon pad on top of another to minimize bonding area on top of a die
- Ribbon bond angle – Forcing a ribbon at various angles to allow for offset pad locations
- Bond pad interfaces – One end of each ribbon will be bonded to a silicon die and the other end to a DBC's top Cu surface

The ribbon material and geometry variations cover a design space likely used within a power electronics unit if wire bonds were to be replaced with ribbon bonds. The ribbon bond variations are listed in Table 1 below.

Table 10. Ribbon Bond Variations

| Criteria | Variation | | |
|--|-------------|----|-------------|
| Material | Al | | Al/Cu |
| Ribbon Cross Section (μm) | 2,000 x 200 | | 1,000 x 100 |
| Ribbon Span (mm) | 10 | | 20 |
| Number of Stitches | Single | | Double |
| Ribbon Stacking | Not Stacked | | Stacked |
| Ribbon Bond Angle ($^{\circ}$) | 0 | 20 | 40 |

Multiple instances of each ribbon configuration were arranged on a 14 mm x 19 mm DBC. The DBC itself was sourced from Curamik and is constructed of a 0.635-mm-thick alumina layer sandwiched between two 0.203-mm-thick copper layers. The design of the etch mask for the top copper layer electrically configures four ribbon bonds in series with multiple parallel paths. This layout was chosen for power cycling samples, but remains the same for all samples. Before the ribbon material is attached to the DBC substrate, Vishay 5 mm x 5 mm Schottky diodes are soldered in place. The selected diodes have a breakdown voltage of 100 V and can reach a maximum junction temperature of 175°C. The diode backside adds a chromium/nickel/silver coating for good solderability while the topside includes a 3 μm layer of aluminum (1% silicon) to be compatible with the ultrasonic bonding process. One end of each ribbon interconnect will be bonded to the top copper layer of the DBC, while the second will be bonded to the top surface of a diode. Both Al and Al/Cu ribbon materials have been sourced from Materion and will be attached using an Orthodyne 3600 wedge bonder. The design layout of the samples is shown in Figure 3 below.

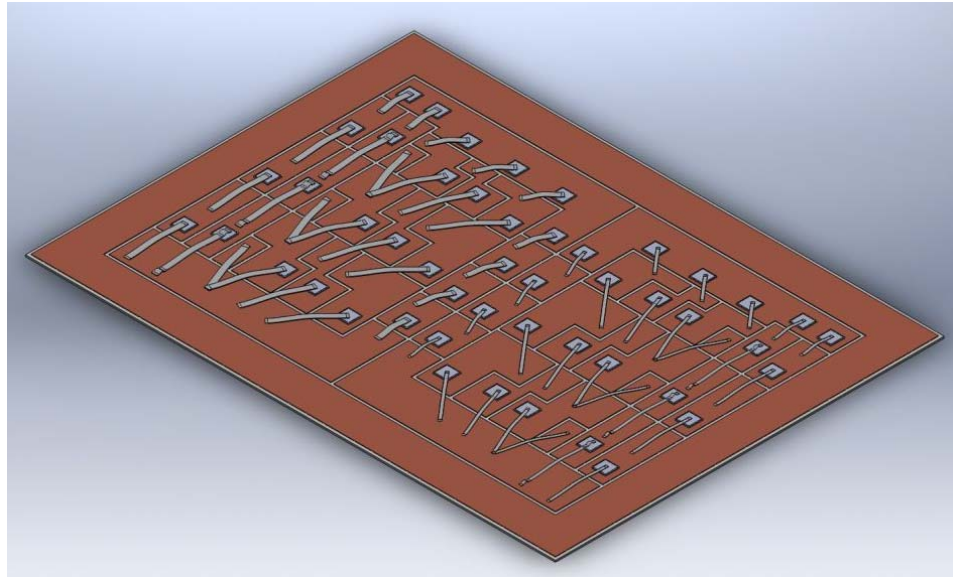


Figure 3. Test sample showing ribbon layout

Ribbon Bonding Mechanical Characterization

Several techniques will be used to evaluate the quality of the ribbon interconnects. An XYZTEC Condor 100-3 mechanical bond tester, shown in Figure 4, will be used to measure the strength of the ribbon bonds. As this is a destructive evaluation, one test sample without any prior accelerated testing will be selected to measure initial ribbon bond strength.



Figure 4. XYZTEC mechanical bond tester

Two mechanical evaluation tests will be completed on a ribbon-bonded test sample. A hook with a diameter smaller than a ribbon bond's loop height will be positioned under the bond as shown in Figure 5. An adequate force in the vertical direction will be applied to break the ribbon bond. The bond strength will be considered sufficient if the ribbon material itself plastically deforms and breaks. A poor bond will result in the ribbon lifting off from one of its bond pads. The failure method and maximum force required to cause failure will be recorded for each ribbon bond. In addition to pull testing, shear testing of the ribbon pad will provide a second measurement method of bond pad strength. A shear tool will align

against a ribbon bond and apply enough force to break it away from its bond pad. Shear tests will be used if pull tests do not result in ribbon bond pad liftoff.

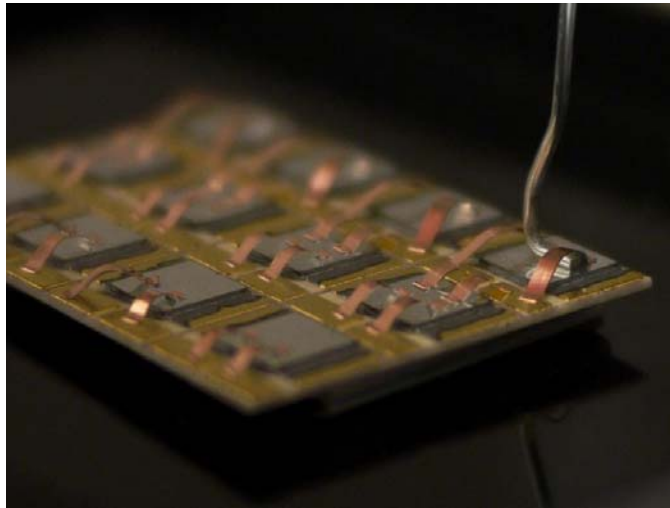


Figure 5. Ribbon pull test

Mechanical tests will be conducted on samples after they have completed their designated accelerated testing procedure. In addition to mechanical evaluation, cross sections of ribbon bond pads will provide a qualitative way to determine if the grain structure has changed after accelerated testing. Bonding of dissimilar metals between the ribbon and pad causes intermetallic formation and Kirkendall voiding under high-temperature storage tests. An example of intermetallic formation is shown in Figure 6 between Au wire and an Al bond pad. Visual analysis will also monitor signs of corrosion development.



Figure 6. Intermetallic formation between Au wire and Al bond pad

Accelerated Testing

Subjecting a component to accelerated testing conditions will identify its failure mechanisms in a reduced amount of time relative to normal operating stress conditions. Various accelerated tests have been selected to evaluate several likely failure mechanisms within ribbon interconnects and are shown in Table 2. Test procedures are based on standards developed by the JEDEC Solid State Technology Association [8].

Table 11. Accelerated Testing Procedures

| JEDEC | Title | Temp (°C) | RH (%) | Vapor Pressure (kPa) | Duration (hours/cycles) | Bias | Dwell Time (min) | Ramp Rate (°C/min) |
|--------------|--|------------------|---------------|-----------------------------|--------------------------------|--------------------------|-------------------------|---------------------------|
| 22-A101-C | Steady State Temperature Humidity Bias Life Test | 85 (dry bulb) | 85 | 49.1 | 1,000 | DC, continuous or cycled | - | - |
| 22-A102-D | Accelerated Moisture Resistance - Unbiased Autoclave | 121 (dry bulb) | 100 | 205 | 96 | - | - | - |
| 22-A103-D | High Temperature Storage Life | 150/200 | - | - | 1,000/96 | - | - | - |
| 22-A104-D | Temperature Cycling | -40 to 150 | - | - | 2,000 | - | 10 | 10 |
| 22-A105-C | Power and Temperature Cycling | -40 to 125 | - | - | 1,500 | cycled every 5 minutes | 10 | 5 |

Accelerated test methods—humidity, thermal, power, or a mixture of the three—are designed to highlight a particular interconnect’s failure mechanism.

- Two humidity-based tests will evaluate the corrosion resistance of the ribbons and their bond pads. Under a humidity bias test, ribbon interconnects will be placed in an 85°C, 85% relative humidity environment for 1,000 hours. A DC bias will be applied during the test. Under a second humidity test, samples will be subjected to a 121°C, 100% relative humidity environment for 96 hours with no electrical bias.
- Samples subjected to high-temperature storage testing will highlight thermally activated failure mechanisms. Ribbon bonds will be stored under two separate tests, at 150°C for 1,000 hours and 200°C for 96 hours.
- Alternating temperature extremes will test the ability of interconnects to withstand thermally induced mechanical stresses. Samples will be cycled from -40°C to 150°C for 2,000 cycles, with ramp rates of 10°C/minute and dwell/soak times of 10 minutes. A thermal shock chamber, shown in Figure 7, will be used for temperature cycling tests.
- Under combined power and thermal cycling, interconnects will be subjected to a periodically applied operating bias while they experience high and low temperature extremes. Samples will be cycled from -40°C to 125°C for 1,500 cycles, with ramp rates of 5°C/minute and dwell/soak times of 10 minutes.



Figure 7. Thermal shock chamber

Physics of Failure Models

Accurate lifetime predictions for wire bonds have been made possible by the development of PoF-based models. PoF models identify the root cause of a failure and then provide a lifetime estimation based on material properties, geometry, and environmental conditions. Wires subjected to thermal cycling undergo flexure due to thermal expansion mismatches among the wire, die, and substrate. Models have been developed to predict the maximum bending stress in the heel of the wire bond due to temperature cycling [9-10]. The stress within the wire bond can be approximated using the theory of curved beams, shown as

$$\sigma = 6E_w \frac{r}{D_s} \left(\frac{L}{D_s} - 1 \right)^{\frac{1}{2}} \left(2\alpha_s + \frac{\alpha_s - \alpha_w}{(1 - D_s/L)} \right) \Delta T \quad (1)$$

where

- α_s is the thermal expansion coefficient of the substrate material,
- α_w is the thermal expansion coefficient of the wire material,
- E_w is the Young's modulus of the wire material,
- L is the length of the wire,
- D_s is the span length of the wire bond,
- r is the radius of the wire, and
- ΔT is the amplitude of the temperature cycles.

The number of cycles to failure from flexure fatigue can be estimated by the Coffin-Manson equation

$$N_f = C_w \sigma^{-m_w} \quad (2)$$

where σ has been previously found, and C_w and m_w are fatigue properties found through material tensile tests. This model can evaluate the effect of loop height on the reliability of the wire bond, where loop height is altered by a change in the L/D_s ratio [9]. The number of cycles to failure is predicted in Figure 8, where the wire-bond lifetime changes based on the L/D_s ratio and temperature range ΔT .

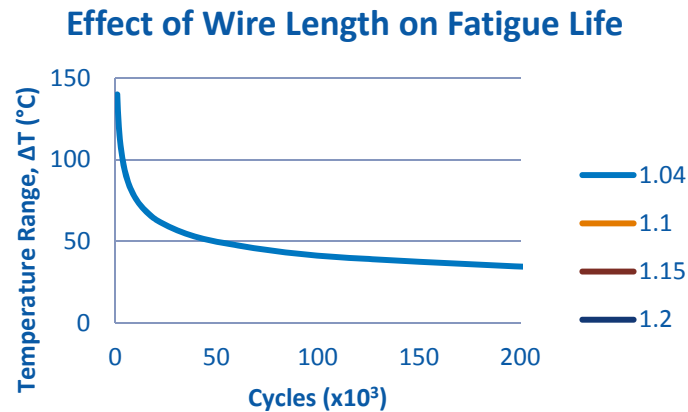


Figure 8. Analytical prediction of wire bond life based on flexure fatigue

By updating this wire flexure model to accommodate a ribbon bond's cross-sectional shape, similar stress values can be generated. Additional tensile fatigue tests will need to be completed on ribbon material for an accurate number of cycles to failure estimation with the Coffin-Manson equation. The stresses determined through PoF models will be compared with finite element analysis (FEA) of wire and ribbon bonds. In Figure 9, the geometries of an Al wire bond, an Al ribbon bond, and an Al/Cu ribbon bond have been evaluated in the ANSYS finite element software package. Under the same loading conditions, the ribbon bond exhibits less deflection than the wire bond, and stress concentrations present in the heel of the wire bond are lower in the ribbon geometries. Accelerated testing results will validate both analytical and FEA model predictions.

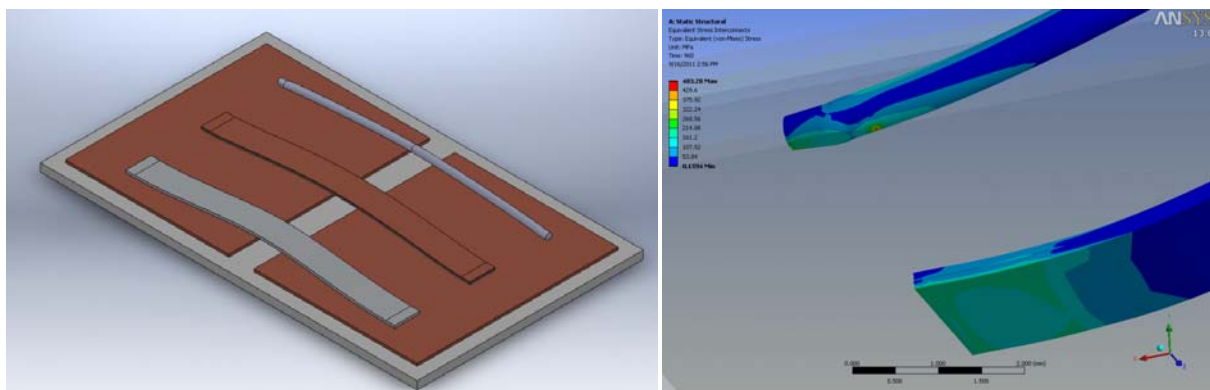


Figure 9. FEA of 500μm Al wire bond, 2,000 μm x 200 μm Al ribbon, and 2,000 μm x 200 μm Al/Cu ribbon

Summary of Procedure

The preceding sections have described the experimental and modeling procedure that will be followed to obtain reliability predictions for ribbon interconnects. This is summarized in Figure 10 below.

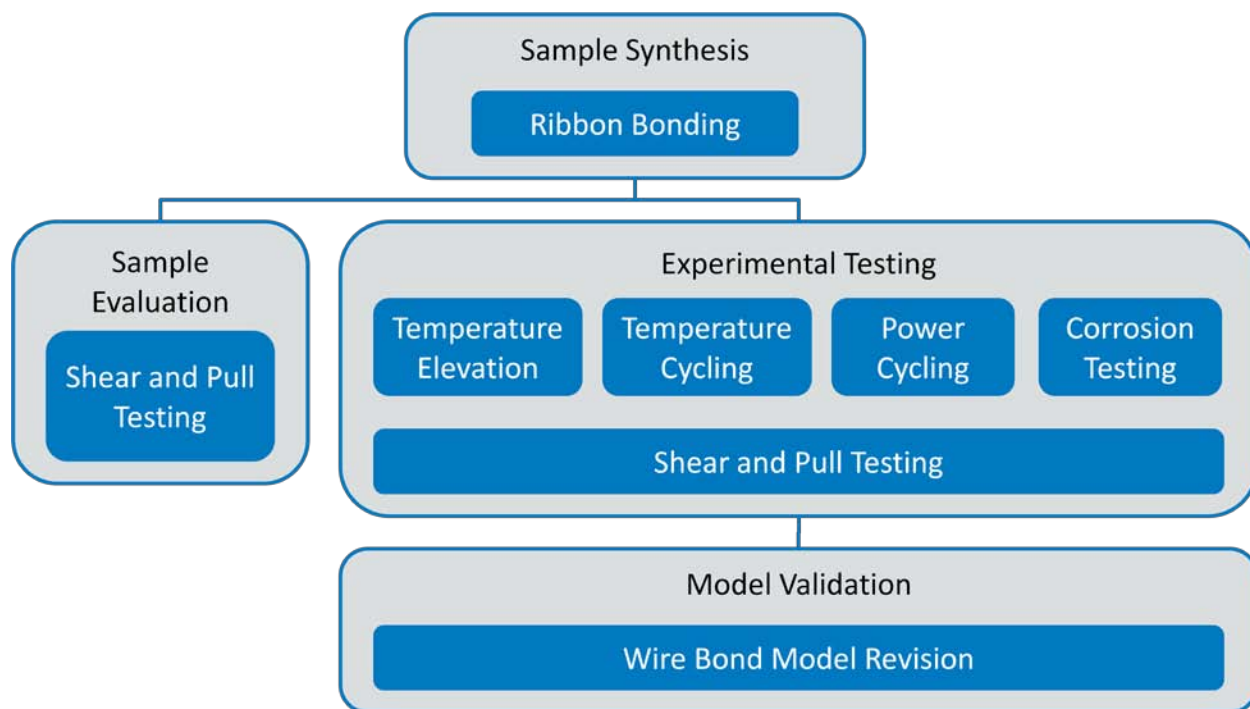


Figure 10. Flowchart of ribbon interconnects reliability testing procedure

Conclusion

The work accomplished in FY2011 establishes the foundation for a comprehensive evaluation of the reliability of ribbon bond interconnects. A variety of materials and geometries will be tested under various accelerated testing conditions to highlight failure mechanisms. Industry partners have been selected to aid in the bonding process, and evaluation criteria have been set to monitor the quality of ribbon bonding before and during testing. Combining experimental results with previous wire bond lifetime-to-failure models will enable reliability predictions for ribbon bonds.

References

1. L. Ménager, C. Martin, B. Allard, and V. Bley. "Industrial and lab-scale power module technologies: A review." *IEEE 32nd Annual Conference on Industrial Electronics, IECON 2006*; Paris, 2006; pp. 2426-2431.
2. M. Ciappa. "Selected failure mechanisms of modern power modules." *Microelectronics Reliability*; Vol. 42, 2002; pp. 653-667.
3. F. Farassat and J. Sedlmair. "More Performance at Lower Cost – Heavy Aluminum Ribbon Bonding." *F & K Delvotec Bondtechnik GmbH*, 2007.
4. K. Guth, D. Siepe, J. Görlich, H. Torwesten, R. Roth, F. Hille, and F. Umbach. "New assembly and interconnects beyond sintering methods." *Proceedings PCIM 2010*; Nuremberg, Germany, 2010.
5. C. Luechinger, T. Loh, K. Oftebro, and G. Wong. "Composite Aluminum-Copper Ribbon Bonding – Heel Reliability." *Proceedings of IMAPS 2007*; San Jose, CA, 2007.
6. C. Luechinger. "Ribbon bonding – A Scalable Interconnect for Power QFN Packages." *IEEE 9th Electronics Packaging Technology Conference*; Singapore, 2007; pp. 47-54.

7. E. Almagro and H. Granada Jr. "Stack Bonding Technique Using Heavy Aluminum Ribbon Wires." *IEEE 10th Electronics Packaging Technology Conference*; Singapore, 2008; pp. 976-981.
8. "Standards & Documents Search," JEDEC, <<http://www.jedec.org/standards-documents>>.
9. J. Hu, M. Pecht, and A. Dasgupta. "A Probabilistic Approach for Predicting Thermal Fatigue Life of Wire Bonding in Microelectronics." *ASME Journal of Electronic Packaging*; Vol. 113, 1991; pp. 275-285.
10. K. Meyyappan. *Failure Prediction of Wire Bonds Due to Flexure*. Ph.D. Thesis. College Park, MD: University of Maryland, 2004.

5.7 Two-Phase Cooling Technology for Power Electronics with Novel Coolants

Principal Investigator: Gilbert Moreno

National Renewable Energy Laboratory

Center for Transportation Technologies and Systems

1617 Cole Blvd MS 1633

Golden, CO 80401

Voice: 303-275-4450; Fax: 303-275-4415; E-mail: Gilbert.Moreno@nrel.gov

DOE Technology Development Manager: Susan A. Rogers

Voice: 202-586-8997; Fax: 202-586-1600; E-mail: Susan.Rogers@ee.doe.gov

Objectives

The overall project objective is to demonstrate improved thermal performance and reduced system cost through the implementation of two-phase heat transfer technology. Two-phase heat transfer offers high heat transfer rates and provides near isothermal characteristics. This technology may enable high insulated-gate bipolar transistor (IGBT) power densities, which could result in a decrease in the IGBT device count or size (i.e., reduced cost, weight, and volume). The intent is to contribute toward achieving the Advanced Power Electronics and Electric Motors Program cost, power density, and specific volume targets.

Approach

This project conducts both fundamental and system-level studies to evaluate two-phase (boiling/evaporation) heat transfer as a potential power electronics cooling scheme. The fundamental study is focused on characterizing the pool boiling performance of novel coolants/refrigerants as well as investigating promising boiling enhancement techniques. Additional efforts are geared toward conducting a mechanistic study to understand boiling heat transfer on enhanced surfaces. Fundamental research results then feed into the design of the system-level components.

The system-level study is focused on developing a prototype two-phase cooling system capable of dissipating several kilowatts of heat. The intent is to demonstrate superior thermal performance and reduced cost with the two-phase cooling system developed. Air-cooled, passive (pump-less) two-phase systems will be considered due to their inherent efficiency and potentially lower cost.

Major Accomplishments

- The pool boiling performance of a new refrigerant, HFO-1234yf, was characterized and compared to the performance of HFC-134a (R134a). Experiments were carried out at various saturation temperatures (25°C–60°C), with and without boiling enhancement techniques, up to the critical heat flux condition. Results from this study will be published in the 2011 ASME IMECE Conference Proceeding [1] making the National Renewable Energy Laboratory (NREL) the first institution to publish this information. This work was a collaborative effort between NREL, 3M, and DuPont.
- NREL in collaboration with 3M, Delphi, and Oak Ridge National Laboratory (ORNL) demonstrated a 60% reduction in thermal resistance of an automotive power electronics module using immersion boiling (two-phase) in conjunction with surface enhancement techniques [2-4]. The thermal performance enhancement was in comparison to the existing automotive cooling system.
- A new experimental system was designed and will be used to test the long-term reliability of boiling enhancement coatings. The system will stress multiple coated samples by subjecting them to

power/temperature cycling (on/off operation) to simulate extreme two-phase cooling operation for extended durations. The system can operate at pressures as high as 20 atmospheres (300 psi) and can be used with various refrigerants/coolants. The system is currently being fabricated.

- Design of various two-phase cold-plates and a water-cooled condenser was completed. These components will be assembled together to form a thermosyphon system intended as a new two-phase based, indirect cooling scheme. This indirect-cooling approach is intended to increase system reliability.

Future Direction

- The water-cooled thermosyphon systems designed in FY11 will be fabricated and evaluated for thermal performance. Fluid-vapor flow patterns and fluid quantity requirements within these systems will be characterized. Knowledge gained from these systems will be used in the design of air-cooled thermosyphons. (FY12)
- The boiling enhancement coating reliability test system designed in FY11 will be fabricated. Experiments will then be carried out to investigate the long-term reliability of boiling enhancement coatings. (FY12)
- Experiments will be conducted to characterize the forced convective (i.e., flow boiling and spray cooling) boiling performance of HFO-1234yf. (FY12)
- Air-cooled, two-phase thermosyphons capable of dissipating several kilowatts of heat will be designed and fabricated. The thermal performance of these systems will be characterized at various operating conditions (e.g., elevated temperatures) and under transient heat loads. (FY12-FY13)
- Experiments will be conducted to investigate the reliability of the two-phase thermosyphons. These experiments will subject the two-phase cold-plates to temperature cycling. The effect of this on system seals (i.e., refrigerant/coolant leakage) and performance will be evaluated. (FY13)
- The effect of contaminants on boiling heat transfer performance will be evaluated. (FY13)
- A mechanistic study will be conducted to investigate boiling on microporous coatings. (on-going)

Technical Discussion

Although two-phase heat transfer is not used as a means of cooling power electronics in the automotive industry, its use has been applied to power electronics cooling in other industries. For example, large mining haul trucks and high-speed trains (France's Train à Grande Vitesse) currently utilize passive, immersion (pool) boiling schemes to cool the power electronics (gate turn-off thyristors) [5-8]. The advantages of passive two-phase systems include greater efficiency (pump-less) and superior cooling performance. With regard to cooling performance, Barnes and Tuma [5] have reported thermal resistance (junction-to-liquid) values as low as 0.07 K/W using a passive two-phase cooling scheme on an IGBT package. A study by Ayers et al. [9] demonstrated that the improved heat transfer capacity of two-phase heat transfer can reduce the volume of a power electronics system by more than 50%.

A potential strategy for implementing a two-phase cooling solution for automotive power electronics involves using the same refrigerant to cool both the cabin and power electronics. This approach minimizes the number of automotive coolants and may also allow for integration of cooling systems to further reduce costs. HFC-134a is the current automotive air-conditioning refrigerant; however, due to its high global warming potential (GWP), it will be phased out and replaced with a more environmentally benign refrigerant. The likely successor to HFC-134a is a new refrigerant called HFO-1234yf (hydrofluoroolefin 2,3,3,3-tetrafluoropropene).

HFO-1234yf's nearly identical thermophysical properties to HFC-134a [10] and low GWP (GWP = 4) [11] make it the leading candidate as the next-generation refrigerant in automotive air-conditioning/cabin cooling systems. Because HFO-1234yf is a new refrigerant, little is known about its boiling heat transfer characteristics and no critical heat flux (CHF) data exists. To date, there are only a few published studies

that document the two-phase heat transfer performance of HFO-1234yf. Park and Jung [12] conducted pool boiling experiments using smooth and finned heater surfaces to characterize the boiling heat transfer coefficients of HFO-1234yf. Their experiments were conducted at a saturation temperature of 7°C ($P_{\text{sat}} = 0.39 \text{ MPa}$) and did not reach the CHF. They reported that the nucleate boiling heat transfer coefficients of HFO-1234yf are similar to those of HFC-134a and can be predicted, with reasonable accuracy, using existing correlations. HFO-1234yf condensation heat transfer coefficients have also been reported by Del Col et al. [13] and Park et al. [14]. Both studies reported lower condensation heat transfer coefficients for HFO-1234yf as compared with HFC-134a. Del Col et al. [13] attributed the lower condensation heat transfer coefficients of HFO-1234yf to its lower thermal conductivity (18% lower than HFC-134a at 40°C saturation temperature). These findings differ from Park et al. [15], who reported minimal differences in the condensation heat transfer coefficients of HFO-1234yf and HFC-134a.

HFO-1234yf Pool Boiling Performance

This study characterized the pool boiling performance of a new refrigerant, HFO-1234yf, with implications for two-phase cooling of automotive power electronics. Experiments were conducted with pure (oil-free) HFO-1234yf and its performance was compared to the performance of HFC-134a (R134a). The study evaluated the effects of saturation temperature and a boiling enhancement coating on nucleate boiling heat transfer coefficients and CHF.

Experimental Apparatus

A schematic of the experimental apparatus used for these tests is shown in Fig. 1. The high pressure system has a maximum operating pressure of 2 MPa and was fabricated from materials compatible with a variety of refrigerants. The system was designed for both pool and forced convection boiling experiments. System components include a test section, flat-plate heat exchangers, gear pump, mass flow meter, vacuum pump (not shown), and a pneumatic compressor (not shown). Pool boiling experiments were conducted within the test section using horizontally-oriented heat sources. A schematic of the heated test article is provided in Fig. 1. The test article consisted of a 10×10×3 mm oxygen-free copper block, a 50-ohm film resistor, and a polytetrafluoroethylene (PTFE) substrate. Test article temperature measurements were performed using a calibrated K-type thermocouple that was embedded 1.5 mm below the heated surface in the copper block. Test article wall temperatures (T_{wall}) were then calculated assuming one-dimensional, steady-state heat transfer through the copper block. Pool boiling experiments were controlled and monitored using a program created in LabVIEW. The program controlled a data acquisition system and power supply to generate heat-flux-controlled boiling curves. A more detailed apparatus description and uncertainty analysis can be found in [1].

Experiments were conducted to evaluate the effect of a microporous copper coating on boiling heat transfer. The microporous coating is a 3M product designed to enhance boiling heat transfer [16]. The coating consisted of micrometer-sized copper particles fused onto a surface at elevated temperatures to form an approximately 150- μm -thick porous structure. Scanning electron microscope images of the microporous coating revealed a structure that does not resemble spherical shapes but instead takes the form of irregular, elongated structures (Fig. 2). Coated sample mass and volume measurements indicated the porosity of the coating to be approximately 40%–50%. The baseline/reference surface, to which the microporous coating performance was compared to, consisted of a sand-paper (600 grit) polished copper surface with an average surface roughness of $R_a = 0.3 \text{ }\mu\text{m}$, as measured by a stylus profilometer.

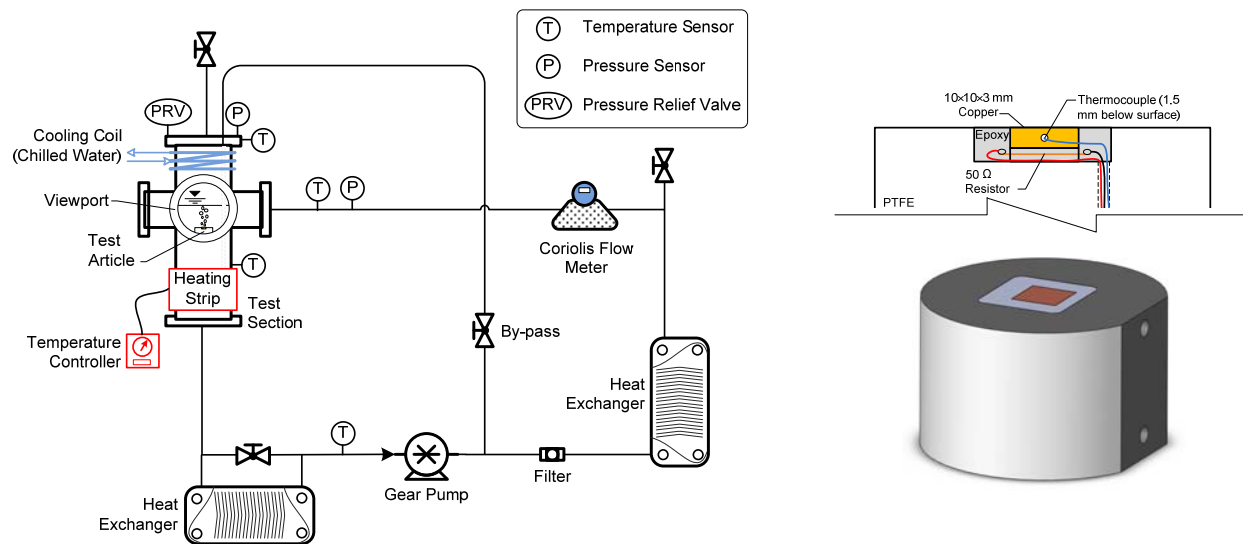


Figure 32. High-pressure apparatus/flow loop (left) and test article (right) schematics

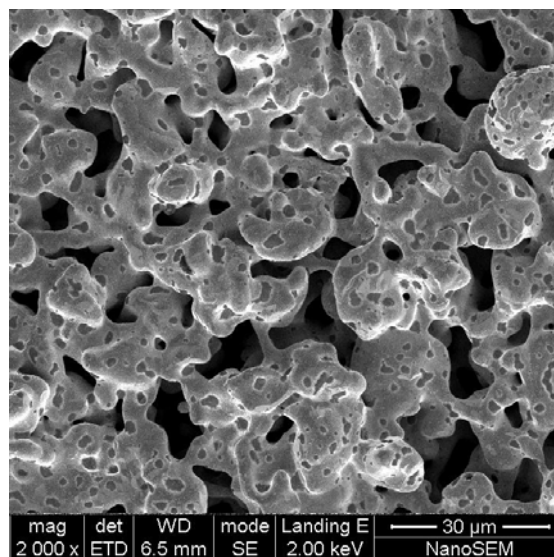


Figure 33. Scanning electron microscope image of the microporous coating

Results and Discussion

HFO-1234yf pool boiling curves obtained with a baseline/smooth surface are provided in Fig. 3a. Four boiling curves pertaining to saturation temperatures of 25°C ($P_{\text{sat}} = 0.8$ MPa), 40°C ($P_{\text{sat}} = 1.0$ MPa), 50°C ($P_{\text{sat}} = 1.3$ MPa), and 60°C ($P_{\text{sat}} = 1.6$ MPa) are provided. Results demonstrated increasing boiling heat transfer coefficients with increasing saturation temperature. Heat transfer coefficients increased from about 30,000 W/m²-K at $T_{\text{sat}} = 25^\circ\text{C}$ to about 45,000 W/m²-K at $T_{\text{sat}} = 60^\circ\text{C}$.

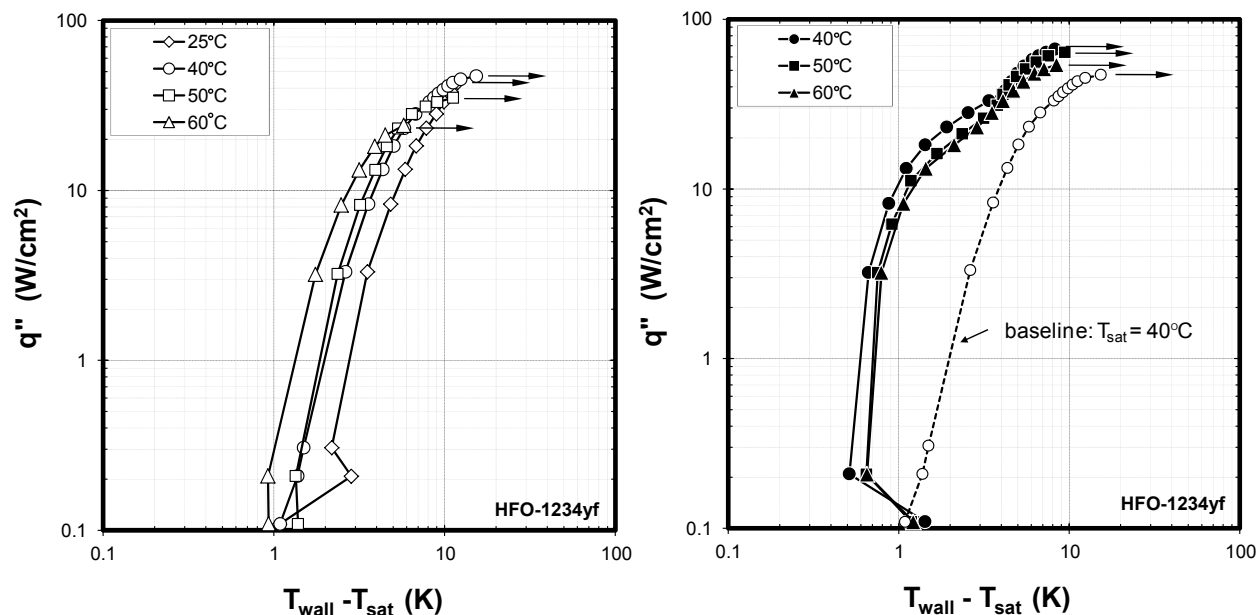


Figure 34. HFO-1234yf pool boiling curves for a baseline/smooth surface (a) and a microporous coated surface (b) at various saturation temperatures. Arrows denote the onset of CHF.

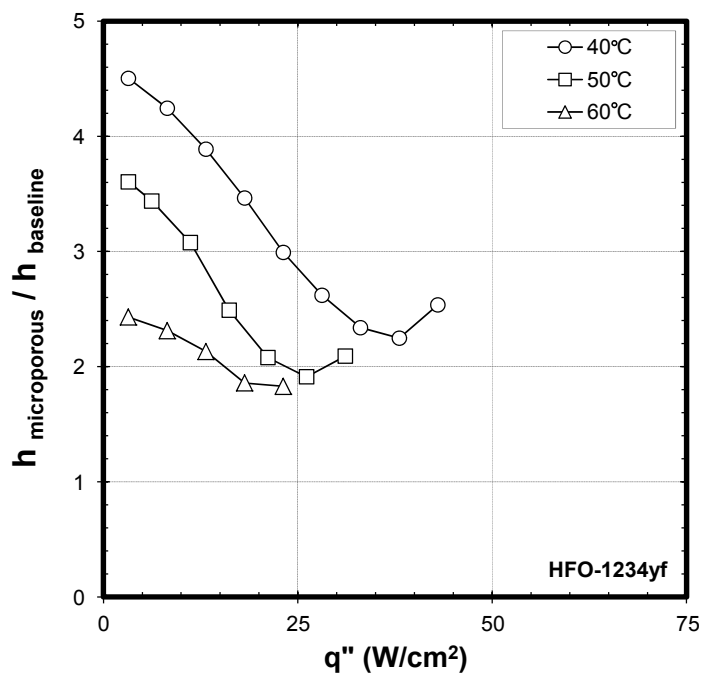


Figure 35. HFO-1234yf boiling heat transfer coefficient enhancement from the microporous coating versus heat flux

HFO-1234yf boiling curves for microporous coated surfaces are shown in Fig. 3b. Experiments were conducted at saturation temperatures of 40°C, 50°C, and 60°C. For reference, a baseline surface boiling curve is also provided in this figure. As shown in the figure, the microporous coating significantly enhanced heat transfer coefficients and critical heat fluxes. Heat transfer coefficients and CHF values for

the microporous coated surfaces achieved values as high as $120,000 \text{ W/m}^2\text{-K}$ and 66 W/cm^2 , respectively. The coating's enhancements are believed to be mostly a result of an increase in the liquid/vapor/solid contact line length within the numerous tunnels of the coating's porous structure, which increases evaporation. Additional enhancement mechanisms include increased nucleation site density and wetted area as well as capillary wicking, which provides a passive means of fluid transport through the coating. The effect of increasing saturation temperature on microporous coating heat transfer enhancement is plotted in Fig. 4. This figure plots the ratio of heat transfer coefficients, microporous over baseline, versus the heat flux dissipated. As shown in the figure, the microporous coating enhancements are found to decrease with increasing pressure. At a heat flux of 20 W/cm^2 , the microporous surface enhancement decreased from more than 200% at $T_{\text{sat}} = 40^\circ\text{C}$ to about 80% at $T_{\text{sat}} = 60^\circ\text{C}$.

Because HFO-1234yf may replace HFC-134a in automotive air-conditioning systems, there is value in comparing the performance of the new refrigerant to its predecessor. For this reason, pool boiling experiments were also conducted with HFC-134a with and without the use of a microporous coating. Boiling heat transfer coefficients versus the heat flux dissipated at 40°C and 60°C saturation temperatures are plotted in Fig. 5 for both HFO-1234yf and HFC-134a. Heat transfer coefficients for baseline/smooth surfaces and microporous coated surfaces are plotted in Fig 5a and Fig 5b, respectively.

As shown in Fig. 5a, baseline surface heat transfer coefficients for the two refrigerants are nearly identical at the lower heat fluxes. At higher heat fluxes, HFO-1234yf heat transfer coefficients are lower than those of HFC-134a. The divergence of HFO-1234yf heat transfer at $T_{\text{sat}} = 60^\circ\text{C}$, for the last data points, is likely a result of localized dry-out near CHF. However, the divergence between HFC-134a and HFO-1234yf heat transfer coefficients at lower saturation temperatures ($<T_{\text{sat}} = 60^\circ\text{C}$) occurs well below CHF and thus is likely not associated with localized dry-out. HFO-1234yf's lower heat transfer at higher heat fluxes is due, in part, to its lower latent heat (about 20% lower) and lower thermal conductivity [13], as compared with HFC-134a. The reason why the heat transfer discrepancy only occurs at higher heat fluxes is not fully clear.

Figure 5b provides the heat transfer coefficients for the microporous coated surface at 40°C and 60°C saturation temperatures. The magnitude of the heat transfer coefficient enhancement from the coating is evident when comparing Fig. 5a and Fig. 5b. As was the case with the baseline surface, microporous coated surface heat transfer coefficients for the two refrigerants were essentially identical at lower heat fluxes. Differences in the microporous coating performance began to appear at higher heat fluxes, and were more apparent at lower saturation temperatures ($T_{\text{sat}} = 40^\circ\text{C}$), where HFO-1234yf performed worse. At the highest saturation temperature tested (60°C), the heat transfer coefficients for both refrigerants were similar.

Perhaps the biggest difference in boiling performance between HFO-1234yf and HFC-134a is in their CHF values. Figure 6 plots the CHF ratio (defined as the HFO-1234yf CHF over the HFC-134a CHF) versus the saturation temperature. With regard to the baseline surface, HFO-1234yf CHF values can be 20%–40% lower than HFC-134a CHF values. Moreover, the CHF disparity between the two refrigerants increases with increasing temperature (i.e., increasing pressure). With the microporous coating, HFO-1234yf CHF values are about 20% lower than their HFC-134a counterparts. HFO-1234yf's lower CHF values are attributed, in part, to its lower latent heat and liquid/vapor density ratio as compared with HFC-134a.

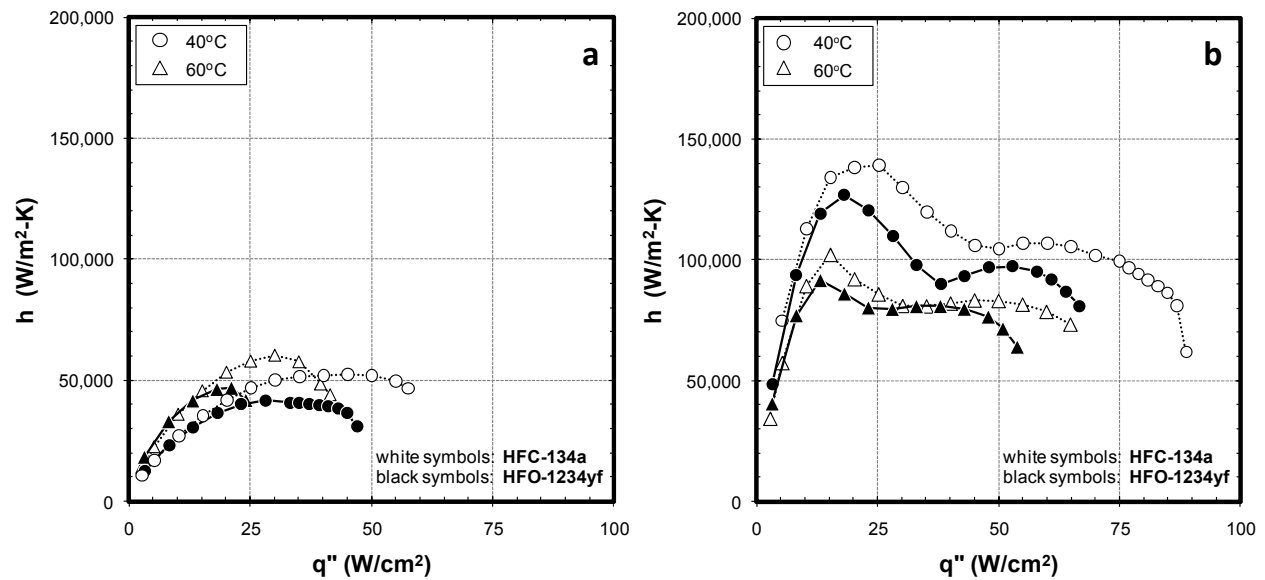


Figure 36. HFO-1234yf and HFC-134a heat transfer coefficients for a baseline surface (a) and a microporous coated surface (b)

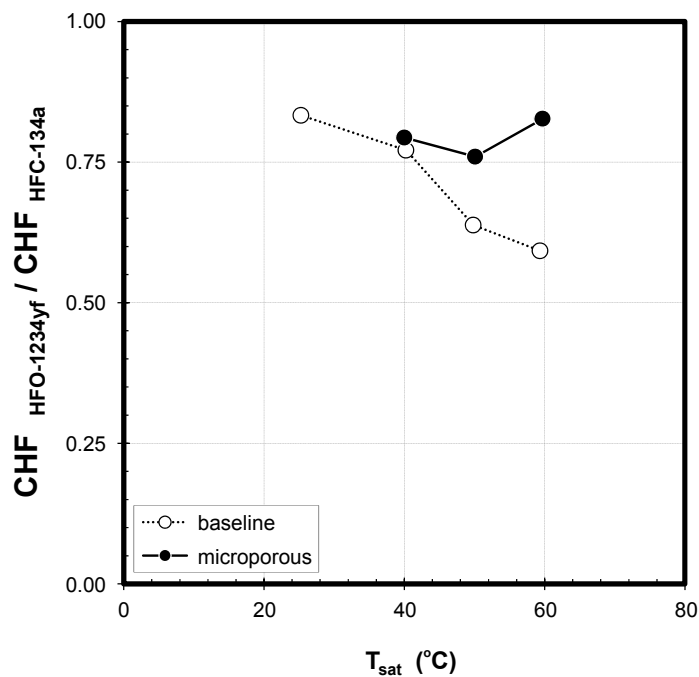


Figure 37. HFO-1234yf CHF over HFC-134a CHF ratio plotted versus the saturation temperature for the baseline and microporous surfaces

Immersion Cooling (Pool Boiling) of an Automotive Power Electronics Module

System-level experiments were conducted to demonstrate a two-phase cooling solution on an automotive power electronics module. The module chosen was a power electronics module taken from a 2008 Lexus LS 600H hybrid vehicle. The two-phase cooling solution implemented was a passive, immersion boiling (two-phase) scheme chosen for its inherent efficiency (pump-less) and simplicity. The thermal

performance of the two-phase cooling scheme was then compared to the thermal performance of the existing automotive cooling system which consisted of a single-phase, water-ethylene glycol heat exchanger.

Experimental Apparatus

A schematic of the immersion boiling vessel used for these experiments is shown in Fig. 7. The vessel has a 15.24 cm inner diameter and is fabricated from aluminum. Two borosilicate glass viewports are located on both sides of the vessel to allow for observation. The vessel operates at ambient pressures. It is open to ambient through a pipe that extends upward from the vessel through a concentric tube heat exchanger to an open vent. The heat exchanger serves as a condenser during experiments and degassing procedures.

The power electronics modules were mounted inside the vessel for the immersion boiling experiments. Dielectric HFE-7100 fluid was then introduced into the vessel. Sufficient fluid was added to the vessel to fully submerge the modules (Fig. 7). Cartridge heaters embedded within the vessel walls were used to raise the fluid temperature up to saturation conditions (i.e., $\sim 55^\circ\text{C}$ at 83 kPa). Once saturated conditions were achieved, the fluid was degassed by boiling the fluid for one hour. During the degassing process, non-condensable gasses (e.g., air) dissolved in the fluid were expelled from the system through the open condenser. HFE-7100 vapor generated during this process was condensed in the condenser/heat exchanger and returned to the vessel. Saturated and degassed conditions were verified through vapor and liquid temperature and vapor pressure measurements.

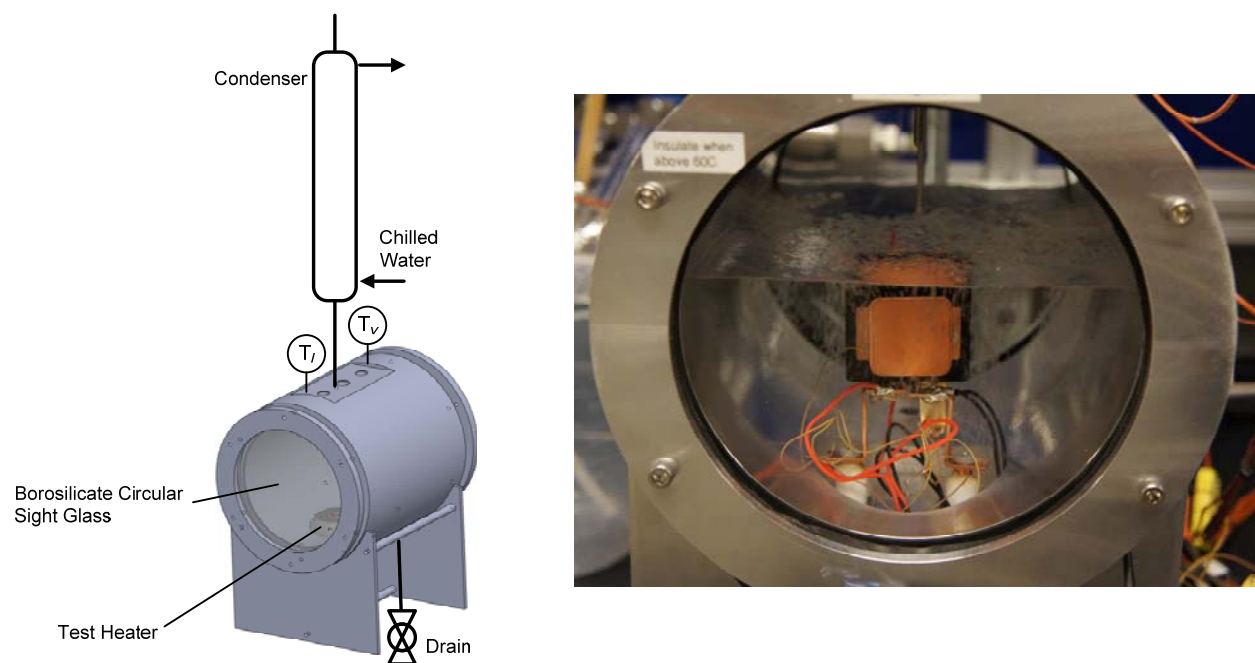


Figure 38. Schematic of the immersion boiling vessel (left) and a picture of the automotive power electronics module within the vessel and immersed in a HFE-7100 fluid bath (right)

The power electronics modules used for these experiments were taken from a 2008 Lexus hybrid vehicle. Each module consisted of an IGBT-diode pair and utilized a dual-side cooling approach (i.e., heat dissipating from both sides). Two modules were tested; a module with a microporous, boiling-enhancement coating applied on both sides and a baseline/non-coated module. The microporous coating used here was the same one shown in Fig 2. The intent was to demonstrate the advantages of immersion

boiling and to utilize boiling enhancement techniques (i.e., microporous coating) to increase thermal performance.

A Transient Thermal Tester (T3Ster) was used to power the modules for these tests. This was achieved by running a high current, at low voltage, through the IGBTs while gating the IGBTs with 10 VDC. Power levels up to 164 Watts (100 W/cm^2 at the IGBT level) were supplied until steady-state conditions were achieved. After temperature equilibrium was reached, the transient thermal tester shut off power and immediately sent a 100 mA current pulse through the IGBTs. IGBT junction temperatures were then inferred by measuring the resulting voltage drop (V_{ce}), which is correlated to the IGBT temperature through calibrations performed prior to testing. The transient thermal tester collects V_{ce} (i.e., temperature) measurements in one micro-second increments. The initial 100 μs seconds of data, following the power shut off, are discarded due to electrical transients. IGBT steady-state temperatures are then inferred by performing linear regression on a portion of the remaining data and extrapolating back to time = 0 (i.e., just before power shut down).

Results and Discussion

The thermal performance results for the modules cooled using immersion boiling (with and without the microporous coating) and the modules cooled using the conventional single-phase heat exchanger are provided in Fig. 8. This figure plots total thermal resistance (junction-to-liquid) versus the heat dissipated. Tests were conducted at power levels of 9 W, 27 W, 65 W, 110 W, and 164 W. Thermal performance data for the conventional automotive single-phase, liquid-cooling system was taken from a report by Sakai et al. [17].

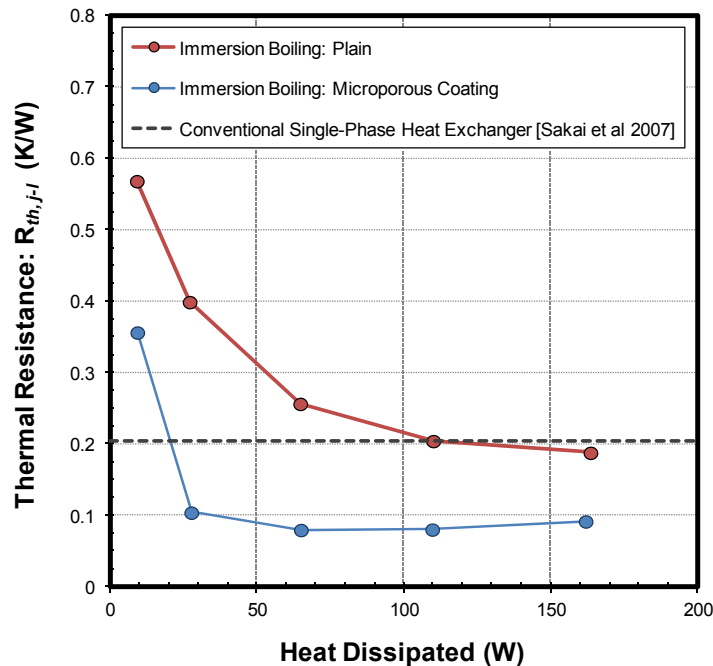


Figure 39. Thermal performance of an automotive power electronics module cooled through immersion boiling. Immersion boiling in conjunction with a microporous coating reduced the module thermal resistance by 60% as compared to the conventional automotive heat exchanger.

As shown in Fig. 8, immersion boiling with the microporous boiling enhancement coatings offers the best thermal performance. This two-phase solution produced thermal resistance values that were about 60% lower than those provided by existing automotive cooling system. This reduction in the thermal resistance

means that each device can dissipate more than twice as much heat resulting in decreased IGBT die count and/or size and potentially leading to cost savings. The superior thermal performance from two-phase cooling is a result of heat absorbed in the vaporization of the fluid as well as the turbulent/churning nature of the fluid as the vapor leaves the heated surface. These mechanisms are enhanced by the microporous coating that facilitates phase change, thus improving performance. In addition to offering better performance, the passive (pump-less) nature of immersion two-phase cooling also offers greater efficiency. The use of dielectric fluid also benefits thermal performance as it allows for direct cooling of the electrical devices, which decreases the package stack thermal resistance.

High-speed video images from these experiments are shown in Fig. 9. This figure shows a microporous coated module and a baseline/non-coated module both submerged in HFE-7100 and dissipating 28 W of heat. As shown in the images, the module with the coating is experiencing significant amount of boiling (phase-change) on its heated surfaces. The phase change provides this module with superior cooling performance. In contrast, the module without the coating is experiencing minimal boiling on its heated surfaces.

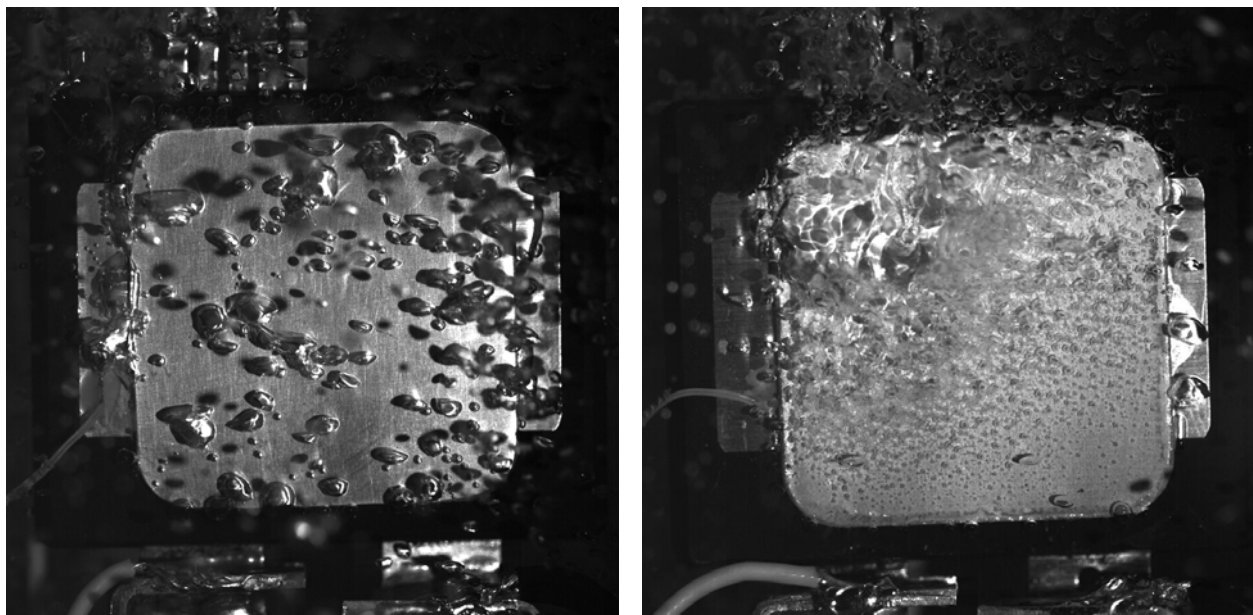


Figure 40. High-speed video images of a baseline/non-coated (left) and a microporous coated automotive power electronics modules (right) both dissipating 28 W and being cooled through boiling heat transfer

Two-Phase Thermosyphon for Power Electronics Cooling

A potential means to implement two-phase cooling for automotive power electronics is through a thermosyphon configuration. A thermosyphon utilizes vapor pressure and gravity to circulate vapor to the condenser and fluid back to the boiler/evaporator. This approach is both simple and efficient (pump-less). NREL has completed the design of several thermosyphon configurations that are currently under fabrication (Fig. 10). These initial thermosyphon designs utilize an indirect-cooling approach to cool the power electronics. The indirect-cooling approach means that the power electronics mount to either side or both sides of a two-phase-based cold plate. The electronics then transmit heat through the cold plate to the fluid within, where phase change occurs. This approach eliminates electrical feed-through penetrations into the refrigerant/coolant chamber and thus decreases the potential for leakage and contamination. A direct-cooling (i.e., electronics immersed in a fluid) thermosyphon approach may also be implemented in

the future. This effort is intended as system-level demonstration of a complete two-phase-based cooling system. Initial efforts will be focused on optimizing the cold-plate for performance.

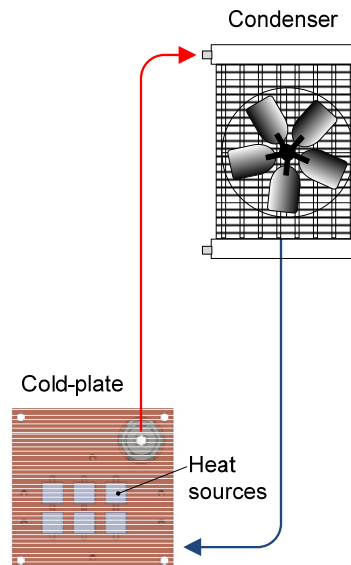


Figure 41. Two-phase thermosyphon concept

Boiling Enhancement Coating Reliability

To address reliability concerns, NREL has completed the design of an apparatus/system in which the long-term reliability of boiling enhancement coatings will be tested (Fig. 11). This apparatus is currently under fabrication. The apparatus was designed to simulate accelerated boiling heat transfer operation on multiple coated samples. Samples will be subjected to power/temperature cycling (i.e., on/off operation) for long durations. The effect of this cycling on coating delamination and long-term thermal performance will be evaluated.

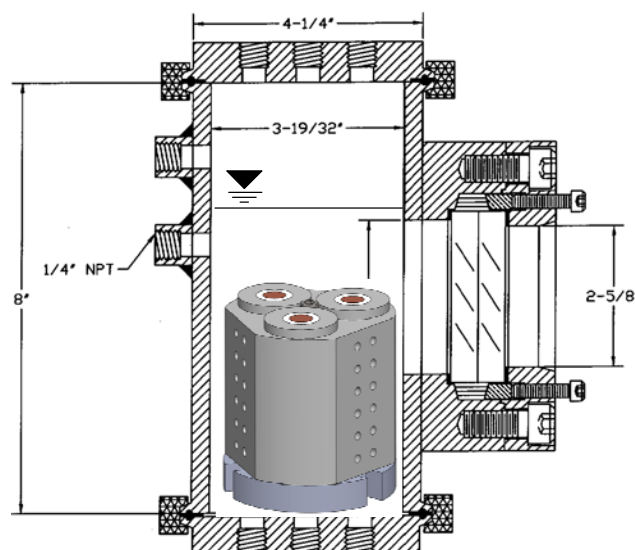


Figure 42. Apparatus designed to test the long-term reliability of multiple boiling enhancement coated samples

Conclusions

This project conducted fundamental and system-level experiments to evaluate two-phase heat transfer as a potential power electronics cooling solution. Fundamental experiments were carried out to characterize the pool boiling performance of a new refrigerant, HFO-1234yf. System-level efforts were focused on demonstrating the advantages of two-phase heat transfer for cooling automotive power electronics modules. Some of the major conclusions from this project are presented below.

- NREL was the first institution to fully-characterize and publish the pool boiling performance of HFO-1234yf [1]. Results show that the boiling heat transfer coefficients of HFO-1234yf and HFC-134a (R134a) are nearly identical at lower heat fluxes. HFO-1234yf yielded lower heat transfer coefficients at higher heat fluxes and lower CHF as compared with HFC-134a. A microporous coating was found to enhance boiling heat transfer coefficients by over 300% and CHF by as much as 120% for HFO-1234yf.
- NREL demonstrated a two-phase cooling solution for an automotive power electronics module. The two-phase cooling scheme provided superior cooling performance—decreasing thermal resistance by 60% as compared to the conventional automotive, single-phase (water-ethylene glycol) cooling system.
- Design of a thermosyphon system (cold-plate and condenser) intended as a system-level demonstration of a two-phase cooling solution was completed. Design of a system to test the long-term reliability of boiling enhancement coatings was also completed. Both systems are currently under fabrication.

Acknowledgments

The authors would like to acknowledge the support provided by Susan Rogers and Steven Boyd, technology development managers for Advanced Power Electronics and Electric Motors, Vehicle Technologies Program, U.S. Department of Energy Office of Energy Efficiency and Renewable Energy. The contributions of Sreekant Narumanchi, Charles King, and Kevin Bennion (NREL) to the project are acknowledged. The authors would also like to acknowledge Phil Tuma at 3M, Mary Koban at DuPont and Oak Ridge National Lab for contributing to this project.

Publications

1. Moreno, G., Narumanchi, S., and King, C. "Pool Boiling Heat Transfer Characteristics of HFO-1234yf with and without Microporous Enhanced Surfaces." *ASME 2011 International Mechanical Engineering Congress & Exposition Proceedings; Denver, Colorado*. 2011.
2. Moreno, G., Narumanchi, S., Thiagarajan, S. J., Bennion, K., and Venson, T. "Enhanced Surfaces to Improve Power Electronics." *MEPTEC: The Heat is On Proceedings; San Jose, California*. 2011.
3. Narumanchi, S., Moreno, G., Thiagarajan, S. J., Bennion, K., and Venson, T. "Enhanced Surfaces in Conjunction with Single and Two-Phase Flows for Power Electronics Cooling." *International Conference on Metallurgical Coatings and Thin Films Proceedings; San Diego, California*. 2011.
4. Tuma, P., Moreno, G., Narumanchi, S., Bennion, K., Brandenburg, S., Olszewski, M., and Burress, T. "Passive 2-Phase Immersion Cooling of Commercial and Developmental Insulated Gate Bipolar Transistor (IGBT) Modules." *IMAPs ATW on Thermal Management Proceedings; Palo Alto, California*. 2010.

References

1. Moreno, G., Narumanchi, S., and King, C. "Pool Boiling Heat Transfer Characteristics of HFO-1234yf with and without Microporous Enhanced Surfaces." *ASME 2011 International Mechanical Engineering Congress & Exposition Proceedings; Denver, Colorado*. 2011.
2. Moreno, G., Narumanchi, S., Thiagarajan, S. J., Bennion, K., and Venson, T. "Enhanced Surfaces to Improve Power Electronics." *MEPTEC: The Heat is On Proceedings; San Jose, California*. 2011.
3. Narumanchi, S., Moreno, G., Thiagarajan, S. J., Bennion, K., and Venson, T. "Enhanced Surfaces in Conjunction with Single and Two-Phase Flows for Power Electronics Cooling." *International Conference on Metallurgical Coatings and Thin Films Proceedings; San Diego, California*. 2011.
4. Tuma, P., Moreno, G., Narumanchi, S., Bennion, K., Brandenburg, S., Olszewski, M., and Burrell, T. "Passive 2-Phase Immersion Cooling of Commercial and Developmental Insulated Gate Bipolar Transistor (IGBT) Modules." *IMAPs ATW on Thermal Management Proceedings; Palo Alto, California*. 2010.
5. Barnes, C. M., and Tuma, P. E. "Practical Considerations Relating to Immersion Cooling of Power Electronics in Traction Systems." *IEEE Trans. on Power Electron.*, vol. 25(9), pp. 2478–2485, 2010.
6. Brown, G. M., Elbacher, B. J., and Koellner, W. G. "Increased Productivity with AC Drives for Mining Excavators and Haul Trucks." *IEEE Industry Applications Conference Proceedings*. Vol. 1, pp. 28–37, 2000.
7. Koellner, W. G., Brown, G. M., Rodriguez, J., Pontt, J., Cortes, P., and Miranda, H. "Recent Advances in Mining Haul Trucks." *IEEE Trans. on Ind. Elec.*, vol. 51(2), pp. 321–329, 2004.
8. Tantolin, C., Lallemand, M., and Eckes, U. "Experimental Study of Immersion Cooling for Power Components." *IEEE International Conference on Control Proceedings*. CONTROL'94, 1, pp. 723–727, 1994.
9. Ayers, C. W., Conklin, J. C., Hsu, J. S., and Lowe, K. T. "A Unique Approach to Power Electronics and Motor Cooling in a Hybrid Electric Vehicle Environment." *IEEE Vehicle Power and Propulsion Conference Proceedings*. pp. 102–106, 2007.
10. Leck, T. J., "Evaluation of HFO-1234yf as a Potential Replacement for R-134a in Refrigeration Applications." *3rd IIR Conference on Thermophysical Properties and Transfer Processes of Refrigerants Proceedings; Boulder, Colorado*. 2009.
11. "Dupont™ Opteon™ Yf Refrigerant for Mobile Air Conditioning." http://www2.dupont.com/Refrigerants/en_US/uses_apps/automotive_ac/SmartAutoAC/HFO-1234yf.html. Accessed October 2011.
12. Park, K.-J., and Jung, D. "Nucleate Boiling Heat Transfer Coefficients of R1234yf on Plain and Low Fin Surfaces." *Int. J. Refrigeration*; Vol. 33(3), 2010; pp. 553–557.
13. Del Col, D., Torresin, D., and Cavallini, A. "Heat Transfer and Pressure Drop During Condensation of the Low GWP Refrigerant R1234yf." *Int. J. Refrigeration*; Vol. 33(7), 2010; pp. 1307–1318.
14. Park, J. E., Vakili-Farahani, F., Consolini, L., and Thome, J. R. "Experimental Study on Condensation Heat Transfer in Vertical Minichannels for New Refrigerant R1234ze(E) Versus R134a and R236fa." *Exp. Thermal and Fluid Science*; Vol. 35(3), 2011; pp. 442–454.
15. Park, K.-J., Kang, D. G., and Jung, D. "Condensation Heat Transfer Coefficients of R1234yf on Plain, Low Fin, and Turbo-C Tubes." *Int. J. Refrigeration*; Vol. 34(1), 2011; pp. 317–321.

16. "3M™ Microporous Metallic Boiling Enhancement Coating (BEC) L-20227." 3M, 2009.
17. Sakai, Y., Ishiyama, H., and Kikuchi, T. "Power Control Unit for High Power Hybrid System." SAE International, 2007.

6. Small Business Innovative Research Grants

6.1 Small Business Innovative Research Projects

Steven Boyd

*Vehicle Technologies Program – DOE Office of Energy Efficiency and Renewable Energy
1000 Independence Ave. SW
Washington, DC 20585
Voice: 202-586-8967; Fax: 202-586-1600; E-mail: steven.boyd@ee.doe.gov*

DOE Technology Development Manager: Susan A. Rogers

Voice: 202-586-8997; Fax: 202-586-1600; E-mail: Susan.Rogers@ee.doe.gov

Objectives

- Use the resources available through the Small Business Innovation Research (SBIR) and Small Business Technology Transfer (STTR) programs to conduct research and development of technologies that can benefit the Advanced Power Electronics and Electric Motors (APEEM) effort within the Vehicle Technologies Program.
- Achieve the four SBIR objectives: (1) to stimulate technological innovation; (2) to increase private sector commercialization of innovations; (3) to use small business to meet federal research and development needs; and (4) to foster and encourage participation by minority and disadvantaged persons in technological innovation.

Approach

- The Small Business Innovation Research (SBIR) program was created in 1982 through the Small Business Innovation Development Act. Eleven federal departments participate in the SBIR program and five departments participate in the STTR program, awarding a total of \$2billion to small high-tech businesses.
- A 1982 study found that small businesses had 2.5 times as many innovations per employee as large businesses, while large businesses were nearly three times as likely to receive government assistance. As a result, the SBIR Program was established to provide funding to stimulate technological innovation in small businesses to meet federal agency research and development needs. After more than a decade, the STTR program was launched. The major difference is that STTR projects must involve substantial (at least 30%) cooperative research collaboration between the small business and a non-profit research institution.
- Small Business Innovation Research (SBIR) and Small Business Technology Transfer (STTR) are U.S. Government programs in which federal agencies with large research and development (R&D) budgets set aside a small fraction of their funding for competitions among small businesses only. Small businesses that win awards in these programs keep the rights to any technology developed and are encouraged to commercialize the technology.
- Each year, DOE issues a solicitation inviting small businesses to apply for SBIR/STTR Phase I grants. It contains technical topics in such research areas as energy production (Fossil, Nuclear, Renewable, and Fusion Energy), Energy Use (in buildings, vehicles, and industry), fundamental energy sciences (materials, life, environmental, and computational sciences, and nuclear and high energy physics), Environmental Management, and Nuclear Nonproliferation. Grant applications submitted by small businesses MUST respond to a specific topic and subtopic during an open solicitation.

- SBIR and STTR have three distinct phases. Phase I explores the feasibility of innovative concepts with awards up to \$100,000 for about 9 months. Only Phase I award winners may compete for Phase II, the principal R&D effort, with awards up to \$750,000 over a two-year period. There is also a Phase III, in which non-Federal capital is used by the small business to pursue commercial applications of the R&D. Also under Phase III, Federal agencies may award non-SBIR/STTR-funded, follow-on grants or contracts for products or processes that meet the mission needs of those agencies, or for further R&D.

Phase II Topics for 2010

Under the SBIR/STTR process, companies with Phase I awards from FY 2010 are eligible to apply for a Phase II award in FY 2010. The FY 2010 Phase I subtopics were:

- a. High-Performance DC Bus Capacitors for Power Inverters in Electric Drive Vehicles*
- b. Alternative Production Techniques for Homogenous Magnet Alloys*
- c. High Temperature Packaging*
- d. Non Obtrusive Semiconductor Die Temperature Measurements*

Phase II Awards Made in 2010

Four Phase I awards were made in FY 2010 as Phase I projects, and resulted in the following Phase II award for FY 2011.

A Low Cost Continuous Process to Produce Magnet Alloys

Materials and Electrochemical Research (MER) Corporation

7960 S. Kolb Road, Tucson, AZ 85756

Principal Investigator: Dr. James C. Withers, jcwithers@mercorp.com

Statement of the Problem: The current processes to produce Nd-Fe-B alloy powders for producing high magnetic strength permanent magnets for application in electric traction motors for use in electric vehicles requires a significant number of steps resulting in high cost as well as 96.8% supply of Nd-Fe-B which is controlled predominately by China. To meet the cost goals for traction motors to expand the availability of electric vehicles, substantial reductions in cost to produce the Nd-Fe-B alloy powders must be achieved as well as providing a U.S. base of supply.

Technical Approach: Neodymium oxide (Nd₂O₃), the DOE specified starting material, is transformed to anhydrous neodymium chloride (NdCl₃) by demonstrated low cost processing which is the feed along with iron chloride (FeCl₂) and boron trichloride (BCl₃) to an electrolytic fused salt cell that directly produces the ideal alloy Nd₂Fe₁₄B fine powder at a fraction of the state-of-the-art process cost. The Nd₂Fe₁₄B is vacuum separated from the salt that is recycled to the electrolytic cell and the Nd₂Fe₁₄B powder is sintered to form a magnet without exposure to air producing a high quality magnet at low cost.

What was done in Phase I: The phase I demonstrated Nd₂O₃ could be transformed to anhydrous NdCl₃ using a carbothermic reduction/chlorination demonstrated process. The anhydrous NdCl₃ was co-fed with FeCl₂ and BCl₃ to an electrolytic fused salt cell that electrolytically directly deposited the ideal alloy Nd₂Fe₁₄B as a very fine powder in the desirably nano size range that translates to magnets with higher energy density. The simplified flow chart that directly produces the Nd₂Fe₁₄B alloy predicts a cost significantly less than the current price of material.

What is planned for Phase II: Technical feasibility has been demonstrated in Phase I. Phase II proposes to scale-up processing utilizing neodymium oxide or lower cost carbonate to produce anhydrous NdCl_3 which will be co-fed with FeCl_2 and BCl_3 in a scaled-up electrolytic cell to define reproducibility of producing very fine/nano particle $\text{Nd}_2\text{Fe}_{14}\text{B}$ powder that is vacuum separated from the salt which is recycled back to the electrolytic cell in a benign environmental cycle. The separated $\text{Nd}_2\text{Fe}_{14}\text{B}$ alloy powder will be sintered into low cost magnets without exposure to the atmosphere. This project establishes a U.S. source to produce $\text{Nd}_2\text{Fe}_{14}\text{B}$ alloy powder and high quality magnets.

Commercial Applications and Other Benefits: Substantially reducing the cost and energy in an environmentally friendly process to produce low cost $\text{Nd}_2\text{Fe}_{14}\text{B}$ alloy powder provides the material to produce high quality permanent magnets at low cost that translates to producing more electric vehicles. The greater use of electric vehicles reduces pollution, reduces the need for oil/petroleum and the attendant advantages of reduced importing of oil. A greater use of electric vehicles emanating from low cost permanent magnets is a benefit to the entire Nation. The low cost $\text{Nd}_2\text{Fe}_{14}\text{B}$ is also applicable for magnets for wind generation of electricity as well as defense applications. This program establishes a U.S. source for $\text{Nd}_2\text{Fe}_{14}\text{B}$ that overcomes the Chinese monopoly of 96.8% of the supply.

This document highlights work sponsored by agencies of the U.S. Government. Neither the U.S. Government nor any agency thereof, nor any of their employees, makes any warranty, express or implied, or assumes any legal liability or responsibility for the accuracy, completeness, or usefulness of any information, apparatus, product, or process disclosed, or represents that its use would not infringe privately owned rights. Reference herein to any specific commercial product, process, or service by trade name, trademark, manufacturer, or otherwise does not necessarily constitute or imply its endorsement, recommendation, or favoring by the U.S. Government or any agency thereof. The views and opinions of authors expressed herein do not necessarily state or reflect those of the U.S. Government or any agency thereof.



U.S. DEPARTMENT OF
ENERGY | Energy Efficiency &
Renewable Energy

For more information
eere.energy.gov

DOE/EE-0676 January 2012
Printed with a renewable-source ink on paper containing
at least 50% wastepaper, including 10% post consumer waste.